Thermochemical Processes

Principles and Models

DropBooks

Thermochemical Processes

Principles and Models

C.B. Alcock DSc, FRSC

BUTTERWORTH HEINEMANN

OXFORD AUCKLAND BOSTON JOHANNESBURG MELBOURNE NEW DELHI

Butterworth-Heinemann
Linacre House, Jordan Hill, Oxford OX2 8DP
225 Wildwood Avenue, Woburn, MA 01801-2041
A division of Reed Educational and Professional Publishing Ltd

A member of the Reed Elsevier plc group

First published 2001

© C.B. Alcock 2001

All rights reserved. No part of this publication
may be reproduced in any material form (including
photocopying or storing in any medium by electronic
means and whether or not transiently or incidentally
to some other use of this publication) without the
written permission of the copyright holder except
in accordance with the provisions of the Copyright,
Designs and Patents Act 1988 or under the terms of a
licence issued by the Copyright Licensing Agency Ltd,
90 Tottenham Court Road, London, England W1P 9HE.
Applications for the copyright holder's written permission
to reproduce any part of this publication should be addressed
to the publishers

British Library Cataloguing in Publication Data
Alcock, C. B.
Thermochemical processes:principles and models
1 Thermodynamics 2 Chemical processes 3 Materials at high temperatures
I Title
660.2′969

Library of Congress Cataloguing in Publication Data
Alcock, C. B.
Thermochemical processes:principles and models/C.B. Alcock.
p. cm.
Includes bibliographical references.
ISBN 0 7506 5155 5
1 Thermodynamics 2 Chemical processes 3 Materials at high temperatures
I Title
TP155.2.T45 T47 2000
660′.2969–dc21 00-049367

ISBN 0 7506 5155 5

Typeset by Laser Words, Chennai, India
Printed in Great Britain

PLANT A TREE
BTCV British Trust for Conservation Volunteers
FOR EVERY TITLE THAT WE PUBLISH, BUTTERWORTH-HEINEMANN WILL PAY FOR BTCV TO PLANT AND CARE FOR A TREE.

DropBooks

Contents

Preface xi

Part 1: Processes with gaseous reaction control 1

1 Vapour deposition processes 3
Vapour deposition for the preparation of thin films 3
Vapour pressure data for the elements 4
The kinetic theory of a gas in a container 4
Molecular effusion 6
Vapour deposition of elements 6
The deposition rate on a cool substrate 8
Vapour deposition of alloys 8
Vapour deposition of compounds 10
Free evaporation coefficients of solids 11
Other techniques for the preparation of thin films 16
Single and epitaxial films in semiconducting systems 16
Thin film production by the sputtering of metals 17
The production of nanoparticles 20
Coating with thin diamond films 22
Plasma evaporation and pyrolysis of carbon to form Fullerenes 23
Materials science and the formation of thin films 24
The formation of nuclei from the vapour phase 24
The formation of a film from nuclei 28
Grain growth in the initial deposit 30
Point defects in solids 31
Edge and screw dislocations 33
Interfacial energies in solid systems 35
Bibliography 38
Appendix: Vapour pressure data for the elements 38

2 Gaseous reaction kinetics and molecular decomposition 42
Theories of reaction kinetics 42
Thermal energies and the structures of molecules 43
The collision theory of gaseous reactions 45
Transition state theory of gaseous reactions 47
Empirical estimates of the activation energy 49
The order of chemical reactions 50

Time dependence of the extent of reaction 52
Chain reactions 52
Combustion chain reactions 53
Chain reactions in the combustion of gaseous fuels 56
Fuel/air mixing in combustion systems 58
The thermal efficiencies of combustion engines 59
Bibliography 62
Molecular dissociation and chain reactions in chemical vapour deposition 62
Thermochemical data for the dissociation of gaseous molecules 63
Bond character in gaseous heteronuclear compounds 64
Hybridization of covalent bonds 66
Bond energies of gaseous polyvalent metal halides 67
Thermal decomposition of hydrides and organometallic compounds 68
Bibliography 71
Radiation and electron decomposition of molecules 72
Photochemical reactions 73
Dissociation cross-sections 75
Substrate heating by transmitted radiation 77
Radiation and convection cooling of the substrate 82
Laser production of thin films 82
Molecular decomposition in plasma systems 84
Bibliography 85

3 Vapour phase transport processes 86
Vapour transport processes 86
Thermodynamics and the optimization of vapour phase transport 86
The direction of vapour transport across a thermal gradient 89
The choice of halogen in transport reactions 91
The vapour phase refining and separation of metals 91
The thermodynamics of the vapour phase transport of compounds 93
Multicomponent thermodynamics in gaseous systems 95
Sintering by vapour phase transport 99
Grain growth by vapour phase transport 100
Vapour transport in flowing systems 102
Transport along a thermal gradient 102
Mass transport across a flowing gas 103
Material deposition from a flowing gas 106
Transport and thermal properties of gases 108
Equations of state for ideal and real gases 112
Molecular interactions and the properties of real gases 114
Bibliography 117

4 Heterogeneous gas–solid surface reactions 118
The zeroth order reaction 118
Adsorption of gases on solids 119
Surface structures of catalytic materials 124
Adsorption and the surface energies of metals 125

DropBooks

Bond mechanisms of adsorbed molecules 126
Supported metal catalysts 128
Examples of industrially important catalysts 129
Thermodynamics of the water–gas shift and steam reforming reactions 129
Kinetic factors in steam reforming 132
The Fischer–Tropsch production of organic molecules 134
The production of ammonia from its elements 136
The catalytic converter for automobile exhaust 138
Catalysis by metal oxides 140
Coupling reactions of methane 142
Reactors for catalytic processes 143
Bibliography 145

Part 2: Rate processes in the solid state 147

5 Electrical charge and heat transport in solids 149
The transport of electrons and positive holes 149
Metals and alloys 149
Electromigration in alloys 153
Elemental and compound semiconductors 154
Metal oxides 158
Thermal transport in condensed phases 163
Heat capacities 164
Thermal conductivity 166
Bibliography 169

6 Rate processes in metals and alloys 170
Structure and diffusion-controlled processes in metallic systems 170
The structures of metals 170
Volume diffusion in pure metals 170
Diffusion in inter-metallic compounds 176
Diffusion in alloys 177
Steady state creep in metals 180
Diffusion in interstitial solutions and compounds 181
Phase transformations in alloys 184
The decomposition of Austenite 184
Transformations in substitutional alloys 188
Order–disorder transformation 189
The age-hardening of copper–aluminium alloys 190
Spinodal decomposition of binary alloys 190
Metals and alloys in nuclear power reactors 194
Bibliography 195
Grain boundary and surface-driven properties in metallic systems 195
The measurement of the surface energies of metals 196
Diffusion in grain boundaries and dislocations 197
Surface diffusion on metals 199

Powder metallurgy 201
The production of metal powders 201
The sintering of solid metal particles 204
Hot pressing 207
Ostwald ripening 209
Grain growth in polycrystalline metals 213
Processing of powders to form metallic articles 214
Self-propagating combustion reactions 216
Inter-diffusion and interaction in thin film microelectronic structures 219
Bibliography 221

7 Rate processes in non-metallic systems 223
Diffusion in elemental semiconductors 223
Structures and diffusion in metal oxides 224
The measurement of diffusion coefficients in simple oxides 229
Surfaces and surface energies in ionic crystals 232
Sintering of metal oxides 233
The production and applications of ceramic oxide materials 234
Electroceramic oxides 236
Dielectric or ferroelectric oxides 236
Magnetic oxides 237
Solid electrolyte sensors and oxygen pumps 239
Solid oxide fuel cells and membranes 244
Ceramic superconductors 247
The redistribution of fission products in UO_2 nuclear fuels 249
Bibliography 250

8 Gas–solid reactions 251
The oxidation of metals and compounds 251
The parabolic rate law 251
The linear and logarithmic rate laws 252
Oxidation of metals forming more than one oxide 253
The oxidation of nickel: volume and grain boundary diffusion 254
The oxidation of silicon 255
Complex oxide formation in the oxidation of alloys 256
Internal oxidation of alloys 257
The theory of the parabolic oxidation law 260
The carburizing and oxidation of transition metals 262
The oxidation of metallic carbides and silicides 266
The oxidation of silicon carbide and nitride 268
Bibliography 269

9 Laboratory studies of some important industrial reactions 270
The reduction of haematite by hydrogen 270
Erosion reactions of carbon by gases 271
The combustion of coal 273
The oxidation of FeS – parabolic to linear rate law transition 274
Oxidation of complex sulphide ores – competitive oxidation of cations 275

DropBooks

The kinetics of sulphation roasting 276
Heat transfer in gas–solid reactions 277
Industrial reactors for iron ore reduction to solid iron 279
The industrial roasting of sulphides 281
The corrosion of metals in multicomponent gases 283
Bibliography 285
Appendix: Thermodynamic data for the Gibbs energy of formation of metal oxides 285

Part 3: Processes involving liquids 289

10 Physical properties and applications of liquid metals 291
The structures and mechanism of diffusion of liquid metals 291
Thermophysical properties of liquid metals 294
Viscosities of liquid metals 294
Surface energies of liquid metals 295
Thermal conductivity and heat capacity 296
The production of metallic glasses 297
Liquid metals in energy conversion 300
Liquid phase sintering of refractory materials 301
Bibliography 304
The production of crystalline semiconductors 304
Zone refining of semiconducting elements 304

11 Physical and chemical properties of glassy and liquid silicates 307
Metal solubilities in silicate glasses 310
The production of silicate glasses and glass-containing materials 310
The production of porcelains 311
Ceramic electrical insulators 313
The production of glass-ceramics 313
Cements 314
Optical fibres 315
Chalcogenide glasses 315
Bibliography 316

12 The structures and thermophysical properties of molten salts 317
Hot corrosion of metals by molten salts 319
Molten carbonate fuel cells 321
Bibliography 322

13 Extraction metallurgy 323
The principles of metal extraction 324
Metal–slag transfer of impurities 324
The electron balance in slag–metal transfer 327
Bubble formation during metal extraction processes 328
The corrosion of refractories by liquid metals and slags 329
Extractive processes 330
The production of lead and zinc 330
Co-production of lead and zinc in a shaft furnace 332

The ironmaking blast furnace 333
The reduction of stable oxides in carbon arc furnaces 335
Steelmaking and copper production in pneumatic vessels 337
Steel 337
Copper 339
The reduction of oxides and halides by reactive metals 341
Magnesium 341
Chromium 342
Manganese 343
Heat losses in crucible reactions 344
Zirconium 345
Uranium 346
The electrolysis of molten salts 347
Magnesium 347
Sodium 347
Aluminium 348
Refractory metals 349
Bibliography 349

14 The refining of metals 351
The effect of slag composition on impurity transfer 351
The thermodynamics of dilute solutions 354
The refining of lead and zinc 356
The separation of zinc and cadmium by distillation 357
De-oxidation of steels 360
Vacuum refining of steel 361
Refining by liquid salts and the Electroslag process 363

15 Factorial analysis of metal-producing reactions 365
Bibliography 369

Index 371

DropBooks

Preface

This book is intended to be a companion to Kubaschewski's *Metallurgical Thermochemistry*, and as such deals primarily with the kinetic and transport theory of high temperature chemical reactions. I have chosen the title *Thermochemical Processes* rather than *High Temperature Materials Chemistry* since many of the important industrial processes which are described hardly deserve the high temperature connotation, and such a title would have implied a larger structural and thermodynamic content than is required for the description of the industrial processing of materials. It will be seen that the book has a significant content from the chemical engineer's approach, and I feel that this rapprochement with the materials scientist is overdue.

The origins of the material contained in this book are to be found in the rapid growth of the scientific description of extractive metallurgical processes which began after World War II. This field was dominated by thermodynamics originally, and the development of kinetic and transport descriptions of these processes followed later. At that time the study of glasses and ceramics was largely confined to phase diagrams of the multicomponent systems, and processes in which gaseous reaction kinetics were rate-controlling were of more interest to the chemist than to the materials scientist, a field which, practically, did not exist in that era.

The quantitative description of materials processing has now advanced to the state where most of the processes which are in industrial use can be described within a logical physico-chemical framework. The pace of development in this field has largely been determined by the rate of improvement of our experimental capabilities in high temperature chemistry; the *ab initio* theoretical contribution to the building of our present knowledge is growing rapidly under the influence of computer capabilities which simplify the fundamental basis for *a priori* calculation. However, the processes and substances with which the materials scientist works are usually complex, and the precision of the information which is required to describe a process accurately is still too high to be calculated theoretically. The practical situation can now be assessed from the substantial results of experimental studies which cover almost every situation to be found on the present industrial scene.

The role of the physico-chemical study of materials processing has been consigned to a secondary position of interest by those engaged directly in

manufacturing processes. This has probably come about for two reasons. The first and most obvious reason is that economic factors more than physical chemistry play the important part in industrial decision-making. Those who direct the production aspects of industry seldom have equally developed skill in the physico-chemical aspects as well as in economics. As a result, the decision-making tends to be under financial direction, and the decision-makers draw their scientific advice from research in a digested form. The second reason is that high temperature chemists have been fully occupied up till now in the business of understanding the processes already in use and their contributions to industrial progress seem always to be *post hoc*. At present, it is true to say that their efforts have been more of value in teaching the student laboratory workers than in predicting potentially new processes. To some extent, this state of affairs has been brought about by empirical industrial progress which has built up a formidable amount of knowledge over decades by the use of works trials. These aspects of industrial development together with the financial constraints of process innovation probably account for the fact that the physical chemist has had no really outstanding impact on the materials industry to date, apart from providing experimental tools for the appraisal of new processes, and the 'tools of thought' which can be transferred from the analysis of an established process to prognosis when new methods are being sought.

The treatment in this book is intended for those who have already received the basic courses in classical thermodynamics which nearly all students of materials science and chemical engineering must assimilate nowadays before passing on to courses in materials processing. For the interested graduate, a brief refresher in any of the standard textbooks of physical chemistry is recommended if he/she is not comfortable in thermodynamic analysis. References are given at the end of each section to other works and original literature sources which are normally available to the student of materials science. Rather than present the reader with a plethora of original references, I have collected a number of review articles, and monographs which have seemed to me to be valuable oversights in this subject. A parallel study of these reference materials will augment the value of this book very considerably, but it is hoped that the main ideas which are germane to the analysis of processes are to be found here.

In conclusion, any author who has had the experience of seeing a subject grow from its early beginnings should acknowledge his debt to the leading men in the field who have taught him how to reach a level of competence and 'feel' for the subject. Among the many colleagues who have played this role for me, I would place F.D. Richardson and O. Kubaschewski as the prime movers during the years I spent in the Nuffield Research Group, and others, such as H.J.T. Ellingham, L.S. Darken, and of course, C. Wagner, with whom I 'sat at the master's feet'. To all of those who remember having worked

DropBooks

with me over the last fifty years, I would extend my thanks for friendship coupled with instruction. Finally I must acknowledge the ever-present support and encouragement which I have received from my wife who has never failed to help me in high times and low with her insight into what forms scientists outside of their working persona.

Part 1

Processes with Gaseous Reaction Control

Introduction

This first part is concerned with processes in which the kinetic behaviour of a gaseous phase is rate-determining. The range of processes includes some which are carried out in vacuum systems in which Knudsen or free evaporation occurs from a condensed phase, to transport reactions where a chemical reaction occurs between a solid and the gaseous phase to produce molecular species containing some or all of the elements occurring in the solid phase. In this latter case, the examples are drawn from those systems in which the mechanism of transport of these molecules through the gaseous phase is rate-determining.

The rates of these reactions both in the gas phase and on the condensed phase are usually increased as the temperature of the process is increased, but a substantially greater effect on the rate can often be achieved when the reactants are adsorbed on the surface of a solid, or if intense beams of radiation of suitable wavelength and particles, such as electrons and gaseous ions with sufficient kinetic energies, can be used to bring about molecular decomposition. It follows that the development of lasers and plasmas has considerably increased the scope and utility of these thermochemical processes. These topics will be considered in the later chapters.

DropBooks

As with all of the processes described, these are first studied in detail in the laboratory with an industrial application as the objective. Those processes which pass the criterion of economic potential are used in a pilot plant study, and then, if successful, at the production level which must be optimized. The materials which are produced are mainly, in the present instance, for application in the electronics industry where relatively high costs are acceptable. It will be seen that the simple kinetic theory of gases is adequate to account for the rates of these processes, and to indicate the ways in which production may be optimized on the industrial scale.

Chapter 1

Vapour deposition processes

Vapour deposition for the preparation of thin films

Thin films of metals, alloys and compounds of a few micrometres thickness, which play an important part in microelectronics, can be prepared by the condensation of atomic species on an inert substrate from a gaseous phase. The source of the atoms is, in the simplest circumstances, a sample of the collision-free evaporated beam originating from an elementary substance, or a number of elementary substances, which is formed in vacuum. The condensing surface is selected and held at a pre-determined temperature, so as to affect the crystallographic form of the condensate. If this surface is at room temperature, a polycrystalline film is usually formed. As the temperature of the surface is increased the deposit crystal size increases, and can be made practically monocrystalline at elevated temperatures. The degree of crystallinity which has been achieved can be determined by electron diffraction, while other properties such as surface morphology and dislocation structure can be established by electron microscopy.

As the condensed film increases in thickness, the properties of the condensate are no longer determined solely by the original surface, now a substrate to the film. However, the interface between the substrate and the growing film does have a large effect on the subsequent ability of the film to grow into a single crystal. If the lattice parameters of the film and the substrate are similar, i.e. within 15% of each other, and of the same crystal type, a single crystal thin film is readily prepared under these conditions of *epitaxial growth*. If there is a significant disparity in either condition for epitaxy, the thin film may not adhere to the substrate. In the extreme case where the substrate is amorphous, as for example a glass substrate, the deposited film might develop a single crystal structure in the right temperature regime but lack adhesion to the substrate. The encouragement of monocrystalline growth by heating the substrate also increases the probability of the re-evaporation of the atoms comprising the thin film, and hence there is this practical limit on the choice of the substrate temperature during film formation.

The individual processes which take part in thin film production are thus:

1. The vaporization of elements.
2. Formation of nuclei of the condensing substance on a support.

3. Growth of nuclei by surface diffusion of atoms to form a continuous layer.
4. Establishment of the film morphology as determined by the film/substrate physical relationships.
5. Further growth of the film to a useful thickness.

Vapour pressure data for the elements

The design of vapour deposition processes requires an accurate knowledge of the vapour pressures of the chemical elements. A considerable body of experimental data for the vapour pressures of the elements is now available as a result of the adaptation of classical methods of vapour pressure measurement to high temperatures, and by the relatively recent development of techniques requiring the establishment of high vacuum, such as mass spectrometry. The data can be represented in a simple form by a two-term equation, which is usually accurate to within 10% over a wide range of temperature, but sometimes a more accurate three-term equation is necessary. These two forms are sufficient for the present needs. These equations are related to the thermodynamics of vaporization, particularly to the Gibbs energy of vaporization, ΔG_e°.

$$\Delta G_e^\circ(\text{solid} \longrightarrow \text{gas}) = \Delta H_e^\circ - T\Delta S_e^\circ$$

$$\Delta G_e^\circ \cong A - BT = A' - B'T + CT\log T = -RT\ln p^\circ$$

where p° is the vapour pressure of the pure element at the temperature T, ΔH_e and ΔS_e are the standard heat and entropy of vaporization. (See Appendix for current data for many elements.)

DropBooks

It will be seen throughout this discussion of thermochemical processes that these require a knowledge of both thermodynamic and kinetic data for their analysis, and while kinetic theory obviously determines the *rate* at which any process may be carried out, the thermodynamic properties determine the *extent* to which the process can occur.

The simplest system in which useful products are obtained by thermochemical processing involves the evaporation of an element or elements in vacuum in order to produce thin films on a selected substrate. This process is usually limited to the production of thin films because of the low rates of evaporation of the elements into a vacuum under conditions which can be controlled. These rates can be calculated by the application of the kinetic theory of ideal gases.

The kinetic theory of a gas in a container

A cornerstone of the analysis of vaporization processes in a vacuum is the classical theory of gases. In this theory, a gas is assumed to consist of non-interacting molecules which undergo elastic collisions with one another and

the containing walls. Between collisions the molecules move in field-free space an average distance denoted the *mean free path*. The average velocity of the molecules is determined by their mass and the temperature of the system. The motion of the molecules is chaotic and the distribution of the molecules within the container is uniform in three dimensions. The fraction dn of a gas containing n molecules with velocity between c and $c + \mathrm{d}c$ is given by the Maxwell–Boltzmann equation

$$\frac{\mathrm{d}n}{n} = \frac{4}{\sqrt{\pi}\alpha^3} \exp - \left(\frac{c^2}{\alpha^2}\right) c^2 \, \mathrm{d}c$$

where $\alpha^2 = 2\overline{c}^2/3$.

The mean square velocity is defined by

$$\overline{c}^2 = \frac{\int_0^\infty c^2 \, \mathrm{d}n}{n} = \frac{3kT}{m}$$

where m is the mass of one molecule. This last equation leads to the law of *equipartition of energy*, which states in its simplest form that the average contribution to the kinetic energy of a monatomic species in a gas is $3/2kT$, where k is Boltzmann's constant, and hence in one gram-atom the kinetic energy is $3/2NkT$, or $3/2RT$, where N is Avogadro's number, and R is the gas constant.

The relationships which can be derived from this distribution which will be applied here are as follows:

1. The number of molecules of mass m impinging on 1 cm^2 of the container in unit time, n', is given by:

$$n' = (1/4)n\overline{c}$$

where n is the number of molecules per cm^3, and $\overline{c}$ is the average velocity.

2. The pressure, p, exerted on the walls of the container is the force acting on each cm^2 due to the motion of the molecules

$$p = (1/3)nm\overline{c}^2 \times 10^{-5} \text{ atmos}$$

(Note: 1 atmosphere $\cong 10^6$ dynes cm^{-2} $= 1.013 \times 10^5$ Pa.)

3. The value of the mean square velocity, $\overline{c}^2$, is given by

$$\overline{c}^2 = 3p/\rho = 3p/nm \times 10^{-2} \text{ (cm s}^{-1})^2$$

where ρ is the density of the gas in particles/cm^3.

The relationship between the average velocity $\overline{c}$ and $\overline{c}^2$ is

$$(1/3)\overline{c}^2 = (\pi/8)(\overline{c})^2$$

$$\overline{c} = (8p/\pi\rho)^{1/2} = (8RT/\pi M)^{1/2}$$

($R = 8.314 \times 10^7$ ergs K^{-1} $\mathrm{mol}^{-1} = 8.314\,\mathrm{J\,K^{-1}\,mol^{-1}}$) and therefore

$$n' = (1/4)n\overline{c} = 3.64 \times 10^3 n(T/M)^{1/2}$$

where T is the absolute temperature and M is the molecular weight of the gas. The mass of gas impinging on 1 cm^2 of the container per second, G, is therefore

$$G = (p\rho/2\pi)^{1/2} = 44.33\,p(M/T)^{1/2}\ \mathrm{g\,s^{-1}}$$

where p is the pressure in atmospheres.

The mean free path, which is the average distance a molecule travels between collisions, is

$$\lambda = 1/\sqrt{2}\pi n d^2$$

which varies as the inverse of the pressure. The molecular diameter is d, which has a typical value of 0.2 to 1.0 nm.

Molecular effusion

DropBooks

According to Knudsen if a small circular orifice of diameter less than the mean free path of the molecules in a container, is opened in the wall of the container to make a connection to a high vacuum surrounding the container, the mass of gas effusing through the orifice, of area A, is given by an equation derived from the kinetic theory, where the pressure is in atmospheres.

$$G(A) = 44.33\,pA(M/T)^{1/2}\ \mathrm{g\,s^{-1}}$$

If the external pressure is increased to p_e the mass effusing is

$$G'(A) = 44.43(p - p_e)A(M/T)^{1/2} \times 10^{-4}\ \mathrm{g\,s^{-1}}$$

If a monatomic gas escapes from a Knudsen cell into an atmosphere in which the mean free path is λ_e, the fraction of the atoms, I, which traverse a distance L without collision is given by

$$I = I_0 \exp -(L/\lambda_e)$$

Vapour deposition of elements

Thin films of metal can be prepared by vacuum evaporation and condensation on a suitable support. For example, thin films of silver can be formed on a

sodium chloride single crystal support. If this crystal is held at room temperature, the condensate is a polycrystalline film, but if the sodium chloride crystal is heated to around 600 K during deposition, the deposit is a single crystal. This shows that the crystalline state of a deposit depends on the mobility of the atoms forming the epitaxial deposit on the surface, as well as the crystallographic deposit/substrate relationship. An ideal source of atomic vapour is the Knudsen cell, which has the advantage that the atomic beam is concentrated in the forward direction according to Lambert's law,

$$I(\theta) = I_0 \cos\theta$$

where I_0 is the total flux leaving the cell, and θ is the angle between the normal to the surface carrying the orifice, such as a crucible lid, and the direction of propagation of the chosen segment of the beam. For a substrate of radius r which receives the effusate I at a distance L from the source I_0 where $r \ll L$, the total effusate received is given by

$$I = \int_0^{\theta} I_0 \cos\theta = [I_0 \sin\theta]_0^{\theta} \cong I_0\, r/L$$

By contrast, in *free* evaporation from an open sample of the element, the condensate is widely distributed about the target area.

Another aspect of the use of a Knudsen source is that complex deposits, containing more than one element, can be prepared by the use of several cells, one for each element. The temperature of each cell is independently adjusted to provide the appropriate *flux* in the proportions required in the final deposit. The flux, J, is the number of atoms arriving at the condensate in unit time over unit area, which is equal to the mass arriving divided by the molecular weight of the species and multiplied by Avogadro's number 6.022×10^{23}. The ratio of the fluxes of two species impinging on a surface is therefore given by

$$J_A/J_B = (p_A^{\circ}/p_B^{\circ})\,(M_B/M_A)^{1/2}$$

when the two sources are at the same temperature.

The condition for Knudsen effusion that the mean free path of the effusate should be less than the diameter of the circular orifice, limits the usable vapour pressure of the material in the Knudsen cell to about 10 Pa, since the orifice diameter would have to be less than 1 mm at a higher pressure.

Some elements, such as the rare earths and the refractory metals, have a high affinity for oxygen, so vaporization of these elements in a 'normal' vacuum of about 10^{-4} Pa, would lead to the formation of at least a surface layer of oxide on a deposited film. The evaporation of these elements therefore requires the use of ultra-high vacuum techniques, which can produce a pressure of 10^{-9} Pa.

The deposition rate on a cool substrate

The flux of atoms emerging from a Knudsen cell at 1000 K in which an element of vapour pressure 10^{-4} atmospheres and atomic weight 100 g is contained in a cell of orifice diameter 1 mm, is

$$J = 44.43 \times 10^{-4}(p) \times (\pi/4 \times 10^{-2})(A) \times \sqrt{(1/MT)}\,\text{mol s}^{-1}$$
$$= 6.63 \times 10^{16}\,\text{particles/second}$$

At a distance of 20 cm from the orifice a plate of 1 cm diameter receives 1.67×10^{15} particles/second. If all these particles are condensed, and each has a diameter of 0.2 nm, the time to form a monolayer of condensate is 1.5 seconds.

Vapour deposition of alloys

In order to form a binary alloy it is necessary to use separate Knudsen cells for each element, which are thermally isolated from one another, to provide fluxes in the proportion of the atom fractions of the elements in the required alloy. This is because the fluxes of atoms leaving the surface of an alloy will only be in the ratio of the atom fractions in the alloy at one composition, the *congruent* vaporization composition, and this will vary with the temperature of the alloy. The vaporization rates of the elemental species from a binary alloy source can be calculated under equilibrium conditions using data for the thermodynamics of the alloy. The Gibbs free energy of formation per gram-atom of the alloy ΔG_m° for the binary alloy $A - B$ which forms a continuous range of solid solutions is related to the partial molar Gibbs energies of the components $\Delta\overline{G}_i$ by the equation

$$\Delta G_m^\circ = X_A \Delta\overline{G}_A + X_B \Delta\overline{G}_B$$
$$= X_A RT \ln(p_A/p_A^\circ) + X_B RT \ln(p_B/p_B^\circ)$$

The relationship of the vapour pressure of an element p_i over a binary alloy, to the vapour pressure of the pure species p_1° as determined by the thermodynamic *activity*, a, of the component in the alloy

$$\Delta\overline{G}_i = RT \ln a_i = RT \ln \gamma_i X_i = RT \ln p_i/p_i^\circ = \mu - \mu^\circ = \Delta\mu$$

where X_i is the mole fraction of the component in the alloy, and where γ_i is the activity coefficient, and $\Delta\mu$ is the *chemical potential*. A useful graphical representation of these relationships in terms of the chemical potential for systems which form a continuous range of solid solution, or a number of stoichiometric compounds, or one in which a non-stoichiometric compound with a significant range of composition occurs is shown in Figure 1.1.

DropBooks

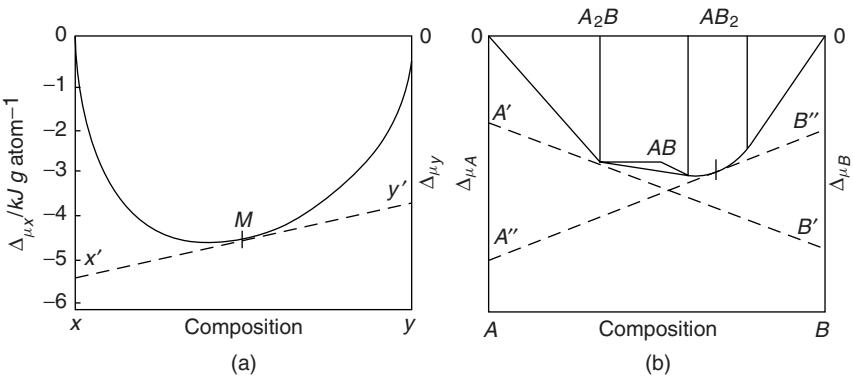


Figure 1.1 *(a) Chemical potential diagrams for systems forming a complete range of solid solutions. The tangent shows at its terminal points, X′, Y′ the chemical potentials of the elements x and y which are in equilibrium with the solid solution of composition M; (b) Potentials for the system A–B, which forms the two stable compounds the stoichiometric A_2B and the non-stoichiometric AB_2. The graph shows that there are many pairs of potentials A′, B′ in equilibrium with A_2B and only one pair for a particular composition of $AB_2 \cdot AB$ is metastable with respect to decomposition to A_2B and AB_2*

The rate of evaporation from the surface of an alloy into the surrounding vacuum, will usually be different for each component and at the temperature T is given by

$$G_i = \alpha p_i A (M_i/T)^{1/2}$$

where α is the vaporization coefficient of the ith component, and A is the area of the alloy surface. The vaporization coefficients of metals are usually unity, but lower values can be expected for the non-metallic elements, such as arsenic, and the non-metallic components of a glass or ceramic, such as alumina (see below).

The Knudsen equation for vaporization, expressed in the form

$$G_A = p_A (M_A/2\pi RT)^{1/2} \,\mathrm{g\,cm^{-2}\,s^{-1}}$$

gives the expression for the flux

$$J_A = p_A (1/2\pi M_A RT)^{1/2}$$

where M_A is the molecular weight of the species A. It follows that in the evaporation of a binary alloy,

$$J_A/J_B = (p_A/p_B)(M_B/M_A)^{1/2}$$

and on substituting for the vapour pressure ratio using the thermodynamic functions, that

$$J_A/J_B = (\gamma_A X_A p_A^\circ/\gamma_B X_B p_B^\circ)(M_B/M_A)^{1/2}$$

Hence, the evaporation rate of each element will only be in the proportion of the alloy composition at one composition, the congruently vaporizing composition. If there is a large difference between the vapour pressures of the elements then the element having the higher vapour pressure could be completely evaporated first.

Vapour deposition of compounds

If two elements form a series of intermetallic compounds, then the fluxes must be arranged in the proportions of the compound it is desired to produce. In many cases, each compound can show a small range of non-stoichiometry, and a range of flux ratios can be chosen to form the compound, each ratio forming the compound at a specific point on the non-stoichiometric composition. Here again, the most satisfactory procedure is to use separate Knudsen sources operating at separately controlled temperatures, one for each element. Most compounds have a very small range of composition, such as SiC, but others have a wide range, such as TiC, Figure 1.2.

DropBooks

In the case of SiC if one attempts to use the compound as the evaporating source, the surface is soon depleted of silicon, because of the large difference in the elementary vapour pressures of silicon and carbon. A steady state is only achieved in the evaporating rates of the elements when the silicon source results from the restricted flow of atoms from below a carbon-rich surface into the vacuum. This process of diffusion of the silicon atoms through the carbon surface layer will depend on the physical state of this layer and will be a function of time and temperature, i.e. depending on the rate at which the carbon layer can *sinter* so as to restrict the flow of silicon atoms to the free surface. Clearly the use of two Knudsen cells, one for each element, operating at different temperatures so as to match the fluxes to the correct ratio, is the practical approach to the preparation of thin films of SiC, with the carbon source operating at a considerably higher temperature than the silicon source. Another advantage of this procedure is that the material of construction of each Knudsen cell may be chosen so as to minimize chemical interaction with the element contained in the cell.

In the case of TiC, preferential evaporation of titanium leads to a change in the stoichiometry of the compound towards the carbon-rich end, the excess carbon being left diffuses into the carbide phase, and so the flux ratio of the two elements changes with time until congruent vaporization is achieved.

The thermodynamic data can only be used in an assessment of the most likely *initial* behaviour of a binary system undergoing free vaporization using

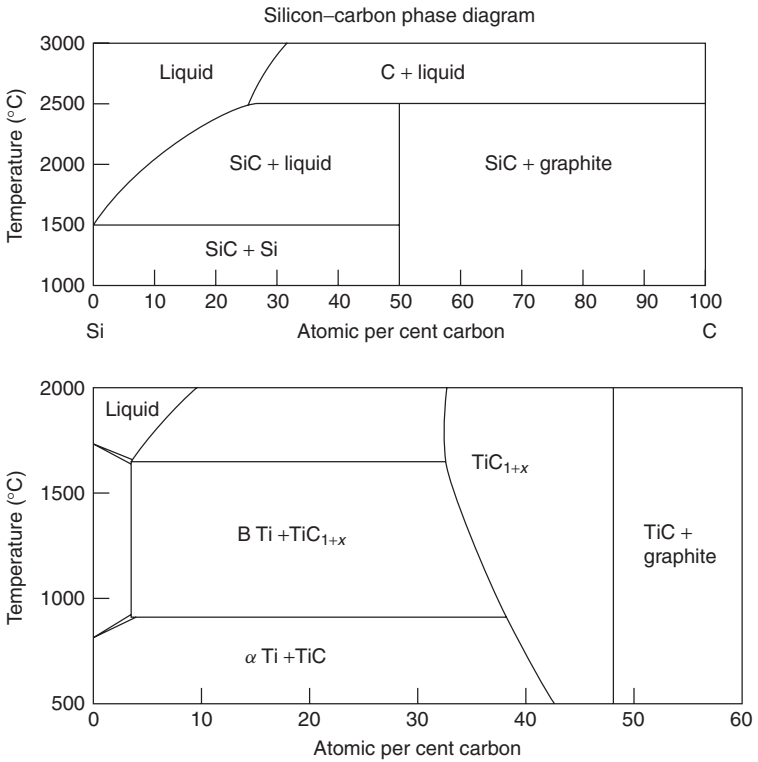


Figure 1.2 *Phase diagrams for the formation of the stoichiometric SiC, and the titanium-deficient* TiC_{1+x}

the ΔG_m diagram per gram-atom as a guide, since the tangent to the resulting curve will intersect the two ordinates at the *equilibrium* chemical potential of each element. The subsequent vaporization behaviour of the system will be determined not only by these considerations, but also by the rearrangement of the atoms by diffusion processes in the compound source.

Free evaporation coefficients of solids

For the majority of metals, the evaporation coefficient is found to be unity, but, as mentioned before, the coefficient of many non-metallic elements with a complex vaporization mechanism such as

$$As(s) \longrightarrow As(g) + As_2(g) + As_4(g) \text{ as major species}$$

$$S(s) \longrightarrow S(g) + S_2(g) \text{ and higher polymers}$$

is less than unity, and increases with temperature.

Oxides such as MgO and Al_2O_3, also have coefficients which are less than unity, between 0.1 and 0.5, depending on the temperature. Data for the evaporation mechanisms of these systems can be obtained from mass spectrometry and, as is the case for the elements with a low coefficient, the vapour does not usually consist of one species only, but has a number of components. The partial pressures of the various species are a function of the oxygen partial pressure, and in the vaporization of alumina and magnesia where the processes

$$\begin{aligned} Al_2O_3 &\longrightarrow 2Al + 3O \qquad MgO \longrightarrow Mg + O \\ &\quad\; Al_2O + 2O \qquad\qquad\quad MgO(g) \\ &\quad\; 2AlO + O \end{aligned}$$

are the major components, the principal mechanism of vaporization changes among these various possibilities, the first predominating at low oxygen pressures, as for example in vacuum, and the third in the case of alumina and the second in the case of magnesia at atmospheric pressure. The middle option predominates for alumina in the presence of a high aluminium activity, for example, when the oxide is in contact with the pure metal. The evaporation of the oxides ZrO_2 and ThO_2 occur principally as the dioxide molecules, and thus the rate is independent of the oxygen pressure.

The overall rates of vaporization of oxides are also a function of the crystallographic nature of the surface, and will decrease for a given sample with time leading to a minimization of the surface Gibbs energy ΔG_s, which will change the surface morphology until a constant rate is achieved. An example of the change in morphology resulting from high temperature evaporation which introduces ledges on initially flat surfaces is shown in Figure 1.3. In the free evaporation of metals, where the evaporation coefficient is unity, this effect is not marked.

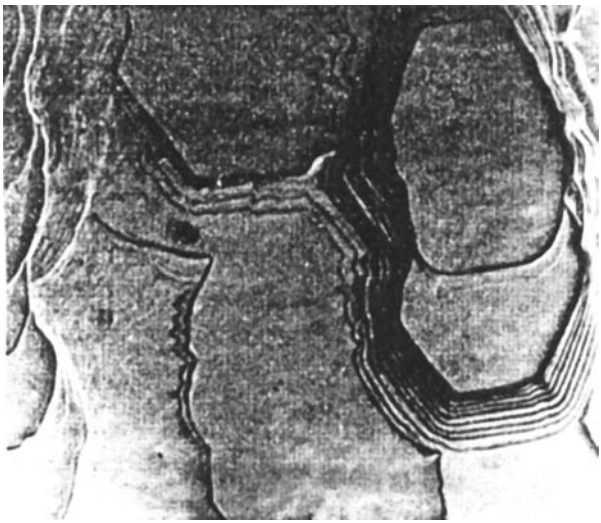
DropBooks

The surface energy of a given crystal plane in a metal can be estimated by multiplying the number of bonds which will be broken per atom when the crystal is cleaved along the direction of the plane by the energy of each bond broken, divided by two. The factor of two is introduced because when the crystal is cleaved, two new surfaces are formed. As an example of the relative surface energies of two crystal planes (111) and (100) in a closed-packed structure, where each atom has six neighbours in the plane and three above and below the plane, three bonds are broken per atom on cleavage in the (111) plane, and four bonds per atom on the (100) plane (Figure 1.4).

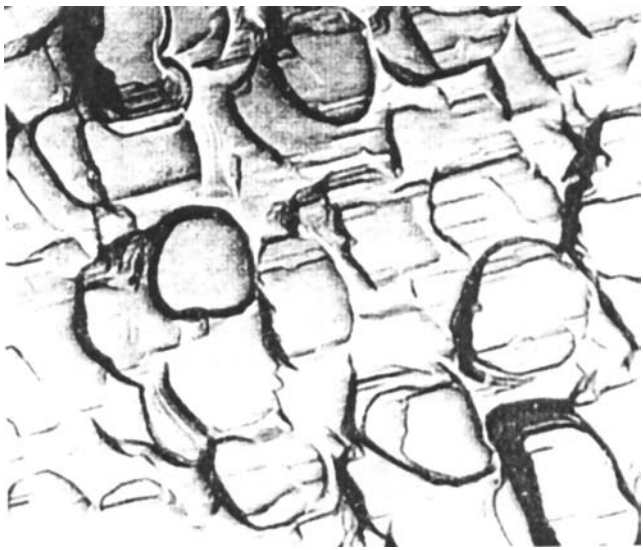
The number of atoms per unit area, N/A, multiplied by the bond energy, ε, and the net number of bonds which are broken yields the surface energy. The relative surface energies of the (111) and (100) planes is derived thus

$$N/A(111) = 2/a_0^2\sqrt{3}; \qquad N/A(100) = 1/a_0^2$$

$$E(111) = N/A(111)(3/2)\varepsilon; \qquad E(100) = N/A(100)(4/2)\varepsilon$$

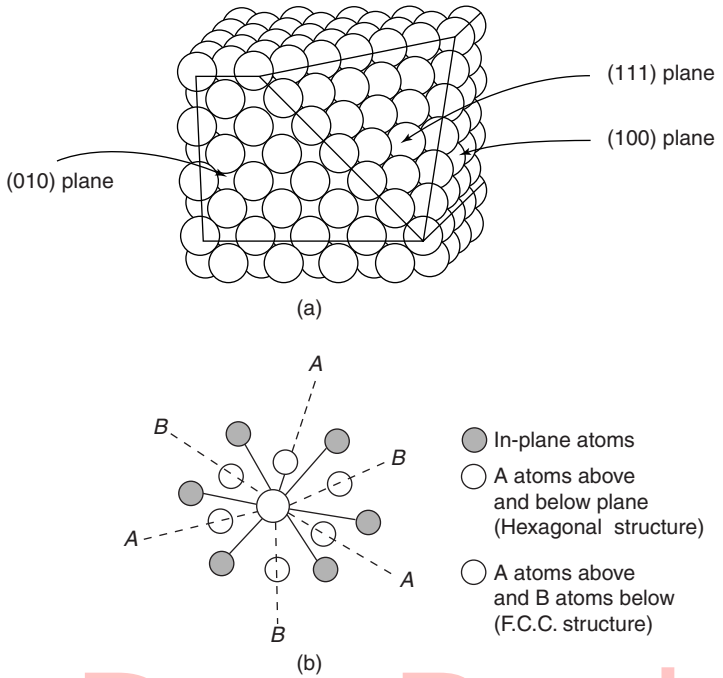


(a)



(b)

Figure 1.3 *Surface morphology of Al_2O_3 single crystal after evaporation in vacuo at 2000°C. (a) the basal plane, and (b) a plane normal to the basal plane. Note the formation of ledges on the (0110) plane*



DropBooks

Figure 1.4 *(a) Close packing of atoms in a cubic structure, showing six in-plane neighbours for each atom; (b) An expanded diagram of the packing of atoms above and below the plane. A above and A below represents the location of atoms in the hexagonal structure, and A above with B below, the face-centred cubic structure*

and hence the ratio of the surface energies is given by

$$E_s(111)/E_s(100) = \sqrt{3}/2$$

Here a_0 is the lattice parameter of the crystal. An approximate value for the bond energy, ε, for this structure where the co-ordination number, Z, equals twelve is given by

$$\varepsilon = \Delta E_{\text{sub}}/0.5ZN = \Delta E_{\text{sub}}/6N$$

where ΔE_{sub} is the energy of sublimation per gram-atom. This assumes that the bonds between atoms in a metal arise by interaction of nearest neighbours only, and atoms further away have no effect on the bonding, and that the interatomic distance is the same on the surface as deep in the crystal. In the case of ionic crystals, this calculation is more complex due to the fact that ions below the surface contribute significantly to the bonding of the surface

ions. The resultant effect of this difference in surface energies between the various crystal planes of a solid is that the shape of a single crystal changes during evaporation to expose those surfaces with the lowest energy. The final equilibrium shape can be obtained from Wulff's theorem which states that the relative extension of each crystal face, area A, will be determined by minimizing the product of the surface area of each plane by the respective surface energy, γ_i. It follows that surface energy divided by the distance of the face from the centre of the crystal r_i, is constant. Thus

$\Sigma\gamma_i \, \mathrm{d}A_i$ is a minimum and γ_i / r_i is a constant

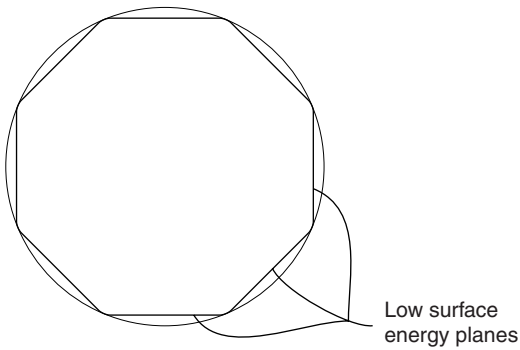


Figure 1.5 *Evolution of an initially spherical particle to expose the low-energy planes, as a result of evaporation*

Atoms in the surface layer (*adatoms*) migrate over the surface to find those sites where the binding energy to the underlying atoms is minimal before the process of evaporation takes place. In the case of a metal, the evaporation will take place from those surface sites in which the evaporating atom has the least number of bonds to the adjacent atoms. This process of surface diffusion will also occur on the surface of a deposit which is formed by condensation, but now the condensing atoms will seek those sites of strongest binding.

Finally, it is to be expected that the evaporation coefficient of a very stable compound, such as alumina, which has a large heat of sublimation resulting from the decomposition into the elements, will be low. Since the heat of evaporation must be drawn from the surface, in the case of a substance with a low thermal conductivity such as an oxide, the resultant cooling of the surface may lead to a temperature gradient in and immediately below the surface. This will lower the evaporation rate compared to that which is calculated from the apparent, bulk, temperature of the evaporating sample as observed by optical pyrometry, and thus lead to an apparently low free surface vaporization coefficient. This is probably the case in the evaporation of alumina in a vacuum,

which has an apparent evaporation coefficient of about 0.3. Zirconia, on the other hand, which is as stable as alumina, evaporates as ZrO_2 molecules and has a coefficient of evaporation equal to unity.

Other techniques for the preparation of thin films

Single and epitaxial films in semiconducting systems

Monomolecular films of semiconductors in the II–VI group and the III–V compounds have been prepared by the interaction of monolayers of the Group II or III elements with gases containing the V or VI elements. The earliest experiments involved the vacuum evaporation of Zn or $ZnCl_2$ on a glass substrate to form a monolayer, followed by reaction of this layer with H_2S or S gas to form the sulphide (Suntola and Hyvarinen, 1985). Similarly a vapour-deposited monolayer or a single crystal sample of Ga was reacted with AsH_3 to form a monolayer of GaAs. The formation of III–V compounds has also been carried out with an organometallic source for Ga atoms, $Ga(CH_3)_3$ for example, and AsH_3 for the As atoms (Usui and Watanabe, 1991). A monolayer of As is first laid down on a substrate heated to temperatures in the range 700 K to 900 K, by thermal or light-assisted decomposition of AsH_3. The organometallic gallium source is then adsorbed on this surface. The reverse procedure, in which the organometallic was introduced first did not lead to monolayer formation of the compound. It was therefore concluded that the Ga layer was formed by the adsorption and subsequent decomposition of the trimethyl with the Ga atoms in direct contact and bonded to the As layer, leaving the methyl radicals to prevent further immediate adsorption of $Ga(CH_3)_3$ molecules. The resultant Ga layer after the removal of the methyl radicals, which occurs in a few milliseconds, also prevents the further adsorption of trimethyl molecules. To reduce the unwanted decomposition of the molecules in the gas phase, the process is carried out by admitting the gases sequentially into an evacuated chamber containing the substrate, and removing the excess of each reactant before admitting the other.

A very important technology in laser production makes use of two-phase systems involving semiconductors. The properties of the combined solids determine the lowest energy states in which electrons are at thermal equilibrium or are excited to the conducting state under illumination. For example, the junction between GaAs and GaAs–AlAs alloys is one between the narrow band gap GaAs in which electrons are easily excited to the conduction state, and the wider band gap GaAs–AlAs, which requires a greater energy of excitation to produce conduction electrons. The conduction electrons are therefore confined to the GaAs phase under equilibrium at normal temperatures. Electrons may be transferred to the GaAs–AlAs phase by suitable illumination

DropBooks

and this inverse population can be light-stimulated to produce laser action. Since AlAs and GaAs form a continuous range of solid solutions, the lattice parameter of the alloy can be adjusted to achieve a good match to the GaAs lattice parameter, leading to epitaxy.

When a mismatch is inevitable, as in the combination $Ge_xSi_{1-x} - Si$, it is found that up to a value of $x = 0.4$, there is a small mismatch which leads to a strained silicide lattice (known as *commensurate* epitaxy) and at higher values of x there are misfit dislocations (incommensurate epitaxy) at the interface (see p. 35). From these and other results, it can be concluded that up to about 10% difference in the lattice parameters can be accommodated by commensurately strained thin films.

There are a number of methods for the preparation of these materials, and the production of thin films may be carried out using Knudsen cells for each element which are thermally isolated from one another. Although elementary sources of the components are generally used, it should be pointed out that the use of compound sources might be preferable in many cases. For example the formation of arsenides, sulphides and tellurides could be more readily controlled if metallic compounds involving these elements were used rather than the elements. This is because the production of the thin film requires the addition of these elements, atom-for-atom to the Group III element, and the complex molecular species must dissociate to provide the Group V or VI atom, leaving the rest of the molecule to evaporate. The gaseous species evolved by the elementary sources are complex, but the vapour species over sulphur, $S_n (n = 1 - 8)$ for example, reduce to a mixture of predominantly monatomic with diatomic sulphur only, over a mixture of Fe–FeS in Knudsen evaporation. Also the higher temperature of operation of the Knudsen cell is much easier to control in a vacuum system when the metallic compound source is used.

Thin film production by the sputtering of metals

Thin films may be produced by the evaporation of metals through *sputtering* by ion bombardment as well as by thermal evaporation methods (Gautherin, Bouchier and Schwebel, 1985). The source of the ions is usually a plasma, which produces ions and electrons at equal concentrations to a degree of ionization of about 10^{-5} ($10^9 - 10^{12}$ electrons and ions cm^{-3}) of a neutral gas such as argon. The plasma is sustained by applying a DC or AC potential gradient to the inert gas at a pressure of about 10^2 Pa, either by metal electrodes which confine the plasma, or by external electrodes when AC is used, usually at RF frequencies (5–30 MHz) (Figure 1.6).

In DC sputtering, the plasma is formed between a metal target which acts as the source of atoms, and which is held at a negative potential with respect to the condensation substrate, which may be a metal or an insulator. The source

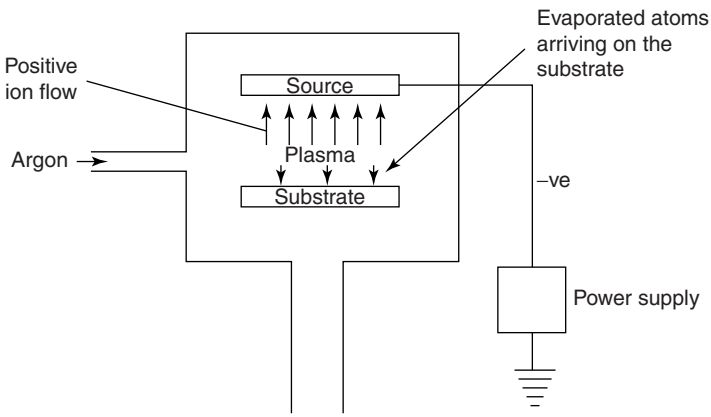


Figure 1.6 *Sputtering device for the formation of thin films by the bombardment of a source material by ions extracted from a plasma*

is bombarded by ions from the plasma and the evaporated atoms collect in part on the target substrate. The negative potential is applied between the source and the substrate to cause the movement of the positive ions of the plasma towards the source. The collisions between the incident ions and the metal target lead to dislodgement of the target atoms, and these atoms can then diffuse towards the substrate through the plasma.

DropBooks

The origin of the sputtered atoms may result from displacement below the surface of the source, a so-called *thermal spike*, as well as directly from the surface, depending on the incident energy of the bombarding ions, E_i. This must reach a threshold value, E_t, before any atoms are dislodged from the target and

$$E_{\text{evap}} \leq E_t \leq E_d$$

where E_{evap} is the energy of vaporization of a target atom, and E_d is the energy to create a thermal spike. In a thermal spike the bombarding ion penetrates the surface, and imparts energy to a cluster of atoms in its path before coming to rest. The energy is dissipated throughout the lattice subsequently by thermal conduction, but for a brief period, probably of the order of 10^{-11} s, the effective temperature is much higher than the rest of the lattice, and this can liberate more than one atom per ion from the target. If T_m is the energy transferred from the incident ion of kinetic energy E_i, to the target atom in a head-on collision, this can be calculated according to classical mechanics

$$T_m = \frac{4m_i m_t}{(m_i + m_t)^2} E_i = \tau E_i$$

where m_i and m_t are the masses of the ions and the target atoms respectively. Clearly, $(1 - T_m)$ is the energy carried away by the reflected ion after collision, and so the threshold energy is given by

$$E_t = \frac{E_{\text{evap}}}{\tau(1 - \tau)}$$

which agrees with the experimental data to within a factor of two (Bohdansky, Roth and Bay, 1980) when $m_i < m_t$. The number of atoms produced per ion at the threshold (a few eV) is about 10^{-2} rising to unity at a bombarding energy of 10^2–10^3 eV, and exceeding unity at higher ion energies where thermal spikes play an important role. The sputtering efficiency for surface evaporation is therefore determined in part by the ratio of the energy of the incident ions to the evaporation energy of the substrate, but also by the relative masses of the ionic species and the target atoms. An equation which relates the sputtering efficiency, S, to these factors is

$$S = (3\alpha/4\pi^2)T_m/E_{\text{evap}}$$

where α is a transfer coefficient of the order of 0.1–1 (Sigmund, 1969). An empirical formula for α (Gautherin *et al.*, loc.cit.) which shows the dependence of this factor on the relative masses of the incident and target atoms is

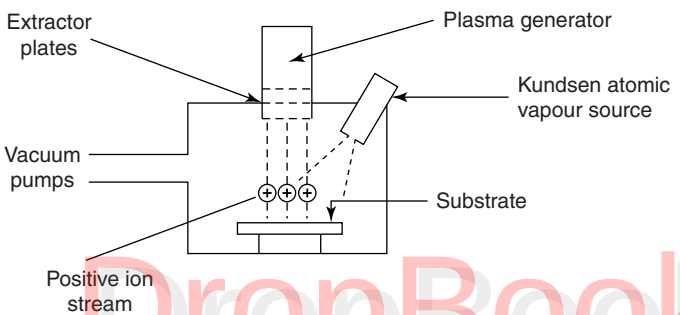
$$\alpha = 0.15 + 0.12\, M_t/M_i$$

Because the energy which is imparted to the target by ion bombardment is finally transformed into thermal energy, the target plate is normally water-cooled in a sputtering apparatus.

Experimental values for the sputtering efficiency tend to show lower values of α for elements, such as aluminium and tungsten which form stable oxides, compared with the metals such as gold and platinum which do not under normal experimental conditions. This is probably due to the presence of a surface oxide, since industrial sources of argon, which are used as a source of ions for example, usually contain at least 1 ppm of oxygen, which is more than enough to oxidize aluminium and tungsten.

Growth rates of the order of 1–10 nm min^{-1} are produced by this technique for a wide range of materials, metals, intermetallic compounds and semiconductors for example. These rates are similar to those attained in Knudsen evaporation, but it is possible that the cohesion could be better if the atoms arriving at the substrate have a high energy (superthermal), which depends on the potential gradient across the plasma. The ion density of the discharge in these devices can be increased if a magnetic field is incorporated in the source to cause the electrons to follow helical paths through the argon. This is most efficiently achieved in the *magnetron* configuration, in which the electron source is a cylindrical filament with the anode in the form of a concentric cylinder. A magnetic field is applied perpendicular to the discharge to increase the electron path-length between the electrodes.

An alternative procedure which is effective in providing a controlled flux of metal atoms and condensing some of these on a clean substrate, is the method known as *ion plating*. An apparatus for this method of thin film formation consists of a plasma which is principally used to provide ions which clean the substrate surface by ion bombardment. A separately heated Knudsen cell or a heated filament provide the source of metal atoms to form the deposit, and these must diffuse through the plasma, either in the charged state, or as excited or neutral atoms. This procedure appears to be more efficient than the simple sputtering of a metal target due to the separation of the control of the metal atom source from the plasma, the first merely serving as a source, and the latter as a method for preparing a clean substrate to receive the deposit (Figure 1.7).



DropBooks

Figure 1.7 *Ion plating device in which the substrate is cleaned by ion bombardment and the material to be deposited is supplied by a Knudsen cell*

These sputtering procedures have an advantage over Knudsen evaporation, since metallic alloys and some metal compounds can be directly sputtered without significant difference between the composition of the film and the source material. As there is most probably a difference between the sputtering efficiencies of the elements in the alloy, the one with the higher efficiency will be sputtered first, enriching the surface of the alloy with the other element, which will subsequently be sputtered, until the surface composition is restored. The relative rates of Knudsen evaporation and sputtering are, however, not significantly different in most practical cases. The independence of the sputtering mechanism of the relative vapour pressures of the alloying elements clearly presents an experimental advantage over the use of a number of Knudsen cells, one for each element.

The production of nanoparticles

Films consisting of nanoparticles of between 1 and 10^2 nm in diameter can be produced by the evaporation of metals, using either a freely evaporating,

heated, metal sample or a metal block which is heated with a focused laser beam, which evaporates into a low-pressure (10^{-2}–10^{-3} atmos) inert atmosphere followed by condensation on a cold plate or liquid-nitrogen-cooled cold finger.

In laser heating, energy densities of 106–107 W cm^{-2} are directed on the surface of the metal during a laser pulse of 10 ns duration and 10^{-2} cm^2 in area and at a repetition rate of 5000 s^{-1} to cause the formation of a vaporized plume. This typically contains about 10^{15} atoms at an atom density equivalent to about 10^{18} atoms per cm^3. As an example of this process, the evaporation of 10^{15} atoms of zinc would require about 10^{-9} of the molar heat of evaporation of zinc (130.4 kJ mol^{-1}), or about 10^{-4} joule, which is negligible in comparison with the total energy imparted by the laser beam, and therefore most of this energy is used in raising the temperature of the gaseous products in the plume to temperatures as high as 10 000 K, to form a plasma containing free ions and electrons. The laser beam is scanned across the surface of the target in order to make the maximum use of the beam energy, and reduce the conduction of heat away from the surface and into the interior of the metal sample.

If the surrounding inert gaseous atmosphere is heated from below the metal sample to cause convection currents, the plume of the evaporated metal is conveyed upwards to the cold plate, which is placed above the irradiated metal sample, for rapid condensation. Condensation of atoms occurs within the plume during ascent to the condensing plate to yield the fine particle deposit because the plume is super-saturated in metal vapour as the temperature of the plume approaches that of the surrounding atmosphere by radiation, and subsequently by collision, cooling. Metal oxide, nitride, and carbide nanoparticle films can be produced by adding oxygen, ammonia or methane to the inert atmosphere surrounding the metal target during irradiation, and scanning the laser beam to find unreacted metal. The final average size of the nanoparticles can be controlled through the temperature of the condensing plate. For example, the average diameter of ZnO particles was found to increase from 10–20 nm at 173 K, to 50–60 nm at 230 K condensation temperature.

Nanofilms of oxides can also be produced by heating gaseous metal compounds, such as halides, e.g. $TiCl_4$, in an oxidizing flame. In this technique the gaseous compound is introduced into the central axis of an oxygen–methane flame, and the resultant product is condensed on a cold plate. Composite materials may also be prepared by mixing suitable gaseous compounds of the elements contained in the composite. A published example of this procedure is the formation of an Fe_3O_4/SiO_2 composite by simultaneous oxidation of iron pentacarbonyl, $Fe(CO)_5$ and hexamethylsiloxane, $(CH_3)_3SiOSi(CH_3)_3$, in a methane/oxygen/nitrogen flame (Goldstein 1997) (Figure 1.8).

The potential technological importance of nanoparticles is due to the increase in sinterability with a substantial decrease in the sintering temperature

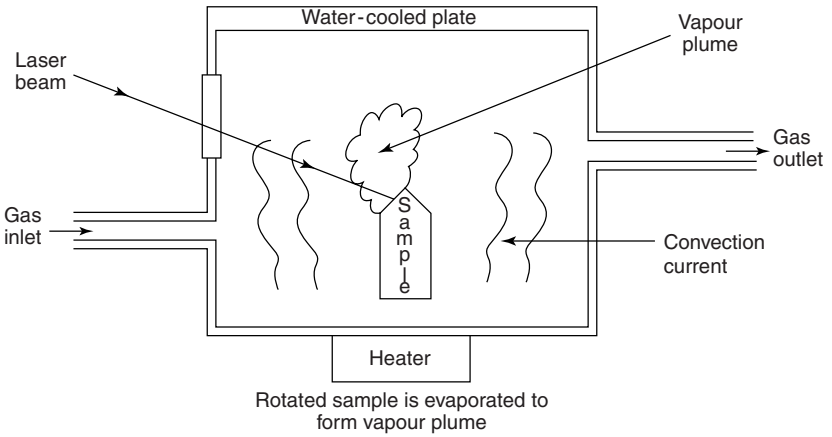


Figure 1.8 *Evaporation of a metal by laser beam irradiation to provide a source for the deposition of nanoparticles on a water-cooled substrate*

when compared to conventional materials since grain boundaries with high-diffusivity paths form a substantial fraction of a nanoparticle assembly. Also cold-compacted assemblies of nanoparticles have very much higher rates of atomic transport due to the fact that about 10% of the atoms in the compact are in the grain boundaries.

DropBooks

Coating with thin diamond films

The reaction between hydrogen and methane at high-temperatures has recently found an important application in the coating of cutting tools, for example, with thin films of diamond. A pre-requisite appears to be to be the inoculation of the tool surface with diamond paste to provide *nuclei* for the film formation. The film is grown in a gas mixture of >95% hydrogen and 1–4% methane, with or without the addition of a small partial pressure of water vapour. This gas mixture has been passed through a high-frequency discharge or over a tungsten filament held at about 2000–2500 K before arriving at the tool surface. The substrate on which the film is to be formed must be held at a temperature between 1000 and 1500 K.

For the analysis of the process it is suggested that the high-temperature treatment of a hydrogen–methane mixture produces atomic hydrogen and acetylene as the important products. The thermodynamic analysis of the mixture shows the composition as detailed in Table 1.1, which indicates that atomic hydrogen is at a much lower concentration than molecular hydrogen. A proposed mechanism is that the surface of the diamond paste particles is covered with hydrogen atoms which are bonded to surface carbon atoms and these react with hydrogen atoms from the gas phase to produce hydrogen molecules which are desorbed

Table 1.1 *Equilibrium composition of gas mixtures at 2300 K and 0.1 atmos pressure (mole fractions of the major gases only)*

$95\%H_2 + 5\%CH_4$		$95\%H_2 + 4\%CH_4 + 1\%H_20$	
H_2	0.947	H_2	0.947
C_2H_2	0.0234	C_2H_2	0.0140
H	0.0296	H	0.0296
CH_4	4.69×10^{-5}	CO	0.00 938
CH_3	2.74×10^{-5}	CH_4	3.62×10^{-5}
		CH_3	2.12×10^{-5}

to the gas phase, leaving spare bonding electrons on the diamond surface. These bonds are then the sites of acetylene adsorption on the surface which couple to spread the diamond structure across the substrate. During the adsorption of acetylene on the diamond nucleus surface, the bond nature of the adsorbed molecule changes from that found in the acetylene molecule to the graphite structure in the adsorbed state, and finally to bonds between the adsorbate diamond substrate and the neighbouring adsorbed acetylene molecule.

The alternative to diamond formation is, of course, the formation of graphite, which is the stable phase under these conditions. The structure of graphite involves triangular carbon–carbon bonding to form edge-joined benzene rings in flat planes, separated from one another by weak bonding which allows the planes to glide over one another easily. It will be seen that the carbon–carbon bond is stronger in benzene than in diamond, and in fact, the Gibbs energy of the transformation

$$\text{C (diamond)} \longrightarrow \text{C (graphite)}$$

has the Gibbs energy change, at one atmosphere

$$\Delta G^\circ = -1372 - 4.53T \quad \text{J mol}^{-1}$$
$$= -5905 \quad \text{J mol}^{-1} \text{ at } 1000\,\text{K}$$

The presence of water vapour in the ingoing gas mixture has been found to suppress the formation of graphite and thus to favour diamond formation. The significant change in composition when water vapour is added, is the presence of carbon monoxide in about half the proportion of hydrogen atoms.

Plasma evaporation and pyrolysis of carbon to form Fullerenes

The vapour phase in the evaporation of carbon at high temperatures contains a number of gaseous species C, C_2, C_3 and higher polymers. Of these the first

three molecules constitute the major species at 4000 K, the relative partial pressures favouring the trimer at 1 atmos pressure, and the monomer when the pressure is decreased to 10^2 Pa. This is a temperature which is typically achieved at the surface of the electrodes when carbon electrodes are used in a plasma heater. New materials have been synthesized from the condensates of carbon evaporation resulting from a DC plasma formed between carbon electrodes in a low pressure (about 10^3 Pa) inert gas such as helium or argon. In the discharge the anode is evaporated by electron bombardment, and the condensates are found, in part, on the anode as a thin web-like structure. These include the first complex of this kind to be discovered, the spherical C_{60} giant molecule and more recently single and double wall tubes of nanodimensions.

The tube walls have the graphite six-membered ring structure, and the tubes are frequently sealed at each end by caps made of five-membered carbon rings, which can be removed by selective oxidation. The nanotubes have interesting electrical properties which suggest future applications in electronic microcircuits. Also of considerable interest are the nanoparticles which are formed when a 1:1 mixture of graphite powder and an oxide powder such as NiO, Fe_2O_3 or a lanthanide oxide such as Y_2O_3 is placed in a central cavity drilled into the carbon anode electrode. Nanoparticles of approximately spherical shape in which the metal carbide is encapsulated in a graphite layer of varying thickness are produced. Because of the low sinterability of graphite the particles retain their shape at high temperatures, and the metal carbide particles function as catalysts for the preparation of organic compounds without the disadvantages of similar metal catalyst particles mounted on the surface of an inert carrier, such as a ceramic (see Chapter 4).

DropBooks

The method of laser evaporation of carbon has also produced nanotubes, but a promising development of potentially great flexibility is in the thermal decomposition (*pyrolysis*) at temperatures around 1000–1300 K of organic molecules containing C–C double bonds, such as benzene. A number of organic species have been tested in this way, and aligned nanotubes have been produced by the decomposition of iron ferrocene $Fe(C_5H_5)_2$, in which an iron atom is sandwiched between two cyclopentadiene molecules. Given the enormous variation of organic molecules which can be tested in this procedure, many new possibilities of the production of nanotubes in a wide range of configurations appear available (Terrones *et al*., 1999).

Materials science and the formation of thin films

The formation of nuclei from the vapour phase

The growth of deposits on a substrate requires the initial formation of nuclei and their subsequent growth and agglomeration into a film, most probably a

monolayer. The classical theory of the growth of condensed phase nuclei from a gas by *homogeneous* nucleation, shows that the initial nuclei, which contain a very small number of atoms, are unstable and can re-disperse into atoms. However, once a critical size is surpassed, the nuclei become more stable as growth proceeds, until finally the nucleus attains thermodynamical stability. The growth of nuclei towards stability can be simply treated in the case of spherical liquid nuclei growing in a gaseous environment, by consideration of the Gibbs energy of transfer of atoms from the gas to the nuclei ΔG_f. This has two opposing components, one corresponding to the *endothermic* contribution of the surface energy of the material of the nucleus, γ, and the other to the *exothermic* formation of the equilibrium condensed phase ΔG_s from the gas. The Gibbs energy of formation of the nucleus is then given by

$$\Delta G_f = 4\pi r^2\gamma + 4/3\pi r^3 \Delta G_s$$

The Gibbs energy of formation of the equilibrium condensed phase of the nucleus is equal in magnitude but opposite in sign to the Gibbs energy of vaporization of the condensed phase. The contribution of the two terms on the right-hand side of this equation can be combined graphically to form a composite diagram showing the Gibbs energy of the nucleus as a function of the nucleus radius (Figure 1.9).

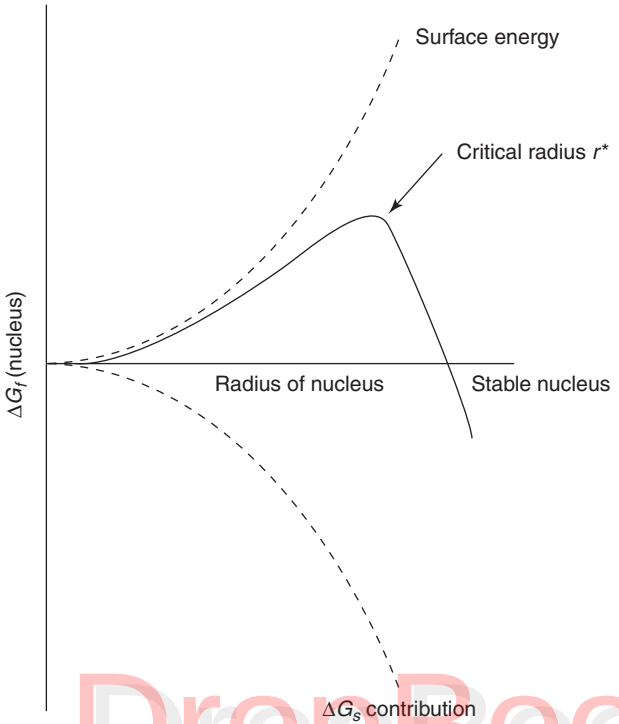
The surface energy term causes the Gibbs energy of nucleus formation to increase endothermically at small nucleus radius, but this is eventually converted to an exothermic process at larger nucleus radius by the effect of the second, volume, term. The shape of the resultant curve is typical of the progress of many chemical reactions, where an energy barrier exists between the reactants and the product which must be overcome by 'activation' of the reactants before the product can be formed (see Chapter 2) The critical size of the nucleus radius beyond which the nucleus becomes more stable, r^*, and the critical Gibbs energy ΔG_f^*, is given by

$$r^* = 2\gamma/\Delta G_s$$

$$\Delta G_f^* = 16\pi\gamma^3/3\Delta G_s^2$$

These terms are obtained from the equation above by differentiation with respect to r, and setting the resultant equal to zero. This is equivalent to taking the point on the graph of the Gibbs energy of nucleus formation versus the size of the nucleus where the tangent has zero slope.

When the nucleus is formed on a solid substrate by heterogeneous nucleation the above equations must be modified because of the nucleus–substrate interactions. These are reflected in the balance of the interfacial energies between the substrate and the environment, usually a vacuum, and the nucleus–vacuum and the nucleus–substrate interface energies. The effect of these terms is usually to reduce the critical size of the nucleus, to an extent dependent on



DropBooks

Figure 1.9 *The balance of endothermic surface energy and the exothermic formation of the stable condensed phase during nucleation from the vapour phase. The critical radius, above which the nuclei become stable, is where the resultant Gibbs energy change has zero slope*

the magnitudes of these three factors. The modified form of the nucleation equation for heterogeneous nucleation now becomes

$$\Delta G_f^* = (16\pi\gamma_{n-g}^3/3\Delta G_s^2)((2+\cos\theta)(1-\cos\theta)^2)/4$$

where the interfacial energy terms define the angle θ through the relationship

$$\gamma_{n-s} = \gamma_{s-g} - \gamma_{n-g}\cos\theta$$

where γ_{n-s} is the interfacial energy between the substrate and the nucleus, γ_{s-g} and γ_{n-g} are the interfacial energies between the substrate and the gas, and between the nucleus and the gas (Figure 1.10).

When the nucleus is a liquid, the angle θ is called the *wetting angle*. It can be seen that the critical radius in heterogeneous nucleation is given by the same equation as that for homogeneous nucleation, but the radius now refers

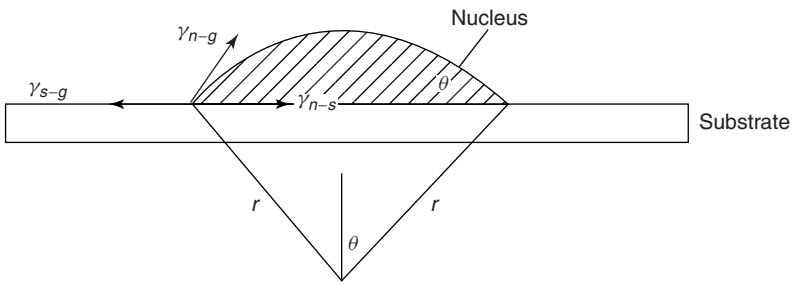


Figure 1.10 *The formation of a spherical-cap nucleus of radius r on a substrate upon which the nucleus has a wetting angle* θ

to the radius of the spherical cap formed by the nucleus at the plane of contact with the substrate.

These classical considerations of liquid–solid interactions apply only qualitatively to the case of a solid nucleus, since the periphery of the nucleus will not be circular in this case but will develop a morphology which is determined by the surface energy of a stepped surface built from rows of atoms of varying length. The equivalent in the solid state to the droplet radius of curvature in the solid state is the step length between the neighbouring rows of atoms, which increases with decreasing size of the nucleus. It is to be expected that this periphery will contain these steps, and that the planes which in the bulk have the minimum surface energy, the close-packed planes, will predominate in the solid nucleus. As in the liquid example, there will be a critical size of the nucleus below which it will tend to decrease in size due to the detachment of atoms from the most weakly bound positions on the periphery. Studies of gold nuclei on a silica substrate show that the interatomic distances in these nuclei are larger than that of the bulk solid, indicating a relative weakening of the metal–metal bonds. This will also lead to a greater instability in the solid nuclei the smaller they are, than would be calculated using bulk data, such as the vaporization energy in the calculation of the detachment energy of an atom.

When the nucleus is formed by condensation of a single element on a reactive substrate, the Gibbs energy change may be altered because of the thermal nature of the adsorption process. This effect will usually reduce the two terms in ΔG_f^* because of the heat and entropy of *adsorption* decrease when gas atoms become confined to the surface of the substrate. The energy of re-evaporation also depends on the nature of the bonds between the nucleus and the substrate, being reduced when these are less strong than those of the parent element. The structure of the nucleus appears to depend on these factors, together with the activation energy for the migration of the adatoms, over the surface of the substrate. Metal nuclei have been found to have two-dimensional

structures when

$$\Delta E_{\text{evap}} \leq 3(E_{\text{des}} - E_{\text{diff}})$$

ΔE_{evap} is the energy of vaporization of the parent element, E_{des} is the energy of *desorption* of an adatom from the nucleus, and E_{diff} is the energy of migration of the adatom over the substrate. If the energy of vaporization of the element is greater than three times the desorption energy, then three-dimensional nuclei are formed. The desorption energy will usually approach the energy of vaporization of the parent element when the nucleus is four or more atom layers thick (Niedermayer, 1975). However, the initial film is frequently two-dimensional, but after two or three layers have been formed over the film, the nucleus continues to grow with the lattice properties of the bulk phase.

The atomic structure of the nuclei of metal deposits, which have the simplest form since they involve only one atomic species, appear to be quite different from those of the bulk metals. The structures of metals fall mainly into three classes. In the face-centred cubic and the hexagonal structures each atom has 12 co-ordination with six neighbours in the plane. The repeat patterns obtained by laying one plane over another in the closest fit have two alternative arrangements. In the hexagonal structure the repeat pattern is A–B–A–B etc., whereas in the face-centred cubic structure the repeat pattern is A–B–C–A–B–C. In the body-centred cubic structure in which each atom is eight co-ordinated, the repeat pattern is A–B–A–B. (See Figure 1.4.)

DropBooks

Some experimental (Ogawa and Ino, 1972) and theoretical studies suggest that in the formation of three-dimensional films, tetrahedral co-ordination predominates in the initial formation of nuclei involving four atoms, but thereafter the structure changes to five-fold co-ordination, a seven-atom nucleus consists of bipentagonal pyramids and so on, and the subsequent stage involves some twenty corner-sharing *tetraheda* forming an icosahedron with one central atom. The icosahedra can join together by face-sharing into larger structures, eventually deforming into a basic octahedral structure, leading to the normal structure of the parent element. It is not until the nucleus contains a large number of atoms, and the diameter reaches 5–10 nm that the structure changes to the normal close-packed structure of the bulk (Hoare and Pal, 1972) (Figure 1.11).

The nature of the bonding must alter during this structural change in co-ordination, as will the electrical conductivity of the film.

The formation of a film from nuclei

Once a number of nuclei are formed on the surface of the substrate, the next stage of the film formation process involves the transport of nuclei or their constituent atoms across the surface in order to cover the area available to form the complete film. It is clear from the relationship between the Gibbs energy

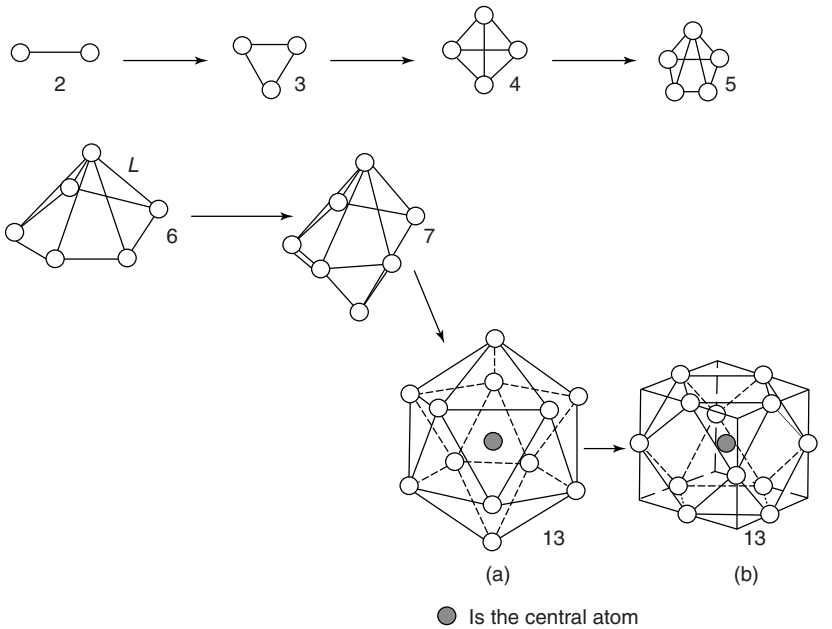


Figure 1.11 *The formation of metal clusters during the nucleation of a new phase. The co-ordination is first tetrahedral, leading to 5-fold symmetry, until the 13-atom icosahedron is formed which transforms into the cubic icosahedron of the stable phase*

and nucleus size that the small nuclei are unstable compared to the larger nuclei. It follows that atoms can be transferred from the smaller, less stable nuclei to the larger nuclei by diffusion across the surface of the substrate. All diffusion processes are described by a general equation due to Einstein where M is the *mobility*, which is the velocity under unit chemical potential gradient, N is Avogadro's number, and $\delta\mu/\delta x$, is the chemical potential gradient in the x direction.

$$J = -(MkT/N)\delta\mu/\delta x$$

and μ is the chemical potential equal to $RT \ln a$.

An empirical formula, due to Fick, shows that, under simple circumstances where the chemical potential of a component in a system is defined by the equation

$$\mu_i - \mu_i^\circ = RT \ln c_i$$

the diffusional flux is given by

$$J_i = -D_i \, \mathrm{d}c_i/\mathrm{d}x$$

where D is a phenomenological coefficient having the dimensions $cm^2\,s^{-1}$. Comparing this equation with the Einstein equation, it can be seen that when $\ln a = \ln c$.

$$D = MkT$$

The mobility or diffusion of the atoms over the surface of the substrate, and over the film during its formation, will occur more rapidly as the temperature increases since epitaxy can be achieved, under condition of crystallographic similarity between the film and the substrate, when the substrate temperature is increased. It was found experimentally that surface diffusion has a closer relationship to an activation-dependent process than to the movement of atoms in gases, and the temperature dependence of the diffusion of gases. For surface diffusion the variation of the diffusion coefficient with temperature is expressed by the Arrhenius equation

$$D = D_0 \exp -A/T$$

where T is the absolute temperature and D_0 and A are constants for a given system, A being the activation energy divided by the gas constant. The energy of activation for surface migration is approximately the same as that for migration within a crystal. This has led to some speculation that surface migration involves vacancy–adatom place exchange during surface diffusion. The pre-exponential factor is typically of the order of $10^{-3}\,cm^2\,s^{-1}$.

DropBooks

Grain growth in the initial deposit

When the film is first completed, it consists of grains with a distribution of grain sizes. The smaller grains have the largest radius of curvature at the grain boundaries, and they tend to disappear in time. Atoms are transferred from the smaller grains to the larger grains across the boundaries at a rate which can be deduced using Einstein's equation together with the Gibbs–Thomson equation.

This equation is derived by considering the transfer of material from a flat surface to a droplet. For the transfer of a small mass δm from the flat surface of vapour pressure p° to the droplet of vapour pressure p, the Gibbs energy of transfer is

$$\Delta G_{\text{transfer}} = RT \ln \frac{p}{p^\circ} \frac{\delta m}{M}$$

where M is the molecular weight of the fluid.

The addition of this small mass increases the radius of the droplet, r, to $r + \mathrm{d}r$, and the surface area by $8\pi r\,\mathrm{d}r$. If the fluid density is ρ, then the

corresponding increase in mass is given by

$$\delta m = 4\pi r^2 \rho \, \mathrm{d}r$$

The increase in surface energy, S, is given by

$$S = 8\pi r\gamma \, \mathrm{d}r = \frac{8\pi\gamma\delta m}{4\pi r\rho} = \frac{2\gamma}{r}\frac{\delta m}{\rho} = \Delta G_{\text{transfer}}$$

Hence

$$RT \ln \frac{p}{p^\circ} = \frac{2\gamma}{r}\frac{M}{\rho} = \frac{2\gamma}{r}V_m \qquad (V_m \text{ is the molar volume})$$

The term $RT \ln p/p^\circ$ is clearly the chemical potential of a surface of radius r with respect to a flat surface of the same material as standard state. It follows that the difference in chemical potential between two surfaces, $\mu^{\mathrm{I}} - \mu^{\mathrm{II}}$, where surface I is convex of radius r_1, and the other surface II is concave of radius r_2 is given by

$$\mu^{\mathrm{I}} - \mu^{\mathrm{II}} = 2V_m\gamma(1/r_1 + 1/r_2)$$

which, since r_1 is equal and opposite in sign to r_2 at the grain boundary, yields the equation

$$\mathrm{d}\mu/\mathrm{d}x = (\mu^{\mathrm{I}} - \mu^{\mathrm{II}})/\delta_{\mathrm{GB}} = 4V_m\gamma/r_1\delta_{\mathrm{GB}}$$

where V_m is the molar volume, γ is the interfacial surface energy and δ_{GB} is the thickness of the grain boundary.

The Einstein equation for the flux of atoms across the interface is

$$J = -(MkT/N)\,\mathrm{d}\mu/\mathrm{d}x$$

and so this may be approximated by the equation

$$J = -(MkT/N)(\mu^{\mathrm{I}} - \mu^{\mathrm{II}})/\delta_{\mathrm{GB}} = -(MkT/N)4\gamma/r_1\delta_{\mathrm{GB}}$$

The mobility, M, is a function of the substance, and obeys an Arrhenius expression $M = M_0 \exp -(\Delta E/RT)$ where ΔE is the energy of transfer across the grain boundary.

Point defects in solids

A crystalline solid is never perfect in that all of the lattice sites are occupied in a regular manner, except, possibly, at the absolute zero of temperature in a perfect crystal. Point defects occur at temperatures above zero, of which the principal two forms are a *vacant* lattice site, and an *interstitial* atom which

occupies a volume between a group of atoms on normal sites. The creation of both of these defects is endothermic, and providing the number in unit volume is small, the energy of creation of each defect can be assumed to require a constant amount of energy. The increase in the number of point defects with increasing temperature is due to the balance between the energy of formation of the defects and the entropy of their formation, which is proportional to the number of defects.

The vacant sites will be distributed among the N_l lattice sites, and the interstitial defects on the N_i interstitial sites in the lattice, leaving a corresponding number of vacancies on the N_l lattice sites. In the case of ionic species, it is necessary to differentiate between cationic sites and anionic sites, because in any particular substance the defects will occur mainly on one of the sublattices that are formed by each of these species. In the case of vacant-site point defects in a metal, Schottky defects, if the number of these is n, the random distribution of the n vacancies on the N_l lattice sites can be achieved in

$$D = \frac{N_l!}{(N_l - n)!n!}$$

distinguishable ways.

Using Stirling's approximation

$$\ln x! = x \ln x - x \text{ (for large numbers)}$$

DropBooks

and the Boltzmann relation between the entropy, S, of a system of particles and this number, which is also the most probable distribution, gives

$$S = k \ln D \text{ where } \ln D = N_l(\ln(N_l/N_l - n) - n \ln(n/N_l - n)$$

and since the crystal was perfectly ordered before the introduction of these point defects, this is also the entropy of formation of n point defects, ΔS_n, usually referred to as the *configurational* entropy, to distinguish it from the thermal entropy arising from heat capacities. If the energy of formation of a single vacancy is E, the Gibbs energy of formation of n defects is

$$\Delta G = nE - T\Delta S_n$$

and since the variation of the Gibbs energy with respect to the number of defects is at a minimum at each temperature T, upon setting the differential of this expression with respect to n equal to zero, the stable value of n defects on the lattice sites at the temperature T, is found to be

$$n = N_l \exp -E/kT \text{ where } n \ll N_l$$

where k is the Boltzmann constant. In a stoichiometric ionic crystal, there will be an equal number of cation vacancies and anion vacancies, the number of each being given by the equation above.

When there are n_i interstitial defects distributed on N_i sites each requiring E_i energy of formation, the equilibrium number of these at temperature T is given by

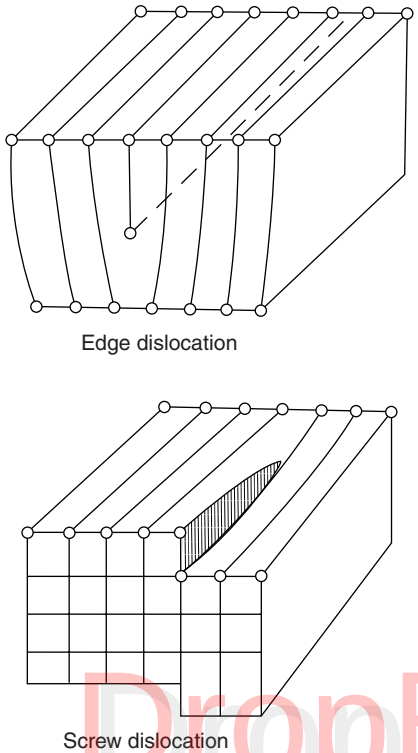
$$n_i = N_l N_i \exp -E_i/2kT$$

The difference between these two equations reflects the fact that a particle on an interstitial site having left a vacant site at which it was originally located in the crystal lattice, there are *two* defects produced in this process. The vacant lattice sites are usually referred to as Schottky–Wagner defects, and the interstitial defect as Frenkel defects. The energy of formation of the Schottky defect is 1–2 eV, and there are usually about 10^{10} per gram-mole at room temperature. All of these point defects play an important part in the migration of atoms within and on the surface of a solid, the mechanism involving the counter-migration of particles and defects. The vacant sites allow the diffusion of atoms within a solid by atom–vacancy site exchange, and the interstitial sites allow rapid transport by the diffusion of atoms from one interstitial site to a neighbouring site.

Edge and screw dislocations

The other major defects in solids occupy much more volume in the lattice of a crystal and are referred to as *line defects*. There are two types of line defects, the edge and screw defects which are also known as *dislocations*. These play an important part, primarily, in the plastic non-Hookeian extension of metals under a tensile stress. This process causes the translation of dislocations in the direction of the plastic extension. Dislocations become mobile in solids at elevated temperatures due to the diffusive place exchange of atoms with vacancies at the core, a process described as dislocation *climb*. The direction of climb is such that the vacancies move along any stress gradient, such as that around an inclusion of oxide in a metal, or when a metal is placed under compression.

The model for the formation of an edge defect consists of the insertion of an extra half-plane of atoms in a crystal, and the screw dislocation is formed by making a cut into the lattice and shearing one–half of the crystal with respect to the other. The introduction of the extra half-plane in creating the edge dislocation results in the volume immediately below the newly inserted plane being in a state of tension, a negative dislocation, and that above the point of entry of the half-plane being in a state of compression, a positive dislocation. The core of the dislocation, at the point where the inserted half-plane ends, will clearly have a strain energy content which is absent in the rest of the normal lattice, since the lattice is in compression on the positive side, and in tension on the other side of the core. Similarly the volume on one side of a screw



DropBooks

Figure 1.12 *The structures of an edge and a screw dislocation*

dislocation will contain strain energy greater than that in the rest of the lattice due to the shear energy generated by the atomic displacements (Figure 1.12).

Dislocations are characterized by the Burgers vector, which is the extra distance covered in traversing a closed loop around the core of the dislocation, compared with the corresponding distance traversed in a normal lattice, and is equal to about one lattice spacing. This circuit is made at right angles to the dislocation core of an edge dislocation, but parallel to the core of a screw dislocation.

In crystal growth, the attachment of atoms to screw dislocations emerging at the free surface is thought to be the most important role of dislocations during this process. The attachment of condensate atoms to the emerging edge of the screw dislocation will continue the propagation of the dislocation through the new film in the form of a helix, and thus the dislocation is always available as an energetically favourable sink for the attachment of new atoms at the surface. This process compares favourably with the addition of atoms to a pre-existing disc-shaped nucleus, since the advance in the area of the disc

leaves a ledged surface on the disc, and the attachment of new atoms can only be made to this surface. The sites on the growing face of an emerging screw dislocation can be referred to as the 'active' sites, and will be found to be very important in a number of heterogeneous gas–solid surface processes.

The interface between the substrate and the fully developed film will be coherent if the conditions of epitaxy are met. If there is a small difference between the lattice parameter of the film material and the substrate, the interface is found to contain a number of equally spaced edge dislocations which tend to eliminate the stress effects arising from the difference in the atomic spacings (Figure 1.13).

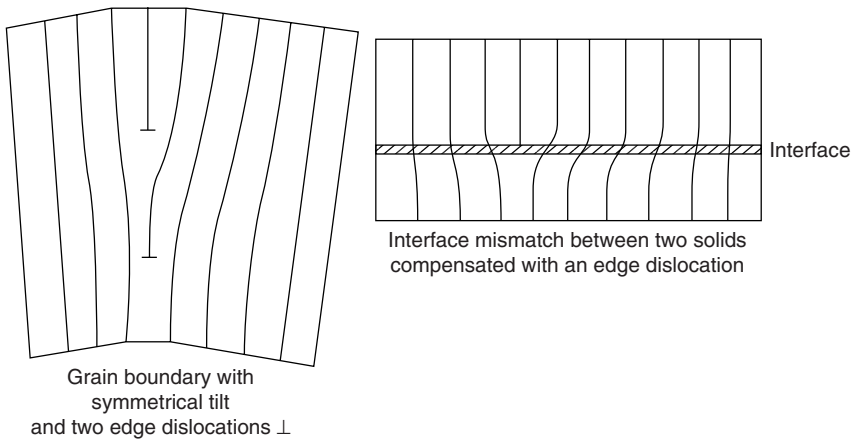


Figure 1.13 *The grain boundary and interface which can be formed between two crystals with the insertion of dislocations. In the grain boundary the two crystals are identical in lattice structure, but there is a difference in lattice parameters in the formation of the interface*

As mentioned earlier, if there is a large disparity in structure at the film–substrate interface, such as a crystalline phase growing on an amorphous, glassy, substrate, the film may detach and grow a separate morphology.

Interfacial energies in solid systems

It is generally observed that the interface between two solids which results from the growth of one phase by condensation to form a film on the other is one in which the number of nearest neighbour bonds between the two phases is maximized. The close-packed planes tend to be found at the interface, which is consequently usually nearly atomically flat and this minimizes the interfacial

energy. The values of interfacial energies between a film and the substrate are very difficult to calculate in solid–solid contacts, but an approximate method is to assume that the dislocation model of grain boundary structure would be equally applicable to the interface.

In this model a grain boundary is assumed to involve the contact between two single crystals with different orientations of the atomic planes at the interface. The atoms in each face are assumed to have their normal spacings as dictated by the bulk lattice parameters, and the mis-match between the two lattices is relieved at the interface by the introduction of edge dislocations. This model of grain boundary structure can be tested, because the grain boundary emerging at a free surface will form a surface groove, the angle of which is determined by equilibrium between the grain boundary energy and the solid–gas interfacial energy at the exposed sides of the groove. The dislocation model predicts a grain boundary energy according to the Read–Shockley equation (1950)

$$\gamma_{GB} = E_0\theta(A_0 - \ln\theta)$$

where $A_0 = 1 + \ln(\mathbf{b}/2\pi r_0)$, $\mathbf{b}$ being the Burgers' vector, r_0 being the radius of the dislocation core, and E_0 is the energy per unit length of the dislocation. The term in $\ln\theta$ accounts for the overlap of the stress fields of the neighbouring dislocations as the angle of tilt increases.

Measurements of the grain boundary energy from the values of the groove angle show that the dislocation model is only adequate at intergranular orientation mismatches of less than about 15°, and at greater inclinations the grain boundary begins to show a constant structure, with an approximately constant grain boundary energy of about 20% of the free surface energy.

In the corresponding model of an interface, when the lattice parameters of the two phases in contact are different, there will be a dis-registry at the interface defined by

$$\delta = \frac{d_\alpha - d_\beta}{d_\alpha} \qquad d_\beta < d_\alpha$$

where d_α and d_β are the interplanar spacings in the direction normal to the interface. The dislocation model then suggests that edge dislocations are inserted at intervals L, where

$$L = \frac{d_\beta}{\delta} = \frac{d_\beta d_\alpha}{d_\alpha - d_\beta}$$

Also according to the corresponding dislocation model of grain boundary energies, the spacing between the edge dislocations, D, required to remove the effects of a tilt angle θ between corresponding planes in grains which

DropBooks

meet at a boundary is given by

$$D = \frac{\mathbf{b}}{\sin\theta}$$

where **b** is the Burgers vector of the dislocation. Putting $\mathbf{b} = d_\alpha$, and equating the two functions for dislocation spacing

$$D\sin\theta = L\frac{d_\alpha - d_\beta}{d_\beta} \cong D\theta \text{ (radians)}$$

An alternative, but to some extent complementary approach to the structure of grain boundaries notes that as the tilt angle between the crystals forming the grain boundary increases, planes of lower atomic concentrations, the high index planes, such as (221), (331) and (115) in the face-centred structure, become parallel to the grain boundary. There is therefore a decrease in the number of metal–metal bonds at the boundary as the tilt angle increases.

This loosening of the local bonding leads to a volume expansion at the boundary, compared with the bulk phase, which becomes larger the larger the tilt angle. This model of the grain boundary thus suggests that it is a volume in which the number of the metal–metal bonds at the interface is less than that in the bulk metal. This model does not exclude the dislocation model, since the core of the dislocation may also be regarded as a volume in which bonds are broken to accommodate the inserted-half plane in the case of the edge dislocation (Wolf and Merkle, 1992).

This model of the structure of the interface leads to an estimate of the factors M_0 and ΔE_{trans} grain boundary motion, since an atom crossing the boundary becomes an adatom on the opposite wall of the boundary, and the energy of detachment of the atom is of the order of the energy of the creation of a vacancy at the surface of the solid. Alternatively, in the dislocation model, this would represent a process of climb of a segment of the dislocation at the interface, into one side of the boundary, the driving force being the greater surface energy of the smaller grain. In both models the activation energy of transfer is about the same as the energy of diffusion of atoms by the atom–vacancy exchange mechanism within the solid. Regarding the pre-exponential as the entropy of mobility divided by R, the gas constant, suggests that the term is related to the probability that an atom will acquire the activation energy when moving in the direction of the wall. This in turn is related to the vibrational frequency of the atoms within the solid, ν, and so

$$\text{Rate of transfer} = \nu P(d/R)\exp -\Delta E_{\text{diff}}/RT$$

where P is the probability that an atom moves in the direction of the interface, a factor roughly equal to the inverse of the number of nearest neighbours times the jump length, d. The Arrhenius energy of activation will be determined by diffusive processes in the grain boundary.

Bibliography

P.W. Atkins. *Physical Chemistry*, A88 (1994) QD 453.2.
J.W. Evans and L.C. de Jonghe. *The Production of Inorganic Materials*, Macmillan, New York (1991) TN665.E94.
O. Kubaschewski, C.B. Alcock and P.J. Spencer. *Materials Thermochemistry*, Pergamon Press. Oxford (1993) QD 511.
D.V. Ragone. *Thermodynamics of Materials*, Vols. I and II, J. Wiley and Sons, New York (1995) TA 418.52.
M. Ohring. *The Materials Science of Thin Films*, Academic Press (1992) TA 418.9.
K.J. Klabunde (ed.). *Thin Films from Free Atoms and Particles*, Academic Press (1985) QC.176.83 T47 (1983).
L. Holland. *Vacuum Deposition of Thin Films*, Chapman and Hall, London (1966) TS 695 H6.
J.P. Hirth and M. Pound. *Condensation and Evaporation*, Pergamon Press New York (1963).
J.M. Howe. *Interfaces in Materials*, J. Wiley and Sons, New York (1997) QC 173.4.I57 H68.
A.V. Goldstein (ed.). *Handbook of Nanomaterials*, Marcel Dekker, New York (1997) TA418.9.
C.B. Alcock, V.P. Itkin and D.M. Horrigan, Vapour pressures of the elements, *Can. Met. Quart.* **23**, 309 (1984).
R. Niedermayer, *Angew. Chem. Int. Ed. Engl.*, **14**, 212 (1975).
G. Gautherin, D. Boucher and C. Schwebel, part 5 in *Thin Films from Free Atoms and Particles*, K.J. Klabunde (ed.). Academic Press (1985).
J. Bohdansky, J. Roth and H.L. Bay, *J. Appl. Phys.* **51**, 2861 (1980).
P. Sigmund, *Phys. Rev.*, **184**, 383 (1969).
M.R. Hoare, *Adv. Chem. Phys.,* **40**, 49 (1979).
S. Ogawa and S. Ino, *J. Crystal Growth*, **13/14**, 48 (1972).
D. Wolfe and K.L. Merkle, *Materials Interfaces*, p. 87, D. Wolf and S. Yip (eds). Chapman and Hall London (1992).
M. Hoare and P. Pal. *J. Crystal Growth*, **17**, 77 (1972).
W. Shockley and W.T. Read, *Phys. Rev.* **78**, 275 (1950).
T. Suntola and J. Hyvarinen, *Ann. Rev. Mater. Sci.,* R.A. Huggins (ed.), **15**, 177 (1985).
A. Usui and H. Watanabe. ibid **21**, 185 (1991).
M. Terrones *et al*., *Topics in Current Chem.,* **199**, 189 (1999).

DropBooks

Appendix. Vapour pressure data for the elements

(Data from Alcock, Itkin and Horrigan (loc.cit.))

$$\log p(\text{atm}) = A + BT^{-1} + C\log T + DT10^{-3}$$

Element	A	B	C	D	Range
Li sol	5.667	−8310			298–m.p.
Li liq	5.055	−8023			m.p.–1000
Na sol	5.298	−5603			298–m.p.
Na liq	4.704	−5377			m.p.–700
K sol	4.961	−4646			298–m.p.
K liq	4.402	−4453			m.p.–600

Element	A	B	C	D	Range
Rb sol	4.857	−4215			298–m.p.
Rb liq	4.312	−4040			m.p.–550
Cs sol	4.711	−3999			298–m.p.
Cs liq	4.165	−3830			m.p.–550
Be sol	8.042	−17 020	−0.4440		298–m.p.
Be liq	5.786	−15 731			m.p.–1800
Mg sol	8.489	−7813	−0.8253		298–m.p.
Ca sol	10.127	−9517	−1.4030		298–m.p.
Sr sol	9.226	−8572	−1.1926		298–m.p.
Ba sol	12.405	−9690	−2.2890		298–m.p.
Ba liq	4.007	−8163			m.p.–1200
Al sol	9.459	−17 342	−0.7927		298–m.p.
Al liq	5.911	−16 211			m.p.–1800
Ga sol	6.657	−14 208			298–m.p.
Ga liq	6.754	−13 984	−0.3413		m.p.–1600
In sol	5.991	−12 548			298–m.p.
In liq	5.374	−12 276			m.p.–1500
Tl sol	5.971	−9447			298–m.p.
Tl liq	5.259	−9037			m.p.–1100
Sn sol	6.036	−15 710			298–m.p.
Sn liq	5.262	−15 332			m.p.–1850
Pb sol	5.643	−10 143			298–m.p.
Pb liq	4.911	−9701			m.p.–1200
Sc sol	6.650	−19 721	0.2885	−0.3663	298–m.p.
Sc liq	5.795	−17 681			m.p.–2000
Y sol	9.735	−22 306	−0.8705		298–m.p.
Y liq	5.795	−20 341			m.p.–2300
La sol	7.463	−22 551	−0.3142		298–m.p.
La liq	5.911	−21 855			m.p.–2450
Ti sol	11.925	−24 991	−1.3376		298–m.p.
Ti liq	6.358	−22 747			m.p.–2400
Zr sol	10.008	−31 512	−0.7890		298–m.p.
Zr liq	6.806	−30 295			m.p.–2500
Hf sol	9.445	−32 482	−0.6735		298–m.p.
V sol	9.744	−27 132	−0.5501		298–m.p.
V liq	6.929	−25 011			m.p.–2500
Nb sol	8.822	−37 818	−0.275		298–2500
Ta sol	16.807	−41 346	−3.2152	0.7437	298–2500
Cr sol	6.800	−20 733	0.4391	−0.4094	298–2000

Element	A	B	C	D	Range
Mo sol	11.529	−34 626	−1.1331		298–2500
W sol	2.945	−44 094	1.3677		298–2350
W liq	54.527	−57 687	−12.2231		2200–2500
Mn sol	12.805	−15 097	−1.7896		298–m.p.
Re sol	11.543	−40 726	−1.1629		298–2500
Fe sol	7.100	−21 723	0.4536	−0.5846	298–m.p.
Fe liq	6.347	−19 574			m.p.–2100
Ru sol	9.755	−34 154	−0.4723		298–m.p.
Os sol	9.419	−41 198	−0.3896		298–2500
Co sol	10.976	−22 576	−1.0280		298–m.p.
Co liq	6.488	−20 578			m.p.–2150
Rh sol	10.168	−29 010	−0.7068		298–m.p.
Rh liq	6.802	−26 792			m.p.–2500
Ir sol	10.506	−35 099	−0.7500		298–2500
Ni sol	10.557	−22 606	−0.8717		298–m.p.
Ni liq	6.666	−20 765			m.p.–2150
Pd sol	9.502	−19 813	−0.9258		298–m.p.
Pd liq	5.426	−17 899			m.p.–2100
Pt sol	4.882	−29 387	1.1039	−0.4527	298–m.p.
Pt liq	6.386	−26 856			m.p.–2500
Cu sol	9.123	−17 748	−0.7317		298–m.p.
Cu liq	5.849	−16 415			m.p.–1850
Ag sol	9.127	−14 999	−0.7845		298–m.p.
Ag liq	5.752	−13 827			m.p.–1600
Au sol	9.152	−19 343	−0.7479		298–m.p.
Au liq	5.832	−18 024			m.p.–2050
Zn sol	6.102	−6776			298–m.p.
Zn liq	5.378	−6286			m.p.–750
Cd sol	5.939	−5799			298–m.p.
Cd liq	5.242	−5392			m.p.–650
Hg liq	5.116	−3190			298–400
Ce sol	6.139	−21 752			298.–m.p.
Ce liq	5.611	−21 200			m.p.–2450
Pr sol	8.859	−18 720	−0.9512		298–m.p.
Pr liq	4.772	−17 315			m.p.–2200
Nd sol	8.996	−17 264	−0.9519		298–m.p.
Nd liq	4.912	−15 824			m.p.–2000
Sm sol	9.988	−11 034	−1.3287		298–m.p.
Eu sol	9.240	−9459	−1.1661		298–m.p.

DropBooks

Element	A	B	C	D	Range
Gd sol	8.344	−20 861	−0.5775		298–m.p.
Gd liq	5.557	−19 389			m.p.–2250
Tb sol	9.510	−20 457	−0.9247		298–m.p.
Tb liq	5.411	−18 639			m.p.–2200
Dy sol	9.579	−15 336	−1.1114		298–m.p.
Ho sol	9.785	−15 899	−1.1753		298–m.p.
Er sol	9.916	−16 642	−1.2154		298–m.p.
Er liq	4.688	−14 380			m.p.–1900
Tm sol	8.882	−12 270	−0.9564		298–1400
Yb sol	9.111	−8111	−1.0849		298–900
Lu sol	8.793	−22 423	−0.6200		298–m.p.
Lu liq	5.648	−20 302			m.p.–2350
Th sol	8.668	−31 483	−0.5288		298–m.p.
Th liq	−18.453	−24 569	6.6473		m.p.–2500
Pa sol	10.552	−34 869	−1.0075		298–m.p.
Pa liq	6.177	−32 874			m.p.–2500
U sol	0.770	−27 729	2.6982	−1.5471	298–m.p.
U liq	20.735	−28 776	−4.0962		m.p.–2500
Np sol	19.643	−24 886	−3.9991		298–m.p.
Np liq	10.076	−23 378	−1.3250		m.p.–2500
Pu sol	26.160	−19 162	−6.6675		298–600
Pu sol	18.858	−18 460	−4.4720		500–m.p
Pu liq	3.666	−16 658			m.p.–2450
Am sol	11.311	−15 059	−1.3449		298–m.p.
Cm sol	8.369	−20 364	−0.5770		298–m.p.
Cm liq	5.223	−18 292			m.p.–2200

Chapter 2

Gaseous reaction kinetics and molecular decomposition

Theories of reaction kinetics

The kinetics of reaction in the gaseous state has been studied mainly with a view to elucidating the atomic and molecular processes which are involved in chemical change. There are two alternative procedures for doing this, in one, the classical approach relates chemical change to the kinetic energies of colliding molecules, the decomposition of which leads to the reaction products, and the other, the *transition state* theory, assumes the existence of an equilibrium between the reactants and an intermediate species which decomposes to form the reaction products. Whereas the interpretation using the classical theory is conceptually simple, the transition state theory requires the calculation of the stability of the *intermediate* species, which does not occur as a separate species, and hence for which there are no thermodynamic data. This task has only become possible with the advent of the digital computer, excepting for molecules of the simplest kind, e.g. in the exchange reaction between the isotopic species of hydrogen, H_2 and D_2

DropBooks

$$H_2 + D_2 = \begin{array}{c} H - H \\ | \quad | \\ D - D \end{array} = 2HD$$

with the intermediate species H_2D_2. It will be seen that the complete understanding of chemical reactions at the molecular level requires information about the various energy states, kinetic, rotational and vibrational as well as the dissociation energies to the chosen reacting and reaction products. All of these states can be described by an approximate application of the quantum theory using data derived from spectroscopic studies in the complete range of spectral energies, the infra-red, visible and ultra-violet regions.

In many gaseous state reactions of technological importance, short-lived intermediate molecules which are formed by the decomposition of reacting species play a significant role in the reaction kinetics. Thus reactions involving the methane molecule, CH_4, show the presence of a well-defined dissociation product, CH_3, the methyl *radical*, which has a finite lifetime as a separate entity and which plays an important part in a sequence or 'chain' of chemical reactions.

The deposition of thin films may be achieved by the dissociation of molecules in the gaseous state which are in contact with a cool or a heated substrate as well as by the vacuum technique previously described. The dissociation is brought about either by the use of high temperature or by the use of intense sources of radiation such as laser beams or by collision with energetic ions and electrons in plasma discharges. The energies of dissociation are obtained from thermodynamic data for the formation of molecules, and the rates of deposition from the mechanisms and kinetics of the dissociative reactions, together with cross-sectional data of molecules interacting with radiation, ions or electrons.

Thermal energies and the structures of molecules

The relationship between the thermal energies of molecules and their molecular structures, which determine the conditions for decomposition, can be analysed approximately by the use of the following simplified quantum theory of molecular structure. This shows that the energy levels of molecules are separated by specific amounts, or *quanta*, of energy depending on the molecular structure and the chemical bonding. The path of decomposition of a molecule is determined by the absorption of energy from the surroundings, and by any ancillary chemical reaction which can be applied to change the reaction energetics.

The energy levels of a molecule include:

1. Translational energy, which may be directly calculated from the classical kinetic theory of gases since the spacings of these quantized energy levels are so small as to be negligible. The Maxwell–Boltzmann distribution for the kinetic energies of molecules in a gas, which is based on the assumption that the velocity spectrum is continuous is, in differential form,

$$\mathrm{d}n = \frac{2\pi n}{(\pi kT)^{3/2}} \mathrm{e}^{-\frac{\varepsilon}{kT}} \varepsilon^{1/2} \mathrm{d}\varepsilon$$

where

$$(1/2)m\overline{c}^2 = \varepsilon$$

for n molecules, leading to the equipartition law

$$E_{\mathrm{kin}} = (3/2)NkT \ \mathrm{mol}^{-1}$$

2. Rotational energy, which, as its name implies, is the energy a molecule contains by virtue of rotations around the centre of mass. These energy levels are quite narrowly spaced from the energetic point of view, but they

are larger than the translational level spacings, and so must be treated using quantum theory. The rotational energy levels are described by the equation

$$E_{\text{rot}} = \frac{h^2}{8\pi^2 I} J(J+1)$$

where I is the moment of inertia of the molecule, and J is a quantum number which takes all integral values from one upwards.

3. Vibrational energy, which is associated with the alternate extension and compression of the chemical bonds. For small displacements from the low-temperature equilibrium distance, the vibrational properties are those of simple harmonic motion, but at higher levels of vibrational energy, an *anharmonic* effect appears which plays an important role in the way in which atoms separate from the molecule. The vibrational energy of a molecule is described in the quantum theory by the equation

$$E_{\text{vib}} = (v + 1/2)h\nu_e$$

where v is an integral quantum number, and ν_e is the fundamental frequency of vibration of the molecule for small displacements. At large displacements the anharmonicity term must be included according to the equation

$$E = (v + 1/2)h\nu_e - (v + 1/2)^2 hA\nu_e$$

where A is the anharmonicity constant. The presence of the anharmonicity constant leads to molecular decomposition at large internuclear distances. An empirical curve-fitting equation for the variation of the energy of a diatomic molecule as a function of the internuclear distance is the Morse equation:

$$E(r) = D_e(1 - \exp[-A(r - r_0)])^2$$

where D_e is the dissociation energy plus the vibrational energy at the absolute zero of temperature, where v equals zero, the so-called 'zero point energy', E_0

$$D_e = D + E_0$$

$$A = \nu_0 \sqrt{(2\pi^2 \mu D_e)}$$

D is the chemical energy of dissociation which can be obtained from thermodynamic data, and μ is the reduced mass of the diatomic molecule

$$1/\mu = 1/m_A + 1/m_B$$

in the AB molecule. The zero point energy can be described as arising from the uncertainty of position of the bonded atoms, and hence of the bond length, at the absolute zero of temperature.

DropBooks

Experimental information about the energy levels of molecules is obtained from spectroscopic studies, in the infra-red for the rotational states and in the ultra-violet for the vibrational and most of the dissociation energies. Some thermodynamic data are also obtained for the dissociation energies using mass spectroscopy.

The collision theory of gaseous reactions

The science of reaction kinetics between molecular species in a homogeneous gas phase was one of the earliest fields to be developed, and a quantitative calculation of the rates of chemical reactions was considerably advanced by the development of the collision theory of gases. According to this approach the rate at which the classic reaction

$$H_2 + I_2 \longrightarrow 2HI$$

proceeded, which was measured by the rate of formation of the product species, HI, was proportional to a rate constant and the concentrations of the reacting gases

$$\frac{\mathrm{d}p_{\mathrm{HI}}^2}{\mathrm{d}t} = k p\mathrm{H}_2\, p\mathrm{I}_2$$

The reaction constant k was related to a *collision* number Z, the number of reactant molecules colliding/unit time, and an activation energy E by the Arrhenius equation

$$k = Z\exp(-E/RT)$$

where R is the gas constant, and T the absolute temperature. The activation energy is envisaged in this collision theory as the critical collision energy between molecules which must be achieved to bring about reaction. It might also be characterized as indicating the number of molecules in the high-energy tail of the Maxwell distribution which have sufficient kinetic energy to convert to potential energy at the point of collision, leading to favourable conditions for bond breaking and reforming into the most thermodynamically stable configuration. These 'hot' molecules behave in the same way as the average molecules would behave at a higher temperature. The collision number can be derived from the classical kinetic theory of gases where σ_{AB} is the collision cross-section of A and B atoms or molecules having masses m_A and m_B and concentrations n_A and n_B atoms or molecules/unit volume respectively.

$$Z = \sigma_{AB}^2 \left[8\pi kT\frac{m_A + m_B}{m_A m_B}\right]^{1/2} n_A n_B$$

A typical value of the collision number is $10^{30}s^{-1}$ in gases at one atmosphere pressure and room temperature, and the number of successful collisions which can bring about the chemical reaction is equal to this number multiplied by the Arrhenius or probability factor, $\exp(-E/RT)$, where E is the activation energy, the critical collision energy needed for reaction to occur.

From experimental studies of gaseous reactions, the activation energy, which is obtained from a plot of $\log k$ vs $1/T$, is found to be in the range 80–200 kJ. If we assume, following Goodeve (1948), that a reaction is just measurable when 10^{13} molecules undergo change per second, and too fast to measure at 10^{17} molecules per second, the data in Table 2.1 can be used to estimate the temperature range over which chemical reaction is rate-determining as a function of the activation energy and temperature when multiplied by the collision number.

Table 2.1 *Values of* $\exp(-E/RT)$ *as a function of temperature*

Temperature °C	Tempered activation energy			
	$10\,000^T$	$20\,000^T$	$30\,000^T$	$40\,000^T$
200	6.58×10^{-10}	4.33×10^{-19}	2.85×10^{-28}	1.88×10^{-37}
400	3.52×10^{-7}	1.24×10^{-13}	4.37×10^{-20}	1.54×10^{-26}
600	1.06×10^{-5}	1.12×10^{-10}	1.19×10^{-15}	1.26×10^{-20}
800	8.96×10^{-5}	8.04×10^{-9}	7.20×10^{-13}	6.46×10^{-17}
1000	3.88×10^{-4}	1.50×10^{-7}	5.82×10^{-11}	2.26×10^{-14}
1200	1.13×10^{-3}	1.27×10^{-6}	1.43×10^{-9}	1.61×10^{-12}
1400	2.54×10^{-3}	6.43×10^{-6}	1.63×10^{-8}	4.13×10^{-11}

N.B. A typical range of values of Z is 10^{28}–10^{31} collisions $s^{-1}\,cm^{-3}$, for gas pressures between 10^{-3} and 1 atmosphere, and for one g-mole of gas.
The 'Tempered activation energy', is the activation energy divided by R, the gas constant, and is dimensionless. It will be shown here with a superscript T, e.g. $10\,000^T$.
A reaction with an activation energy of 100 kJ will occur at too high a rate to be measurable at 500 K, one with 200 kJ will be measurable in the temperature range around 800 K, with 300 kJ at temperatures around 1000 K, and finally a reaction having an activation energy of 400 kJ or more will become measurable above 1300 K.

DropBooks

The gaseous reaction

$$H_2 + I_2 \longrightarrow 2HI$$

has its counterpart in the reverse direction

$$2HI \longrightarrow H_2 + I_2$$

and clearly thermodynamic equilibrium is achieved when the rates of reaction are the same in both directions:

$$\text{forward rate} = k_F\, pH_2\, pI_2$$

$$\text{reverse rate} = k_R\, p^2HI$$

when $k_F\, p\mathrm{H_2}\, p\mathrm{I_2} = k_R\, p^2\mathrm{HI}$

$$K_{\text{equilibrium}} = \frac{k_F}{k_R} = \frac{p^2\mathrm{HI}}{p\mathrm{H_2}\, p\mathrm{I_2}}$$

which provides a link with classical thermodynamics. This link is most clearly utilized in the 'transition state theory' of chemical reactions.

Transition state theory of gaseous reactions

A more general, and for the moment, less detailed description of the progress of chemical reactions, was developed in the transition state theory of kinetics. This approach considers the reacting molecules at the point of collision to form a complex intermediate molecule before the final products are formed. This molecular species is assumed to be in thermodynamic equilibrium with the reactant species. An equilibrium constant can therefore be described for the activation process, and this, in turn, can be related to a Gibbs energy of activation:

$$\mathrm{H_2} + \mathrm{I_2} = \mathrm{H_2I_2}$$

$$K_F = \frac{p\mathrm{H_2I_2}}{p\mathrm{H_2}\, p\mathrm{I_2}} = \exp - \left(-\frac{\Delta G_F^\circ}{RT}\right)$$

By the usual thermodynamic relationships

$$\Delta G_F^* = \Delta H_F^* - T\Delta S_F^*$$

where ΔH_F^* and ΔS_F^* are now the enthalpy and entropy of activation respectively. The reverse reaction can similarly be described by

$$K_R = \frac{p\mathrm{H_2I_2}}{p^2\mathrm{HI}} = \exp\left(-\frac{\Delta G_R^*}{RT}\right); \quad \Delta G_R^* = \Delta H_R^* - T\Delta S_R^*$$

Finally the link with equilibrium can be made through the relationship

$$\Delta G^\circ_{\text{equilibrium}} = \Delta G_R^* - \Delta G_F^*$$

and similarly for ΔH^* and ΔS^*. These equilibrium states must be present at all times, but there must be a rate factor which determines the relative forward and backward rates of the kinetic process. For homogeneous gaseous reactions, this factor is taken to be a constant of value kT/h. The reason for this choice is to be found in the quantum statistics of molecular vibrations, and this constant is related to the, assumed, vibrational properties of the transition state molecule.

It is clear by comparing the transition state theory with the collision model that the corresponding entropy of activation can be calculated from the value

for the collision theory constant, once the energy of activation has been obtained. The statistical mechanical treatment of equilibria uses the *partition functions* of molecules, and in the simple case of an equilibrium constant for the formation of a diatomic species from two atomic species

$$\mathrm{A} + \mathrm{B} \longrightarrow \mathrm{AB}$$

the constant is defined by

$$K = \frac{PF_{AB}}{PF_A PF_B} \exp\left(-\frac{\Delta E_0^\circ}{RT}\right)$$

where PF is the total partition function and ΔE_0° is the energy of formation of the molecule AB at the absolute zero of temperature.

The total partition function may be approximated to the product of the partition function for each contribution to the heat capacity, that from the translational energy for atomic species, and translation plus rotation plus vibration for the diatomic and more complex species. Defining the partition function, PF, through the equation

$$PF = \sum_i \exp\left(-\frac{\varepsilon_i}{kT}\right)$$

where ε_i are the quantized energy levels, and using the quantum results, if we omit any vibrational partition function contribution the product of the translational and rotational functions yields

$$PF_{\text{trans}} = \frac{(2\pi mkT)^{3/2}}{h^3} \text{ in three dimensions}$$

and

$$PF_{\text{rotation}} = \frac{8\pi^2 IkT}{h^2}$$

where I is the moment of inertia of the molecular species.

$$I = \sigma^2 \frac{m_A m_B}{m_A + m_B}$$

The equilibrium constant in terms of the partition function is,

$$K^* = \frac{(2\pi(m_A + m_B)kT)^{3/2}}{(2\pi m_A kT)^{3/2}(2\pi m_B kT)^{3/2}} h^3 8\pi\sigma_{AB}^2 \left(\frac{m_A m_B}{m_A + m_B}\right) \exp\left(-\frac{\Delta E_0^\circ}{kT}\right)$$

if we omit any vibrational partition function contribution. The right-hand side of this equation becomes identical with the collision theory expression for the

DropBooks

reaction constant

$$k = Z \exp\left(\frac{-\Delta E}{RT}\right)$$

after multiplication by kT/h.

This factor can be obtained from the vibration partition function which was omitted from the expression for the equilibrium constant stated above and is, for one degree of vibrational freedom where υ_0 is the vibrational frequency in the lowest energy state.

$$PF_{\text{vibration}} = \left(1 - \exp\left(-\frac{h\nu_0}{kT}\right)\right)^{-1}$$

If $h\upsilon_0$ is small compared with kT, the partition function becomes $kT/h\upsilon_0$. The function kT/h which pre-multiplies the collision number in the transition state theory of the bimolecular collision reaction can therefore be described as resulting from vibration of frequency ν_0 along the transition bond between the A and B atoms, and measures the time between each potential transition from reactants to product which will only occur provided that the activation energy, ΔE_0° is available.

Empirical estimates of the activation energy

Approximate calculations of this activation energy have been made in a number of examples using the quantum theory of molecular binding, by making assumptions concerning the structure and partition functions of the transition state molecule.

The entropy of activation may be estimated from experimental data for gaseous molecules, and in the special case of HI formation, which may be regarded as involving the intermediate formation of the dimer H_2I_2, using the general empirical relationship

$$S^\circ(\text{dimer})/S^\circ(\text{monomer}) = 1.52 \pm 0.05 \quad \text{J mol}^{-1}\,\text{K}^{-1}$$

This yields a value of the entropy of formation of the transition state molecule

$$\begin{aligned}\Delta S^* &= 313[1.52(S^\circ_{298}\text{HI})] - 130.6(S^\circ_{298}\text{H}_2) - 260.6(S^\circ_{298}\text{I}_2)\\ &= -77.2 \quad \text{J mol}^{-1}\,\text{K}^{-1}\end{aligned}$$

An estimate of the enthalpy change which corresponds to the activation energy of the collision theory analysis of $167\,\text{kJ mol}^{-1}$ may be made by assuming that the formation of the dimer from two molecules of the monomer is energetically equivalent to the dipole–dipole and dispersion interactions of two HI molecules. These exothermic sources of interaction are counterbalanced

to a small extent by the rotational energy of the transition state molecule. This procedure would require an estimate of the intermolecular distance between the two reacting molecules in the transition state. A simpler, more empirical, procedure suggests that the activation energy of this reaction may be obtained by using the equation

$$\Delta H^* = 1/4[\Delta H^\circ_0(\mathrm{H_2}) + \Delta H^\circ_0(\mathrm{I_2})] = 136\,\mathrm{kJ\,mol^{-1}}$$

where the heats of formation of the reactants, in this case, are also close to the dissociation energies of the reactants (Glasstone, Laidler and Eyring, 1941). The fact that the observed activation energy is higher than this value probably results from the fact that the transition state molecule is not an equilibrium entity, but is a molecule in an energy level probably well above the ground state.

Another empirical equation due to Semenov relates the activation energy to the formation energy of the product molecule reaction ΔH°_{298}. For two gram-molecules of HI this is 600 kJ, and substituting in the equation

$$E_{\mathrm{act}} = 48.1 + 0.25\Delta H^\circ_{298}$$

for the HI reaction this would be 48.1 + 149 or 197 kJ, which *overestimates* the activation energy. It appears that these two approaches serve as lower and upper bounds respectively, and the activation energy lies approximately at the average.

DropBooks

The order of chemical reactions

Reactions involving collisions between two molecular species such as H_2 and I_2, or between two HI molecules are called *bimolecular* or second-order homogeneous reactions, because they involve the collision between two molecular species, and they are homogeneous since they occur in a single gas phase. The rates of these reactions are dependent on the product of the partial pressure of each reactant, as discussed above, and for the formation of HI, and the decomposition of HI,

$$-\frac{\mathrm{d}\,p\mathrm{HI}}{\mathrm{d}t} = k p^2\mathrm{HI}$$

$$\frac{\mathrm{d}\,p\mathrm{HI}}{\mathrm{d}t} = k p\mathrm{H_2}\, p\mathrm{I_2}$$

Unimolecular and *trimolecular* or first and third-order reactions are also known, but these are less frequent in occurrence than bimolecular reactions.

Examples of each of the three orders of gaseous reaction are:

First order: $2\mathrm{N_2O_5} \longrightarrow 4\mathrm{NO_2} + \mathrm{O_2}$ where $-\mathrm{d}\dfrac{[\mathrm{N_2O_5}]}{\mathrm{d}t} = k[\mathrm{N_2O_5}]$

[X] is a commonly-used shorthand notation for pX.

$$\frac{\mathrm{d}[NO_2]}{\mathrm{d}t} = 2k[N_2O_5]$$

since two molecule of NO_2 are formed by the decomposition of each N_2O_5 molecule.

It also follows that

$$\frac{\mathrm{d}[O_2]}{\mathrm{d}t} = (1/2)k[N_2O_5]$$

The classical example of a second-order reaction is the formation of HI(g) which was discussed above for which the reaction rate is given by

$$\text{second order } \frac{\mathrm{d}[HI]}{\mathrm{d}t} = k[H_2][I_2]$$

An example of a third-order reaction is the formation of nitrogen oxy-chloride according to the reaction

$$2NO + Cl_2 \longrightarrow 2NOCl$$

$$\text{third order: } -\frac{\mathrm{d}[NO]}{\mathrm{d}t} = k[NO]^2[Cl_2]$$

In these equations the minus sign always indicates a partial pressure which decreases in time, i.e. the partial pressure is that of a reactant.

In all of these expressions the order appears to be related to the number of molecules involved in the original collision which brings about the chemical change. For instance, it is clear that the bimolecular reaction involves the collision between two reactant molecules, which leads to the formation of product species, but the interpretation of the first and third-order reactions cannot be so simple, since the absence of the role of collisions in the first order, and the rare occurrence of three-body collisions are implied.

An explanation which is advanced for these reactions is that some molecules collide, but do not immediately separate, and form dimers of the reactant species which have a long lifetime when compared with the period of vibration of molecules, which is about 10^{-11} seconds. In the first-order reaction, the rate of the reaction is therefore determined by the rate of break-up of these dimers. In the third-order reaction, the highly improbable event of a three-body collision which leads to the formation of the products, is replaced by collisions between dimers of relatively long lifetime with single reactant molecules which lead to the formation of product molecules.

An alternative explanation which has been advanced for the first-order reaction is that one molecule is activated during a bimolecular collision, and can retain the activation energy until it finally decomposes some time after the

original collision. Both the dimerization and the long-term activation of a single molecule would conform to the experimentally observed effect that a reduction of the total pressure leads to the order of the reaction changing to the usual bimolecular kinetics.

Time dependence of the extent of reaction

When a unimolecular reaction occurs with an initial product partial pressure of the reactant A, to yield an amount of the product, x, the first-order reaction rate equation reads

$$dx/dt = k_r(A - x)$$

which in the integrated form is

$$\ln A/(A - x) = k_r t$$

$$x = A(1 - \exp(k_r t))$$

This equation demonstrates the exponential decay of the rate of formation of products in a first-order reaction with time. When

$$x = A/2; \quad t_{0.5} = \ln 2/k_r$$

where $t_{0.5}$ is the *half-life*, which is the time when the reaction is half completed.

A similar treatment for a bimolecular reaction

$$dx/dt = k_2(A - x)(B - x)$$

where A and B are the initial partial pressures of the two reactants, yields a half-life given by

$$t_{0.5} = 1/k_2 A$$

when $A = B$.

Chain reactions

The time dependence of the reaction

$$H_2 + Br_2 \longrightarrow 2HBr$$

was found to be very much more complicated than that for the simple bimolecular reaction of hydrogen and iodine. The experimentally determined rate equation is

$$\frac{d[HBr]}{dt} = k\frac{[H_2][Br_2]^{1/2}}{\left(m + \dfrac{[HBr]}{[Br_2]}\right)}$$

DropBooks

where k and m are constants. The time dependence of the rate of formation of HBr was explained by the intermediate formation of hydrogen atoms resulting from bimolecular collisions and from the thermal dissociation of bromine molecules to bromine atoms.

There are a number of processes contributing to the reaction rate which lead to the formation of atomic species, and these are

	$Br_2 \longrightarrow 2Br$	Thermal dissociation	k_1
	$Br + H_2 \longrightarrow HBr + H$	Chain propagation (a relatively slow, endothermic reaction)	k_2
	$H + Br_2 \longrightarrow HBr + Br$	Chain propagation (rapid)	k_3
	$H + HBr \longrightarrow H_2 + Br$	Chain inhibition (rapid, but destroying product molecules)	k_4
and	$2Br \longrightarrow Br_2$	Chain termination	k_5

Collecting all of the rate expressions for these five reactions to yield one equation for the formation of HBr it was found that the reaction rate could be described by

$$\frac{d[HBr]}{dt} = \frac{k_1^{1/2} k_2 k_3 k_4^{-1} k_5^{-1/2} [H_2][Br_2]^{1/2}}{k_3 k_4^{-1} + \dfrac{[HBr]}{[Br_2]}} \qquad \text{(A)}$$

which identifies the values of k and m in the general equation given above. The equation (A) may be decomposed thus

$$[Br] = \left(\frac{k_1}{k_5}[Br_2]\right)^{1/2}; \quad [H] = \frac{k_2 \left(\dfrac{k_1}{k_5}\right)^{1/2} [H_2][Br_2]^{1/2}}{k_3[Br_2] + k_4[HBr]}$$

and these expressions yield the equation

$$\frac{d[HBr]}{dt} = k_2[Br][H_2] + k_3[H][Br_2] - k_4[H][HBr]$$

Combustion chain reactions

The conversion of chemical energy by oxidative processes at high temperatures is a major source of heat for many industrial processes and, on a more sophisticated plane, for the propulsion of aircraft and advanced rockets, such as the Shuttle. The generation of high temperatures by these reactions

involves the burning of carbon as coal, or hydrogen and hydrocarbons as natural gas or fuel oil. Except in special circumstances, such as rocket propulsion, air is the source of oxygen, the nitrogen acting as an inert thermal reservoir excepting when oxides of nitrogen, NO_x are formed. The natural sources such as coal and natural gas, usually contain a small percentage of sulphur-containing compounds, such as FeS_2 and H_2S, which form a mixture of sulphur oxides, usually denoted as SO_x, in the combustion chamber. NO_x and SO_x are the major pollution problems arising from these oxidation energy sources.

Proposed mechanisms for the gaseous combustion processes which involve a series of chain reactions such as those for the oxidation of hydrogen to form water vapour,

$$\begin{aligned} H_2 + O_2 &\longrightarrow H_2O_2 \longrightarrow 2OH \\ &\longrightarrow HO_2 + H \\ OH + H_2 &\longrightarrow H + H_2O \\ H + O_2 &\longrightarrow O + OH \quad \text{(branching)} \\ O + H_2 &\longrightarrow H + OH \quad \text{(branching)} \\ 2OH &\longrightarrow H_2O + O \end{aligned}$$

DropBooks

and so on, have been elaborated to explain the propagation of chain mechanisms in this reaction. The reactions marked 'branching' produce more radicals than are consumed, and it is these processes which can lead to a rapid increase in the concentrations of radicals and eventually an explosive reaction rate.

The oxidation of hydrocarbons involves the sequential formation of a number of similar reactions in which various intermediate radicals which are combinations of carbon, hydrogen and oxygen are formed. In the simplest case, the oxidation of methane, the methyl radical CH_3 plays an important part both in direct oxidation to CO(g) and in indirect oxidation through the formation of higher hydrocarbons such as C_2H_6 before CO is formed. The chain reactions include

$$\begin{aligned} CH_4 + H &\longrightarrow CH_3 + H_2 \\ CH_3 + O &\longrightarrow HCHO \quad \text{(formaldehyde)} \\ HCHO + H &\longrightarrow CHO + H_2 \\ CHO + H &\longrightarrow CO + H_2 \\ CHO + O_2 &\longrightarrow CO + OH + O \end{aligned}$$

or this radical may produce further radicals by thermal decomposition

$$CHO \longrightarrow CO + H$$

There are also branching processes in this system such as those found in hydrogen oxidation, e.g.

$$H_2 + O \longrightarrow H + OH$$

The alternative route in the oxidation of methane, with C_2H_6 formation, follows a similar path with the intermediate formation of CH_3 by thermal decomposition and CHO radicals before CO is formed.

The final step of the oxidation process is the formation of CO_2, and this also occurs by a number of chain sequences such as

$$CO + O_2 \longrightarrow CO_2 + O$$

and

$$CO + OH \longrightarrow CO_2 + H$$

The latter reaction only occurs in the presence of water vapour, which increases the rate of oxidation markedly.

A feature of chain reactions where branching occurs is the extreme reaction rate which is termed an *explosion*. The origin of this rate is in the branching processes, and there exist pressure limits for a given reaction above and below which explosive rates do not occur. Below the lower explosion limit the chain reaction is limited by the destruction of radicals which diffuse to the walls of the container without reaction. This view is substantiated by the fact that the lower limit is raised as the containing vessel diameter is decreased. Above the upper limit chain-terminating reactions with neutral molecules constrain the branching processes. These neutral molecules which can be foreign to the reaction, such as argon, also inhibit the diffusion of the radicals to the walls of the container (Figure 2.1).

This type of explosive behaviour is not to be confused with explosions such as that of gunpowder, where the explosion is caused by the extremely rapid expansion of the gases which are liberated by chemical reaction with a large release of heat.

Confirmation of the formation of the radicals during combustion reactions has been made by introducing a sample of the flames into a mass spectrometer. The sample is withdrawn from a turbulent flame which is formed into a thin column, by admitting a sample of the flame to the spectrometer through a pinhole orifice, usually of diameter a few tenths of a millimetre. An alternative procedure which has been successful in identifying the presence of radicals, such as CHO, has been the use of laser-induced fluorescence.

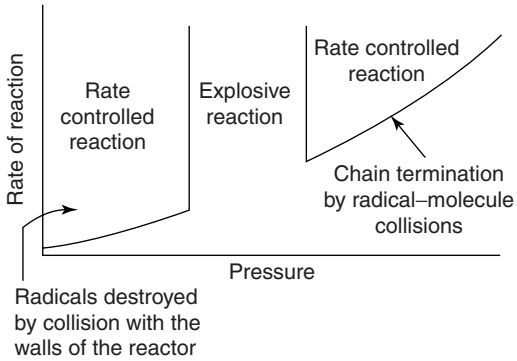


Figure 2.1 *The lower and upper limits of an explosive chain reaction as a function of temperature and pressure.*

Another important diagnostic for the existence of a chain reaction is, as might be expected, the fact that the reaction is slowed down when the reaction vessel is partially filled with an inert material having a large surface area. This is probably due to the recombination of radicals which are chemisorbed on the new surface, a process which also occurs on the walls of the vessel, thus terminating their further role in the chain reaction. Conversely, some substances may be used as coatings on the walls of a reactor in which a chain reaction is occurring which reflect the radicals back into the reaction volume, sustaining the reaction. Examples of such materials are to be found among the iodides of the alkali metals, such as KI.

DropBooks

The individual steps in chain reactions involving radicals are characteristically of small activation energy, between about 10 and 50 kJ mol^{-1}, and so these reactions should occur at an immeasurably high rate at temperatures above 500 K (see Table 2.1), which is a low temperature for a useful combustion process. The overall rate of the process will therefore depend mainly on the concentrations of the radicals.

Chain reactions in the combustion of gaseous fuels

Domestic heat sources make use of mixtures of gaseous fuels, such as natural gas, which is principally methane, with air, or mixtures of oil droplets with air. In internal combustion engines the fuel is a mixture of relatively long chain hydrocarbons which are derived by refining from oil. All of these fuels in the vapour state undergo chain reactions similar to those which occur in the oxidation of methane, although a new type of reaction involving the attachment of an oxygen molecule to a hydrocarbon radical to form a peroxy molecule leads to the subsequent formation of a number of organic products, such

as ketones, aldehydes and carboxylic acids. For example, the oxidation of n-heptane (C_7H_{16}) involves the formation of a peroxy compound which removes a hydrogen atom from the hydrocarbon chain, leaving one carbon atom with an unused bond. This radical can then capture another oxygen molecule to form another peroxy group.

$$\begin{aligned} CH_3(CH_2)_5CH_3 &\longrightarrow CH_3CH(CH_2)_4CH_3 + H + O_2 \\ &\longrightarrow CH_3CHOOHCH(CH_2)_3CH_3 + O_2 \\ &\longrightarrow CH_3CHOOHCHOO(CH_2)_3CH_3 \\ &\longrightarrow (CH_3)_2CO, CO, OH \ \& \ C_3H_7 \end{aligned}$$

The formation of the hydrocarbon radical with the release of a hydrogen atom is a common feature in these chain reactions.

The performance of automobile engines in which a pure hydrocarbon is used as the fuel is limited by engine 'knock' which appears to be due to limited explosive reactions occurring at the end of the compression cycle, and after the normal flame of combustion has propagated through most of the compression chamber volume. It is believed that this phenomenon arises because heat which is transmitted from the laminar flame front to the unburnt gases, causes an increase in pressure as well as temperature in the residual volume, and thus bringing about the conditions for explosive reaction rates. The introduction of metal alkyls such as lead tetra-ethyl was widely made to suppress engine knock, and it is thought that the effect was due to the capture of oxygen by the metal atom from the peroxy compounds hence leading to some chain termination. The metal was introduced as the organometallic compound as this was a simple means of introducing the metal as a vapour at room temperature. Subsequent environmental concerns have led to the omission of metallic knock suppressants, and their replacement by organic compounds such as naphthols.

The thermodynamic data for the oxidation (combustion) of the normal and iso-paraffins (alkanes), C_2H_{2n+2}, can be represented to within a few kilojoules by the equation

$$\Delta H^\circ \text{ (combustion)} = 659.4n + 234 \text{ kJ mol}^{-1}$$

and thus the heat evolved during combustion, the 'calorific value', increases with the number of carbon atoms in the compound. However, the range of hydrocarbons which can be employed as fuels depends on the volatilities, i.e. melting and boiling points of these compounds. For example, butane, which is commonly used as a heating gas, boils at approximately 273 K, and of the liquid fuels, pentane boils at 309 K, and iso-octane at about 400 K. Hydrocarbons which are solid at room temperature, the paraffin waxes, having more carbon atoms per molecule than hexadecane $C_{16}H_{34}$. These data may be

used to calculate the adiabatic flame temperature, in which it is assumed that the heat of combustion is entirely absorbed in the reaction products, leading to an increase in temperature which can be calculated from a knowledge of their respective heat capacitites.

Fuel/air mixing in combustion systems

The two types of domestic heating, gas/air and droplet/air, present different flow patterns in the combustion chamber. The gas/air system is premixed before combustion, while the droplet/air mixture undergoes combustion in which the droplets are consumed by oxidation within the burning mixture. This latter process clearly depends on the vaporization of the droplets, and the diffusion of the vapour into the surrounding atmosphere where combustion occurs, hence the name *diffusion* flame. The two flow regimes which these systems generate are usually streamline or laminar flow in the pre-mixed gases, and turbulent flow in the burning of droplets, excepting in the slow process of burning a candle.

The familiar combustion process which occurs in automobile engines, is one in which gaseous hydrocarbons are oxidized by oxygen in air. In the Otto cycle a mixture of fuel vapour and air is drawn into the combustion region and compressed before being ignited by a spark. In the Diesel engine, liquid fuel droplets are injected into the combustion zone during the compression stroke, which raises the temperature of the intake air to the ignition temperature of the fuel, and reaction takes place between the vapour phase and the oxygen content of the entrained air without spark ignition. In jet engines the source of oxidant is compressed air (supercharging), and thrust is generated by the formation of combustion products with an increase in the volume and temperature of the air/fuel mixture.

DropBooks

Since the air and fuel come originally from different sources it is important to allow optimium conditions for mixing of these reactants before combustion takes place. In laminar flames, the reactants are pre-mixed before entering the combustion volume, as in the Otto engine and enter in streamline flow. In turbulent flames the velocity is considerably higher and the reactants are separately introduced into the combustion volume, the extent of reaction depending on the mixing by inter-diffusion of the fuel and air streams, which is the case in the Diesel engine.

A criterion for the nature of flow, either laminar or turbulent flow in fluid systems is the value of the Reynolds number. This number, R_e is defined by the equation

$$R_e = Lu\rho/\eta$$

where L is a characteristic length depending on the configuration of the fluid flow, u is the fluid velocity, ρ is the fluid density, and η is its viscosity. R_e is

a dimensionless number and can be described as the ratio between two forces, the inertial force which causes movement, and the viscous force which resists movement of the fluid.

The value of the Reynolds number which approximately separates laminar from turbulent flow depends, as previously mentioned, on the particular configuration of the system. Thus the critical value is around 50 for a film of liquid or gas flowing down a flat plate, around 500 for flow around a sphere, and around 2500 for flow through a pipe. The characteristic length in the definition of the Reynolds number is, for example, the diameter of the sphere or of the pipe in two of these examples.

The distribution of the gas velocity across the profile of a moving column of gas changes in the transition from laminar to turbulent flow. In the case of flow through a pipe of radius r_0, the laminar flow variation is given by

$$u = u_{\max}(1 - r/r_0)^2 \text{ with } u_{\text{av}} = (1/2)u_{\max}$$

where u_{av} and $u_{\max}$ are the average and maximum velocities respectively, which is therefore parabolic. For turbulent flow the corresponding relationship is

$$u = u_{\max}(1 - r/r_e)^{1/2} \text{ with } u_{\text{av}} = 0.8u_{\max}$$

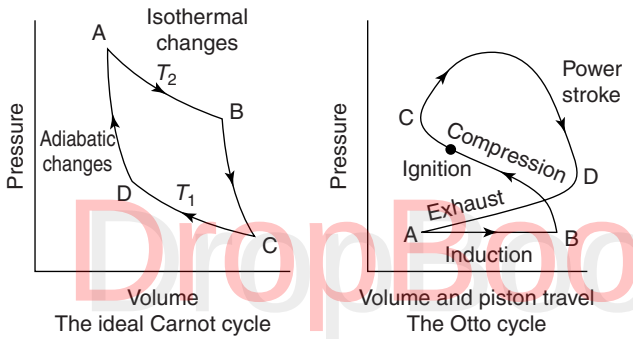
which is more rounded than the laminar case. In obtaining these equations it is assumed that the velocity of the gas is zero in contact with the wall of the pipe.

The thermal efficiencies of combustion engines

The behaviour of the Otto four-stroke engine can be described by showing the pressure acting on the gas phase as a function of the percentage of the containing piston stroke or the volume containing the gases. This is referred to as the Otto indicator diagram. After an initial admission of the fuel/air mixture in the downward stroke of the piston, followed by the compression of the unreacted fuel, together with any retained gases from the previous cycle, a spark is applied and the pressure increases as a result of the increase in volume following the chemical fuel oxidation reaction. This forces the piston to descend, the so-called power stroke. The piston then rises in the cylinder, sweeping out the majority of the combustion products and completing the cycle. Since air consists of 80% nitrogen, the main thermal effect in the combustion cycle is the heating of this volume of nitrogen together with the combustion products. If the combustion process were brought to thermodynamic equilibrium, the combustion products would be CO_2 and H_2O together with nitrogen. This ideal situation is not achieved in practice, and the engine exhaust must be passed over a catalyst to complete the process (see Chapter 4).

The air/fuel ratio can be varied, usually in the range 0.8 (rich) to 1.1 (lean), and a typical limit of the compression ratio is set at about 10:1 by the tendency of the engine to knock at higher ratios, leading to severe mechanical stresses in the engine components.

The thermal efficiency of the process (QE) should be compared with a thermodynamically ideal Carnot cycle, which can be done by comparing the respective indicator diagrams. These show the variation of temperature, volume and pressure in the combustion chamber during the operating cycle. In the Carnot cycle one mole of gas is subjected to alternate isothermal and adiabatic compression or expansion at two temperatures. By the first law of thermodynamics the isothermal work done on (compression) or by the gas (expansion) is accompanied by the absorption or evolution of heat (Figure 2.2).



DropBooks

Figure 2.2 *The indicator diagrams for the Carnot and the Otto engines. The Carnot cycle operates between the two temperatures T_1 and T_2 only, whereas the Otto cycle undergoes a temperature increase as a result of combustion.*

The adiabatic expansion and compression serve only to change the temperature of the gas without heat being absorbed or evolved, i.e. *iso-entropic* changes. The heat changes are therefore only related to the work which is done during the isothermal stages, which is given by

$$|Q| = RT \ln \frac{\text{final volume}}{\text{original volume}}$$

The modulus indicates that heat is absorbed (+), during the isothermal expansion, but released (−) during the isothermal compression. In the adiabatic processes no heat is supplied or removed from the working gas, and so

$$C_v \, \mathrm{d}T + p \, \mathrm{d}v = 0 = C_v \, \mathrm{d}T + RT \, \mathrm{d}v/v$$

which on integration yields

$$-C_v \ln T_2/T_1 = R \ln(v_2/v_1) = (C_p - C_v) \ln(P_1/P_2)$$
$$= (C_p - C_v) \ln(1/r)$$

(r, the compression ratio $= P_2/P_1$).

Since $R = C_p - C_v$ for an ideal gas, then

$$-\ln T_2/T_1 = (\gamma - 1) \ln(1/r)$$

where γ is the ratio of the specific heats C_p/C_v, and

$$T_2/T_1 = 1/r^{\gamma-1}$$

The efficiency, QE, is then defined as the heat absorbed minus the heat released divided by the heat absorbed in the cycle. This expression can, in turn, be transformed to show that the efficiency is equal to the difference between the two temperatures of operation, divided by the upper temperature.

$$QE = (T_2 - T_1)/T_2 = 1 - 1/r^{\gamma-1}$$

It follows that the efficiency of the Carnot engine is entirely determined by the temperatures of the two isothermal processes. The Otto cycle, being a real process, does not have ideal isothermal or adiabatic expansion and contraction of the gas phase due to the finite thermal losses of the combustion chamber and resistance to the movement of the piston, and because the product gases are not at thermodynamic equilibrium. Furthermore the heat of combustion is mainly evolved during a short time, after the gas has been compressed by the piston. This gives rise to an additional increase in temperature which is not accompanied by a large change in volume due to the constraint applied by the piston. The efficiency, QE, expressed as a function of the compression ratio (r) can only be assumed therefore to be an approximation to the ideal gas Carnot cycle.

The power of the engine is expressed by the mean effective pressure, *mep*, where

$$mep = \frac{\text{area of the indicator diagram}}{\text{cylinder volume displacement}}$$
$$= QE\Delta H^{\circ}_{\text{comb}}(P_i/RT_i)$$

where P_i and T_i are the pressure and temperature of the input fuel and $\Delta H^{\circ}_{\text{comb}}$ is the heat of combustion, and hence the power of the engine increases almost linearly with the compression ratio.

In the Diesel engine, a higher compression ratio can be achieved, up to about 18, before knock presents a problem, and the fuel is injected into the combustion chamber near the end of the compression stroke as a spray. The

indicator diagram for this engine is very similar to the Otto diagram, but the efficiency over the same compression range is lower, probably owing to the less complete mixing of the fuel vapour and air. At the higher compression levels the efficiency approaches that of the Otto engine, and the lack of complete mixing of the fuel/air mixture is overcome by using a lower ratio (lean) than the optimum in the Otto engine. The fuel used for the Diesel engine usually contains higher, and therefore cheaper, hydrocarbons than that which is used in the Otto engine, the principal component, known as 'kerosene', being mainly $C_{12}H_{26}$.

The gas turbine has a compressor for the inlet air before reaching the combustion chamber where kerosene is combusted. The combustion products are then mixed with a further supply of air, reducing the temperature of the gases to about 1000 K before they impinge on the turbine blades. This is done to reduce the corrosion of the blades by the gases which might be significant at higher temperatures. The indicator diagram and the efficiency are, again, similar to the Otto engine, but the compression ratio is less than the optimum for that engine. The advantages of the turbine engine in practical use largely derive from the low cost of maintenance, the low weight and the ability to use cheaper fuel. The thermal efficiency is improved by using the exhaust gases from the turbine as a pre-heater for the air reaching the combustion chamber.

DropBooks

Bibliography

F. Goodeve, *Disc. Far. Soc.*, **4**, 9 (1948).
K.J. Laidler, *Chemical Kinetics*, 3rd edn. Harper & Row NY (1987) QD 501 L17.
S. Glasstone, K.J. Laidler and H. Eyring. *The Theory of Rate Processes*, McGraw-Hill NY (1941).
B. Lewis and G. von Elbe. *Combustion, Flames and Explosions of Gases*, 3rd edn, Academic Press, NY (1987).
T. Takano, *Turbulence and Molecular Processes in Combustion*, (ed.) Elsevier, Amsterdam (1993) TJ 254.5.

Molecular dissociation and chain reactions in chemical vapour deposition

Chain reactions such as those described above, in which atomic species or radicals play a rate-determining part in a series of sequential reactions, are nearly always present in processes for the preparation of thin films by the decomposition of gaseous molecules. This may be achieved by thermal dissociation, by radiation decomposition (photochemical decomposition), or by electron bombardment, either by beams of electrons or in plasmas. The molecules involved cover a wide range from simple diatomic molecules which dissociate to atoms, to organometallic species with complex dissociation patterns. The

choice of a process for the production of a specific deposition product mainly centres on thermodynamic properties, and once the kinetics of formation of atomic or free radical species has been achieved, the subsequent reactions involving these species proceed rapidly with typically small activation energies. The kinetics of formation and growth of deposits proceeds as described above for the physical deposition of thin films.

Thermochemical data for the dissociation of gaseous molecules

The basic thermodynamic data for the design of such reactions can be used to assess the dissociation energies for various degrees of dissociation, and to calculate, approximately, the relevant equilibrium constants. One important source of dissociation is by heating molecules to elevated temperatures. The data below show the general trend in the thermal dissociation energies of a number of important gaseous molecules.

$H_2 = 2H$	Gibbs energy change:	$451\,950 - 119.6\,T$ joules
$N_2 = 2N$		$958\,650 - 132.7\,T$
$P_2 = 2P$		$496\,790 - 118.9\,T$
$O_2 = 2O$		$509\,990 - 133.6\,T$
$S_2 = 2S$		$435\,290 - 121.7\,T$
$F_2 = 2F$		$168\,200 - 128.5\,T$
$Cl_2 = 2Cl$		$253\,160 - 121.5\,T$
$Br_2 = 2Br$		$195\,990 - 110.7\,T$
$I_2 = 2I$		$153\,660 - 105\,T$

In these examples the entropy change does not vary widely, and the value of the equilibrium constant is mainly determined by the heat of dissociation. It can be concluded, therefore, that nitrogen is one of the most stable diatomic molecules, and that chlorine is the most stable diatomic halogen molecule.

As further examples of some important polyatomic molecules.

$H_2O = 2H + O$	$958\,130 - 244\,T$
$H_2S = 2H + S$	$760\,420 - 229\,T$
$NH_3 = N + 3H$	$1\,212\,000 - 361.9\,T$
$PH_3 = P + 3H$	$995\,950 - 345.4\,T$
$CH_4 = CH_3 + H$	$435\,900 - 141.5\,T$
	(better as $425\,800 - 57.91\,T - 10.48\,T \log T$)
$CH_3 = CH_2 + H$	$463\,000 - 125.9\,T$
$CH_2 = CH + H$	$441\,000 - 101\,T$
$CH = C(g) + H$	$351\,000 - 85\,T$
$HF = H + F$	$590\,180 - 123.5\,T$
$HCl = H + Cl$	$450\,070 - 116.2\,T$

These data can be used to obtain the value of the equilibrium constant at any temperature and this in turn can be used to calculate the degree of dissociation through the equation for the concentration dependence of the constant on the two species for a single element, the monomer and the dimer, which coexist. Considering one mole of the diatomic species which dissociates to produce $2x$ moles of the monatomic gas, leaving $(1 - x)$ moles of the diatomic gas and producing a resultant total number of moles of $(1 + x)$ at a total pressure of P atmos, the equation for the equilibrium constant in terms of these concentrations is

$$K = 4x^2P/(1 - x)(1 + x) = 4x^2P/(1 - x^2)$$

and when $x \ll 1$, the simple equations for x are

$$K = 4x^2P; \quad x = (K/4P)^{1/2}$$

In the case of hydrogen, for example, at a temperature of 2500 K, the equilibrium constant for dissociation has the value, calculated from the thermodynamic relation between the Gibbs energy of formation and the equilibrium constant of 6.356×10^{-4} and hence at a total pressure of 10^{-2} atmos, the degree of dissociation is 0.126 at 2500 K, which drops to 8.32×10^{-3} at 2000 K.

As was stated above, nitrogen has one of the highest atomization energy, and iodine has one of the lowest. These facts reflect the nature of the chemical bonds in these molecules, and the trend within a given Group of the Periodic Table shows that the higher molecular weight species in a given Group tend to have bond energies lower than those of the earlier members. This is so with the exception of the halogens where the trend only begins at chlorine, the bond energies of bromine and iodine following the more general trend. It is also of interest to note that the three stages of decomposition of methane to methyl, CH_3, methylene, CH_2 and methine, CH, require about the same heat input.

DropBooks

Bond character in gaseous heteronuclear compounds

Chemical bonding in gaseous compounds is only purely covalent when the two atoms are identical. If atoms of different species are bonded, the bond usually has a character between the covalent and ionic extremes. The estimation of the fractions of these two forms of bond in a given molecule may be made using Pauling's Table of *electronegativities*. These values attempt to reflect the relative attraction for an electron of each element, and can be calculated a number of ways. The original table due to Pauling (loc.cit) was based on assumptions about the direct relationship between the electronegativity numbers and the heats of formation of heteronuclear diatomic molecules.

Later methods, especially that of Gordy (1955), and later Allred and Rochow (1958) make use of screening constants of the electron structure for the nuclear charge of each atom. This determines the attraction between the nucleus of the atom and an electron outside the normal electron complement, and is the effective nuclear charge. The empirical equation for the values of electronegativity obtained in this manner by Allred and Rochow is

$$x = 1.282Z_e/r_{\text{cov}}^2 + 0.744$$

where Z_e is the effective, *screened* nuclear charge, and r_{cov} is the radius of the atom in a covalently bonded diatomic molecule. This procedure leads to the conclusion that the values of electronegativity should decrease in a particular Group of the Periodic Table with increasing atomic size, and increase from Group I to Group VII across a given Period.

Using the values of electronegativity, Pauling further suggested that the fractional ionic contribution to the bond energy (FIC) is related to the electronegativities x_{A} and x_{B} in the A–B molecule and given by

$$\text{FIC} = 0.16(x_{\text{B}} - x_{\text{A}}) + 0.035(x_{\text{B}} - x_{\text{A}})^2$$

The iodides will always be more covalent in bonding than the chlorides presumably because of the increased nuclear screening.

A further aspect of these calculations is that the *dipole moments* of gases, which arise from the displacement of electronic charge from the centre of symmetry of the bond, should also be directly related to the electronegativity difference. Pauling showed that the dipole moments of the hydrogen halides followed the values predicted by the respective electronegativities. The lack of symmetry in the bonds, could be taken to indicate a displacement of the electrons from the geometric centre they would occupy in a purely covalent bond. Alternatively this may be regarded as indicating that the electrons spend a larger fraction of time in the ionic mode, and the rest of the time in the covalent mode.

An alternative solution to this problem is to ignore the approach via electronegativity, and conclude that the dipole moment arises from the distortion of the normally spherical larger anion by the smaller cation in an otherwise ionic bond. This *polarization* effect of the cation of charge ze and radius r, which is referred to as the *ionic potential*, equal to ze/r, will be more marked the higher the charge, and the smaller the ionic radius of a cation species. Also since larger anions are more easily polarized it can be concluded that iodides will be the most covalently bonded of the halogens.

The compounds of carbon and silicon with hydrogen would be expected to be completely covalent according to these models, but the directionality of the bonds, which is towards the apices of a regular tetrahedron, is not explained by these considerations. Another of Pauling's suggestions which accounts for this type of directed covalent bonding involves so-called *hybrid* bonds.

Hybridization of covalent bonds

Carbon and silicon being in Group IV of the Periodic Table can form four bonds with hydrogen, as in methane, and these bonds are equal in strength and oriented towards the apices of a regular tetrahedron. Carbon also forms other compounds, such as ethylene and acetylene, in which there are double and triple bonds between carbon atoms with correspondingly different spatial distributions of the carbon–hydrogen bonds from those in methane. The bonds in these compounds are not simple bonds involving electrons with the same energies, e.g. s or p electrons, but are 'hybrid' bonds which have spatial properties which are a mixture of the s and p orbitals. The term *orbital*, which arises from the quantum theory of atomic structure, describes the volume around an atom in which an electron is most probably to be found, and has a different shape according to the azimuthal quantum number of the state occupied by the electron. For azimuthal quantum number zero, the s electrons, the orbital is a sphere centred on the nucleus of the atom. The p electrons occupy the next level of quantum number, and the volume occupied by these electrons has the form of a dumbell, with the mid-point of the dumbell located at the nucleus, and there are three of these at right angles to one another, each accommodating two electrons. In carbon two p orbitals contain one electron, and the third is empty. The outer electronic configuration of the carbon atom which can therefore be described by the shorthand notation, s^2p^2, would provide bonds directed about the nucleus in a different arrangement from that found in methane. Pauling's explanation of this revolves around the fact that covalent bonding is stronger the more the electron orbitals on each atom forming the bond can overlap without significant repulsion arising from the closed electron shells nearer each nucleus. The ground level s^2p^2 state of the carbon atom can be promoted to the *excited* sp^3 state by the absorption of $272\,kJ\,mol^{-1}$, and the strength of each carbon–hydrogen bond in methane is about $411\,kJ\,mol^{-1}$, and hence the promotion energy is more than compensated by bond formation. Similarly, carbon can form three sp^2 bonds which lie in one plane at 120° to one another with a bond energy of $440\,kJ\,mol^{-1}$ to hydrogen in ethylene, and two sp bonds of energy $500\,kJ\,mol^{-1}$ in acetylene. The remaining bonds in these two molecules, the carbon–carbon bonds, each use one of the hybrid bonds together with bonds involving the remaining s and p orbitals. The overlap of the hybrid orbitals in carbon–carbon bonds is greatest in acetylene, less in ethylene and least in methane, leading to bond lengths, 0.1061 nm in C_2H_2, 0.1086 nm in C_2H_4, and 0.1093 nm in CH_4 (Figure 2.3).

An extreme example of hybidization is the structure proposed for sulphur hexafluoride, SF_6. The six S-F bonds are directed to the apices of a regular octahedron. An arrangement which would satisfy this number of covalent bonds is sp^3d^2 hybridization. The ground state of the sulphur atom is s^2p^4 and

DropBooks

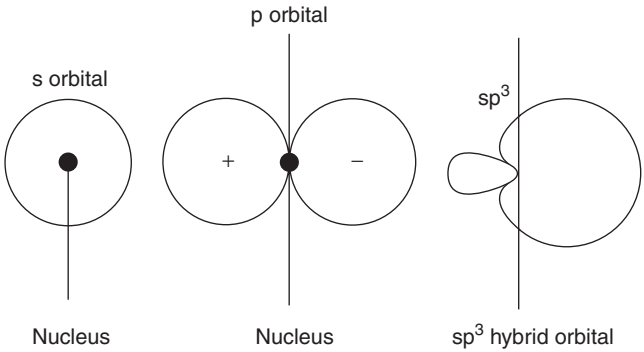


Figure 2.3 *The shapes of orbitals for the s electron pair, the three pairs of p electrons with obitals mutally at right angles, and the sp^3 orbitals which have the major lobes pointing towards the apices of a regular tetrahedron.*

so one of the s electrons and one of the p electrons must be promoted to the 3d level to form the hybrid bonds.

Bond energies of gaseous polyvalent metal halides

Elements forming solid halides in more than one valency state may produce gaseous species which reflect a number of different valencies. Thus gallium forms GaCl(g) and $GaCl_3$(g), and titanium forms TiI_2, TiI_3 and TiI_4 gases. It is generally true that the strength of the metal–halogen bond is higher in the lower valence states. Therefore a partial dissociation of the higher valency compounds may be achieved at the lowest temperatures. A general, approximate, rule can be obtained from experimental data to show that the bond energy of each metal–halogen bond decreases by 10 to 15% as the valency increases. Mass spectrometric data for the atomization energies of a number of metal–halogen systems are shown in Table 2.2 for the elements of Group III together with the ratio of the average bond energies, E_{III}/E_I.

Table 2.2 *Heats of atomization of metal chlorides*

BCl	515 kJ	BCl_3	1268 kJ	$E_{III}/E_I = 0.82$
AlCl	494*	$AlCl_3$	1276*	0.85
GaCl	490	$GaCl_3$	1100	0.75
InCl	439	$InCl_3$	979	0.74

*The data for the aluminium halides are not very accurate.

These data also show that the bond energies decrease as the atomic number of the metal increases in the same Group of the Periodic Table.

Another trend which can be anticipated from electronegativity data, is that the bromides will be more easily decomposed thermally than the chlorides, and the iodides more readily than the bromides. A typical comparison is between the compounds of titanium and those of hafnium, which play a significant role in vapour deposition.

Zirconium	$ZrCl_4(g)$;	$\Delta H^\circ_{298} = -868.6$
	$ZrBr_4(g)$;	$\Delta H^\circ_{298} = -643.5$
	ZrI_4 (g);	$\Delta H^\circ_{298} = -353.8$
Hafnium	$HfCl_4(g)$;	$\Delta H^\circ_{298} = -882.8$
	$HfBr_4(g)$;	$\Delta H^\circ_{298} = -657$
	HfI_4 (g);	$\Delta H^\circ_{298} = -364^*$

*estimated Heat of vaporization of 130 kJ.

It can be seen that the bromides are about 225 kJ mol^{-1}, and the iodides about 515 kJ mol^{-1} less stable than the chlorides.

The deposition of metals directly from these halides would require high temperatures to be efficient, but because of the thermodynamic stabilities of the hydrogen halides, direct reduction can readily be carried out with hydrogen at lower temperatures. The general reaction

$$MeX_n + (n/2)H_2 = Me(g) + nHX$$

will produce a metallic film on a substrate at the temperature where the metal vapour pressure provided by this reaction becomes equal to the vapour pressure of the condensed metal. If it is difficult to maintain the substrate at a lower temperature than the rest of the system gas phase–substrate–container, then once the film began to form on the substrate, deposition would occur over the walls of the container as well. However if the element is to be reduced to form a compound with another element, as in the production of the III–V semiconductors, then the reaction could be carried out at a temperature where the metal vapour pressure at equilibrium is less than that to produce the pure metal, due to the stability of the III–V compound in this case. Any tendency to re-evaporation from the film will also be reduced.

Thermal decomposition of hydrides and organometallic compounds

One of the earliest studies of deposition from organometallics was the discovery that when some metal *alkyls*, such as lead tetramethyl $Pb(CH_3)_4$,

DropBooks

prepared by reaction between alkyl halides and metals, are passed through a high temperature region they could be decomposed to form a mirror of the metal, and the exit gas phase removed a metal film further along the gas train. These early studies established the existence of methyl and ethyl free radicals, CH_3 and C_2H_5 with a significant lifetime as the products of these reactions. Propyl, C_3H_7, and butyl, C_4H_9, radicals appeared to be unstable with respect to decomposition to methyl and ethyl radicals. The subsequent development of organometallic chemistry has made available many other sources of these radicals by pyrolysis. The reaction between the methyl and ethyl radicals with hydrogen was also found to lead to the formation of atomic hydrogen, the exit gas containing methane and ethane

$$CH_3 + H_2 = CH_4 + H; \quad CH_3 + CH_3 = C_2H_6$$

This makes possible numerous further decomposition reactions involving the hydrogen atom as an intermediate in chain reactions.

An important method for the production and doping of thin films of semiconductor elements and compounds by chemical vapour deposition, CVD, involves the thermal decomposition of organometallic compounds either singly or in the presence of a chemically reactive species such as SiH_4 or AsH_3. The organometallic compounds are frequently metal methyls or ethyls, e.g. $Ga(CH_3)_3$ or $Ga(C_2H_5)_3$, which involve metal–carbon bonds. More complex compounds than these have also been used, such as the acetonylacetonates, but accurate thermochemical data for these compounds do not exist, and so no quantitative analysis can be attempted at the present time except by the addition of calorimetric values of the strength of each bond in the compound. From these considerations it can be concluded that the metal–carbon bond strength in the more complex organic molecules should not be significantly different from the simple methyls or ethyls. However, the possibility of secondary reactions between dissociation fragments, which may include oxygen atoms, may contribute to metal atom production.

As an example of carbon bond strengths the data for the stages in the atomization of methane are shown below, together for the less accurate data for silane

$CH_4 \longrightarrow CH_3 + H$	$D_0 = 427\,\text{kJ}$
$CH_3 \longrightarrow CH_2 + H$	456
$CH_2 \longrightarrow CH + H$	420
$CH \longrightarrow C + H$	332

which yields the total dissociation energy

$CH_4 \longrightarrow C + 4H$	1635

For the corresponding silicon–hydrogen system

$$\begin{aligned} SiH_4 &\longrightarrow SiH_3 + H \qquad D_0 = 381\,\text{kJ} \\ SiH_3 &\longrightarrow SiH_2 + H \qquad 281 \\ SiH_2 &\longrightarrow SiH + H \qquad 308 \\ SiH &\longrightarrow Si + H \qquad 295 \end{aligned}$$

with the total dissociation energy

$$SiH_4 \longrightarrow Si + 4H \qquad 1265$$

The above data are correct to about $\pm 20\,\text{kJ mole}^{-1}$, but it will be seen that the general trend among these more covalent bonds does appear to be a decrease in stability from carbon to silicon, i.e. the same way as was found for more ionic bonds in the halides. Thermodynamic data for metallorganic methyl compounds used in the production of semiconductor systems are shown in Table 2.3.

Table 2.3 *Metal–carbon bond energies for some methyls*

Group	III		
	$Al(CH_3)_3$	Al–C bond energy =	326 kJ
	$Ga(CH_3)_3$	Ga–C	251
	$In(CH_3)_3$	In–C	197
Group	IV		
	$Ge(CH_3)_4$	Ge–C	292
	$Si(CH_3)_4$	Si–C	264
Group	V		
	$As(CH_3)_5$	As–C	264
	$Sb(CH_3)_5$	Sb–C	238

DropBooks

The preparation of semiconductors by thermal decomposition would appear to be impossible because of the high amount of energy required to break all of the metal–carbon bonds before the atomic species could be formed. However, the thermal method is successful because the reaction to form free methyl radicals, which combine to form ethane, lowers the energetic requirements for the formation of gallium, for example, according to the equation

$$2Ga(CH_3)_3 \longrightarrow 2Ga + 3C_2H_6$$

Similarly it is believed that the dissociation of ethyls occurs with the formation of ethylene,

$$Ga(C_2H_5)_3 \longrightarrow Ga{-}H + 3C_2H_4 + H_2$$

If trimethyl gallium is mixed with arsine, AsH_3, the hydrogen atoms released by the dissociation of this gas react with the methyl radicals released from gallium trimethyl according to the equation

$$Ga(CH_3)_3 + AsH_3 \longrightarrow Ga{-}As + 3CH_4$$

The temperature at which this reaction is carried out is limited by considerations of the possibility of re-evaporation of As_2 molecules and gallium atoms from the GaAs film. The semiconducting compounds are less susceptible to this problem than the separate elements because of the thermodynamic stabilities of these compounds, as discussed above.

Table 2.4 *Heats of formation of semiconducting compounds*

GaAs	74.1 kJ mol^{-1}	CdS	69.0 kJ mol^{-1}
InSb	30.5	CdSe	83.3
		ZnS	205.2
		ZnSe	163.2

Some metal *carbonyls*, such as nickel, cobalt and manganese compounds have been used to produce metallic deposition. The decomposition occurs in a stepwise manner, producing one CO(g) molecule at each step.

$$Co(CO)_5 \longrightarrow Co(CO)_4 + CO(g)$$

The *sandwich* compounds, ferrocene and nickelocene, $Fe(C_5H_5)_2$ and $Ni(C_5H_5)_2$, so called because the metal atom is 'sandwiched' between the organic radicals, C_5H_5, have also been used to prepare iron and nickel deposits.

The major problem in the production of semiconductors by the decomposition of organometallics appears to be the unwanted carbon contamination of the products.

Bibliography

L. Pauling. *The Nature of the Chemical Bond*, 3rd edn Cornell Univ. Press (1960).
R. McWeeny. *Coulson's Valency*, 3rd edn, Oxford University Press (1979).
W. Gordy, *Disc. Far. Soc.*, **19**, 14 (1955).
A.L. Allred and E.G. Rochow, *J. Inorg. Nucl. Chem.*, **5**, 264 (1958).

Radiation and electron decomposition of molecules

There are two broad ways in which gaseous molecules may be dissociated other than by use of high temperatures. Decomposition may be effected photochemically, where the quantal energy of radiation directed towards the gas, usually in the ultra-violet, is sufficient to break the molecular bonds in the gas. The result is to produce neutral or excited atoms from simple molecules, or fragments from more complex molecules such as organic species. The resulting decomposition products have a chemical reactivity much greater than that of the simple molecular species from which they derive as seen above. The quantal energies required for dissociation of simple molecules can be calculated from thermochemical data, and some important examples are given in Table 2.5.

Table 2.5 *Dissociation quanta of some diatomic molecules*

Molecule	Dissociation energy (kJ) at 298 K	Absorption wavelength range
$H_2 \longrightarrow 2H$	$436 \equiv 4.52\,eV$	(ultra-violet)
$O_2 \longrightarrow 2O$	$500 \equiv 5.18\,eV$	(ultra-violet)
$N_2 \longrightarrow 2N$	$945 \equiv 9.88\,eV$	(far U.V.)
$Cl_2 \longrightarrow 2Cl$	$242 \equiv 2.5\,eV$	(visible)
$I_2 \longrightarrow 2I$	$151 \equiv 1.56\,eV$	(visible)
$HCl \longrightarrow H + Cl$	$431 \equiv 4.47\,eV$	(ultra-violet)
$HI \longrightarrow H + I$	$351 \equiv 3.64\,eV$	(visible)

DropBooks

The absorption wavelengths quoted here are for the complete dissociation of these molecules to the atoms in their ground state. The thermochemical data also show that a temperature of nearly 4000 K is required before the atomic oxygen concentration is equal to that of molecular oxygen, and almost 7000 K for the nitrogen atom population to be equal to the molecular nitrogen concentration, at one atmosphere pressure.

The use of irradiation or electron bombardment offers an alternative approach to molecular dissociation to the use of elevated temperatures, and offers a number of practical advantages. Intensive sources of radiation in the visible and near-visible are produced by flash photolysis, in which a bank of electrical capacitors is discharged through an inert gas such as krypton to produce up to 10^5 joule for a period of about 10^{-4} s, or by the use of high power laser beams (Eastham, 1986 (loc.cit.)). A more sustainable source of radiation is obtained from electrical discharge devices usually incorporating

an inert gas such as argon at less than one atmosphere pressure. These include plasma discharges using DC and low potential AC sources, as well as radio-frequency sources.

The advantage of the former is that charged particles which are formed along with neutral atomic species can be directed in a suitable electrical arrangement to the surface of a metal, which is an efficient way of delivering the charged species to this surface. In *microwave* discharges it is possible to produce an atomic population without the accompanying heat generation typical of plasma discharge sources.

In both plasma and microwave discharges in which argon is the gas, the current is carried mainly by electrons which are formed by ionization of argon atoms. Collisions between molecules introduced into the plasma volume and these electrons can lead to the formation of positively charged ionized species from the gaseous molecules. The electrons gather kinetic energy from the applied electric field between collisions. This process also creates further electrons and thus can increase the number of ions per unit volume (Venugopalan and Avni, 1985)

Photochemical reactions

The complex form of the rate equation for the formation of hydrogen bromide is due to the role of atomic species in the reaction mechanism. The formation of hydrogen iodide, on the other hand, is much simpler, conforming to that of a bimolecular rection, although there is evidence of a change in the activation energy at high temperatures, above about 700 K, which might indicate an increasing trend towards a chain reaction mechanism. The reaction between hydrogen and chlorine follows the same complex path as the bromine reaction, and this was the first in which the influence of light on the rate of a chemical reaction was studied. The intermediate stages of this reaction involve atom–molecule collisions, where the chlorine atoms have been mainly formed photochemically. Thus the reaction path is

$$Cl_2 \longrightarrow 2Cl$$

$$Cl + H_2 \longrightarrow HCl + H$$

$$H + Cl_2 \longrightarrow HCl + Cl$$

The changes in the strengths of molecular bonding in the sequence of hydrogen–halogen reactions is

$$Cl_2 > Br_2 > I_2$$

and

$$HCl > HBr > HI$$

These data suggest that both the chain reactions and the bimolecular reactions occur simultaneously in all systems but that the bimolecular reaction, which dominates the formation of HI, occurs only to a minor extent in the formation of HCl and HBr. To analyse the difference between these alternate mechanisms of hydrogen–halogen reactions, we should first consider the relative energies of each of the chain reaction steps for each system. The results for ΔH°_{298} for each reaction are show in Table 2.6.

Table 2.6 *Reaction steps in hydrogen halide formation*

X =	Cl	Br	I
$H_2 + X = HX + H$	+4 kJ	+70 kJ	+138 kJ
$H + X_2 = HX + X$	−189	−174	−148
$H_2 + X_2 = 2HX$	−185	−104	−101
$X_2 = 2X$	+243	+193	+151

The standard entropy change for the atom–molecule reactions is in the range 5–20 J K^{-1} $mole^{-1}$, and the halogen molecule dissociation has an entropy change of about 105 e.u. The halogen molecule dissociation energy decreases from chlorine to iodine, but the atom–molecule reactions become more endothermic from chlorine to iodine, and this latter effect probably influences the relative contributions to the mechanism from chain reaction and bimolecular reaction.

DropBooks

Estimates of the activation energies of the atom–molecule reactions are between 20–30 kJ $mole^{-1}$, and the measured activation energy of the reaction for the bimolecular formation of HI is 169 kJ $mole^{-1}$, which is significantly higher. It might therefore be concluded that it is the reaction involving the halogen atoms as reactants to dissociate the hydrogen molecules which determine the overall predominating mechanism, whether chain or bimolecular collision.

The effect of light in the visible region on the speeds of these reactions is measured by the quantum efficiency, QE, which is defined by

$$\text{QE} = \text{Number of molecules decomposed} / \text{Number of radiation quanta absorbed}$$

The quantum efficiency of the irradiation of a hydrogen–chlorine mixture has the apparent value between 10^4 and 10^6, but the corresponding value for the parallel bromine reaction is only about 10^{-2}. Of course the real quantum efficiency can only reach the value of unity as an upper limit, and the large apparent value for the chlorine reaction indicates that once two chlorine atoms

are formed by photon absorption, these products can then lead to the formation of many other atomic species through the chain reactions and it is only the stability of the chlorine molecule that prohibits this effect under purely thermal activation. The fact that the iodine–hydrogen steps are so endothermic prevents the occurrence of the chain reaction, despite the weak iodine molecule bonds.

The next step is to consider the cross-sections of the absorption of radiation by the diatomic halogen molecules in order to decide if the relative effects result from the efficiency of the radiation photon–molecule interactions. These are reflected in the dissociation cross-sections of these interactions.

Dissociation cross-sections

The interaction between radiation and a mass of gas can be treated as a collision problem. In this case the number of photon–molecule collisions, N_x, in unit length of an absorbing gas is given by

$$N_x = I_x n\sigma$$

where I_x is the radiation flux, n is the number of gas molecules in the path of the beam per cm^2 of projected area, and σ is the cross-section of absorption. Alternatively, the absorption coefficient, is defined through the Beer–Lambert equation

$$I_{\text{trans}} = I_0 \exp(-\mu x)$$

where I_{trans} is the intensity of radiation after absorption by the gas, I_0 is the incident intensity, μ is the absorption coefficient and x is the length of the gas column having unit cross-section. It follows that

$$\mu x = n\sigma x$$

if μx is small. The larger values of adsorber thickness show departures from the first equation, because of the 'shadowing' by the first layers of subsequent layers of the absorber from the incident radiation.

These coefficients, the cross-section and the absorption coefficient are a function of the radiation frequency, and hence the photon energy. When this is less than the dissociation energy of the irradiated species, the molecules can be raised to an energetically excited state from the initial ground state, with or without subsequent decomposition. Alternatively, a low photon energy may be used to raise the rotational energy of the molecule. When the photon energy is greater than the dissociation energy of the molecules, the presence of the dissociation products is observed, and depending on the excess energy of the photons above the molecular dissociation energy, the kinetic energy of the product molecules could trigger further reaction.

Experimental data for some molecules of technical interest have been obtained by the use of high-intensity discharge lamps and high-power lasers to yield cross-sections in the range 10^{-17} to $10^{-20}\,cm^2$ for single photon absorption. At higher intensity and energy levels of photon energy (>5 eV for example), double photon absorption with a cross-section of about $10^{-40}\,cm^2$ becomes possible, leading to the formation of different products from the single photon case. An example of this is the irradiation of aluminium trimethyl, $Al(CH_3)_3$ in which the Al–C bond has a dissociation energy of 3.38 eV. When the photon energy is 4.9 eV, one methyl–aluminium bond is broken, but above 5.4 eV two of these bonds are broken. As an extreme example the decomposition of arsine, AsH_3, can lead to differing degrees of dissociation, depending on the photon energy. Thus

$$AsH_3 + h\nu \longrightarrow AsH_2 + H \text{ (photon energy 6.5 eV)}$$
$$AsH_3^+ \text{ (an ionized state at 10 eV)}$$
$$AsH_2^+ \text{ (at 13 eV)}$$
$$As^+ \text{ (at 15 eV)}$$

(Koplitz *et al.*, 1988).

The effective absorption of radiation by a gas can be increased by the addition of a *sensitizer*. For example, when mercury vapour is added to silane gas, the mercury vapour absorbs radiation to form an excited atom Hg^* which collides with a silane molecule to lead to partial dissociation

$$Hg + h\nu \longrightarrow Hg^*$$
$$Hg^* + SiH_4 \longrightarrow Hg + SiH_3 + H$$
$$H + SiH_4 \longrightarrow H_2 + SiH_3$$

(Kamisako *et al.*, 1988) or alternatively, an addition of ammonia gas leads to a different route for achieving the same product by the photolysis of ammonia to produce hydrogen atoms

$$NH_3 + h\nu \longrightarrow NH_2 + H$$
$$H + SiH_4 \longrightarrow SiH_3 + H_2$$

(Hellner *et al.*, 1984).

This mixture of gases has been used to prepare silicon nitride particles photochemically, the overall reaction being represented by

$$3SiH_4 + 4NH_3 + h\nu = Si_3N_4 + 12H_2$$

although the reaction path includes the formation of the radicals shown above as intermediates. The reaction produces fine particles of silicon nitride which

DropBooks

have commercial application. The photons were provided by a CO_2 laser with a photon energy of 0.117 eV. The thermodynamics of this reaction in the absence of radiation is described by

$$\Delta G^\circ = -607\,900 - 416.5T \quad \text{J mol}^{-1}$$

Clearly this reaction is highly exothermic and could be carried out by thermal means alone, but this would require that the gas mixture be passed through a furnace and, as a result, the product would not be expected to be a fine powder, but a somewhat coarser agglomerate.

There is a great deal of flexibility in the choice of laser radiation in the production of thin films by photochemical decomposition, and many routes for achieving the same objective can be explored. In most reactions of industrial interest the reaction path is via the formation of free radicals as intermediates, and the complete details of the reaction paths are not adequately defined. However, it may be anticipated that the success of the photochemical production of new materials in thin films and in fine powder form will lead to considerably greater effort in the elucidation of these kinetics.

The energy of photons in the visible range is limited to a relatively low level of photon energy compared to molecular binding energies, and for dissociation studies ultra-violet radiation is mainly used. Table 2.7 shows the range in wavelength and quantal energy of light which can be generated in this fashion.

Table 2.7 *Wavelength and energy of electromagnetic radiation*

Red light	640–750 nm	186.44–159.09 kJ/einstein
Yellow	580–640	205.73–186.44
Green	495–580	241.73–205.73
Blue	440–495	271.19–241.73
Violet	380–440	314.88–271.73
Near Ultraviolet	300–380 nm	390.83–314.88
Far Ultraviolet	200–300	598.29–390.83.

1 einstein = Avogadro's number (6.03×10^{23}) of quanta
1 eV/molecule = 96.48 kJ mole^{-1}

Substrate heating by transmitted radiation

Another consideration in the production of thin films by photochemical processes is that the fraction of the beam which is not used in photodecomposition will heat any substrate on which it is desired to form the film. The power of the light source which can be used for photodecomposition in the gaseous phase only is therefore limited by the transmission of energy. Clearly this transmitted beam represents a constant source of energy which

impinges on the substrate. If this is absorbed at the surface, the resulting heating effect is a function of the thermal conductivity of the substrate according to the time-dependent (unsteady-state) solution of Fourier's equation for heat conduction in one dimension,

$$\alpha \frac{\partial^2 Q}{\partial x^2} = \frac{\partial Q}{\partial t}$$

for the heat distribution, or alternatively

$$\alpha \frac{\partial^2 T}{\partial x^2} = \frac{\partial T}{\partial t}$$

for the temperature distribution.

Here Q is the amount of heat contained per unit volume in the substrate, x is the distance down into the substrate, and t is the time of irradiation. The solutions of this equation depend on the physical conditions of the irradiation. Thus if the surface is subject to a constant energy supply, Q_0, the solution is

$$Q(x, t) = Q_0(1 - \operatorname{erf} x/(4\alpha t)^{1/2}$$

which yields the temperature distribution throughout the substrate as a function of time

$$T(x, t) = (Q_0/\kappa)(4\alpha t)^{1/2} \operatorname{ierfc} x/(4\alpha t)^{1/2}$$

DropBooks

Here, $\operatorname{erfc} x$ is the error function complement of x and ierfc is its inverse. The physical properties are represented by α, the *thermal diffusivity*, which is equal to $\kappa/\rho C_P$, where κ is the thermal conductivity, ρ is the density and C_P, the specific heat capacity at constant pressure. The surface temperature during this irradiation, T_s, at $x = 0$, is therefore

$$T_s = \frac{2Q_0}{\kappa}\sqrt{\frac{\alpha t}{\pi}}$$

The analytical methods for solving the Fourier equation, in which Q and T are functions of the spatial co-ordinate and time, include a change of variables by combination, and in the more general case the use of Laplace transforms.

To find the temperature distribution, the first procedure requires a change of variables to the variable, z, defined by the equation

$$z = x/t^{1/2}$$

and writing

$$T = f(z)$$

thus

$$\frac{\partial T}{\partial x} = \frac{\mathrm{d}f}{\mathrm{d}z}\frac{\partial z}{\partial x} = \frac{1}{t^{1/2}}\frac{\mathrm{d}f}{\mathrm{d}z}; \quad \frac{\partial^2 T}{\partial x^2} = \frac{1}{t}\frac{\mathrm{d}^2 f}{\mathrm{d}z^2}$$

and

$$\frac{\partial T}{\mathrm{d}t} = \frac{\mathrm{d}f}{\mathrm{d}z}\frac{\partial z}{\partial t} = -\frac{1}{2}\frac{x}{t^{3/2}}\frac{\mathrm{d}f}{\mathrm{d}z}$$

which leads to the time-independent differential equation and its first integral

$$\alpha\frac{\mathrm{d}^2 f}{\mathrm{d}z^2} = -\frac{1}{2}z\frac{\mathrm{d}f}{\mathrm{d}z}; \quad \frac{\mathrm{d}f}{\mathrm{d}z} = A\exp\left(-\frac{z^2}{4\alpha}\right)$$

and, from the definition of $f(z)$, this yields

$$\frac{\partial T}{\partial x} = At^{-1/2}\exp\left(-\frac{x^2}{4\alpha t}\right)$$

It can be found, by substitution, that

$$T = At^{-1/2}\exp\left(-\frac{x^2}{4\alpha t}\right)$$

is a solution of the Fourier equation for the temperature distribution. A, the integration constant may be evaluated by use of the equation for the distribution throughout the solid of the amount of energy received by the solid at the time, τ, and in the interval of irradiation, $\delta\tau$,

$$Q_0\delta\tau = [\int_0^\infty \rho C_p T\,\mathrm{d}x]\delta\tau = \kappa A\sqrt{\frac{\pi}{\alpha}};$$

$$\delta T = \frac{Q_0}{\kappa}\sqrt{\frac{\alpha}{\pi}}(t-\tau)^{-1/2}\mathrm{e}^{\frac{-x^2}{4\alpha(t-\tau)}}\,\delta\tau$$

and δT is the temperature increase due to diffusion of this quantity of heat during the remaining time $(t-\tau)$. Integrating with respect to t as $\delta\tau$ tends to zero, and setting $x = 0$, the surface temperature T_s is given by

$$T_s = \frac{2Q_0}{\kappa}\sqrt{\frac{at}{\pi}}$$

The Laplace transform technique also allows the reduction of the partial differential equation in two variables to one of a single variable In the present case,

time is eliminated as a variable by using the Laplace transform $L(x, t)$ thus

$$L[(Q(x,t)] = \int_0^\infty \mathrm{e}^{-st} Q(x,t)\,\mathrm{d}t$$

$$L\frac{\partial^2 Q}{\partial x^2} = \frac{\mathrm{d}^2 \overline{Q}}{\mathrm{d}x^2}; \quad L\frac{\partial Q}{\partial t} = s\overline{Q}$$

Tables of Laplace transforms for a large number of functions have been calculated, and can be obtained from published data. In the present example, the transformed equation is

$$\frac{\mathrm{d}^2 \overline{Q}}{\mathrm{d}x^2} - \frac{s}{\alpha}\overline{Q} = 0$$

for which the solution is

$$\overline{Q} = A_1 \mathrm{e}^{-q'x} + A_2 \mathrm{e}^{q'x}$$

where $q'^2 = s/\alpha$.

Applying the boundary conditions it follows that A_2 above must be zero since Q remains finite as $x \to \infty$. At x equal to zero,

$$\overline{Q} = \frac{Q_0}{s} \text{ thus } A_1 = \frac{Q_0}{s}$$

DropBooks

From tables for the Laplace function the inverse Laplace function can then be read and this yields

$$Q = Q_0 \operatorname{erfc} \frac{x}{2}\sqrt{\alpha t}$$

which is given above for the solution to the laser heating problem.

An alternative method of solution to these analytical procedures, which is particularly useful in computer-assisted calculations, is the *finite-difference technique*. The Fourier equation describes the accumulation of heat in a thin slice of the heated solid, between the values x' and $x' + \mathrm{d}x$, resulting from the flow of heat through the solid. The accumulation of heat in the layer is the difference between the flux of energy into the layer at $x = x'$, $J_{x'}$ and the flux out of the layer at $x = x' + \mathrm{d}x$, $J_{x'+\mathrm{d}x}$. Therefore the accumulation of heat in the layer may be written as

$$\mathrm{d}x\frac{\partial Q}{\partial t} = J_{x'} - J_{x'+\mathrm{d}x} = -\mathrm{d}x\left[\frac{\partial J}{\partial x}\right]_{x=x'}$$

but at any given point in the heat profile in the solid

$$J = \alpha\frac{\partial Q}{\partial x} \text{ hence } \frac{\partial Q}{\partial t} = \frac{\partial}{\partial x}\left[\alpha\frac{\partial Q}{\partial x}\right]$$

which is the Fourier equation. For the numerical solution of this equation the variables are first changed to dimensionless variables

$$q = Q/Q_0; \quad \beta = x/l; \quad \tau = \alpha t/l^2$$

where l is the total thickness of the substrate.

The heat conduction equation in terms of these variables has the components

$$\frac{\partial Q}{\partial x} = \frac{\partial Q}{\partial \beta}\frac{\mathrm{d}\beta}{\mathrm{d}x} = \frac{\partial Q}{\partial \beta}\frac{1}{l}; \quad \frac{\partial^2 Q}{\partial x^2} = \frac{\partial^2 Q}{\partial \beta^2}\frac{1}{l^2}$$

$$\frac{\partial Q}{\partial t} = \frac{\partial Q}{\partial \tau}\frac{\mathrm{d}\tau}{\mathrm{d}t} = \frac{\partial Q}{\partial \tau}\frac{\alpha}{l^2}$$

The thickness of the solid is then divided into thin slices, and the separate differentials at the mth slice in the Fourier equation can be expressed in terms of the functions

$$\left(\frac{\partial^2 q}{\partial \beta^2}\right)_m = \frac{(q_{m+1} - q_m) - (q_m - q_{m-1})}{(\partial\beta)^2}$$

$$\left(\frac{\partial q}{\partial t}\right)_m = \frac{(q_m^* - q_m)}{\delta\tau}$$

where q^* is the value of q after a time increment $\delta\tau$, and finally, on substituting in the heat conduction equation,

$$q_m^* = q_m + \frac{\delta\tau}{(\delta\beta)^2}(q_{m+1} - 2q_m + q_{m-1})$$

Successive steps in this distribution can then be obtained to calculate the values of Q at a given value of x in a sequence of time intervals.

Methods for numerical analyses such as this can be obtained from commercial software, and the advent of the computer has considerably eased the work required to obtain numerical values for heat distribution and profiles in a short time, or even continuously if a monitor supplies the boundary values of heat content or temperature during an operation.

Returning to laser heating of the film which is deposited on a substrate, it is possible to control the temperature of the film and the substrate through the power of the light source or by scanning the laser beam across the surface of the substrate at a speed which will allow enough time for the deposit to be formed (laser writing). In the practical situation it is simpler to move the substrate relative to the laser beam in order to achieve this. The speed must be selected so as to optimize the rate of formation of the film while maintaining the desired relation of the physical properties of the film and the substrate such as cohesion and epitaxial growth.

Radiation and convection cooling of the substrate

This calculation is subject to two further considerations. The first of these is that a substrate such as quartz, which is transparent in the visible region, will not absorb all of the incident light transmitted through the gas phase. The Fourier calculation shown above considers only the *absorbed* fraction of the energy at the surface. Secondly, if the absorption of radiation at the surface of the substrate is complete, leading to the formation of a hot spot, this surface will lose heat to its cooler surroundings by radiation loss. The magnitude of this loss can be assessed using the Stefan–Boltzmann law,

$$Q_x = Fe\sigma(T_s^4 - T_m^4)$$

Here, Q_r is the energy loss per second by a surface at temperature T_s to its surroundings at temperature T_m, the emissivity of the substrate being e, the view factor F being the fraction of the emitted radiation which is absorbed by the cool surroundings, and σ being the Stefan–Boltzmann radiation constant ($5.67 \times 10^{-8}\,\mathrm{J\,m^{-2}\,s^{-1}\,K^{-4}}$). In the present case, the emissivity will have a value of about 0.2–0.3 for the metallic substrates, but nearly unity for the non-metals. The view factor can be assumed to have a value of unity in the normal situation where the hot substrate is enclosed in a cooled container.

There will also be heat loss from the substrate due to convection currents caused by the temperature differential in the surrounding gas phase, but this will usually be less than the radiation loss, because of the low value of the heat transfer coefficient, h, of gases. The heat loss by this mechanism, Q_c, can be calculated, approximately, by using the Richardson–Coulson equation

$$Q_c = h(T_s - T_m) = 5.6(T_s - T_m)^{1/4}\,\mathrm{J\,m^{-2}\,s^{-1}\,K^{-1}}$$

which indicates a heat loss by this mechanism which is about one quarter of the radiation loss for a substrate at 1000 K and a wall temperature of 300 K. The major effect of the convection currents will be to mix the gas phase so that the surface of the substrate does not become surrounded by the reaction products.

Laser production of thin films

There are therefore two ways in which lasers may be used to bring about photon-assisted film formation. If the laser emits radiation in the near-ultra-violet or above, photochemical decomposition occurs in the gas phase and some unabsorbed radiation arrives at the substrate, but this latter should be a minor effect in the thin film formation. This procedure is referred to as *photolysis*. Alternatively, if the laser emits radiation in the infra-red, and the photons are only feebly absorbed to raise the rotational energy levels of the gaseous

DropBooks

species, the major absorption occurs at the substrate, which therefore generates a 'hot-spot', as described above, at the point where the beam impinges. This spot heats the gas phase in its immediate environment to bring about thermal dissociation. This is therefore a *pyrolytic* process. Lasers which provide a continuous source of infra-red are of much greater power than the pulsed sources which operate at higher frequencies, so the pyrolytic process is more amenable to industrial processing where a specific photochemical reaction is not required.

Because of the possibility of focusing laser beams, thin films can be produced at precisely defined locations. Using a microscope train of lenses to focus a laser beam makes possible the production of microregions suitable for application in computer chip production. The photolytic process produces islands of product nuclei, which act as preferential nucleation sites for further deposition, and thus to some unevenness in the product film. This is because the substrate is relatively cool, and therefore the surface mobility of the deposited atoms is low. In pyrolytic decomposition, the region over which deposition occurs depends on the thermal conductivity of the substrate, being wider the lower the thermal conductivity. For example, the surface area of a deposit of silicon on silicon is narrower than the deposition of silicon on silica, or on a surface-oxidized silicon sample, using the same beam geometry.

The energy densities of laser beams which are conventionally used in the production of thin films is about $10^3 - 10^4\,\mathrm{J\,cm^{-2}\,s^{-1}}$, and a typical substrate in the semiconductor industry is a material having a low thermal conductivity, and therefore the radiation which is absorbed by the substrate is retained near to the surface. Table 2.8 shows the relevant physical properties of some typical substrate materials, which can be used in the solution of Fourier's equation given above as a first approximation to the real situation.

Table 2.8 *Thermal conductivities and heat capacities of some metals and oxides*

Material	Thermal conductivity ($\mathrm{W\,m^{-1}\,K^{-1}}$)		Heat capacity ($\mathrm{J\,mol^{-1}\,K^{-1}}$)	
	300 K	1300 K	300 K	1300 K
Copper	397	244	24.35	32.19
Iron	73.3	28	25.02	34.84
Silicon	138		20.0	26.57
Beryllia	202	15	25.38	51.58
Magnesia	46	6.3	37.43	52.78
Silica	1.5	2.5	44.82	71.96
Alumina	39	5	79.36	128.78

Molecular decomposition in plasma systems

Apart from thermal and photon decomposition, the production of atoms and radicals in gaseous systems always occurs in plasma. This is because of the presence of both high energy electrons as well as photons in the plasma volume. The energy spectrum of the electrons is determined by the ionization potential of the plasma gas, the mean free path of the electrons between collisions, which depends on the pressure, and the applied electric potential gradient. Measurements of the energy spectrum in a glow discharge have yielded electron energy values of the order of 2–10 eV (200–1000 kJ mole^{-1}), and the photon spectrum can extend to 40 eV. The plasma therefore contains electrons and photons which can produce the free radicals which initiate chain reactions, and the novel feature is the capability to produce significant quantities of ionized gaseous species. The ions which are co-produced in the plasma have a much lower temperature, around 7–800 K, and hence the possibility that the target will be excessively heated during decomposition using plasma is very unlikely. However, there is not the capability of easy control of the energy of the dissociating species as may be exercised in photodecomposition.

All of the atomic species which may be produced by photon decomposition are present in plasma as well as the ionized states. The number of possible reactions is therefore also increased. As an example, the plasma decomposition of silane, SiH_4, leads to the formation of the species, SiH_3, SiH_2, H, SiH_2^+, SiH_3^+ and H_2^+. Recombination reactions may occur between the ionized states and electrons to produce dissociated molecules either directly, or through the intermediate formation of excited state molecules.

DropBooks

$$AB + e^- \longrightarrow A + B : AB + e^- \longrightarrow AB^* + e^- \longrightarrow A + B + e$$

where AB^* represents a molecule in an excited state in which an energy level is reached involving some electron re-arrangement, such as *spin decoupling* in the stable bonding configuration of the molecule. The lifetime of these excited states is usually very short, of the order of 10^{-7} seconds, and thus they do not play a significant part in reactions which normally occur through the reaction of molecules or atoms in the ground, most stable, state. They may provide the activation energy for a reaction by collision with normal molecules before returning to the ground state, similar to the behaviour of the activated molecules in first-order reactions.

A useful application of plasma is in the *nitriding* of metals or the formation of nitrides. Thermal methods for this require very high temperatures using nitrogen gas as the source, due to the high stability of the nitrogen molecule, and usually the reaction is carried out with ammonia, which produces nitrogen and hydrogen by dissociation. There is therefore a risk of formation of a nitrohydride in some metals, such as titanium and zirconium, which form stable hydrides as well as the nitrides. In a nitrogen plasma, a considerable degree of

dissociation of the nitrogen molecules occurs, together with positively charged species such as N^+ and N^{2+}. The rate of nitriding of metals such as titanium may be increased by imposing a negative potential on the metal to be nitrided with respect to the plasma.

Carbides may also be prepared, either by direct carburizing, as in the case of steel, in which a surface carbide film dissolves into the substrate steel, or by refractory metal carbide formation as in the cases when one of the refractory metal halides is mixed with methane in the plasma gas.

Bibliography

D.A. Eastham. *Atomic Physics of Lasers*, Taylor & Francis, London (1986) QC 688 E37.
J. Mazumdar and A. Kar. *Laser Chemical Vapor Deposition*, Plenum NY (1995) TS 695 M39.
J.G. Eden. *Photochemical Vapor Deposition*, J. Wiley (1992) TS 693 E33.
B. Koplitz, Z. Xu and C. Wittig, *Appl. Phys. Lett.*, **52**, 860 (1988).
K. Kamisako, T. Imai, and Y. Tarui, *Jpn. J. Appl. Phys.*, **27**, 1092 (1988).
L. Hellner, K.T.V. Grattan and M.H.R. Hutchinson, *J. Chem. Phys.*, **81**, 4389 (1984).
V.G. Jenson and G.V. Jeffreys. *Mathematical Methods in Chemical Engineering*, Academic Press, London (1963).
M. Venugopalan and R. Avni, Chapter 3 in Klabunde loc. cit. (1985).

Chapter 3

Vapour phase transport processes

Vapour transport processes

A rapidly developing technique in the materials science of thin film and single crystal growth involves the transport of atoms across a temperature gradient by means of gas–solid reactions. The objectives may be many, and include the separation of elements from an unwanted impurity and the removal of atoms from a polycrystalline sample to form a single crystal among others. The atomic species are transported by molecules which are formed by reaction of the solid with a specially chosen reactant gas, and may occur up or down the temperature gradient, depending on the nature of the transport reaction.

In most circumstances, it can be assumed that the gas–solid reaction proceeds more rapidly than the gaseous transport, and therefore that local equilibrium exists between the solid and gaseous components at the source and sink. This implies that the extent and direction of the transport reaction at each end of the temperature gradient may be assessed solely from thermodynamic data, and that the rate of transport across the interface between the gas and the solid phases, at both reactant and product sites, is not rate-determining. Transport of the gaseous species between the source of atoms and the sink where deposition takes place is the rate-determining process.

DropBooks

Thermodynamics and the optimization of vapour phase transport

The choice of the transporting reagent for a given material is made so that the reaction is as complete as possible in one direction, in the uptake, and the reverse reaction in the opposite direction at the deposition site. This requires that not only the choice of the reagent, but also the pressure and temperature ranges under which the reaction is most effectively, or quantitatively, performed, must be calculated (Alcock and Jeffes, 1967; 1968). There will always be limitations placed on this choice by the demands of the chemical inertness and temperature stability of the containing materials in which the reaction is carried out.

These considerations apart, the selection of the optimum conditions for the performance of a transporting reaction requires the choice of the best average value of the equilibrium constant. The effect of the range in the

Table 3.1 *Values of pXY_2 at equilibrium with $X(s)$ at varying values of $K(p = 1\,atmos)$ for the reaction*

$$X(\mathrm{s}) + Y_2(\mathrm{g}) = XY_2(\mathrm{g})$$

K	pXY_2 (atmos)
10^{-3}	9.1×10^{-4}
10^{-2}	9.1×10^{-3}
10^{-1}	9.1×10^{-2}
1	0.50
10	0.91
10^2	0.99
10^3	0.999

equilibrium constant of a transporting reaction on the partial pressure variation of a transporting gas is exemplified by Table 3.1 for the reaction:

$$X(\mathrm{s}) + Y_2(\mathrm{g}) = XY_2(\mathrm{g})$$

This shows the partial pressure of transporting molecules which are formed at various values of the equilibrium constant, for the reaction carried out at one atmosphere pressure. It can be seen that the greatest change in the equilibrium partial pressure occurs around the value of the equilibrium constant of unity, and hence where the standard Gibbs energy change has the value zero. It is true that the greatest value of the partial pressure of the transporting molecule is to be found at the highest value of the equilibrium constant, but the greatest change is about the value of unity.

The optimal choice depends on the total pressure of the system, and on the stoichiometry of the reaction. As an example, the transportation of zirconium as the tetra-iodide is made at low pressure, while the purification of nickel by tetracarbonyl formation is made at high pressure. These reactions may be written as

$$\mathrm{Zr} + 4\mathrm{I(g)} = \mathrm{ZrI_4(g)} \quad \Delta G^\circ = -784\,900 + 321.73T \quad \mathrm{J\,mol^{-1}}$$
$$= 0 \text{ at } 2440\,\mathrm{K}$$

and

$$\mathrm{Ni} + 4\mathrm{CO(g)} = \mathrm{Ni(CO)_4} \quad \Delta G^\circ = -138\,860 + 368.7T \quad \mathrm{J\,mol^{-1}}$$
$$= 0 \text{ at } 377\,\mathrm{K}$$

Both reactions involve the formation of a vapour-transporting species from four gaseous reactant molecules, but whereas the tetra-iodide of zirconium is a stable molecule, the nickel tetracarbonyl has a relatively small stability. The equilibrium constants for these reactions are derived from the following considerations:

For the general reaction

$$X(\mathrm{s}) + 4Y(\mathrm{g}) = XY_4(\mathrm{g})$$

when x moles of product are formed, leaving $4(1-x)$ moles of reactant gas, and yielding a total number of moles $(4-3x)$, the equilibrium constant is given by

$$K = \frac{1}{P^3}\frac{x(4-3x)^3}{(4-4x)^4}$$

where P is the total pressure. Considering only the value of the equilibrium constant, and ignoring the temperature effect on the actual value in any particular process, the optimum value of K will be found at the maximum value of the *efficiency function*

$$F = p\,\mathrm{d}p/\mathrm{d}K$$

for the product gas.

DropBooks

Efficient transport of material across a temperature gradient depends not only on the change in the equilibrium constant of the transporting reaction, but also on the mean partial pressure of the transporting species. The product $p\,\mathrm{d}p/\mathrm{d}K$ can be used to assess the effectiveness of a given reaction, and the maximum of this function is to be found at different values of K, depending on the total pressure and the stoichiometry. According to Le Chatelier's principle it is to be expected that a change in total pressure will have an effect on the maximum of this function, and in the examples of zirconium and nickel refining given above, there is a marked difference in the optimum conditions for carrying out these reactions. This is due to the large difference in the heats of formation of these transporting species and the effect of these heats on the value of the equilibrium constants. Figure 3.1 shows that the optimum for a reaction involving no change in the number of gaseous molecules, which we shall call a 1:1 reaction, is independent of the total pressure. The change due to pressure in a 4:1 reaction, such as the refining reactions discussed above, is very marked however, leading to different values in the optimum value of the equilibrium constant, thus a low pressure system is best for zirconium transport where the equilibrium favours the iodide, while a high-pressure system is used for nickel purification, since the equilibrium constant produces a small partial pressure of the carbonyl at one atmosphere pressure.

The direction of vapour transport across a thermal gradient

In some transport reactions the transporting species is carried up a temperature gradient and in others the transport is in the opposite direction. For example the transport of aluminium by reaction with $AlCl_3$ to form the monochloride, AlCl, occurs down the temperature gradient. This reaction is written as

$$2Al + AlCl_3(g) = 3AlCl(g) \quad \Delta G^\circ = 391\,600 - 261.3T \quad J\,mol^{-1}$$

and the lower chloride is the transporting gas. The difference between this reaction, a 1:3 reaction, and the zirconium transport reaction 4:1, which occurs up a temperature gradient, lies in the entropy change. This is mainly determined by the change in the number of gaseous molecules which occurs in each reaction. The 1:3 reaction shown above will be accompanied by an increase in the

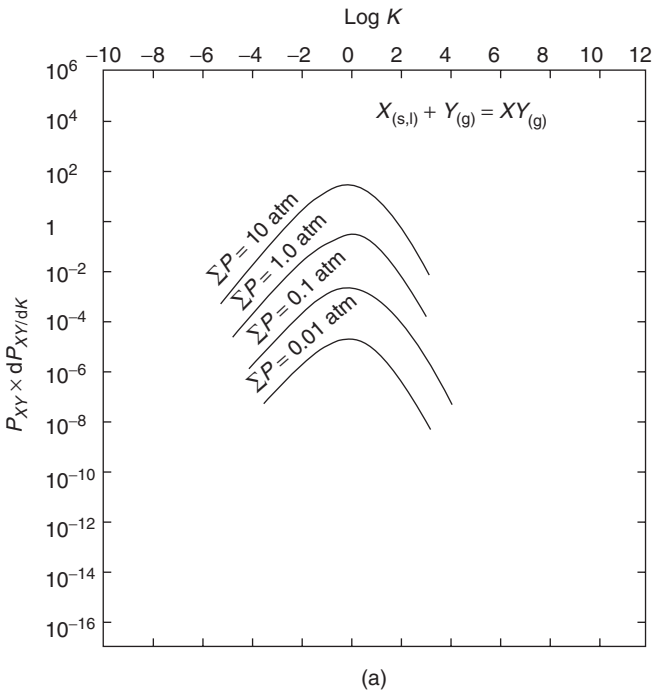
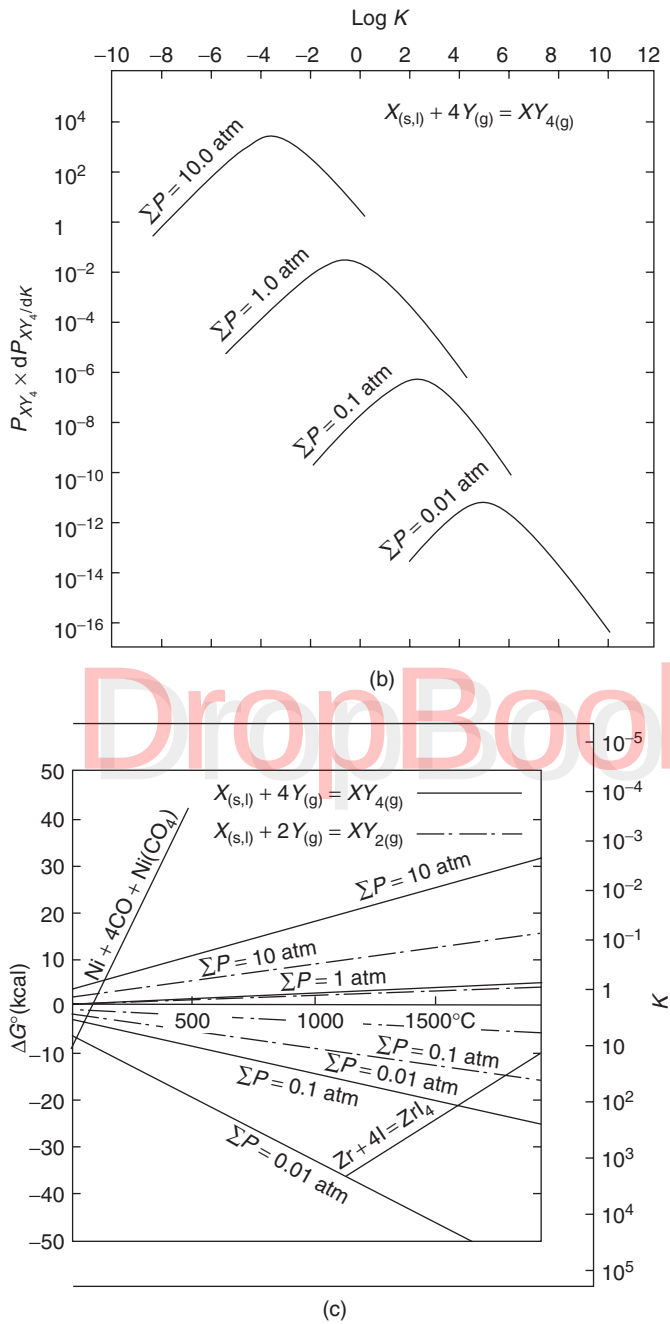


Figure 3.1 *(a) & (b) The efficiency of 1:1 and 1:4 vapour phase transport reactions, showing the marked dependence of the optimum for the 1:4 reaction on the pressure. (c) The dependence of the 1:2 and 1:4 reaction Gibbs energy on temperature and pressure, showing that the formation of nickel carbonyl is favoured by high pressure, and that of zirconium tetra-iodide, which is much more stable, is favoured by low pressures*


Log K
−10 −8 −6 −4 −2 0 2 4 6 8 10 12
$X_{(s,l)} + 4Y_{(g)} = XY_{4(g)}$
$\Sigma P = 10.0$ atm
$\Sigma P = 1.0$ atm
$\Sigma P = 0.1$ atm
$\Sigma P = 0.01$ atm
$P_{XY_4} \times dP_{XY_4}/dK$
(b)
$X_{(s,l)} + 4Y_{(g)} = XY_{4(g)}$
$X_{(s,l)} + 2Y_{(g)} = XY_{2(g)}$
$Ni + 4CO = Ni(CO)_4$
$\Sigma P = 10$ atm
$\Sigma P = 1$ atm
500 1000 1500°C
$\Sigma P = 0.1$ atm
$\Sigma P = 0.01$ atm
$Zr + 4I = ZrI_4$
ΔG° (kcal)
K
(c)

DropBooks

Figure 3.1 *(continued)*

entropy content, while the zirconium refining 4:1 reaction shows a decrease from left to right in the equation of transport.

The standard entropies of monatomic gases are largely determined by the translational partition function, and since this involves the logarithm of the molecular weight of the gas, it is not surprising that the entropy, which is related to the translational partition function by the Sackur–Tetrode equation,

$$S = 3/2R \ln M + (5/2)R \ln T - 2.300$$

should also be an approximately linear function of the logarithm of the molecular weight, having a value of $200\,\mathrm{J\,K^{-1}}$ at 298 K for light molecules, rising to about $600\,\mathrm{J\,K^{-1}}$ at a molecular weight of 200 for polyatomic molecules. It also follows that the iodides will have the largest entropy change when compared with the other halides due to this mass effect in transporting reactions, especially when combined with light metals.

The choice of halogen in transport reactions

The value of the change in partial pressure of the transporting gas, at one atmosphere where pressure, with temperature indicates the balance between the standard heat of the reaction and temperature times the standard entropy change. In the case of chloride transport this balance sometimes occurs only at an unacceptably high temperature due to the large heats of formation of most chlorides. The optimum temperature for vapour transport is significantly reduced by the use of bromine, by approximately $100\,\mathrm{kJ\,mol^{-1}}$, and even more by the use of iodine, by roughly double that amount, as the transporting halogen. This is because the heats of formation of corresponding gaseous halides reflect the decrease in the electron affinities of the halogens in the sequence Cl > Br > I, and the fact that the metal–halogen bond length increases in the opposite sequence, M–Cl < M–Br < M–I. The electron affinities determine the magnitude of the ionic contribution to the metal–halogen bond, and the bond length determines the covalent as well as the ionic contributions. Furthermore, iodine is the most practical species when the reaction is carried out on a small scale in a sealed system, or under vacuum conditions, because it may be introduced into the container in solid form, and the container can be sealed at room temperature before the experiment or application is begun.

The vapour phase refining and separation of metals

The classical examples of the transporting of metals by halogens are the van Arkel refining of metals, and the prolongation of the working life of tungsten lamps. Both of these use iodine to provide the transporting molecule and function by transporting the metal across a temperature gradient. In van

Arkel refining a sample of the impure metal, for example zirconium, is heated to a temperature around 550 K in contact with low pressure iodine gas in a sealed system which has a heated tungsten filament in the centre. The filament temperature is normally about 1700 K. At the source the iodides of zirconium and some of the impurities are formed and these diffuse across the intervening space, where the total pressure is maintained at 10^{-3} atmos, and are decomposed on the filament. The iodine then returns to form fresh iodide at the source, and the transport continues.

The anticipated content of impurities in the refined metal may be calculated *a priori* by assuming thermodynamic equilibrium at both metal/gas interfaces, and using the relevant stabilities of the gaseous iodides. Adequate thermodynamic data could provide the activities of the impurities with that of zirconium close to unity, but the calculation of the impurity transport obviously requires a knowledge of activity coefficients in the original impure material, which are not sufficiently well known.

The three impurities, iron, silicon and aluminium are present in the metal produced by the Kroll reduction of zirconium tetrachloride by magnesium to the extent of about 1100 ppm. After the iodide refining process the levels of these impurities are 350, 130 and 700 ppm respectively. The relative stabilities of the iodides of these metals compared to that of zirconium can be calculated from the exchange reactions

$$\mathrm{Zr} + \mathrm{SiI_4(g)} = \mathrm{Si} + \mathrm{ZrI_4(g)} : \Delta G^\circ_{550} = -241\,600 - 8.26T = -246\,500$$

$$\log K = \log \frac{a\mathrm{Si}\, p\mathrm{ZrI_4(g)}}{a\mathrm{Zr}\, p\mathrm{SiI_4(g)}} = 21.5$$

$$3\mathrm{Zr} + 2\mathrm{Al_2I_6(g)} = 4\mathrm{Al} + 3\mathrm{ZrI_4(g)} : \Delta G^\circ = -89\,040 - 150.4T = -171\,019$$

$$\log K = \log \frac{a^4\mathrm{Al}\, p\mathrm{ZrI_4(g)}}{a^3\mathrm{Zr}\, p^2\mathrm{Al_2I_6(g)}} = 16.20$$

and there are no reliable data for the iron gaseous iodides. Since silicon and aluminium are both present in the impure zirconium as the stable compounds Zr_3Si and Zr_3Al respectively, their activity coefficients should be less than one, and it is clear that the thermodynamic data suggest that zirconium should be transported preferentially initially. The final experimental amounts of silicon and aluminum transported are significantly higher than these data would indicate. They must therefore be transported as a result of iodination when the surface has been depleted of zirconium. The low temperature at which the reaction with iodine is carried out supports the conclusion that thermodynamic data will only be of limited value in the estimation of the transport of impurities in this process.

This is an instructive example of the fact that thermodynamic data can only be used to calculate the extent to which a reaction can be carried out

before equilibrium is reached, but the kinetics of the reaction depend on the mechanism of the reaction in the context of the reacting substances.

The separation of niobium from tantalum through the gaseous chlorides is carried out at higher temperature, about 900 K, and it is therefore to be expected, as is the case, that the thermodynamic data will provide a useful guide. These metals form a number of chlorides, mainly the tri- tetra- and pentachlorides. These latter are much more volatile than the tetrahalides, and the exchange reaction at 900 K

$$\mathrm{NbCl_5(g) + TaCl_4 = TaCl_5(g) + NbCl_4}:$$

$$\Delta G^\circ = -181\,300 + 180.4T \quad \mathrm{J\,mol^{-1}}$$

$$= 0 \text{ at } 1005\,\mathrm{K}$$

and hence this reaction, which is not affected by a change in the total pressure, is found to be an efficient means of separating the two metal chlorides.

The thermodynamics of the vapour phase transport of compounds

In this more complicated case, both components must be transported in the proportions indicated by the chemical composition. In the simplest cases, one of the components is an elementary species during transport, which is generally so in the transport of oxides and arsenides by elementary halogens, for example. The identity of the gas or gases which may be transporting the metal are frequently difficult to decide because of the complexity resulting from the possibility of forming a number of species. For example, the transport of niobium oxides by chlorine could involve the species $NbCl_5$, $NbCl_4$ and $NbCl_3$ as well as some oxychlorides such as $NbOCl_3$.

The Gibbs energy of formation of the more important molcules are,

$$\mathrm{NbO_2 + (3/2)Cl_2 = NbOCl_3(g) + (1/2)O_2}$$

$$\Delta G^\circ = 34\,140 - 59.1T \quad \mathrm{J\,mol^{-1}}$$

$$\mathrm{NbO_2 + (5/2)Cl_2 = NbCl_5(g) + O_2}$$

$$\Delta G^\circ = 88\,980 - 5.57T \quad \mathrm{J\,mol^{-1}}$$

which shows that the oxychloride is, in fact, the more stable gas under these circumstances.

In the transport of gallium arsenide by chlorine, there is a competition between the monochloride and the trichloride for the transport of gallium after arsenic has evaporated as the element or as a chloride. The probability

of formation of the monochloride may be determined from the data for the reaction

$$GaCl_3(g) + 2Ga = 3GaCl(g) \quad \Delta G^\circ = 196\,900 - 249.4T \quad J\,mol^{-1}$$
$$= 0 \text{ at } 790\,K$$

Below this temperature, mainly $GaCl_3$ transports gallium, but above this temperature, the monochloride will begin to predominate.

A graphical method involving the Gibbs energies of formation per gram-atom can be used to assess the feasibility of potential transport reactions. If the Gibbs energy of formation of the various gaseous species which can be formed in a ternary system are known, the relative partial pressures of all of these gases can be calculated for known activities of the elements in the solid phase to be transported. The feasibility of a vapour phase transport reaction of a binary solid such as SiC in the ternary Si–C–Cl requires that the transport reactions carry the proper amounts of each component in the solid, for example the transport of silicon and carbon in SiC in 1:1 proportion. This can be assessed from the chemical potential diagrams for the gases in the binary systems Si–Cl, Si–C and C–Cl, by joining the common axes in the sequence (Cl–Si)-(Si–C)-(C–Cl). The Cl–Si system must have a common chemical potential of chlorine with the C–Cl system in any equilibrium situation. In this the partial pressures of each of the gaseous species in the transporting reaction must be calculated for all of those silicon and carbon activities which are together in equilibrium with SiC. It is clear from the graph (Figure 3.2) that the process cannot be used because of the much lower stability of CCl_4 than $SiCl_4$. For the quaternary system Si–C–H–Cl the Gibbs energy data are joined in the following sequence, Cl–Si–C–H–Cl, and a common chlorine activity must apply to the Si–Cl and H–Cl systems.

DropBooks

This technique is a useful graphical approach to the problem together with the solution of the multicomponent Gibbs minimization equations using computerized procedures and the ancillary data for the Gibbs energies for all of the potential species. For example, it is clear that whereas chlorine cannot be used as a transporting agent for silicon carbide, hydrogen chloride gas is a good choice. The Gibbs energy of this reaction

$$SiC + 4HCl(g) = SiCl_4(g) + CH_4(g)$$
$$\Delta G^\circ = -305\,040 + 255.3T \quad J\,mol^{-1}$$
$$= 0 \text{ at } 1195\,K$$

This is a 4:2 reaction, and is thus pressure dependent. However, it is necessary to compute the equilibrium partial pressure of some alternative gaseous species, such as $SiCl_3$, and other hydrocarbons such as C_2H_2 and for this a Gibbs energy minimization calculation should be made.

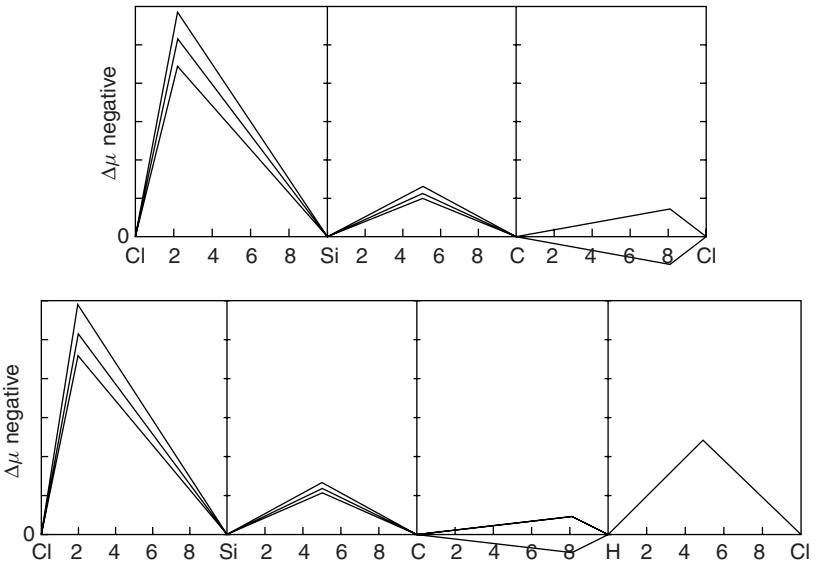


Figure 3.2 *Chemical potential diagrams for the transport of silicon carbide by chlorine, showing that the much greater stability of $SiCl_4$ than CCl_4 makes this process very inefficient, while the use of HCl as the transporting gas can be operated under optimum conditions*

Multicomponent thermodynamics in gaseous systems

A simple example of the analysis of multicomponent systems will suffice for the present consideration, such as the calculation of the components in a gaseous mixture of oxygen, hydrogen and sulphur. As a first step, the Gibbs energy of formation of each potential compound, e.g. S_2, H_2S, SO, SO_2, H_2O etc. can be used to calculate the equilibrium constant for the formation of each compound from the atomic species of the elements. The total number of atoms of each element will therefore be distributed in the equilibrium mixture in proportion to these constants. Thus for hydrogen with a starting number of atoms n_H, and the final number of each species n'_i,

$$n_H = n'_H + 2n'^2_H K'_1 + 2n'^2_H n'_S K'_2 + 2n'^2_H n'_O K'_3$$

K'_1, K'_2, and K'_3 are the equilibrium constants for the formation of hydrogen molecule, H_2S and H_2O gases respectively from the atomic elements. The equations for each of the atomic elements form simultaneous non-linear equations which can be solved for example by Newton's method, starting with very small initial values of the number of each atomic and molecular species, i.e. 10^{-8}.

Since in most practical circumstances at temperatures where vapour transport is used and at around one atmosphere pressure, the atomic species play a minor role in the distribution of atoms, it is simpler to cast the distribution equations in terms of the elemental *molecular* species, H_2, O_2 and S_2, the base molecules, and the derived molecules H_2O, H_2S, SO_2 and SO_3, and eliminate any consideration of the atomic species. In this case, let X_i be the initial mole fraction of each atomic species in the original total of N^0 atoms, and the variables x_i represent the equilibrium number of each molecular species in the final number of molecules, N_f. Introducing the equilibrium constants for the formation of each molecule from the elemental atomic species, with a total pressure of one atmos, we can write

$$(X_H + X_O + X_S)N^0 = 2(x_1 + x_2 + x_3) + 3x_1x_2^{1/2}K_{H_2O}/N_f^{1/2} + 3x_1x_3^{1/2}K_{H_2S}/N_f^{1/2} \ldots$$

and so on for the other species, such as SO_2.

The balance for each atomic species now runs,

$$X_H N^0 = 2x_1 + 2n_{H_2O} + 2n_{H_2S}$$

$$X_O N^0 = 2x_2 + n_{H_2O} + 2n_{SO_2} + 2n_{SO_3}$$

$$X_S N^0 = 2x_3 + n_{H_2S} + n_{SO_2} + 3n_{SO_3}$$

DropBooks

and if the final pressure is P_t, each molecular species partial pressure can be evaluated following this example for water vapour

$$K_{H_2O} = pH_2O/pH_2(pO_2^{1/2}); \quad pH_2O = xH_2O(P_t/N_f)$$
$$= K_{H_2O}\, xH_2\, x^{1/2}O_2(P_t/N_f)^{3/2}$$

$x_{H_2O} = K_{H_2O}\, x_1\, x_2^{1/2}(P_t/N_f)^{1/2}$ and so on for other molecular species.

Hence the total contribution of water vapour to the combined form of hydrogen is $3x_1x_2^{1/2}\,K_{H_2O}(P_t/N_f)^{1/2}$ allowing for contributions to the hydrogen balance and the corresponding oxygen balance. N_f is simply equal to the sum of the final number of molecules

$$N_f = 2x_1 + 2x_2 + 2x_3 + \Sigma n_i \text{ (all other molecules)}$$

The total equation can now be decomposed into a set of equations for each atomic species, which are re-arranged to yield functions equal to zero. Thus

$$F(x_1) = 2x_1 + 2x_1x_2^{1/2}K_{H_2O}/N_f^{0.5} + 2x_1x_3^{1/2}K_{H_2S}/N_f^{1/2} - X_H N^0 = 0$$

is the equation for hydrogen distribution. These equations are differentiated partially with respect to each component element, F'_{ij}, and the results used in

the iterative solution

$$x_{1(k+1)} = x_{1(k)} - F(x_{1(k)})/F'(x_{1(k)})$$

where

$$F'x_1(k) = \partial\frac{Fx_1(k)}{\partial x_1} + \partial\frac{Fx_1(k)}{\partial x_2} + \partial\frac{Fx_1(k)}{\partial x_3}$$

At higher pressures, the total pressure P_t must be included in the equations, and at low pressures, such as are used in the van Arkel process, the atomic species cannot be ignored.

When one of the elements is solid, as in the case of carbon in the calculation of the partial pressures of the gaseous species in the reaction between methane and air, CO(g) can be used as a basic element together with hydrogen and oxygen molecules, and thus the calculation of the final partial pressure of methane must be evaluated using the equilibrium constant for CH_4 formation

$$K_{CH_4} = p\mathrm{CH_4}(p^{1/2}\mathrm{O_2}/p\mathrm{CO})p^2\mathrm{H_2} = K_{CH_4}\, p\mathrm{CO}\, p^2_{H_2O}\, K_{H_2O}$$

These multicomponent calculations are now computerized, and complicated systems, such as the Si–C–H–Cl quaternary, may be solved by the use of commercially available software, e. g. the IVTAN database. The solution to this multicomponent system which is obtained by this means is somewhat subjective, since, at the time of writing for example, data are available for 72 gaseous species in the quaternary system Si–C–H–Cl. Choosing 19 of the most probable of these, and using the IVTAN software to solve this multicomponent equilibrium, yields the following results for the most probable species (see Table 3.2).

Table 3.2 *Partial pressures of some species in the gaseous system Si–C–H–Cl at 1195 K*

Gaseous species	Partial pressure (atmos)
CH_4	3.51×10^{-1}
$SiCl_4$	4.60×10^{-1}
H_2	1.29×10^{-1}
HCl	2.52×10^{-3}
C_2H_4	3.36×10^{-2}
C_2H_2	2.09×10^{-2}
C_2H_6	7.17×10^{-4}
SiH_4	7.35×10^{-4}
$SiCl_3$	7.04×10^{-4}
SiH_4	9.85×10^{-5}

It therefore appears that other hydrocarbons than methane take part, but to a lesser extent. The other species which were considered in this calculation were SiCl, SiH_4, CH_3Cl, SiH_3, H, Si, Si_2, Cl and Cl_2, all of which are gaseous at this temperature. It is difficult to predict before this calculation what will be the major species, and attempts to limit the number of compounds which are included is to some extent subjective, but this can be corrected by using the graphical method as a preliminary.

To return to the problem of the vaporization of the tantalum silicides, which could be transported as the tetraiodide of each element, but not as the elementary species. From these data it can be concluded that whatever the starting point in the composition range, the composition of the surface phase will tend towards Ta_5Si_3, which is the most nearly congruently vaporizing composition.

The exchange reaction

$$TaCl_4(g) + Si = Ta + SiCl_4(g)$$

has the equilibrium constant given by

$$K = \frac{p\mathrm{SiCl_4}\, a\mathrm{Ta}}{p\mathrm{TaCl_4}\, a\mathrm{Si}}$$

has a value of about 10^3 at 1000 K, which shows that in the vapour phase above a tantalum–silicon mixture, be it compound or alloy, the partial pressures of the two gases will only be approximately equal when a_{Ta} is much larger than a_{Si}. Alternatively, if the iodides were used for this reaction the heat change would be reduced by the difference in heats of formation of the halides. Thus

$$\Delta H^\circ(SiCl_4) - \Delta H^\circ(TaCl_4) = 662.7 - 566.9 = 95.8\,\mathrm{kJ\,mol^{-1}}$$

The heat of formation of $SiI_4(g)$ is $-125.1\,\mathrm{kJ\,mol^{-1}}$ and so the heat of formation of TaI_4 may be estimated to be $-29\,\mathrm{kJ\,mol^{-1}}$, and the entropies may be estimated from the empirical equation

$$S^\circ(298) = -131.8 + 207.1 \log M \text{ (Kubaschewski } \textit{et al.} \text{ loc. cit.)}$$

to be for SiI_4, $S^\circ(298) = 433$ and for TaI_4, $S^\circ(298) = 456\,\mathrm{J\,K^{-1}\,mol^{-1}}$.

This estimated Gibbs energy of the transporting reaction is,

$$Ta + Si + 4I_2(g) = TaI_4(g) + SiI_4(g) = -396\,290 + 220.4T$$

which passes through zero at 1800 K. The heats of formation of the silicides Ta_5Si_3 and Ta_3Si_2 are about $40\,\mathrm{kJ\,gram\text{-}atom^{-1}}$, with entropies of formation

DropBooks

approximately equal to zero entropy units per gram-atom. The Gibbs energy of the reaction to form the gaseous iodides from the compound Ta_5Si_3 is therefore obtained from the reactions

$$5Ta + 3Si + 16I_2(g) = 5TaI_4(g) + 3SiI_4(g);$$
$$\Delta G^\circ = -1\,490\,610 + 864.8T\ \text{J}$$
$$5Ta + 3Si = Ta_5Si_3; \quad \Delta G^\circ = -339\,300 + 9.8T\ \text{J}$$

and hence

$$Ta_5Si_3 + 16I_2(g) = 5TaI_4(g) + 3SiI_4(g)$$
$$\Delta G^\circ = -1\,151\,300 + 873.8T\ \text{J}$$

which passes through zero at approximately 1300 K.

The chemical potential diagram for this ternary system (Figure 3.3) shows that the reaction with the elements would reduce the iodine pressure to a very low value, which is not suitable for CVD, whereas the compound Ta_5Si_3, in which the chemical potentials of the two elements are about 40 kJ gram-atom^{-1}, would be suitable for CVD at about 1300 K.

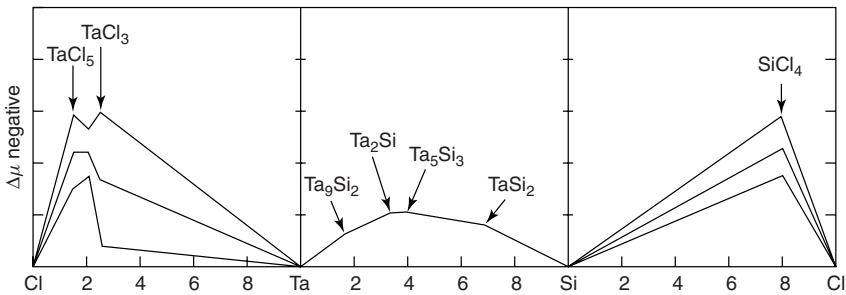


Figure 3.3 *Chemical potential diagram for the transport of titanium silicides by chlorine, showing that only $TaSi_2$ can provide the proper ratio of Ta and Si for stoichiometric transport*

Sintering by vapour phase transport

The particle size distribution in a polycrystalline aggregate changes towards a larger average size when the solid is at high temperature, by a process of sintering. The increase in the average particle size which reduces the aggregate surface area is sometimes brought about by vapour phase transport. A classical example of this is the sintering of sodium chloride. If a number of equally sized NaCl spheres are laid side by side on a flat plate at a temperature of 1000 K, the particle shape becomes elongated, and the points of contact between the

spheres grow into a solid neck. The simplest explanation of this is that NaCl molecules evaporate from the surfaces of the spheres and condense into the points of contact. During the whole process of vapour phase sintering, the centre-to-centre distance of two particles remains constant. The geometry of this process may therefore be represented by this simple model and the rate of sintering may be calculated to show that the neck radius and area and volume at any instant are

$$r = x^2/2a \quad A = \pi^2 x^3/2a \quad v = \pi x^4/2a$$

where x is the thickness, v is the volume, and a is the radius of the two spheres in contact. The mass, m, evaporating from the surface of the spheres under free evaporation conditions is given by the Kinetic Theory equation and the pressure difference by the Kelvin equation,

$$m = \alpha \Delta p \left(\frac{M}{2\pi RT}\right)^{1/2}; \quad \Delta p = \frac{\gamma p^\circ}{\rho r}\frac{M}{RT}; \quad \frac{mA}{\rho} = \frac{\mathrm{d}v}{\mathrm{d}t}$$

where α is the material vaporization coefficient and ρ is the density of the solid.

The dependence of the thickness of the neck on the time of sintering, t, is given by

$$\frac{x^3}{a} = \left(\frac{9\pi}{2MRT}\right)^{1/2} \frac{V_m^2 \gamma p^\circ}{RT} t$$

DropBooks

where p° is the vapour pressure of the solid, γ is the surface energy, V_m is the molar volume, T is the temperature, and M is the molecular weight of the vapour molecules.

Clearly the rate of thickening of the neck will be determined by the rate of transport of the NaCl molecules, and hence by the equilibrium vapour pressure at the sintering temperature. The gaseous transport process has a low temperature coefficient, as already indicated for diffusion in gases, but the heat of sublimation of the solid is high, and hence the activation energy of the vapour phase sintering process will be very close to the heat of sublimation of NaCl. The change in shape of the spheres is consistent with this model.

Grain growth by vapour phase transport

The process of sintering by vapour phase transport is probably important to the growth of single crystals of solids from polycrystalline samples in a closed system, where the vapour species are the transporting gas, which may have the same or different chemical composition from the solid. An example where

the transporting species has the same composition as the solid phase is in the growth of grains in UO_2 nuclear fuel rods during operation of a nuclear reactor. These are fabricated from uranium dioxide powders, and they operate in a nuclear reactor with a large temperature difference between the centre of a fuel rod and its external surface; of the order of 1800 K difference across a fuel rod of radius 1 cm. In normal operation, there is a short initial restructuring of the fuel rod such that an axial void appears along the rod, and the temperature gradient becomes relatively constant. The outside surface of a rod usually operates at temperatures around 500 K. It follows that there is a considerable temperature gradient across any void in the rod material in the radial direction. Material will therefore transport from the higher temperature surface of a void to the lower temperature surface and the void will move *up* the temperature gradient and towards the central void. During the transport of matter, either by vaporization or by surface migration around the walls of the pore, there is ample opportunity for the molecules, which are transported across the void, to condense to form single crystal material. A rod which is sectioned after some time in operation is found to have three crystalline zones (Figure 3.4). The central region has an almost transparent crystal structure, approximating to single crystals separated by radial cracks, which is surrounded by an equi-axed crystal zone showing some crystal growth, and the outer zone has the particle size distribution of the original material. The vaporization of UO_2 may

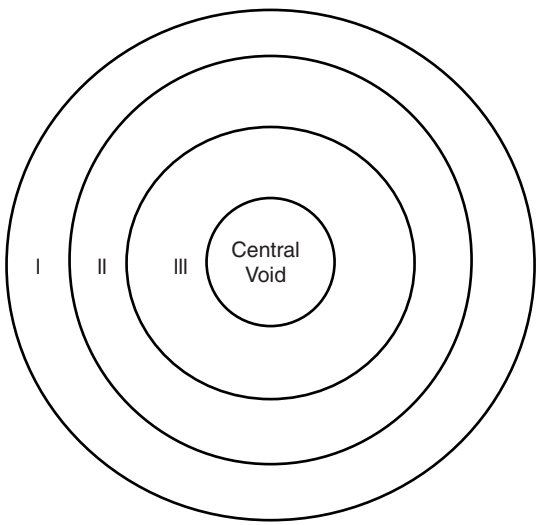


Figure 3.4 *Grain growth in a UO_2 fuel rod during high-temperature service, showing the three zones of the original grain structure (I), the equi-axed central zone (II), and the mainly single crystal zone (III) surrounding the central void*

be represented by the Gibbs energy equation

$$\mathrm{UO_2(s)} \longrightarrow \mathrm{UO_2(g)} \quad \Delta G^\circ = 567\,000 - 150T \quad \mathrm{J\,mol^{-1}}$$
$$= -RT \ln p\mathrm{UO_2(g)}$$

and the vapour pressure difference between 1000°C and 2000°C, which are roughly the temperatures at the extremes of the single crystal region, is therefore $10^{-15.4} - 10^{-5.2}$ atmospheres.

Vapour transport in flowing systems

The discussion so far can be applied to closed systems, but the more important mode of operation in many industrial applications uses an open system, in which the gases flow through the temperature gradient, the transporting molecules being carried by an inert gas, such as argon, or in a gaseous mixture resulting from a transporting chemical reaction. Since the creation of the transporting species takes place at the surface of the solid reactant, the vapour species must diffuse into the carrier gas, and the degree of saturation, i.e. the extent to which the carrier gas transports the thermodynamic equilibrium products of the transporting reaction, depends on the gas flow rate and temperature.

DropBooks

It is clear that the achievement of equilibrium is assisted by the maximum contact between the reactant and the transporting gas, but the diffusion problem is complex, especially in a temperature gradient, when a process known as *thermal diffusion* occurs. The ordinary concentration-dependent diffusion process occurs *across* the direction of gas flow, but the thermal diffusion occurs *along* the direction of gas flow, and thus along the temperature gradient.

Transport along a thermal gradient

In the stationary state, the gaseous components of a mixture of gases in a temperature gradient tend to separate such that the higher molecular weight species moves to the lower temperature region, and this results in a lower relative partial pressure of this species in the higher temperature region than in the original mixture, and vice versa for the lower molecular weight species. A simple kinetic theory by Gillespie (1939) of this phenomenon in a static binary gas mixture yields the equation

$$\frac{\mathrm{d}\ln x_1}{\mathrm{d}\ln T} = \frac{x_2(m_2 - m_1)}{2(m_1 x_1 + m_2 x_2)}$$

where x_i are the mole fractions of the gases, and m_i is the square root of the molecular weights. A similar equation for a multicomponent mixture of

gases is

$$\frac{\mathrm{d}\ln x_1}{\mathrm{d}\ln T} = \frac{1 - m_1}{2\Sigma m_i x_i}$$

where the summation is over all species. The effect of a foreign inert gas on the separation of two components is given by

$$\frac{\mathrm{d}\ln(x_1/x_2)}{\mathrm{d}\ln T} = \frac{m_2 - m_1}{2\Sigma m_i x_i}$$

Thus the addition of an inert gas which does not intervene chemically in the transport reaction but adds to the density of the gas, reduces the segregation due to thermal diffusion. An example of this is the reduction of thermal separation in a mixture of H_2 and H_2O by the addition of Hg vapour (Dastur and Chipman, 1948).

The effect of thermal diffusion in transport reactions can be seen when measuring the vapour pressure of a pure metal by the gas transport process in which metal vapour is carried by a neutral gas from the experimental zone holding the metal sample to a lower temperature where the metal vapour is condensed. The effect can also be seen in the measurement of a solid–gas equilibrium constant when the gas phase is a mixture of two gases with a large difference in the molecular weights, e.g. in H_2/H_2S mixtures. At low flow rates of the transporting gas, the result obtained for the vapour pressure is substantially higher than the true equilibrium pressure when the molecular weight of the metal vapour is higher than that of the transporting gas, e.g. gold in argon (Figure 3.5). There is an intermediate flow regime where the correct vapour pressure can be measured as shown by Knudsen cell measurements, and at high flow rates the system shows undersaturation.

Mass transport across a flowing gas

Transport across the direction of flow can be determined using Fick's first law of diffusion for the flux of material in particles/cm^2 sec^{-1} in a steady, time-independent state

$$J = -D\frac{\partial c}{\partial x}$$

together with a description of the velocity distribution in the flowing gas in the neighbourhood of the solid phase to be transported. The flow regime can be described with reasonable accuracy by the use of dimensionless numbers, or more easily and approximately by the use of the concept of a boundary layer. In this, the non-linear concentration change across the layer of gas in immediate contact with the solid is replaced by a hypothetical constant gradient over the

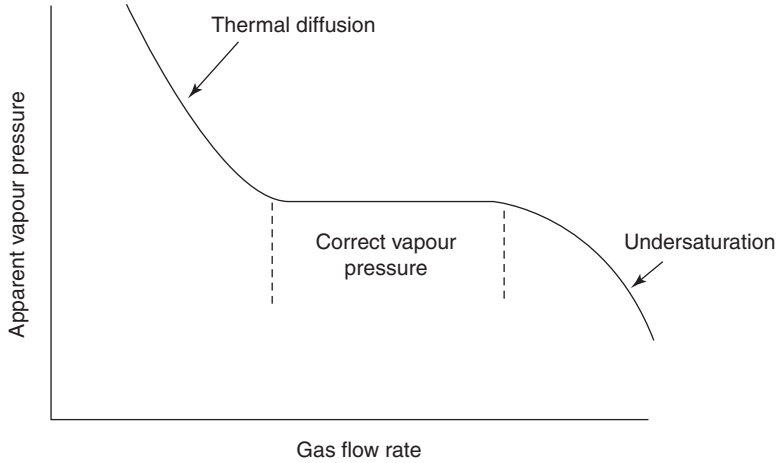


Figure 3.5 *The apparent vapour pressure of gold in gas transportation measurements as a function of the gas flow rate. Low flow rates, which were used earlier to assure equilibrium, are now known to be too high as a result of thermal diffusion in the gas mixture which is saturated with gold vapour*

DropBooks

thickness of a *boundary* or *diffusion* layer, δ, and the concentration is assumed to be constant at each surface of the boundary layer; c_s at the solid surface and c_g in the entraining gas. The differential in Fick's law is thus replaced by $(c_s - c_g)/\delta$. The ratio D/δ is referred to as the *mass transport coefficient*, k_d. An approximate thickness for the boundary layer may be expressed in dimensionless numbers for the case of streamline flow along a surface, where L is the distance which the gas has covered from the leading edge of the solid at a linear velocity, u, η is the viscosity and D_{A-B} is the diffusion coefficient in the boundary layer.

$$\delta = \frac{3L^{1/2}}{u^{1/2}} \eta^{1/6} D_{A-B}^{1/3}$$

For a gas in laminar flow over a condensed phase sample of length L, the mass transport across the boundary layer, in terms of the flux of molecules from the sample to the gas phase, is therefore

$$J_x = k_d(c_s - c_g) = k_d\, p_{eq}/RT(c_g = 0)$$

where k_d is the mass transport coefficient of the gas, and p_{eq} is the equilibrium partial pressure of the metal-transporting vapour species at the gas–solid interface.

The mass transport coefficient in this example can be related to the properties of the flowing gas by the equation

$$k_x L/D_{v/g} = 0.332 N_{Re}^{1/2} N_{Sc}^{1/3} = N_{Sh}$$

The dimensionless numbers in this equation are the Reynolds, Schmidt and the Sherwood number, N_{Sh}, which is defined by this equation. $D_{v/g}$ is the diffusion coefficient of the metal-transporting vapour species in the flowing gas. The Reynolds and Schmidt numbers are defined by the equations

$$N_{Re} = \frac{u\rho L}{\eta} \qquad N_{Sc} = \frac{\eta}{\rho D_{v/g}}$$

where u is the gas velocity, ρ is the density, η is the gas viscosity, and L is a length whose magnitude is determined by the solid/gas configuration. For example when a gas is flowing over a finite solid sample, L is the length of the sample, and when it flows along a tube, this length is the diameter of the tube. The average value of the mass transport coefficient over the length of the sample is derived from the Sherwood number, N_{Sh}.

$$N_{Sh}\ (\text{mean}) = (1/L) \int N_{Sh}(x) = 0.664 N_{Re}^{1/2} N_{Sc}^{1/3} = k_d\ (\text{mean})\ L/D_{v/g}$$

from which it follows that

$$J = k_d\ (\text{mean})\ p_{eq}/RT$$

The advantage of the use of dimensionless numbers in calculations such as these is that they may be applied independent of the physical size of the system being described.

The above discussion relates to diffusion-controlled transport of material to and from a carrier gas. There will be some circumstances where the transfer of material is determined by a chemical reaction rate at the solid/gas interface. If this process determines the flux of matter between the phases, the rate of transport across the gas/solid interface can be represented by using a rate constant, h, so that

$$J_{chem} = h p_{eq}/RT = h c_s$$

where h takes a value between 0 and 1. Any value of h less than one corresponds to some degree of reaction rate control. If J_{chem} is equal to or greater than J_{diff}, the transfer will be diffusion controlled and vice versa. The resultant equation using the boundary layer approximation for a mixed chemical-diffusion control is therefore

$$J = (D/\delta)(h p_{eq}/RT - c_g)$$

Material deposition from a flowing gas

Apart from the reactions described above for the formation of thin films of metals and compounds by the use of a solid source of the material, a very important industrial application of vapour phase transport involves the preparation of gas mixtures at room temperature which are then submitted to thermal decomposition in a high temperature furnace to produce a thin film at this temperature. Many of the molecular species and reactions which were considered earlier are used in this procedure, and so the conclusions which were drawn regarding choice and optimal performance apply again. For example, instead of using a solid source to prepare refractory compounds, as in the case of silicon carbide discussed above, a similar reaction has been used to prepare titanium boride coatings on silicon carbide and hafnium diboride coatings on carbon by means of a gaseous input to the deposition furnace (Choy and Derby, 1993); (Shinavski and Diefendorf, 1993).

The reactions

$$TiCl_4(g) + 2BCl_3(g) + 5H_2 = TiB_2 + 10HCl$$

and

$$HfCl_4(g) + 2BCl_3(g) + 5H_2 = HfB_2 + 10HCl$$

were used respectively. The first study was carried out in the temperature range 1323–1723 K and pressure in the range 6–23 kPa and the second in the temperature range 983–1573 K with a pressure range 0.7–7 kPa, with a heated carbon rod providing the condensation surface. These two successful studies differ widely in the thermodynamic properties of the reactions. The titanium diboride deposition was carried out with a range in the logarithm of the equilibrium constant for the reaction of 1.81 to 4.55 and the hafnium diboride deposition with a corresponding range of −8.03 to −1.0. The essential differences between the two studies in the gas phase was the range of pressures and the magnitude of the equilibrium constant.

It would be anticipated, as was found, that the TiB_2 deposit would be polycrystalline and smooth at the lower temperatures and higher pressures since both of these factors produce a lower rate of diffusion in the gas phase and thus of growth which is still acceptable, while the higher temperature range produced coarse-grained material. The activation energy of formation of the HfB_2 deposits was found to be typical of a gaseous diffusion process at temperatures above about 1100 K, but below this the rate was determined by an apparent activation energy of about 380 kJ mol^{-1}, but again there were advantages in the form of the product at the lower temperature operation.

Since the objective of these processes is the formation of a smooth layer of the deposit, probably fine-grained, the efficiency considerations which apply to

DropBooks

vapour phase transport are no longer of significance. The only chemical consideration in the design of CVD processes appears to be the presentation of the elements forming the deposit in the correct proportions as gaseous molecules which can be pyrolysed to form the required compound. However, the temperature at which the decomposition must be carried out can be considerably affected by the reactant which is chosen to remove the unwanted elements in the reactants. Thus, the temperature of decomposition of the chlorides in the studies reported above can be substantially reduced by the use of bromides and iodides.

The thermodynamic data for the formation of the IVB diborides together with the corresponding hydrogen halides are as follows:

TiB_2:

$$TiCl_4(g) + 2BCl_3(g) + 5H_2; \quad \Delta G^\circ = 298\,780 - 260.6T \quad J\,mol^{-1}$$

$$TiBr_4(g) + 2BBr_4(g) + 5H_2; \quad \Delta G^\circ = 255\,150 - 265T$$

$$TiI_4(g) + 2BI_3(g) + 5H_2; \quad \Delta G^\circ = 67\,140 - 258.8T$$

ZrB_2:

$$ZrCl_4(g) + 2BCl_3(g) + 5H_2; \quad \Delta G^\circ = 402\,760 - 258T$$

$$ZrBr_4(g) + 2BBr_3(g) + 5H_2; \quad \Delta G^\circ = 336\,100 - 253.1T$$

$$ZrI_4(g) + 2BI_3(g) + 5H_2; \quad \Delta G^\circ = 126\,400 - 257.7T$$

HfB_2:

$$HfCl_4(g) + 2BCl_3(g) + 5H_2; \quad \Delta G^\circ = 409\,840 - 256.5T$$

$$HfBr_4(g) + 2BBr_3(g) + 5H_2; \quad \Delta G^\circ = 348\,250 - 252.9T$$

$$HfI_4(g) + 2BI_3(g) + 5H_2; \quad \Delta G^\circ = 161\,280 - 260T$$

From these data it can be concluded that the entropy change for the diboride production is relatively constant, but the enthalpy change decreases in all cases in going from the chlorides to the iodides, and hence the temperature of deposition of the diboride will decrease.

Similar results are obtained for the deposition of the carbides of these metals using methane as a source of carbon, and silicon tetrahalides for the preparation of silicides. These reactions are more complex than the preparation of the diborides because of the number of carbides and silicides that the transition metals form, some of which have wide ranges of non-stoichiometry. The control of the ratio of the partial pressures of the ingoing gases is therefore important as a process variable.

The deposition of material along the length of a collecting surface will decrease uniformly initially, but as the first segment becomes saturated with the deposit, the film thickness will become progressively uniform along the

collecting surface. If the flow rate of the gas is v, the initial deposition rate in the x direction along parallel plates with a spacing of b in the y direction, is given by

$$G(x) = 2\frac{c_i M_d}{b\rho M_t} D \exp\left(-\pi^2 \frac{Dx}{4vb^2}\right)$$

where c_i is the concentration of the transporting species of molecular mass M_d and M_t is the molecular mass of the, inert, carrier gas or reaction product(s). This is a solution of Fick's second law of diffusion. The equation for this problem is,

$$\frac{\partial c(x,\, t)}{\partial t} = D\nabla^2 c(x,\, y) - v\frac{\partial c(x,\, y)}{\partial x}$$

where c is a function of concentration and time, and v is the flow velocity of the gas. This equation must be solved for a set of boundary conditions, which in the example above are $c = 0$ when $y = 0$; $x > 0$: $c = c_i$ when $y = b$; $x \geq 0$

$$\frac{\partial c}{\partial y} = 0 \text{ at } y = b; \quad x \geq 0$$

A situation which is frequently encountered in the production of micro-electronic devices is when vapour deposition must be made into a re-entrant cavity in an otherwise planar surface. Clearly, the gas velocity of the major transporting gas must be reduced in the gas phase entering the cavity, and transport down the cavity will be mainly by diffusion. If the mainstream gas velocity is high, there exists the possibility of turbulent flow at the mouth of the cavity, but since this is rare in vapour deposition processes, the assumption that the gas within the cavity is stagnant is a good approximation. The appropriate solution of the diffusion equation for the steady-state transport of material through the stagnant layer in the cavity is

$$J_i = \frac{D_{\mathrm{A-B}}}{L} \ln \frac{p_{\mathrm{g}}}{p_{\mathrm{c}}}$$

for the ith species, where L is the depth of the cavity, and p_{g} and p_{c} are the partial pressures of this vapour component in the gas, and at the base of the cavity respectively. The partial pressures will correspond to the composition of the ingoing gas, and the equilibrium composition at the temperature of deposition.

Transport and thermal properties of gases

The kinetic theory of gases has been used so far, the assumption being that gas molecules are non-interacting particles in a state of random motion. This

DropBooks

theory indicates that the diffusion of atoms and molecules has a different temperature dependence from the activated processes in condensed phases, and the equation for the diffusion coefficient derived from the theory is

$$D = (1/3)\lambda\overline{c}$$

Using the expressions given earlier for the mean velocity and the mean free path

$$\overline{c} = (8RT/\pi M)^{1/2}$$

$$\lambda = 1/\left(\sqrt{2}\pi n d^2\right)$$

where d is the molecular diameter, and R the gas constant, the equation for the diffusion coefficient becomes

$$D = 1/(3\sqrt{2}\pi n d^2)(8RT/\pi M)^{1/2}$$

which is quite different in form from the empirical equation for an activated diffusion process.

In a binary gas mixture, the diffusion coefficient of the species i at a mole fraction x_i, with respect to that of the species j is given after evaluating the constants by the equation

$$D_{ij} = 2.265 \times 10^{-5}[T(1/M_i + 1/M_j)]/x_i d_{ij}^2$$

where

$$d_{ij} = 1/2(d_i + d_j)$$

and in a multicomponent mixture, the diffusion coefficient of the ith species with respect to the other species, D_{im}, is given by;

$$D_{im} = [(1 - x_i)/\Sigma x_j D_{ij}]$$

where the summation clearly excludes $j = i$.

An empirical equation which has been found to be quite accurate (within 2%) was proposed by Andrussov (1950), which v_i is the molar volume of the ith species.

$$D_{ij} = \frac{0.0606T^{1.78}}{p\left(v_i^{1/3} + v_j^{1/3}\right)^2} \frac{(1 + \sqrt{M_i + M_j})}{\sqrt{M_i M_j}}$$

This equation has a different temperature coefficient from that calculated from kinetic theory, and shows a shortcoming in the theory which is due to the assumption of non-interaction between the molecules.

Another property of gases which appears in the Reynolds and the Schmidt numbers is the viscosity, which results from momentum transfer across the volume of the gas when there is relative bulk motion between successive layers of gas, and the coefficient, η, is given according to the kinetic theory by the equation

$$\eta = (1/3)\rho\bar{c}\lambda = \frac{m\bar{c}}{3\sqrt{2}\pi d^2} = 1.81 \times 10^{-5}\frac{(MT)^{1/2}}{d^2} \text{ poise}$$

where ρ is the density of the gas, and d is in angstroms (10^{-8} cm). The viscosity of a gas mixture, η_{mix}, can be calculated from the equation

$$\eta_{\text{mix}} = \frac{\Sigma x_i \eta_i m_i^{1/2}}{\Sigma x_i m_i^{1/2}}$$

The viscosity increases approximately as $T^{1/2}$, and there is, of course, no vestige of the activation energy which characterizes the transport properties of condensed phases.

The thermal conductivity is obtained in terms of λ and c through the equation

$$\kappa = (1/3)\rho C_v \bar{c}\lambda = \eta C_v$$

DropBooks

where C_v is the specific heat at constant volume. The heat capacity at constant volume of a polyatomic molecule is obtained from the equipartition principle, extended to include not only translational, but also rotational and vibrational contributions.

The classical values of each of these components can be calculated by ascribing a contribution of $R/2$ for each degree of freedom. Thus the translational and the rotational components are $3/2R$ each, for three spatial components of translational and rotational movement, and $(3n - 6)R$ for the vibrational contribution in a non-linear polyatomic molecule containing n atoms and $(3n - 5)R$ for a linear molecule. For a diatomic molecule, the contributions are $3/2R_{\text{trans}} + R_{\text{rot}} + R_{\text{vib}}$.

The classical value is attained by most molecules at temperatures above 300 K for the translation and rotation components, but for some molecules, those which have high heats of formation from the constituent atoms such as H_2, the classical value for the vibrational component is only reached above room temperature. Consideration of the vibrational partition function for a diatomic gas leads to the relation

$$\frac{E - E_0}{T} = \frac{Rxe^{-x}}{1 - e^{-x}}$$

where E_0 is the zero point energy and x is equal to $h\nu/kT$. By differentiation with respect to temperature the heat capacity at constant volume due to the vibrational energy is

$$C_v = \left(\frac{\partial E}{\partial T}\right)_V = \frac{Rx^2}{2(\cosh x - 1)}$$

This function approaches the classical R value of $8.31\,\mathrm{J\,mol^{-1}\,K^{-1}}$, when x is equal to or less than 0.5. Above this value, the value of C_v decreases to four when x reaches 3 (Figure 3.6).

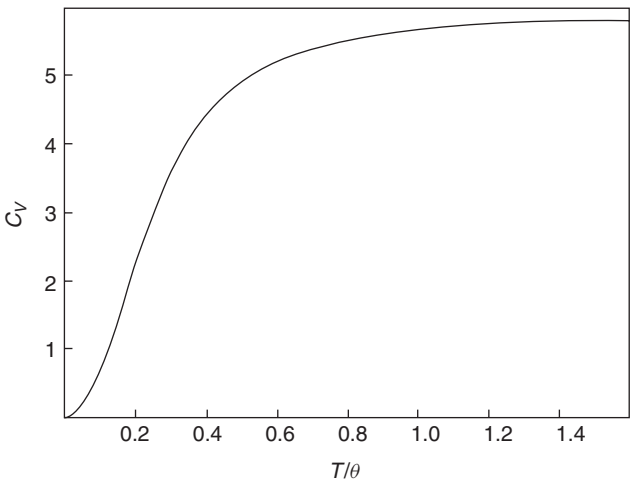


Figure 3.6 *The heat capacity of a solid as a function of the temperature divided by the Debye temperature*

Treating the atomic vibration as simple harmonic motion yields the expression

$$\nu = \frac{1}{2\pi}\sqrt{\frac{k}{\mu}}$$

where k is the force constant and μ is the reduced mass defined by

$$\frac{1}{\mu} = \frac{1}{m_\mathrm{A}} + \frac{1}{m_\mathrm{B}}$$

in the AB molecule. The force constant is roughly inversely proportional to the internuclear distance, the product, kd^2, having the value about $8 \times 10^{-2}\,\mathrm{N\,nm^{-1}}$ for the hydrogen halide molecules.

It follows from this discussion that all of the transport properties can be derived in principle from the simple kinetic theory of gases, and their interrelationship through λ and c leads one to expect that they are all characterized by a relatively small temperature coefficient. The simple theory suggests that this should be a dependence on $T^{1/2}$, but because of intermolecular forces, the experimental results usually indicate a larger temperature dependence even up to $T^{3/2}$ for the case of molecular inter-diffusion. The Arrhenius equation which would involve an enthalpy of activation does not apply because no 'activated state' is involved in the transport processes. If, however, the temperature dependence of these processes is fitted to such an expression as an algebraic approximation, then an 'activation enthalpy' of a few kilojoules is observed. It will thus be found that when the kinetics of a gas–solid or liquid reaction depends upon the transport properties of the gas phase, the apparent activation enthalpy will be a few kilojoules only (less than 50 kJ).

Some typical results for the physical properties of common gases which are of industrial importance are given in Table 3.3. The special position of hydrogen which results from the small mass and size of the H_2 molecule should be noted.

Equations of state for ideal and real gases

DropBooks

The equation of state for a gas consisting of non-interacting point particles has the form

$PV = RT$ for one mole of gas

The assumptions involved in this equation clearly do not accurately describe real gases in which the atoms or molecules interact with one another, and occupy a finite volume in space the size of which is determined by the complexity and mass of the particles. The first successful attempt to improve on the ideal equation was that of van der Waals

$$(P + a/V^2)(V - b) = RT$$

The correcting term in the pressure reflects the diminution in the impact velocity of atoms at the containing walls of the gas due to the attraction of the internal mass of gas, and the volume term reflects the finite volume of the molecules. Data for these two constants are shown in Table 3.4.

The interaction forces which account for the value of a in this equation arise from the size, the molecular vibration frequencies and dipole moments of the molecules. The factor b is only related to the molecular volumes. The molar volume of a gas at one atmosphere pressure is 22.414 l mol^{-1} at 273 K, and this volume increases according to Gay–Lussac's law with increasing

Table 3.3 *Thermophysical properties of common gases*

	Temp (K)	Viscosity (micropoise)	Sp. heat at constant pressure ($J\,g^{-1}\,K^{-1}$)	Thermal conductivity ($W\,cm^{-1}\,K^{-1} \times 10^5$)
H_2	300	84	14.48	166.53
	1100	210	14.72	447.69
Ar	300	209	0.519	15.90
	1100	550	0.519	43.93
N_2	300	170	1.046	5.65
	1100	415	1.138	64.85
O_2	300	189	0.941	24.10
	1100	500	1.067	75.32
CO	300	166	1.046	22.97
	1100	450	1.142	67.36
CO_2	300	139	0.994	14.35
	1100	436	1.025	71.96
SO_2^*	300	116	0.678	8.53
	800	310	0.786	33.93
H_2O^*	400	125	1.924	23.89
	700	241	2.025	55.23

Note the smaller range of temperature for SO_2 and H_2O. This was due to lack of high temperature viscosity data.

Table 3.4 *van der Waals constants for some common gases*

	$a = 0.244\,l^2\,\text{atmos}\,\text{mol}^{-2}$	$b = 26.6 \times 10^{-3}\,l\,\text{mol}^{-1}$
H_2		
O_2	1.36	31.8
H_2O	5.46	30.5
CO	1.49	39.9
CO_2	3.59	42.7
HCl	3.8	41.0
SO_2	6.7	56.0

temperature. At a temperature T(K)

$$V_T = V_{273}T/273$$

Clearly the effects of the van der Waals corrections will diminish significantly at 1000 K, and the ideal gas approximation will become more acceptable. The

effects will also diminish considerably as the pressure is decreased below one atmosphere. Expressing the deviation from the ideal gas laws by the parameter z, so that

$$PV = zRT$$

the value of z for SO_2 at 1000 K and one atmos pressure, at which temperature the molar volume is 82.10l, is less than 1.001, compared with 1.013 at 298 K.

The effects of the constants in the van der Waals equation become more marked as the pressure is increased above atmospheric. Early measurements by Regnault showed that the PV product for CO_2, for example, is considerably less than that predicted by Boyle's law

$$P_1V_1 = P_2V_2$$

the value of this product being only one quarter, approximately, of the predicted value at 100 atmos using one atmosphere data, i.e. the molar volume is 22.414 litres at room temperature.

The parameter z can be obtained from Regnault's results and these show a value of z of 1.064 for hydrogen, 0.9846 for nitrogen, and 0.2695 for carbon dioxide at room temperature and 100 atmospheres pressure. These values are related to the corrections introduced by van der Waals.

DropBooks

Molecular interactions and the properties of real gases

The classical kinetic theory of gases treats a system of non-interacting particles, but in real gases there is a short-range interaction which has an effect on the physical properties of gases. The most simple description of this interaction uses the Lennard–Jones potential which postulates a central force between molecules, giving an energy of interaction as a function of the inter-nuclear distance, r,

$$E(r) = 4\varepsilon \left\{ \left(\frac{d_c}{r} \right)^{12} - \left(\frac{d_c}{r} \right)^{6} \right\}$$

where d_c is the collision diameter, and ε is the maximum interaction energy.

The collision diameter is at the value of $\varepsilon(r)$ equal to zero, and the maximum interaction of the molecules is where $\varepsilon(r)$ is a minimum. The interaction of molecules is thus a balance between a rapidly-varying repulsive interaction at small internuclear distances, and a more slowly varying attractive interaction as a function of r (Figure 3.7).

Chapman and Enskog (see Chapman and Cowling, 1951) made a semi-empirical study of the physical properties of gases using the Lennard–Jones

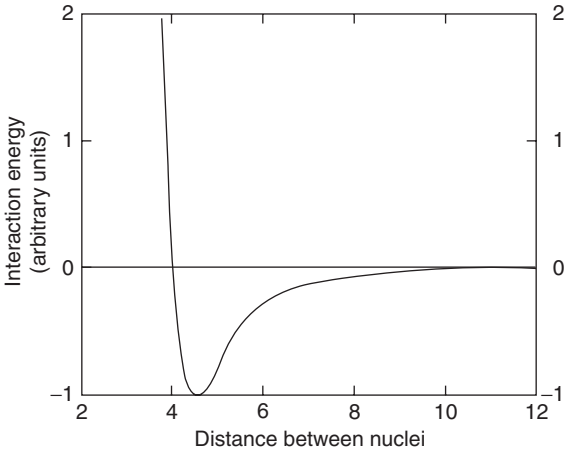


Figure 3.7 *The Lennard–Jones potential of the interaction of gaseous atoms as a function of the internuclear distance*

potential, and deduced equations for these properties which included the collision integral, Ω, which is a function of kT/ε. Their equations for the viscosity, thermal conductivity and diffusion coefficient are

$$\eta = 2.67 \times 10^{-5} \frac{(MT)^{1/2}}{d_c^2 \Omega_\eta}$$

$$\kappa = 1.981 \times 10^{-4} \frac{(MT)^{1/2}}{d_c^2 \Omega_k}$$

and for the inter-diffusion coefficient of the gases A and B,

$$D_{\mathrm{AB}} = 1.86 \times 10^{-3} \frac{\left(\left[\frac{1}{M_A} + \frac{1}{M_B} \right] T^3 \right)^{1/2}}{P d_c^2 \Omega_d}$$

where P is the total pressure in atmospheres and M is the molecular weight. The values of Ω, which is a slowly varying function of kT/ε, are slightly different from one property to another, but within 10%, and the average value is about 1.4–1.6 at kT/ε equal to one, and about 1.0 at kT/ε equal to 2.5 for the diffusion value, and 3.5 for viscosity and thermal conductivity (Hirschfelder, Bird and Spotz, 1949). The temperature dependence of the inter-diffusion coefficient is in satisfactory agreement with experimental observation.

The values of ε/k are less than 600 K for most of the simple molecules which are found in high temperature systems, and hence the collision integral may be assumed to have a value of unity in these systems.

An approximate value for d_c in the equation for the Lennard–Jones potential, quoted above, may be obtained from the van der Waals constant, b, since

$$b = (2/3)\pi N d_c^3$$

and the values of ε are obtained from experimental values of the polarizability of molecules, α, where

$$\alpha = \frac{f}{e^2}$$

f is the restoring force constant for the relative displacement of nuclei and electrons. Using the London theory of the van der Waals interaction which relates the ionization potential, I, times the electronic charge, e, to the vibration frequency of the electrons with respect to the nuclei in gas atoms, ν, by the equation

$$Ie = h\nu$$

the result for the interaction energy $\varepsilon_{\text{dis}}(r)$ between gas atoms is

$$\varepsilon_{\text{dis}}(r) = -\frac{3h\nu e^4}{4f^2 r^6} = -\frac{3Ie\alpha^2}{4r^6}$$

DropBooks

which is in accord with the attractive energy expression used in the Lennard–Jones potential for monatomic gases. This theory envisages the interaction between molecules as being due to dipole–dipole interactions which arise from the separation of nuclear and electron charge density centres during atomic vibrations (dispersion effect). Clearly this effect will be larger in magnitude the larger the molecule, as in the comparison between H_2 and Cl_2, where the latter is about 40 times larger.

This dispersion interaction must be added to the dipole–dipole interactions between molecules, such as HCl, NH_3 and H_2O which have a permanent dipole, μ. The magnitude of the dipole moment depends on the differences in electronegativity of the atoms in the molecule. Here again, the energy of interaction varies as r^{-6} (orientation effect).

$$\varepsilon_{\text{dip}}(r) = \frac{2\mu^4}{3r^6 kT}$$

As examples of the relative magnitudes of these contributions, only the dispersion effect applies to monatomic gases, and in the case of HCl ($I = 12.74$ eV, $\mu = 1.03$ debye), the dispersion effect predominates, in NH_3 ($I = 10.2$ eV, $\mu = 1.49$ d) these effects are about equal, and in H_2O ($I = 12.6$ eV, $\mu = 1.85$ d), the orientation effect predominates.

Bibliography

H. Schafer. *Chemical Transport Reactions*. Academic Press, New York (1964).
C.B. Alcock and J.H.E. Jeffes. *Trans. Inst. Min. Met.*, **C76**, 245 (1967) and *J. Mater. Sci.*, **3**, 635 (1968).
L.J. Gillespie. *J. Chem. Phys.*, **7**, 530 (1939).
M.N. Dastur and J. Chipman. *Disc. Far. Soc.*, **4**, 100 (1948).
W.R. Smith and R.W. MIssen. *Chemical Reaction Equilibrium Analysis*. J. Wiley and Sons. New York (1982).
K.L. Choy and B. Derby. *Chemical Vapor Deposition*, XII, Electrochem. Soc. 408 (1993).
R.J. Shinavski and R.J. Diefendorf. *ibid*, 385 (1993).
R.B. Bird, W.E. Stewart and E.N. Lightfoot. *Transport Phenomena*, pp. 249–261 and 502–513. J. Wiley & Sons New York (1960).
L. Andrussov. *Z. Elektrochem.*, **54**, 567 (1950).
S. Chapman and T.G. Cowling. *Mathematical Theory of Non-uniform Gases*, 2nd ed, Cambridge University Press (1951).
J.O. Hirschfelder, R.B. Bird and E.L. Spotz. *Chem. Rev.*, **44**, 205 (1949) see also Tables in Bird, Stewart and Lightfoot (above).

Chapter 4

Heterogeneous gas–solid surface reactions

In this chapter we consider systems in which a reaction between two gaseous species is carried out in the adsorbed state on the surface of a solid. The products of the reaction will be gaseous, and the solid acts to increase the rate of a reaction which, in the gaseous state only, would be considerably slower, but would normally yield the same products. This effect is known as *catalysis* and is typified in industry by the role of adsorption in increasing the rate of synthesis of many organic products, and in the reduction of pollution by the catalytic converter for automobile exhaust.

The zeroth order reaction

DropBooks

The elucidation of chemical effects in gaseous reactions which are accelerated by the presence of a metal, began with a study of the reaction for HI decomposition which is bimolecular in the gaseous state. It was found that the rate of this reaction was considerably increased in the presence of metallic gold and that the rate was directly dependent on the surface area of the gold sample exposed to the gas. The order of the reaction could be described mathematically as a zero order reaction, i.e. one in which the rate was independent of the amount of HI present in the system and of the amount of products which were formed. The conclusion was that the reaction was taking place on the gold surface, where rapid decomposition of the HI molecules was taking place as a result of bimolecular collisions between adsorbed HI molecules. HI collisions could occur much more frequently in the absorbed layer on the metal surface than in the gas phase. The activation energy of this heterogeneous reaction was approximately one half of that of the homogeneous gas phase reaction. When the pressure of HI is reduced below a critical value at a given temperature, the reaction order changes to the unimolecular type.

The flux of the adsorbed species to the catalyst from the gaseous phase affects the catalytic activity because the fractional coverage by the reactants on the surface of the catalyst, which is determined by the heat of adsorption, also determines the amount of uncovered surface and hence the reactive area of the catalyst. Strong adsorption of a reactant usually leads to high coverage, accompanied by a low mobility of the adsorbed species on the surface, which

limits the rate at which new molecules can arrive at the active area. It can happen that the *products* of reaction are more strongly adsorbed than the reactants, and hence the surface mobility of the reactants is restricted by collisions with the relatively immobile adsorbed product molecules. This reduces the frequency of collisions between adsorbed reactants, and hence decreases the rate of product formation. An example of this effect is to be found in the catalysis of SO_3 formation from SO_2 and oxygen by platinum. The rate of reaction is expressed by

$$\mathrm{d}[SO_3]\mathrm{d}t = k[O_2]/[SO_3]^{1/2}$$

when SO_2 is in excess, and

$$\mathrm{d}[SO_3]/\mathrm{d}t = k[SO_2]/[SO_3]^{1/2}$$

when O_2 is in excess. The denominator of these expressions reflects the strong degree of adsorption of the SO_3 molecules on the catalyst.

Although it is generally true that the catalyst is not affected physically by the catalysed reaction, in many instances it is probable that the catalyst supplies electrons during the course of the reaction to the reacting molecules thus enhancing the bond exchanges. In the case of hydrocarbon adsorbates there is evidence that dehydrogenation occurs as a result of the interaction between the catalyst and the adsorbate, and oxidation of non-stoichiometric oxide catalysts occurs in some reactions involving oxygen and oxygen-containing gases. The ability to supply electrons is why metals form a large part of catalytic materials, and a number of oxide catalyst are more active when the positive hole concentration is high, leading to semi-conductivity. In some catalysts, nickel for example, non-metallic elements such as hydrogen, oxygen and carbon are soluble to a limited extent, and this solution provides a means to transport the interstitial atoms from one site, through the catalyst, to another site.

Adsorption of gases on solids

It is well established that catalytic behaviour is fairly specific, thus platinum has much less activity than gold in HI decomposition, and also shows weaker adsorption of HI molecules than gold. The description of the process of adsorption given by Langmuir proposes that a certain fraction of the solid is covered by the adsorbed layer depending on the partial pressure of the species to be adsorbed in the gas phase in contact with the catalyst. Further adsorption can therefore occur only on the unoccupied sites on the surface. Desorption takes place from the adsorbed species, there being an equilibrium between these two processes at any given time. The amount of surface coverage is greater the more exothermic the process of adsorption. If θ is the fraction of a surface covered at equilibrium, then $1 - \theta$ must represent the uncovered fraction and

the steady state for adsorption/desorption can be described using k_c and k_e as the rate constants, so that at adsorption equilibrium

$$k_e\theta = k_c(1-\theta)$$
$$\theta = (k_c/k_e)p/(1+(k_c/k_e)p)$$

Here, k_e and k_c are rate constants for desorption (evaporation) and condensation respectively. The sites on the solid at which adsorption takes place were denoted as *active sites* by Langmuir.

Modern studies of surfaces by electron microscopy and electron diffraction show that single crystals have level terraces bounded by ledges which can be straight over many atom lengths, but also include kinks along a ledge. In transmission electron microscopy the presence of dislocations at or near the surface is also detected in a thin film of a solid. In electron diffraction, information can be gathered about the atomic structure, and the smoothness of the surface layers. In low-energy electron diffraction (LEED) a monokinetic beam of electrons of about 100 eV energy is directed normally to the surface of a solid. Since the penetration of electrons in solids is very much less than X-rays, the diffraction pattern due to the wave nature of electrons is formed in the first few layers of the solid. Furthermore because the wavelength of electrons, even of such a low energy, is substantially smaller than those of the X-rays which are used in diffraction studies, the conditions for the formation of a diffraction pattern are less rigorous. Thus diffraction patterns can be obtained with a static polycrystalline sample in electron diffraction, whereas in X-ray diffraction it would be necessary to rotate the sample, as in the Debye–Scherrer procedure, or use a 'white' X-ray beam containing a range of wavelengths.

DropBooks

This difference is explained by the application of the principle of the *Ewald sphere* used in X-ray diffraction studies. This will now be exemplified for the two-dimensional case to simplify the analysis. To begin this construction, a diagram is made representing the original lattice in reciprocal space. Points on the diagram represent the reciprocal distances, $2\pi/d$ of each plane from the origin (000) in a direction normal to the plane. Thus the family of {100} planes would be represented by points for the planes (100) (010), (010) (-100), (0-10), (00-1) etc. A vector, k_0, of length $2\pi/\lambda$ where λ is the wavelength of the X-radiation, pointing in the direction of the incident beam is superimposed on this diagram with the tip at the point (000). A sphere is then drawn with radius k_0. When the point representing a particular lattice plane (hkl) touches the Ewald sphere, diffraction will occur, producing a spot on the recording film. The vector representing the diffracted beam connects the centre of the sphere with the representative point of the diffracting plane and is therefore of the same length as the incident beam vector. It can be seen in Figure 4.1

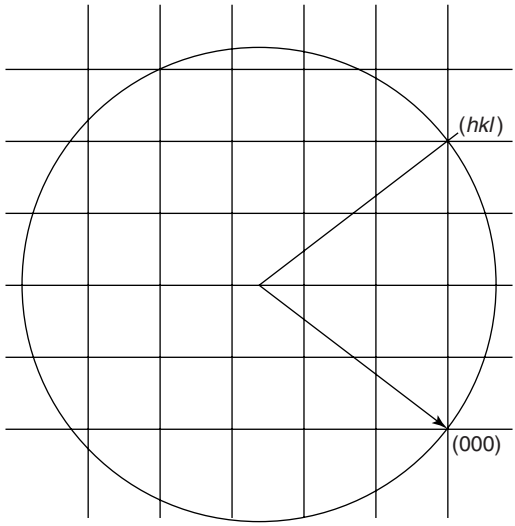


Figure 4.1 *The Ewald diagram showing the diffraction of a beam represented by the vector originating at (000), by the plane (hkl)*

that by dropping a perpendicular to the resultant vector, r, that the equation

$$\lambda = 2d_{hkl} \sin\theta$$

which is a form of the Bragg relationship for diffraction, can be confirmed on the figure. The representative point for the (hkl) plane in reciprocal space is inversely related to the interplanar spacing of the plane and d_{hkl} is related to the lattice parameter, d, by the equation

$$d_{hkl} = d/(h^2 + k^2 + l^2)^{1/2}$$

and hence the equation given above can be converted into the Bragg equation in its usual form

$$n\lambda = 2d \sin\theta$$

where

$$n = (h^2 + k^2 + l^2)^{1/2}$$

Because of the much shorter wavelength of electron beams, the Ewald sphere becomes practically planar in electron diffraction, and diffraction spots are expected in this case which would only appear in X-ray diffraction if the specimen were rotated.

In reflection high-energy electron diffraction (RHEED), a monokinetic electron beam of much higher energy, 50–100 keV is directed at grazing incidence to the solid. If the surface of the solid is atomically smooth, the diffraction pattern consists of streaks which are spaced proportionally to the spacing between the rows of atoms on the surface. If the surface is not smooth, some part of the beam will pass through surface ledges, leading to a diffraction pattern of regularly spaced spots which more closely resembles the three-dimensional diffraction pattern which is obtained in LEED. This technique can therefore be used to study the surface morphology continuously when the film is built up in a vacuum system, such as in Knudsen evaporation. It follows that a complete picture of the surface structure and inter-atomic spacings can only be obtained by rotating the sample around the direction of the incident beam in order to bring rows of atoms in different crystallographic directions parallel to the incident beam. The relative intensities of spots and streaks is thus a measure of the surface smoothness.

When a ledge is formed on an atomically smooth monolayer during the formation of a thin film the intensity of the diffraction pattern is reduced due to the reduction in the beam intensity by inelastic scattering of electrons at the ledge–monolayer junction. The diffraction intensity can thus be used during deposition of several monolayers to indicate the completion of a monolayer through the relative increase in intensity at this time. Observation of this effect of intensity oscillation is used in practice to count the number of monolayers which are laid down during a deposition process.

DropBooks

The number of atoms bound to one particular atom on the surface of a solid depends on its position in this morphology. In a simple cubic lattice, where each atom has a coordination number six, atoms on the planar terraces will have one bond less than those deep in the solid. Those at the edge of a terrace, a ledge site, will have two less and those at the corner of a kink will have three less than the deep-atom bonding of an atom in the solid. In a close-packed structure, a terrace atom on a (100) plane has four bonds less than an atom in the bulk, the ledge atom has five bonds less, and the atom on the edge of a kink site has six bonds less than the deep atom. These latter will be sites on the surface of the solid where the bonding is therefore much weaker than in others, and it is from these sites that evaporation will most easily occur. The converse is true of the more completely bonded atoms on the terraces (Figure 4.2).

Since the evaporation of a solid would occur at the kink sites because the bonding is weaker, atoms would diffuse also to these sites before evaporation. A demonstration of this is to be found on the morphologies of single crystals after a period of heating in vacuum to cause substantial evaporation. The resultant surface shows an increase in the number of ledges and kinks relative to the area of the terraces. It is also to be expected that dislocations emerging at the surface of catalysts, either as edge or screw dislocations, would play a

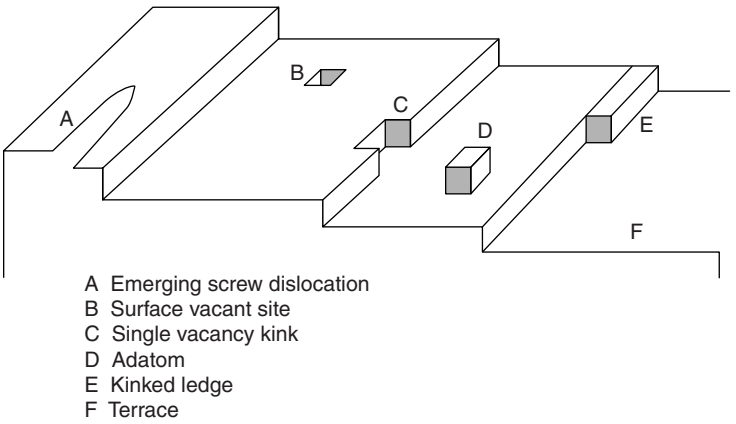


Figure 4.2 *Terraces, ledges and kinks on a solid surface, together with an emerging screw dislocation, a vacant site, and an adatom*

significant role in catalysis, since these would present a large number of atoms in the ledge and kink configurations.

Adsorbed molecules are more strongly held at the sites where the weakest metal–metal bonding is to be found, and these correspond to the active sites of Langmuir. A demonstration of this effect was found in studies of the adsorption of H_2S from a H_2S/H_2 mixture on a single crystal of copper of which the separate crystal faces had been polished and exposed to the gas. The formation of copper sulphide first occurred on the [100] and [110] planes at a lower H_2S partial pressure than on the more densely packed [111] face. Thus the metal atoms which are less strongly bonded to other metal atoms can bond more strongly to the adsorbed species from the gas phase.

The adsorption and desorption of hydrogen on platinum also shows that the hydrogen atoms are more readily adsorbed on the kink sites, followed by the ledges and finally on the flat terrace surfaces. The desorption kinetics shows that adsorbed hydrogen atoms are desorbed from the terraces more readily than the ledges, and finally from the kink sites (Somorjai and Davis, 1980). It is therefore to be expected that the heat of adsorption of hydrogen on the surface of platinum will decrease with increasing surface coverage as the kink and edge sites become successively filled with adsorbed atoms. The terrace sites will show the lowest energy of adsorption, and the rate of decrease of the energy of adsorption on a platinum surface will depend on the particular morphology of the surface. Decomposition reactions occur more readily at kink and ledge sites. Thus the decomposition of ethylene occurs at lower temperatures on the ledge sites of nickel than on the terraces (Lehwald and Ibach, 1980). Finally, sites at the leading edge of a screw dislocation emerging at the surface would also be expected to show stronger adsorption of gaseous

species than the terrace sites because of the weaker bonding of the atoms at the leading edge to the solid.

Surface structures of catalytic materials

The surface layers of single crystals which have been found by LEED and RHEED show that the atomic arrangement of the surface layer may be quite different from that on the underlying structure. There are shorter metal–metal bonds in the surface layer and between the surface atoms and those in the next layer of atoms below the surface, than the bond lengths in the interior of the substrate. Frequently there is a different coordination structure in the surface layer than in the interior. This process of re-arrangement or re-construction of the surface layer has been studied for metal catalysts, such as platinum. The reconstruction of the surface layer on this important catalyst results in a surface with a hexagonal structure, above the bulk face-centered cubic structure. This change in structure from bulk to surface results in an undulating structure and surface buckling, which should add active sites to the surface. However when a molecular species such as CO or CH_4 is adsorbed on the surface, the metal atoms on the surface move back to the cubic co-ordination characteristic of the bulk phase structure.

Semiconducting elements silicon and germanium and the III–V compounds GaAs and InSb are linked by covalent bonds, four per atom, in tetrahedral co-ordination. These bonds are hybrid orbital bonds of sp^3 configuration. The surface of these elements have a different co-ordination from the interior because the tetrahedral structure of the bulk can no longer be sustained. The surface structure consists of strings of atoms, and there is re-construction of an intermediate nature in the next few atomic layers. The surface atoms thus have a lower co-ordination number than four, and the bonding electrons form a new configuration with σ bonding involving s electrons (such as that in the hydrogen molecule) on the surface and trigonal sp^2 bonding (such as that in elementary boron) between the surface and the lower layers.

DropBooks

Turning to non-metallic catalysts, photoluminescence studies of alkaline-earth oxides in the near-ultra-violet region show excitation of electrons corresponding to three types of surface sites for the oxide ions which dominate the surface structure. These sites can be described as having different cation co-ordination, which is normally six in the bulk, depending on the surface location. Ions on a flat surface have a co-ordination number of 5 (denoted 5c), those on the edges 4 (4c), and the kink sites have co-ordination number 3 (3c). The latter can be expected to have higher chemical reactivity than 4c and 5c sites, as was postulated for the evaporation mechanism.

The spectroscopic evidence suggests that on adsorption of CO, an adsorbed CO_3^{2-} ion and a polymeric form of the CO molecule are formed thus

$$2O^{2-} + (n+1)CO \longrightarrow CO_3^{2-} + (CO)_n$$

The value of n in the polymeric adsorbed species $(CO)_n$ is larger on the 3c sites than on the 4c and 5c sites. The CO_2 molecule is much more strongly adsorbed, indicating CO_3^{2-} ion formation on the oxide surface, and the evidence suggests that in this case the differentiation between the 3c and the 4c and 5c sites is much less clearly marked. The relative occurrence of these three types of surface sites on heating the alkaline earth oxides indicates that with increasing temperature there is increasing surface roughness, the 3c sites only occurring in significant amounts above 1000 K.

An important property of the surface behaviour of oxides which contain transition metal ions having a number of possible valencies can be revealed by X-ray induced photoelectron spectroscopy. The energy spectrum of these electrons give a direct measure of the binding energies of the valence electrons on the metal ions, from which the charge state can be deduced (Gunarsekaran *et al.*, 1994).

Adsorption and the surface energies of metals

The adsorption studies of sulphur on copper single crystals referred to above show that solid metals do not have single values of surface energy for all large-grain samples, but that the value for a given material depends on the crystalline orientation of the surface grains. A rough estimate of the surface energy is the energy change due to the breaking of bonds when two new surfaces are prepared by cleavage of a single crystal. Since the number of bonds which are broken depends on the number of atoms in the bulk bonded or significantly interacting with each atom at the surface, it is clear that the density of atoms, which changes from plane to plane, will determine the surface energy.

The approximate calculation of the surface energies of metals as a function of crystal structure described earlier uses the enthalpy of sublimation, ε, and the co-ordination number to calculate the energy as a function of the atomic concentration on the surface. The atomic areas of the principal configurations are as follows:

> the (100) plane has $1/a^2$ atoms/cm^2 with four bonds below the surface
> the (110) plane has $2/a^2$ atoms/cm^2 with four bonds and the (111) plane, the most densely packed, has $2/a^2\sqrt{3}$ atoms/cm^2 with three bonds, where a is the cell edge length.

It follows that the total bonding energy lost when a new surface is formed is $4\varepsilon/a^2$ per atom in the (100) plane, $4\varepsilon/\sqrt{2}a^2$ in the (110) and $6\varepsilon/\sqrt{3}a^2$ in the (111) planes. This indicates the relative magnitudes of these surface energies. This calculation yields surface energies of the correct order of magnitude when compared with the measured values and shows the surface plane orientation effect. It is to be expected, then, that the surface morphology will tend towards that which minimizes the surface energy, and surface migration

will tend to extend the low surface energy planes at the expense of the high energy planes.

The above model applies to the surface energy of a pure metal only. In a binary alloy, for example, Hondros and Seah have shown that the observed surface enrichment of a solute of limited solubility is related to the thermodynamics of solution of the solute in the host and the surface energies of the pure components. The bulk and surface phases will have different compositions if surface enrichment occurs. If the solute has a small solubility in the host, the activity coefficient of the host will be nearly unity across the range of solid solution, while that of the solute, γ_2, will obey Henry's law, having a constant and large activity coefficient in the bulk phase. If the respective surface areas of the atoms of solvent and solute are A_1 and A_2 and their surface energies in the pure state are σ_1 and σ_2 respectively, the segregation ratio, R, is given by

$$R = \frac{X_2^{\text{surface}}}{X_2^{\text{bulk}}} = \frac{X_1^{\text{surface}}}{X_1^{\text{bulk}}} \gamma_2 \exp\left(-\frac{\Delta G^s}{RT}\right)$$

where

$$\frac{\Delta G^s}{RT} \cong \left[\frac{\sigma_1 A_1 - \sigma_2 A_2}{RT}\right]$$

If a thin film is formed in a partial or moderate vacuum, in which the residual gases contain a chemically active species, such as oxygen or sulphur, these atoms can become adsorbed on the surface of the film, altering the surface properties of the film. The effect of a strongly adsorbed species on the surface of a film is to decrease the orientation dependence of the surface energy, and therefore to affect the nucleation and growth kinetics by removing preferential growth on low-energy planes.

DropBooks

Bond mechanisms of adsorbed molecules

An important effect in the selectivity of catalytic activity is the relation between the bond lengths in the molecule being adsorbed and those in the surface layer of the catalyst. For example, it was once thought that the variation of catalytic activity across the composition ranges of copper alloys was due to the change in the free electron concentration in the alloys. It now appears that is more probably due to the variation of lattice spacing with alloy composition, and it is therefore the bond-length matching between catalyst and adsorbed species which is the important factor.

Studies of the state of adsorbed molecules on clean surfaces have been made using high-resolution energy loss spectroscopy (HREELS) in which low-energy monochromatic electron beams in the energy range 1–20 eV, are reflected from the surface of a metal bearing an adsorbed layer. The reflection spectrum shows the absorption excitation of the vibration spectrum of

the adsorbed layer by the electrons, which can then be compared with that of the adsorbed molecule in the gaseous state. For example, CO molecules are adsorbed on metals either lying flat on the surface, or standing up with the component which interacts most strongly with the substrate in contact with the substrate. For example, in the adsorption of CO by rhodium at room temperature, the bridge configuration only becomes occupied after 50% coverage of the surface by CO molecules forming a strong Rh–C bond, the oxygen atom being above the carbon atom. This is accompanied by absorptions in the HREELS spectrum corresponding to the stretching vibrations of the C–O and Rh–C bonds. The onset of bridge formation is shown by the appearance of an additional absorption band in the HREELS spectrum to those shown at lower degrees of surface coverage which corresponds to the stretching frequency of the bridge C–O bond. The strong Rh–C bond also appears in the adsorption of small organic molecules on the surface of this catalyst and platinum. For example, the adsorption of ethylene leads to the formation of carbon–metal bonds. Adsorbed hydrocarbons undergo hydrogen evolution as the temperature is increased, leading to the formation of less saturated molecules having an increased metal–carbon contact. Finally a graphitic layer of carbon atoms is left on the surface which diminishes the catalytic activity, at temperatures around 800 K. The importance of the strength of the metal–carbon bond in catalysed reaction of hydrocarbons and the orientation of CO molecules on the surface of noble metal catalysts is reflected in the fact that the heat of adsorption of CO on the transition metals is highest on those metals forming the most stable carbides, e.g. titanium and niobium, where the heat of adsorption is three times higher than on the noble metals (about $200\,\mathrm{kJ\,mol^{-1}}$).

On oxide substrates, oxygen molecules are adsorbed flat on the surface of a filled oxide structure, or with one oxygen atom inserted in a surface oxygen vacancy in non-stoichiometric oxides. The charge state of an oxygen adsorbate depends on the nature of the oxide. Stoichiometric oxides with a single cation valency, e.g. MgO are unchanged by oxygen adsorption, but those with a higher cation valency state available can release electrons to form adsorbed O_2^- or O_2^{2-} ions, e.g. Mn_2O_3, and those with oxygen ion vacancies, e.g. TiO_{2-x} can form O^- ions. Other small molecules undergo a reactive adsorption, the nature of which depends on the adsorbate. For example, the adsorption of water vapour occurs with the formation of two hydroxyl groups,

$$H_2O + O^{2-} = 2OH^-$$

and for CO and CO_2, the formation of carbonate groups as described, and SO_2 forms a sulphite ion, SO_3^{2-} by addition of an O^{2-} ion.

A common feature of the interaction of oxides with organic molecules is the breaking of C–H bonds, but rarely C–C bonds. The reaction to form C_2H_6

from methane probably occurs by the reaction

$$CH_4 + O^- = CH_3 + OH^-$$

and with molecules containing double bonds or hydroxyl groups, charged organic species are formed

$$(RCH = CH_2) + O^{2-} = (RCH = CH^-) + OH^-$$

where R represents a hydrocarbon radical, e.g. CH_3, C_2H_5, C_6H_5 etc.

Supported metal catalysts

Apart from the surface structure of a catalyst, the most effective sample of a catalyst will be the one with the largest surface area. A large surface area is frequently achieved in practice by supporting fine particles of a catalyst on an inert support, e.g. platinum particles on an alumina support. Problems associated with this arrangement arise from the relative ease with which very small particles can evaporate when compared with the bulk material, and the tendency for the average particle size to increase due to surface diffusion of atoms from the smaller to the larger particles. This is because the smaller particles have a higher thermodynamic activity, and hence chemical potential, according to the Kelvin equation

$$\mu_r - \mu^\circ = 2V_m\gamma/r$$

DropBooks

where μ_r and μ° are the chemical potentials of a particle of radius r and a flat surface respectively, V_m is the molar volume and γ is the surface energy. The process involving surface diffusion, which is known as *Ostwald ripening* increases the average particle size, and hence reduces the catalytic activity.

Another mechanism for the growth of particles and a decrease in the number in unit surface area, is collision and coalesence between particles by migration over the support surface. Movement of quite large particles involving 100 atoms and more have been observed in a number of systems, the apparent diffusion coefficient of theses particles having an activation energy which increases as the particle size increases. This kind of movement has been likened to *Brownian motion* which can be seen in liquid colloidal dispersions, where the average velocity is $(2kT/\pi m)^{1/2}$ for a two-dimensional gas, and the diffusion coefficient can be calculated from the general equation

$$D = \bar{x}^2/2\tau$$

$\bar{x}$ being the average displacement of the particles in the time τ. The obvious difference between these colloidal dispersions and the catalyst particles on the surface of a support, is that the above model would require that the particles

can slide across the support surface with zero frictional constraint, and the coalescence would require atomic re-arrangement on the interface between the colliding particles. It is therefore to be expected that this simple model would represent an upper limit to the possible movement and coalescence of solid particles.

Chemical interaction between the metal particles and the support can sometimes have the effect of changing the contact angle between the catalyst and the support, in some cases leading to an increase in catalytic activity, due to the increased surface area of the catalyst. Platinum, for example, when supported on TiO_2 forms small particles on the stoichiometric oxide, but after reduction in hydrogen at high temperature, where the oxide is probably reduced to Ti_3O_5, the metal forms small flattened islands having a larger surface area than in the original sample. Rhodium on the same support becomes encapsulated in titanium oxide after this reduction stage. The covering layer of oxide is removed on subsequent oxidation. These elements react with many oxides, however, to form inter-metallic compounds which have a high chemical stability. For example, platinum interacts with alumina and zirconia to form several inter-metallic compounds as well as very stable solid solutions at the platinum-rich end of the composition range. Palladium, on the other hand, which is not regarded as a metal as chemically and catalytically active as platinum, does not form such stable compounds and solid solutions with oxides, although they are similar to the platinum compounds in variety and composition, and therefore functions more like a simple metal catalyst on an oxide support.

Examples of industrially important catalysts

The catalyst metals are usually transition metals, either of Group IB or VIII having an electronic structure in the condensed state in which there are electron holes in the conduction band. These play an important role in electron exchange reactions occurring on the surface of the metals during heterogeneous gas–solid reactions. The metals and their alloys have a wide range of applications in the preparation of organic compounds, but we shall restrict interest here to reactions involving the simple molecules such as methane and methanol. Table 4.1 shows some examples of industrial processes in which catalysis plays a vital role.

Thermodynamics of the water–gas shift and steam reforming reactions

These two reactions, which have been in industrial use for many decades, have equilibrium constants (Table 4.2) where it can be seen that the equilibrium

Table 4.1 *Transition metal catalysts of industrial processes*

Element	Catalytic reactions
Group IB	
Copper	Water–gas shift reaction: $CO + H_2O = CO_2 + H_2$
Silver	Oxidation of ethylene, synthesis of HCN from NH_3 and CH_4
Gold	Decomposition of HI and oxidation of SO_2.
It will be observed that copper, which is easily oxidized or halogenated, is restricted as a catalyst to reactions where the oxygen potential is low, as in CO/CO_2 mixtures containing an excess of CO.	
Group VIII	
Nickel	Steam reforming of CH_4: $CH_4 + H_2O = CO + 3H_2$
Iron	NH_3 synthesis from the elements
Iron or Cobalt	Hydrogenation of CO and CO_2 to form hydrocarbons (Fischer–Tropsch synthesis)
These elements can only be used at low oxygen potentials.	
Palladium	Oxidation of hydrocarbons
Platinum	Oxidation of hydrocarbons, CO and NH_3 and nitrogen oxides
These metals can be used at high oxygen potentials, but the use of platinum is limited in high oxygen potentials and high temperatures by the formation of gaseous PtO_2.	

DropBooks

Table 4.2 *Thermodynamic data for ideal reforming reactions*

$H_2O + CO = H_2 + CO_2$	$: \Delta G^\circ = -35\,600 + 32.74T$	J/mole H_2O
	$K = 0$ at 1078 K	
$H_2O + CH_4 = 3H_2 + CO$	$: \Delta G^\circ = 224\,900 - 251.90T$	J/mole H_2O
	$K = 0$ at 892 K	
$4Cu + O_2 = 2Cu_2O$	$: \Delta G^\circ = -341\,800 + 145.2T$	J/mole O_2
$2Ni + O_2 = 2NiO$	$: \Delta G^\circ = -470\,000 + 171.8T$	J/mole O_2

constants pass through the value of unity at temperatures between 800 K and 1100 K. The metals which can be used as catalysts form oxides at oxygen partial pressures above 10^{-15}–10^{-8} atmos for copper, and 10^{-21}–10^{-13} atmos for nickel in this temperature range. It would appear that both metals can be oxidized during these reactions, unless the kinetics of oxidation are slow, or the oxygen potential can be maintained at a low value.

There are a number of major industrial problems in the operation of the steam reforming of methane. These include the formation of carbon on the surface of the catalyst, the sulphidation of the catalyst by the H_2S impurity in commercial natural gas, and the decline of catalytic activity due to Ostwald ripening of the supported catalyst particles by migration of catalyst atoms from the smaller to the larger particles, as the temperature is increased. A consideration of the thermodynamics of the principal reaction alone would suggest that the reaction shifts more favourably to the completion of the reaction as the temperature is increased.

The carbon activity of the gas, which is determined by the CO/CO_2 ratio is given by the equation

$$2CO = CO_2 + C : \Delta G^\circ = -171\,400 + 176T \quad \text{joules}$$

$$\ln K = \ln a_c + \ln (pCO_2/p^2CO)$$

At the average temperature 900 K, the activity of carbon will reach unity, i.e. pure carbon may be formed, when

$$\ln K = \ln(pCO_2/p^2CO) = 1.73$$

In the steam reforming reaction, $pCO_2/p^2CO = 2.08$ ($\ln = 5.64$) at this temperature, and at 1000 K the results are $\ln K = 0.55$ for carbon formation, and the pCO_2/p^2CO ratio is 0.155 ($\ln K = 1.16$), and thus the tendency for carbon formation passes from zero to unity in this temperature range. The presence of CO_2 is not indicated in this reaction as given above, but its partial pressure can be obtained from data for the concurrent reaction

$$CH_4 + 2H_2O = CO_2 + 4H_2 : \Delta G^\circ = 224\,000 - 250T \quad \text{joules}$$

The total composition of the product gas phase can be calculated using Gibbs energy minimization calculations. The results for the partial pressures of the major components of the water–gas shift equilibrium (Table 4.3) show that the pCO_2/p^2CO ratio at 900 K is 7.67, which indicates a higher CO_2 partial pressure than that at which the carbon activity reaches unity, and thus that this reaction would not be expected to produce carbon deposition on the catalyst. The steam reforming of methane reaction however, should produce a pCO_2/p^2CO ratio of 3.64 at equilibrium at 900 K, and this is quite close to the conditions for carbon formation.

The principle of Le Chatelier shows that when the pressure applied to a gaseous system is increased, the equilibrium composition will change in order to reduce the number of gaseous molecules. In the case of the steam reforming of methane, the partial pressures of methane and steam will increase as the pressure is increased. In the water–gas reaction, where the number of molecules is the same on both sides of the equation, the effect of increasing

Table 4.3 *Equilibrium composition in the steam-reforming reaction at 900 K as a function of pressure (molar fraction)*

Pressure	1 atmos	10 atmos	100 atmos
H_2	0.564	0.326	0.153
CO	0.158	0.031	0.0052
CH_4	0.119	0.322	0.421
H_2O	0.106	0.264	0.387
CO_2	0.052	0.058	0.038
The corresponding data for the water-gas shift reaction at 1000 K are			
H_2	0.272		
CO_2	0.272	at all pressures (1–100 atmos)	
CO	0.228		
H_2O	0.228		

or decreasing the total pressure has no effect on the equilibrium composition. As a corollary to this, it is clear that increasing the temperature will favour an endothermic reaction, such as the steam reforming reaction, but lowering the temperature will favour the exothermic water–gas shift reaction, to produce the reaction products.

DropBooks

Kinetic factors in steam reforming

The rate of formation of the products of steam reforming is extremely slow in the homogeneous reaction, and the reaction only proceeds at a useful rate in the presence of the catalyst. This indicates that adsorption of the reactant gases on the catalyst surface is a necessary step in the initiation of a useful reaction. The nature of the adsorption processes can be described by the equations:

$$\begin{aligned} CH_4 + n^* &\longrightarrow CH_x - n^* + (4-x)/2H_2 \\ CH_x - n^* + O{-}^* &\longrightarrow CO + (x/2)H_2 + (n+1)^* \\ H_2O + {}^* &\longrightarrow O - {}^* + H_2 \\ H_2 + 2^* &\longrightarrow 2H - {}^* \end{aligned}$$

Here 'n^*' indicates an active surface site, and $X{-}^*$ indicates the species X adsorbed on an active site. The first reaction allows for the possibility that methane may occupy more than one active site on adsorption. The third and fourth reactions show the observed retarding effects of steam and hydrogen

on the rate of the overall reaction, since they compete with methane for active sites.

The overall reaction kinetics corresponding to these stages of surface adsorption followed by reaction can be represented by the equation

$$\text{Rate} = k p_{CH_4}/(1 + k_1\sqrt{p_{H_2}} + k_2\sqrt{p_{O_2}})^n$$

Similar expressions have been found to be applicable to the steam reforming of higher hydrocarbons. For example, it has been shown that if it is assumed that ethane, C_2H_6 is adsorbed on two neighbouring sites, the overall reaction rate can be expressed by the equation

$$\text{Rate} = 2.2 \times 10^5 \exp(-9100/T) p_{C_2H_6}^{0.54} p_{H_2O}^{-0.33} p_{H_2}^{0.2}$$

Another aspect of the mechanisms of these reactions is that all of these non-metallic elements, carbon, oxygen and hydrogen, are soluble in nickel to a small extent. There is therefore a transport mechanism for the elements through the catalyst, apart from adsorption on the surface sites. The role of carbon solution in nickel appears to be to act as a transport path for the formation of carbon whiskers on the surface. These reduce the efficiency of the catalyst, and must be removed by the addition of a surplus of steam above the reaction stoichiometry, leading to an oxidizing condition. It has recently been shown that the addition of gold to a nickel catalyst decreases the formation of carbon whiskers. This can be understood as resulting from the reduction of the solubility of carbon, due to the fact that the solubility of carbon in gold is very small, and the solubility of carbon in the alloy is given approximately by the relation

$$\ln C_{Ni-Au} = X_{Ni} \ln C_{Ni} + X_{Au} \ln C_{Au} + \Delta G_{Ni-Au}^{xs}/RT$$

where the excess energy of mixing applies to the composition of the alloy (Figure 4.3).

The role of oxygen and hydrogen solutions in the metal catalyst does not appear to be that of impeding the major reactions, but merely to provide a source of these reactants which is uniformly distributed throughout the catalyst particles, without decreasing the number of surface sites available to methane adsorption. It is therefore quite possible that a significant fraction of the reaction takes place by the formation of products between species adsorbed on the surface, and dissolved atoms just below the surface, but in adjacent sites to the active surface sites.

Another contribution to the reaction involving steam is thought to be the role of the oxide support in the provision of hydrogen to the surface of adjacent catalyst particles. It is suggested that the water molecule is adsorbed on the surface of oxides such as alumina, to form hydroxyl groups on the surface, thus

$$H_2O + O^{2-} = 2OH'$$

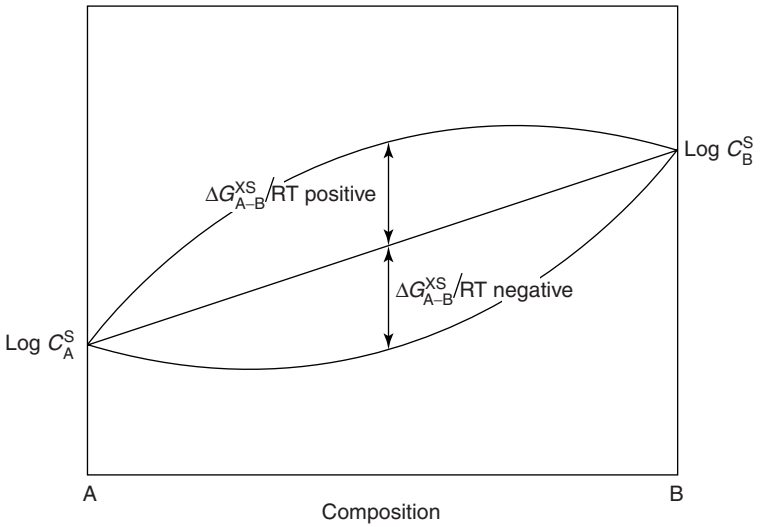


Figure 4.3 *The variation of the solubility of a dilute solutes in an A–B alloy*

and if these hydroxyl groups migrate to the catalyst/support interface, this reaction can reverse, leaving an oxygen atom adsorbed on an active site of the catalyst.

DropBooks

The Fischer–Tropsch production of organic molecules

The products of the water–gas shift reaction contain CO and H_2 as the principal content, together with CO_2 and H_2O which are by-products of the main reaction. The resultant mixture of CO and H_2 is referred to as 'synthesis gas', since it can be used in the Fischer–Tropsch reaction to prepare hydrocarbons and oxygenated organic molecules. The same synthesis gas can be prepared by burning coal in an oxygen/steam mixture, when the carbon content is oxidized to CO and the hydrocarbon content of the coal provides some of the hydrogen. The final ratio CO/H_2 can be controlled through the oxygen/steam ratio of the incoming gas. The oxygen for this process is prepared in a cryogenic air separation plant. The exit gas from this gasification contains a small partial pressure of methane accompanying the CO/H_2 mixture together with sulphur-containing gases, the quantity of which depends on the quality of the coal. After removal of the sulphur, the residual gas is sent to the Fischer–Tropsch reaction vessel.

The catalyst is typically iron, which is promoted by the addition of copper, SiO_2 and an alkali oxide, usually K_2O. The catalyst can be prepared by

fusing, magnetite with the appropriate amounts of the additions at 1800 K, followed by reduction in hydrogen to form a porous metal catalysts in the form of islands, separated by the alkali silicate. The presence of the silicate coating of the metallic particles probably reduces the tendency to Ostwald ripening and sintering, and therefore retains the catalytic activity of the metal. In some practice more silica is added to form a support for the metal phase. Cobalt has also been used successfully as the catalyst, but the addition of copper is eliminated in this case. Since the pure synthesis gas would produce carbon deposition on the iron surface, reducing the activity of the catalyst, the role of the CO_2 content of the inlet gas is to lower the carbon potential. The H_2/CO ratio is frequently maintained as high as 5:1 in the process at a temperature of operation of about 550 K, and a pressure of 1 atmos or greater.

A typical analysis of the gaseous products of the process shows a wide range of hydrocarbons, both saturated and unsaturated, from methane up to C_{18}, including gasolene C_8 and Diesel fuel $C_{12}-C_{16}$, and waxy products of higher carbon content. The oxygenated products range from acetaldehyde, CH_3CHO to methyl alcohol, CH_3OH, dimethyl ketone, CH_3COCH_3 and higher members of these series, together with a minor content of the lower carboxylic acids, acetic, proprionic and butyric acids.

The thermodynamic expectation is far removed from the practical results which yield a much higher content of the higher hydrocarbons than would be expected for the temperature of operation and the composition of the in-going gas. It is apparent that further reactions among the hydrocarbons leading to increased chain length must occur in the reactor. This probably involves the formation of free radicals as in the coupling reactions of methane (see below) followed by chain growth of the higher hydrocarbons. The data from industrial production units has been shown to conform with the simple assumption of a constant ratio between chain growth and chain termination. Thus if a fraction, α, of the molecules of formula C_nH_{2n+2} in the saturated hydrocarbon series undergo growth to form the species $C_{n+1}H_{2n+4}$, then $(1-\alpha)$ is the fraction of molecules terminated at the composition C_nH_{2n+2} which appear in the process yield. The statistics of a polymerization process, where a molecular species, C_1, undergoes growth to form larger molecules C_n, may be treated by assuming that each step in the polymerization process consists of the addition of a C_1 radical, CH_3, where C_1 represents methane, at each step. The chain of the number of molecules of each stage are then represented by

$$C_1 \longrightarrow \alpha C_1 + (1-\alpha)C_1 \text{ remaining as } C_1$$

$$\alpha C_1 \longrightarrow C_2 \longrightarrow \alpha C_2 + (1-\alpha)\alpha C_1 \text{ remaining as } C_2$$

$$\alpha C_2 = \alpha^2 C_1 \longrightarrow \alpha C_2 + (1-\alpha)\alpha^2 C_1 \text{ remaining as } C_3$$

and the general term for the remaining content of C_n is $(1-\alpha)\alpha^{n-1}C_1$. The mole fraction of each component, X_i, is then calculated by summing the series for the total number of all molecules Although each stage in the polymerization requires the addition of a CH_3 radical to the chain, the total number of molecules, N, in the chain remains constant and hence

$$N = \Sigma_{\text{all species}}(1-\alpha)\alpha^{n-1}C_1 = C_1; \quad X_n = [(1-\alpha)/\alpha]\alpha^n$$

The weight fraction can be calculated by multiplying each remaining fraction by nw_1, where w_1 is the molecular weight of the monomer, then for the nth species

$$\begin{aligned} W_n &= nw_1[(1-\alpha)\alpha^{n-1}]/\Sigma_{\text{all species}}nw_1[(1-\alpha)\alpha^{n-1} \\ &= n\alpha^{n-1}/\Sigma nw_1\alpha^{n-1} = n\alpha^{n-1}/(\partial/\partial\alpha)\Sigma\alpha^n \\ &= n\alpha^{n-1}/(\partial/\partial\alpha)(1-\alpha)^{-1} \\ &= n\alpha^{n-1}(1-\alpha)^2 \end{aligned}$$

Data from the results of an industrial reactor study produced the result

$$\alpha = 0.606 + 0.012n$$

The effect of increasing pressure is to move the average hydrocarbon content towards the heavier species, but increasing temperature seems to favour the production of lighter species. The final proportions are also determined by the state of the catalyst, and the physical arrangement of the reactor. The formation of the oxygenated compounds could also involve reactions between the H_2O content of the gas in the form of adsorbed OH^- radicals and hydrocarbon radicals since the production of these molecules is also well beyond the thermodynamic expectation.

A further stage in the synthesis of organic compounds is the production of aromatic cyclic compounds, such as benzene, C_6H_6, from aliphatic compounds, such as hexane, C_6H_{14}. Platinum is the catalyst which is used for this process, and the average temperature and pressure are 750 K, and 20 atmos respectively. Surface studies of the thermolysis of hydrocarbons adsorbed on platinum show dehydrogenation reactions which eventually leave a carbon film on the catalyst. This reduces the activity of the catalyst, but the formation of the film can be eliminated by the addition of a small partial pressure of hydrogen, which inhibits the dehydrogenation in the final stages before carbon formation.

The production of ammonia from its elements

The 'fixing' of nitrogen in ammonia is the first step in the industrial production of many nitrogen-containing materials, such as fertilizers. The industrial

DropBooks

process, the Haber process, is carried out at moderate temperatures and high pressures using an iron catalyst. The starting material for the preparation of the iron catalyst is iron oxide, mixed with about 2.5 wt per cent Al_2O_3 and 1 per cent K_2O. The mixture is fused at 1800 K and then reduced in hydrogen to produce a porous iron structure in which the iron particles are separated by a thin film containing the alumina and potash. The function of the thin film is to maintain the iron porosity during the synthesis of ammonia.

The industrial reaction using nitrogen and hydrogen gases

$$N_2 + 3H_2 = 2NH_3$$

is carried out at 1000 atmos pressure, the elevated pressure being indicated because of the decrease in the number of molecules which occurs in the reaction. The temperature of the operation when the catalyst described above is used is about 800 K. The thermodynamic data for the reaction indicate an equilibrium constant under these conditions

$$K_p = p^2NH_3/pN_2\,p^3H_2 = 10$$

corresponding to about one-third conversion of the original gas mixture. The kinetics of the formation reaction is rate-determined by the adsorption of nitrogen to form adsorbed separated atoms

$$N_2 = 2N(ads)$$

with the heat of adsorption decreasing from 200 kJ mol^{-1} at the initial adsorption, almost linearly to 50 kJ at 50% coverage.

The reverse reaction to ammonia synthesis, the decomposition to nitrogen and hydrogen, is used in the nitriding of iron and carried out industrially at temperatures around 800 K and atmospheric pressure to produce surface-hardening. This dissolution reaction must also play a part in the synthesis of ammonia by the industrial process. The attempt to nitride iron by reaction with nitrogen gas is very slow under atmospheric pressure, presumably due to the stability of the nitrogen molecule.

The kinetic parameters for NH_3 decomposition at high pressures and temperature around 650 K are found to be

$$\text{Rate} = k\ pNH_3^{0.6}/pH_2^{0.85}$$

with an activation energy of 192 kJ mol^{-1}.

The overall rate for the formation of ammonia must therefore be a balance between the formation and the decomposition of the product species. Experimental data suggest that this balance can be represented by the equation

$$\text{Rate} = k_f\,pN_2[p^3H_2/p^2NH_3]^{0.5} - k_d[p^2NH_3/p^3H_2]^{0.5}$$

with an activation energy of 170 kJ mol^{-1}.

The catalytic converter for automobile exhaust

The metallic catalysts for exhaust pollution control are designed to perform three functions. The air/fuel ratio employed in combustion engines creates exhaust products which are a mixture of hydrocarbons, carbon oxides, and nitrogen oxides. These must be rendered environmentally innocuous by reactions on the catalyst such as

$$CO + (1/2)O_2 = CO_2$$

$$\text{Hydrocarbons} + O_2 \longrightarrow H_2O + CO_2$$

$$NO + CO = (1/2)N_2 + CO_2$$

$$NO + H_2 = (1/2)N_2 + H_2O$$

The proportions of these unwanted species in the exhaust are strongly affected by the air/fuel ratio, and the optimum performance of the engine is usually found at the ratio 14–15:1. No single catalyst has been found to perform all of these functions efficiently, and the solution has been to use different catalysts for each reaction. The so-called 'three way catalysts' that are employed to carry out these various reactions are mainly composed of platinum, rhodium and palladium. Of these, platinum plays the major role in the oxidation of hydrocarbons and carbon monoxide, rhodium is the most efficient catalyst for the reduction of nitrogen oxides, and palladium is sometimes used to replace platinum, in order to reduce the cost. Alumina is the most frequent support for the catalyst, either in the form of pellets, or as a surface coating to a monolith consisting of thin-walled honeycombs of cordierite ($2MgO{\cdot}2Al_2O_3{\cdot}5SiO_2$). The structure of the monolith made of cordierite is an effective support because of its light weight, low coefficient of thermal expansion and physical resistance to the effects of vibration.

DropBooks

There is a significant difference between rhodium and the other metals in that rhodium forms a relatively stable oxide, Rh_2O_3. The Gibbs energy of formation of this oxide is given by the equation

$$(4/3)Rh + O_2 = (2/3)Rh_2O_3$$

$$\Delta G^\circ = -229\,030 + 163.4T \quad \text{J mol}^{-1}$$

and for the reaction with NO,

$$2Rh + 3NO = Rh_2O_3 + (3/2)N_2$$

$$\Delta G^\circ = -609\,070 + 276.8T \quad \text{J mol}^{-1}$$

It is therefore very probable that the success in using rhodium to reduce nitric oxide, and any other higher oxides of nitrogen, is the result of the stability of the rhodium oxide, probably only as a surface layer. Needless to say, the reducing gases in the exhaust, such as carbon monoxide and the hydrocarbons would cause the reduction of this oxide, thus regenerating the metal surface. Palladium also forms a relatively stable oxide, PdO, the Gibbs energy of formation equation being

$$2\mathrm{Pd} + \mathrm{O_2} = 2\mathrm{PdO}$$

$$\Delta G^\circ = -221\,840 + 182T \quad \mathrm{J\,mol^{-1}}$$

and the reaction for the reduction of NO is

$$\mathrm{Pd} + \mathrm{NO} = \mathrm{PdO} + 0.5\mathrm{N_2}$$

The kinetics of the oxidation of CO on a platinum surface indicate that CO and oxygen are adsorbed to about the same extent. The rate of oxidation depends on the oxygen partial pressure when CO is in excess, and on the CO partial pressure when oxygen is in excess.

Since the ratio of fuel to air does not remain constant during operation, it is necessary to arrange for the catalyst to function as an oxygen storage material during 'lean' combustion periods, when the fuel/air ratio exceeds the most efficient range. Efforts to achieve this centre around the addition of an alloying element to platinum, such as cerium, which is readily oxidized. Since the oxide formed on cerium can be reduced in stages to form the non-stoichiometric CeO_{2-x}, it is found that such additions to the catalyst are readily oxidized to yield CeO_2 during the high air/fuel ratio 'rich' regime of operation, but the oxide is only partially reduced to the non-stoichiometric oxide during the lean phase of operation. Thus the CO level of the exhaust changes rapidly following a rich/lean step, but reaches a new level only after several seconds in a lean/rich step.

These noble metal catalysts are subject to deterioration in time due to Ostwald ripening, but another consideration arises when a mixture of metals is used to form a catalyst system. To understand this, it is necessary to consider the composition of the surface of a binary metal alloy. According to the Gibbs surface energy theorem, the surface will tend to be covered by the metal with the lowest surface energy, and this in the case of the binary alloy will lead to a surface composition different from the bulk. It is therefore to be expected that the surface of an initially homogeneous binary alloy will change in the direction of minimizing the surface energy during high temperature operation.

Before leaving metallic catalysts, it is interesting to note that it was at first thought that the formation of iron carbide, Fe_3C played an important intermediate role in the Fischer–Tropsch process. Although this has not been proved to occur, nevertheless some metal carbides, such as WC, Mo_2C and VC are finding useful application in the production of organic species. One aspect of these compounds is that the tendency to form surface oxycarbide phases, which also act as catalysts, makes some new organic syntheses possible in an oxygen and sulphur-containing atmosphere.

Catalysis by metal oxides

Metal oxides present structures of a wide range from the alkaline earth oxides with the simple rocksalt structure to the cage-like structures of the zeolites, and the Ruddlesden–Popper phases in which layers of rocksalt structure are interspersed with perovskite unit cells, as in the ceramic superconductors. The oxygen anions, which dominate the surface structures of oxides are co-ordinated with metal ions of varying ionic charge and cation size, and thus the overall spacing between the anions varies with the cationic radius, providing a significant variable in the fit of adsorbed molecules on the oxide surface. Many cations can exist in more than one valency in the same oxide, leading to semiconduction, or even metallic conduction, depending on the particular cation, and the oxygen potential of the gas phase. It is clear that oxides are very versatile catalysts, and a wide range of studies have been made to compare the efficiencies of a number of oxides for the catalysis of a particular reaction.

DropBooks

One feature of oxides is that, like all substances, they contain point defects which are most usually found on the cation lattice as interstitial ions, vacancies or ions with a higher charge than the bulk of the cations, referred to as 'positive holes' because their effect of oxygen partial pressure on the electrical conductivity is the opposite of that on free electron conductivity. The interstitial ions are usually considered to have a lower valency than the normal lattice ions, e.g. Zn^+ interstitial ions in the zinc oxide ZnO structure.

An important species which occurs on the surface of oxygen-deficient compounds is the singly charged oxygen ion. This results from the filling of an oxygen vacancy by an adsorbed oxygen atom according to the equation

$$(1/2)O_2 + V(O^{2-}) + O_1{}^{2-} = 2O^-$$

where $V(O^{2-})$ is an oxygen vacancy, and $O_1{}^{2-}$ is an oxygen ion on a neighbouring lattice site. The presence of the singly-charged oxygen ion confers positive hole conduction on the oxide. When the cation has a number of

valencies the adsorption of oxygen more usually leads to the formation of higher valency cations.

There is some distortion at the surface, the oxygen ions being displaced towards the underlying cations when compared with anions in the bulk of the material, in part because the co-ordination of a surface ion is less than in the bulk, especially on ledges and kinks. It has been estimated that in a crystal of MgO, the Madelung constant, which measures the binding of an ion to its environment, decreases from the bulk value of 1.748, to 1.567 on a ledge site and 0.873 on a kink corner ion. Since the second ionization potential of oxygen is endothermic, it is quite probable that the singly-charged oxygen ion could occur on the low Madelung constant sites, such as these corner sites, as a predominant species.

Because of the existence of surface point defects, such as vacancies in the anion structure and O^- ions, oxides can function as receptors of water molecules by reactions involving the formation of surface hydroxyl groups. These were invoked above in the catalytic interactions at the nickel–alumina interface referred to in the context of methane reforming. They can be quite stable at room temperature, leading to the formation of a hygroscopic layer on the surface, e.g. of BaO, but are largely evaporated at high temperature. It should be noted that this hydroxylation of the surface is possible in the transition state of a surface reaction, and that other oxidizing gaseous reagents, such as nitrous oxide, can undergo analogous reactions.

$$N_2O + V(O^{2-}) = N_2 + O_1{}^{2-}$$

An effect which is frequently encountered in oxide catalysts is that of promoters on the activity. An example of this is the small addition of lithium oxide, Li_2O which promotes, or increases, the catalytic activity of the alkaline earth oxide BaO. Although little is known about the exact role of lithium on the surface structure of BaO, it would seem plausible that this effect is due to the introduction of more oxygen vacancies on the surface. This effect is well known in the chemistry of solid oxides. For example, the addition of lithium oxide to nickel oxide, in which a solid solution is formed, causes an increase in the concentration of the major point defect which is the Ni^{3+} ion. Since the valency of the cation in the alkaline earth oxides can only take the value two the incorporation of lithium oxide in solid solution can only lead to oxygen vacancy formation. Schematic equations for the two processes are

$$Li_2O + V(Ni^{2+}) \longrightarrow 2Li_1{}^+ + O^{2-} + Ni^{3+}; \quad \text{on NiO}$$

and

$$Li_2O \longrightarrow 2Li_1{}^+ + O^{2-} + V(O^{2-}); \quad \text{on BaO}$$

Coupling reactions of methane

The reaction shown above for the steam reforming of methane led to the formation of a mixture of CO and H_2, the so-called *synthesis gas*. The mixture was given this name since it can be used for the preparation of a large number of organic species with the use of an appropriate catalyst. The simplest example of this is the coupling reaction in which methane is converted to ethane. The process occurs by the dissociative adsorption of methane on the catalyst, followed by the coupling of two methyl radicals to form ethane, which is then desorbed into the gas phase.

A closer analysis of the equilibrium products of the 1:1 mixture of methane and steam shows the presence of hydrocarbons as minor constituents. Experimental results for the coupling reaction show that the yield of hydrocarbons is dependent on the redox properties of the oxide catalyst, and the oxygen potential of the gas phase, as well as the temperature and total pressure. In any substantial oxygen mole fraction in the gas, the predominant reaction is the formation of CO and the coupling reaction is a minor one.

The reaction of CH_4 with hydrogen, at the other end of the oxidation scale, produces mainly acetylene, C_2H_2, ethylene C_2H_4 and ethane, C_2H_6. These reactions are favoured by operating at high temperatures. In fact the production of acetylene is most efficient if the gas mixture is passed through an arc struck between carbon electrodes, which probably produces a reaction temperature in excess of 2500 K.

DropBooks

It would seem that the coupling of methane can be carried out at oxygen potentials in between these two extremes using a catalyst which is to some extent reducible at moderately high oxygen potentials. A further constraint on the selection of the oxide is that the volatility of the oxide must be low at the operating temperature, about 1000–1200 K. Manganese forms a series of oxides MnO_2, Mn_2O_3, Mn_3O_4 and MnO spanning an oxygen dissociation pressure between 1 atmos for the MnO_2/Mn_2O_3 equilibrium, about 10^{-3} atmos for Mn_2O_3/Mn_3O_4, to less than 10^{-9} for the Mn_3O_4/MnO equilibrium. The oxide Mn_2O_3 can therefore undergo reduction on adsorption of methane with subsequent regeneration by oxygen in the gas phase. Methyl radicals produced by the adsorption process undergo coupling to form ethane on the surface, which is then desorbed into the gas phase. Alternatively, it has been proposed that methyl radical combination can take place primarily in the gas phase.

The lithium oxide-promoted barium oxide also functions as a catalyst for the methane coupling reaction, but the mechanism is not clearly understood at the present time. The only comment that might be offered here is that the presence of O^- ions on the surface of this material might enhance the formation of methyl radicals through the formation of hydroxyl groups thus

$$CH_4 + O^- = CH_3 + OH'$$

followed by the desorption reaction

$$2OH' = H_2O(g) + O_1^{2-}$$

A comparative study of oxides which were closely related, but had different electrical properties, showed that both *n*- and *p*-type semiconduction promoted the oxidation reaction, forming CO as the major carbon-containing product. In a gas mixture which was 30% methane, 5% oxygen, and 65% helium, reacted at 1168 K the coupling reactions were best achieved with the electrolyte $La_{0.9}Sr_{0.1}YO_{1.5}$ and the *p*-type semiconductor $La_{0.8}Sr_{0.2}MnO_{3-x}$ and the *n*-type semiconductor $LaFe_{0.8}Nb_{0.2}O_{3-x}$ produced CO as the major oxidation product (Alcock *et al.*, 1993). The two semiconductors are non-stoichiometric, and the subscript $3 - x$ varies in value with the oxygen pressure and temperature. Again, it is quite probable that the surface reactions involve the formation of methyl radicals and O^- ions.

Reactors for catalytic processes

The industrial production of compounds by catalytic reactions is carried out mainly in one of two types of reactor. In the fixed, or *packed bed* reactor, particles of the catalyst are held in close contact in a cylindrical container. The gases flow through the unoccupied volume of this packed bed, and the temperature of reaction is achieved by a combination of control of the container temperature, pre-heating the inlet gas, and by the generation or absorption of heat on the catalyst as a result of the gaseous reaction. The transfer of heat to and from the gas phase and the rate of reaction are therefore important in fixing the dimensions of the catalyst particles which at a small diameter will restrict gas flow, and at a large size will present too little surface, and hence catalyst, to the reactants. The overall diameter of the containing vessel will determine the throughput of gas to the reaction, once the optimum particle diameter has been decided. The pressure drop, ΔP, across a packed bed of length L consisting of particles of average diameter d_p, for a gas of density ρ_g, and viscosity η_g, flowing at a velocity u_g, is given approximately by the empirical Ergun equation

$$\frac{\Delta P}{L} = K_1\eta_g u_g + K_2 u_g^2$$

$$K_1 = \frac{150(1-\varepsilon)^2}{\varepsilon^3 d_p^2}; \quad K_2 = \frac{1.75\rho_g(1-\varepsilon)}{\varepsilon^3 d_p}$$

Here ε is the porosity of the bed, which is equal to the difference between the bed volume and the volume of particles, divided by the bed volume. It can

be assumed that the gas phase is in turbulent, and hence well mixed, motion throughout the reaction volume.

It follows that the position of thermodynamic equilibrium will change along the reactor for those reactions in which a change of the number of gaseous molecules occurs, and therefore that the degree of completion and heat production or absorption of the reaction will also vary. This is why the external control of the independent container temperature and the particle size of the catalyst are important factors in reactor design.

In the *fluidized bed* the catalyst is suspended as separate particles in the gaseous reactants, which have been suitably pre-heated. The advantages of this form of reactor include excellent heat transfer to and from the catalyst particles, maximum contact between the catalyst and the gas, and the elimination of the possibility of particle–particle sintering during the production run. There is also very little pressure drop across the reactor, and so there is negligible effect on the position of equilibrium. The principal disadvantages include the necessity of particle size control of the catalyst to minimize sweeping of the light particles from the reactor, and the settling of the oversize particles into the reactor entry port. The gas transit time is also not as easily controlled as in the fixed bed because of the need to suspend the catalyst particles. The problem of fine particle entrainment can be decreased by reducing the gas velocity to a level where the mass of particles has the appearance of a boiling liquid, which decreases the overall rate of reaction. Alternatively at high gas input rates, the entrained particles can be separated from the effluent gases in a precipitator and recycled with the fresh particle input. The gas velocity at which fluidization occurs is given by

DropBooks

$$u_{\mathrm{mf}} = \frac{d_p^2 g(\rho_s - \rho_g)}{1650\eta_g}$$

for large particles, when the Reynolds number, N_{Re}, of the gas is large (>1000), and

$$u_{\mathrm{mf}} = \frac{d_p g(\rho_s - \rho_g)}{24.5\rho_g}$$

for small particles, with a small gas Reynolds number (<20). This dimensionless number is defined in the case of a particle suspended in a gas by the equation

$$N_{\mathrm{Re}} = \frac{d_p u_g \rho_g}{\eta_g}$$

and for a particle of diameter 1 mm, and density 3 g cm^{-3}, suspended in air (viscosity 0.04 cp, and density 3×10^{-4} g cm^{-3}) which is flowing at u_g cm s^{-1},

the Reynolds number is

$$N_{\mathrm{Re}} = \frac{(0.1) \times 0.0003 u_g}{0.0004} = 0.075 u_g$$

The gas velocity required to suspend these small particles is

$$u_{\mathrm{mf}} = \frac{(0.1)^2 \times 981 \times 3}{1650 \times 0.0003} = 59.5\,\mathrm{cm\,s^{-1}}$$

which yields a Reynolds number of 4.46.

It can be seen from the above equations that the viscosity of the gas only becomes important at these low gas velocities for typical particle sizes which are used in fluidized beds.

As an example of the chemical significance of the process technology, the products of the Fischer–Tropsch synthesis, in which a significant amount of gas phase polymerization occurs vary markedly from fixed bed operation to the fluidized bed. The fixed bed product contains a higher proportion of straight chain hydrocarbons, and the fluidized bed produces a larger proportion of branched chain compounds.

Bibliography

M. Prutton. *Surface Physics*, 2nd edn. Oxford University Press (1983).

J.T. Richardson. *Fundamental and Applied Catalysis*, Plenum, New York (1989) TP159 C3R47.

J.R. Anderson and M. Boudart (eds), *Catalysis, Science and Technology*, Several volumes. Springer Verlag, Berlin TP156 C35 C375 Volume 1: M.E. Dry, The Fischer-Tropsch synthesis, pp. 160–255.

J.H. Sinfelt. Catalytic reforming of hydrocarbons, ibid. pp. 259–300.

A. Ozaki and K. Aika. Catalytic Activation of dinitrogen, ibid. pp. 87–158, Volume 7: B.E. Koel and G.A. Somorjai. Surface structural chemistry, pp. 159–218.

J.M. Thomas and K.I. Zamaraev (eds). *Perspectives in Catalysis*, Blackwell Scientific for I.U.P.A.C., London (1992).

V.E. Henrich and P.A. Cox. *The Surface Science of Metal Oxides*, Cambridge University Press (1994).

N. Gunarsekaran, S. Rajadurai, J.J. Carberry, N. Bakshi and C.B. Alcock, *Solid State Ionics*, **73**, 289 (1994).

C.B. Alcock, J.J. Carberry, R. Doshi and N. Gunarsekaran, *J. Catalysis*, **143**, 533 (1993).

J. Szekely and N.J. Themelis. *Rate Phenomena in Process Metallurgy*, Chapter 18, p 639. Wiley-Interscience. New York (1971).

G.C. Kuczynski (ed.). *Sintering and catalysis*, Plenum Press, New York (1975).

G.A. Somorjai and S.M. Davis, *Surface. Sci.*, **92**, 73 (1980).

S. Lehwald and H. Ibach, ibid, **89**, 425 (1980).

Part 2

Rate Processes in the Solid State

Introduction

Processes in which solids play a rate-determining role have as their principal kinetic factors the existence of chemical potential gradients, and diffusive mass and heat transfer in materials with rigid structures. The atomic structures of the phases involved in any process and their thermodynamic stabilities have important effects on these properties, since they result from the distribution of electrons and ions during the process. In metallic phases it is the diffusive and thermal capacities of the ion cores which are prevalent, the electrons determining the thermal conduction, whereas it is the ionic charge and the valencies of the species involved in non-metallic systems which are important in the diffusive and the electronic behaviour of these solids, especially in the case of variable valency ions, while the ions determine the rate of heat conduction.

DropBooks

The structural effects in solids are not confined to atomic distribution, but are also dependent upon the 'graininess' of the solid, both with respect to the degree of crystallinity and the grain structure of a reacting sample of a solid. Most samples of solids which are used in processes are polycrystalline, the single crystals mainly serving as 'test-beds' where the effects of grain boundaries are eliminated, or made with a controlled structure, as in bicrystals which are used to investigate grain boundary properties. To some measure solid state process kinetics involve dislocations and grain boundaries which provide short circuits for reaction paths.

Chapter 5

Electrical charge and heat transport in solids

The transport of electrons and positive holes

The electrical properties of solids are categorized into classes of conductivity through Ohm's law which states a relationship between conductivity σ, current density J and applied potential E

$$J = \sigma E$$

where σ can vary over twenty orders of magnitude between metals and insulators. For example, metals have conductivities around 10^5 ohm^{-1} cm^{-1}, silicon and germanium semiconductors are around 10^{-5} Ω^{-1} cm^{-1} and ceramic oxides are 10^{-10} to 10^{-15} Ω^{-1} cm^{-1} at room temperature.

Metals and alloys

The free electron theory of metals envisages conduction electrons as moving through a crystalline array of ion cores the charge of which relates to the Group of the metal in the Periodic Table, namely 1+ for sodium, 2+ for magnesium and so on. Because of the large mass difference, the electron loses kinetic energy at each collision with an ion core, and then gathers momentum again under the influence of an applied electrical field but initially in a random direction from its previous trajectory. Between collisions the electron acquires an average drift velocity $\overline{v}$ in the direction of the field such that

$$J = ne\overline{v}$$

where n is the number of electrons per unit volume in the metal, and e is the electronic charge.

If the average time between collisions is 2τ then the *relaxation time* is defined by

$$\frac{m\overline{v}}{eE} = \tau$$

and setting the *mobility*, μ, which is the mean drift velocity in unit field (units, $cm^2\,v^{-1}s^{-1}$) as equal to $e\tau/m$ it follows that

$$J = ne\mu E \text{ and } \sigma = ne\mu$$

The temperature coefficients of conductivity of metallic systems are characteristically negative because of the increased scattering of the electrons brought about by the increasing amplitude of vibration of the ion cores.

When electrons traverse an alloy rather than a pure metal, the scattering of electrons is different at the ion core of each chemical species and so the conductivity reflects a mixture of the effects due to each species. In a series of copper alloys it was found that the resistance, which is the reciprocal of the conductivity, is a parabolic function of the concentration of the major element

$$1/\sigma \propto X(1 - X)$$

where X is the mole fraction of copper. This is Nordheim's empirical rule for the conductivity of concentrated alloys ($1 \geq X \geq 0.7$).

In dilute alloys of copper containing 1% of alloying element the conductivity decreases as the valency of the dilute solute increases. The modern view of the electron concentration around such a dilute solute suggests a localization of some conduction electrons which almost screen the extra charge brought by the alloying element ion core. Thus the conduction electrons in a Cu–Zn alloy will 'see' a partially screened Zn^{2+} ion, and the potential around an ion being given by

DropBooks

$$E_r = \frac{Ze^2}{r}\exp(-qr)$$

at a distance r from an ion core of charge Z. The screening constant, q, has a reciprocal value of about 0.05 nm in copper. In the preparation of high-conductivity copper it is necessary to remove as much as possible any impurity, because those with a different valency will reduce the conductivity as shown above, and those in the same Group such as silver will form solid solutions which also decrease the conductivity. This is usually done industrially by a combination of high-temperature processing, the so-called *fire refining* and finally room temperature electrolysis with an aqueous electrolyte.

The behaviour of electrons in metals shows the translational properties of quantum particles having quantized energy levels. These cannot be approximated to the continuous distribution describing particles in a gas because of the much smaller mass of the electron when compared with atoms. If one gram-atom of a metal is contained in a cube of length L, the valence electrons have quantum wavelengths, λ, described by the de Broglie equation

$$\lambda = h/mv$$

and hence the kinetic energy

$$E = \frac{1}{2}mv^2 = \frac{m^2v^2}{2m} = \frac{h^2}{2m\lambda^2} = \frac{h^2k^2}{8\pi^2m}$$

where k is the *wave number*, $2\pi/\lambda$. The values of λ are constrained to those values which have a node at each face of the cube,

$$\lambda = 2L, L, \frac{2L}{3}, \ldots, \frac{2L}{n}$$

where L equals $V^{1/3}$ and

$$\lambda^2 = \frac{4V^{2/3}}{n^2} = \frac{1}{\left[n_x^2 + n_y^2 + n_z^2\right]}4V^{2/3}$$

where n is a quantum number taking the integral values n_x, n_y and n_z which take the values 1, 2, 3 etc., are the components of n along the axes of the cube.

In a metal of molar volume, V_m, these energy levels are filled with paired-spin electrons up to a maximum energy level described by

$$E_{\max} = n_{\max}^2 \frac{h^2}{8mV_m^{2/3}}$$

and in a monovalent metal, such as copper, the total number of states which are occupied by paired-spins electrons is given by the octant of a sphere having $n_{\max}$ as a radius

$$\frac{1}{8}\frac{4}{3}\pi n_{\max}^3 = \frac{N}{2}; \quad n_{\max}^3 = \frac{3N}{\pi}$$

where N is Avogadro's number which is also the number of conduction electrons. It follows that the number of states with a quantum number n, the *density of states*, is proportional to $E^{1/2}$. The value of $n_{\max}$ defines the *Fermi surface*, and any electron having n less than this maximum value cannot be promoted to any of the filled higher levels. The electrons at the Fermi surface have empty energy levels immediately above the surface, and so these electrons can be promoted at elevated temperatures to free electron gas behaviour, and give rise to the very small classical electron contribution to the heat capacity of a metal. Since this is such a small proportion of the total electron concentration in these conduction electrons, the effect on the overall heat capacity is also small. This is why the $3R$ contribution of the vibrational energy of the ion cores is the principal contribution to the heat capacity and the conduction electron gas contribution which, according to the principle of equipartition, should be $(3/2)R$ mol^{-1} for a gaseous component is absent.

In the Sommerfield model of metals it is postulated that all valence electrons move in a constant potential, U, under the attraction of the ion cores, the total energy of electrons in the metal is thus the sum of the kinetic energy calculated above plus the energy due to the interaction with the ion cores. Since these are of opposite sign, the maximum electron energy is thus $E_{max} - U$. Since U is greater in magnitude than E_{max}, the resultant energy of the electron at the Fermi surface, which is called the *Fermi energy*, is less than that of an electron in free space and the electron *work function*, which is the energy required to remove an electron from a metal, is therefore equal to the negative of the electron energy at the Fermi surface.

There are restrictions on the values of the quantum numbers which electrons can occupy in three-dimensional metal structures which can be determined by application of the Bragg diffraction equation

$$n\lambda = 2d \sin\theta$$

Since electrons travelling at an angle θ to planes in the lattice having wavelengths which satisfy this equation would be diffracted in the lattice, these electrons do not give rise to translational energies, but can be described in wave-mechanical terms as standing waves. The result is that there are ranges of conduction electron kinetic energy which will not occur in crystals, depending on the crystal structure and interplanar spacing. The electrons are therefore

DropBooks

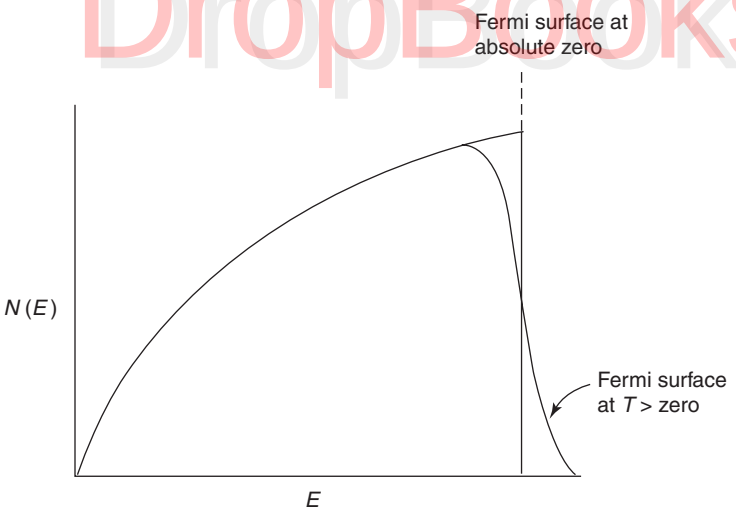


Figure 5.1 *The parabolic distribution in energy, $N(E)$, as function of energy, E, for free electrons. The Fermi surface represents the upper limit of electron energy at the absolute zero of temperature, but at higher temperatures a small fraction of the electrons can be excited to higher energy levels*

collected into bands of kinetic energy known as Brillouin zones which may be separated from one another energetically, or may overlap. In the latter case the material is a metal, but when the bands are separated the material is a semiconductor if the gap in energy between bands is small, but it is an insulator if this is large.

One further effect of the formation of bands of electron energy in solids is that the *effective mass* of electrons is dependent on the shape of the $E-k$ curve. If this is the parabolic shape of the classical free electron theory, the effective mass is the same as the mass of the free electron in space, but as this departs from the parabolic shape the effective mass varies, depending on the curvature of the $E-k$ curve. From the definition of E in terms of k, it follows that the mass is related to the second derivative of E with respect to k thus

$$E = \frac{h^2k^2}{8\pi^2 m}; \quad \frac{\mathrm{d}^2E}{\mathrm{d}k^2} = \frac{h^2}{4\pi^2 m}$$

As might be anticipated, the above relationship does not imply that electrons in metals are essentially different in mass from the electron in free space, but merely that the response of these electrons to an applied force is different, being reflected in the effective mass.

$$m = \frac{h^2}{4\pi^2 \dfrac{\mathrm{d}^2E}{\mathrm{d}k^2}}$$

Electromigration in alloys

Studies which have been made of the electrical conductivities of metallic alloys have shown that there is a compositional change along the direction of flow of the electric current. This change is related to the current passed during an experiment, and its duration. There appears, therefore, to be a diffusional flux of the ion cores associated with the passage of current, which has been named *electromigration*. It was thought, at one time, that the relative movement of species under the passage of current would always indicate the relative charges of each of the ion cores present in the structure, and therefore would indicate which species was relatively cathodic, and which anodic. Thus early studies of carbon dissolved in solid iron indicated a flow of carbon atoms towards the cathode, which could be interpreted to indicate a more positive charge on the carbon atoms than that on the iron atoms, whereas oxygen dissolved in titanium migrated to the anode, indicating a negative charge on the oxygen atoms as might be expected.

Further analysis, which is not yet complete, has indicated that the flow of current should be described as having two effects. The first, the purely

electrolytic effect, drives oppositely charged particles to opposite electrodes, as in the electrolysis of an ionic substance. The second effect, which moves particles in the direction of current flow, regardless of what charge they may carry, can be described as a frictional effect, or an electronic 'wind'.

Some quantitative aspects have emerged from experimental studies which can be described in terms of these two effects. In interstitial alloys, such as those of carbon, hydrogen and nitrogen, the frictional effect drives these interstitial atoms, which have a much higher mobility than the matrix transition metal solvent atoms, towards the cathode. This is consistent with the assumption that momentum exchange of the electrons and the interstitial atoms which propels these to cathode-directed holes is the predominant transport mechanism. Oxygen interstitial atoms are transported towards the anode in a number of transition-metal solutions because, it is thought, oxygen atoms do carry a net negative charge with respect to the metallic species (Verhoven, 1963).

In substitutional metallic solid solutions and in liquid alloys the experimental data have been described by Epstein and Paskin (1967) in terms of a predominant frictional force which leads to the accumulation of one species towards the anode. The relative movement of metallic ion cores in an alloy phase is related to the scattering cross-section for the conduction electrons, which in turn can be correlated with the relative resistance of the pure metals. Thus iron, which has a higher specific resistance than copper, will accumulate towards the anode in a Cu–Fe alloy. Similarly in a germanium–lithium alloy, the solute lithium atoms accumulate towards the cathode. In liquid alloys the same qualitative effect is observed, thus magnesium accumulates near the cathode in solution in bismuth, while uranium, which is in a higher Group of the Periodic Table than bismuth, accumulated near the anode in the same solvent.

DropBooks

A number of attempts have been made to quantify this model by means of fundamental quantum-mechanical calculations on the free electron transport in metals and alloys, but at the present time, the qualitative data presented in Table 5.1 will suffice to indicate the trends.

Elemental and compound semiconductors

In most metals the electron behaves as a particle having approximately the same mass as the electron in free space. In the Group IV semiconductors, this is usually not the case, and the effective mass of electrons can be substantially different from that of the electron in free space. The electronic structure of Si and Ge utilizes hybrid orbitals for all of the valence electrons and all electron spins are paired within this structure. Electrons may be thermally separated from the electron population in this bond structure, which is given the name the *valence band*, and become conduction electrons, creating at the same time

Table 5.1 *Electromigration in alloys*

Solvent	Solute	Direction of solute accumulation	
Solid interstitial solutions			
α-Fe	H, C, N	Cathode	
γ-Fe	H, C, B	Cathode	
β-Ti	O	Anode	
Zr	O	Anode	
Th	C, N, O	Anode	
Ag	O	Anode	
Solid substitutional alloys			$\Delta\rho$ (ohm cm)
Cu-Fe	Fe	Anode	+72
Cu-Au	Au	Anode	+26
Ag-Sb	Sb	Anode	+71
Al-Ag	Ag	Anode	+19
Si-Li	Li	Cathode	−20
Si-Cu	Cu	Cathode	−28
Si-In	In	Cathode	−47
Fe-Al	Al	Cathode	−100
Liquid substitutional solutions			
Na-Hg	Hg	Anode	+67
Na-Tl	Tl	Anode	+49
Cu-Ge	Ge	Anode	+19
Au-Ge	Ge	Cathode	+28
Bi-Mg	Mg	Cathode	−102

an equal number of positive holes in the valence band which are also able to carry current but in the opposite direction from electrons. The concentration of these thermally activated carriers can be calculated from the statistical mechanical equation to be

$$c = 2\left(\frac{2\pi m_0 kT}{h^2}\right)^{3/2} \exp\left(-\frac{E_g}{2kT}\right) \cong 4.83 \times 10^{15} T^{3/2} \exp\left(-\frac{E_g}{2kT}\right)$$

where m_0 is the mass of the free electron, E_g is the band gap, which is the potential energy difference between the band containing the valence electrons together with the positive holes and that containing the conduction electrons, and c is the concentration in particles/unit volume, of both electrons and positive holes. It will be recognized that this concentration function contains the

translation partition function of the conduction species which are co-produced with an activation energy of E_g, and the 'equation of the reaction' may be represented as

$$0 = \mathrm{n} + \mathrm{p}$$

where zero represents the original ground state of the element, and n and p are the electron and positive hole respectively (Figure 5.2).

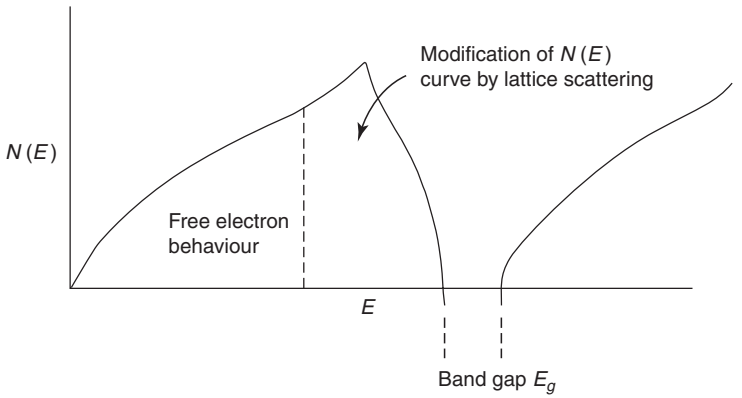


Figure 5.2 *The modification of the electron energy distribution curve by the presence of diffraction limits in a crystal. The lower filled band is separated from upper unoccupied states in a semiconductor by a small energy difference, so that some electrons can be promoted to conduction by an increase in temperature*

DropBooks

The effective masses of holes and electrons in semiconductors are considerably less than that of the free electron, and the conduction equation must be modified accordingly using the effective masses to replace the free electron mass. The conductivity of an *intrinsic* semiconductor is then given by

$$\sigma = ne\mu_e + pe\mu_p$$

which would be zero if

$$\mu_e = \mu_p$$

Usually this is not the case and Table 5.2 shows values for E_g, μ_e and μ_p for a number of semiconductors having the diamond structure. It will generally be observed from this table that the mobilities of electrons are greater than those of positive holes making these materials n-type semiconductors.

Additional n or p-type character may be added to the conduction properties by the addition of small amounts of impurities such as boron to generate holes in Si and Ge, and phosphorus to generate free electrons.

Table 5.2 *Electrical properties of elemental and compound semiconductors*

Semiconductor	Band gap (eV)	m_e/m_0	μ_e	m_h/m_0	μ_h
Silicon	1.10	1.1	1600	0.56	400
Germanium	0.70	0.55	3800	0.30	1800
GaP	2.4	0.35	300	0.50	150
GaAs	1.53	0.07	8800	0.50	400
GaSb	0.80	0.05	4000	0.23	1400
InP	1.34	0.067	4600	0.40	150
InAs	0.45	0.022	33 000	0.41	460
InSb	0.25	0.014	78 000	0.18	750

Notes:

1. The data for mobilities (at room temperature) are in units of $\mathrm{cm^2\ v^{-1}s^{-1}}$.
2. These data should be compared with the typical value for a metal where

   $\mu_e \cong 50\,\mathrm{cm^2\ v^{-1}\ s^{-1}}$.

3. A temperature coefficient for these data may be obtained from the equation for lattice scattering

   $\mu = \mu_0(m_e)^{-5/2}T^{-3/2}$

   for electrons and similarly for positive holes.

When dilute solutions of these elements are made, the electrons or holes which are generated give rise to *extrinsic* semiconduction at low temperatures with an activation energy contribution to the conductivity. The holes or electrons are trapped around the impurity atoms at low temperatures, behaving like the electron around the nucleus in a hydrogen atom. Because of the high dielectric constant of the semiconductors, about 14, which appears in the denominator of the Bohr equation for the hydrogen atom as the square, this ionization energy is reduced from the value of 13.54 eV for the hydrogen atom to the values shown in Table 5.3. As the temperature increases, all extrinsic current carriers are freed from their trapping Groups III or V atoms increasing the conductivity which then decreases with increasing temperature due to increased scattering by the thermally vibrating atomic structure. The situation thus resembles the scattering of electrons by ion cores in metals. At higher temperatures still, the intrinsic conduction due to thermal excitation of electrons from the valence band becomes predominant.

It is because these extrinsic electrons can so readily be activated thermally to the conduction band, that great care must be taken in producing the elementary semiconductors to a high state of purity, by such processes as *zone refining*.

Generally speaking the mobilities of electrons and positive holes decrease and the band gaps increase as the bonding in the semiconductors becomes more

Table 5.3 *Donor and acceptor ionization energies in silicon and germanium*

Impurity	Type	Si (eV)	Ge (eV)
P	n	0.045	0.120
As	n	0.05	0.013
Sb	n	0.04	0.010
B	p	0.045	0.010
Al	p	0.06	0.010
Ga	p	0.07	0.011
In	p	0.16	0.011

ionic, or as the electronegativity difference between the elements becomes larger. The band gaps for GaP and GaSb are 2.4 and 0.8 eV respectively, those of InP and InSb are 1.34 and 0.25 eV respectively, while that of ZnS is 3.7 eV and of ZnSe, 2.6 eV.

In the (Cd, Zn) (S, Se, Te) family of compounds the principal crystal structure is sphalerite, a face-centred cubic structure of the metal atoms with the Group VI elements along the cube diagonals in four coordination with the metal atoms. The exceptions are CdS and CdSe which have the related wurtzite (h.c.p) structure. The lattice parameters of the sphalerite phases range between 0.54 nm for ZnS to 0.64 nm for InSb. There are therefore a number of solid solutions which can be formed between these compounds, where the lattice parameters differ by less than about 15%, such as GaAs–InAs. A practical example is the solid solution between CdTe (band gap = 1.44 eV, $a = 0.6488$ nm) and HgTe (band gap = 0.15 eV, $a = 0.6459$ nm). This solution has a variable band gap as a function of the Cd/Hg ratio, and a wide range of miscibility. Another example is the solid solution between InP ($a = 0.5969$ nm) and GaAs ($a = 0.5654$ nm) in which the band gap varies directly as the mole fraction of each component. These solutions are best prepared by vapour phase deposition under ultra-high vacuum conditions, using separate Knudsen cells for each element because of the widely differing vapour pressures of the constituent elements.

DropBooks

Metal oxides

It is to be expected that the conduction data for ceramic oxides would follow the same trends as those found in semiconductors, i.e. the more ionic the metal–oxygen bond, the more the oxides behave like *insulators* or *solid electrolytes* having a large band gap between the valence electrons and holes, and

the conduction electrons. Table 5.4 shows data for the much larger band gaps of some important oxides, indicating the concentrations of thermally excited electrons to be calculated from the equation given above, and values for the electron mobilities.

Table 5.4 *Intrinsic semiconducting properties of ceramic oxides*

Oxide	E (eV)	$E_g/2k$	Electrons (cm^{-3})		
			1000 K	1500 K	2000 K
MgO	8.0	$46\,400^T$	1.07	1.03×10^7	3.61×10^{10}
NiO	4.2	$23\,380^T$	3.92×10^9	2.44×10^{13}	2.18×10^{15}
Al_2O_3	7.4	$42\,960^T$	33.42	1.02×10^8	2.01×10^{11}
Fe_2O_3	3.1	$18\,000^T$	2.31×10^{12}	1.71×10^{15}	5.3×10^{16}
SiO_2	8.0	$46\,400^T$	1.071	1.03×10^7	3.61×10^{10}
UO_2	5.2	$30\,200^T$	1.16×10^7	5.03×10^{11}	1.19×10^{14}

For free electrons in the conduction band

$$C = 4.83 \times 10^{15} T^{3/2} \exp(-E_g/2kT)$$

and for electrons of effective mass m_e and holes of effective mass m_h in the valence band

$$C_e = C_h = 2\left(\frac{2\pi k}{h^2}\right)^{3/2} (m_e m_h)^{3/4} T^{3/2} \exp\left(-\frac{E_g}{2kT}\right)$$

The insulating materials such as CaO, MgO, Al_2O_3 and SiO_2 which have the largest band gaps, are also *refractories*, i.e. they have a high melting point, and find important application in industry as container materials for high-temperature metallurgical reactors. The *solid electrolyte* materials are also oxides with a very low intrinsic conductivity, and include many of the rare earth oxides and ZrO_2 and ThO_2. These materials are finding important potential applications in solid electrolyte *fuel cells*.

Another important group of oxide materials with a very low electrical conductivity is the *oxide dielectrics*. A number of these are based upon the perovskites, MXO_3 or $MO{\cdot}XO_2$. The archetype of these materials is $BaTiO_3$, which has a high dielectric constant, or relative permittivity to vacuum, the value at room temperature being 1600, and commercial use is made of the isostructural $PbTiO_3$ and $ZrTiO_3$ which form solid solutions, the PZT dielectrics. These materials lose their dielectric properties as the temperature

is increased due to the increased vibration of the ion cores in the crystal structure.

Apart from these intrinsic properties, extrinsic effects can be produced in many oxides by variation of the metal/oxygen ratio through control of the atmospheric oxygen potential. The p-type contribution is increased as the oxygen pressure increases, and the n-type contribution as the oxygen pressure decreases. The pressure dependence of these contributions can usually be described by a simple power dependence thus

$$\sigma_p = k p^{1/n}; \quad \sigma_n = k' p^{-1/m}$$

where n and m are integers between 2 and 6.

In oxides where a large concentration of oxygen vacancies is generated by the addition of *aliovalent ions*, such as when CaO or Y_2O_3 are dissolved in ZrO_2 or CeO_2, there is a wide range of oxygen pressures over which the conductivity is independent of oxygen pressure. This behaviour indicates that the major transport process is the diffusion of oxygen ions in the solid which is now described as a solid electrolyte. Recent studies suggest that the enhancement of the anion mobility by the addition of an aliovalent ion is largest when the ionic radius of the added ion is approximately equal to that of the host cation.

The relative contributions of ions, electrons and positive holes to the conductivity is described through the *transport number* which is related to a partial conductivity defined by

$$t_i = \frac{\sigma_i}{\sum_i \sigma_i}$$

DropBooks

and takes values between zero and unity. In the general oxide showing n- and p-type semiconduction as well as an electrolytic range, Schmalzried (1963) has shown that the ionic transport number is usefully defined by the equation

$$t_i = \left[1 + \left(\frac{p_{O_2}}{pO_2^+}\right)^{1/n} + \left(\frac{p_{O_2}}{pO_2^-}\right)^{-1/m}\right]^{-1}$$

where pO_2^+ and pO_2^- are the oxygen pressures at which the p-type and n-type semiconduction contributions are equal to the ionic contribution (Figure 5.3).

The oxide solid electrolytes have electrical conductivities ranging from $10^{-1}\,\Omega^{-1}\,cm^{-1}$ to $10^{-6}\,\Omega^{-1}\,cm^{-1}$ at 1000°C and these can be converted into diffusion coefficient data, D, for the oxygen ions by the use of the Nernst–Einstein relation

$$\frac{\sigma}{D} = \frac{C_i Z^2 e^2}{kT}$$

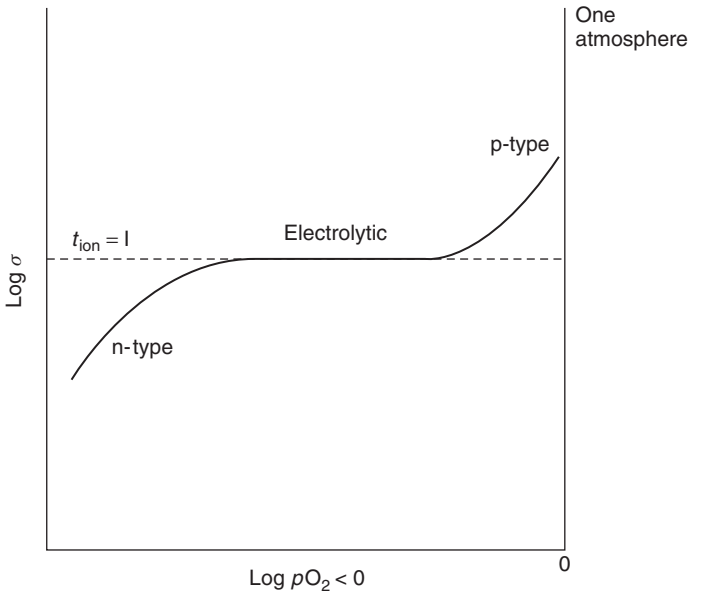


Figure 5.3 *The dependence of the conductivity of typical solid electrolytes on the oxygen pressure, showing the limits of electrolytic behaviour where* t_{ion} *is very close to unity*

where C_i is the number of anions/unit volume of charge Ze. A typical range of diffusion coefficients for oxygen in solid electrolytes is therefore 10^{-6} to $10^{-10}\,cm^2\,s^{-1}$ at 1000°C. The relative scarcity of solid electrolyte systems is explained by a comparison of the semiconducting contribution as a function of band gap for oxides with this electrolytic contribution. Figure 5.4 shows the contribution to electrical conductivity due to electrons thermally excited across band gaps of energy 0–500 kJ (0–5 eV) having the free electron mass, compared with an ionic contribution at various values of the diffusion coefficient, D. It is clear from this diagram that when D has the average value of $10^{-8}\,cm^2\,s^{-1}$, the band gap should be of the order of 5 eV or greater to yield electrolytic behaviour.

At the other end of the conduction spectrum, many oxides have conductivities dominated by electron and positive hole contributions to the extent that some, such as ReO_3, SnO_2 and the perovskite $LaCrO_3$ have conductivities at the level of metallic conduction. High levels of p-type semiconduction are found in some transition metal perovskites especially those containing aliovalent ions. Thus the lanthanum-based perovskites containing transition metal ions, e.g. $LaMO_3$ (M–Cr, Mn, Fe, Co, Ni) have enhanced p-type semiconduction due to the dependence of the transition metal ion valencies on the ambient

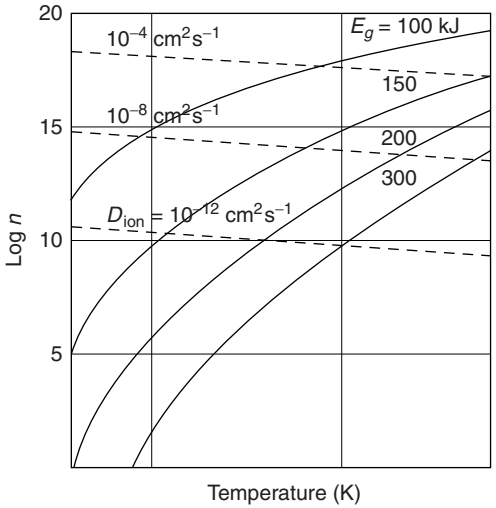


Figure 5.4 *The intrinsic conduction electron concentration as a function of temperature and band gap energy together with the values of the ionic diffusion coefficient which would provide an equal contribution to the conduction*

DropBooks

oxygen pressure, and enhanced oxygen ion mobility when some of the La^{3+} ions are replaced by Sr^{2+}. This leads to the formation of *oxygen vacancies*, and thus to the enhanced oxygen diffusion coefficient as well. Because of the oxygen vacancies, the stoichiometry is a function of oxygen pressure in for example $La_{1-x}Sr_xCrO_{3-y}$ due to the reaction

$$2Cr^{3+} + 1/2O_2 \longrightarrow 2Cr^{4+} + O^{2-}$$

in which the increase in valency of the transition metal ion is accompanied by the introduction of oxygen ions into the vacant oxide sites. This enhances the electrical conductivity in an approximately linear fashion, each Cr^{4+} ion contributing equally to the p-type semiconductivity. Such materials are promising oxygen atomic *membranes* by virtue of the parallel migration of oxide ions and the accompanying positive holes according to the scheme:

$$O_v + 2\oplus + 1/2O_2(p') \Big| \longleftarrow \begin{matrix} O^{2-} \\ 2\oplus \end{matrix} \Big| O_v + 2\oplus + 1/2O^2(p'')$$

where $p'' > p'$, and both the oxygen vacancies and positive holes are provided by the membrane oxide.

The kinetics of this transport, virtually of oxygen atoms through the solid, is determined by the diffusion coefficient of the less mobile oxide ions, and local

Table 5.5 *Measured and estimated mobilities in oxides*

Oxide	Electrons μ_n ($cm^2\ v^{-1}\ s^{-1}$)	Positive holes μ_p ($cm^2\ v^{-1}\ s^{-1}$)
UO_2	–	7×10^{-2}(1000)
CeO_{2-x}	8×10^{-3}(1000)	–
Al_2O_3	3 (room temp.)	–
ReO_3	33 (room temp.)	–
Ta_2O_5	5×10^{-2}(1100)	–
MgO	13 (1400)	4.0(1400)
FeO	–	1.0(1000)
CoO	1	0.3(1000)
NiO	–	9.33(1000)
TiO_2	0.2(1000)	–
$La_{1-x}Sr_xCrO_3$	–	4.6×10^{-3}(1000)

The values in parenthesis are the temperatures of measurement in degrees Centigrade.

electroneutrality is maintained throughout the membrane by the, balanced, parallel transport of ions and positive holes (Table 5.5).

Thermal transport in condensed phases

In addition to the transport of atoms, ions and electrons in condensed phases, the mechanisms of reactions involve the creation or loss of energy by chemical change, and the transport of this thermal energy through the reactants and products. The local temperature change which can be brought about by chemical reaction can be estimated by using the heat capacities of reactants and products by the *adiabatic* approximation. In this approximation, the temperature change brought about by reaction can be calculated by an adaptation of Hess's law if the heats of formation of the products and the heat capacities of the product species are known. Thus a heat change generated by a reaction at temperature T_R will yield products at a temperature T_F according to the equation

$$\Delta H_R = \Sigma C_p \text{ (products) } (T_F - T_R)$$

For the reaction

$$A + B \longrightarrow C + D$$

the sum of heat capacities of the products will relate to the amounts of those products which are formed when ΔH_R is generated. Thus ΔH_R per mole will

relate to one mole of C and D. This approximation assumes that the heat generated by the chemical reaction is retained without loss at the reaction site, hence the use of the term 'adiabatic'. However, in the real case, the heat which would be generated at a reaction interface, for example, would be conducted away by the reaction products according to their respective thermal conductivities. Both the heat capacities and the thermal conductivities have specific values for each chemical species at a given temperature, and we will now consider the approximate values of these quantities in terms of atomic structure and components.

Heat capacities

The heat capacity, the heat required to raise 1 g-mole through one kelvin, can be calculated at temperatures generally above 300 K by two simple empirical rules. The first of these, Dulong and Petit's rule, was discovered in the course of calorimetric studies of the heat capacities of the elements and shows that the heat capacity has a value,

$$C_V \cong 25.1\,\mathrm{J\,K^{-1}\,mol^{-1}}$$

This rule conforms with the principle of equipartition of energy, first enunciated by Maxwell, that the heat capacity of an elementary solid, which reflected the vibrational energy of a three-dimensional solid, should be equal to $3R\,\mathrm{J\,K^{-1}\,mol^{-1}}$. The 'anomaly' that the free electron theory of metals described a metal as having a three-dimensional structure of ion-cores with a three-dimensional 'gas' of free electrons required that the electron gas should add another $(3/2)R$ to the heat capacity if the electrons behaved like a normal gas as described in Maxwell's kinetic theory, whereas the quantum theory of free electrons shows that these quantum particles do not contribute to the heat capacity to the classical extent, and only add a very small component to the heat capacity.

DropBooks

The 'law' of Dulong and Petit was extended to molecular substances by Neumann and Kopp, who suggested that the heat capacity of a compound containing n atoms per molecule would be given by

$$C_V = 3nR$$

because there would be n gram-atoms of vibrating species per mole of compound.

These heat capacity approximations take no account of the quantal nature of atomic vibrations as discussed by Einstein and Debye. The Debye equation proposed a relationship for the heat capacity, the temperature dependence of which is related to a characteristic temperature, θ_D, by a universal expression by making a simplified approximation to the vibrational spectrum of the

atoms (ions) in a solid. The Debye temperature θ_D is normally located around or below room temperature but for low molecular weight substances such as beryllium, this temperature is above room temperature (see Table 5.6).

Table 5.6 *The Debye temperatures of some elements*

Element	Debye temperature	Element	Debye temperature
Lithium	400 K	Zinc	234 K
Sodium	150 K	Cadmium	120 K
Potassium	100 K	Boron	1250 K
Copper	315 K	Aluminium	394 K
Silver	215 K	Iron	420 K
Beryllium	1000 K	Nickel	375 K
Magnesium	318 K	Platinum	230 K

From a survey of experimental data for a large number of compounds, Kelley concluded that the heat capacity at constant pressure above room temperature could usefully be represented by an empirical equation using only the temperature as variable:

$$C_p = \alpha + \beta T + \frac{\gamma}{T^2} + \delta T^2$$

This equation in no way resembles the Debye equation

$$C_V = 3R\left(\frac{T}{\theta_D}\right)^3 \int_0^{\frac{\theta_D}{T}} \frac{e^x x^4 \, dx}{(e^x - 1)^2}$$

where $x = h\nu/kT$ and ν takes a range of values from 0 to ν_m, the maximum frequency of the vibration spectrum in the solid. However, the Debye temperature is not known for the majority of solids for which Kelley's temperature dependence can be used. An approximate equation, due originally to Lindemann, which brings out the dependence of the atomic vibration frequency on the mass of the vibrating species can be written as

$$\theta_D = \frac{A}{V_m^{3/2}}\left(\frac{T_m}{M}\right)^{1/2}$$

where A is a universal constant, V_m is the molecular volume, T_m is the melting point, and M is the atomic mass of the vibrating species. This equation is consistent with the fact that both beryllium and BeO have high Debye θ values.

Gruneisen showed that a number of properties of monatomic solids could be correlated if the pairwise interaction between atoms was of the form

$$\varepsilon(r) = -\frac{a}{r^m} + \frac{b}{r^n} \qquad n > m$$

where m and n are parameters in the so-called 'Mie equation', which includes the Lennard–Jones potential equation for the interaction of atoms in the gaseous phase. For the relationship involving the value of θ_D, Gruneisen gave the equation

$$\frac{n+2}{6} = -\frac{1}{\theta_D}\frac{d\theta_D}{dV_m}$$

It may be assumed that the differential $d\theta/dV_m$ can be obtained from data for similar materials.

Thermal conductivity

The vibrational spectra of solids which were referred to above can be described as containing *quanta* of vibrational energy. These quanta are referred to as *phonons* by analogy with the term *photons* for quanta of light energy. When a solid is placed in a temperature gradient the hot and cold regions are characterized by different phonon energies and concentrations. Phonons will therefore be transmitted from the higher energy density (the hot region) to the lower energy density (the cold region). Phonons can be regarded as being transmitted with the speed of sound through the solid and with a mean free path which decreases as the temperature increases. The total number of phonons is not conserved in transporting thermal energy across a solid but can be regarded as being created in the hot region, and destroyed in the cold region.

DropBooks

By analogy with the thermal conduction equation for a gas, given by the kinetic theory of gases, we can write for the thermal conductivity, K, of a solid

$$K = (1/3)C_P V\lambda$$

where V is the velocity of sound in the solid and λ is the phonon mean free path. This latter quantity will generally decrease as the temperature increases, but the actual value for a given substance depends, among other things, on the state of crystallinity of the sample. A single crystal has a longer mean free path for phonons than a corresponding polycrystalline sample because of phonon scattering at grain boundaries or voids.

When a substance is transparent to visible light, such as single crystals of simple inorganic solids which do not contain transition metal ions, or some glasses, another significant component in the thermal conductivity is the transmission of photons in the infra-red region, which becomes more important with

increasing temperature. Some solids therefore show a minimum in the thermal conductivity due to a decreasing phonon contribution to energy transfer with increasing temperature but an increasing contribution due to photon transmission as the temperature increases.

Substances containing a significant porosity also show an increasing photon transfer of energy as the temperature increases due to the superior transmissivity of infra-red photons through the pores over the surrounding solid.

As described above, quantum restrictions limit the contribution of the free electrons in metals to the heat capacity to a very small effect. These same electrons dominate the thermal conduction of metals acting as efficient energy transfer media in metallic materials. The contribution of free electrons to thermal transport is very closely related to their role in the transport of electric current through a metal, and this major effect is described through the Wiedemann–Franz ratio which, in the Lorenz modification, states that

$$\frac{\kappa}{\sigma T} = \text{a constant} \cong 2.2 \times 10^{-8}\,\text{W S deg}^{-2}$$

where K is the thermal conductivity in units of watts per metre per degree Kelvin, and the conductivity σ is in $\text{ohm}^{-1}\,\text{m}^{-1}$ or Siemens (S).

Thus for silver these values at room temperature are

$$\kappa = 428\,\text{W m}^{-1}\,\text{K}^{-1} \quad \sigma = 0.62 \times 10^{8}\,\text{S}$$

and for aluminium

$$236\,\text{W m}^{-1}\,\text{K}^{-1} \text{ and } 0.36 \times 10^{8}\,\text{S}$$

Some comparative values of thermal conductivity for a number of important materials in the solid state are shown in Table 5.7.

The formation of solid solutions in both metallic and non-metallic systems leads to a decrease in thermal conductivity below the composition-weighted average of the two pure components. This applies whether the principal conduction process is by electron or ionic transmission of phonons. It follows that solids showing a wide-range on non-stoichiometry such as UO_{2+x} ($x = 0$–0.25) have a decreasing thermal conductivity as the departure from stoichiometry, and hence the point defect content, increases. In the case of UO_2 which has an exceptionally wide range of non-stoichiometry, the thermal conductivity decreases by at least a factor of two, according to present data over this range of non-stoichiometry.

Finally, it can be shown from the quantum theory of vibrational energy in the solid state that, at temperatures above the Debye temperature θ_D, the density of phonons, n_p, is inversely related to θ_D according to the equation

$$n_p = q^N \left(\frac{T}{\theta_D}\right) \text{ per mole}$$

Table 5.7 *Thermal conductivities of metals and oxides ($W\,m^{-1}\,K^{-1}$)*

Metal	298 K	1273 K	Liquid
Beryllium	218	70	
Copper	401	340	
Iron	83	30	
Molybdenum	139	103	
Platinum	72	84	
Aluminium	236	–	105
Cadmium	104	–	45
Gallium	41	–	35
Lead	35.5	–	20
Sodium	135	–	80
Silver	428	–	180
Tin	70	–	35
Zinc	122	–	55
Oxide	298 K	1273 K	
Beryllium oxide	242	17	
Alumina	68	6	
Magnesia	52	4	
Fused silica	<1	5	
Ceria	11.0	1	
Urania	8.5	3	

DropBooks

where N is Avogadro's number. It follows that the lowest phonon concentrations are expected to be found in light metals and oxides, such as BeO, containing low atomic weight cations where θ_D has the highest value. But according to the kinetic theory of gases, which can be used to describe thermal conduction in solids by analogy, the mean free path for phonon transmission is inversely proportional to the density of particles in the gaseous state, or the density of phonons in the solid state. Hence theory would indicate, as is found in practice, that BeO would have a higher thermal conductivity than all other oxide ceramics, and that the thermal conductivity would decrease with increasing cation atomic weight.

Metals, on the other hand being predominantly conduction electron dominated phonon transport, would not show the same relationship, but would mainly reflect the electrical conductivity.

Bibliography

M.C. Lovell, A.J. Avery and M.W. Vernon. *Physical Properties of Materials*, Chapter 7. Van Nostrand (1976).
J. Hafner. *From Hamiltonians to Phase Diagrams.* Springer-Verlag, Berlin (1987).
J. Verhoven. *Met. Rev.*, **8**, 311 (1963).
S.G. Epstein. *Adv. Phys.*, **16**, 325 (1967).
S.G. Epstein and A. Paskin. *Phys. Lett.*, **24A**, 309 (1967).
H. Schmalzried. *Z. Phys. Chem.*, **38**, 87 (1963).

Chapter 6

Rate processes in metals and alloys

Structure and diffusion-controlled processes in metallic systems

The structures of metals

The crystal structures of most metals are simple and have a high degree of symmetry. In the *hexagonal* close-packed structure each atom is surrounded by six other atoms in the same plane, and the planes are stacked in A–B–A–B repeat pattern there being a translation between neighbouring planes which provides the closest packing between planes (Figure 6.1). In the *face-centred* cubic close-packed structure the corresponding planes are stacked in an A–B–C–A–B–C repeat pattern. In the *body-centred* cubic structure, which is a more open structure than in the close-packed structures, each atom is surrounded by eight atoms at the corners of a cube, and the next-nearest neighbours are six atoms at a distance from the central atom equal to the surrounding cube edges.

DropBooks

These three structures are the predominant structures of metals, the exceptions being found mainly in such heavy metals as plutonium. Table 6.1 shows the structure in a sequence of the Periodic Groups, and gives a value of the distance of closest approach of two atoms in the metal. This latter may be viewed as representing the atomic size if the atoms are treated as hard spheres. Alternatively it may be treated as an inter-nuclear distance which is determined by the electronic structure of the metal atoms. In the free-electron model of metals, the structure is described as an ordered array of metallic ions immersed in a continuum of free or unbound electrons. A comparison of the ionic radius with the inter-nuclear distance shows that some metals, such as the alkali metals are ‘empty’ i.e. the ions are small compared with the hard sphere model, while some such as copper are ‘full’ with the ionic radius being close to the inter-nuclear distance in the metal. A consideration of ionic radii will be made later in the ionic structures of oxides.

Volume diffusion in pure metals

The *self-diffusion* coefficients of metals, which describe the movement of atoms within a pure metal, vary over a very wide range of values at any

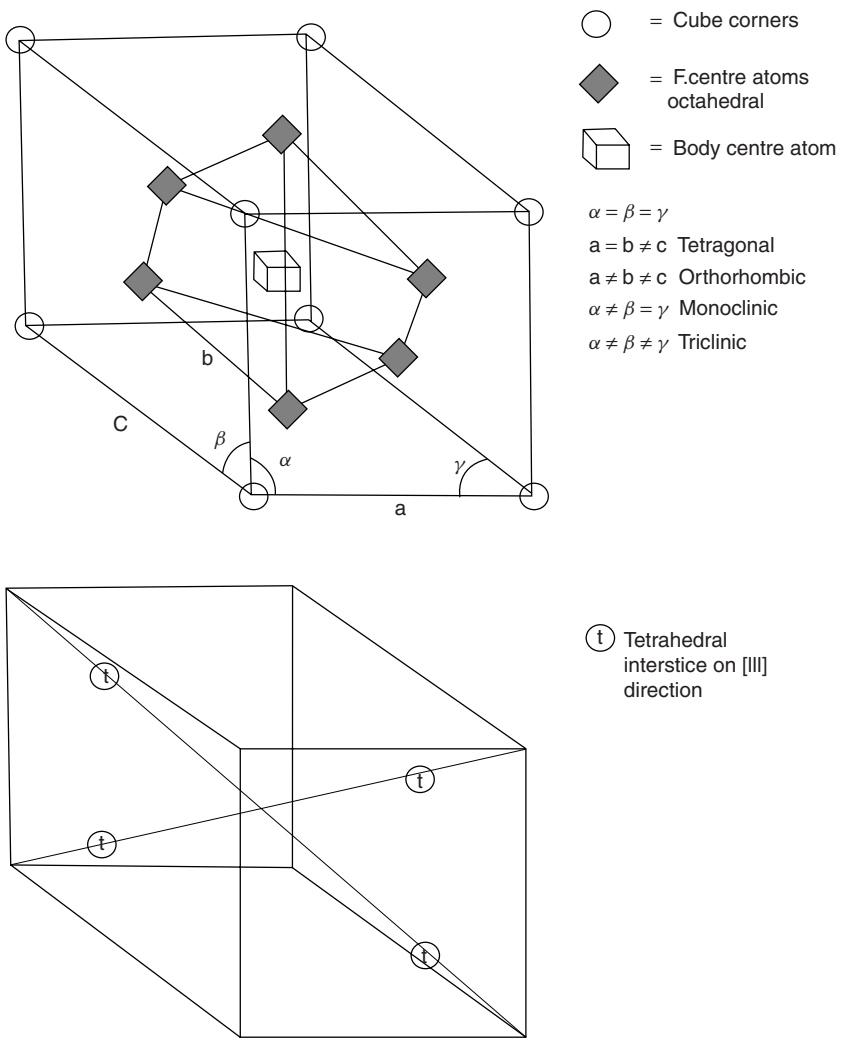


Figure 6.1 *The placement of ions in the face-centred or body-centred structures, and the location of interstitial particles on the [111] cell diagonal directions*

given temperature, but the value for most metals approaches $10^{-8}\,\mathrm{cm^2\,s^{-1}}$ near the melting point. The coefficient for any given metal shows the Arrhenius temperature dependence and may be written as a function of temperature according to the equation

$$D = D_0 \exp(-\Delta H^*/RT)$$

Table 6.1 *Structures of the common metals at room temperature (diameters in angstroms)*

Metal	Structure	Metallic diameter
Lithium	b.c.c	3.039
Sodium	b.c.c	3.715
Potassium	b.c.c	4.627
Copper	f.c.c	2.556
Silver	f.c.c	2.888
Gold	f.c.c	2.884
Magnesium	c.p.h	3.196
Calcium	f.c.c	3.947
Zinc	c.p.h	2.664
Cadmium	c.p.h	2.979
Aluminum	f.c.c	2.862
Lead	f.c.c	3.499
Titanium	c.p.h	2.89
Zirconium	c.p.h	3.17
Vanadium	b.c.c	2.632
Tantalum	b.c.c	2.860
Molybdenum	b.c.c	2.725
Tungsten	b.c.c	2.739
Iron	b.c.c	2.481
Cobalt	c.p.h	2.506
Nickel	f.c.c	2.491
Rhodium	f.c.c	2.689
Platinum	f.c.c	2.775
Uranium	orthorhombic	2.77
Plutonium	monoclinic	3.026
Rare earths		
Scandium	h.c.p	1.641
Yttrium	h.c.p	1.803
Lanthanum	h.c.p	1.877

DropBooks

where D_0 is a constant for each element, and ΔH^* is called, by analogy with the Arrhenius equation for gas reaction kinetics, the 'activation energy'. Since the quantity which is involved relates to a condensed phase under constant pressure in this instance, it is more correct to call this term an 'activation enthalpy'. The pre-exponential term has a fairly constant range of values for most metals of approximately 0.1 to 1, and the activation energies follow the

same trend as the heats of vaporization. The latter observation gives a hint as to the nature of the most important mechanism of diffusion in metals, which is vacancy migration. It is now believed that the process of self-diffusion in metals mainly occurs by the exchange of sites between atoms and neighbouring vacancies in the lattice. The number of such vacancies at a given temperature will clearly be determined by the free energy of vacancy formation. The activation enthalpy for self-diffusion ΔH_{diff} is therefore the sum of the energy to form a vacancy ΔH_{vac} and the energy to move the vacancy.

It has been found that the heat of formation of vacancies is approximately half the total enthalpy of activation for diffusion, for the lower values of activation energy, rising to two-thirds at higher energies (see Table 6.2) and hence it may be concluded that it is roughly equal to the enthalpy of vacancy movement. This contribution can be obtained by measurements of the electrical resistance of wire samples which are heated to a high temperature and then quenched to room temperature. At the high temperature, the equilibrium concentration of vacancies at that temperature is established and this concentration can be retained on quenching to room temperature (Figure 6.2).

Table 6.2 *Data for diffusion coefficients in pure metals*

Element	Crystal structure	D_0 ($\text{cm}^2\,\text{s}^{-1}$)	ΔH_{vac}	ΔH_{diff}	$\Delta H_{\text{sub}}^{298}$
Cu	f.c.c.	0–16	124	200	337
Ag	f.c.c.	0.04	108	170	285
Mg	Hex	1.0	–	134	147
Al	f.c.c.	0.05	65.5	123	330
Pb	f.c.c.	1.37	54.8	109	195
γFe	f.c.c.	0.49	135	284	416
Zr	Hex	0.06	–	210	601
V	b.c.c.	0.02	424	283	514
Ta	b.c.c.	0.02	269	392	781
Mo	b.c.c.	0.10	289	386	658
W	b.c.c.	1.80	385	586	851
αFe	b.c.c.	2.0	154	239	(415)

The total electrical resistance at room temperature includes the contribution from scattering of conduction electrons by the vacancies as well as by ion-core and impurity scattering. If the experiment is repeated at a number of high temperature anneals, then the effects of temperature on the vacancy contribution can be isolated, since the other two terms will be constant providing that

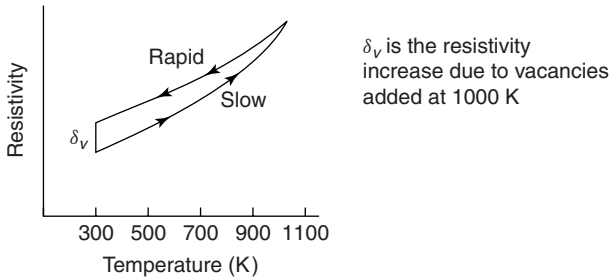


Figure 6.2 *The increase in electrical conductivity when a metal sample is heated to a high temperature and then quenched to room temperature, arising from the introduction of vacant sites at high temperature*

the temperature at which the resistance is measured is always the same. The energy to form vacancies is then found from the temperature coefficient of this contribution

$$R_{\text{vacancy}} = R_0 \exp -\frac{\Delta H_{\text{vac}}}{RT}$$

where R_0 is a constant of the system.

Typical values of the energy to form vacancies are for silver, 108 kJ mol^{-1} and for aluminium, 65.5 kJ mol^{-1}. These values should be compared with the values for the activation enthalpy for diffusion which are given in Table 6.2. It can also be seen from the Table 6.2 that the activation enthalpy for self-diffusion which is related to the energy to break metal–metal bonds and form a vacant site is related semi-quantitatively to the energy of sublimation of the metal, in which process all of the metal atom bonds are broken.

DropBooks

At high temperatures there is experimental evidence that the Arrhenius plot for some metals is curved, indicating an increased rate of diffusion over that obtained by linear extrapolation of the lower temperature data. This effect is interpreted to indicate enhanced diffusion via *divacancies*, rather than single vacancy–atom exchange. The diffusion coefficient must now be represented by an Arrhenius equation in the form

$$D = D_0(1) \exp\left(\frac{-\Delta H_1}{RT}\right) + D_0(2) \exp\left(\frac{-\Delta H_2}{RT}\right)$$

Examples of this analysis are given in the data as follows:

$$\text{Gold (f.c.c.)} \quad D = 0.04 \exp -\frac{20\,500^T}{T} + 0.56 \exp -\frac{27\,500^T}{T}$$

$$\text{Vanadium (b.c.c.)} \quad D = 0.014 \exp \frac{-34\,060^T}{T} + 7.5 \exp \frac{-43\,200^T}{T}$$

It can be seen that the divacancy diffusion process leads to a larger value of D_0, but only a fractional increase in ΔH_{diff}.

The measurements of self-diffusion coefficients in metals are usually carried out by the sectioning technique. A thin layer of a radioactive isotope of the metal is deposited on one face of a right cylindrical sample and the diffusion anneal is carried out at a constant temperature for a fixed time. After quenching, the rod is cut into a number of thin sections at right angles to the axis, starting at the end on which the isotope was deposited, and the content of the radioisotope in each section is determined by counting techniques. The diffusion process in which a thin layer of radioactive material is deposited on the surface of a sample and then the distribution of the radioactive species through the metal sample is analysed after diffusion, obeys Fick's second law

$$D\frac{\partial^2 c}{\partial x^2} = \frac{\partial c}{\partial t}$$

with the following boundary conditions:

$$c = c_0, \quad x = 0, \quad t = 0; \quad c = 0, \quad x > 0, \quad t = 0$$

D can be regarded as a constant of the system in this experiment since there is no change of chemical composition involved in the exchange of radioactive and stable isotopes between the sample and the deposited layer. The solution of this equation with these boundary conditions is

$$c = \frac{c_0}{\sqrt{\pi Dt}} \exp\left(-\frac{x^2}{4Dt}\right)$$

The procedure in use here involves the deposition of a radioactive isotope of the diffusing species on the surface of a rod or bar, the length of which is much longer than the length of the metal involved in the diffusion process, the so-called *semi-infinite* sample solution.

An alternative procedure which is sometimes used is to place a rod in which the concentration of the isotope is constant throughout c_0, against a bar initially containing none of the isotope. The diffusion profile then shows a concentration at the interface which remains at one-half that in the original isotope-containing rod during the whole experiment. This is called the *constant source* procedure because the concentration of the isotope remains constant at the face of the rod which was originally isotope-free. The solution for the diffusion profile is with the boundary condition $c = c_0/2$, $x = 0$, $t \geq 0$ is

$$c = \frac{c_0}{2}(1 - \text{erf}(x/2\sqrt{Dt}))$$

It follows that a plot of the logarithm of the concentration of the radioactive isotope in each section against the square of the mean distance of the section

below the original surface transfer ($x = 0$) should be linear with slope $-(1/4)Dt$. Since t, the duration of the experiment, is known, D may be calculated.

Diffusion in intermetallic compounds

Inter-metallic compounds have a crystal structure composed of two interpenetrating lattices. At low temperatures each atomic species in the compound of general formula A_mB_n occupies a specific lattice but at higher temperatures a second-order transition involving a disordering of the atoms to a random occupation of all atomic sites takes place. The mean temperature at which the order–disorder transformation takes place depends upon the magnitude of interaction energy of A–B pairs. This is exothermic, which brings about the low-temperature order, the more so the higher the transition temperature.

In the ordered state an atom cannot usually undergo a vacancy exchange with an immediately neighbouring site because this is only available to the other atomic species. Thus in the CuAu inter-metallic compound having the NaCl crystal structure, a copper atom can only exchange places with a site in the next nearest neighbour position. In disordered CuZn, nearest neighbour sites can be exchanged as in the self-diffusion of a pure metal.

It is quite probable that ordered metallic compounds have a partial ionic contribution to the bond between unlike atoms resulting from a difference in electronegativity of the two metals. Miedema's model of the exothermic heats of formation of binary alloys uses the work function of each metallic element in determining the ionic contribution to bonding in the solid state, instead of Pauling's electronegativity values for the gaseous atoms which are used in the bonding of heteronuclear diatomic molecules. However, in the solid metallic state the difference in valency electron concentration in each pair of unlike atoms, adds a repulsive (endothermic) term to the heat of formation, and thus reduces the resultant value. This repulsive component has been found to be proportional to the bulk modulus, B, where

$$B = s/(\Delta V/V)$$

which is the relative volume change in response to an applied stress, s.

Vacancies on each site will therefore carry a virtual charge due to the partial transfer of electrons between the neighbouring atoms, and vacancy interaction between the two lattices should therefore become significant at low temperatures, leading to divacancy formation at a higher concentration than is to be found in simple metals. These divacancy paths would enhance atomic diffusion in two jumps for an A atom passing through a B site to arrive at an A site at the end of the diffusive step. Above the order–disorder transformation the entropy contribution to the Gibbs energy of formation outweighs the exothermic heat of formation, and thus any atom–vacancy pair can lead to diffusion in the random alloy.

DropBooks

There is not sufficient experimental evidence to continue this discussion quantitatively at the present time, but the sparse experimental data suggests that for a given compound, the D_0 value is significantly lower than is the case in simple metals. This decrease may be attributed to a low value in the correlation factor which measures the probability that an atom may either move forward or return to its original site in its next diffusive jump. In simple metals this coefficient has a value around 0.8.

Diffusion in alloys

If samples of two metals with polished faces are placed in contact then it is clear that atomic transport must occur in both directions until finally an alloy can be formed which has a composition showing the relative numbers of gram-atoms in each section. It is very unlikely that the diffusion coefficients, of A in B and of B in A, will be equal. Therefore there will be formation of an increasingly substantial vacancy concentration in the metal in which diffusion occurs more rapidly. In fact, if chemically inert marker wires were placed at the original interface, they would be found to move progressively in the direction of slowest diffusion with a parabolic relationship between the displacement distance and time.

At any plane in a Raoultian alloy system parallel to the original interface, the so-called chemical diffusion coefficient D_{chem}, which determines the flux of atoms at any given point, and is usually a function of the local composition so that according to Darken (1948), D_{chem} is given by

$$D_{\text{chem}} = X_2 D_1 + X_1 D_2$$

$$D_{\text{chem}} = -\frac{J}{\left(\frac{\mathrm{d}c}{\mathrm{d}x}\right)}$$

where X_1, X_2 are the atom fractions of the components and D_1, D_2 are their self-diffusion coefficients, in this case of each element in alloys of this composition. This equation also shows that as $X_2 \to 0$, $D_{\text{chem}} \to D_2$, or that in a dilute alloy, the diffusion coefficient for the dilute constituent should approach that of its own self-diffusion coefficient in the dilute alloy. In an alloy showing departures from the ideal behaviour, this equation must be modified accordingly to

$$D_{\text{chem}} = (X_2 D_1 + X_1 D_2)(1 - d \ln \gamma / d \ln X_1)$$

An experimental technique for the determination of D_{chem} in a binary alloy system in which the diffusion coefficient is a function of composition was originally developed by Matano (1932), based on a mathematical development

of Fick's equations due to Boltzmann. The average diffusion length of particles in a time t can be calculated from Fick's 2nd law to be given by

$$(\overline{x})^2 = 2Dt$$

This suggests that $x/t^{1/2}$ could be a useful variable transformation. Then the flux accumulation rate can be expressed as

$$\frac{\partial c}{\partial t} = \frac{\mathrm{d}c}{\mathrm{d}z}\frac{\partial z}{\partial t} = -\frac{1}{2}\frac{x}{t^{3/2}}\frac{\mathrm{d}c}{\mathrm{d}z}$$

where $z = \dfrac{x}{t^{1/2}}$

and substituting into the general form of Fick's 2nd law

$$-\frac{x}{2t^{3/2}}\frac{\mathrm{d}c}{\mathrm{d}x} = \frac{\partial}{\partial x}\left(D\frac{\partial c}{\partial x}\right) = \frac{1}{t}\frac{\mathrm{d}}{\mathrm{d}z}\left(D\frac{\mathrm{d}c}{\mathrm{d}z}\right)$$

which is now a single variable differential equation.

Integrating the equation in the form

$$-\frac{z}{2}\frac{\mathrm{d}c}{\mathrm{d}z} = \frac{\mathrm{d}}{\mathrm{d}z}\left(D\frac{\mathrm{d}c}{\mathrm{d}z}\right)$$

using as boundary conditions

$c = c_0$ for $x < 0$ at $t = 0$

$c = 0$ for $x > 0$ at $t = 0$

DropBooks

the result is

$$-\frac{1}{2}\int_{c=0}^{c=c'} z\,\mathrm{d}c = \left[D\frac{\mathrm{d}c}{\mathrm{d}z}\right]_{c=0}^{c=c'}$$

and substituting for z from the original definition yields the equation

$$-\frac{1}{2}\int_{0}^{c'} x\,\mathrm{d}c = Dt\left(\frac{\mathrm{d}c}{\mathrm{d}x}\right)_{c=c'}$$

since $\mathrm{d}c/\mathrm{d}x = 0$ at $x = 0$, and t is the (known) duration of the experiment, which is fixed, and c is a function of x only.

This also requires that

$$\int_{c=0}^{c=c_0} x\,\mathrm{d}c = 0$$

and the point where $x = 0$ can be found by equating the area above the curve for c' as a function of x when $x < 0$ with that below the curve when $x > 0$.

The chemical diffusion coefficient at any concentration C' in the experimental diffusion profile is then given by

$$D_{\text{chem}}(c') = -\frac{1}{2t}\left(\frac{\mathrm{d}x}{\mathrm{d}c}\right)_{c'} \int_0^{c'} x\,\mathrm{d}c \text{ where } t \text{ is known}$$

This analysis makes possible the determination of a chemical diffusion coefficient from experimental data having made no use of a model, and which takes no account of the atomic mechanism of diffusion, and assumes that the same chemical diffusion coefficient applies to each component of the alloy.

If we now place chemically inert markers at the original interface between the two metal samples before the diffusion anneal, more information about the diffusion process can be obtained. Imagine that more atoms of type A move from left to right in the joined samples, J_A, than those of type B moving from right to left, J_B. Then if both diffusion processes are by atom–vacancy exchange, there must be a corresponding vacancy flow from left to right, J_v, equal to the difference between these two fluxes

$J_A \longrightarrow$

$J_B \longleftarrow$

$J_v \longleftarrow$ vacancies

A concentration gradient of vacancies will therefore appear across the original interface. The concentration of vacancies will be less than the equilibrium value on the B-rich side and more than the equilibrium value on the A-rich side. In a classical experiment to determine how this accumulation of vacancies would affect the position of the markers, Kirkendall and Smigelskas showed that when marker molybdenum wires were placed around a brass bar which was then electroplated with a thick layer of copper, the markers moved inward to the centre of the bar while zinc diffused out of the brass and into the copper. Clearly vacancy creation would originally take place on the brass side of the original marker position, and the wires have moved in the direction of the vacancy flux with a $t^{1/2}$ dependence on time. The excess vacancies are removed from the interface by diffusional exchange. Otherwise they may tend to aggregate to form pores on the side of the markers containing the more rapidly moving species, the brass side in this case.

Darken assumed that the accumulated vacancies were annihilated within the diffusion couple, and that during this process, the markers moved as described by Smigelskas and Kirkendall (1947). His analysis proceeds with the assumption that the sum of the two concentrations of the diffusing species $(c_1 + c_2)$ remained constant at any given section of the couple, and that the markers, which indicated the position of the true interface moved with a velocity v.

The statement of Fick's 2nd law then becomes

$$\frac{\partial c}{\partial t} = \frac{\partial c_1}{\partial t} + \frac{\partial c_2}{\partial t} = \frac{\partial}{\partial x}\left(D_1\frac{\partial c_1}{\partial x} + D_2\frac{\partial c_2}{\partial x} - cv\right) = 0 \qquad \text{(i)}$$

Integrating with $\partial c/\partial t = 0$

$$D_1\frac{\partial c_1}{\partial x} + D_2\frac{\partial c_2}{\partial x} - cv = \text{a constant} = 0$$

The constant of integration must be zero because at points on the diffusion couple far from the interface,

$$\frac{\partial c_1}{\partial x}, \frac{\partial c_2}{\partial x} \text{ and } v = 0$$

$$\text{thus } v = \frac{1}{c}\left(D_1\frac{\partial c_1}{\partial x} + D_2\frac{\partial c_2}{\partial x}\right)$$

substituting for v in (i)

$$\frac{\partial c_1}{\partial t} = \frac{\partial}{\partial x}\left(D_1\frac{\partial c_1}{\partial x} - \frac{c_1}{c}D_1\frac{\partial c_1}{\partial x} - \frac{c_1}{c}D_2\frac{\partial c_2}{\partial x}\right)$$

$$= \frac{\partial}{\partial x}\left(\frac{c_1D_2 + c_2D_1}{c}\frac{\partial c_1}{\partial x}\right) \text{ since } \frac{\partial c_1}{\partial x} = -\frac{\partial c_2}{\partial x}$$

$$J_1 = -D\frac{\partial c_1}{\partial x} + vc_1 \text{ and } \frac{\partial c_1}{\partial t} = -\frac{\partial J_1}{\partial x}$$

DropBooks

Since X_i is a mole fraction equal to c_1/c

$$D_{\text{chem}} = \frac{c_1D_2 + c_2D_1}{c} = X_1D_2 + X_2D_1$$

$$\text{and } v = (D_1 - D_2)\frac{\mathrm{d}X_1}{\mathrm{d}x}$$

Steady state creep in metals

Dislocations are known to be responsible for the short-term plastic (non-elastic) properties of substances, which represents departure from the elastic behaviour described by Hooke's law. Their concentration determines, in part, not only this immediate transport of planes of atoms through the solid at moderate temperatures, but also plays a decisive role in the behaviour of metals under long-term stress. In processes which occur slowly over a long period of time such as secondary creep, the dislocation distribution cannot be considered geometrically fixed within a solid because of the applied stress.

This movement of dislocations leads to the formation of networks of dislocations which mutually reduce their mobility, and this produces *work-hardening*, which is the increased resistance of metals to an applied stress. This effect is decreased in time through the diffusion of vacancies into the dislocation core leading to dislocation *climb*. The presence of stress-induced diffusion can therefore enhance dislocation climb through the increased atom–vacancy exchange. It is also observed that the process of creep involves some degree of movement of grains relative to one another by *grain boundary sliding*.

An account of the mechanism for creep in solids placed under a compressive hydrostatic stress which involves atom–vacancy diffusion only is considered in Nabarro and Herring's (1950) volume diffusion model. The counter-movement of atoms and vacancies tends to relieve the effects of applied pressure, causing extension normal to the applied stress, and shrinkage in the direction of the applied stress, as might be anticipated from Le Chatelier's principle. The opposite movement occurs in the case of a tensile stress. The analysis yields the relationship

$$-\frac{1}{L}\frac{\mathrm{d}L}{\mathrm{d}t} = \frac{AD_v s V_m}{RTL^2}$$

where L is the length of the grain of a material under a compressive stress, s, and having a molar volume V_m. A is a shape factor which has a value between 10 and 40. If this process occurs by grain boundary diffusion as well, Coble (1963) has shown that

$$-\frac{1}{L}\frac{\mathrm{d}L}{\mathrm{d}t} = \frac{AD_b \delta s V_m}{RTL^3}\left[1 + \frac{D_v L}{3D_b \delta}\right]$$

where D_b is the grain boundary diffusion coefficient and δ is the boundary width. Note that the dimensionless ratio $D_b\delta/D_vL$ determines whether boundary or volume diffusion predominates in the creep process.

Diffusion in interstitial solutions and compounds

Although the face-centred cubic structure of metals is close packed, it is still possible for atoms which are much smaller than the host metal atoms to fit into interstitial sites inside the structure, while maintaining the essential properties of metals such as electrical conductivity and heat transport. These interstitial sites are of two kinds. The *octahedral* interstitial sites have six metal atoms at equal distances from the site, and therefore at the apices of a regular octahedron. The *tetrahedral* interstitial sites have four nearest neighbour metal atoms at the apices of a regular tetrahedron. A smaller atom can just fit into the octahedral site if the radius ratio is

$$\left[0.732 \geq \frac{r \text{ interstitial}}{r \text{ metal}} = \geq 0.414\right]$$

and into a tetrahedral site if the radius ratio is

$$\left[0.414 \geq \frac{r \text{ interstitial}}{r \text{ metal}} = \geq 0.225\right]$$

In many of the transition metals, such as titanium, vanadium and molybdenum, carbon, nitrogen and oxygen atoms can fit into octahedral holes, and hydrogen into the tetrahedral holes. The 'fit' here is estimated by assuming the atoms all have incompressible radii, and the contact must be such that the interstitial atoms do not 'rattle around' in the holes.

In the face-centred cubic structure there are four atoms per unit cell, $8 \times 1/8$ cube corners and $6 \times 1/2$ face centres. There are also four octahedral holes, one body centre and $12 \times 1/4$ on each cube edge. When all of the holes are filled the overall composition is thus 1:1, metal to interstitial. In the same metal structure there are eight cube corners where tetrahedral sites occur at the 1/4, 1/4, 1/4 positions. When these are all filled there is a 1:2 metal to interstititial ratio. The transition metals can therefore form monocarbides, nitrides and oxides with the octahedrally coordinated interstitial atoms, and dihydrides with the tetrahedral coordination of the hydrogen atoms.

From thermodynamic measurements, it can be concluded that there is a small repulsive interaction between neighbouring interstitial particles, and many such compounds are stable over a range of compositions, showing considerable non-stoichiometry. Extensive ranges of solid solution are also formed where only a fraction of the vacant interstitial sites are filled, depending on the thermodynamic properties of the co-existing equilibrium vapour phase which controls the thermodynamic activity of the non-metal. In these dilute solid solutions interstitial atoms have a high probability of finding a vacant neighbouring site into which to diffuse. The activation energy of diffusion therefore does not include a term for the creation of a vacancy, and is therefore lower than in the case of the metallic diffusion step. The frequency factor D_0 can be calculated by assuming that one-sixth of the vibrations an interstitial atom makes are in the right direction for diffusion, and the total frequency of the vibrations is about $10^{13}\ s^{-1}$, a typical vibration frequency for atoms in solids. The calculated value for D_0 is then obtained from the equation

$$D_0 = (1/6) f d^2$$

where d is the distance between the interstitial atoms. Thus if we consider two planes of interstitial sites separated by one layer of metal atoms, then if the concentrations of interstitials are c_1, and c_2 atoms/unit volume the flux relationship becomes

$$\text{Flux} = \frac{1}{6} f (c_1 - c_2) d = -D \frac{(c_1 - c_2)}{d}$$

DropBooks

since $c\,d$ is the number of interstitial atoms in a plane of unit area in size, in a volume where the concentration is c per unit volume. If D in this equation is identified with D_0 in the Arrhenius expression, and d is of the order of 10^{-8} cm, the resulting value of D_0 is $10^{-3}\,\mathrm{cm^2\,s^{-1}}$ which is in fair agreement with experimental data (Table 6.3).

Table 6.3 *Diffusion data for interstitials in metals*

Solvent	Solute	D_0 ($\mathrm{cm^2\,s^{-1}}$)	ΔH_{diff} ($\mathrm{kJ\,mol^{-1}}$)
Iron	Carbon	0.004	80.0
	Nitrogen	0.005	77.0
	Oxygen	0.002	86.0
Vanadium	Carbon	0.009	116
	Nitrogen	0.040	148
	Oxygen	0.025	123
Molybdenum	Carbon	0.01	172
	Nitrogen	0.004	109
	Oxygen	0.03	130

According to the transition state theory, the diffusion process can be described by the equation

$$D = F(t) \exp \frac{\Delta S^*}{R} \exp\left(-\frac{\Delta H^*}{R}\right)$$

where $F(t)$ is a function of time. Since the interstitial diffusion coefficient pre-exponential term D_0 is well accounted for by the simple expression above, it may be concluded that the entropy of activation for diffusion by this process is quite small. Conversely in the case of volume diffusion, where D_0 is substantially larger, the entropy of activation must be correspondingly greater. The difference in D_0 for interstitial and volume diffusion suggests a value for the latter of

$$\exp \frac{\Delta S^*}{R} \cong 10; \quad \frac{\Delta S^*}{R} \simeq 2$$

In the transition-metal monocarbides, such as TiC_{1-x}, the metal-rich compound has a large fraction of vacant octahedral interstitial sites and the diffusion jump for carbon atoms is therefore similar to that for the dilute solution of carbon in the metal. The diffusion coefficient of carbon in the monocarbide shows a relatively constant activation energy but a decreasing value of the pre-exponential

D_0 as the stoichiometric composition is approached. The experimental results for TiC may be represented by the equation

$$D = 345(1 - x)\exp\left(-\frac{54\,000^T}{T}\right)\ \text{cm}^2\,\text{s}^{-1}$$

The value of the activation energy approaches $50\,000^T$ near the stoichiometric composition. This diffusion process therefore approximates to the self-diffusion of metals at stoichiometry where the vacancy concentration on the carbon sub-lattice is small.

Phase transformations in alloys

The decomposition of Austenite

The iron–carbon solid alloy which results from the solidification of iron blast-furnace metal is saturated with carbon at the metal–slag temperature of about 2000 K, which is subsequently refined by the oxidation of carbon to produce steel containing less than 1 wt% carbon, the level depending on the application. The first solid phases to separate from liquid steel at the eutectic temperature, 1408 K, are the (f.c.c) γ-phase *Austenite* together with cementite, Fe_3C, which has an orthorhombic structure, and not the thermodynamically stable carbon phase which is to be expected from the equilibrium diagram. Cementite is thermodynamically unstable with respect to decomposition to iron and carbon from room temperature up to 1130 K

$$\Delta G^\circ = 27\,860 - 24.64T \quad \text{J mol}^{-1}$$

The austenite phase which can contain up to 1.7 wt% of carbon decomposes on cooling to yield a much more dilute solution of carbon in α-iron (b.c.c), 'Ferrite', together with cementite, again rather than the stable carbon phase, at temperatures below a solid state eutectoid at 1013 K (Figure 6.3).

The higher solubility of carbon in γ-iron than in α-iron is because the face-centred lattice can accommodate carbon atoms in slightly expanded octahedral holes, but the body-centred lattice can only accommodate a much smaller carbon concentration in specially located, distorted tetrahedral holes. It follows that the formation of ferrite together with cementite by eutectoid composition of austenite, leads to an increase in volume of the metal with accompanying compressive stresses at the interface between these two phases.

In the most frequently used steels, having less than the eutectoid content of carbon (about 0.8 wt%), the various forms in which the cementite phase can be produced in dispersion in ferrite depend upon the rate of cooling to

DropBooks

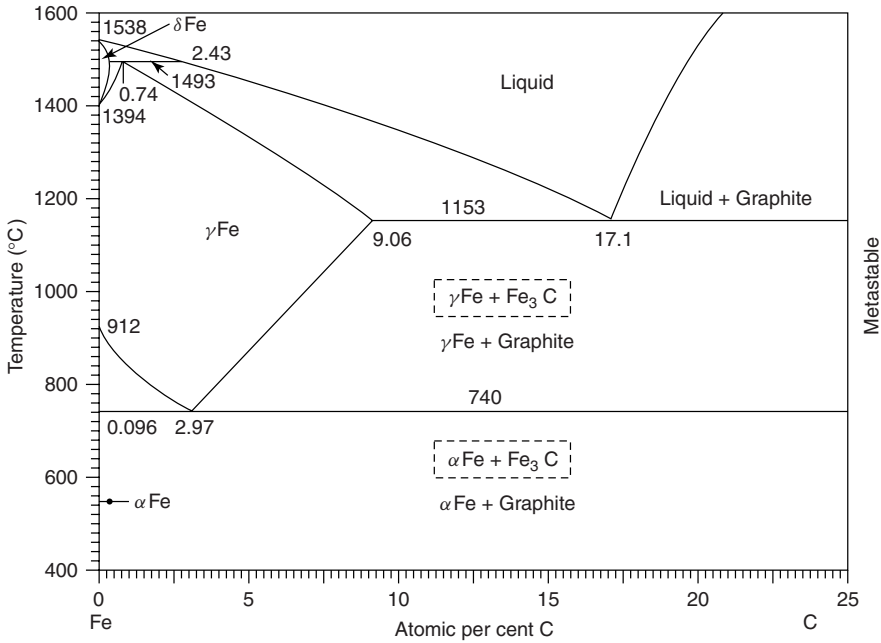


Figure 6.3 *The iron–carbon phase diagram showing the alternative production of iron and cementite from the liquid alloy, which occurs in practice, to the equilibrium production of graphite*

room temperature. Thus, pearlite, which consists of alternate layers of ferrite and cementite, can be produced by cooling the alloy slowly. The nucleation of pearlite begins at grain boundaries, and so fine grain steels transform most rapidly. The thickness of the ferrite–cementite layers is a function of temperature, because the growth of these layers is determined by the transfer of carbon by diffusion from the ferrite to the cementite layers, and clearly this rate will decrease with decreasing temperature. Bainite, which consists of platelets of ferrite containing islands of cementite is formed if the alloy is rapidly cooled to a temperature between 825 K and 700 K. The structure of bainite is divided into upper bainite, which forms at the high temperature, and consists of cementite deposited between the ferrite platelets, and lower bainite, which is formed at the lower temperatures, less than 700 K, in which the cementite particles are formed within the ferrite particles. The rate of lower bainite formation decreases substantially at temperatures less than this because the diffusion coefficient of carbon decreases. If the alloy is cooled rapidly to temperatures between 700 K and room temperature, martensite, which consists of lens-shaped needles of composition about $Fe_{2.4}C$ with a

body-centred tetragonal structure dispersed in a matrix of ferrite is produced. The c/a ratio of the martensite needles increases with the carbon content of the original alloy, indicating an increase in the carbon content of the martensite phase.

Alloy steels contain small amounts of elements which have a marked effect on the relative stability of austenite and ferrite. For example, nickel at a concentration of about 10% extends the austenite and ferrite phases to higher carbon content than in the Fe–C system, and chromium suppresses the formation of austenite, stabilizing ferrite to cover the complete temperature range from room temperature to the melting point when the chromium content is greater than 12%. Elements, such as tungsten and vanadium together with chromium form stable carbides, and tend to remove carbon from the alloy as carbides, either pure or mixed with cementite in solid solution. The phase diagrams and cooling behaviour of the alloy steels is therefore complicated, especially as the most commonly used steels contain a mixture of alloying elements. The best-known composition in corrosion-resistant stainless steels is the 18:8 composition of chromium and nickel. These produce austenitic steels on slow cooling, but martensitic steels on rapid cooling (Pascoe, 1978).

The products of the decomposition of austenite which are thus determined by the rate of cooling, have a marked effect on the hardness of the resultant steel. Pearlite formation leads to a malleable form of the metal, while martensite is a hard brittle material. The hardness of a martensitic steel can be modified by the process of tempering. The temperature distribution in a cooling alloy will clearly show that the outer layers of the alloy cool more rapidly than the interior. Thus the surface can develop a martensitic skin during rapid cooling, and as the interior cools and undergoes transformation with an accompanying dilatation, the outer layer will tend to crack. In ‘martempering’, the steel is cooled to a temperature just above the onset of martensite formation, and retained at this temperature until the sample has a uniform temperature distribution. Bainite cannot be formed at this low temperature due to the slow diffusion rate of carbon. The metal is then allowed to cool slowly to room temperature, when martensitic needles are formed, hardening the resultant sample.

DropBooks

The type of products of austenite decomposition therefore depends on the rate of cooling, which can be variable or constant, and varies as a function of the temperature at each point of the cooling cycle. The results of cooling can be graphically represented by showing the products which are formed as a function of time and temperature during the cooling cycle, in a time–temperature–transformation diagram. The shape of the resulting curves for the onset and completion of the transformation at a constant temperature are related to the interstitial migration of carbon, which would decrease in rate as the temperature decreases, and the Gibbs energy of nucleation, compensated in part by the chemical potential driving forces which increase

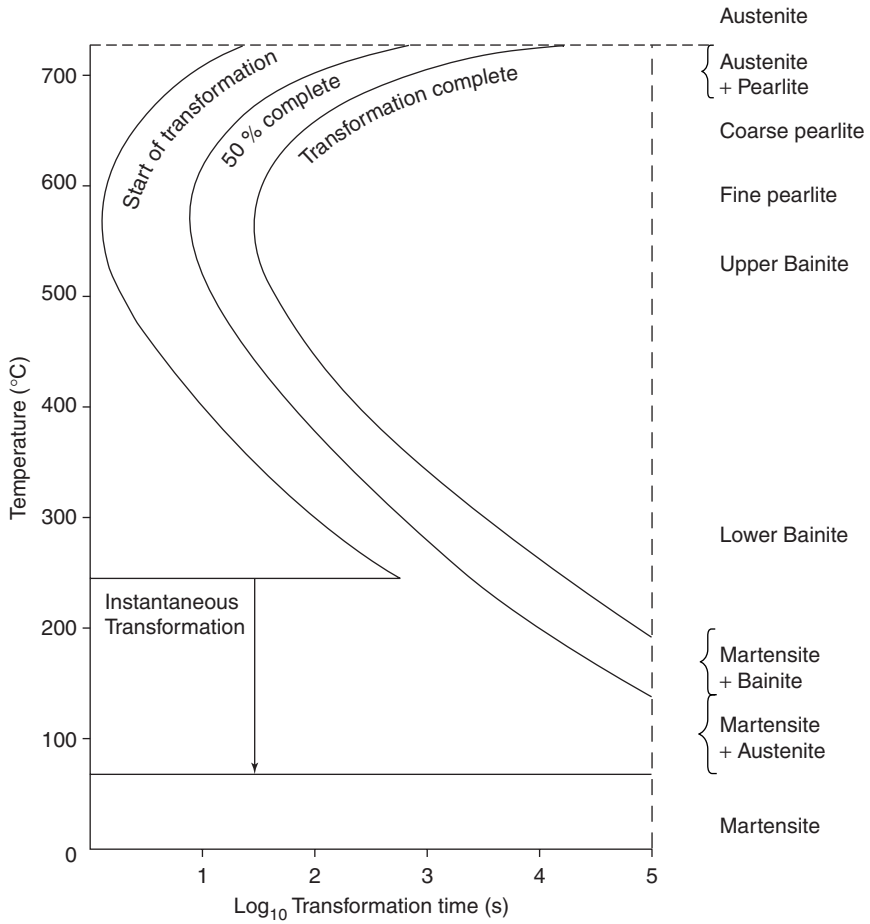


Figure 6.4 *The time–temperature–transformation diagram of the iron–carbon system, beginning at the composition of austenite*

with decreasing temperature. The T–T–T curves thus show a maximum rate of transformation at the temperature where these forces are simultaneously optimized (Figure 6.4).

Since the rate of formation of cementite is determined by nucleation, and therefore proceeds more rapidly in fine-grained steels, it follows that the T–T–T diagram will show a more rapid onset of austenite decomposition than in steels of the same composition, but a coarser grain size. The shape of the T–T–T curve is also a function of the steel composition, and is altered by the presence of alloying elements at a low concentration. This is because the common alloying elements such as manganese, nickel and chromium decrease

the diffusion coefficient of carbon, and thus slow down the rate of austenite decomposition at a given temperature. In some alloys the general shape of the T–T–T curve is also changed.

In any solid state transformation, such as the growth of a new phase from the homogeneous austenite phase, or in the recrystallization of a metal, the T–T–T curve arises from the competing effects of the decrease in the diffusion rate versus the increase in the Gibbs energy change in the process as the temperature decreases. The 'knee' in the T–T–T curve represents the optimum in the balance between these two rate-determining effects. A general empirical equation which describes the shape of the T–T–T curve is the Johnson–Mehl equation

$$F = 1 - \exp\left(-\frac{\pi}{3}\frac{\mathrm{d}n}{\mathrm{d}t}\frac{\mathrm{d}x}{\mathrm{d}t}t^4\right)$$

where F is the fraction transformed in the time t, and the differentials represent the nucleation rate and the change in size of a principal dimension of the nucleus, such as the radius of a spherical nucleus or the length of a needle, respectively. This equation has been modified by Avrami to give a more general expression

$$F = 1 - \exp(-Kt^n)$$

where K is a rate constant and n varies depending on the morphology of the nucleus. Thus the value of n can change during the coarsening of a precipitate nucleus, from 4 to 3 for three-dimensional precipitates, to between 3 and 2 for sheets, and 2 to 1 for needle-shaped precipitates. The value of the exponent can be obtained from a plot of $\log\log(1 - F)$ vs negative $\log t$.

DropBooks

Transformations in substitutional alloys

In the previous example of austenite decomposition, the mobile species was the interstitial carbon atom. Industrially important transformations also occur in alloys between metals which have a significant heat of mixing or solution range in the solid state. In such systems, there is usually a difference in molar volume between the parent alloy and the separating phase which brings the Gibbs energy of volume change into play in determining the tendency to transform. The final precipitate will give rise to misfit strain energy in the surrounding structure, which is the result of the work done to accommodate the precipitate in the matrix. Also, in the light of modern knowledge about the structures of solids, at a two-phase interface the mismatch in lattice parameters between the two phases leads initially to a coherency strain energy. This source of misfit energy can be accommodated by the inclusion of dislocations, in which the lattice parameters of the contiguous phases are assumed to remain

constant up to the interface and any lack of registry between the atoms at the interface is accommodated by the inclusion of equally spaced dislocations. This is a non-coherent interface, and represents a possible final stage of phase separation. Alternatively the interface between a precipitate and the matrix can represent complete detachment, and any strain energy is removed.

In the examples given below, the physical effects are described of an order–disorder transformation which does not change the overall composition, the separation of an inter-metallic compound from a solid solution the range of which decreases as the temperature decreases, and the separation of an alloy into two phases by spinodal decomposition.

Order–disorder transformation

The simplest example of an order–disorder transformation in which only one element is involved is the ferro- to diamagnetic transformation of b.c.c. α-iron, when the magnetic properties change over a range of temperature, the completion of the transformation being at the Curie temperature. Since this transformation only requires a randomization of electron spins without atomic diffusion, the process is very rapid, and the degree of spin disorder closely follows the thermodynamic model as the temperature of the solid is brought up to the Curie temperature.

Some intermetallic compounds melt congruently without change of composition or of atomic order. These are the compounds with a large heat of formation due, according to Miedema *et al*. (loc. cit. de Boer *et al*., 1989), to a significant ionic contribution to the inter-metallic bond. Other less strongly bonded compounds undergo a transformation in the solid state from an ordered to an atomically disordered state before melting. The change occurs over a range of temperature, and is also characterized by a Curie temperature at which the transformation is complete.

The simple Bragg–Williams treatment of this behaviour assumes an unlike atom bond strength which is greater than the like atom bonding and calculates the entropy of mixing as a function of the disorder which counterbalances this negative heat of formation. The relationship between the Curie temperature, T_c, and the bond energies is

$$kT_c = -4[E_{AB} - (E_{AA} + E_{BB})/2]$$

where E_{AB} is the bond energy between unlike atoms in the A–B systems.

The process requires the interchange of atoms on the atomic lattice from a state where all sites of one type, e.g. the face centres, are occupied by one species, and the cube corner sites by the other species in a face-centred lattice. Since atomic re-arrangement cannot occur by direct place-exchange, vacant sites must play a role in the re-distribution, and the rate of the process is controlled by the self-diffusion coefficients. Experimental measurements of the

change in resistance of a sample which was originally an ordered compound as the temperature is increased show the kinetics of this transformation since the disordered phase has a higher resistivity than the ordered phase. The rate of disorder at each incremental change of temperature as a function of time is used to determine the overall rate of disorder, and the results show that the energy of acivation is very close to the energy of formation of vacancies, and the transformation follows an Arrhenius temperature relationship.

The age-hardening of copper–aluminium alloys

An alloy consisting of a dilute solution of copper in aluminium, about 2 atom % of copper, develops hardness on cooling from 800 K to room temperature. This is because a second phase, $CuAl_2$, separates from the homogeneous solution, and under a slow rate of cooling the precipitate forms in thin platelets which are epitaxial to the matrix. The initial phase of transformation, at a temperature of about 400 K, involves the formation of *Guinier–Preston zones* which are about 2 atoms thick by between 2 and 20 atoms long which precede the formation of the precipitate phase. The G–P zones are coherent with the matrix, and further growth, accompanied by coherency strain energy, can occur without detachment of the zones from the aluminium matrix, until a critical size is reached at which the inter-metallic compound appears as a separate phase, dispersed in the matrix. The rate of growth of the G–P zones and the eventual detachment of the $CuAl_2$ particles from the aluminium matrix can be fixed by control of the cooling rate of the alloy from the solution phase to room temperature. It has been found that the alloys which have been brought to the stage preceding the separation of the $CuAl_2$ particles from the matrix, show a considerable degree of hardening, i.e. resistance to plastic deformation, with respect to the original solid solution phase and the final stage of detachment of the precipitate from the matrix. The degree of hardness of the alloy increases with time at constant temperature, which may be as low as room temperature in some alloy systems, but in the Al–Cu system occurs at about 400 K. It is because of the relatively slow growth of hardness which occurs in these alloys, that they are known as *age-hardened* alloys.

DropBooks

The crystallographic requirement for the formation of G–P zones is that the material within the zones shall have an epitaxial relationship with the matrix, and thus the eventual precipitate should have a similar unit cell size in one direction as tha matrix. In the Al–Cu system, the f.c.c. structure of aluminium has a lattice parameter of 0.4014 nm, and the tetragonal $CuAl_2$ compound has lattice parameters $a = 0.4872$ and $b = 0.6063$ nm respectively.

Spinodal decomposition of binary alloys

When solid alloys have a positive heat of mixing, ΔH_M, complete solid solution occurs above the temperature where $T\Delta S_M$ is more negative than the heat

of mixing, but on cooling the effect of the heat of mixing becomes greater than the entropy contribution to the Gibbs energy of formation of the alloy over a range of composition, and so phase separation occurs in that range. Both of these components of the Gibbs energy vary with composition, so the region where this change occurs is usually limited in composition, and the separation of phases is determined not only by the alloy thermodynamics, but also by the diffusive separation of the phases as the temperature decreases. From the thermodynamic aspect, below the temperature where phase separation begins, the Gibbs energy of formation of the alloy develops two inflections, and separation of two new phases of composition represented by the points of inflection should appear, but these do not represent the compositions of the final equilibrium phases. This is the spinodal decomposition of the alloy, which produces two separate phases whose composition change as the temperature is decreased and the points of inflection move further apart (Figure 6.5).

The kinetics of spinodal decomposition is complicated by the fact that the new phases which are formed must have different molar volumes from one another, and so the interfacial energy plays a role in the rate of decomposition. Another important consideration is that the transformation must involve the appearance of concentration gradients in the alloy, and therefore the analysis above is incorrect if it is assumed that phase separation occurs to yield equilibrium phases of constant composition. An example of a binary alloy which shows this feature is the gold–nickel system, which begins to decompose below 810°C.

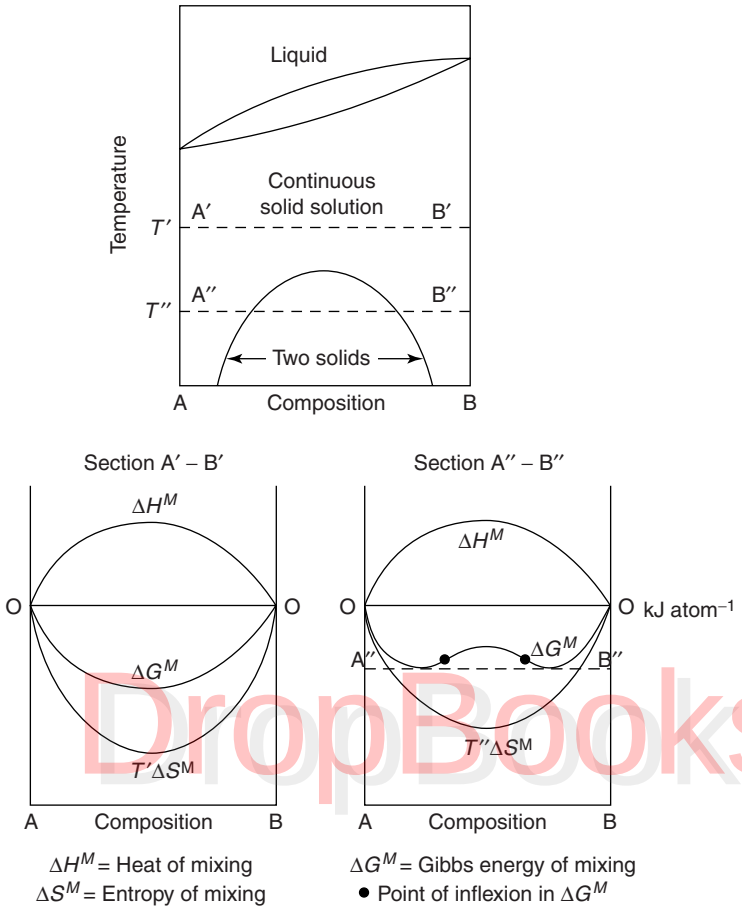
The experimental observation is that the decomposition occurs in bands, so that regions of each spinodal phase are formed, separated by regions of the other, with a variation of the composition in both regions around the compositions predicted by the inflection points in the thermodynamic Gibbs energy of mixing. These regions initially show an approximately sinusoidal variation in composition across the bands. The driving force for the separation includes the Gibbs energy gradient, and the first step in calculating this quantity is to calculate the variation of composition around a local concentration fluctuation using a Taylor's expansion. If the Gibbs energy at the centre of the fluctuation is c_0, and the fluctuation leads to concentrations varying by the amount $\pm\delta$, the change in Gibbs energy is represented by the equation

$$\Delta G = 1/2[(\delta c)G' + 1/2(\delta c)^2 G''] + 1/2[(-\delta c)G' + 1/2(-\delta c)^2 G']$$

$$\Delta G = 1/2(\delta c)^2 G''$$

where G' represents the first spatial differential, and G'' the second differential of the Gibbs energy, and δc may be replaced by $\mathrm{d}c/\mathrm{d}x$.

These fluctuations lead to two more components to the Gibbs energy changes in the process. The first arises from the fact that the fluctuations represent a local gradient in composition, and hence there is a change in the number of



DropBooks

Figure 6.5 *The appearence of spinodal decomposition as the temperature is lowered from a range of complete solubility, to the separation of two phases. In the range of composition between the inflection points, the equilibrium spinodal phases should begin to separate*

like and unlike atoms which surround a given atom. Since the heat of mixing is positive for the system, the unlike atom bonds are weaker than the like atom bonds, and the gradient energy will reflect this (Hillert, 1961). The total Gibbs energy of the fluctuation can then be written as the sum of the two components (Cahn and Hilliard, 1958)

$$\Delta G = \left[\frac{1}{2}G'' + K\left(\frac{\mathrm{d}c}{\mathrm{d}x}\right)^2\right]$$

where K represents the effect of unlike atom bonding on the stability of the fluctuation. Since G'' is negative in the composition region of the spinodal decomposition, the fluctuation Gibbs energy change will only be negative if

$$\frac{1}{2}|G''|(\delta c)^2 > K\left(\frac{\mathrm{d}c}{\mathrm{d}x}\right)^2$$

If the fluctuation is assumed to follow a cosine distribution

$$c - c_0 = A\cos\beta x$$

then the Gibbs energy change due to the variation in composition is given by

$$\Delta G_s = \pi A^2[G'' + 2K\beta^2] \text{ where } \beta = 2\pi/\lambda$$

Hence the critical value of λ is

$$\lambda_c = \left(-8\pi^2\frac{K}{\Delta G_{c_0}}\right)^{1/2}$$

If a fluctuation has a wavelength which is less than this critical value, it will not be stable but will decay.

Here K represents the effect of the change in bonding accompanying the fluctuation. Since a positive heat of mixing usually results from a significant difference in the atomic radii of the two metals, there will be a contribution of this factor to the Gibbs energy, the coherency strain energy, which is given by

$$\Delta G_s = m^2(\delta c)^2 E\, V_{av}$$

where m, the lattice misfit, is given by

$$m = \frac{1}{a}\frac{\mathrm{d}a}{\mathrm{d}c}$$

E is Young's modulus and V_{av} is the average molar volume. Summing these terms the total Gibbs energy change accompanying the fluctuation, ΔG_t, is

$$\Delta G_t = \left[G'' + \frac{2K}{\lambda^2} + 2m^2 E\, V_{av}\right]\frac{(\delta c)^2}{2}$$

It follows that the total Gibbs energy change will be negative, and a fluctuation will be stable, when a wavelength component of the fluctuation spectrum corresponds to the relationship

$$\lambda^2 > \frac{2K}{G'' + 2m^2 E\, V_{av}}$$

The kinetics of spinodal decomposition follows the equation

$$A(\beta, t) = A(\beta, 0)\exp[R(\beta, t)]$$

where (r, β), the amplitude factor, given by

$$R(\beta, t) = -M\beta^2[G'' + 2K\beta^2] \quad \text{(Cahn 1961)}$$

where M is the atomic mobility and omitting the strain energy term. The fastest growing fluctuation is given by

$$(\beta^*)^2 = 2\left[-\frac{\mathrm{d}^2G}{\mathrm{d}c^2}\,\frac{1}{2K}\right]$$

Metals and alloys in nuclear power reactors

The early reactors were gas-cooled, mainly by CO_2 or helium, using a metallic uranium fuel element clad in a metallic container. The development of these reactors has depended very much upon the improvement in performance which can be brought about by alloy formation. In the Calder Hall reactor, the first to produce electric power on a commercial scale, the cladding element was Magnox, an alloy of magnesium with minor amounts of Al, Be, Ca and Fe. The alloying elements provide corrosion resistance to the CO_2 coolant. The main disadvantage of the fuel in this system is the fact that uranium undergoes a phase transformation at 661°C which leads to significant dimensional change. Because of this the Calder Hall reactor was operated at a fuel temperature below this phase change.

DropBooks

The metallic elements which are produced by nuclear fission involving neutrons at thermal energies, include the elements, caesium, strontium and barium from Group II, many of the rare earths, zirconium, molybdenum and the Group VIII elements rhodium, ruthenium and palladium. Also produced are the gaseous elements iodine, xenon and krypton. Most of these elements interact with uranium to form inter-metallics, while caesium and the gases do not, but tend to accumulate in the grain boundaries as pores. This leads to swelling of the metal, and together with the unwanted absorption of thermal neutrons by fission products, limits the useful life of the fuel element, the burn-up, which is typically less than 10% of the available fuel, U^{235}. The water-cooled reactors using oxide fuels dominate the commercial stage today, but these also presented problems to the metallurgist. The cladding element most commonly in use is a zirconium alloy, Zircalloy. This is designed to prolong the life of the cladding material against corrosion by the high temperature, high pressure water coolant, and consists of zirconium with small amounts of iron, chromium and nickel, at levels less than 1 wt%. The alloying elements are not dissolved in the metal, but appear to form surface layers of inter-metallics among themselves which reduce the oxidation of zirconium.

Uranium forms a continuous range of solid solutions with molybdenum at high temperatures, and it is possible by alloying to remove the phase change which limits the upper temperature of operation of metallic fuel elements. However the absorption of thermal neutrons by molybdenum is unacceptably high for gas-cooled reactors, but viable for use in fast neutron reactors. This fuel element undergoes fission of U^{235} together with the formation of Pu^{239} from U^{238}, which also undergoes fission with fast neutrons to produce 2–3 neutrons per fission event. A prototype reactor functioned satisfactorily with stainless steel cladding and cooling with a sodium–potassium liquid alloy. Attempts to make larger commercial reactors of this type have not yet been successful. The modern developments of commercial nuclear reactors have all been centred on oxide fuels, which will be considered later.

Bibliography

J. Crank. *The Mathematics of Diffusion*, 2nd edn. Oxford University Press (1975) QC185.
C.J. Smithells. *Metals Reference Book*, 7th edn. Butterworth-Heinemann (1996) TN761. S55.
C. Matano *Jpn. J. Phys.*, **8**, 109 (1932–3).
L.S. Darken. *Trans. AIME*, **175**, 184 (1948).
E. Smigelskas and E. Kirkendall. *Trans. AIME*, **171**, 130 (1947).
P. Shewmon. *Diffusion in Solids*. TMS. (1989).
C. Herring. *J. Appl. Physics*., **21**, 301 (1950).
R.L. Coble. ibid, **34**, 1679 (1963).
D.A. Porter and K.E. Easterling. *Phase Transformations in Metals and Alloys*. Van Nostrand (UK) (1982) TN 690P597 (2nd edition Chapman & Hall (1992).
F.R. de Boer, R. Boom, W.C.M. Mattens, A.R. Miedema and A.K. Niessen. *Cohesion in Metals*. North-Holland (1989).
M. Hillert. *Acta Met.* **9**, 525 (1961).
J.W. Cahn. *Acta Met.* **9**, 795 (1961).
J.W. Cahn and J.R. Hilliard. *J. Chem. Phys.*, **28**, 258 (1958).
B.R.T. Frost. *Nuclear Fuel Elements*. Pergamon Press, Oxford (1982).

Grain boundary and surface-driven properties in metallic systems

Under most processing conditions a metal sample will be polycrystalline, and consists of individual grains connected at boundaries which are sinks for vacancies and dislocations. Under some circumstances, impurities also tend to concentrate around grain boundaries. The strength of grain boundaries therefore plays a significant role in the mechanical properties of normal metallic materials. It follows that atoms may be transported through the sample not only by volume diffusion through the individual crystals, but also along grain boundaries and over exposed surfaces. At the surface of such polycrystalline solids, grain boundaries intersect the surface at grooves. The widths and shapes

of the grooves are determined by the equilibrium between the surface–gas interface and the grain boundary surface energies. Clearly the equilibration angle Θ is determined by the condition

$$2\gamma_{s-g}\cos\Theta = \gamma_b$$

for the surface tension, for the solid–gas γ_{s-g}, and the grain boundary, γ_b. The magnitude of the grain boundary energy can be estimated for small values of $\cos\Theta$ by the use of the dislocation model.

The measurement of the surface energies of metals

One useful technique for the measurement of the average surface energy of a metal is to find the condition where a metal wire of radius, r, and length, l, just fails to elongate under stress from an applied weight at constant temperature, over a long period of time. The process of creep, which would lead to this extension, increases the surface area of the wire, and thus the limiting weight occurs when the work to extend the wire by the weight is just counter-balanced by the work of surface extension. If the sample consists of transverse grains, the vacancies which are removed from the surface during creep migrate to the grain boundaries, as in Nabarro–Herring creep. The total superficial energy of the system, E_s, is given by

$$E_s = 2\pi rl\gamma_s + N\pi r^2\gamma_B$$

$$\frac{\partial E_s}{\partial l} = \pi r\gamma_s\left(1 - \frac{Nr}{l}\frac{\gamma_B}{\gamma_s}\right) = mg$$

DropBooks

where mg is the applied load which causes creep to begin.

These data relate to the surface Gibbs energy, and this has both an energy, U_s, and an entropy, S_s, contribution hence

$$\gamma_s = U_s - TS_s$$

The experimental data show that S_s has a typical value of $1\,\mathrm{mJ\,m^2}$ where U_s is typically $1–2\,\mathrm{J\,m^2}$ (Table 6.4).

The relationship of the surface energy to the heat of sublimation can be readily seen in these data. An empirical equation for this relationship has been given by Miedema *et al.*, (1980)

$$\gamma = 2\times10^{-6}\Delta H_{\mathrm{sub}}/V_m^{2/3} \quad \mathrm{J\,m^{-2}}$$

where V_m is in $\mathrm{m^3\,mol^{-1}}$. These calculated values are for the absolute zero.

It will be remembered that the surface energy is the energy loss when particles are brought to the surface from the interior, and therefore the energy

Table 6.4 *Surface energies of solid elements*

Element	Surface energy ($J\,m^2$)	Temp. of measurement	ΔH_{sub} ($kJ\,mol^{-1}$) (298 K)
Cu	1.5	1000°C	337
Ag	1.1	950°C	285
Au	1.4	1000°C	368
Fe	1.93	1475°C	416
Ni	1.72	1400°C	430
Ga	0.77	20°C	272
In	0.63	140°C	240
Al	0.98	450°C	330
Sn	0.67	200°C	301
W	2.80	2000°C	851

change to bring 1 gram-atom of material to the surface is typically

$$\frac{10^{-4}}{d^2}N \quad \text{joule} \cong 1\,\text{kJ gram-atom}^{-1}$$

where N is Avogadro's number and d is the atomic diameter, and hence the term $1/d^2$ gives the number of surface atoms cm^{-2}.

Diffusion in grain boundaries and dislocations

Diffusion paths in grain boundaries are paths of more rapid diffusion than is to be found within the grains of a solid. Because the volume of material which is in the grain boundary region is small compared to the grain volume, the contribution to material flux of the grain boundaries is usually small except at low temperatures and deep penetration into the matrix. The enhanced diffusion rate in grain boundaries is probably related to the structure of matter in them. This structure, which has been described earlier, has atoms arranged in a less ordered manner than within the grains and probably at a lower density. This would imply that in *amorphous* solids which are completely structureless, these high diffusivity paths which are characteristic of grain boundaries might be the major routes for materials transport. The alternative description of grain boundary structure in terms of the dislocation model of grain boundaries, discussed above, suggests that diffusion along these line dislocations will be more rapid than within grains due to the absence there of atoms. Hence the rapid diffusion in grain boundaries may, in some cases, be ascribed to *pipe* diffusion down the line dislocations. It follows that grain boundary diffusion

between two single crystals will depend on their relative orientation at the boundary. This dependence has been found experimentally for angles of inclination between 0 and 20°. The experimentally-derived Arrhenius expression for pipe diffusion in silver is

$$D_p = 0.1 \exp\left(-\frac{10\,200^T}{T}\right) \text{ cm}^2\,\text{s}^{-1}$$

which is to be compared with the volume diffusion relationship

$$D_v = 0.04 \exp\left(-\frac{20\,500^T}{T}\right) \text{ cm}^2\,\text{s}^{-1}$$

It can be seen that the major difference lies in the activation energy being lower in the grain boundary. Data for a number of metals show that the activation energy for grain boundary diffusion is about one-half of that for volume diffusion.

A formal derivation of diffusion in a restricted, high diffusivity path which uses no atomic model of the grain boundary is that due to Fisher, who made a flux balance in unit width of a grain boundary having a thickness of δ. There is flux accumulation in the element according to Fick's second law given by

$$\frac{\partial C_b}{\partial t} = \frac{D}{v}\frac{\partial^2 C_b}{\delta y^2}$$

DropBooks

y being the axis pointing down the grain boundary from the free surface and v being the volume element of a grain boundary of unit width in the direction z along the grain boundary, dy in length along the diffusion direction and δ in thickness in the x direction.

There is a loss of material along the x direction at each face of the boundary and into the grains adjacent to the boundary given by

$$-J_x = \frac{2}{\delta} D_1 \left(\frac{\partial C_1}{\partial x}\right)_{x=\frac{\delta}{2}}$$

and at the boundary $C_b(\delta/2) = C_1(\delta/2)$ to ensure flux continuity.

An approximate, but sufficient, solution of this equation for the thin tracer film experimental technique shows that the penetration curve has two components A_I, A_II and b being known constants.

$$\log c = A_\text{I} \exp\left(-\frac{x^2}{4Dt}\right) + A_\text{II} \exp\left(\frac{-x^{6/5}}{b}\right)$$

The first term predominates at low values of x and the long tail in the $\log c$ vs x^2 plot which is normally used when only volume diffusion is

anticipated, follows the second term. The assumption that boundary diffusion is significantly more rapid than volume diffusion indicates that the $x^{6/5}$ tail will become predominant in the penetration curve at low temperatures, especially since the major difference in the Arrhenius equations for volume and boundary diffusion is almost entirely due to the difference in activation energies. Since the boundary is a rapid diffusion path into the volume of an aggregate of grains, it is to be expected that in fine grain material, or in materials containing a high dislocation density, and especially at low temperatures, the transport of atoms through an aggregate would be more rapid than would be expected by using data for volume diffusion. This is because the diffusion profile formed by radial diffusion from dislocation pipes, or normally to grain boundaries in the more general case, would soon overlap at depths in the aggregate which had not yet been affected by volume diffusion from a free surface.

If the weak bonding model is valid for high angle grain boundaries ($>20°$) it follows that diffusion in amorphous preparations of a given material should also show this measure of enhanced diffusion, when compared with the crystalline material.

Surface diffusion on metals

Extensive computer simulations have been carried out on the near-surface and surface behaviour of materials having a simple cubic lattice structure. The interaction potential between pairs of atoms which has frequently been used for inert gas solids, such as solid argon, takes the Lennard–Jones form where d is the inter-nuclear distance, ε is the potential interaction energy at the minimum corresponding to the point of

$$E(r) = 4\varepsilon \left[\left(\frac{\sigma}{d}\right)^{12} - \left(\frac{\sigma}{d}\right)^{6} \right]$$

contact, the collision diameter, σ, between the two interacting atoms.

There are many conclusions to be drawn from these calculations. First it appears that the inter-nuclear spacing in the surface layers increases towards the free surface layers. Secondly, the surface becomes increasingly rough as the temperature increases, becoming largely covered in ledges and islands of atomic groups at temperatures corresponding to about $2kT/3\varepsilon$. Diffusive steps on solids are simple unit translations at low temperatures, there is considerable movement in the positions of atoms in the surface and the surface layer of the solid due to migration from terraces, ledges and kinks, and there is migration of groups of atoms by Brownian motion over the surface at much lower velocities than that of single atoms. At higher temperatures diffusive steps can be longer than one interatomic distance. The value of the net transport diffusion coefficient is about $10^{-4}\,\mathrm{cm^2\,s^{-1}}$ at temperatures near the melting

point and appears to conform to an Arrhenius expression for the temperature dependence. Although the Lennard–Jones potential is only a rough approximation to the potential energies of metals, the general features brought out by these simulations are probably close to what happens at the surfaces of metals.

The measurement of surface diffusion has yielded values for a number of metals, indicating that the Arrhenius expression contains a pre-exponential similar to that for volume diffusion, between 10^{-1} and $10^{-4}\,\mathrm{cm^2\,s^{-1}}$. The activation energies are therefore significantly smaller than those for volume diffusion, which accounts for the larger surface diffusion coefficients. The procedures for measurement are relatively few, and some, such as field ion microscopy, are specific to certain refractory metals. One more general technique exploits the time evolution of the shape of grain boundary emergence at surfaces or of surface scratches or grooves. A simplified model due to Shewmon (loc. cit.) assumes that the chemical potential of atoms, of volume Ω, on the surface takes the form

$$\Delta\mu = \Omega K\gamma \quad \begin{array}{l}\text{where } \gamma \text{ is the surface free energy/cm}^2\\ \text{and } K \text{ is the surface curvature}\end{array}$$

$$K = \frac{\dfrac{\mathrm{d}^2 y}{\mathrm{d}x^2}}{\left[1 - \left(\dfrac{\mathrm{d}y}{\mathrm{d}x}\right)^2\right]^{3/2}} \cong \frac{\mathrm{d}^2 y}{\mathrm{d}x^2}$$

DropBooks

where the x axis is parallel to the initial sample surface, and the y axis is normal to the surface at a grain boundary/surface intersection. The thermodynamics of curved surfaces in which the surface energy is independent of orientation, as in liquids, is described by the Gibbs–Thomson equation.

The Einstein flux equation for surface diffusion in this situation is

$$J = -\frac{D_s}{kT}\frac{1}{\Omega}\frac{\mathrm{d}\Delta\mu}{\mathrm{d}x}$$

and Fick's 2nd law yields

$$\frac{\mathrm{d}J}{\mathrm{d}x} = -\frac{D_s}{kT}\frac{1}{\Omega}\frac{\mathrm{d}^2\Delta\mu}{\mathrm{d}x^2}$$

If the rate of advance of the surface at a particular value of y is

$$\frac{\mathrm{d}y}{\mathrm{d}t} = -\frac{\mathrm{d}J}{\mathrm{d}x}\delta\Omega \quad \text{where } \delta \text{ is the surface layer thickness}$$

for which equation the solution is

$$y(x, t) = \tan\theta(Bt)^{1/4} F\left[\frac{x}{(Bt)^{1/4}}\right]$$

where $B = \dfrac{D_s \delta \gamma \Omega}{kT}$ and $F\left[\dfrac{x}{(Bt)^{1/4}}\right]$ is a power series

The power series has a complicated structure

$$F(u) = \sum_{n=\infty}^{n=0} a_n u^n \text{ where } u = \frac{x}{(Bt)^{1/4}}$$

When θ, the groove angle is small, the width between the two maxima, W, on either side of a surface groove is obtained from the values

$$a_0 = -\frac{1}{\sqrt{2}\Gamma(5/4)}; \quad a_1 = 1, \quad a_2 = -\frac{1}{2^{3/2}\Gamma(3/4)}; \quad a_3 = 0$$

and the Γ function is defined by

$$\Gamma(Z) = \int_0^\infty \mathrm{e}^{-t} t^{z-1}\,\mathrm{d}t$$

and so

$$W = 4.6(Bt)(1/4)$$

and the height of the maxima above the root of the groove d is

$$d = 0.97 \tan\theta(B/t)(1/4)$$

Note here that at a grain boundary, if θ is small,

$$\tan\theta \cong \sin\theta = \frac{\gamma_b}{2\gamma_s}$$

γ_b is the boundary energy, and γ_s the energy of the surface.

Powder metallurgy

The production of metal powders

In the production of metallic objects for technological applications, an important way to produce these is via the compacting of metal powders. One

conventional method for producing metal powders is by the use of ball mills, in which lathe turnings of metals are ground to fine particles by crushing the turnings with balls made of very hard materials in a rotating ceramic-lined cylindrical jar (comminution). Another process, for example for the production of iron powder, involves the reduction of previously ground oxide particles with hydrogen. The most widely used large-scale method for metallic powder production is the atomization of a liquid metal stream by the rapid expansion of a carrier gas though a nozzle. The molten metal is drawn into the nozzle by the carrier gas, and breaks into fine particles in the gas emerging from the nozzle.

The particle size distribution of ball-milled metals and minerals, and atomized metals, follows approximately the Gaussian or normal distribution, in most cases when the logarithn of the diameter is used rather than the simple diameter. The normal Gaussian distribution equation is

$$f(D) = (1/\sigma\sqrt{2\pi})\exp[-0.5\{(D - D_{\text{mean}})/\sigma\}2]$$

where D is the particle size in a given group of particles, and D_{mean} is the mean particle size, defined by

$$D_{\text{mean}} = \frac{\int D f(D)\,\mathrm{d}D}{\int f(D)\,\mathrm{d}D}$$

DropBooks

the integrals being from minus to plus infinity. The variance, σ, measures the spread of the distribution, and 95% of the observed diameters lie within 2σ of the average value. In the lognormal distribution, the size and the mean particle size are replaced in the Gaussian distribution by their logarithms. Whereas the Gaussian distribution curve is symmetrical about the arithmetic average diameter, the average size in the lognormal distribution is the geometric mean, and thus shows the typical skewness towards the higher particle size diameters which commonly occurs in comminuted materials.

This mathematical form of the size distribution does not take account of the fact that the particle size does not stretch over the range from minus to plus infinity but has a limited range, and a modification such as the empirical Rosin–Rammler (1933) equation

$$f(D) = \alpha M D^{\alpha-1}\exp[(-M D^{\alpha})]$$

where M and α are determined from experimental data, or the Gaudin–Melloy equation

$$f(D) = (m/D_{\max})[1 - D/D_{\max}]^{m-1}$$

where m is an adjustable parameter, are empirical attempts to take account of this factor. However, the Gaussian normal, but preferably the lognormal,

distributions are adequate if this shortcoming is ignored, in describing real particle size distributions.

The *cumulative* function, F, for all of these distributions is defined through the equation

$$F(D) = \int_{D_{\min}}^{D} f(D)\,\mathrm{d}D$$

Substituting in the Rosin–Rammler function

$$x = \alpha M\, D \text{ and so } F(x) = 1 - \exp[-x]$$

the values of α and M can be obtained as the intercept and slope respectively of a plot of

$$\log[-\log(1 - F)] \text{ against } \log D$$

Similarly, substituting in the Gaudin–Melloy equation

$$z = D/D_{\max} \text{ yields } F(z) = 1 - (1 - z)^m$$

and the value of z may be obtained from a plot of $\log[1 - F]$ against $\log[1 - z]$ which has a slope of m.

A typical range of particle size for ball-milled powders is 10–5000 microns, but the shapes of particles produced by the usual comminution methods are not the ideal spherical shape envisaged in the Gaussian distribution, but are, on average, of a much more irregular shape. In order to apply the equations quoted above, an approximate value for the equivalent ideal spherical particle diameter must be determined, and this may be obtained by measurement of the surface area of a sample of particles, from which an average radius of the circle of equal surface area can be obtained. This method clearly requires the accurate measurement of a large number of particles to yield a statistically significant result, and a simpler, again approximate method of estimation is to separate the particles into finite size ranges by the use of metallic screens. Screen sizes from 50 to 7000 μm in opening cross-section are commercially available, and sizes down to 5 μm can be obtained for special applications. The disadvantage of these small aperture screens is that particles of very small size tend to agglomerate or adhere to one another, making the particle size analysis meaningless. Such small particles are better analysed for size distribution by measuring the terminal velocity, v, of settling of the particles in air or some inactive fluid, as given by Stokes' law

$$v = \frac{gD^2(\rho_m - \rho_f)}{18\eta}$$

where g is the gravitation constant, D is the particle diameter, ρ_m and ρ_f are the densities of the particles and the suspending fluid respectively, and η is the viscosity of the fluid.

The advantage of the method of screen analysis is that the particle size distribution can readily be calculated from the weight of material in each size interval. The commercially available screen intervals range from 37 μm at the lower limit (400 mesh), increasing to 6.685 mm at the upper limit (3 mesh), in a geometric progression. Each mesh opening is $\sqrt{2}$ wider than the previous, finer, opening, e.g. 52–74–104–147 μm with mesh numbers 270–200–150–100. The mesh number is defined by the number of mesh wires per linear inch, thus 200 mesh has 200 wires per inch, leaving an opening of width 74 μm.

The sintering of solid metal particles

The sintering process is used extensively in powder metallurgy and in the preparation of dense ceramic bodies. In both cases the process can be carried out in the solid state, and the mechanism whereby small isolated particles can be consolidated into an article of close to theoretical density involves the growth of necks which join the particles together, and which gradually increase in time to produce consolidation. The sintering of a large collection of fine particles is a many body problem with complicated growth patterns, but the scientific understanding of the process is greatly assisted by the analysis of simple assemblies containing only a few particles. Broadly speaking, two principal mechanisms are responsible for the transfer of matter from the individual particles to cause neck growth, and these are mass transfer via the gas phase (see Part I), or solid state diffusion processes, namely volume, grain boundary and surface diffusion.

DropBooks

There is a qualitative distinction between these two types of mass transfer. In the case of vapour phase transport, matter is subtracted from the exposed faces of the particles via the gas phase at a rate determined by the vapour pressure of the solid, and deposited in the necks. In solid state sintering atoms are removed from the surface and the interior of the particles via the various diffusion vacancy-exchange mechanisms, and the centre-to-centre distance of two particles undergoing sintering decreases with time.

For diffusion-controlled sintering there are two sources of atoms which migrate to the neck. The first source is from the surface of the spheres where diffusion may occur either by simple surface migration, or by volume diffusion from the surface and through the volume of the spheres. These processes involve the surface and volume self-diffusion coefficients of the sphere material in the transfer kinetics. The second source is from the grain boundary which can be imagined to form across the centre section of the neck. This will again involve the volume diffusion coefficient and also a grain boundary diffusion coefficient of the sphere material (Figure 6.6).

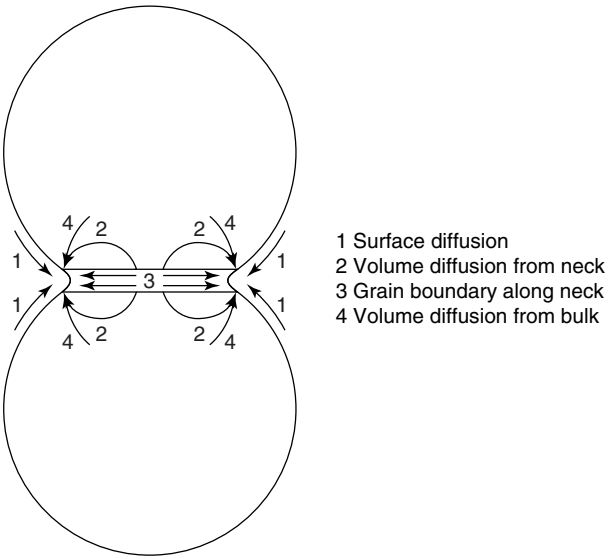


Figure 6.6 *The paths for atom movement to form the sintered neck between two particles in the solid state*

In the operation of the first source, the driving force for sintering is the difference in curvature between the neck and the surface of the sphere. The curvature force K_1, is given by

$$K_1 = \left(\frac{1}{r} - \frac{1}{x}\right) + \frac{2}{a}$$

where x is the neck radius, r the radius of curvature of the neck and the two radii of curvature of the spheres are equal to a.

The second, the grain boundary driving force, K_2, is given by

$$K_2 = \left(\frac{1}{r} - \frac{1}{x}\right)$$

where r and x are of opposite sign.

The differential equations for neck growth by these four mechanisms are (Ashby, 1974)

$$\frac{\mathrm{d}x}{\mathrm{d}t} = 2D_s\delta_s F K_1^3 \text{ for surface diffusion}$$

$$= \frac{4D_B\delta_B F K_2^2}{x} \text{ for grain boundary diffusion within the neck}$$

where δ_B is the grain boundary thickness

$= 4D_V F K_2^2$ for volume diffusion within the neck

$= 2D_V F K_1^2$ for volume diffusion

Both these diffusion controlled and the vapour phase transport processes may be described by the general equation

$\left(\frac{x}{a}\right)^n = \frac{F(T)t}{a^m}$ $F(T)$ is a function of temperature, and molar volume

(where $F = \frac{\gamma V_m}{RT}$ and δ_s is the surface thickness)

with the corresponding values of m and n

$m = 2; \quad n = 3$ for vapour phase transport,
$m = 3; \quad n = 5$ for volume diffusion,
$m = 4; \quad n = 6$ for grain boundary diffusion,
$m = 4; \quad n = 7$ for surface diffusion.

The values of m given above conform to Herring's 'scaling' law (1950) which states that since the driving force for sintering, the transport length, the area over which transport occurs and the volume of matter to be transported are proportional to a^{-1}, a, a^2 and a^3 respectively, the times for equivalent change in two powder samples of initial particle size $a_{1,0}$ and $a_{2,0}$ are

$$\frac{\Delta t_2}{\Delta t_1} = \left(\frac{a_{2,0}}{a_{1,0}}\right)^m$$

DropBooks

where m takes the values 2 for evaporation-condensation, 3 for volume diffusion and 4 for grain boundary or surface diffusion. The diffusion-controlled processes all lead to a decrease in the centre-to-centre distance of the spheres being sintered. Kuczynski (1949) suggested the two equations

$$\frac{x^5}{a^3} = \frac{40\gamma V_m}{RT} D_V t \text{ for diffusion control}$$

and $$\frac{x^7}{a^3} = \frac{56\gamma V_m^{4/3}}{RT} D_s \delta_s t \text{ for grain boundary control}$$

He studied the sintering of copper particles in the diameter range 15–100 microns and of silver particles of diameter 350 microns. The results for the larger volume fraction of copper and for silver were shown to fit the volume diffusion mechanism and yielded the results for volume self-diffusion

$$D_V^{\text{Cu}} = 70 \exp\left(-\frac{28\,000}{T}\right) \text{ cm}^2\,\text{s}^{-1}$$

and

$$D_V^{\mathrm{Ag}} = 0.6 \exp\left(-\frac{21\,000}{T}\right) \mathrm{cm}^2\,\mathrm{s}^{-1}$$

Ashby pointed out that the sintering studies of copper particles of radius 3–15 microns showed clearly the effects of surface diffusion, and the activation energy for surface diffusion is close to the activation energy for volume diffusion, and hence it is not necessarily the volume diffusion process which predominates as a sintering mechanism at temperatures less than 800°C.

Ashby also constructed 'sintering maps' in which x/a is plotted versus the 'homologous' temperature T/T_m where T_m is the melting point. These maps, which must be drawn for a given initial radius of the sintering particles, use the relevant diffusion and vapour pressure data. Isochrones connect values of x/a which can be achieved in a fixed time of annealing as a function of the homologous temperature.

The results for silver particles show the way in which the average particle size of the spheres modifies the map of the predominating mechanisms which depend on the sphere diameter, a, in differing ways as shown above in the variation in the values of m which can be shown in the form of a general equation

$$\left(\frac{x}{a}\right)^n = \frac{F(T)t}{a^m}$$

In the practical application of this theory, interest centres around the sintering of a large agglomeration or compact of fine particles. The progress of the sintering reaction is gauged by the decrease in the overall dimensions of the compact with time. Kingery and Berg found that the volume shrinkage $\Delta V/V_0$ which is given by

$$\frac{\Delta V}{V_0} = 3\frac{\Delta L}{L_0}$$

the shrinkage in length, changes with time according to

$$\frac{\Delta L}{L_0} = \frac{31}{16}\left(\frac{\gamma V D_V t}{RTa^3}\right)^{2/5}$$

for volume diffusion control

Hot pressing

When three spherical particles are sintered together, the volume between them decreases as the necks increase until a spherical cavity is left. The source of material to promote further neck growth is now removed by the coalescence of

the spherical surfaces, and the necks cease to grow according to the previous models. This limits the extent to which densification can be achieved, and sintered bodies usually attain only 90–95% of the theoretical density. Further densification may be achieved by applying an external pressure at sintering temperature, and this process, 'hot pressing', can lead to higher final densities than sintering under atmospheric pressure. A model of the various contributions to this process due to Wilkinson and Ashby (1975), assumes that the particles can be approximated by a spherical shell with a central cavity. Denoting the shell radius by b and the cavity radius by a then the pressure exerted on the cavity, when an external pressure p_{ext} is applied to the shell is

$$p = p_{\text{ext}} - p_{\text{int}} + \frac{2\gamma}{a}$$

where p_{int} is the pressure generated by the gases trapped in the cavity. The relative density of the sample is denoted by ρ and the density of the shell material ρ_0 and

$$\rho_s = \frac{b^3 - a^3}{b^3} = 1 - \left(\frac{a}{b}\right)^3$$

Assuming that the average diffusion length of particles to the cavity from the shell surface is equal to the thickness of the shell, and conversely that there is a counter-current of vacancies from the cavity to the shell surface, the rate of densification $\mathrm{d}\rho/\mathrm{d}t$ is given by

$$\rho_1 = \frac{\mathrm{d}\rho}{\mathrm{d}t} = \frac{3D_V V_m}{RTb^2}\,\frac{a}{b-a}\,p$$

for volume diffusion, and

$$\rho_2 = \frac{\mathrm{d}\rho}{\mathrm{d}t} = \frac{a}{2}\,\frac{D_B \delta V_m}{RTb^3}\,\frac{b}{b-a}\,p$$

for grain boundary diffusion, and so

$$\rho_2 = \frac{3}{2}\,\frac{D_B \delta}{aD_V}\rho_1$$

This latter equation defines the relative roles in hot pressing densification of volume and grain boundary processes.

It was shown earlier that the Nabarro–Herring model of creep in solids involved the migration of vacancies out of the stressed solid accompanied by counter-migration of atoms to reduce the length of the solid in the direction of the applied stress. This property could clearly contribute to densification under an external pressure, given sufficient time of application of the stress

DropBOOKS

and the appropriate mechanical properties of the solid. The normal objectives of hot pressing are to produce dense bodies at temperatures of sintering which are less than those applied in conventional atmospheric sintering. Materials having very low diffusion coefficients and especially ceramic materials which are brittle would not be expected to densify more rapidly under an applied stress than at one atmosphere pressure, the normal condition. Nevertheless in the case of metallic materials, creep, both volume and grain boundary, and plastic deformation can play a significant role in pressure sintering as was shown by Wilkinson and Ashby.

Ostwald ripening

This phenomenon was found to limit the usefulness of dispersed-phase strengthened metallic alloys at high temperature since the dispersed phase particles of materials such as ThO_2 and Y_2O_3 have a particle-size distribution, and the smaller particles have a higher solubility in the surrounding metallic matrix than the larger particles, according to the Gibbs–Thomson equation. The smaller particles dissolve and transfer matter to the larger particles, thus releasing pinned dislocations, and weakening the matrix. According to the Gibbs–Thomson equation the vapour pressures p_1 and p_2, of particles of diameter r_1 and r_2 take the form

$$RT \ln \frac{p_1}{p_2} = 2\gamma V_m \left(\frac{1}{r_1} - \frac{1}{r_2} \right) = \Delta\mu_1 - \Delta\mu_2; \quad \Delta\mu_i = RT \ln \frac{p_i}{p^\circ}$$

where $\Delta\mu_i$ is the chemical potential of the ith species, and p° is the vapour pressure of a flat surface in the standard state.

Greenwood (1956) described the behaviour of an assembly of n groups of particles undergoing Ostwald ripening by solution-diffusion controlled transfer between particles according to a general relationship

$$\frac{\mathrm{d}Q}{\mathrm{d}t} = 4\pi\rho a_2^2 \frac{\mathrm{d}a_2}{\mathrm{d}t} = -4\pi\rho a_1^2 \frac{\mathrm{d}a_1}{\mathrm{d}t}$$

where $\mathrm{d}a$ is the amount of material transferred from the particles of radius a_1, to those of radius a_2 in time $\mathrm{d}t$, and ρ is the material density. Denoting the solubilities in the matrix by the appropriate form of the Gibbs–Thomson equation by

$$S_{a_1} - S_{a_2} = \frac{2V_m S^\circ \gamma}{RT} \left(\frac{1}{a_1} - \frac{1}{a_2} \right)$$

where V_m is the molar volume, and S° is the solubility of a flat sample of the particulate material in the metallic matrix, then Fick's law for the transport of

material from one particle to the other may be expressed by the equation

$$\frac{dQ}{dt} = D\frac{A}{x}(S_{a_1} - S_{a_2})$$

where D is the diffusion coefficient of the particulate material in the matrix, and A/x is the ratio of cross-section to distance in the matrix between the two particles (Figure 6.7).

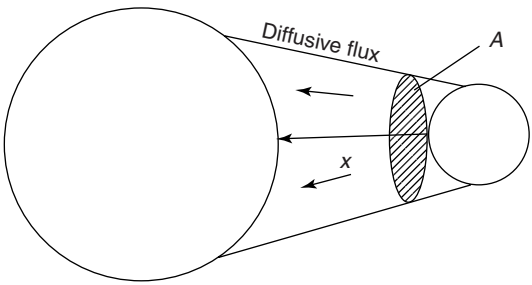


Figure 6.7 *The model for atom transfer during Ostwald ripening, showing the flux of atoms from the smaller particle to the larger*

DropBooks

In the total particle size distribution, some particles of small diameter decrease in radius, and those in the larger diameter range increase in radius during Ostwald ripening. There will therefore be a radius at which particles neither decrease nor grow in size and if a_u is this critical radius

$$4\pi a^2 \rho \frac{da_u}{dt} = \frac{DS^\circ V_m \gamma}{RT} \sum_1^n \left(\frac{A}{x}\right)_i \left(\frac{1}{a_i} - \frac{1}{a_u}\right)$$

$$\text{but } \frac{da_u}{dt} = 0; \text{ hence } \sum_1^n \left(\frac{A}{xa_i}\right) = \frac{1}{a_u}\sum_1^n \left(\frac{A}{x}\right)_i$$

From conservation of mass considerations

$$\sum_1^n 4\pi\rho a_i^2 \frac{da_i}{dt} = 0$$

The problem in the solution of Fick's law when applied to this problem lies in the difficulty in expressing analytically the A/x ratio for each pair of particles in the dispersion. Greenwood provided a limiting case solution to this problem by dealing only with a dilute dispersion in which each particle supplies or receives atoms from the surrounding average concentration solution. In such a dilute dispersion, each particle can be considered to be surrounded only by

the solvent, which has an average composition at a point distant from each particle, S_∞ and then the solution rate for a particle is given by solving the diffusion equation

$$4\pi a^2 \rho \frac{\mathrm{d}a}{\mathrm{d}t} = 4\pi r^2 D \frac{\mathrm{d}s}{\mathrm{d}r}$$

where

$$\int_r^\infty \frac{a^2 \rho}{Dr^2}\,\mathrm{d}r\,\frac{\mathrm{d}a}{\mathrm{d}t} = \int_{S_r}^{S_\infty} \mathrm{d}s = S_\infty - S_a \text{ when } r = a$$

and for the exchange between a_i and a_u particles

$$\frac{\mathrm{d}a_i}{\mathrm{d}t} = \frac{D}{\rho a_i} S_{a_i} - \frac{D}{\rho a_u} S_{a_u} = \frac{2Dv_m\gamma}{RT\rho}\left(\frac{1}{a_u^2} - \frac{1}{a_i^2}\right) \text{ [Gibbs–Thomson]}$$

and, replacing a_u by a_m, the mean particle radius, yields

$$\frac{\mathrm{d}a_i}{\mathrm{d}t} = \frac{2DV_m\gamma}{RT\rho}\left(\frac{1}{a_m^2} - \frac{1}{a_i^2}\right)$$

The graphical representation of this equation showed that the fastest growing radius in the distribution $a_{\max}$ is twice the mean radius, and therefore

$$a_m^2 \left(\frac{\mathrm{d}a}{\mathrm{d}t}\right)_{\max} = \frac{2DV_m\gamma}{RT\rho}$$

and integrating

$$a_\mathrm{F}^3 - a_\mathrm{I}^3 = \frac{6DS^\circ V\gamma}{RT\rho}t$$

where a_F is the final radius, and a_I the initial radius, for this maximum rate of growth.

Wagner (1961) examined theoretically the growth kinetics of a Gaussian particle size distribution, considering two growth mechanisms. When the process is volume diffusion controlled

$$r^3(t) - r^3(0) = \frac{8DS^\circ V^2\gamma}{9RT}t$$

where $r(t)$ and $r(0)$ are the average particle radius at times t and zero.

The alternative rate-determining process to diffusion is the transfer of atoms across the particle–matrix interface. In this case there is a rate constant for

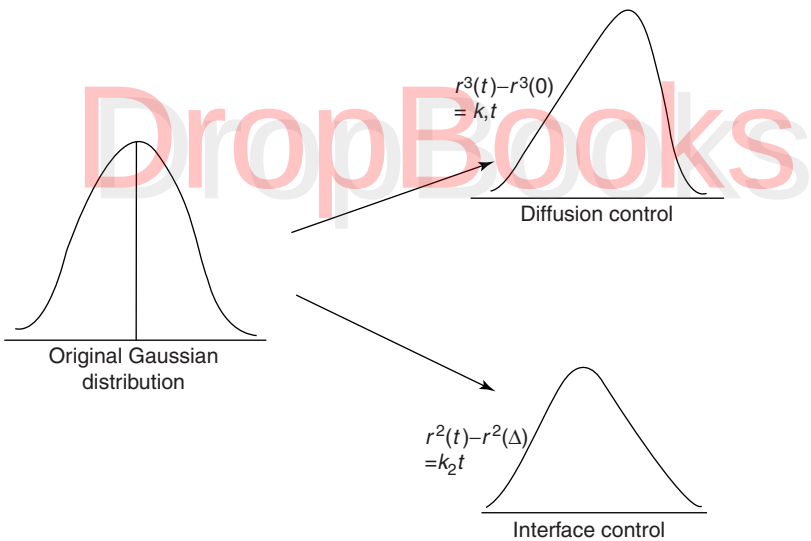
dissolution, usually designated, K. If the concentration gradient at the surface of the ith particle is $(S_i - S_m)$ and hence

$$\frac{da_i}{dt} = -KV_m(S_i - S_m)$$

the rate equation deduced by Wagner for this process is

$$r_m^2(t) - r_m^2(0) = \frac{KS^\circ\gamma V_m^2}{RT}t$$

Wagner further deduced that for this Gaussian size distribution curve, the particle size distribution should evolve in two different ways according to the growth mechanism (Figure 6.8). The diffusion-controlled growth shows a steeper leading edge to the distribution curve, than is the case for reaction-controlled growth. In most practical situations, the initial particle size distribution is rarely Gaussian, a lognormal or a bimodal distribution are more frequent, and Ostwald ripening with this initial distribution has not been considered theoretically.



DropBooks

Figure 6.8 *The change in particle size distribution which is brought about by Ostwald ripening of an initial Gaussian distribution of particle size*

An illuminating example is the effect of Ostwald ripening on pore size distribution in a sintered body, resulting from vacancy transfer from the smaller to the larger pores, where the decrease in the number and the increase in average diameter of the pores can be clearly seen. The distribution curve for

this study also shows the persistence of the long tail to the distribution, which is not described by a theoretical treatment but seems to be typical of the ripening of real systems.

Grain growth in polycrystalline metals

The final state of sintering of particles consists of a solid with grains of varying shapes and sizes, with intergranular pores. When a polycrystalline material is maintained at high temperatures for a long period of time, grain growth occurs by the transfer of atoms from grain boundaries of positive curvature to those of negative or less positive curvature. The grain boundaries therefore move in the opposite direction to the direction of atom transfer. If the 'force' acting on a boundary is calculated using the Gibbs–Thomson equation, the grain boundary velocity can be written as

$$V_b = AM_b\gamma\left(\frac{1}{r_1} + \frac{1}{r_2}\right)$$

where A is a geometric factor, M_b is the grain boundary mobility and r_1 and r_2 are the convex and concave radii of curvature of neighbouring grains respectively.

The mobility of the boundary should be closely related to the volume diffusion process in the solid, and would therefore be expected to show an Arrhenius behaviour with an activation energy close to the volume diffusion activation energy.

If the radius of curvature of the grain boundary is approximated to the grain diameter D_g.

$$\frac{1}{D_g} \cong \frac{1}{r_1} + \frac{1}{r_2} \text{ and } V_b = \frac{AM_b\gamma}{D_g} = \frac{\mathrm{d}D_g}{\mathrm{d}t}$$

Hence

$$D_g^2 - D_0^2 = AM_b\gamma_b t$$

The mobility of grain boundaries is substantially reduced by the presence of the pores and the restraining force may be calculated simply to have a maximum value.

$$F_{\max} = n\pi r_n\gamma$$

when there are n pores cm^2 of a given cross-section and the average pore radius is r_n. This follows from the fact that the force retarding the movement of a pore is given by

$$F = \pi r_n\gamma\sin 2\theta$$

and setting $\theta = 45^\circ$ yields the maximum value.

If the volume fraction of the pores is f, the number of pores appearing in unit cross-section

$$n = \frac{2fr_n}{4/3\pi r_n^3} = \frac{3f}{2\pi r_n^2}$$

From the value given above for maximum retarding force

$$n\pi r_n\gamma = \frac{3f\pi r_n\gamma}{2\pi r_n^2} = \frac{3f\gamma}{2r_n}$$

When this force is equal to the force to grow grains, growth by boundary migration will cease. If the limiting grain diameter is D_1 then by the Gibbs–Thomson relationship

$$\frac{2\gamma}{D_1} = \frac{3f\gamma}{2r_n} \text{ and } D_1 = \frac{4r_n}{3f}$$

If the pore size distribution is finally the result of Ostwald ripening, it follows that $D_1 \propto t^{1/3}$.

Processing of powders to form metallic articles

DropBooks

The production of metallic objects from powders makes possible the formation from mixtures of metals as well as pure metals, even those systems forming alloys which might be unstable at high temperatures. Furthermore these objects can be prepared very close to final shape, thus reducing considerably the amount of milling, etc., which is required for billets of cast metal. This process starts from a compact produced under high pressure, either at room temperature or higher, containing the final composition mixture of metals in the appropriate proportions. The compact is then fired to promote densification until an acceptable density is attained. This need not be very close to the theoretical density, since there are applications which need a porous product, such as filters and self-lubricating alloys containing a lubricant in the compact porosity.

Another advantage of working in the solid state only is the possibility of making objects of pure refractory elements and their alloys without having to achieve the high temperatures required for formation in the liquid state. Two-phase mixtures such as copper–carbon or 'soft' metals containing carbides for cutting tools can also be easily prepared in this manner. The latter usually require hot pressing rather than fabrication at atmospheric pressure, or the liquid-phase sintering process.

In order to make a dense material it is necessary to eliminate pores which form as a result of sintering. Pores can be moved through a compact by grain boundary dragging, so that the adhesion of the pores to the boundaries

must be encouraged to prevent breakaway from the boundaries, and their isolation within a single grain. The mobility of boundaries is related to the diffusion coefficient of the material, while the migration of pores can either occur by surface migration or, as was seen in the case of UO_2, by vapour phase transfer. Since this process only becomes significant when the vapour pressure of the material reaches about 10^{-5} atmos, it is not expected to play a large role in metal sintering processes. It follows that the smaller the average particle size in the original material, the more likely will a high density be achieved.

In a binary alloy system the rate of the sintering process is determined by the inter-diffusion properties of the composite elements, which control densification as a function of temperature both with regard to volume and grain boundary diffusion, as well as pore elimination by grain boundary migration and Ostwald ripening. A rough guide to the time and temperature required for the homogenization of binary mixtures states that the time to homogenize, t, is related to the inter-diffusion coefficients of the component metals, D, and the initial particle diameters, d, by the equation

$$\frac{Dt}{d^2} = 1$$

The mean distance that particles will migrate is given by the classical expression

$$\overline{x^2} = 2Dt$$

and hence the mean diffusion distance is half the particle diameter.

An example where one metal melts before the densification process, is the formation of bronze from a 90:10 weight percentage mixture of copper and tin. The tin melts at a temperature of 505 K, and the liquid immediately wets the copper particles, leaving voids in the compact. The tin then diffuses into the copper particles, leaving further voids due to the Kirkendall effect. The compact is therefore seen to swell before the final sintering temperature of 1080 K is reached. After a period of homogenization dictated by the criterion above, the alloy shrinks on cooling to leave a net dilatation on alloy formation of about 1%.

When there is a disparity in the inter-diffusion coefficients, the alloys containing a smaller content of the slowly diffusing component will show swelling, which decreases as this proportion is increased. Thus alloys with 10% nickel in copper have a greater tendency to swelling than those containing 30% nickel. The effect arises again from the Kirkendall effect, but is eliminated by long annealing periods of several hours.

The elimination of pores comes about by the combined effects of grain growth and Ostwald ripening in the final stages of sintering.

Self-propagating combustion reactions

Some refractory carbides, silicides and borides can be synthesized by using the heat supplied by interaction of the elements. For this procedure, the sample is in the form of a compact in order to achieve a rapid reaction rate. The compact is ignited at one end, and the reaction proceeds through the compact as a result of the heat evolved during the reaction. An estimate of the temperature that can be achieved by the use of the adiabatic approximation and Hess's law. If it is assumed that the compact loses no heat to its surroundings, which is the adiabatic approximation, then the whole of the reaction heat is available to heat the products. It has been found that this approximation is a useful guide to calculating the temperature achieved at the reaction front as this moves through the compact and away from the initial point of ignition.

As a further approximation, it may be assumed that the elements conform to Neumann and Kopp's rule that the heat capacities of compounds and elements are about $25\,\mathrm{J\,g\,atom^{-1}}$. Consequently the final temperature, T_f, which is achieved at the reaction front is given by

$$-\Delta H^{\circ}_{298} = 25n(T_f - 298)$$

where n is the number of gram-atoms taking part in the reaction. Thus for the formation of niobium carbide, NbC,

$$\mathrm{Nb(s) + C(s) = NbC(s)}$$

DropBooks

where the heat of formation at 298 K is $-141\,\mathrm{kJ\,mol^{-1}}$, the calculated reaction temperature should be above 3000 K. The measured values for the heat capacities show that these are between 26 and 27 J gram-atom at this temperature, and so the equation given above should overestimate the final temperature. The temperature obtained from experimental measurement of the reaction temperature profile in a compact is about 400 K less than this calculation.

For $MoSi_2$ ($\Delta H^{\circ}_{298} = -132\,\mathrm{kJ\,mol^{-1}}$), which is used as a heating rod in high temperature furnaces, the calculation gives a reaction temperature of 1957 K, and the measured value is 1920 K. For NiAl which is used in high temperature alloys, where the heat of formation is $-118\,\mathrm{kJ\,mol^{-1}}$, the calculated temperature achieved through the reaction

$$\mathrm{Ni + Al = NiAl}$$

is 2650 K, and the measured value is 1900 K. This indicates that the adiabatic approximation is less accurate when the reactants and products are metallic, and thus have a higher thermal conductivity than the refractory materials.

Apart from simple compounds, composite materials may also be prepared by combustion synthesis. Thus a composite of TiB_2 and MgO can be formed

by the reaction

$$TiO_2 + B_2O_3 + 5Mg = TiB_2 + 5MgO$$

and a composite of MgO and B_4C can be prepared through the reaction

$$6Mg + C + 2B_2O_3 = 6MgO + B_4C$$

and where there is sufficient heat evolution, a reacting mixture such as Ti/C can be mixed with a thermally neutral material such as Al_2O_3, provided that the oxide is present to less than about 40% by weight in the original mixture, to make a TiC/Al_2O_3 composite. When a mixture of $Ti + C + Al_2O_3$ is ignited, the velocity of propagation of the reaction through the compact is slower than that of a Ti + C mixture due to the lower thermal conductivity of the Al_2O_3. It follows that the velocity of propagation through a compact will also decrease as the original or 'green' density of the compact decreases.

As an example of the production of oxide systems, the ceramic superconductor $YBa_2Cu_3O_{7-x}$ has been prepared through the reaction

$$Y_2O_3 + 4BaO_2 + 6Cu \longrightarrow 2YBa_2Cu_3O_{7-x}$$

as well as many other inter-oxide compounds. The heat requirement of these oxide-forming reactions can usually be supplied by reaction between a metal which forms a more stable oxide, as in the above example which involves the reduction of BaO_2 to BaO by copper.

The reaction mechanisms are quite complicated in these syntheses, the kinetics depending on inter-diffusion rates in neighbouring particles, the formation of transient liquid phases, and in some cases, the vapour transport of a reactant. The presence of the latter can be detected by the retarding effect of increased pressure in an inert surrounding atmosphere.

Despite these effects, the extent of reaction of a composite can be expressed in terms of the properties of the reactants by the general simplified equation

$$\xi(x) = \frac{C_p \rho u(T - T_0) - \kappa_1 \dfrac{dT}{dx}}{(\kappa_1 - \kappa_2)\dfrac{dT}{dx} + Q\rho u}$$ (Holt and Dunmead, 1991)

where $\xi(x)$ is the extent of the reaction, having the value zero for unreacted material, and one for completely reacted material. C_p, ρ, are the heat capacity and density of the product, u is the velocity of the combustion front, Q is the heat of the reaction, T and T_0 are the temperatures of the combustion front and the original sample respectively, and κ_1 and κ_2 are the thermal conductivities of the reactants and the products. This equation is obtained by solving the heat balance equation under the simplified conditions that heat losses by the

reacting system to its surroundings are negligible and that in this equation

$$C_p\rho\frac{\partial T}{\partial t} = \kappa\frac{\partial^2 T}{\partial x^2} + Q\rho\phi(T, \xi)$$

where $\phi(T, \xi)$ is a function describing the extent of the reaction which can be replaced by writing

$$\phi(T, \xi) = \frac{\partial \xi}{\partial t} = u\frac{\partial \xi}{\partial x}$$

and

$$C_p\rho\frac{\partial T}{\partial t} = C_p\rho u\frac{\mathrm{d}T}{\mathrm{d}x}$$

and u is the velocity of the reaction front. Upon integration with respect to x, the heat balance equation becomes

$$\kappa\frac{\partial T}{\partial x} - C_p\rho u(T - T_0) + Q\rho u\xi = 0$$

and the value for κ may be approximated by the expression

$$\kappa = \xi(\kappa_2 - \kappa_1) + \kappa_1$$

which is the arithmetic average of the conductivities, weighted by the degree of advancement. The neglect of heat losses by the compact during the reaction is more valid the smaller the surface area/volume ratio, and thus larger samples are to be preferred to ones of smaller diameter. These heat loss terms include the convective heat transfer to the surroundings and radiative loss. While the first term may be readily ignored, the radiation term could be significant in the synthesis of compounds having a large heat of formation, such as NiAl.

A further kinetic equation, suggested by Zenin *et al.* (1980) relates the reaction rate to the energy of activation, thus

$$\phi(T, \xi) = u\frac{\mathrm{d}\xi}{\mathrm{d}x} = A\xi^{-p}\exp\left(-\frac{\Delta E^*}{RT}\right)$$

Here $p = 1$ for a diffusion-controlled reaction.

The reactions can also be initiated through the application of a shock wave from a mechanical source, and synthesis of GaAs has been achieved without any external heating, which would lead to arsenic evaporation, being applied to the mixture of the elements.

The results of combustion reactions are normally products in which the final density is somewhat lower than the theoretical value, normally about 70%. Increased densification can be achieved if the hot product, which is still relatively plastic, is compressed. This procedure combines the thermal

DropBooks

efficiency of the combustion reaction with the high-density product of hot pressing.

The simple model in which the reaction is entirely carried out at the combustion leading edge must normally be modified to take account of the fact that the material in front of the combustion zone will be pre-heated by thermal conduction, and the material left behind the zone is at a high temperature, and therefore reactions can continue after the zone has passed. For example, it has been shown that an important step in the synthesis of TiC is the melting of the titanium before the arrival of the combustion zone, and the wetting of the carbon particles by the liquid metal, thus improving the contact which was originally established in the compact and speeding the subsequent reaction in the combustion zone. As an example of reaction after the zone has passed, the synthesis of Ti_5Si_3 has several intermediate stages involving the formation of the lower silicides, such as TiSi, before the desired material is formed in the combustion products.

Finally, the combustion zone does not always proceed at a uniform rate, but oscillates in time, slowing down and then advancing rapidly. This effect is probably due to the non-uniform packing and distribution of the reactants in the compact. Also visual observation shows that the zone is not uniformly distributed around the periphery of the compact, and the observed movement of a hot spot around the periphery is usually referred to as 'spin' combustion.

Inter-diffusion and interaction in thin film microelectronic structures

The physical structures of microchip assemblies usually contain a number of thin films in contact, each of which plays a separate role in the performance of the device. As an example, in one structure a silicon thin film would be contacted on one face by a copper rod which conducts away the heat generated during computer operations, and on the other face by an aluminium thin film which acts as a connector to other silicon films. This aluminium film is in turn in contact with a ceramic layer containing other thin film devices, and with copper pins which plug into the circuit board.

In thin film structures such as this, the films are formed by some form of vapour deposition, and thus have a granular structure in which grain boundary diffusion plays a more significant role at the low temperature of operation than does volume diffusion. This is because the grain boundary thickness between two grains (ca 5 μm) is of the order of 1 to 10% of the average grain radius, whereas the grain boundary diffusion coefficient can be orders of magnitude greater than the volume diffusion coefficient. The possibility of inter-diffusion of the layers via grain boundary interaction must be considered in order to ensure a long period of service.

Another problem in the construction of these devices, is that materials which do not play a direct part in the operation of the microchip must be introduced to ensure electrical contact between the electronic components, and to reduce the possibility of chemical interactions between the device components. The introduction of such materials usually requires an annealing phase in the construction of the device at a temperature as high as 600 K. As a result it is also most probable, especially in the case of the aluminium–silicon interface, that thin films of oxide exist between the various deposited films. Such a layer will act as a barrier to inter-diffusion between the layers, and the transport of atoms from one layer to the next will be less than would be indicated by the chemical potential driving force. At pinholes in the Al_2O_3 layer, aluminium metal can reduce SiO_2 at isolated spots, and form the pits into the silicon which were observed in early devices. The introduction of a thin layer of platinum silicide between the silicon and aluminium layers reduces the pit formation. However, aluminium has a strong affinity for platinum, and so a layer of chromium is placed between the silicide and aluminium to reduce the invasive interaction of aluminium.

The contact between the aluminium layers and the ceramic substrate requires a joining material which will wet both metal and ceramic, and solders such as the conventional Pb–Sn alloy have been used which are molten during the annealing process. The contact between the solder and the aluminium layer is frequently unsatisfactory because of the intervention of the Al_2O_3 layer, and a practical solution appears to be to place three layers of metal; chromium in contact with the aluminium, copper in contact with the chromium, and gold between the copper layer and the solder.

DropBooks

The materials problems in the construction of microchips are related to both diffusion and chemical interactions between the component layers, as shown above. There is probably a link between these two properties, since the formation of inter-metallic compounds of medium or high chemical stability frequently leads to the formation of a compound barrier in which the diffusion coefficients of both components are lower than in the pure metals.

A guide to the stabilities of inter-metallic compounds can be obtained from the semi-empirical model of Miedema *et al.* (loc. cit.), in which the heat of interaction between two elements is determined by a contribution arising from the difference in work functions, $\Delta\phi$, of the elements, which leads to an exothermic contribution, and the difference in the electron concentration at the periphery of the atoms, Δnw, which leads to an endothermic contribution. The latter term is referred to in metal physics as the concentration of electrons at the periphery of the 'Wigner–Seitz cell' which contains the nucleus and electronic structure of each metal atom within the atomic volume in the metallic state. This term is also closely related to the bulk modulus of each element. The work function difference is very similar to the electronegativity difference. The equation which is used in the Miedema treatment to

describe the heat of interaction between two elements at the equimolar composition is

$$\Delta H = [-P\Delta\phi^2 + Q(\Delta nw^{0.33})^2]V^{0.66}/(\Delta nw^{-0.33})av - R$$

where P and Q are approximately constant, and R has a finite value when the one element is a transition metal, and the other is a non-transitional metal, such as in the silicides and aluminides. Values for the elements which are mentioned above for microchip construction, are shown in Table 6.5. The value of the parameter, R, is a function of the group of the non-transitional element in the Periodic Table, being higher for silicon than aluminium, and empirical values for the three parameters in this treatment have been obtained as follows: Q/P has an average value 9.4 with P having an average value of 12.35, while R/P has a value of 2.1 for silicides and 1.9 for aluminides (Table 6.5).

Table 6.5 *Miedema constants for the microchip elements*

Element	ϕ, electron volts	nw, electron density	V, atomic volume
Al	4.20	2.70	10.0
Au	5.15	3.87	10.20
Cr	4.65	5.18	7.23
Cu	4.45	3.18	7.12
Pd	5.45	4.66	8.90
Pt	5.65	5.64	9.10
Si	4.70	3.18	8.60

These data underline the phase diagrams for the pairs of elements which are in contact in microchips, where Pd–Si and Pt–Si form stable inter-metallic compounds, and Au–Si forms a eutectic system.

Bibliography

T. Allen. *Particle Size Measurement*. Chapman & Hall, London (1990).
N.G. Stanley-Wood and R.W. Lines. *Particle Size Analysis*. Roy. Soc. Chem. Special Publication #102 (1992) TA 418.8 P32.
G.C. Kuczynski. *Trans. AIME*, **185**, 169 (1949).
G.W. Greenwood. Ostwald ripening, *Acta. Met.*, **4**, 243 (1956).
C. Wagner. *Z. Elektrochemie*, **65**, 581 (1961).
M.F. Ashby. *Acta Met.*, **22**, 275 (1974).

D.S. Wilkinson and M.F. Ashby. In *Sintering & Catalysis*, G.C. Kuczynski (ed.). Plenum Press (1975) TN695. I56.

R.M. German. *Powder Metallurgy Science*. Metal Powder Industries Federation, Princeton (1994) TN695 G47.

J.B. Holt and S.D. Dunmead. Self-Heating synthesis of materials, *Ann. Rev. Mater. Sci.*, **21**, 305 (1991).

A.A. Zenin, A.G. Merzhanov and G.A. Nersisyan. *Dokl. Akad. Sci. USSR (Phys. Chem.)* **250**, 83 (1980).

DropBooks

Chapter 7

Rate processes in non-metallic systems

Diffusion in elemental semiconductors

The technology of silicon and germanium production has developed rapidly, and knowledge of the self-diffusion properties of these elements, and of impurity atoms has become reasonably accurate despite the experimental difficulties associated with the measurements. These arise from the chemical affinity of these elements for oxygen, and from the low values of the diffusion coefficients.

The structures of these Group IV semiconductors is described in terms of covalent bonding through sp^3 hybrid orbitals. These elements, together with carbon, have an external atomic electron structure s^2p^2, but by promotion of one s electron to a p orbital and hybridization of the resulting orbitals, four bonds are formed pointing to the apices of a regular tetrahedron, which leads to a structure similar to the diamond structure.

Because of the rigidity and directionality of the covalent bonds the energies of self-diffusion have been found to be higher than those of metals. In the case of silicon, it appears that a further complication is that an interstitialcy mechanism predominates above 1000°C. Below this temperature, both elements appear to self-diffuse by atom–vacancy exchange as for the metals.

The diffusion of Group II and IV impurities in Si and Ge is more rapid than self-diffusion by approximately one to two orders of magnitude, the more rapid diffusion being of Group IV impurities in silicon, and the Group V elements in germanium. This suggests that the electron defect accompanying the introduction of the Group III element in silicon enhances interstitial diffusion, but is not effective in germanium where diffusion only occurs by the vacancy mechanism.

Quite extraordinary diffusion coefficients of impurities from other parts of the Periodic Table are found, and especially in the important case of lithium or copper diffusion, where the enhancement over self-diffusion is by six to eight orders of magnitude. This indicates that these atoms do not form part of the sp^3 network in the structure, but more closely resemble separate atoms in the sp^3 matrix.

The incorporation of oxygen either on the surface due to the presence of a SiO_2 layer, or within the volume following diffusion away from the surface,

has a marked effect on the diffusion of impurities in silicon. It is believed that this incorporation enhances the interstitial concentration, and lowers the vacancy concentration through a Frenkel equilibrium, and hence the Group II elements undergo enhanced diffusion, while the Group V elements are retarded due to the decrease in vacancy concentration.

It will be noted that because of the low self-diffusion coefficients the numerical values for representations of self-diffusion in silicon and germanium by Arrhenius expressions are subject to considerable uncertainty. It does appear, however, that if this representation is used to average most of the experimental data the equations are for silicon

$$D_{\mathrm{Si}}^{\mathrm{Si}} = 60 \exp\left(-\frac{400\,000}{RT}\right) \quad (850\text{–}1200^{\circ}\mathrm{C})$$

and for germanium

$$D_{\mathrm{Ge}}^{\mathrm{Ge}} = 30 \exp\left(-\frac{300\,000}{RT}\right) \quad (550\text{–}850^{\circ}\mathrm{C})$$

The pre-exponentials are about one order of magnitude higher than those for metallic diffusion.

Structures and diffusion in metal oxides

DropBooks

The oxides which find a large industrial application as electroceramics are based on relatively few crystal structures. The insulators such as MgO have the sodium chloride structure with octahedral co-ordination of both ionic species. Oxides which conduct electricity principally by oxygen ion migration have the CaF_2 structure. This consists of a face-centered cubic structure of the cations, with the anions on each of the cube diagonals at the 1/4, 1/4, 1/4 positions. There are thus $8 \times (1/8) + 6 \times (1/2)$ equals four cations per unit cell, and 8 anions. Al_2O_3 and many of the rare earth oxides have a hexagonal structure, with the anions forming the close-packed structure and two-thirds of the interstitial holes being filled by the cations.

The criteria which were applied to the co-ordination of a smaller species in a larger in the metallic interstitial compounds apply to ions. However, the appropriate value of the ionic radius of the cation is not fixed but depends on the co-ordination, being relatively smaller in the smaller co-ordination. Thus Ca^{2+} has a radius in eight co-ordination (0.11 nm) which is larger by about 10% than in six co-ordination (0.10 nm). Complete data for most cations is given by Shannon and Prewitt (1969). Other phases of minor occurrence and significance in the electrical industry such as TiO_2 and WO_3 are more specific in structure than these materials and are not of such a general nature as those above. An important structure which is of relatively recent industrial importance is the *perovskite* structure. The perovskite structure having the

overall composition ABO_3 involves two cationic species with a significant difference in their ionic radii. One cation species, the smaller, is placed at the centre of a face-centered structure and has octahedral co-ordination with oxygen ions, while the larger cations, which are located on the corners of the unit cell, have a co-ordination number of 12. This structure is found in important ferroelectric materials, and in some superconductors having the K_2NiF_4 structure, where two cells of perovskite structure are separated by a unit cell having the sodium chloride structure. Other variants of this structure are the Ruddlesden–Popper systems in which the perovskite structures are separated by a number of sodium chloride unit cells.

Another important crystal structure incorporating two ionic species is *spinel*, which has the composition AB_2O_4, or $AO{\cdot}B_2O_3$. In this phase one-third of the cations occupy tetrahedrally oxygen co-ordinated sites, and two-thirds occupy octahedrally co-ordinated sites.

In all of these oxide phases it is possible that departures from the simple stoichiometric composition occur through variation of the charges of some of the cationic species. Furthermore, if a cation is raised to a higher oxidation state, by the addition of oxygen to the lattice, a corresponding number of vacant cation sites must be formed to compensate the structure. Thus in nickel oxide NiO, which at stoichiometric composition has only Ni^{2+} cations, oxidation leads to Ni^{3+} ion formation to counterbalance the addition of extra oxide ions. At the same time vacant sites must be added to the cation lattice to retain the NaCl structure. This balanced process can be described by a normal chemical equation thus

$$2Ni^{2+} + (1/2)O_2 \longrightarrow 2Ni^{3+} + V(Ni^{2+}) + O^{2-}$$

This type of point defect formation is summarized by the general notation due to Kroger and Vink in the equivalent form

$$(1/2)O_2 = O_0 + 2h' + V_{Ni}^{\cdot\cdot}$$

Here O_0 represents the oxide ion which is incorporated, h' represents the Ni^{3+} ion which is a positive hole, and an extra negative charge being indicated by the superscript dot, thus $V_{Ni}^{\cdot\cdot}$ is the vacant cation site where the double dot represents the absence of two positive charges at that site.

Another source of departure from stoichiometry occurs when cations are reduced, as for example in the reduction of zinc oxide to yield an oxygen-defective oxide. The zinc atoms which are formed in this process dissolve in the lattice, Zn^+ ions entering interstitial sites and the corresponding number of electrons being released from these dissolved atoms in much the same manner as was found when phosphorus was dissolved in the Group IV semiconductors. The Kroger–Vink representation of this reduction is

$$ZnO = Zn_{int}^{\cdot} + e^{\cdot} + (1/2)O_2$$

The trioxides of molybdenum and tungsten, MoO_3 and WO_3 may be reduced to yield a number of intermediate compounds before the dioxides MoO_2 and WO_2 are formed. In the whole series of oxides, the basic unit structure of the systems consists of a metal ion co-ordinated octahedrally by six oxygen ions. When each octahedron touches its neighbours only at the corners, then each oxygen ion is shared by two metal ions, and the compound formula is MO_3. If oxygen ions are now removed by a chemical reduction process then isolated point defects are formed where the ions are removed. The situation in which these point defects are randomly distributed throughout the structure corresponds to the non-stoichiometric oxide case which we have previously described $MO_{3-\delta}$. It has been found, however, that such a random distribution only occurs for a very small value of δ and that with increasing departure from stoichiometry a new phenomenon arises which can give rise to a large number of stable intermediate oxides between MO_3 and MO_2. If a number of vacancies can be imagined to line up on one row of oxygen ions, then the vacant sites can be annihilated by the translation of the neighbouring rows of octahedra which incorporate the defective row. Such a translation, which involves the movement of groups of metal atoms together, is called a crystallographic shear, and the shear plane is a new structural unit in the compound (Figure 7.1). Since the vacant oxygen ion sites are removed as a result of the shear, a new stoichiometric compound can be formed, and the overall stoichiometry is determined by the spacing between the shear planes.

A number of compounds in the series W_xO_{3x-1} and W_xO_{3x-2} were found by Magnéli (1950) in the original discovery of this phenomenon and many more examples have been found. Molybdenum also forms the Magnéli shear plane compounds and other examples are found in the groups of compounds which are formed by the reduction of TiO_2 to give Ti_nO_{2n-1} and VO_2 to give V_2O_{2n-1} series of oxides where n takes all integral values from unity upwards. As examples, the phases Ti_4O_7, Ti_5O_9, Ti_6O_{11} are phases which have been identified in the Ti–O system. The transport properties of ions in the shear plane structures have not been sufficiently elucidated to date for a worthwhile comment to be made.

By analogy with similar materials in which free electrons and electron holes are formed, NiO is called a p-type compound having vacant site Schottky defects, and ZnO is an n-type compound having interstitial Frenkel defects. The concentrations of these defects and their relation to the oxygen pressure in the surrounding atmosphere can be calculated, for a dilute solution of defects by the application of a mass action equation. The two reactions shown above are represented by the equations

$$K_{\mathrm{NiO}} = \frac{C^2_{\mathrm{Ni}^{3+}} C_{V_{\mathrm{Ni}^{2+}}}}{p^{1/2}\mathrm{O}_2} = \frac{C^3_{\mathrm{Ni}^{3+}}}{p^{1/2}\mathrm{O}_2} \quad (\text{since } C_{\mathrm{Ni}^{3+}} = C_{V_{\mathrm{Ni}^{2+}}})$$

$$C_{\mathrm{Ni}^{3+}} = 2C_{V_{\mathrm{Ni}^{2+}}} = K p^{1/6}\mathrm{O}_2$$

DropBooks

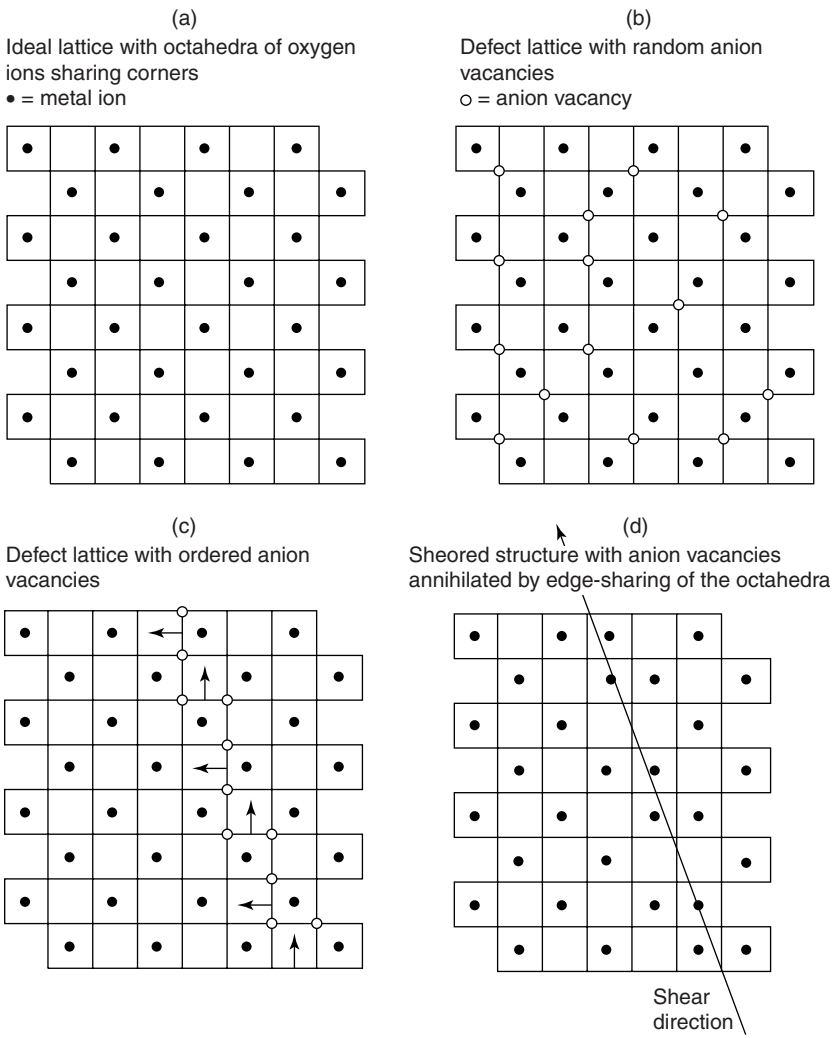

(a)
Ideal lattice with octahedra of oxygen ions sharing corners
• = metal ion
(b)
Defect lattice with random anion vacancies
○ = anion vacancy
(c)
Defect lattice with ordered anion vacancies
(d)
Sheored structure with anion vacancies annihilated by edge-sharing of the octahedra
Shear direction

Figure 7.1 *The generation of shear planes in a non-stoichiometric oxide resulting from the elimination of oxygen ions*

and

$$K_{\mathrm{ZnO}} = C^2_{\mathrm{Zn}_i^+} C_{e^-}\, p^{1/2}\mathrm{O}_2$$

$$= C^3_{\mathrm{Zn}_i^+}\, p^{-1/2}\mathrm{O}_2 \text{ (since } C_{\mathrm{Zn}^+} = C_{e^-})$$

$$C_{\mathrm{Zn}_i^+} = 2C_{e-} = K\, p^{-1/6}\mathrm{O}_2$$

where the concentrations are ionic fractions counted on the cation and anion lattices separately thus

$$C_{Ni^{3+}} = \frac{number\ of\ Ni^{3+}\ ions}{total\ number\ of\ Ni\ ions\,(Ni^{2+} + Ni^{3+})}$$

$$C_{Zn^{+}} = \frac{number\ of\ interstitial\ Zn^{+} ions}{total\ number\ of\ interstitial\ cation\ sites}$$

An important feature of oxide systems is that non-stoichiometry can also be achieved by the substitution of aliovalent ions which change the charge balance between cations and anions. Thus if Li_2O or Al_2O_3 are substituted molecule for molecule on the NiO lattice, the excess Li^+ ions are accommodated in vacant cation positions and the Al^{3+} ions substitution increases the cation vacancy concentration. Similar additions to ZnO causes the increase of the number of interstitial Zn^+ ions on Li_2O addition, and the adsorption of interstitial Zn^+ ions on the normal cation sites when Al_2O_3 is added. The cationic vacancy and interstitial ion concentration can therefore be modified by these additions. Conversely, the hole or electron concentrations in these two oxides must be altered in the opposite sense to the change in vacancy concentration, to maintain the value of the mass action constants for defect formation. When the principal cation cannot be readily reduced it is possible to make aliovalent ion additions which are compensated by the formation of oxygen vacancies in the lattice. Thus, the addition of CaO to ZrO_2 can be represented by the equation

DropBooks

$$CaO \longrightarrow Ca^{2+}_{Zr^{4+}} + O_0 + V''_0$$

It is not necessary for a compound to depart from stoichiometry in order to contain point defects such as vacant sites on the cation sub-lattice. All compounds contain such intrinsic defects even at the precisely stoichiometric ratio. The Schottky defects, in which an equal number of vacant sites are present on both cation and anion sub-lattices, may occur at a given temperature in such a large concentration that the effects of small departures from stoichiometry are masked. Thus, in $MnO_{1+\delta}$ it is thought that the intrinsic concentration of defects (Mn^{3+} ions) is so large that when there are only small departures from stoichiometry, the additional concentration of Mn^{3+} ions which arises from these departures is negligibly small. The non-stoichiometry then varies as $p^{1/4}O_2$ in this region. When the departure from non-stoichiometry is large and the concentration of defects arise from non-stoichiometry, the extrinsic defect concentration is large compared with the intrinsic concentration, the dependence of non-stoichiometry follows a $p^{1/6}O_2$ law.

Another example of the effects of non-stoichiometry on diffusion is to be found in $UO_{2+\delta}$. Here the defect consists of interstitial oxygen ions of high

mobility, and it is found that the diffusion coefficient of oxygen increases with increasing values of δ. The oxygen dependence is more complicated in this case than in NiO and the following is an explanation of the observed effects. The mass action equation can be written thus

$$\frac{1}{2}O_2 + 2U^{4+} \longrightarrow {O_i}^{2-} + 2U^{5+} \quad K = \frac{C^2_{U^{5+}} + C_{{O_i}^{2-}}}{p^{1/2}_{O_2}}$$

If it is assumed that the U^{5+} ions and the interstitial O^{2-} ions are associated, i.e. not free to migrate in the lattice independently of one another, then we write for the equilibrium constant which involves the *defect complex*, $U^{5+} - O^{2-} - U^{5+}$

$$K = \frac{C\left[U^{5+} - {O_i}^{2-} - U^{5+}\right]}{p^{1/2}_{O_2}}$$

and δ varies as $p^{1/2}O_2$. This idea of associated defects has found some value in systematizing results for non-stoichiometric behaviour which does not follow the simple mass action rule. However, a preferable model, which is not so easily quantified as the association model, derives from some early X-ray studies of the non-stoichiometric compound FeO, which has a significant range of non-stoichiometry. The system does not obey a simple vacancy or association model, but was found to give results suggesting the existence of *micro-domains* of Fe_3O_4 dispersed in a matrix of cubic FeO (Koch and Cohen, 1969). This model suggests that the non-stoichiometry of UO_{2+x} may be due to the formation of micro-domains of U_4O_9, which is the next highest phase in oxygen content.

The measurement of diffusion coefficients in simple oxides

The diffusion coefficients of cations in metal oxides are usually measured through the use of radioactive isotopes. Because of the friable nature of oxides it is extremely difficult to use the sectioning technique employed for metal samples. The need for this can be avoided by the application of radio-isotopes which emit radiation having a well established absorption law in matter. Isotopes which emit γ radiation are very useful when the cation has a relatively high diffusion coefficient because of the long-range penetration of γ rays. The absorption law is

$$I = I_0 \exp(-\mu x)$$

where μ is the absorption coefficient. When the thickness of a diffusion sample is reduced by grinding or polishing the sample down to a depth x' below the original surface, the total intensity of γ ray emission of the residual sample is given by

$$I = \int_{x=x'}^{x=\infty} C_X \exp -\mu(x - x')\mathrm{d}x$$

$$= \int_{x=x'}^{x=\infty} \frac{C_0}{(\pi Dt)^{1/2}} \exp\left(-\frac{x^2 + \mu(x - x')}{4Dt}\right) \mathrm{d}x$$

when C_0 is the concentration of isotope in the thin layer deposited on the original surface of a cylindrical sample, as for metallic diffusion studies.

For shorter penetration the use of β emitting isotopes is widely made applying much the same absorption law for β radiation as for γ rays, with a minor modification. An alternative procedure used by Kingery and Paladino for the study of Al^{3+} diffusion in Al_2O_3 employs two right cylinders, one only containing the radioactive Al^{26} isotopic species which emits relatively low energy ($E_{max} = 0.511$ MeV) β particles.

If the total amount of radioactivity transferred from one cylinder to another is measured the solution of the diffusion equation is

$$C = \frac{C_0}{2}\left[1 - \mathrm{erf}\frac{x}{2Dt}\right]; \mathrm{erf}\, x = \frac{2}{\sqrt{\pi}}\int_0^x \mathrm{e}^{-t^2}\mathrm{d}t$$

DropBooks

Differentiating with respect to x at $x = 0$

$$J = -D\left(\frac{\partial C}{\partial x}\right)_{x=0} = \frac{C_0}{2}D^{1/2}\left(\frac{1}{\pi t}\right)^{1/2}$$

$$\left[\frac{\partial C}{\partial x}\right]_{x=0} = \frac{C_0}{2}\left(\frac{1}{\pi Dt}\right)^{1/2}$$

The total amount of diffused material in a time t is

$$S = A\int_0^t J\,\mathrm{d}t$$

$$= \frac{AC_0}{\sqrt{\pi}}(Dt)^{1/2}$$

where A is the cylinder cross section, and from which the diffusion coefficient D may be calculated.

For extremely small penetrations a technique may be employed which depends upon the weak penetration of charged atoms with a known absorption law. The α-particles, which are He^{2+} ions, have a linear absorption

law in matter so that the diffusion coefficients of elements with α-emitting isotopes may be obtained by measuring the energy spectrum of α particles emitting from the surface of a diffusion sample initially coated with a thin layer of the radioisotope. This technique was used to measure the diffusion coefficient of uranium in UO_2 and thorium in ThO_2 (Hawkins and Alcock, 1968).

The measurement of oxygen diffusion is usually made by the use of O^{18} as the labelling isotope. If a gas containing an initial concentration C_i of O^{18} in O^{16}, and C_0 is the initial concentration of O^{18} in a right cylinder oxide sample of thickness $2l$, and α is the ratio of oxygen atoms in the original gas phase compared with that in the solid, then after a time t, when the O^{18} concentration in the gas phase is C_f

$$\frac{C_f - C_0}{C_i - C_0} = \exp\left(\frac{Dt}{l^2\alpha^2}\right) \operatorname{erfc}\left(\frac{Dt}{l^2\alpha^2}\right)^{1/2}$$

where erfc $= 1 -$ erf.

This assumes that the gas–solid exchange kinetics at the interface is rapid. When this process affects the O^{18} exchange kinetics significantly then analysis of O^{18} concentrations layer by layer in the diffused sample is necessary. This can be done by the use of SIMS (secondary ion mass spectrometry) and the equation used by Kilner, Steele and co-workers for this diffusion study employs a surface exchange component.

For surface exchange

$$K(C_{\text{gas}} - C_{\text{solid}}) = -D\left(\frac{\partial C}{\partial x}\right)_{x=0}$$

Then at a depth x below the original surface

$$C = \frac{C_x - C_0}{C_g - C_0} = \operatorname{erfc}\left(\frac{x}{2(Dt)^{1/2}}\right) - \exp(hx + h^2Dt) \operatorname{erfc}\left[\frac{x}{2(Dt)^{1/2}} + h(Dt)^{1/2}\right]$$

where $h = K/D$. The measurements of the relative values of the surface exchange coefficient and the self diffusion coefficients in a number of solid electrolyte-forming oxides, show that the exchange coefficients are about 10^2 times larger for the exchange coefficient (Steele, 1995). The general conclusion from diffusion studies of simple oxides is that the cation diffusion coefficient is larger then the oxygen diffusion coefficient in NaCl structure oxides such as MgO and NiO, the two coefficients are approximately equal in the hexagonal structure materials such as Al_2O_3, and that oxygen diffuses much more rapidly in the CaF_2-structure oxides such as UO_2 (Table 7.1).

Table 7.1 *Ionic diffusion coefficients in oxides at 1000°C*

Oxide	D_{cation}	D_{anion}
BeO	$10^{-12}(34\,000T)$	$10^{-16}(32\,000T)$
MgO	$10^{-15}(38\,000T)$	$10^{-17}(31\,000T)$
Al_2O_3	$10^{-17}(57\,000T)$	$10^{-17}(58\,000T)$
Cr_2O_3	$10^{-15}(50\,000T)$	$10^{-16}(52\,000T)$
Fe_2O_3	$10^{-16}(56\,000T)$	$10^{-13}(39\,000T)$
UO_2	10^{-19}	$10^{-9}(33\,000T)$
ThO_2	10^{-17}	$10^{-11}(33\,000T)$
CSZ*	10^{-17}	$10^{-6}(14\,000T)$
Non-stoichiometric oxides near the metal-rich border		
FeO	10^{-7}	–
CoO	10^{-9}	10^{-12}
NiO	10^{-11}	10^{-18}

*CSZ = Calcia–stabilized zirconia.

Surfaces and surface energies in ionic crystals

DropBooks

The structures of ionic solids may be accounted for quite accurately by the use of a *coulombic interaction* potential between neighbouring ion pairs together with a suitable ion-core repulsion.

$$E(r) = -\frac{MZ^2e^2}{r^2} + B\exp^{-r/\rho}$$

where ρ is a constant, M is the Madelung constant and B the repulsion constant. This form has been employed for most significant calculations of the stability of ionic compounds. However, the electronegativity considerations suggest that bonding in many ceramic oxides has a covalent contribution which cannot be ignored. This effect can be taken into account by the use of a more general repulsion term such as the Buckingham potential

$$V(r) = Be^{-r/\rho} - Cr^{-6}$$

together with the Madelung contribution. Computer simulations of structures at and near the surface of ionic crystals using these potentials confirm the earlier calculations. From these it was concluded that the lattice relaxes near the surface with the larger anions extending from the bulk slightly more than the cations in the surface layer (surface rumpling). These effects are ignored in a simple method devised by Gilman for the calculation of the surface energies of

ionic systems. He concludes that the surface energy can be directly calculated from Young's modulus, Y, through the relation

$$U_s = \frac{Yx_0}{4\pi^2}$$

where x_0 is the equilibrium internuclear distance of cation–anion pairs.

This procedure can be checked against experimental values which are obtained from the energy to cleave single crystals along specific directions. The agreement is good (see Table 7.2), and since it is of a general nature, the method could even be extended to the elemental semiconductors.

Table 7.2 *Calculated surface energies of ceramic oxides*

Oxide	r (cation) + r (anion) (Å)	Young's modulus (GPa)	σ calculated ($J\,m^{-2}$)
BeO	1.67	311	1.32
MgO	1.98	207	1.04
Al_2O_3	1.83	380	1.76
ZrO_2	2.11	138	0.74
UO_2	2.29	173	1.00

The experimental result for MgO from cleavage studies is $\sigma = 1.30\,J\,m^{-2}$.

Sintering of metal oxides

When inorganic compounds, such as the ceramic oxides are sintered, the neck growth must occur by the parallel migration of both species, metal ions and oxygen ions, in the stoichiometric amounts required by the overall composition, and to maintain local electroneutrality. Each species may diffuse by surface, volume or grain boundary diffusion, and the diffusion coefficients are normally quite different between cations and anions. Furthermore in transition metal oxides the vacancy concentration on the cation sites, and hence the cation diffusion coefficient, is a function of oxygen pressure in the surrounding atmosphere as well as temperature. A study which brings out a number of factors involved in the sintering of oxides is exemplified by a study of the sintering of MnO by Porter *et al.* (1979). The sintering rate of MnO spheres, 35–45 micron diameter, was observed microscopically in the temperature range 900–1100°C in a CO/CO_2 gas mixture which controlled pO_2 to the limits 10^{-8}–10^{-14} atmos.

The fractional shrinkage was expressed by the general equation

$$y = \frac{\Delta L}{L_0} = \left[\frac{k\gamma VD}{RTa^n}\right]^m t^m$$

where $m = 0.46–0.49$ for volume diffusion control and
$m = 0.31–0.33$ for grain boundary control
D is the relevant diffusion coefficient
$n = 3$ for volume control and 4 for grain boundary control
a is the diameter of the MnO particles.

The results at 1000°C in which $\log y - \log t$ was plotted as a function of log pO_2 shows that grain boundary migration is dominant at low pO_2 where there is a small vacancy Mn^{2+} concentration, then volume diffusion takes over as the dominant mode at intermediate pressures, and finally grain boundary predominates again at high oxygen pressures. This suggests that at low defect concentration VMn^{2+}, both species diffuse along the grain boundary. At intermediate oxygen pressures, the metal ion diffuses principally by the enhanced volume mode, and at high defect concentrations where defect interaction reduces the relative diffusion coefficients between volume and grain boundary, the preferred mode of cation diffusion is again via grain boundary movement. Oxygen which has a much lower diffusion coefficient in oxides with the NaCl structure always contributes to sintering via grain boundary migration, according to this model.

The production and applications of ceramic oxide materials

DropBooks

The production of objects from powders is the principal method for the consolidation of ceramics and for the manufacture of machine parts by powder metallurgy techniques. The latter procedure is very much simpler in the case of metals which can usually be obtained in the form of bars which can be reduced to powder either by milling or via liquid atomization. These can be blended to form a mixture of the desired composition before consolidation by sintering. The fabrication of ceramic parts begins in the majority of cases with the compaction of prepared powders obtained by the ball-milling of naturally occurring minerals or from solids derived from solutions. In both cases a period of sintering is necessary before the final object appears, and the industrial objective is to reduce energy costs by reducing the sintering time and temperature.

In the ceramics field many of the new advanced ceramic oxides have a specially prepared mixture of cations which determines the crystal structure, through the relative sizes of the cations and oxygen ions, and the physical properties through the choice of cations and their oxidation states. These include, for example, solid electrolytes and electrodes for sensors and fuel cells, ferrites and garnets for magnetic systems, zirconates and titanates for piezoelectric materials, as well as ceramic superconductors and a number of other substances

for application in the field generally described as *electroceramics*. For the preparation of these materials with a precisely defined mixture of cations, the earlier technique in which powders of the constituent simple oxides were mixed and alternatively fired and re-ground until homogeneity could be established, has been replaced by methods employing room temperature liquid mixtures, frequently of organic metal-bearing compounds. Some examples of this procedure are shown in Table 7.3. This source of materials produces very fine particles in a narrow size-distribution range, and because of the use of liquid precursors, the cations are mixed on an atomic scale. The firing time and temperature are considerably reduced in comparison with the traditional powder-mix method because of the fine particle size and the elimination of long periods for cation inter-diffusion. Typical particle sizes which are obtained by the methods, both traditional and from liquid precursors, are from 1–10 microns.

Table 7.3 *Newer techniques for ceramic powder formation*

Chemical vapour deposition
Example. The preparation of films of titanium dioxide. $TiCl_4 + O_2$(or $2H_2O$) $\longrightarrow TiO_2 + 2Cl_2$ (or 4HCl)
Spray drying of aqueous suspensions
Example. (Ni, Zn, Fe) sulphates (in air) $\longrightarrow$ Ni, Zn ferrite.
Precipitation of oxalates
Example. (Ca, ZrO) nitrates + $(COOH)_2 \longrightarrow$ (Ca, ZrO)$(COO)_2$ calcium and zirconyl nitrates solution to which oxalic acid is added. The oxalate solid solution of cations is then fired to 1300 K
Hydrolysis of metal-organic solutions
Example. $Ba(OC_3H_7)_2 + Ti(OC_5H_{11})_4 + H_2O \longrightarrow BaTiO_3$ {Barium isopropoxide and Titanium tertiary amyloxide are refluxed in isopropanol and then hydrolyzed with de-ionized water to produce a sol-gel.}
Pyrolysis of sol-gel products
Example. The Pechini method for fuel cell electrode preparation. La, Ba, Mn nitrates + $C_5H_8O_7 \longrightarrow$ citrate complex + $C_2H_6O_2 \longrightarrow$ gel. Metal nitrates are complexed with citric acid, and then heated with ethylene glycol to form a transparent gel. This is then heated to 600 K to decompose the organic content and then to temperatures between 1000 and 1300 K to produce the oxide powder. The oxide materials prepared from the liquid metal-organic procedures usually have a more uniform particle size, and under the best circumstances, this can be less than one micron. Hence these particles are much more easily sintered at lower temperatures than for the powders produced by the other methods.

Electroceramic oxides

Oxides play many roles in modern electronic technology from insulators which can be used as capacitors, such as the perovskite $BaTiO_3$, to the superconductors, of which the prototype was also a perovskite, $La_{0.8}Sr_{0.2}CuO_{3-x}$, where the value of x is a function of the temperature cycle and oxygen pressure which were used in the preparation of the material. Clearly the chemical difference between these two materials is that the capacitor production does not require oxygen partial pressure control as is the case in the superconductor. Intermediate between these extremes of electrical conduction are many semiconducting materials which are used as magnetic ferrites or fuel cell electrodes. The electrical properties of the semiconductors depend on the presence of transition metal ions which can be in two valence states, and the conduction mechanism involves the transfer of electrons or positive holes from one ion to another of the same species. The production problem associated with this behaviour arises from the fact that the relative concentration of each valence state depends on both the temperature and the oxygen partial pressure of the atmosphere.

Dielectric or ferroelectric oxides

DropBooks

The earliest example of a ferroelectric oxide to be studied in detail is the perovskite, $BaTiO_3$. This material has a high capacity to store electricity by virtue of the behaviour of the titanium Ti^{4+} ion in the body-centre of the unit cell. There are two energetically equivalent off-centre sites for this ion at low temperature, separated by a low energy barrier. On heating the solid, an order–disorder transition occurs above which each titanium ion occupies the two sites equally in random fluctuation. The high storage capacity comes from the localization of each ion in one of the two sites, which leads to the formation of an electric dipole within the unit cell, the particular site which is occupied being determined by the direction of the applied electric field. These dipoles are aligned by dipole–dipole interaction between neighbouring unit cells in small, randomly oriented, groups known as *domains*, which are oriented on the application of the field in the field direction. This is very similar to the behaviour of magnetic domains in ferromagnetic materials, and hence the name ferroelectric for these materials.

In lead zirconate, $PbZrO_3$, the larger lead ions are displaced alternately from the cube corner sites to produce an antiferroelectric. This can readily be converted to a ferroelectric by the substitution of Ti^{4+} ions for some of the Zr^{4+} ions, the maximum value of permittivity occurring at about the 50:50 mixture of $PbZrO_3$ and $PbTiO_3$. The resulting PZT ceramics are used in a number of capacitance and electro-optic applications. The major problem in the preparation of these solid solutions is the volatility of PbO. This is overcome by

sintering the original PZT material in a sealed crucible, and finally adding pure $PbZrO_3$ to the sealed volume. Alternative methods of preparation with the use of water-soluble acetates, or sol-gel procedures have been used successfully to prepare PZT at lower temperatures, thus minimizing the loss of lead oxide, but the conventional mixing of ball-milled individual oxides is a cheaper procedure. Additional substitution of Pb^{2+} by La^{3+} is also possible in varying the properties of the PLZT ceramics,

Magnetic oxides

The magnetic spinels are derived structurally from the mineral $MgO{\cdot}Al_2O_3$, in which the divalent ions occupy the tetrahedral holes in the cubic oxide ion structure and the trivalent ions occupy the octahedral holes. Magnetite, which can be written as $FeO{\cdot}Fe_2O_3$, has the tetrahedral holes occupied by the ferric ions, and the octahedral holes contain an equal amount of ferrous and ferric ions. Because there are five unpaired spins on each ferric ion, and four on the ferrous ion, the total number of unpaired spins per formula is thus fourteen. The ferric ion spins on the tetrahedral holes are aligned antiparallel with those on the octahedral sites by *superexchange*. This process can be envisaged by consideration of the electronic structure of the oxygen ion. This ion has all p electrons spin-paired, and the three 2p orbitals are mutually at right angles. The orbital linking ions on the tetrahedral sites with those on the octahedral sites has paired spins, one occupying each lobe of the orbital. The cation spins are therefore each linked to the electron in one lobe, and the ferric ions on the octahedral holes are aligned anti-parallel to the ferric ions on the tetrahedral sites. The compound therefore contains four unpaired spins per formula residing on the ferrous ions, and is magnetic as a result.

The fact that the site occupation in magnetite is opposite to that of spinel arises from the interaction of the d electrons on the cations with the surrounding anions. The energy for the exchange

$$\{M^{2+}\} + [R^{3+}] \longrightarrow [M^{2+}] + \{R^{3+}\}$$

where { } represents an ion on a tetrahedral site, and [ ] represents one on an octahedral site, is determined by the relative octahedral site preference energy, OSPE, of the M^{2+} ion compared with that of the R^{3+} ion, which is assumed to be temperature-independent. The Gibbs energy of this exchange may be replaced, by the enthalpy of the exchange since the entropy change is approximately equal to zero, and thus for the compound $\{M_xR_{1-x}\}{\cdot}[M_{1-x}R_{1+x}]O_4$, where the compound is a normal spinel when $x = 1$ and inverse spinel when $x = 0$, the equilibrium constant of the degree of inversion is given by

$$\Delta E \text{ (OSPE)} = -RT \log K = -RT \log \frac{(1-x)^2}{x(1+x)}$$

In this approximation it is assumed that the enthalpy of exchange is equal to the energy of exchange, and the thermal entropy of exchange is equal to zero. Both of these imply that there is no change in heat capacity when this exchange is carried out, which is not normally the case, although the effect is small.

Results of quantum-mechanical calculations (Dunitz and Orgel, 1957) have given values for the OSPEs of a number of transitional metal ions and the degree of inversion of mixed spinels

$$\{M_{1-x-y}N_{y-z}R_{x+z}\}[M_xN_zR_{2-x-z}]$$

which is composed of $1 - y$ moles of MR_2O_4 and y moles of NR_2O_4 can be calculated using these data with some confidence. It follows from the equation given above for the equilibrium constant of the exchange process, that the degree of inversion of any spinel will decrease as the temperature increases, and the magnetic properties are lost at the Curie temperature, as a result of the order–disorder transformation.

There are therefore two factors of importance in the production of magnetic spinels. The first of these is the oxygen potential required to be applied at the sintering temperature, in order to maintain the cations in the correct valencies, and the magnitude of the temperature cycle which must be used to obtain satisfactory sintering. This latter must always involve a final quench to room temperature, unless it is possible to control the oxygen potential of the sintering atmosphere during a slower cooling process. Spinels may usually be assumed to be stoichiometric compounds, or as having a very narrow range of non-stoichiometry.

DropBooks

Another important group of magnetic materials is the rare-earth garnets, of composition $3R_2O_3{\cdot}5Fe_2O_3$, with 8 formula units per unit cell. There are 24 tetrahedral and 16 octahedral sites in the unit cell which are occupied by ferric ions and 24 sites of dodecahedral symmetry which are occupied by the rare earth ion or, in the important yttrium iron garnet, by Y^{3+} ions. The spins in the tetrahedral and octahedral Fe^{3+} ion sites are coupled by superexchange, and hence there are 2×5 unpaired spins due to the ferric ions for each formula. The rare earth ions, all M^{3+} ions, occupy the dodecahedral sites and their unpaired spins are coupled weakly with the ferric ions on the tetrahedral sites. The alignment of these electron spins is a function of temperature.

There is a temperature for most of the rare earth garnets at which the unpaired spins of the rare earth ions and the ferric ions produce zero magnetization, the compensation point. This temperature decreases for Ga^{3+} to Lu^{3+} from room temperature to zero Kelvin. Yttrium iron garnet has no compensation point. The rare earth ions in this structure can be readily substituted one for another, and so it is possible to prepare garnets with magnetic properties which vary over a range of temperature, some of which produces constant properties. It can be seen that providing the oxygen potential in the gas phase

during sintering is sufficiently high to retain the iron ions in the ferric state, the only process control which is required is that of the temperature cycle.

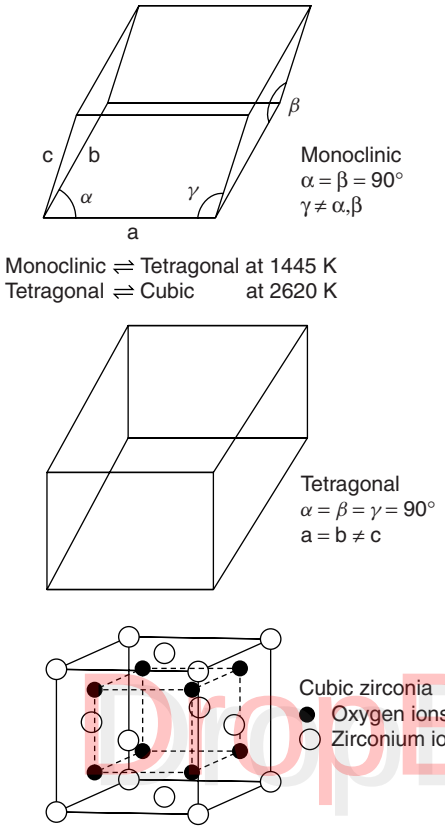
The magnetoplumbites have a hexagonal structure, and are of composition $BaO:Fe_2O_3$. There are four layers of oxide ions which alternate with two layers of Ba^{2+} ions in a ten-layer repeat pattern. The Fe^{3+} ions fit into the interstices of this structure, some with tetrahedral co-ordination, some with octahedral co-ordination and some with five-fold co-ordination of oxygen ions. In the unit cell there are 16 Fe^{3+} ions with spins in one direction and eight Fe^{3+} ions with spins anti-parallel to these. The net spin magnetic moment is therefore $8 \times 5\,\mu$ magnetons. The barium ions can be substituted with magnetic ions, such as cobalt, to vary the magnetic properties.

The spinel and magnetoplumbite magnetic materials differ considerably in behaviour, and therefore have different applications. The spinels are 'soft' magnets which respond rapidly to changes in the direction of the magnetizing field, H, and hence have a narrow $B-H$ curve where B is the induced magnetization, and are useful in transformer coils. The magnetoplumbites on the other hand are 'hard' magnets which show a broad $B-H$ curve, indicating a high hysteresis loss and are used in loudspeakers and other permanent magnet applications where the retention of magnetization is necessary over a period of time. Finally the garnets are used extensively in microwave circuits where the flexibility of design of the magnetic properties which accompanies the variation in the rare-earth ion composition can be usefully applied.

Solid electrolyte sensors and oxygen pumps

Four solid oxide electrolyte systems have been studied in detail and used as oxygen sensors. These are based on the oxides zirconia, thoria, ceria and bismuth oxide. In all of these oxides a high oxide ion conductivity could be obtained by the dissolution of aliovalent cations, accompanied by the introduction of oxide ion vacancies. The addition of CaO or Y_2O_3 to zirconia not only increases the electrical conductivity, but also stabilizes the fluorite structure, which is unstable with respect to the tetragonal structure at temperatures below 1660 K. The tetragonal structure transforms to the low temperature monoclinic structure below about 1400 K and it is because of this transformation that the pure oxide is mechanically unstable, and usually shatters on cooling. The addition of CaO stabilizes the fluorite structure at all temperatures, and because this removes the mechanical instability the material is described as 'stabilized zirconia' (Figure 7.2).

The addition of MgO leads to the formation of a narrow range of solid solutions at high temperature, which decompose to precipitate inclusions of tetragonal ZrO_2 dispersed in cubic zirconia. The material, which functions as a solid electrolyte, has the added advantage that the inclusions stop the propagation of any cracks which may arise from rapid temperature change.



DropBooks

Figure 7.2 *The structural changes of zirconia as a function of temperature. The placement of the ions is shown only in the cubic oxide structure*

This mechanism of crack inhibition is almost unique among ceramic systems, which do not undergo the plastic deformation under stress which is found in metallic systems (Figure 7.3).

The electrical conductivities of the solid solutions increase markedly up to a solute concentration of about 5 mole per cent, after which further addition of solute no longer increases the conductivity, but does in some instances decrease it. This is used as evidence that the solid no longer consists of a single phase, but contains small amounts of a second, non-conducting, compound between the two oxides, e.g. $CaZrO_3$. Evidence for this is that corresponding solutions with the higher atomic weight alkaline earth elements, strontium and barium, show no sign of the dilute solution, but form the zirconate only.

The electrical conductivities of the solid electrolytes vary over approximately two orders of magnitude, in the sequence Bi > Ce > Zr > Th

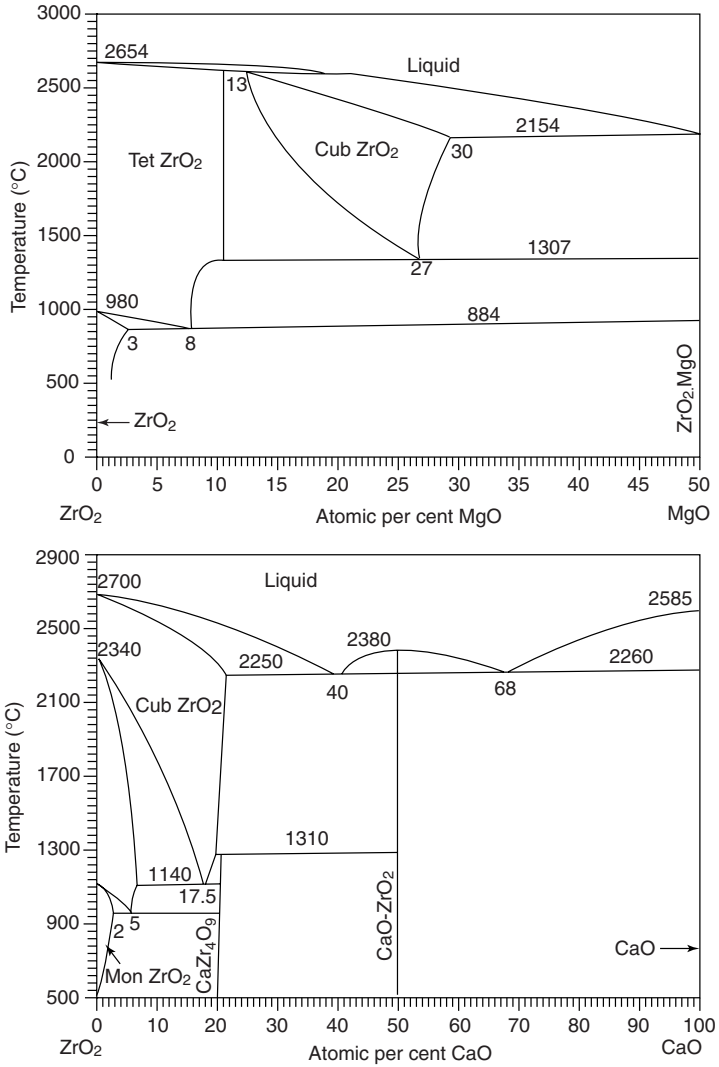


Figure 7.3 *Phase diagrams for the systems $MgO–ZrO_2$ and $CaO–ZrO_2$, showing the lower temperature stability of the $CaO–ZrO_2$ system, which also includes the phases $CaZr_4O_9$ and the perovskite $CaZrO_3$*

oxides, and a range of $10^{-1}-10^{-2}$ S at 1000 K. The ionic transport number in these solid solutions is close enough to unity for the materials to be used in electrochemical cells as the electrolyte between electrodes pasted on the opposite faces of the electrolyte sample. There is a small component of semiconductivity in all of these materials, which may be obtained either

by a measurement of the conductivity as a function of pressure, when the effect is large, as in ThO_2-based electrolytes in the oxygen pressure range $10^{-6}-1$ atmos, or by measurement of the oxygen permeability of the electrolyte. Each electrode in this arrangement is usually platinum sheet in contact with a gas of fixed oxygen potential or a mixture of substances, which has a defined oxygen potential at a given temperature. Examples of these electrodes for which reliable data have been obtained are gas mixtures of oxygen and inert gases, metal/metal oxide or oxide mixtures having two contiguous valencies of a given cation e.g. MnO/Mn_3O_4 and oxygen solutions in solid or liquid metals and alloys. This property is the basis for the use of solid electrolytes as *oxygen sensors*, since if the oxygen potential of one electrode is fixed at a known level, pO_2, that of the other electrode, $p'O_2$, can be obtained from the thermodynamic equation

$$E = \frac{RT}{4F} \ln(pO_2/p'O_2) = 4.96 \times 10^{-2} T \log(pO_2/p'O_2)$$

where E is the EMF of the cell in mV.

Such an electrochemical arrangement can also be used to transport oxygen from one electrode to the other by the imposition of an externally applied potential. This technique, known as 'coulometric titration', has been used to prepare flowing gas mixtures of oxygen/argon with a controlled oxygen partial pressure, to vary the non-stoichiometry of oxides, to study the thermodynamics of dilute oxygen solutions in metals, and to measure the kinetics of metal oxidation, as examples.

DropBooks

A unique application of the solid oxygen electrolytes is in the preparation of mixed oxides from metal vapour deposits. For example, the ceramic superconductors described below, have been prepared from mixtures of the metal vapours in the appropriate proportions which are deposited on the surface of a solid electrolyte. Oxygen is pumped through the electrolyte by the application of a polarizing potential across the electrolyte to provide the oxidant for the metallic layer which is formed.

Another application is in the oxidation of vapour mixtures in a chemical vapour transport reaction, the attempt being to coat materials with a thin layer of solid electrolyte. For example, a gas phase mixture consisting of the iodides of zirconium and yttrium is oxidized to form a thin layer of yttria-stabilized zirconia on the surface of an electrode such as one of the lanthanum-strontium doped transition metal perovskites $La_{1-x}Sr_xMO_{3-z}$, which can transmit oxygen as ions and electrons from an isolated volume of oxygen gas.

The diffusion coefficient of oxygen in solid silver was measured with a rod of silver initially containing oxygen at a concentration c_0 placed end-on in contact with a calcia–zirconia electrolyte and an Fe/FeO electrode. A constant potential was applied across the resulting cell

Pt, Fe/FeO|CaO–ZrO_2|Ag[O], Pt

which would apply an oxygen partial pressure at the face of the silver rod which was so low that the oxygen content of the metal at this surface was reduced to practically zero. This potential can be calculated from the equation given above, knowing the relation between oxygen pressure and the oxygen content of silver. The current density, i, drawn through the cell corresponds to the flux of oxygen, j, leaving the face of the silver by the equation

$$i = 2Fj; \quad j = D\frac{\partial c}{\partial x}_{x=0}$$

The solution of the diffusion equation for the boundary conditions

$$c = c_0 \text{ and } 0 < x < \infty \text{ at } t = 0$$

and

$$c = 0 \text{ for } x = 0 \text{ and } t > 0$$

is

$$c = c_0 \text{ erf}\frac{x}{2\sqrt{Dt}}$$

and hence

$$j = \frac{Dc_0}{(\pi Dt)^{1/2}}; \quad i = \frac{2Fc_0\sqrt{D}}{\sqrt{\pi t}}$$

where F is Faraday's constant. Diffusion coefficients in oxides have also been obtained by the use of this potentiostatic method.

An instructive use has been made of the solid electrolyte, AgI, which conducts by the migration of silver ions. If this material is used as an electrolyte in the cell

$$\text{Ag}/\text{Ag}_2\text{S}|\text{AgI}|\text{Ag}_2\text{S}/p\text{S}_2(\text{g})$$

the sulphur pressure in the gas phase can be obtained, knowing the sulphur potential of the $\text{Ag}/\text{Ag}_2\text{S}$ mixture. If the sulphur gas is replaced with a sample of nickel, the kinetics of nickel sulphide, NiS, formation can be measured by coulometric titration. In the cell

$$\text{Pt, Ag}|\text{AgI}|\text{Ag}_2\text{S}|\text{NiS}|\text{Ni, Pt}$$

the passage of current with the silver metal as the cathode, causes the removal of silver from the sulphide, and the transport of nickel ions across the nickel sulphide, where more nickel sulphide is formed. Since Ag_2S has a negligible range of non-stoichiometry, the removal of silver from this electrode liberates sulphur at the dissociation pressure of the $\text{Ag}/\text{Ag}_2\text{S}$ mixture. As there is no accumulation of charge in the assembly, the current which is passed must represent the transport of nickel ions through the sulphide, which is equal

to the flux of silver ions through the AgI. If a constant potential is applied to the system, the current which is drawn through the assembly will be a function of time, decreasing as the nickel sulphide layer thickens, and the cell resistance increases correspondingly. The dependence of the current, i, in this potentiostatic measurement is related to the thickness of the nickel sulphide layer, and hence to the amount of nickel transferred as ions across the sulphide by the equation

$$X = \frac{V_m}{2F} \int_0^t i \, \mathrm{d}t$$

where x is the thickness at the time t, and V_m is the molar volume of NiS.

Studies of the removal of oxygen from gas mixtures by means of a solid electrolyte, have shown that this process is considerably enhanced by the presence of a small partial pressure of water vapour, which is presumably adsorbed on the electrolyte, and reduced to hydrogen. This can then react with oxygen in the gas phase to re-form water. The oxygen contents of very dry gases are not so easily transferred to the electrolyte, and when a large current is drawn through the cell, greater than about $100\,\mathrm{ma\,cm^{-2}}$, it is possible for the electrolyte to become reduced to a semiconductor at the gas–electrolyte interface.

Oxygen sensors can also be made from substances which conduct by fluoride ion conduction, providing a composite is made between a stable fluoride and the corresponding oxide. For example if a 10 per cent dispersion of La_2O_3 is made in LaF_3 containing 10 mole per cent SrF_2, the composite responds quantitatively to a difference in oxygen potential of two electrodes, such as two platinum sheets, one on each side of a sintered sample of the composite, in contact with separate oxygen partial pressures as in the cell,

$$p'O_2/Pt|LaF_3 - SrF_2 + SrO|Pt/p''O_2$$

Similarly if this electrolyte is made into a composite with SrS, SrC_2 or SrH_2, the system may be used to measure sulphur, carbon and hydrogen potentials respectively, the latter two over a restricted temperature range where the carbide or hydride are stable. The advantage of these systems over the oxide electrolytes is that the conductivity of the fluoride, which conducts by F^- ion migration, is considerably higher.

Solid oxide fuel cells and membranes

Solid oxide fuel cells consist of solid electrolytes held between metallic or oxide electrodes. The most successful fuel cell utilizing an oxide electrolyte to date employs ZrO_2 containing a few mole per cent of yttrium oxide, which operates in the temperature range 1100–1300 K. Other electrolytes based

DropBooks

on cerium oxide, CeO_2, mixed with rare earth oxides M_2O_3, which might operate in the temperature range 800–1000 K, are under development but have not yet reached commercially viable application. The electrode materials are mainly perovskites with the composition $La_{1-x}Sr_xMO_{3-z}$, where x takes values between 0.1 and 0.3, M is one of the transition metals Mn, Fe, Co, Ni, and z is a function of the oxygen potential and temperature. The transition metals are multivalent and the oxygen potential at a given temperature determines the ratio of valencies, and hence the positive hole concentration and electrical conductivity. Iron, cobalt and nickel undergo a 2^+–3^+ valency change, but manganese has the valencies 2, 3, 4^+ under normal operating conditions. The thermodynamic data for these oxides show that nickel is reduced to the single 2^+ valency at higher oxygen potentials than cobalt, which in turn is more easily reduced than iron. Finally, manganese can maintain a significant mixture of valencies between 3^+ and 4^+ at the highest industrially viable oxygen potential, and between 2^+ and 3^+ at the lowest oxygen potential.

In the fuel cell which has a high oxygen potential at one electrode, the cathode, and a low oxygen potential resulting from the oxidation of hydrocarbons at the anode, the cell functions as an oxygen transfer cell in which the reaction

$$O_2(g) + 4e^- = 2O^{2-}$$

occurs at the cathode, and reactions such as

$$CH_4 + 4O^{2-} = CO_2 + 2H_2O + 8e^-$$

occur at the anode. The cell thus combines the two functions of the oxygen pump in removing oxygen from one gas stream, and delivering oxygen at the other. In light of the remarks above concerning oxygen pumping, the problems of the reactions at the cathode which were encountered are related to the adsorption and dissociation of oxygen at the cathode,

$$O_2 \longrightarrow 2\{O\}_{ads}$$

which will depend on the presence of sufficient unoccupied active adsorption sites on the surface of the electrode, and the subsequent transfer of electrons to the adsorbed oxygen atoms.

Alternative mechanisms which have been proposed which involve the surface oxide ion vacancies such as

$$(1/2)O_2 + 2e^- + V'' \longrightarrow O^{2-}$$

and

$$O_2 + 2e^- + 2V'' \longrightarrow 2O^-$$

followed by

$$2O^- + 2e^- \longrightarrow 2O^{2-}$$

The overall process may be described in reaction kinetics terms as

$$O_2 + 4e^- + 2V'' \longrightarrow 2O^{2-}; dO_2^-/dt = kT\, pO_2 c_{e^-}^4 \{V''\}^2$$

showing that the rate of formation of oxide ions is a function of the surface concentrations of vacancies and electrons at a constant oxygen pressure. The rates of supply of these two species are a function of the diffusion coefficient of oxide vacancies in the oxide, and the electronic conductivity. Due to the much higher mobility of electrons in non-stoichiometric oxides than oxide ions, the rate determining step in the overall process must be the rate of supply of oxide vacancies at the surface, which is proportional to the oxygen diffusion coefficient in the oxide.

This mechanism also suggests that the perovskite electrodes should be chosen so that the cathode material undergoes reduction-oxidation at high oxygen potential, in order to provide the electron supply for the charge transfer to the adsorbed oxygen atom, and the anode material undergoes the redox reaction at low oxygen potential for the discharge process. The cobalt and manganese perovskites satisfy the cathode requirements better than the iron or nickel compounds, while there is little to choose between the iron and manganese compounds at the anode.

DropBooks

In a series of studies of oxygen transfer with ceria-based electrolytes at 1000 K, the volume of gas evolved at the anode was measured as a function of the current passing through the cell when an external voltage was applied. (Doshi *et al.*, 1994). It was found that the transfer of oxygen at the cathode from pure oxygen was rate-determining for the evolution of oxygen at the anode, i.e. to the hydrocarbon in a fuel cell, and that the manganese perovskite performed slightly better than the iron perovskite at the anode up to a current of 1250 ma cm^{-2}. Both electrodes performed satisfactorily at the cathode in an atmosphere of pure oxygen, but there was a decreased efficiency of transfer in air when compared to pure oxygen, more than could be accounted for by the decrease of the oxygen partial pressure. It is clear, therefore, that it is the kinetics of the transfer of oxygen from and to these electrodes which may limit the efficiency of a solid oxide electrolyte fuel cell. As a general rule the transfer kinetics improve in direct relation to the diffusion coefficient of oxygen in the electrode or electrolyte. It is also clear that as higher current densities are achieved in a cell, the effect of the electrode surface transfer kinetics will play a more rate-determining role, and this will be an important technical limitation to cell performance. For example, when a Bi_2O_3/SrO electrolyte, which has a higher oxygen conductivity than the ceria-based electrolyte, was used in these experiments, it was found that although current densities as high

as 1000 ma cm^{-2} could be readily achieved, there was evidence of reduction of the electrolyte at higher current densities when the iron perovskite was used as the cathode. Steele (1994) reported that a cobalt perovskite $La_{0.8}Sr_{0.2}CoO_{3-x}$ electrode has a surface exchange constant of 5×10^{-6} at 1000 K which is 100 times higher than that of the manganese-based perovskite, and so this electrode would be expected to perform better than the manganese or iron-based electrodes.

A significant problem in the combination of solid electrolytes with oxide electrodes arises from the difference in thermal expansion coefficients of the materials, leading to rupture of the electrode/electrolyte interface when the fuel cell is, inevitably, subject to temperature cycles. Insufficient experimental data are available for most of the electrolytes and the perovskites as a function of temperature and oxygen partial pressure, which determines the stoichiometry of the perovskites, to make a quantitative assessment at the present time, and mostly decisions must be made from direct experiment. However, Steele (loc. cit.) observes that the electrode $La_{0.6}Sr_{0.4}Co_{0.2}Fe_{0.8}O_{3-x}$ functions well in combination with a ceria–gadolinia electrolyte since both have closely similar thermal expansion coefficients.

Some perovskites can also function as oxygen membranes which permit the transmission of oxygen uniquely from a mixture of gases containing oxygen, such as air, to a gas containing oxygen at a lower partial pressure such as an initially pure inert gas or hydrocarbon. This is possible because these oxides transmit both oxygen ions and positive holes, which also travel down the oxygen potential gradient, and hence essentially transmit oxygen atoms. Another way in which this behaviour can be achieved is by the use of an electrolyte/metal composite material, such as the Bi_2O_3–Er_2O_3 electrolyte containing 40 vol% of silver, or stabilized ZrO_2 containing a dispersed phase of carbide or silicide. These combinations allow electrons to flow through the metal phase to neutralize the charge transfer of the oxide ions through the electrolyte.

Ceramic superconductors

The superconducting oxides include both perovskites and Ruddlesden–Popper compounds which have an orthorhombic arrangement of cubic cells, alternatively of the perovskite and sodium chloride structures. The common feature of all of these is the presence of copper as a major component. The first ceramic superconductor was a lanthanum–strontium substituted cuprate ($La_{1-x}Sr_xCuO_{4-z}$), which is a perovskite, but subsequently the inter-oxide compound Y_2O_3 2BaO 3CuO, commonly referred to as a 123 compound, was shown to have superior performance. The speculation concerning the conduction mechanism is that this involves either Cu^{3+}–Cu^{2+} positive hole

transfer, or $O-O^{2-}$ positive holes in the anion lattice. It is clear from this description that the non-stoichiometric composition of samples of these materials will depend on the oxygen potential at the high temperature end of the sintering cycle, and on the rate of the quench to room temperature subsequently. The experimental data show that the conductivity of these materials is, as would be expected, higher when a high oxygen potential is used during sintering, than in vacuum treatment. This would promote both Cu^{2+} oxidation and the formation of O^- ions by oxygen adsorption on vacant sites in the anionic structure.

The thermodynamics of the 123 compound have been extensively studied and writing the formula as $(YBa_2Cu_3)O_z$ it has been shown that at 1000 K the value of z changes from 6 to 6.6 in the oxygen pressure range 10^{-4} to one atmosphere of oxygen. Above this temperature, the 123 compound decomposes to 211 plus barium cuprate and cuprous oxide according to the reaction

$$2(YBa_2Cu_3)O_6 \longrightarrow Y_2BaCuO_5 + 3BaCuO_2 + Cu_2O$$

The oxygen pressure at which this decomposition begins to occur can be represented as a function of temperature by the equation

$$\log_{10} p(O_2) = -12\,050/T + 7.64$$

and at 1000 K, the decomposition pressure is 4×10^{-5} atmos (Gaskell and Kim, 1995).

For comparison, the decomposition of pure CuO to Cu_2O can be represented by the equation

$$\log_{10}(pO_2) = -14\,935/T + 9.98$$

and the decomposition pressure is approximately 10^{-5} atmos at this temperature. It follows that the activity of CuO in the superconductor at $z = 6$ is about 0.7, allowing for the error in the data.

The early ceramic superconductors were produced as powders by the mix-fire procedure from the component oxides, but some of the more recently discovered and more successful superconducting compounds contain volatile oxides, such as Bi_2O_3 and Tl_2O. In the case of the bismuth containing 2223 and 2212 compounds in the Bi–Sr–Ca–Cu–O system, the temperature of firing can be reduced by the substitution of 10–20% PbO for the bismuth oxide, which leads to the formation of a low-melting Ca_2PbO_4 compound which accelerates compound formation. The lead-doped 2223 compound has a wide range of stoichiometry, depending on the oxygen partial pressure and temperature. In air at 1000 K, a value of z in $Bi_{1.8}Pb_{0.4}Sr_2Ca_2Cu_3O_z$ greater than 10.3 can be obtained, and at the same temperature, this value decreases to 10 in an atmosphere of oxygen at a partial pressure of 10^{-3}. At the lower

DropBooks

pressure decomposition producing Cu_2O occurs at around this temperature. If the high-z compound is cooled slowly in air the stoichiometry can be retained.

For the 2223 compound of the Tl–Ba–Ca–Cu–O compound the loss of thallium is reduced by surrounding a pre-fired, and thallium-deficient, sample with powder of the compound and refiring. These substances also show a temperature–oxygen partial pressure stability relationship, similar to the classical 123 compound, but the details have not yet been elucidated.

The redistribution of fission products in UO_2 nuclear fuels

During the operation of nuclear power reactors, which are fuelled with ceramic UO_2 fuel rods, the fission of the U^{235} nuclei leads to the formation of fission products which are isotopes of elements in all of the Groups of the Periodic Table. The major fission products, present in 1–10% abundance, fall into five groups divided according to the chemical interaction of each product with the fuel:

Metals in a separate phase:Mo, Tc, Rh, Ru and Pd.
Oxides which are not soluble in UO_2:Sr and Ba.
Oxides which dissolve in UO_2:Zr, Ce, Rare earths.
Volatile elements:Cs, Te, Br, I.
Stable inert gases:Xe, Kr.

The fuel rods operate in a temperature gradient from 2000 K in the centre to 800 K at the surface of the rods which is in contact with the zirconium cladding. There is a redistribution of the fission products to form new chemical combinations, and in some cases to be driven down the temperature gradient by chemical potential gradients in the gaseous state. The products of fission are radioactive neutron-rich elements in the mass groups 82–100 and 128–150. The distribution of isotopes within these two atomic mass groups results from the loss of 2–3 neutrons per fission and the emission of about 200 MeV of mass-energy.

The chemical identities of the fission products determine their subsequent redistribution, those elements which are in the gaseous state at the temperature of the operation migrating to the cooler exterior of the fuel rods, and the less voltile elements undergoing incorporation in the fuel rod in solid solution. Thus caesium and iodine migrate to the gas fill which surrounds the fuel rod, and elements such as the rare earths and zirconium are accommodated in solid solution in UO_2 without significant migration along the fuel rod radius. Strontium and barium oxidize to form separate islands which can be seen under the microscope.

As a result of nuclear fission the oxygen/metal ratio increases in the fuel across the wide range of non-stoichiometry of UO_{2+x}. The oxygen potential of

the oxide varies across the fuel radius due not only to the temperature gradient, but also the change in the metal/oxygen ratio. One of the fission products, molybdenum, can be oxidized after fission to form MoO_2, which is also a non-stoichiometric oxide but of very narrow range of composition, depending on the oxygen potential in the fuel at the site of the fission event which produced molybdenum. The extent of burn-up of and non-stoichiometry of the fuel is thus indicated, either by the Mo/MoO_2 ratio, or by the metal/oxygen ratio of the MoO_2.

The elimination of pores by migration towards the centre of the fuel rod, probably occurs by vapour phase transport of $UO_2(g)$ down the local temperature gradient thus moving the pores in the grain structure from the lower to the higher temperature in the form of gas bubbles which finally reach the centre of the fuel rod. The grain size of the fuel rod material, after some days in service can be roughly separated into three zones, The coolest from about 1050–1750 K, preserves the original grain structure of the fuel rod. The next zone, in the temperature range 1750–2100 K, shows considerable equi-axed grain growth, and the central zone, up to 2300 K, has relatively large columnar crystals. The vapour pressure of UO_2 varies across these zones from 10^{-20} to 10^{-9} across the coolest zone, 10^{-9} to 10^{-6} across the middle zone, and 10^{-6} to 10^{-5} atmos across the central zone. These data are consistent with grain growth due to vapour phase transport.

DropBooks

Bibliography

A. Magnéli. *Ark. Kemi*, **1**, 223, 513 (1950).
R.D. Shannon and C.T. Prewitt. *Acta Cryst.*, **B25**, 925 & **B26**, 1046 (1969).
R.J. Hawkins and C.B. Alcock. *J. Nuclear Mater.*, **26**, 112 (1968).
T. Sorenson (eds). *Nonstoichiometric Oxides*. Academic Press New York (1981).
F. Koch and J.B. Cohen. *Acta Cryst.*, **B25**, 275 (1969).
R.L. Porter, P.S. Nicholson and W.W. Smeltzer. Sintering Processes, *Mater. Sci. Res.*, **13**, 129 (1979).
K.G. Nickel (ed.). *Corrosion of Advanced Ceramics.* NATO ASI Series, Kluwer Academic (1994) TA 455 C43C67.
D. Segal. *Chemical Synthesis of Advanced Ceramic Materials*. Cambridge University Press (1989).
L.L. Hench and J.K. West. *Principles of Electronic Ceramics*. John Wiley and Sons New York (1990).
I.J. Hastings. (ed.). *Fission Product Behavior in Ceramic Oxide Fuel*. Adv. in Ceramics **17**, Amer. Ceram. Soc. (1986).
A.L. Moulson and J.M. Herbert. *Electroceramics*. Chapman and Hall London (1992).
R. Beyers and B.T. Ahn. Thermodynamic considerations in superconducting oxides, *Ann. Rev. Mater. Sci.*, **21**, R.A. Huggins (ed.). (1991).
R. Doshi, Y. Shen and C.B. Alcock. *J. Solid State Ionics*, **68**, 133 (1994).
B.C.H. Steele. *J. Power Sources*, **49**, 1 (1994).
D.R. Gaskell and Y.S. Kim. *High Temperature Materials Chemistry*. The Institute of Materials, London (1995).

Chapter 8

Gas–solid reactions

In this chapter a number of reactions are discussed in which the rate-determining step occurs in the solid state, and the solid is chemically changed by the reaction.

The oxidation of metals and compounds

The parabolic rate law

If we postulate that the chemical potentials of all species are equal in two phases in contact at any interface, then Einstein's mobility equation may be simply applied, in Fick's modified form, to describe the rate of a reaction occurring through a solid product which separates the two

$$J_x = -Dc\frac{\Delta \log a}{\Delta x}$$

reactants in a diffusion controlled reaction. $\Delta \log a$ is the activity difference between the two faces of the reaction product and Δx is the thickness of the product.

When the concentration, c, and diffusion coefficient, D of the diffusing species in the reaction product are constant, then the rate of growth of the product in thickness will be given by the simple equation

$$\frac{\mathrm{d}x}{\mathrm{d}t} = \frac{K}{x}; \quad x^2 = 2Kt$$

where K is a constant which yields a *parabolic* law of growth of reaction product as a function of time. This law is frequently observed when a metal is oxidized by a gaseous phase, so that the oxide layer forms a complete diffusion barrier between metal and gas.

A parabolic rate law will also be obtained if part or even all, of the diffusion through the product layer is by grain boundary diffusion rather than diffusion through the volume of each grain. The volume diffusion coefficient is quite simply defined as the phenomenological coefficient in Fick's laws. The grain boundary diffusion must be described by a product, $D_b\delta$, where δ is the grain

boundary thickness. The rate constant in the parabolic law should be revised to take account of these two parallel reaction paths, and one way is by defining an effective diffusion coefficient D_{eff} through the equation

$$D_{\text{eff}} = (1 - \phi)D_V + \phi D_b \delta$$

where ϕ is the fraction of transport due to grain boundary diffusion. The overall rate constant then can be simply expressed by

$$k_{\text{eff}} = (1 - \phi)k_{\text{volume}} + \phi k_{\text{boundary}}$$

It will be seen that both processes operate under the same oxygen potential gradient and therefore the effects are additive. Because the activation energy for grain boundary diffusion is very much lower than that for volume diffusion, the boundary contribution is predominant at low temperature, and the relative contributions at high temperatures is dependent on the grain size, although, generally, the volume diffusion predominates at high temperatures.

The linear and logarithmic rate laws

If the cross-sectional area of the product remains relatively constant but the product layer cracks during growth and so does not impede the access of the gaseous reactants and products to the reacting solid, then a linear rate law is observed

$$\frac{\mathrm{d}x}{\mathrm{d}t} = k'; \quad x = k't$$

DropBooks

The general circumstances under which the linear law will apply to a given reaction have not been very clearly elucidated. Any mechanical or thermal shock to the product layer which can cause the rupture of the layer will lead to a departure from the parabolic law, but unless the cracking occurs continuously, a linear law need not be observed. Other possibilities such as the sealing of cracks during propagation may lead to other time dependencies which can be described by a logarithmic law. This behaviour is also observed when the rate-controlling step in a reaction is transport via the gas phase across sealed-off pores in the product layer.

The logarithmic law is also observed when the oxide film is an electrical insulator such as Al_2O_3. The transport of electrons through the oxide is mainly due to a space charge which develops between the metal–oxide interface and the oxide–gas interface. The incorporation of oxygen in the surface of the oxide requires the addition of electrons, and if this occurs by a charging process

$$(1/2)O_2 + O^{2-} \longrightarrow 2O^-$$

on the surface, there is now an electric potential gradient pulling electrons from the metal surface and into the oxide–gas interface. The transfer of electrons

from the metal will generate the cation required for normal oxide formation

$$M + 2O^- \longrightarrow MO + O^{2-}$$

This process will clearly slow down as the oxide film thickens and hence

$$\frac{dx}{dt} = \frac{k}{t}; \quad x = k \log t$$

A further complication is that in these slowly growing oxide films, the spread of the oxide across the metal surface is limited in the early stages by nucleation and growth control. The bare patches of metal between the oxide nuclei will clearly be exposed to a higher oxygen potential and new oxide nuclei will grow at a different initial rate than on the existing nuclei.

It is clear that the rate of growth of a reaction product depends upon two principal characteristics. The first of these is the thermodynamic properties of the phases which are involved in the reaction since these determine the driving force for the reaction. The second is the transport properties such as atomic and electron diffusion, as well as thermal conduction, all of which determine the mobilities of particles during the reaction within the product phase.

Oxidation of metals forming more than one oxide

A number of metals, such as copper, cobalt and iron, form a number of oxide layers during oxidation in air. Providing that interfacial thermodynamic equilibrium exists at the boundaries between the various oxide layers, the relative thicknesses of the oxides will depend on the relative diffusion coefficients of the mobile species as well as the oxygen potential gradients across each oxide layer. The flux of ions and electrons is given by Einstein's mobility equation for each diffusing species in each layer

$$J_{Cu} = -D_{Cu}\frac{d \ln a_{Cu}}{dx} = D_{Cu}\frac{x_0}{2x_{Cu}}\frac{d \ln pO_2}{dx}$$

and the situation when two oxides are formed, e.g. Cu_2O/CuO, can be represented by the diagram

$$\text{Cu metal} \left| \begin{array}{ccccc} & Cu_2O & | & CuO & | \text{ air} \\ J\{Cu^+\} + Je^- & | & J\{Cu^{2+}\} + Je^- & | & \text{air} \end{array} \right.$$

since the metallic ions migrate in both oxides. The overall mechanism of the oxidation may be parabolic, but since the two oxides usually have different crystal structures, the possibility of epitaxial growth, which would ensure that each oxide layer seals off the metal and the lower oxide from direct access of the gas, seldom occurs. Instead, mixed kinetics which can arise from the parabolic formation of the lower oxide and a linear rate of formation of the

higher oxide, is frequently observed. The apparent behaviour of the overall system will be determined by the parabolic growth of the lower oxide at the high temperature range, and the linear growth of the higher oxide will predominate at the lower temperatures.

In part the parabolic law may also apply to multilayer oxide systems where the cation diffusion coefficient is much higher in the lower oxide than in the higher oxide, which, growing as a thin layer, undergoes plastic deformation at high temperatures, thus retaining the overall oxide layer as impervious to entry of the gas.

When a sample of iron oxide, FeO, is oxidized the cations and electrons are drawn from the oxide to form the layer of the next oxide, Fe_3O_4, and the ferrous oxide layer shrinks not only because ions are used up in making the new magnetite layer, but the magnetite layer is thickened at the FeO/Fe_3O_4 because the extraction of ferrous ions leaves magnetite behind. Thus if a Kirkendall experiment is conducted by placing gold wires at the original surface of the FeO the interface moves towards the centre of the sample because of the effects of these two processes.

Since the relative thicknesses of the oxides which are formed by a multivalent element depend on the oxygen potential at each phase boundary, and the diffusion coefficient of the mobile species in each oxide, it frequently occurs that microscopic observation of the oxide layers on the elements fails to show the presence of some of the equilibrium complexity of the metal–oxygen system. For example, although the titanium–oxygen system forms many oxides, TiO, Ti_2O_3, Ti_3O_5 and the Magneli phases as well as TiO_2, the dioxide is the only oxide which appears in the parabolic law oxidation of the metal, under normal circumstances, up to 1000°C. Above this temperature, the lower oxides have been found in the scale which grows by a linear rate mechanism. Between room temperature and 600°C, the rate equation has a complex dependence on temperature, due to the influence of the formation of the oxygen solution in the metal which becomes more significant with increasing temperature.

DropBooks

The oxidation of nickel:volume and grain boundary diffusion

Nickel oxide, NiO, which is the only oxide formed by nickel during oxidation in air, has a very narrow range of non-stoichiometry, the maximum oxygen/nickel ratio probably being 1.001. The oxygen dependence of the deviation from non-stoichiometry is $p'^{1/6}O_2$, and hence the oxidation rate would be expected to depend on the oxygen partial pressure surrounding a nickel sample at high temperatures in the same way. Measurements of the oxidation rate fulfill this expectation at temperatures of 1000°C and above, but at lower temperatures there is clearly a major contribution from processes occurring more rapidly than could be accounted for using the known volume diffusion coefficient of nickel in the oxide as the major process. The relative

diffusion coefficients have been measured for both nickel and oxygen for volume and grain boundary diffusion. The data show that the cation volume diffusion coefficient is 10^2 times larger than the anion diffusion coefficient, and the grain boundary diffusion coefficients of both species are about 10^2 times larger than the volume coefficients. The enhanced oxidation rate as temperatures less than 1000°C can be quantitatively accounted for by assuming that grain boundary diffusion of nickel ions is rate controlling. There is an epitaxial relationship between the nickel ions in the oxide layer and the nickel metal substrate, which is accommodated by the insertion of line dislocations at regularly spaced intervals. These dislocations effectively eliminate the stress at the interface which might arise due to the 18% difference in the f.c.c. lattice parameters of the metal and its monoxide.

The addition of a small amount of chromium at concentrations less than 1%, increase the oxidation rate proportionately to the chromium content. This is to be expected since the replacement of three nickel ions in NiO by two chromium ions in Cr_2O_3 will introduce one cation vacancy/Cr_2O_3 molecule.

$$Cr_2O_3 \longrightarrow 2Cr^{3+} + V''Ni + 3O^{2-}$$

Yttrium, on the other hand, which has a larger cation radius than Cr^{3+}, appears to affect the grain boundary cation diffusion and not the volume diffusion of Ni^{2+}. The effects of the addition of small amounts of yttrium to nickel is to decrease the rate of the low temperature grain-boundary dominated oxidation kinetics.

The oxidation of silicon

The oxidation of silicon proceeds by two mechanisms, one being the transmission of oxygen molecules through voids in the structure (permeation), and the other being the migration of atoms along the oxide ion network. The relative importance of these two mechanisms has been elucidated by the use of a 'double oxidation' technique using O^{18} as a tracer combined with SIMS analysis of the resulting oxide. If the element is initially oxidized in a normal O^{16}-containing atmosphere, and subsequently in an atmosphere containing O^{18} only, then the distribution of O^{18} in the final oxide will indicate the relative importance of the two mechanisms. If there is a sharp demarcation between the O^{18}-containing oxide layer next to the silicon, and the now superficial O_{16}-containing oxide, then oxidation is by permeation, and the rate equation should be

$$\text{Rate} = K_p D_p p\text{O}_2^m$$

where K_p is the rate constant, D_p is the permeation constant, $p\text{O}_2$ is the oxygen pressure in the atmosphere and m is equal to unity.

If the movement of ions on the network predominates, the rate will depend on some power of the oxygen pressure, n, which is related to the formation of oxygen ions on the lattice such as

$$\text{Rate} = K_i D_i \, pO_2^n$$

and there will be a diffuse interface between at the gas/solid interface, and the original oxide/O^{18}-containing oxide, due to ionic exchange. For instance, the value of n may be given by the mass action-type equation

$$(1/2)O_2 + 2V_{\ddot{0}} + 2e^- \longrightarrow O^{2-}$$

leading to a value of n of one-sixth.

The overall rate is therefore described by the equation

$$\text{Rate} = K_p D_p \, pO_2^m + K_i D_i \, pO_2^{1/6}$$

Experimental data show that the value of m decreases from 0.6 at 1200°C and 0.3 at 1500°C, indicating a mixed control, as shown in the SIMS analysis.

Complex oxide formation in the oxidation of alloys

The oxidation of metallic alloys presents new features since there is usually a difference of the stabilities of the oxides which are formed by the elements in the alloy which can determine the nature of the oxides which are formed. An extreme example of this is in nickel–gold alloys, where only NiO is formed, but the alloy phase becomes depleted in nickel at the oxide/alloy interface as the oxidation procedes (selective oxidation), leading to a decreasing rate of oxidation. The opposite behaviour is shown by the important nickel–chromium alloys in which the chromium is oxidized to Cr_2O_3 and a spinel phase $NiCr_2O_4$. It is probable that the initial oxidation process is the selective oxidation of nickel, with an increase in the concentration of the chromium content at the metal/oxide interface. Also appearing at the interfaces are voids resulting from the coalescence of the vacancies left behind at the metal/oxide interface by the outward migration of nickel ions and electrons to form the oxide. Since the metal and the oxide are separated at these voids, the oxygen potential at the oxide face of each void can increase above the Ni/NiO interface and further oxidation can occur in which a porous sub-layer of nickel and chromium oxides are formed. These can inter-diffuse to form the spinel $NiCr_2O_4$ which is found as separated particles dispersed in the porous NiO layer. At low chromium contents Cr_2O_3 particles are formed inside the metal phase due to the finite solubility of oxygen in the alloy (internal oxidation). At chromium contents in excess of 20 wt %, the oxide which is predominantly formed is Cr_2O_3, which grows very slowly according to a logarithmic rate law. This is because this oxide has a very low electrical conductivity, and so the oxidation rate is limited by electron transport.

DropBooks

Internal oxidation of alloys

In some binary alloys where a dilute constituent has a greater affinity for oxygen than the major constituent, the oxidation proceeds with the formation of a dispersed phase of oxide particles containing only the dilute constituent for example, Cu–Be alloys form an internal oxidation zone containing BeO particles near the metal/gas interface. This process leads to a depletion of beryllium from the alloy in the same zone, and there is therefore an inward diffusion of oxygen from the gas phase and an outward diffusion of beryllium towards the internal oxidation zone. The rate of this process may be calculated according to the following Fick's law equations (Wagner, 1959).

For the dilute reactive constituent R which forms the oxide RO_n, let the thickness of the internal oxidation zone be ξ, then for the inward diffusion of oxygen, mole fraction N_O

$$\frac{\partial N_O}{\partial t} = D\frac{\partial^2 N_O}{\partial x^2} \qquad x \leq \xi$$

and the outward diffusion of R into the zone

$$\frac{\partial N_R}{\partial t} = D_R\frac{\partial^2 N_R}{\partial x^2} \qquad x \leq \xi$$

and

$$D_O\left(\frac{\partial N_O}{\partial x}\right)_{x=\xi-\delta} = -nD_R\left(\frac{\partial N_R}{\partial x}\right)_{x=\xi+\delta}$$

applying Fick's first law for the formation of the oxide.

$$\text{If } \phi = \frac{D_O}{D_R} \text{ and } \gamma = \frac{\xi}{2(D_O t)^{1/2}} \text{ with } \begin{matrix} N_O = 0; & x \geq \xi \\ N_O = N_O^s \text{ at } x = 0 \end{matrix}$$

the solutions of the second law equations given above are

$$N_O = N_O^s\left\{1 - \frac{\text{erf}\left[\dfrac{x}{2(D_O t)^{1/2}}\right]}{\text{erf}\gamma}\right\}$$

$$N_R = N_R^0\left\{1 - \frac{\text{erfc}\left[\dfrac{x}{2(D_R t)^{1/2}}\right]}{\text{erfc}(\gamma\phi^{1/2})}\right\}$$

where N_O^s is the concentration of oxygen at the metal surface, and N_R^0 is the original concentration of the alloying element R. Substituting these results in

the statement of Fick's first law above has the solution

$$\frac{N_{\mathrm{O}}^{\mathrm{s}}}{N_{\mathrm{R}}^{0}} = \frac{n \exp \gamma^2 \mathrm{erf}\gamma}{\phi^{1/2} \exp(\gamma^2 \phi)\, \mathrm{erfc}(\gamma \phi^{1/2})}$$

as δ tends to zero, from which it can be deduced that

$$\xi = \left(\frac{2 N_{\mathrm{O}}^{\mathrm{s}} D_{\mathrm{O}} t}{n N_{\mathrm{R}}^{0}} \right)^{1/2}$$

for the conditions stated above, $\gamma \ll 1$, and $\gamma \phi^{1/2} \gg 1$, and the rate of internal oxidation is dependent on the oxygen diffusion coefficient and solubility in the base metal.

Rapp (1961) has confirmed this equation in a study of the oxidation in air of Ag–In alloys at 550°C. The reaction proceeds with the internal formation of In_2O_3 particles over a range of indium concentrations, but at a critical mole fraction of indium in the alloy, external oxidation occurs with the growth of a layer of In_2O_3 covering the alloy. The transition from internal to external oxidation was found by Rapp to occur at the mole fraction of indium corresponding to

$$N_{\mathrm{R}} = \left(\frac{\pi}{2} f n N_{\mathrm{O}}^{\mathrm{s}} \phi \right)^{1/2}$$

DropBooks

where f is the mole fraction of the internal oxide in the alloy. When the dilute reactive constituent is present in the initial alloy at a concentration greater than this limiting value, an external layer of RO_n is formed.

As an industrially important example, oxygen dissolves in nickel and so when alloys of nickel containing metals having a higher affinity for oxygen are oxidized, internal oxidation occurs. The Ni–Cr alloys with larger than 10% chromium content show the formation of Cr_2O_3 particles within the metal phase. The oxide NiO is formed simultaneously by the normal oxidation mechanism, the oxide boundary moves into the metal, as a result of the outward migration of Ni^{2+} ions into the oxide, and the counter-migration of vacancies. When the oxide encounters Cr_2O_3 particles which have been previously formed by internal oxidation, the spinel Ni_2CrO_4 is formed by interaction between the oxides. There are thus three oxidation zones in the product, one containing Cr_2O_3 particles dispersed in nickel metal, the next containing $NiCr_2O_4$ particles dispersed in NiO, and the outer layer consisting of pure NiO.

Maak (1961) has obtained the equation governing the oxidation rate of a metal to form both an external oxide and an internally oxidized dilute solute, as for example in Cu–Be alloys, corresponding to the equation given earlier

for single internal oxidation, which is

$$\frac{N_{\mathrm{O}}^{(\mathrm{s})} D_{\mathrm{O}}^{1/2} \exp(-\gamma^2)}{\operatorname{erf} \gamma - \operatorname{erf}\left(\dfrac{k_c}{2D_{\mathrm{O}}}\right)^{1/2}} = \frac{n N_{\mathrm{R}}^{(0)} D_{\mathrm{R}}^{1/2} \exp(-\gamma^2 \phi)}{\operatorname{erfc}(\gamma \phi^{1/2})}$$

for the internal formation of the oxide RO_m, where, as above, $N_{\mathrm{O}}^{(\mathrm{s})}$ is the oxygen content of the metal at the oxide-metal interface, $N_{\mathrm{R}}^{(0)}$ is the original content of R in the alloy, ξ is the thickness of the internal oxidation zone. Using the definitions of γ and ϕ given above, if k_C is the external oxidation constant, for the oxide of thickness x, then

$$k_C = x^2/2t$$

and comparing the equations for the formation of the internal oxidation zone with and without external oxide formation, a simple form of the final equations can be obtained when γ is small compared with unity and when $x < \xi$, then

$$\exp(-\gamma^2) = 1; \quad \operatorname{erf} \gamma = \frac{2}{\pi^{1/2}} \gamma$$

The thickness of the internal zone can be calculated from the equation quoted earlier

$$\xi^2 = \frac{2N_{\mathrm{O}}^{(\mathrm{s})} D_{\mathrm{O}} t}{n N_{\mathrm{R}}^{0}} \text{ without an external oxide}$$

where ξ is measured from the gas/solid interface, and

$$\xi(\xi - x) = \frac{2N_{\mathrm{O}}^{(\mathrm{s})} D_{\mathrm{O}} t}{n N_{\mathrm{R}}^{0}} F\left[\frac{\xi}{2(D_R t)^{1/2}}\right] \text{ with an oxide layer}$$

$$F(u) = \pi^{1/2} u \exp u^2 \operatorname{erfc} u = 1 - (1/2)u^2 + (3/4)u^4 \ldots$$

The oxidation of nickel–copper alloys provides an example of the dependence of the composition of the oxide layer on the composition of the alloy. Nickel–copper alloys depart from Raoult's law, but as a first approximation can be taken as ideal. The Gibbs energy change for the reaction

$$\mathrm{NiO} + 2\mathrm{Cu} \longrightarrow \mathrm{Cu_2O} + \mathrm{Ni} \qquad K = \frac{a_{\mathrm{Ni}} a_{\mathrm{Cu_2O}}}{a_{\mathrm{Cu}}^2 a_{\mathrm{NiO}}}$$

$$\Delta G^\circ = 66\,840 - 12.98T \text{ J}$$

and the diffusion coefficients of Ni^{2+} and Cu^{+} in their respective oxides are given by the equations

$$D_{Ni^{2+}} = 4.4 \times 10^{-3} \exp\left(-\frac{20\,000^{T}}{T}\right) \text{cm}^2\,\text{s}^{-1}$$

$$D_{Cu^{+}} = 2.15 \times 10^{-3} \exp\left(-\frac{17\,000^{T}}{T}\right) \text{cm}^2\,\text{s}^{-1}$$

so that NiO is more thermodynamically stable, but Cu_2O is formed more rapidly given the same chemical potential gradient for the metal. Cu_2O and NiO are mutually insoluble. The oxidation behaviour of nickel–copper alloys reflects these properties in that the pattern of oxidation is a function of alloy composition. At the equimolar composition, NiO islands begin to grow on the surface interspersed with Cu_2O islands, the formation of which results from the nickel depletion at the metal surface. The Cu_2O layer increases more rapidly in thickness until it covers the NiO islands. These latter slowly grow together as nickel atoms arrive at the surface by diffusion within the alloy and reduce the Cu_2O islands near the metal surface. Finally the NiO forms a complete layer which continues to grow while the superficial Cu_2O layer oxidizes in air to CuO. At high copper contents, the oxide is entirely made up of Cu_2O, and NiO particles grow by internal oxidation.

DropBooks

The theory of the parabolic oxidation law

The analysis of oxidation processes to which diffusion control and interfacial equilibrium applied has been analysed by Wagner (1933) who used the Einstein mobility equation as a starting point. To describe the oxidation for example of nickel to the monoxide NiO, consideration must be given to the respective fluxes of cations, anions and positive holes. These fluxes must be balanced to preserve local electroneutrality throughout the growing oxide. The flux equation for each species includes a term due to a chemical potential gradient plus a term due to the electric potential gradient

$$J_i = -B_i c_i \left(\frac{\mathrm{d}\mu_i}{\mathrm{d}x} + z_i e \frac{\mathrm{d}\theta}{\mathrm{d}x}\right)$$

where $\mathrm{d}\mu/\mathrm{d}x$ is the chemical potential gradient and $\mathrm{d}\theta/\mathrm{d}x$ is the electric potential gradient in the x direction and z_i is the ionic charge. These terms can also be joined to form the electrochemical potential gradient

$$\frac{\mathrm{d}\mu}{\mathrm{d}x} = \frac{\mathrm{d}\mu_i}{\mathrm{d}x} + z_i e \frac{\mathrm{d}\theta}{\mathrm{d}x}$$

Substituting for the mobility using the Nernst–Einstein equation and the definition of the transport number

$$J_i = -\frac{C_i t_i \sigma}{(ze)^2}\left(\frac{\mathrm{d}\mu_i}{\mathrm{d}x}\right)$$

The ionic and electron or positive hole chemical potentials are related through thermodynamic relations such as

$$\mathrm{d}\mu_M = \mathrm{d}\mu_{M^{m+}} + m\mathrm{d}\mu_e$$

$$\mathrm{d}\mu_A = \mathrm{d}\mu_{A^{r-}} - r\mathrm{d}\mu_e$$

and

$$\frac{\mathrm{d}\mu_M}{\mathrm{d}x} = -\frac{m}{r}\frac{\mathrm{d}\mu_A}{\mathrm{d}x}$$

the Gibbs–Duhem equation.

The complete flux equations when the cation has a valence $m+$, and the anion a valence $r-$ in the compound $\mathrm{M}_a\mathrm{A}_b$

$$J_{\text{cations}} = \frac{\sigma t_c}{(me)^2}\left(\frac{\mathrm{d}\mu_c}{\mathrm{d}x} + me\frac{\mathrm{d}\theta}{\mathrm{d}x}\right)$$

$$J_{\text{anions}} = \frac{\sigma t_a}{(re)^2}\left(\frac{\mathrm{d}\mu_a}{\mathrm{d}x} - re\frac{\mathrm{d}\theta}{\mathrm{d}x}\right)$$

$$J_{\text{electrons}} = \frac{\sigma t_e}{e^2}\left(\frac{\mathrm{d}\mu_e}{\mathrm{d}x} - e\frac{\mathrm{d}\theta}{\mathrm{d}x}\right)$$

and

$$J_{\text{holes}} = \frac{\sigma t_h}{e^2}\left(\frac{\mathrm{d}\mu_h}{\mathrm{d}x} + e\frac{\mathrm{d}\theta}{\mathrm{d}x}\right)$$

where

$$\frac{\mathrm{d}\mu_e}{\mathrm{d}x} = -\frac{\mathrm{d}\mu_h}{\mathrm{d}x} \text{ and } mJ_{m^+} = rJ_{r-} + J_e - J_h.$$

These equations yield expressions for the electric potential gradient

$$\frac{\mathrm{d}\theta}{\mathrm{d}x} = \frac{1}{me}\frac{\mathrm{d}\mu_{M^{m+}}}{\mathrm{d}x} - t_e\frac{\mathrm{d}\mu_M}{\mathrm{d}x} = -\frac{1}{re}\left(t_e\frac{\mathrm{d}\mu a}{\mathrm{d}x} - \frac{\mathrm{d}\mu_{A^r}}{\mathrm{d}x}\right)$$

On substituting these values into the ionic flux equations we obtain

$$J_{M^{m+}} = -\frac{a}{b}\,\frac{t_c t_e \sigma}{e^2 r^2}\,\frac{\mathrm{d}\mu_A}{\mathrm{d}x}$$

and

$$J_{A^{r-}} = \frac{t_a t_e \sigma}{e^2 r^2} \frac{\mathrm{d}\mu_A}{\mathrm{d}x}$$

Hence the rate of formation of the molecules $M_a A_b\,\mathrm{cm}^{-2}\,\mathrm{s}^{-1}$

$$\frac{\mathrm{d}n}{\mathrm{d}t} = \frac{J_{A^{r-}}}{b} - \frac{J_{M^{m+}}}{a} = \frac{1}{e^2 r^2 b^2} \left\{ \int_{\mu_{Ai}}^{\mu_{A0}} (\sigma t_e (t_c + t_a) b \mathrm{d}\mu_A \right\} \frac{1}{\Delta x}$$

where Δx is the instantaneous thickness of the product, and μA_0 and μA_i are the chemical potentials of A at the outer and inner faces of the reaction product.

For the oxidation of Ni($m+ = 2$),

$$\frac{\mathrm{d}n}{\mathrm{d}t} = \frac{k_t}{\Delta x} = \frac{RT}{8e^2} \left\{ \int_{p_{O_2(\mathrm{metal/oxide})}}^{p_{O_2(\mathrm{oxide/gas})}} t_e (t_{Ni^{2+}} + t_{O^{2-}}) \sigma \,\mathrm{d} \ln p_{O_2} \right\} \frac{1}{\Delta x}$$

Here, $t_e \cong 1$ and $t_{O^{2-}}$ is negligible, and thus the rate of oxidation is determined by the partial conductivity due to the Ni^{2+} ions.

If the oxidizing gas is pure oxygen, and $t_{Ni^{2+}}$ remains approximately constant over the oxide thickness

$$\frac{k}{\Delta x} = -\frac{\sigma}{8e^2} t_{Ni^{2+}} \frac{\Delta G^\circ}{\Delta x}$$

DropBooks

where ΔG° is the Gibbs free energy change of the reaction

$$2\mathrm{Ni} + \mathrm{O_2} \longrightarrow 2\mathrm{NiO}$$

Furthermore, using the Nernst–Einstein equation to substitute in the general equation above yields

$$\frac{k_t}{\Delta x} = \frac{c_0}{2b} \int_{p_{O_2}(\mathrm{metal/oxide})}^{p_{O_2}(\mathrm{oxide/gas})} \frac{m}{r} (D_M + D_0) \mathrm{d} \ln p_{O_2} \,\mathrm{moles/cm^2\,s}$$

The carburizing and oxidation of transition metals

These two processes provide examples of the moving boundary problem in diffusing systems in which a solid solution precedes the formation of a compound. The thickness of the separate phase of the product, carbide or

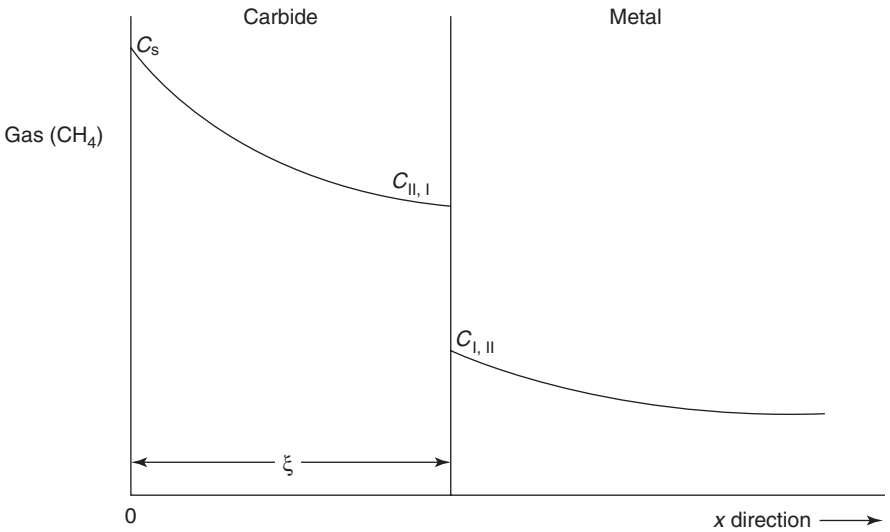


Figure 8.1 *Schematic of the carburization of a metal*

oxide, increases with time thus moving the boundary of the solid solution phase away from the gas–solid interface.

In the kinetics of formation of carbides by reaction of the metal with CH_4, the diffusion equation is solved for the general case where carbon is dissolved into the metal forming a solid solution, until the concentration at the surface reaches saturation, when a solid carbide phase begins to develop on the free surface. If the carbide has a thickness ξ at a given instant and the diffusion coefficient of carbon is D_I in the metal and D_{II} in the carbide, Fick's 2nd law may be written in the form (Figure 8.1)

$$\text{Metal}\ \frac{\partial c}{\partial t} = D_I \frac{\partial^2 c}{\partial x^2} (x > \xi)$$

$$\text{Carbide}\ \frac{\partial c}{\partial t} = D_{II} \frac{\partial^2 c}{\partial x^2} (0 \leq x \leq \xi)$$

for each phase.

When the metal/carbide boundary moves away from the free surface of the sample by an increment $d\xi$, the *flux balance* at this interface reads

$$(C_{II,I} - C_{I,II})d\xi = -D_{II} \left(\frac{\partial c}{\partial x} \right)_{\xi - \delta} + D_I \left(\frac{\partial c}{\partial x} \right)_{\xi + \delta}$$

where $C_{\mathrm{II,I}}$ is the concentration of carbon in the carbide at the carbide/metal interface, and $C_{\mathrm{I,II}}$ is that in the metal at the same interface. Introducing the relationships and definitions which were used earlier

$$\phi = \frac{D_{\mathrm{II}}}{D_{\mathrm{I}}};$$

$$\xi = \frac{2\gamma}{(D_{\mathrm{II}}t)^{1/2}}$$

and replacing

$$\frac{C_{\mathrm{I,II}}}{1 - \mathrm{erf}\ (\gamma\phi)^{1/2}} \text{ by } B_I \text{ and } \frac{C_s - C_{\mathrm{II}}}{\mathrm{erf}\ \gamma} \text{ by } B_{\mathrm{II}}$$

where C_s is the carbon concentration in the carbide at the gas/carbide interface, the solutions of Fick's equations may be represented as follows:

The concentration of carbon in the carbide phase is

$$C_x = C_s - B_{\mathrm{II}}\ \mathrm{erf}\ \left(\frac{x}{2(D_{\mathrm{II}}t)^{1/2}}\right) \qquad 0 \le x \le \xi$$

and in the metal phase

$$C_x = B_{\mathrm{I}}\left(1 - \ \mathrm{erf}\ \left(\frac{x}{2(D_{\mathrm{I}}t)^{1/2}}\right)\right) \qquad x > \xi$$

and substituting into the flux balance equation at the interface

$$C_x = \frac{(C_s - C_{\mathrm{II,I}})}{\pi^{1/2}\gamma\ \mathrm{erf}\ \gamma}\exp(-\gamma^2) - \frac{C_{\mathrm{I,II}}\exp(-\gamma^2)}{(\pi\phi)^{1/2}\gamma[1 - \ \mathrm{erf}\ (\gamma\phi^{1/2})]}$$

and

$$C_{\mathrm{II,I}} - C_{\mathrm{I,II}} = \frac{B_{\mathrm{II}}\exp(-\gamma^2)}{\gamma\pi^{1/2}} - \frac{B_{\mathrm{I}}\exp -(\gamma^2\phi)}{\gamma(\pi\phi)^{1/2}}$$

where $C_{\mathrm{II,I}} - C_{\mathrm{I,II}}$ is the difference in the content of carbon between the carbide and metal phases at equilibrium.

The equation for the rate of oxidation of the transition metals at high temperatures, which form a solid solution of oxygen before the oxide appears at the surface has the same form as that derived for the carburizing of the metal, and

DropBooks

the weight change/unit area, m/A, can be expressed as a function of time by the formula

$$\frac{m}{A} = [K(\text{oxide formation}) + K'(\text{oxygen dissolution})]\sqrt{t} = K''\sqrt{t}$$

where

$$K = 2\gamma(C_{\text{I,II}} - C_{\text{II,I}})D_{\text{oxide}}^{1/2}$$

and using the definition of γ given above

$$K' = \frac{2C_{\text{I,II}}}{\pi^{1/2}1 - \text{ erf }(\gamma\phi^{1/2})}D_{\text{metal}}^{1/2}\exp(-\gamma^2\phi)$$

where $C_{\text{II,I}} - C_{\text{I,II}}$ reflects difference between the the oxygen content of the oxide at the oxide–metal interface, and the saturation solubility of oxygen in the metal and ϕ is the ratio of the oxygen diffusion coefficients $D_{\text{oxide}}/D_{\text{metal}}$.

There can be little doubt that the carburization process occurs by the inward migration of interstitial carbon atoms, and the major sources of evidence support the view that the oxidation process in the IVA metals, Ti, Zr, and Hf, and in the VA metals Nb and Ta, involves a predominant inward migration of oxygen ions with some participation of the metallic ions in the high temperature regime (>1000°C). The mechanism of oxidation is considerably affected by the dissolution of oxygen in the metal, leading to a low-temperature cubic or logarithmic regime, an intermediate region of parabolic oxidation, and then a linear regime in which the vaporization of the oxide can play a significant part. The temperature ranges in which each of these regimes operates varies from metal to metal and to summarize, the parabolic region extends from about 400–1100°C in the Group IVA elements, but the situation is much more complicated in the Group VA elements because of the complexity of the oxide layers which are found in the oxidation product of Nb and Ta. In these latter elements, the parabolic regime is very limited, and mixtures of linear and parabolic regimes are found as a function of the time of oxidation.

It is clear that the dissolution of oxygen in these metals occurs by the inward migration of oxygen, and conforms to the parabolic law. In the oxidation of the Group IVA metals the only oxide to be formed is the dioxide, even though the Ti–O system shows the existence at equilibrium of several oxides. This simplicity in the oxide structure probably accounts for the wide temperature range of parabolic oxidation, although the non-stoichiometry of monoclinic ZrO_2 has been invoked to account for the low-temperature behaviour of the oxidation reaction. The mechanisms at low temperature are complicated by a number of factors, including the stresses in the oxide layer which, unlike the behaviour at high temperatures, cannot be relieved during oxidation. Several explanations are given invoking the relative transport numbers of electrons and ions, the formation of pores at the oxide/metal interface, and unrelieved

stresses in the metal which change during the oxidation period as the oxygen solution becomes more concentrated. Whatever the mechanism(s), it is significant that the oxide is protective for a useful period of time, allowing zirconium cladding to be used for the UO_2 fuel rods in a nuclear reactor, but this lifetime is terminated in breakaway corrosion.

At high temperatures the change in mechanism to a linear oxidation rate, after a short period of parabolic oxidation, indicates that the stresses in the oxide layer which arise from the rapid rate of formation, cause rupture in the oxide, allowing the ingress of oxygen. The cracks which are formed in the oxide will probably vary in morphology and distribution as a function of time of oxidation, due to the sintering process and plastic flow which will tend to close up the cracks. The oxidation of the Group VA elements, Nb and Ta is complicated by the existence of several oxides which are formed in sequence. For example, the sequence in niobium oxidation is

$$\text{Nb}-[\text{O}]\text{solid solution}-\text{NbO}-\text{NbO}_2-\text{Nb}_2\text{O}_5$$

The pentoxide layer always appears to be porous to oxygen gas and therefore provides no oxidation protection. The lower oxides grow more slowly, and can adapt to the metal/oxide interfacial strains, and provide protection. The low temperature oxidation conforms to a linear rate law after a short interval of parabolic behaviour, corresponding to the formation of a solid solution and a thin layer of oxide which is probably an $\text{NbO}-\text{NbO}_2$ (sometimes referred to as NbO_x) layer in platelet form, which decreases in thickness as the temperature increases. This mechanism is succeeded by a parabolic behaviour over a longer period of time which eventually gives way to a linear growth rate as the temperature increases above about 600°C. It is probable that the parabolic behaviour in this regime is rate-determined by the formation of more substantial $\text{NbO}-\text{NbO}_2$ layers before the pentoxide is formed.

DropBooks

The oxidation kinetics of the metals molybdenum and tungsten in Group VI reflect the increasing contribution of the volatility of the oxides MoO_3 and WO_3 as the temperature increases. At temperatures below 1000°C, a protective oxide, is first formed, as in the case of niobium, followed by a linear rate when a porous layer of the trioxide is formed. There appears to be no significant solubility of oxygen in these metals, so the initial parabolic behaviour is ascribed to the formation of the dioxide. At higher temperatures the porous layer of oxide is restricted in thickness by increasing vaporization, and this process further restricts the access of oxygen to the surface until a steady state is reached, depending on the state of motion of the oxidizing atmosphere.

The oxidation of metallic carbides and silicides

The expected oxidation mechanisms of carbides and silicides can be analysed from a thermodynamic viewpoint by a comparison of the relative stabilities

of the oxides of the metals, carbon and silicon. Thus the element having the greater oxygen affinity would be expected to be preferentially oxidized. However, there is a complication arising from the stabilities of the various carbides and their solid solutions, and the stabilities of the numerous silicides which are formed, especially by the transition metals.

The general principle that the respective sequence of oxidation of metal and non-metal will be according to the affinity of the elements to oxygen, must be analysed with due consideration of the thermodynamic activities and the diffusion properties of each element. Thus in the titanium–carbon system the affinity of titanium for oxygen is higher for the formation of rutile than is carbon for the formation of CO(g) in the lower temperature range, and the activity of carbon may be low if the composition of the original carbide, TiC_x is at the upper end of the metal-rich composition. However, as the metal is preferentially oxidized, the unburnt carbon will increase in thermodynamic activity, and the excess of carbon will move the average composition toward the carbon-rich end of the composition range of TiC_x until the two-phase region containing a mixture of the carbide and carbon is reached. The carbon activity will increase as this occurs, and the titanium activity will fall, until the carbon is preferentially oxidized.

The thermodynamic data for the Ti–O–C system are as follows:

$$\mathrm{Ti} + \mathrm{O_2} \longrightarrow \mathrm{TiO_2}; \quad \Delta G^\circ = -938\,860 + 176.4T \text{ J mol}^{-1}$$

$$2\mathrm{C} + \mathrm{O_2} \longrightarrow 2\mathrm{CO}; \quad \Delta G^\circ = -224\,870 - 174.6T \text{ J mol}^{-1}$$

$$\mathrm{Ti} + \mathrm{C} = \mathrm{TiC}; \quad \Delta G^\circ = -182\,750 + 5.83T \text{ J mol}^{-1}$$

(The first equation ignores the existence of the intermediate titanium oxides, which is reasonable for this analysis of the oxidation mechanism.)

When the carbide reaches carbon saturation, the titanium activity is at its lowest value, $\Delta\mu\mathrm{Ti} = -175.754$ kJ at 1200 K and -172.839 kJ at 1700 K, this chemical potential being nearly constant over the temperature range because of the small entropy of formation of TiC from the elements. The oxygen potential required to form TiO_2 is less than that to form CO at one atmosphere pressure in air at 1200 K but much higher than that to form one atmos pressure of CO at 1700 K. There is therefore a change-over in mechanism between these two temperatures. TiO_2 is formed at the lower temperature, and carbon particles are left in the carbide, and at the higher temperature CO is formed, and the composition of the carbide moves towards the liberation of carbon-saturated titanium, thus increasing the tendency for preferential titanium oxidation.

If we combine the Gibbs energy of formation equations above to derive the equation

$$\mathrm{Ti} + 2\mathrm{CO} \longrightarrow 2\mathrm{C} + \mathrm{TiO_2}; \quad \Delta G^\circ = -708\,490 + 347.7T \text{ J mol}^{-1}$$

the temperature at which this reaction has zero Gibbs energy change with the titanium potential of the C–TiC equilibrium is about 1500 K. The changeover in mechanism will therefore occur at about this temperature. Below 1500 K the mechanism is the parabolic oxidation of Ti to TiO_2, but above this temperature the oxidation proceeds according to a linear law, with both elements being oxidized. The CO which is formed during this reaction is oxidized to CO_2 by the air in the atmosphere when the gas reaction takes place away from the sample, and the gas temperature is reduced to room temperature for analysis.

The oxidation rate is decreased by a factor of four in a composite of TiC and Cr. This is because the formation of Cr_2O_3 covers the composite with an oxide which oxidizes slowly because of the low transport number of electrons through the oxide.

The oxidation of the silicides represents a competition between the formation of silica, which is very slow and controlled by oxygen permeation of the oxide, and the oxidation of the accompanying element. The difference between the carbides and the silicides is that there are many more silicides formed in a binary system which vary the activities of each element, than in the carbides. Thus in the Mo–Si system, the compounds $MoSi_2$, Mo_5Si_3, Mo_3Si are formed, and in the TiSi system five silicides are formed, $TiSi_2$, TiSi, Ti_5Si_4, Ti_5Si_3 and Ti_3Si, all of which have a small range of non-stoichiometry. The preferential oxidation of each element in either the Mo–Si or Ti–Si systems would therefore lead to a significant and discontinuous change in the composition near the surface. The thermodynamic activities would show a rapid change at the composition of any of the compounds, but remain constant in any two-phase mixture of the compounds.

DropBooks

Clearly the best protection from oxidation by a silicide as a coating on a reactive substrate would be the disilicide, which has the highest silicon content, and could be expected to provide a relatively protective silica coating.

The oxidation of silicon carbide and nitride

The carbide has an important use as a high-temperature heating element in oxidizing atmospheres. The kinetics of oxidation is slow enough for heating elements made of this material to provide a substantial lifetime in service even at temperatures as high as 1600°C in air. Both elements react with oxygen during the oxidation of silicon carbide, one to produce a protective layer, SiO_2, and the other to produce a gaseous phase, CO(g) which escapes through the oxide layer. The formation of the silica layer follows much the same reaction path as in the oxidation of pure silicon, the structure of the layer being amorphous or vitreous, depending on the temperature, and the oxidation proceeds mainly by permeation of the oxide by oxygen molecules. The escape of CO from the carbide/oxide interface produces a lowering of the oxygen potential at the oxide/gas interface, which reduces the rate of oxidation, to a

level depending on the state of motion of the oxidizing gas, and can reduce the oxide at high temperatures with the formation of SiO(g), which leads to a reduction in the protective nature of the oxide. Because of these effects on the oxidation kinetics, the rate of overall oxidation has been found to depend on the flowrate, through the exchange of CO and O_2 across the boundary layer, in the gas phase.

The nitride is an important high temperature insulator and potential component of automobile and turbine engines and its use in oxidizing atmospheres must be understood for several other applications. It might be anticipated that the oxidation mechanism would be similar to that of the carbide, with the counter-diffusion of nitrogen and oxygen replacing that of CO and O_2. This is so at temperatures around 1400°C, where the oxidation rates are similar for the element, the carbide and the silicide, but below this temperature regime, the oxidation proceeds more slowly, due to the operation of a different mechanism. At temperatures around 1200°C or less, the elimination of nitrogen as N_2 molecules is replaced by a substitution of nitrogen for oxygen on the silica lattice, the N/O ratio decreasing from the nitride/oxide interface to practically zero at the oxide/gas interface. The oxidation rates at 1200°C of the carbide and nitride are about 0.1 and 10^{-2} of that of pure silicon, and at 1000°C, the oxidation rate of the nitride is less than 10^{-2} that of the carbide.

The technical problem in the high temperature application of Si_3N_4 is that unlike the pure material, which can be prepared in small quantities by CVD for example, the commercial material is made by sintering the nitride with additives, such as MgO. The presence of the additive increases the rate of oxidation, when compared with the pure material, by an order of magnitude, probably due to the formation of liquid magnesia–silica solutions, which provide short-circuits for oxygen diffusion. These solutions are also known to reduce the mechanical strength at these temperatures.

Bibliography

P. Kofstad. *High Temperature Oxidation of Metals.* J. Wiley & Sons. New York (1966) TA 462. K57.

N. Birks and G.H. Meier. *Introduction to High Temperature Oxidation of Metals*. Edward Arnold, London (1983) QD 501.

C. Wagner. *Z. Elektrochem.*, **63**, 772 (1959).

F. Maak. *Z. Metallk.*, **52**, 545 (1961).

R.A. Rapp. *Acta Met.*, **9**, 730 (1961).

C. Wagner. *Z. Phys. Chem.*, **21**, 25 (1933).

Chapter 9

Laboratory studies of some important industrial reactions

The reduction of haematite by hydrogen

Two alternative mechanisms were proposed for the reduction of haematite, Fe_2O_3, by hydrogen (McKewan, 1958; 1960). The first proposes that the reduction rate is determined by the rate of adsorption of hydrogen on the surface, followed by desorption of the gaseous product H_2O. The fact that the product of the reaction is a porous solid made of iron metal with a core of unreduced oxides suggests that an alternative rate-determining step might be the counter-diffusion of hydrogen and the product water molecules in the pores which are created in the solid reactant. The weight loss of a spherical sample of iron oxide according to these two mechanisms is given by alternative equations. Using W_0 as the original weight of a sphere of initial radius r_0, W as the weight after a period of reduction t when the radius is r, and W_f as the weight of the completely reduced sphere, the rate equations are:
For the *interface* control,

$$\frac{-\mathrm{d}W}{\mathrm{d}t} = kA = 4\pi kr^2; \text{ and } \frac{\mathrm{d}W}{\mathrm{d}t} = \frac{\mathrm{d}W}{\mathrm{d}r}\frac{\mathrm{d}r}{\mathrm{d}t} = 4\pi r^2 \Delta\rho \frac{\mathrm{d}r}{\mathrm{d}t}$$

where $\Delta\rho$ is the difference in density between the unreduced (oxide) and reduced (iron) material at time t.

On integration and evaluation of the integration constant this yields

$$\Delta\rho(r_0 - r) = kt$$

Since

$$\frac{r}{r_0} = \frac{(W - W_f)^{1/3}}{(W_0 - W_f)} = \Delta W^{1/3}$$

Hence

$$(\Delta W)^{1/3} = 1 - kt/\Delta\rho r_0$$

For *diffusion* control

$$\frac{-\mathrm{d}W}{\mathrm{d}t} = \frac{4\pi D(p - p^0)}{(1/r - 1/r_0)} = -4\pi r^2 \Delta\rho \frac{\mathrm{d}r}{\mathrm{d}t}$$

DropBooks

where p and p^0 are the partial pressures of the gaseous products at the reaction interface and surface of the sphere and D is the diffusion coefficient in the gaseous phase. This equation on integration and substitution yields the result,

$$3(\Delta W)^{2/3} - 2(\Delta W) = 1 - 6Dt/\Delta\rho r_0^2$$

In this derivation, the diffusion coefficient which is used is really a parameter, since it is not certain which gas diffusion rate is controlling, that of hydrogen into a pore, or that of water vapour out of the pore. The latter seems to be the most probable, but the path of diffusion will be very tortuous through each pore and therefore the length of the diffusion path is ill-defined.

Although these two expressions, for surface and diffusion control are different from one another, the graphs of these two functions as a function of time are not sufficiently different to be easily distinguished separately. The decisive experiment which showed that diffusion in the gas phase is the rate determining factor used a closed-end crucible containing iron oxide sealed at the open end by a porous plug, made from iron powder, which was weighed continuously during the experiment. It was found that the rate of reduction of the oxide contained in the crucible was determined by the thickness of the porous plug, and hence it was the gaseous diffusion through this plug rather than the interface reaction on the iron oxide, which determined the rate of reduction (Olsson and McKewan, 1996).

Erosion reactions of carbon by gases

Gases can react with solids to form volatile oxides with some metals which are immediately desorbed into the gas phase, depending on the temperature. These reactions are enhanced when atomic oxygen, which can be produced in a low-pressure discharge, is used as the reagent. Experimental studies of the reaction between atomic oxygen and tungsten, molybdenum and carbon, show that the rate of erosion by atomic oxygen is an order of magnitude higher than that of diatomic oxygen at temperatures between 1000 and 1500 K, but these rates approach the same value when the sample temperature is raised to 2000 K or more. The atomic species is formed by passing oxygen at a pressure of 10^{-3} atmos through a microwave discharge in the presence of a readily ionized gas such as argon. The monatomic oxygen mole fraction which is produced in the gas by this technique is about 10^{-2}.

A typical example of this erosion of metals is the formation of $WO_2(g)$ (Rosner and Allendorf, 1970). The Gibbs energies of formation

$$W + O_2 = WO_2(g); \quad \Delta G^\circ = 72\,290 - 39T \quad \mathrm{J\,mol^{-1}}$$

$$\log K_{2000} = 0.11$$

$$W + 2O = WO_2(g); \quad \Delta G^\circ = -4\,32\,330 + 91.7T \quad J\,mol^{-1}$$

$$\log K_{2000} = -6.46$$

Since the entropies are of the opposite sign, it is clear that these reactions will tend to the same Gibbs energy change at temperatures above 3000 K. If the conversion of oxygen molecules to the monatomic species is complete in the discharge, the partial pressure of $WO_2(g)$ should be about 10 times that in the corresponding molecule pressure from these considerations. These equations may also be used to deduce the Gibbs energy of formation of monatomic from diatomic oxygen

$$O_2(g) = 2O(g); \quad \Delta G^\circ = 504\,620 - 130T \quad J\,mol^{-1}$$

and these data can be used to calculate the monatomic/diatomic ratio at the reduced pressures in space.

The most important industrial reaction of this kind occurs in the ironmaking blast furnace in which iron oxide ore is reduced by carbon in the form of coke. The mixture is heated by the combustion of part of the coke input in air to produce temperatures as high as 2000 K. The reduction reaction is carried out via the gas phase by the reaction

$$3CO(g) + Fe_2O_3 \longrightarrow 2Fe + 3CO_2(g)$$

the lower oxides of iron, Fe_3O_4 and FeO being formed as reaction intermediates. The carbon dioxide is reduced to carbon monoxide by reaction with coke according to

DropBooks

$$CO_2 + C = 2CO$$

The kinetics of this reaction, which can also be regarded as an erosion reaction, shows the effects of adsorption of the reaction product in retarding the reaction rate. The path of this reaction involves the adsorption of an oxygen atom donated by a carbon dioxide molecule on the surface of the coke to leave a carbon monoxide molecule in the gas phase.

$$CO_2 + C \longrightarrow C{-}[O] + CO(g); \text{ rate constant } k_1$$

$$C{-}[O] \longrightarrow CO(g); \text{ rate constant } k_2$$

The adsorption of carbon monoxide retards the reduction reaction with the rate constant k_3, followed by the desorption reaction with a rate constant k_4 in the overall rate equation

$$\text{Rate} = k_1\, pCO_2/1 + (k_3/k_4)\, pCO + (k_1/k_2)\, pCO_2$$

The description of the steady state reaction mechanism in terms of the fraction of the active sites occupied by each adsorbed species, θ_1 for oxygen atoms

and θ_2 for the carbon monoxide molecule, is as follows

$$k_1 p\mathrm{CO_2}(1 - \theta_1 - \theta_2) = k_2\theta_1$$

shows that the rate of adsorption of CO_2, leading to formation of the adsorbed oxygen species, is equal to the rate of desorption of these to form carbon monoxide in the gas phase. The corresponding balance for the adsorption and desorption of the carbon monoxide species is as follows

$$k_3 p\mathrm{CO}(1 - \theta_1 - \theta_2) = k_4\theta_2$$

An alternative surface reaction which has been suggested is a reaction between an adsorbed oxygen atom with an adsorbed carbon monoxide molecule to form carbon dioxide which is immediately desorbed. The reaction rate is again given by the equation above.

The combustion of coal

Coal contains, as well as carbon, water, which may be free in the pores of the solid or bound in mineral hydrates, and a number of other minerals such as SiO_2, Al_2O_3, $CaCO_3$ and FeS_2, together with hydrocarbons which are referred to as 'volatiles'. These comprise some 20–40 wt% of typical coals, and they play an important part in the initiation of ignition prior to combustion. The carbon and the volatiles contribute to heat generation during the combustion, and the minerals usually collect in a solid 'ash', which only absorbs heat, except for pyrites, which gives rise to SO_2 in the off-take gases.

Coal is found in a wide range of carbon contents which consists of carbon and the volatiles, from anthracite and the lower-grade bituminites to lignite, and the relation between the combustion properties of each component of these materials in this range of composition has a profound effect on the combustion process. The anthracites contain the least amount of ash-forming material, but are low in volatiles content compared with some more typical bituminous coal. Since the volatiles play a dominant role in the initiation of combustion, it is clear that the anthracites will not burn so readily as lower grade coals, but have a higher carbon content, and hence represent a more compact source of fuel.

The evolution of the volatile components begins in the temperature range 400–600°C, and ignition in air involves the oxygen–hydrocarbon chain reactions to form CO, CO_2 and water vapour. As the temperature increases, the direct oxidation of carbon begins to take place, probably not only at the surface of the remaining solid material, but also in the pores which are formed during the period of the ignition of the volatiles. The subsequent oxidation process

involves the counter-diffusion of oxygen and CO_2 towards the solid and into the pores, and the outward diffusion of carbon monoxide through a gaseous boundary layer. Experimental data for the combustion of coal particles depend on the flow rate of oxygen around the particles, which will determine the boundary layer thickness, and hence the diffusion length between the atmosphere and the surface of the particle. A further barrier to the burning rate is also the condition of the ash which remains on the surface of a particles during combustion.

More controlled studies, of the oxidation of pure graphite, are indicative of the rates of oxidation of the post-volatilization carbon residue of a burning coal particle (Gulbransen and Jansson, 1970). These results which were carried out at low partial pressures of oxygen of around 40 torr, showed that the oxidation rate depends on a chemical (interface) control at temperatures below 1000 K, and at higher temperatures the reaction rate was determined by the diffusion of oxygen through the boundary layer. The burning of coal in a fluidized bed also shows a change in mechanism between 900 and 1000 K. If the weight loss of a coal particle immersed in a fluidized bed of alumina spheres is measured as a function of the coal particle diameter, the slope of the log (weight loss) vs log (coal particle diameter) is less at the higher temperatures, indicating a change-over from interface control to transport control across a boundary layer.

The oxidation of FeS — parabolic to linear rate law transition

DropBooks

The results for the self-diffusion of iron in $FeS_{1+\delta}$ show that this coefficient is orders of magnitude greater than that of sulphur and, at a given temperature, does not alter by as much as a factor of ten across the whole composition range. This is probably an example of a large intrinsic defect concentration masking the effects of compositional change. It is thus to be expected that the oxidation of ferrous sulphide will proceed by the migration of iron ions and electrons out of the sulphide phase and into the oxide phase, leaving the sulphur-rich sulphide.

Niwa *et al*. (1957) showed that this is in fact the case during the early stages of oxidation at temperatures between 500 and 600°C, the oxide which is formed being Fe_3O_4. The oxidation proceeds according to the parabolic rate law, and the sample weight increases. However, this change in the sulphide composition raises the sulphur pressure at the sulphide–oxide interface until a partial pressure of SO_2 greater than one atmosphere can be generated. The oxide skin then ruptures, and the weight gain as a function of time changes from the parabolic relationship of a solid-state diffusion-controlled process to the linear gas-transport controlled law.

Oxidation of complex sulphide ores — competitive oxidation of cations

Most sulphide minerals contain more than one metal, e.g. chalcopyrite has the formula $CuFeS_2$ and pentlandite $(Fe, Ni)_9S_8$. Thornhill and Pidgeon (1957) have shown semi-quantitatively how such compounds behave during oxidation roasting by means of a metallographic study of the roasted powder specimens. Although there exists no direct experimental evidence at present, it is probable that the diffusion coefficients of both metallic species are about the same, and both are very much larger than that of sulphur. It should then follow that the metal which undergoes the greater reduction in chemical potential by oxidation, i.e. forms the more stable oxide, will be preferentially removed. Thus, FeO is considerably more stable than Cu_2O and so iron should be preferentially oxidized from chalcopyrite. The resulting copper sulphide after a period of oxidation of $CuFeS_2$ was shown by the authors to give the X-ray pattern of digenite Cu_9S_5. The acid-soluble oxide layer which had been formed on the surface was iron oxide (Table 9.1).

Table 9.1 *Roasting of 30–40 mesh $CuFeS_2$ at 550°C*

Time (minutes)	Sulphide analysis		Phase present
	Wt % Cu	Wt % Fe	
Zero	35.3	30.6	Chalcopyrite
20	60.6	8.3	Mauve digenite
35	68.0	zero	Blue digenite (Covellite)

The difference in stability between FeO and NiO is not as large as that between iron and copper oxides, and so the preferential oxidation of iron is not so marked in pentlandite. Furthermore, the nickel and iron monoxides form a continuous series of solid solutions, and so a small amount of nickel is always removed into the oxide phase (Table 9.2).

The kinetics of the processes of oxidation of these complex sulphides have not been established quantitively, but the rate of advance of the oxides into sulphide particles of irregular shapes were always linear. This suggests that the oxide films were ruptured during growth thus permitting the gas phase to have relatively unimpeded access to the sulphide–oxide interface in all cases.

Table 9.2 *Roasting 65–80 mesh* $(Fe, Ni)_9S_8$ *at 600°C*

Sulphide analysis Time (Min.)	Wt % Ni	Wt % Fe	Phases present
Zero	35.1	32.3	Pentlandite
65	42.2	22.0	Pyrrhotite type.

The kinetics of sulphation roasting

The objective in sulphation roasing is to produce water-soluble products which can be used in the hydrometallurgical extraction of metals by aqueous electrolysis. The sulphation reaction is normally carried out on oxides which are the products of sulphide roasting, as described above. A few studies have been made of the rates at which sulphates can be formed on oxides under controlled temperatures and gas composition. The mechanism changes considerably from one oxide to another, and there is a wide variability in the rates (Alcock and Hocking, 1966). The thermodynamics of sulphates shows that the dissociation pressures of a number of the sulphates of the common metals, iron, copper, nickel, etc., reach one atmosphere at quite low temperatures, less than 1000°C. At around 600°C, most of these sulphates have very low dissociation pressures. Thus, $CoSO_4$ has a dissociation SO_3 pressure of 10^{-5} atmos at this temperature. It follows that when a study of the kinetics of sulphation of these oxides is carried out over this temperature range, 600–1000°C, the SO_3 pressure exerted at the oxide–sulphate interface will change by five orders of magnitude if local equilibrium prevails. At the same time, the diffusion processes through the sulphate product layer will increase with increasing temperature over this same interval, following a normal Arrhenius relationship between diffusion coefficients and the temperature. Under the right circumstances, it could, and in some instances does, happen that the overall rate of the process would be seen to pass through a maximum somewhere in the temperature interval 600–1000°C because the rate is dependent on the flux of particles across the product, and hence on the chemical potential gradient multiplied by the diffusion coefficient. This situation is exactly parallel to those which bring about T–T–T transformation in metallic systems.

The sulphation of cobalt oxide, CoO, follows the parabolic law up to 700°C and above 850°C, proceeding by outward diffusion of cobalt and oxygen ions through a sulphate layer which is coherent up to about 700°C. The mechanism

DropBooks

changes above this temperature, which is where the rate optimum should be found, above a limiting thickness at intermediate temperatures and it becomes coherent again above 850°C with parabolic kinetics. The rate of sulphate formation passes through a maximum in the intermediate temperature zone probably because the diffusion coefficients are low at low temperatures while the chemical potential gradients across the sulphate are high, whereas the converse applies at high temperatures. It is observed that the rate law is the linear law in the intermediate, high velocity, region, and the sulphate layer is seen to be cracked. In the upper and lower temperature regions, where the reaction is parabolic, the sulphate layer is smooth and uncracked.

Heat transfer in gas–solid reactions

When a gas reacts with a solid, heat will be transferred from the solid to the gas when the reaction is exothermic, and from gas to solid during an endothermic reaction. The energy which is generated will be distributed between the gas and solid phases according to the temperature difference between the two phases, and their respective thermal conductivities. If the surface temperature of the solid is T_2 at any given instant, and that of the bulk of the gas phase is T_1, the rate of convective heat transfer from the solid to the gas may be represented by the equation

$$\frac{\mathrm{d}Q}{\mathrm{d}t} = h(T_2 - T_1) \text{ per unit area}$$

where h is the heat transfer coefficient of the gas. The fraction of the energy generated in unit time which is transferred to the gas is given by

$$F = \frac{h}{\kappa_s}(T_2 - T_1)$$

where κ_s is the thermal conductivity of the solid.

The value of the heat transfer coefficient of the gas is dependent on the rate of flow of the gas, and on whether the gas is in streamline or turbulent flow. This factor depends on the flow rate of the gas and on physical properties of the gas, namely the density and viscosity. In the application of models of chemical reactors in which gas–solid reactions are carried out, it is useful to define a dimensionless number criterion which can be used to determine the state of flow of the gas no matter what the physical dimensions of the reactor and its solid content. Such a criterion which is used is the Reynolds number of the gas. For example, the characteristic length in the definition of this number when a gas is flowing along a tube is the diameter of the tube. The value of the Reynolds number when the gas is in streamline, or linear flow, is less than about 2000, and above this number the gas is in turbulent flow. For the flow

of a gas around a spherical particle the critical value of the Reynolds number is about 500, the characteristic length being the diameter of the particle. When a gas passes over a flat surface of length L, the heat transfer coefficient is a function of the length x along the surface according to

$$h_x x/\kappa = 0.64(ux\rho/\eta)(1/2)(C_p\eta/\kappa)(1/3)$$

for streamline flow, and

$$h_x x/\kappa = 0.023(ux\rho/\eta)(4/5)(C_p\eta/\kappa)(1/3)$$

for turbulent flow.

There are three dimensionless numbers used in these equations, and their definitions are:

$u_x\rho/\eta$ = Reynolds number, N_{Re}, at the point x along the surface,

$h_x x/\kappa$ is the Nusselt number, N_{Nu}

and $C_p\eta/\kappa$ is the Prandtl number, N_{Pr}.

The relation given above for streamline flow can therefore be expressed as

$$N_{\mathrm{Nu}} = 0.64N_{\mathrm{Re}}^{1/2}N_{\mathrm{Pr}}^{1/3}$$

DropBooks

In the definition of the Prandtl number, C_p is the heat capacity of the gas at constant pressure.

Over the length of the solid the average value of the heat transfer coefficient $h(\mathrm{av})$ is given by

$$h(\mathrm{av}) = (1/L)\int h_x \mathrm{d}x$$

from 0 to L. In most circumstances of streamline flow of a gas, the Prandtl number may be taken as approximately one, since this number only varies between 0.5 and 1.0. The Reynolds number is therefore the most significant number in determining the Nusselt number. Generally speaking, when the surface of the solid is rough, turbulent conditions are likely to apply, even when the Reynolds number has the value of 100.

For low values of the Reynolds number, such as 10, where streamline flow should certainly apply, the Nusselt number has a value of about 2, and a typical value of the average heat transfer coefficient is 10^{-4}. For a Reynolds number of 104, where the gas is certainly in turbulent flow, the value of the Nusselt number is typically 20. Hence there is only a difference of a factor of ten in the heat transfer coefficient between these two extreme cases.

The Nusselt number for the heat transfer between a gas and a solid particle of radius d, is given by the Ranz–Marshall equation

$$N_{\mathrm{Nu}} = 2.0 + 0.6\, N_{\mathrm{Re}}^{1/2} N_{\mathrm{Pr}}^{1/3}$$

where the corresponding Reynolds number is defined by

$$N_{\mathrm{Re}} = du\rho/\nu$$

This yields a value of 4 for the Nusselt number in a situation where N_{Re} is about 10, which is typical of a small laboratory study.

The Rowe–Claxton empirical equation has been found to conform to many experimental studies of heat transfer in a packed bed, such as the reactor typically used in the catalytic processes described earlier. It is first necessary in this situation to define the voidage of the system, ΔV, where

$$\Delta V = \text{total volume of bed} - \text{volume of solid particles}$$

The equation then becomes

$$hd_s/\kappa_g = A + BN_{\mathrm{Re}}^{n} N_{\mathrm{Pr}}^{1/3}$$

where

$$A = 2/(1 - \Delta V)^{1/3}$$

$$B = 2/3\Delta V$$

and the exponent n is defined by the equation

$$\frac{2 - 3n}{3n - 1} = 4.65\, N_{\mathrm{Re}}^{-0.28}$$

d_s is the diameter of the particles, and κ_g is the thermal conductivity of the gas.

The above equations for heat transfer apply when there is no heat generation or absorption during the reaction, and the temperature difference between the solid and the gas phase can be simply defined throughout the reaction by a single value. Normally this is not the case, and due to the heat of the reaction(s) which occur there will be a change in the average temperature with time. Furthermore, in the case where a chemical reaction, such as the reduction of an oxide, occurs during the ascent of the gas in the reactor, the heat transfer coefficient of the gas will vary with the composition of the gas phase.

Industrial reactors for iron ore reduction to solid iron

The reduction of iron ores is carried out on the large industrial scale in the iron-making blast furnace, where CO is the reducing gas and the product is liquid

iron saturated in carbon. Alternatively, several designs of packed bed reactors have been proposed, in which the reducing gas is frequently the reformed mixture of CO, H_2 and N_2 obtained from the reaction between natural gas and air, and the product is solid iron powder which has been sintered to form porous pellets.

The reaction mechanism for the solid state reduction is the same as that described above for the hydrogen reduction of haematite, namely the formation of a porous iron product which results from the penetration of pores in the reacting pellets by reducing gases, and the migration of the reaction products, CO_2 and H_2O through these pores back into the gaseous phase.

The solid iron ore is formed into pellets, which are presented to the gas in a vertical shaft containing the pellets in the form of a packed bed. The reducing gas enters the shaft at the bottom and rises through the packed bed reacting to form gaseous oxidation products, CO_2 and H_2O. The heat required to raise the reactants to a temperature at which the reaction rate is fast enough is usually carried by the inlet gas phase.

In order to analyse the packed bed process, it is necessary to consider both heat transfer from the solid to the gas and reaction heat which may be transmitted to the gas. The composition of the gas, and hence its physical properties, are determined by the rate of reduction, which in turn depends on each layer of the packed bed, and on the degree of reduction which has already occurred. In the reduction of haematite, there are three stages in the reduction, corresponding to the formation of Fe_3O_4 and FeO before the metal is formed. The thermal data for the reduction processes can be approximated by the respective heats of reduction by H_2 and CO gases. Taking 1000°C as a typical mean temperature, the mean value for the heats of reaction per 2 gram-atom of iron are

$$Fe_2O_3 + H_2 \longrightarrow Fe_3O_4 + H_2O \quad \Delta H^\circ = +5.8\,\text{kJ per 2 gram-atom Fe}$$

$$Fe_3O_4 + H_2 \longrightarrow FeO + H_2O \quad \Delta H^\circ = +26\,\text{kJ 2 gram-atom}$$

$$FeO + H_2 \longrightarrow Fe + H_2O \quad \Delta H^\circ = +28\,\text{kJ 2 gram-atom}$$

For complete reduction of Fe_2O_3 by hydrogen

$$\Delta H^\circ = 59.8\,\text{kJ mol}^{-1}\text{Fe}_2\text{O}_3$$

and for CO reduction

$$Fe_2O_3 + CO \longrightarrow Fe_3O_4 + CO_2 \quad \Delta H^\circ = -5.2\,\text{kJ per 2 gram-atom Fe}$$

$$Fe_3O_4 + CO \longrightarrow FeO + CO_2 \quad \Delta H^\circ = 5.3\,\text{kJ 2 gram-atom}$$

$$FeO + CO \longrightarrow Fe + CO_2 \quad \Delta H^\circ = -38.9\,\text{kJ 2 gram-atom}$$

For complete reduction of Fe_2O_3 by carbon monoxide

$$\Delta H^\circ = -38.8\,\text{kJ mol}^{-1}\text{Fe}_2\text{O}_3$$

DropBooks

Since the reforming of CH_4 produces 1 mole of CO for each 2 moles of H_2, the dominant heat effect in the reduction process is the endothermic reduction by hydrogen. However, since the reforming process is carried out with air as the source of oxygen, the heat content of the nitrogen component is a thermal reservoir for the overall reduction process.

The heat of formation of the reformed products is

$$CH_4 + (1/2)O_2 = CO + 2H_2 \quad \Delta H^\circ_{1273} = -21.600\,\text{kJ mol}^{-1}CH_4$$

or at complete reaction

$$CH_4 + 2O_2 = CO_2 + 2H_2O \quad \Delta H^\circ_{1273} = -80\,250\,\text{kJ mol}^{-1}CH_4$$

The heat contents of the Fe_2O_3 and the gases at 1000°C in kJ mol^{-1} which are involved in the process are Fe_2O_3 : 140, H_2 : 29, CO : 25, N_2 : 31, CO_2 : 48, and H_2O : 37.5

It is quite clear from these data that the reducing gas phase must be pre-heated before being used in the reduction shaft, and that the addition of an excess of oxygen over the amount required to form CO and H_2 only, provides a larger source of reaction heat but less reducing power. The pre-heating of the CO/H_2 mixture to 1000°C adds about 84 kJ $mol^{-1}CH_4$ to the ingoing enthalpy content of the gas. In order to avoid the possibility of soot particle formation during the reforming process, it is preferable to add a small excess of oxygen over the stoichiometric composition for CO formation, and thus also profit from the small increase in the heat content of the product, which will now contain a small partial pressure of CO_2 and H_2O. The thermodynamic data for the degree of reduction which can be carried out by the reducing gas, show that about 50% of the reductant can be used to produce iron from 'FeO', the non-stoichiometric oxide of iron and from Fe_3O_4, after which the resulting gas serves only as a reductant for Fe_2O_3 to Fe_3O_4, and as a pre-heater for the unreduced material.

Pilot plant tests which confirm these data show that the percentage utilization of a gas mixture of 2:1 H_2 with CO containing 38% N_2 and a few per cent of CO_2 and H_2O, which is pre-heated to 1000°C, is between 35 and 40%, with a throughput volume of 1400–1600 m^3 of reducing gas per ton Fe_2O_3 (in pellet form of diameter 3.1 cm). The reactor produces about 16 tons of iron sponge per day from a packed bed of 3 m height and 130 cm diameter. Ancillary experimental data show that the time for complete reduction of 400 g Fe_2O_3 pellets is about 20 minutes under comparable flow rates with the same gas mixture in a smaller laboratory system.

The industrial roasting of sulphides

The objective in the roasting of sulphides, such as copper sulphides and zinc sulphides, is to convert these into their corresponding oxides by reaction with

air. The two most successful methods for doing this are the moving bed and the fluidized bed roasters. In both arrangements the reaction of oxidation in air is highly exothermic, and the gaseous products contain oxides of sulphur. The reactions are usually carried out at mean temperatures below 1500 K, and the products are solid oxides in which the total surface area is considerably higher than that of the reactant.

The first successful study which clarified the mechanism of roasting, was a study of the oxidation of pyrite, FeS_2, which is not a typical industrial process because of the availability of oxide iron ores. The experiment does, however, show the main features of roasting reactions in a simplified way which is well supported by the necessary thermodynamic data. The Gibbs energy data for the two sulphides of iron are,

$$\mathrm{Fe} + \mathrm{S_2(g)} = \mathrm{FeS_2(pyrite)}$$

$$\Delta G^\circ = -297\,440 + 196.7\,\mathrm{J\,mol^{-1}}$$

and

$$2\mathrm{Fe} + \mathrm{S_2(g)} = 2\mathrm{FeS\ (pyrrhotite)}$$

$$\Delta G^\circ = -309\,770 + 117.7T\,\mathrm{J\,mol^{-1}}$$

It can be readily calculated that pyrite will exert a sulphur dissociation pressure of 1 atmos only at 1512 K. However, when the sulphide reacts with air the main gaseous product is SO_2, and the reaction is then

$$3\mathrm{FeS_2} + 8\mathrm{O_2} = \mathrm{Fe_3O_4} + 6\mathrm{SO_2}$$

$$\Delta G^\circ = -2\,362\,800 + 142.4T\,\mathrm{J\,mol^{-1}}$$

which is an extremely exothermic reaction. Because of this the oxide layer which is formed on the surface of the sulphide is cracked, thus admitting more oxygen to the residual sulphide kernel.

The corresponding reaction for the oxidation of pyrrhotite has a somewhat different behaviour. There is an initial reaction leading to the formation of SO_2, but no formation of the oxide layer. After a period of oxidation in this mode, the reaction shown by pyrite occurs, with the formation of a cracked oxide product. During the initial 'quiet' period it is found that the sulphur/iron ratio in the sample increases and iron is removed to the surface as magnetite, until a critical state is reached where oxidation of sulphur occurs. Pyrrhotite is known to show a range of composition, and it is this range which is traversed before the oxidation of sulphur occurs. Clearly, the iron is initially removed from the interior of the solid to the gas–solid interface where it has a lower chemical potential in combination with oxygen. This phenomenon is common among sulphides, and when these are complex, i.e. they contain more than

DropBooks

one metal, as in the case of chalcopyrite, $CuFeS_2$, the metal which forms the more stable oxide, in this case iron, is preferentially removed from the sulphide by oxidation, the remaining kernel being more rich in copper than the original ore.

The industrial methods for carrying out these reactions involve the oxidation of separate particles, or the oxidation of thick layers of sulphide. In the *flash roaster* particles are dropped down a tower to fall under gravity, in an atmosphere of air. The particles are assumed to interact completely with the atmosphere during free fall. In *fluosolid roasting* the particles are reacted in an upward flow of air, which keeps the particles floating in the gas phase as well as being separated. The roasted products are removed from the reactor by increasing the gas flow rate. The flow rate of gas necessary to support the particles will clearly be a compromise, because of the distribution of sizes of the particles.

In the fixed-bed and moving-bed roasters, the bed of particles is ignited by the roasting reaction in air and slowly moved through the reactor either by a moving belt, or down a series of horizontal stages by the action of rotary rakes which slowly sweep the material across each stage, finally to fall a short distance to the next stage.

In all of these systems, the rate of generation at the gas–solid interface is so rapid that only a small fraction is carried away from the particle surface by convective heat transfer. The major source of heat loss from the particles is radiation loss to the surrounding atmosphere, and the loss per particle may be estimated using unity for both the view factor and the emissivity as an upper limit from this source. The practical observation is that the solids in all of these methods of roasting reach temperatures of about 1200–1800 K.

The corrosion of metals in multicomponent gases

The reaction of metals with gas mixtures such as CO/CO_2 and SO_2/O_2 can lead to products in which the reaction of the oxygen potential in the gas mixture to form the metal oxides is accompanied by the formation of carbon solutions or carbides in the first case, and sulphide or sulphates in the second mixture. Since the most important aspects of this subject relate to the performance of materials in high temperature service, the reactions are referred to as *hot corrosion* reactions. These reactions frequently result in the formation of a liquid as an intermediate phase, but are included here because the solid products are usually rate-determining in the corrosion reactions.

As an example of the mechanism of these corrosion reactions, the oxidation of metals containing a carbide-forming element, e.g. chromium in Fe–Ni–Cr stainless steels, by CO_2/CO gas mixtures leads to the formation of an oxide which would typically contain grain boundaries. When the reacting gas mixture permeates the oxide, by grain boundary diffusion, the gas mixture will equilibrate with the oxide scale, following the oxygen potential gradient in the

oxide. As the gas approaches the metal/oxide interface, the composition of the gas will have been substantially enriched in CO, and if the resulting CO/CO_2 mixture has a high enough carbon potential, then carbide particles will be formed at or near the interface.

Aircraft turbines in jet engines are usually fabricated from nickel-based alloys, and these are subject to combustion products containing compounds of sulphur, such as SO_2, and oxides of vanadium. Early studies of the corrosion of pure nickel by a 1:1 mixture of SO_2 and O_2 showed that the rate of attack increased substantially between 922 K and 961 K. The nickel–sulphur phase diagram shows that a eutectic is formed at 910 K, and hence a liquid phase could play a significant role in the process. Microscopic observation of corroded samples showed islands of a separate phase in the nickel oxide formed by oxidation, which were concentrated near the nickel/oxide interface. The islands were shown by electron microprobe analysis to contain between 30 and 40 atom per cent of sulphur, hence suggesting the composition Ni_3S_2 when the composition of the corroding gas was varied between SO_2:O_2 equal to 12:1 to 1:9. The rate of corrosion decreased at temperatures above 922 K.

The thermodynamic activity of nickel in the nickel oxide layer varies from unity in contact with the metal phase, to 10^{-8} in contact with the gaseous atmosphere at 950 K. The sulphur partial pressure as $S_2(g)$ is of the order of 10^{-30} in the gas phase, and about 10^{-10} in nickel sulphide in contact with nickel. It therefore appears that the process involves the uphill pumping of sulphur across this potential gradient. This cannot occur by the counter-migration of oxygen and sulphur since the mobile species in the oxide is the nickel ion, and the diffusion coefficient and solubility of sulphur in the oxide are both very low.

DropBooks

It was shown earlier that the oxidation rate of nickel at this temperature is dominated by grain boundary migration, and therefore the possibility exists that SO_2 can diffuse through the boundaries, and penetrate the oxide. If this is so then the diffusing species will come into contact with a decreasing oxygen partial pressure as it penetrates the oxide, and will therefore exert a higher sulphur dissociation pressure. When the oxygen partial pressure is 10^{-16} at the metal/oxide interface, this pressure would be nearly one atmosphere, if the original partial pressure of SO_2 were one atmosphere. This can clearly not be the case since there would be no driving force for SO_2 diffusion from the gas phase, across the boundary layer and through the oxide. Even if this pressure were 10^{-6} atmos at the metal/oxide interface, however, the sulphur pressure would be high enough to allow the formation of Ni_3S_2.

The thermodynamic data for this discussion are:

$$2Ni + O_2 = 2NiO; \quad \Delta G^\circ = -478\,500 + 177T \text{ J}$$

$$3Ni + S_2 = Ni_3S_2; \quad \Delta G^\circ = -350\,400 + 180.7T$$

$$S_2 + 2O_2 = 2SO_2; \quad \Delta G^\circ = -723\,100 + 144.6T$$

Bibliography

W.M. McKewan. *Trans. AIME*, **212**, 791 (1958), ibid. **218**, 2 (1960).
R.G. Olsson and W.M. McKewan. *Trans. AIME*, **236**, 1518 (1966).
D.E. Rosner and H.D. Allendorf. *Heterogeneous Kinetics at Elevated Temperatures*, G.R. Belton and W.L. Worrell (eds), p. 231. Plenum Press, New York (1970).
E.A. Gulbransen and S.A. Jansson. *ibid.*, p. 181.
K. Niwa, T. Wada and Y. Shiraishi. *Trans. AIME*, **209**, 269 (1957).
P.G. Thornhill and L.M. Pidgeon. *ibid.*, **209**, 989 (1957).
C.B. Alcock and M.G. Hocking. *Trans. I.M.M.*, **75**, C27 (1966).
L. von Bogdandy and H.J. Engell. *The Reduction of Iron Ores*. Springer Verlag, Berlin (1971).
M. Radovanovic. *Fluidized Bed Combustion*. Hemisphere Publishing Corp, New York (1985) TJ 254.5 F585.

Appendix: Thermodynamic data for the Gibbs energy of formation of metal oxides

Group IA Oxides		
$4Li + O_2 \longrightarrow 2Li_2O$	$\Delta G^\circ = -1196\,800 + 249.3T$	300–450
Liquid Li	$= -1210\,400 + 279.4T$	450–700
$4Na + O_2 \longrightarrow 2Na_2O$	$\Delta G^\circ = -830\,180 + 260.3$	300–350
Liquid Na	$= -844\,140 + 289.3T$	400–500
$4K + O_2 \longrightarrow 2K_2O$	$\Delta G^\circ = -729\,100 + 287.3T$	400–700
Liquid K only		
$4Rb + O_2 \longrightarrow 2Rb_2O$	$\Delta G^\circ = -699\,840 + 278.9T$	350–700
Liquid Rb only		
$4Cs + O_2 \longrightarrow 2Cs_2O$	$\Delta G^\circ = -685\,720 + 288T$	350–700
Liquid Cs only		
Group IB		
$4Cu + O_2 \longrightarrow 2Cu_2O$	$\Delta G^\circ = -344\,180 + 147.2T$	300–1300
Liquid Cu	$= -328\,510 + 136.2T$	1300–1700
$2Cu_2O + O_2 \longrightarrow 4CuO$	$\Delta G^\circ = -290\,690 + 196.2T$	300–1200
$4Ag + O_2 \longrightarrow 2Ag_2O$	$\Delta G^\circ = -61\,780 + 132T$	298–450
Group IIA		
$2Be + O_2 \longrightarrow 2BeO$	$\Delta G^\circ = -1\,217\,200 + 194.1T$	298–1557
Liquid Be	$= -1\,213\,400 + 191.0T$	1557–2000
$2Mg + O_2 \longrightarrow 2MgO$	$\Delta G^\circ = -1\,206\,300 + 273.7T$	300–900
Liquid Mg	$= -1\,201\,400 + 270.0T$	1000–1350

$2Ca + O_2 \longrightarrow 2CaO$	$\Delta G^\circ = -1\,267\,600 + 206.2T$	298–1124
Liquid Ca	$= -1\,282\,900 + 219.8T$	1124–1760
$2Sr + O_2 \longrightarrow 2SrO$	$\Delta G^\circ = -1\,181\,500 + 191.8T$	300–1000
Liquid Sr	$= -1\,194\,300 + 204.1T$	1050–1600
$2Ba + O_2 \longrightarrow 2BaO$	$\Delta G^\circ = -1\,093\,600 + 178.9T$	300–980
Liquid Ba	$= -1\,106\,800 + 191.8T$	983–1600
Group IIb		
$2Zn + O_2 \longrightarrow 2ZnO$	$\Delta G^\circ = -699\,920 + 198.3T$	300–650
Liquid Zr	$= -711\,120 + 214.1T$	700–1000
$2Cd + O_2 \longrightarrow 2CdO$	$\Delta G^\circ = -515\,500 + 195.5T$	298–590
Liquid Cd	$= -524\,590 + 210.7T$	600–900
$2Hg + O_2 \longrightarrow 2HgO$	$\Delta G^\circ = -108\,900 + 214.3T$	300–600
Liquid Hg only		
Group IIIA		
$4/3B + O_2 \longrightarrow 2/3B_2O_3$	$\Delta G^\circ = -848\,130 + 177.0T$	300–700
Liquid B_2O_3	$= -827\,040 + 147.9T$	750–1200
$4/3Al + O_2 \longrightarrow 2/3Al_2O_3$	$\Delta G^\circ = -1\,115\,700 + 208.3T$	298–923
Liquid Al	$= -1\,124\,800 + 218.3T$	923–1800
$4/3Sc + O_2 \longrightarrow 2/3Sc_2O_3$	$\Delta G^\circ = -1\,268\,900 + 196.1T$	300–1700
$2/3Y + O_2 \longrightarrow 2/3Y_2O_3$	$= -1\,264\,300 + 189.2T$	300–1700
$4/3La + O_2 \longrightarrow 2/3La_2O_3$	$= -1\,191\,800 + 187.4T$	300–1000
Liquid La	$= -1\,196\,400 + 190.4T$	1150–1600
$4/3Sm + O_2 \longrightarrow 2/3Sm_2O_3$	$\Delta G^\circ = -1\,211\,800 + 191.9T$	300–1300
$4/3Eu + O_2 \longrightarrow 2/3Eu_2O_3$	$= -1\,198\,000 + 197.4T$	300–1050
$4/3Gd + O_2 \longrightarrow 2/3Gd_2O_3$	$= -1\,212\,800 + 187.7T$	300–1500
Group IIIB		
$4/3Ga + O_2 \longrightarrow 2/3Ga_2O_3$	$\Delta G^\circ = -731\,090 + 223.7T$	300–1000
Liquid Ga only		
$4/3In + O_2 \longrightarrow 2/3In_2O_3$	$\Delta G^\circ = -618\,160 + 215.2T$	450–1000
Liquid In only		
$4Tl + O_2 \longrightarrow 2Tl_2O$	$\Delta G^\circ = -334\,360 + 192.1T$	300–550
Liquid Tl	$= -350\,670 + 220.8T$	600–850
$Tl_2O + O_2 \longrightarrow Tl_2O_3$	$\Delta G^\circ = -221\,020 + 196.4T$	300–800

DropBooks

Group IV		
$2C + O_2 \longrightarrow 2CO(g)$	$\Delta G^\circ = -227\,140 - 172.6T$	298–2000
$C + 2O_2 \longrightarrow CO_2(g)$	$= -395\,360 - 0.365T$	298–2000
$Si + O_2 \longrightarrow SiO_2$	$= -907\,030 - 175.7T$	300–1700
$Ge + O_2 \longrightarrow GeO_2$	$= -577\,780 + 191.3T$	300–1200
$Sn + O_2 \longrightarrow SnO_2$	$= -581\,440 + 215T$	525–900
Liquid Sn only		
$2Pb + O_2 \longrightarrow 2PbO$	$= -436\,910 + 196.5T$	300–600
Liquid Pb	$= -442\,170 + 204.9T$	600–750
Liquid PbO	$= -438\,090 + 199.6T$	800–1100
$2PbO + O_2 \longrightarrow 2PbO_2$	$\Delta G^\circ = -109\,790 + 193.1T$	300–550
$2Ti_2O_3 + O_2 \longrightarrow 2TiO_2$	$= -744\,910 + 179.3T$	300–1500
$Zr + O_2 \longrightarrow ZrO_2$	$= -1\,096\,100 + 184.3T$	300–1800
$Th + O_2 \longrightarrow ThO_2$	$= -1\,222\,300 + 183.6T$	300–1500
Group V		
$2V_2O_3 + O_2 \longrightarrow 4VO_2$	$\Delta G^\circ = -396\,870 + 142.8T$	300–1000
$4VO_2 + O_2 \longrightarrow 2V_2O_5$	$= -263\,880 + 187.6T$	300–950
$2NbO + O_2 \longrightarrow 2NbO_2$	$= -746\,020 + 177.1T$	300–1100
$4NbO_2 + O_2 \longrightarrow 2Nb_2O_5$	$= -618\,860 + 147.0T$	300–1000
$4/5Ta + O_2 \longrightarrow 2/5Ta_2O_5$	$= 813\,060 + 169.3T$	300–1500
$4/3Bi + O_2 \longrightarrow 2/3Bi_2O_3$	$= -382\,780 + 185.0T$	298–773
Liquid Bi	$= -375\,540 + 179.9T$	773–1100
Group VI		
$4/3Cr + O_2 \longrightarrow 2/3Cr_2O_3$	$\Delta G^\circ = -750\,790 + 171.4T$	300–1600
$Mo + O_2 \longrightarrow MoO_2$	$= -585\,440 + 181.4T$	300–1000
$2MoO_2 + O_2 \longrightarrow 2MoO_3$	$= -311\,070 + 133.6T$	300–1000
$W + O_2 \longrightarrow WO_2$	$= -583\,930 + 175.5T$	300–1500
$2WO_2 + O_2 \longrightarrow 2WO_3$	$= -502\,460 + 145.1T$	300–1000
$U + O_2 \longrightarrow UO_2$	$= -1\,081\,700 + 169.8T$	300–1500
$3UO_2 + O_2 \longrightarrow U_3O_8$	$= -310\,600 + 133.5T$	300–1500

Group VII

$2Mn + O_2 \longrightarrow 2MnO$	$\Delta G^\circ = -768\,990 + 146.2T$	300–1500
Liquid Mn	$= -811\,130 + 174.8T$	1500–1800
$6MnO + O_2 \longrightarrow 2Mn_3O_4$	$= -465\,770 + 256.3T$	300–1000
$Mn_3O_4 + O_2 \longrightarrow 3MnO_2$	$= -174\,050 + 197.6T$	300–1000

Group VIII

$2Fe + O_2 \longrightarrow 2$"FeO"	$\Delta G^\circ = -522\,830 + 130.1T$	300–1640
	$= -548\,150 + 144.2T$	1800–2000
2"FeO" $+ O_2 \longrightarrow 2Fe_3O_4$	$= -624\,420 + 250.2T$	300–1600
$4Fe_3O_4 + O_2 \longrightarrow 6Fe_2O_3$	$= -517\,810 + 307.9T$	300–1500
$2Co + O_2 \longrightarrow 2CoO$	$= -470\,280 + 144.8T$	298–1400
$6CoO + O_2 \longrightarrow 2Co_3O_4$	$= -409\,530 + 338.3T$	300–1200
$2Ni + O_2 \longrightarrow 2NiO$	$= -471\,790 + 172.1T$	300–1700
$Ru + O_2 \longrightarrow RuO_2$	$= -301\,640 + 166.8T$	300–1000
$4/3Rh + O_2 \longrightarrow 2/3Rh_2O_3$	$= -234\,060 + 169.4T$	300–m.pt
$2Pd + O_2 \longrightarrow 2PdO$	$= -227\,770 + 194.9T$	300–m.pt
$Os + O_2 \longrightarrow OsO_2$	$= -291\,310 + 177.9T$	300–m.pt
$Ir + O_2 \longrightarrow IrO_2$	$= -246\,810 + 183.4T$	300–m.pt

DropBooks

Note: These data have been obtained from the complete thermodynamic data tabulated in Kubaschewski *et al.* (loc. cit.), with the approximation of the simple two-term equation. This should serve for calculations not requiring an accuracy of better than $2\,kJ\,mol^{-1}\,O_2$, which is normally the case for industrial applications. Solid state crystal transformations which usually only have relatively small heats of transformation, have been ignored.

Part 3

Processes Involving Liquids

Introduction

In liquid phase processes, there is little to choose in their optimization from the point of view of diffusion, since there is not a large variation in diffusion coefficients, which also have a small temperature coefficient, in the case of liquid metals. In liquid salts there is generally a lower diffusion rate than in metals, and so it is processes in these phases which are rate-determining in metal–salt systems. Again, there is a small temperature dependence of the diffusion coefficients, but other physical properties, such as the viscosity, play a larger role. Thermodynamic factors and interfacial areas are dominant in most high-temperature processes, and optimization is usually achieved by increasing the area of contact and relative states of motion between reacting phases.

Chapter 10

Physical properties and applications of liquid metals

The structures and mechanism of diffusion of liquid metals

The results of the early experimental studies of self-diffusion in liquid metals were interpreted in much the same way as were those for solid metals. The variation of the diffusion coefficient with temperature was fitted to an Arrhenius equation and an activation enthalpy for diffusion, usually around 20 kJ, was obtained. The Arrhenius expression applies to the solid state where a rate process occurs by means of a number of identical unit steps, and thus in the solid state an atom moves to a vacant site in the lattice, leaving behind an identical vacancy to replace the filled one. It is easy to see why the unit step should always be the same for solid systems where the structure is a regular three-dimensional lattice. The same argument cannot be transposed to liquid systems mainly because this long-range structural order is not a property of liquid systems. In these, it is more probable that thermal vibrations will generate unoccupied volumes in the liquid into which atoms may flow by a diffusive step, but that the length of these translations could well vary over a wide range of values. The regular fixed step of the solid is replaced by a step of varying length in the liquid. The activation enthalpy for the formation of these holes in the structure and the enthalpy for the movement of atoms into them will also vary in the liquid (Table 10.1).

DropBooks

A system in which a number of processes occur, with a number of activation enthalpies, does not fit the Arrhenius equation. If this description is applied however, the diffusion process appears to have a low activation enthalpy at low temperatures and a higher value at higher temperatures. In the case of liquid diffusion, this would suggest that the average diffusion steps grows longer as the temperature increases. Swalin (1959) was the first to show conclusively that the apparent fit to an Arrhenius expression for most previous work on liquid metal diffusion was probably due to the narrow range of temperatures which had been employed for measurement in any single system. When a wider range of temperature could be achieved, then significant departures were found from the Arrhenius equation. Instead of the relationship

$$D = D_0 \exp(-(\Delta H/RT))$$

Table 10.1 *Self diffusion coefficients of some liquid metals expressed by an Arrhenius equation*

Metal	Diffusion coefficient	Temp. range (°C)
Copper	$14.6\exp(-4800/T)$	1140–1260
Silver	$7.10\exp(-4070/T)$	1000–1100
Zinc	$8.2\exp(-2540/T)$	450–600
Mercury	$0.85\exp(-500/T)$	0–98
Gallium	$1.07\exp(-560/T)$	30–100
Indium	$2.90\exp(-1220/T)$	170–750
Tin	$3.24\exp(-1380/T)$	300–600
Lead	$9.15\exp(-2230/T)$	600–930
Sodium	$11.0\exp(-1230/T)$	100–220
Potassium	$16.0\exp(-1250/T)$	340–490

Swalin found for liquid tin and indium that the simpler equation which he had derived

$$D = \frac{5.39 \times 10^{-8}}{A} T^2$$

fitted the experimental results adequately. The constant A which has the dimensions $\mathrm{J\,cm^{-2}\,mol^{-1}}$ can be calculated approximately from structural data for the force constants α, of a particular liquid metal, and the heat of vaporization per gram-atom ΔH_v. Swalin assumed that metal atoms interact in a pairwise fashion according to a Morse function. The energy of interaction, according to this function, required to increase the distance between two neighbouring atoms by an amount x, which is related to the energy to form a vacancy for diffusion, is given by

$$E = E_D[1 + \exp(2\alpha x) - 2\exp(-\alpha x)]$$

E_D is the energy required for the breaking of the chemical bond between the atoms and this is obtained in good approximation by the equation which was used for solid metals

$$E_D = \frac{2\Delta H_v}{ZN_0} \text{ per bond}$$

where Z is the co-ordination number of each atom and N_0 is Avogadro's number.

The diffusive movement of atoms is assumed to have a range of values, and the probability that a jump of length between j and $j + \mathrm{d}j$ can occur is

given by Furth's equation

$$p(j)\mathrm{d}j = C j^2 \exp -[E(j)/kT]\mathrm{d}j$$

where C is a constant, and the average distance being

$$\overline{j}^2 = \int_0^\infty j^4 \left[\exp\left(-\frac{E(j)}{kT}\right)\right] \mathrm{d}j \Big/ \int_0^\infty j^2 \left[\exp\left(-\frac{E(j)}{kT}\right)\right] \mathrm{d}j$$

Swalin then uses a Maclaurin expansion of the Arrhenius term to obtain the energy of formation of a cavity in the liquid which permits a small jump, to obtain the equation

$$\overline{j}^2 = \frac{3ZN_0kT}{16\Delta H_v \alpha}$$

and hence using Einstein's equation for the diffusive movement of a particle moving randomly in three dimensions, as in Brownian motion,

$$D = \frac{1}{6}\frac{\overline{j}^2}{\tau} \text{ where } \frac{1}{\overline{\tau}} = \frac{kT}{h}Z$$

with τ obtained from a transition state theory equation for the movement of a particle over an energy barrier with Z neighbours, results in

$$D = \frac{3Z^2N_0k^2T^2}{96\Delta H_v h\alpha}$$

DropBooks

The Morse function which is given above was obtained from a study of bonding in gaseous systems, and this part of Swalin's derivation should probably be replaced with a Lennard–Jones potential as a better approximation. The general idea of a variable diffusion step in liquids which is more nearly akin to diffusion in gases than the earlier treatment, which was based on the notion of vacant sites as in solids, remains as a valuable suggestion.

Further support for this approach is provided by modern computer studies of molecular dynamics, which show that much smaller translations than the average inter-nuclear distance play an important role in liquid state atom movement. These observations have confirmed Swalin's approach to liquid state diffusion as being very similar to the calculation of the Brownian motion of suspended particles in a liquid. The classical analysis for this phenomenon was based on the assumption that the resistance to movement of suspended particles in a liquid could be calculated by using the viscosity as the frictional force in the Stokes equation

$$F = 3\pi d\eta U$$

where d is the particle diameter, and U is the (constant) velocity of the particle through the liquid of viscosity η. This, when combined with a diffusion component obtained from a random walk description yields the Stokes–Einstein equation for Brownian movement. This calculation was then extended to the movement of atoms in liquids, by substituting the diameter of atoms for the diameter of the particles.

$$D = \frac{kT}{3\pi\eta d}$$

The viscosity therefore replaces the restraint on diffusion arising from the interaction of atoms expressed by the Morse potential in Swalin's treatment.

The introduction of molecular dynamical considerations suggests that the the use of the atomic diameter in the Stokes–Einstein equation should be replaced by an expression more accurately reflecting the packing fraction of atoms in liquids, i.e. the volume available to an atom in a close-packed arrangement compared to that which is occupied in a liquid. An average value of this function for liquid metals is about 0.47, corresponding to a ratio of the distance of closest approach of the atoms in a liquid metal to the atomic radius of about 1.55. Each atom must be considered as moving in a 'cage' of nearest neighbours which is larger than that afforded by close packing, as in a solid.

Thermophysical properties of liquid metals

Viscosities of liquid metals

The viscosities of liquid metals vary by a factor of about 10 between the 'empty' metals, and the 'full' metals, and typical values are 0.54×10^{-2} poise for liquid potassium, and 4.1×10^{-2} poise for liquid copper, at their respective melting points. Empty metals are those in which the ionic radius is small compared to the metallic radius, and full metals are those in which the ionic radius is approximately the same as the metallic radius. The process was described by Andrade as an activated process following an Arrhenius expression

$$\eta = \eta_0 \exp Q_{\text{vis}}/RT \text{ poise}$$

where Q_{vis} has a value of about 5–25 kJ, and Eyring *et al*. have suggested that the viscosity is determined by the flow of the ion cores and if the energy for the evaporation of metals ΔE_{vap} is compared with that of viscosity,

$$(\Delta E_{\text{vap}}/Q_{\text{vis}}) \times (r_{\text{ion}}/r_{\text{metal}})^3 = 3 \text{ to } 4$$

A further empirical expression, due to Andrade, for the viscosity of liquid metals at their melting points, which agrees well with experimental data is

$$\eta = 5.1 \times 10^{-4} (MT_{\mathrm{M}})^{0.5} V \text{ poise}$$

where M is the molecular weight in grams, T_{M} is the melting point, and V is the molar volume in cm^3. A further point to note is that the viscosities of liquid metals are similar to that of water at room temperature, about 10^{-2} poise, and so useful models of the behaviour of high-temperature processes involving liquid metals can be made easily visible at room temperature using water to substitute for metals, and a suitable substitute for other phases, usually liquid salts or metallurgical slags, which can have up to 10 poise viscosity.

In connection with the earlier consideration of diffusion in liquids using the Stokes–Einstein equation, it can be concluded that the temperature dependence of the diffusion coefficient on the temperature should be $T(\exp(-Q_{\mathrm{vis}}/RT))$ according to this equation, if the activation energy for viscous flow is included.

Surface energies of liquid metals

A number of experimental studies have supplied numerical values for these, using either the classical maximum bubble pressure method, in which the maximum pressure required to form a bubble which just detaches from a cylinder of radius r, immersed in the liquid to a depth x, is given by

$$p_{\max} = x\rho_{\max} g + 2\frac{\gamma}{r}$$

DropBooks

where γ is the surface energy, and $\rho_{\max}$ is the maximum radius of the bubble just before detachment, or the Rayleigh equation for the oscillation frequency ω in shape of a freely suspended levitated drop of mass m in an electromagnetic field, which is related to the surface energy by

$$\gamma = \frac{3}{8}\pi m\omega^2$$

The resulting data for liquid metals indicate a systematic relationship with the bonding energy of the element, which is reflected in the heat of vaporization $\Delta H^{\circ}_{\mathrm{vap}}$. Skapski suggested an empirical equation

$$\gamma = K\frac{\Delta H^{\circ}_{\mathrm{vap}}}{V_m^{2/3}}$$

where K is a universal constant, and V_m is the molar volume, which provides a fair correlation among the data for elements. Because of the relatively high diffusion coefficients in liquids, and the probability of the rapid convection current distribution of solute elements to their equilibrium sites, the surface energies of liquid metals are found to be very sensitive to the presence

of surface active elements, and to be substantially reduced by non-metallic elements such as sulphur and oxygen, in the surrounding atmosphere. Great care must therefore be taken in the control of the composition of the gaseous environment to assure accurate data for liquid metals. Table 10.2 shows some representative results for elements which should be compared with the data for the corresponding solids (Table 10.2).

Table 10.2 *Surface energies of liquid elements*

Element	Surface energy ($mJ\,m^{-2}$)	ΔH_{vap}^{liquid} ($kJ\,mol^{-1}$)
Sodium	197	104
Antimony	371	244
Bismuth	382	198
Lead	457	190
Indium	556	237
Magnesium	577	138
Germanium	607	325
Gallium	711	267
Silicon	775	400
Zinc	789	123
Aluminium	871	320
Silver	925	274
Copper	1330	326
Uranium	1552	522
Iron	1862	401
Cobalt	1881	408

It will be observed that the surface energy is also approximately proportional to the melting point.

Surface energies of liquid iron containing oxygen or sulphur in solution yield surface energies approximately one-half of that of the pure metal at a concentration of only 0.15 atom per cent, thus demonstrating the large change in the surface energy of a metal when a small amount of some non-metallic impurities is adsorbed to the surface of the metal.

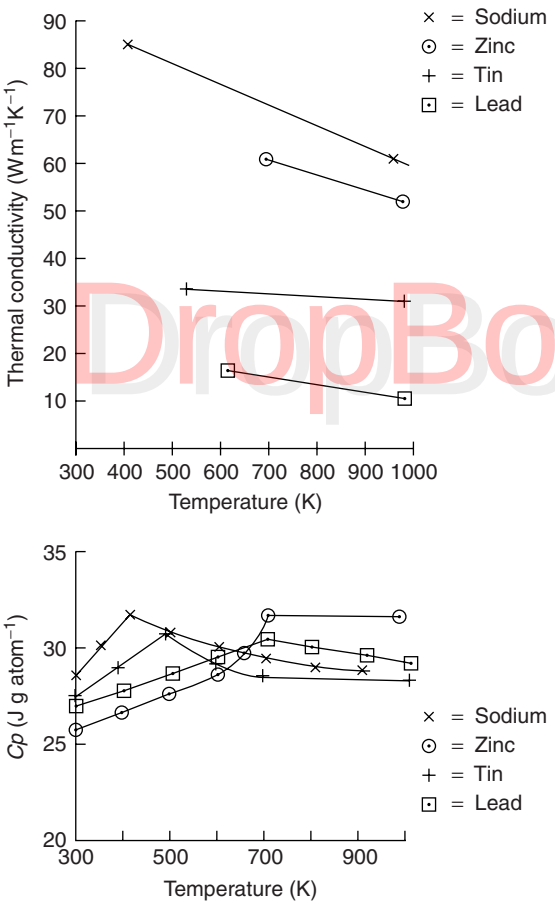
Thermal conductivity and heat capacity

The conduction of heat by liquid metals is directly related to the electronic structure. Heat is carried through a metal by energetic electrons having

translational energies above the energy distribution of the metal ion cores. The conductivity can therefore be calculated using the Lorenz modification of the Wiedemann–Franz ratio

$$\frac{K}{\sigma T} = \text{a constant}$$

where the constant for liquid metals is about 2.5 W ohm K^{-2}. For liquid silver near the melting point, this value is 2.4, and the corresponding value for the solid metal is approximately the same. The thermal conductivity would therefore be about 3.8 W cm^{-1} K^{-1}.



DropBooks

Figure 10.1 *Thermal conductivities and heat capacities of the low-melting elements Na, Zn, Sn and Pb*

The heat capacity is largely determined by the vibration of the metal ion cores, and this property is also close to that of the solid at the melting point. It therefore follows that both the thermal conductivity and the heat capacity will decrease with increasing temperature, due to the decreased electrical conductivity and the increased amplitude of vibration of the ion cores (Figure 10.1).

The production of metallic glasses

A number of metallic alloys form stable glasses when quenched rapidly from the liquid state. These materials fall into two categories, one containing a metalloid dissolved in a metal at about 15–30 atom per cent, and the other containing metals only, with compositions around the 50–50 atom per cent composition. Examples of the first are the systems Ni–P, Au–Si, Pd–Si, Ge–Te and Fe–B. In each of the first group of systems, the phase diagram shows the existence of a low melting eutectic, compared with the melting point of the metallic constituent. In the second group the only similarity appears to be a stronger interaction in the liquid than in the solid state. Some systems form inter-metallic compounds, and others show immiscibility in the solid state. There are also some more complex systems composed of the elements above, such as the ternary systems Fe–Pd–P, Ni–Pt–P, and the Ni–Fe–P–B quaternary.

The structures of the first group of glasses are consistent with the suggestion that the smaller metalloid atoms fill holes in the metal structure, and enable a closer approach of the metal atoms and an increased density. The arrangement of the metal atoms can either be in a random network or in the dense random packing model of Bernal, in which the co-ordination number of the metalloid can be 4, 6, 8, 9 and 10, some of the latter three involving 5 co-ordination of the non-metal. The formation of glass requires that the rate of cooling from the melt must be greater than the rate at which nucleation and growth of a crystalline phase can occur. The minimum rate of cooling to attain the glass structure can be obtained for any system by the observation of the rate of crystallization as a function of supercooling below the liquidus. The extremum of the TTN (time, temperature, nucleation rate) curve shows the maximum rate of nucleus formation as a function of undercooling temperature, and hence the minimum in the rate of cooling required to achieve the formation of a glass.

According to homogeneous nucleation theory, the critical Gibbs energy to form a nucleus is given by

$$\Delta G^* = \frac{16}{3}\frac{\pi\gamma^3}{\Delta G_s^2}$$

In the present case of the nucleation of solid particles from a liquid, the heat capacity change from liquid to solid may be ignored, and hence ΔG_s can be

expressed in terms of the fusion data thus

$$\Delta G_s = \Delta H_s - T\Delta S_s = \frac{\Delta H_f}{T_f}(T - T_f) = \Delta S_f \Delta T$$

(Note: $\Delta H_f = -\Delta H_s$; $\Delta S_f = -\Delta S_s$)

The rate of formation of stable nuclei per unit volume of liquid can be described by the general equation

$$\text{Rate/second} = n f_0 \exp\left(-\frac{\Delta G_M}{RT}\right) \exp\left(-\frac{\Delta G^*}{V_m RT}\right)$$

where ΔG_M is the activation Gibbs energy of diffusion, and describes the rate of arrival of atoms by diffusive jumps at the surface of the nucleus, and n is the number of atoms at the surface of the nucleus. Here, ΔT is the degree of supercooling, and V_m is the molar volume of the solid metal.

The critical size of the stable nucleus at any degree of under cooling can be calculated with an equation derived similarly to that obtained earlier for the concentration of defects in a solid. The configurational entropy of a mixture of nuclei containing n^* atoms with n_0 atoms of the liquid per unit volume, is given by the Boltzmann equation

$$\Delta S_m = k \ln \frac{[n_0 + n^*]!}{n_0!\, n^*!}$$

DropBooks

Eliminating the factorials by Stirling's approximation, which is strictly only correct for large numbers, differentiating the resulting expression for the Gibbs energy of this mixture of nuclei of this size and liquid atoms, with respect to the size of the nucleus, and setting this equal to zero to obtain the most probable value of n^*, it follows that

$$\frac{n^*}{n_0} = \exp\left(-\frac{\Delta G^*}{kT}\right) = \exp\left(-\left[\frac{16}{3}\frac{\pi\gamma^3 V_m^2}{[\Delta S_f \Delta T]^2}\right]\right)$$

for homogeneous nucleation. For most metals, the entropy of fusion is approximately 10 J K^{-1} mol^{-1}, the interfacial energy of solids is about 2×10^{-5} J cm^{-2}, and the molar volume is about 8 cc g atom^{-1} hence this expression may be simplified to

$$\Delta G^* \cong \frac{10^{-13}}{\Delta T^2}\ \text{J}$$

with the critical nucleus diameter of $320/\Delta T$ nm. It will be seen that the rate of nucleation depends on one factor which decreases as the temperature decreases, the diffusion rate to the surface of the nucleus, while the other, the critical nucleus size and formation Gibbs energy, also decreases as the

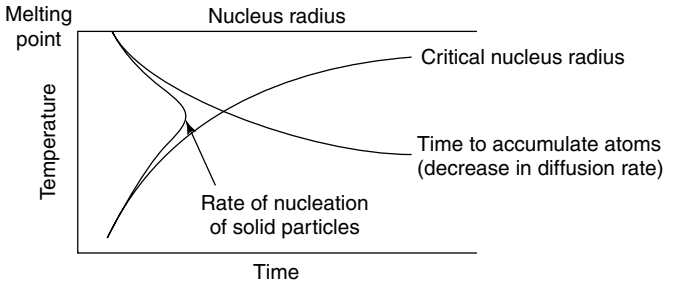


Figure 10.2 *The time–temperature–nucleation curve showing the balance between the rate of nucleation and the critical radius which produces a maximum rate*

temperature decreases. The two factors have opposing temperature effects, and thus the rate of nucleation goes through a maximum at the 'nose' of the TTN curve (Figure 10.2).

Using the Stokes–Einstein equation for the viscosity, which is unexpectedly useful for a range of liquids as an approximate relation between diffusion and viscosity, explains a resulting empirical expression for the rate of formation of nuclei of the critical size for metals

$$\text{Rate} = \frac{K}{\eta} \exp\left(-\frac{0.0205A^*}{\Delta T_r^2 T_r^3}\right)$$

where A^*kT^* is the energy of critical nucleus formation, ΔG^*, $T^* = 0.8T_{\text{M}}$, T_r is the the ratio of the temperature to the melting point and K is a universal rate constant.

Liquid metals in energy conversion

Nuclear and magneto-hydrodynamic electric power generation systems have been produced on a scale which could lead to industrial production, but to-date technical problems, mainly connected with corrosion of the containing materials, has hampered full-scale development. In the case of nuclear power, the proposed fast reactor, which uses fast neutron fission in a small nuclear fuel element, by comparison with fuel rods in thermal neutron reactors, requires a more rapid heat removal than is possible by water cooling, and a liquid sodium–potassium alloy has been used in the development of a near-industrial generator. The fuel container is a vanadium sheath with a niobium outer cladding, since this has a low fast neutron capture cross-section and a low rate of corrosion by the liquid metal coolant. The liquid metal coolant is transported from the fuel to the turbine generating the electric power in stainless steel

ducts. The source of corrosion in this reactor is oxygen dissolved atomically in sodium, which gives rise to a number of inter-metallic oxides, such as $FeO-Na_2O$. A number of fuel element types have been tested, including a metal U–Mo alloy and a UO_2-PuO_2 solid solution. The liquid coolant is pumped around the heat exchanger by electromagnetic forces. If an electric potential is applied across a column of liquid metal which is held in a strong magnetic field, the liquid metal moves through the field in a direction at right angles to the two applied fields.

The converse process is applied in *magneto-hydrodynamic power* conversion, the principle involved being the separation of the conduction electrons from the ion-cores in a liquid metal by pumping a column of the metal through a magnetic field. The container of the liquid metal, usually made of stainless steel, is equipped inside the magnetic field with electrodes which provide an external circuit for the electrons, and thus an electromotive force is generated outside the liquid metal and its container. The propulsive force is appled to the liquid metal which is held in the containing stainless steel loop, the liquid passing through the magnetic field and then heat exchanger of a steam turbine which is a second source of electrical power, a so-called co-production process, which increases the overall efficiency of the plant. The cooler metal is then returned to the magnetic field area.

DropBooks

Liquid phase sintering of refractory materials

An important industrial procedure involving a liquid–solid sintering reaction is the sintering of refractory carbides of the transition metals which have very high melting points, above 2000 K, and would need a high temperature or plasma furnace to produce any significant consolidation of powders in the solid state at atmospheric pressure. The addition of a small amount of nickel, about 5–10 volume per cent, to tungsten carbide before sintering at about 1800 K leads to a considerably greater degree of sintering than could otherwise be achieved. This is because the nickel, which is liquid during the sintering process, can act as a transport medium for the dissolution and precipitation of particles of carbide. The metal additive remains in the fully sintered body as an inter-granular phase which limits the upper temperature of use of the material. This method is used as an alternative to the other successful but technically more difficult industrial process which employs hot pressing of the powders at 2000 K under several atmospheres pressure, using graphite dies, yielding products which can perform at higher temperatures.

In the sintering of such materials as silicon nitride, a silica-rich liquid phase is formed which remains in the sintered body as an intra-granular glass, but this phase, while leading to consolidation, can also lead to a deterioration in the high-temperature mechanical properties.

In order to produce successful liquid-phase sintering, the liquid phase should wet, and to a small extent, dissolve the solid phase to be sintered. A major initial effect of the wetting of the solid phase is to cause the particles to rearrange to a maximum density by surface tension effects during the early stages of sintering. These forces bring about a spreading of the liquid phase among the voids in the initial compact, and the process of dissolution proceeds more rapidly at those parts of the solid grains where there are sharp edges, and hence the highest chemical potential of the solid. This therefore promotes a better packing of the solid particles.

The initial sintering process continues by the dissolution of material at the point of contact of the particles with the formation of a liquid bridge between them. The centre-to-centre distance decreases as material is removed from this region by dissolution in the liquid. Considering the sintering of two spherical particles of radius a which have sintered together with a decrease in the centre-to-centre distance of $2h$ and a bridge of thickness X, it follows by Pythagoras theorem that

$$h = X^2/2a$$

The material in the centre of the bridge has a higher chemical potential than that remote from the bridge on the free surfaces of the spheres because a compressive force acting between the two spheres accompanies the formation of the liquid bridge which generates this chemical potential difference. This force is proportional to the ratio of the interfacial tension, γ, divided by the radius of the bridge free surface, which approximates to half of the centre-to-centre decrease, and can be represented by $K\gamma/h$, where K is a proportionality constant (Figure 10.3).

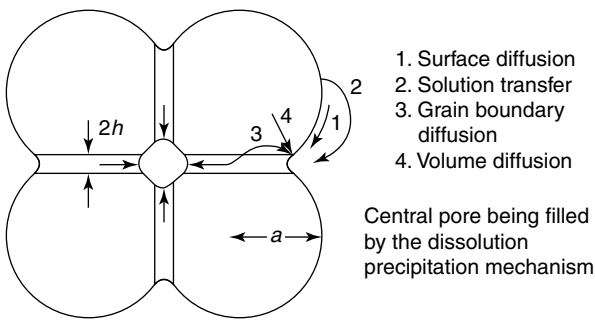


Figure 10.3 *The model for liquid phase sintering of high-melting solids with liquid metals as a sintering aid*

Using the equation which emerges from these considerations, the concentration difference of the dissolved material in the bridge from that in the bulk

of the liquid can be found from the thermodynamic approximation.

$$\mu_{\text{bridge}} - \mu_{\text{bulk}} = K\gamma/h = RT\ln(C_{\text{bridge}}/C_{\text{bulk}}) = RT\Delta C/C_{\text{bulk}}$$

if $(C_{\text{bridge}} - C_{\text{bulk}})$ is small. Approximating the circumference of the bridge to a thin cylinder, the diffusive flux out of the bridge is given by

$$\delta J = 4\pi D\Delta C\,\delta = \mathrm{d}V/\mathrm{d}t = 4\pi D\delta K\gamma C_{\text{bulk}}/hRT$$

where V is the volume of material deposited per second at the bridge, δ is the thickness of the bridge, and D is the liquid diffusion coefficient.

Hence

$$\mathrm{d}V/\mathrm{d}t = 2hJ = 4\pi D\delta K\gamma C_{\text{bulk}}/RT$$

The volume of the bridge is approximately given by

$$V = \pi X^2 h = \pi h^2 a$$

hence

$$\mathrm{d}V/\mathrm{d}t = 2\pi ah\,\mathrm{d}h/\mathrm{d}t$$

and integrating the resulting expression

$$2\pi ah^2\,\mathrm{d}h/\mathrm{d}t = 4\pi D\delta K\gamma C_{\text{bulk}}/RT \text{ with } h = 0 \text{ at } t = 0$$

DropBooks

yields

$$h^3 = (6\pi D\delta K\gamma C_{\text{bulk}}/RT)t/a$$

and the centre-to-centre distance decreases as a function of time according to a $(t/a)^{1/3}$ law. Since the fractional shrinkage of the whole compact, $\Delta L/L$, is proportional to h

$$\Delta L/L = (1/3)(\Delta V/V) \propto t^{1/3}/a^{4/3} \quad \text{(D.W. Kingery, 1959)}$$

Several other sintering mechanisms can become important once the initial phase is over, and the external pressure is no longer a factor in the process. Surface diffusion from the periphery of the particles to the neck (see p. 302) and solution-diffusion through the liquid are the two most probable mechanisms, since other sintering processes would require the parallel diffusion of atoms of each species in the carbide in volume or grain boundary migration. There is always the possibility, however, that the rate of the solution-diffusion process will be decreased by the kinetics of the transfer of material across the boundary layer separating the carbide and the liquid metal. The phase diagram for the nickel–tungsten system, for example, shows the formation

of high-melting solid compounds up to 1525°C, with a wide solubility above that temperature, which is therefore the lower limit for the solution-diffusion mechanism.

Bibliography

T.E. Faber. *An Introduction to the Theory of Liquid Metals*. Cambridge University Press (1972).
R.A. Swalin. Liquid metal diffusion theory, *Acta. Met.*, **7**, 736 (1959).
R.M. German. *Liquid Phase Sintering*. Plenum Press New York (1985) TN695. G469.

The production of crystalline semiconductors

The production of germanium and silicon is carried out by the reduction of the oxides, SiO_2 and GeO_2. There is a considerable difference in the stabilities of the oxides, and GeO_2 can be reduced by hydrogen at temperatures around 1100 K, but SiO_2 must be reduced by carbon at temperatures around 2300 K. The elements only reach a vapour pressure of 10^{-6} atmos at 1500 K and 1750 K respectively, and so the reduction of GeO_2 does not lead to any significant vaporization, but this is not so in the production of silicon. The gaseous composition of a 1:2 mixture of SiO_2 and carbon at 2000 K is as follows:

$$p\mathrm{CO} = 0.75,\ p\mathrm{Si}_2 = 0.17,\ p\mathrm{SiO} = 0.049,\ p\mathrm{C}_3 = 0.016 \text{ and } p\mathrm{Si} = 0.015$$

and with a 1:4 mixture of SiO_2

$$p\mathrm{CO} = 0.61,\ p\mathrm{C}_3 = 0.21,\ p\mathrm{Si}_2 = 0.14,\ p\mathrm{SiO} = 0.016,\ p\mathrm{Si} = 0.014$$

atmos as the major components. It is probable that this mixture of gases plays a major role in promoting the $SiO_2 + C$ reaction.

The products of these reduction reactions are crystalline powders. Further purification is obtained by conversion to the tetrachloride of germanium, and the hydrochloride of silicon, $SiHCl_3$. These chlorides boil at 357 K and 298 K respectively, and hence may be purified by distillation before being reduced to semiconductor-grade elementary powders with hydrogen. Germanium powder can be melted in a carbon crucible without significant contamination, but silicon is best obtained in impure form as a bar by condensing the reduction product of $SiHCl_3$ by hydrogen on a heated silicon rod similar to the van Arkel refining of zirconium.

Zone refining of semiconducting elements

The method of zone refining which was first used in the production of very pure germanium depends for its success on the difference between the thermodynamic properties of an impurity, present as a dilute constituent dissolved in

a nearly pure solid, and those of the impurity dissolved in the coexisting liquid. At solid–liquid equilibrium, the chemical potential of the impurity must be the same in each phase and since

$$RT \ln \gamma = \Delta G^{xs} = \Delta H - T\Delta S^{xs}$$

where γ is the activity coefficient. If X is the mole fraction of the dilute solute the distribution of this impurity between the solid and the liquid phases is

$$\ln(X_S/X_L) = \Delta H \text{ (transfer)} - T\Delta S^{xs} \text{ (transfer)} = \ln K_{S-L}$$

where the transfer terms are for the transfer of the impurity from the solid to the equilibrium liquid phase. The solvent, germanium, is present to more than 95% concentration, and its activity coefficient may be taken as unity. Thus the partition coefficient of the impurity between the solid and liquid K_{S-L} is determined by the heat of transfer and therefore of the activity coefficient ratio of the impurity between the solid and the liquid solvent.

In zone refining, a bar of the impure material can be heated in a radio-frequency heater to produce a thin layer of liquid which is slowly moved through the solid by raising the heater along the bar. Since equilibrium is not achieved in one pass of the liquid through the solid, several passes are made before a usefully high state of purity is reached. Alternatively, the impure bar can be contained in a chemically inert, ceramic tube and the liquid layer can be produced by passing the tube through a short heater. The liquid phase is well stirred by the r.f. field, and hence can be assumed to be uniform in composition except at the boundary layer where atoms of the impurity are re-deposited on one side, and dissolved on the other as the liquid advances.

DropBooks

The removal of impurity in one pass can be calculated by making a mass balance for the advancing liquid phase. If the original impurity content of the bar is C_0, and C_L is the impurity content of the liquid, then for an advance δx of the liquid, the amount dissolved into the advancing liquid minus the amount deposited behind the liquid is equal to the increase in the impurity content of the liquid

$$C_0\delta x - K_{S-L}C_L\delta x = l\delta C_L$$

where l is the liquid zone length, and in differential form this becomes

$$l\,\mathrm{d}C_L = (C_0 - K_{S-L}C_L)\mathrm{d}x$$

which upon integration, and inserting the boundary conditions $C_L = C_0$ when $x = 0$, yields the equation for the resulting content of impurity in the solid as a function of the distance along the bar, C_S,

$$C_S = C_0[1 - (1 - K_{S-L})\exp(-K_{S-L}x/l)]$$

In order to calculate the effect of several passes an iterative calculation is needed using the initial profile at each pass to represent C_0. Clearly for the second pass, the concentration profile given in the right-hand side of the above equation must be used. It is clear that the partition constant of the impurity between the solid and liquid is the most significant parameter in the success of zone refining.

The values of the partition coefficients increase with the valency of the impurity, being about 10^{-5} atom per cent for the elements of Group IB (e.g. copper) in germanium, up to about 1 atom per cent for Group IV (tin). The liquid phases in these systems are approximately Raoultian at the germanium-rich end, showing only small negative deviations in Cu + Ge, and small positive deviations in Sn + Ge. We may therefore neglect the heats of solution of these impurities in germanium at the zone refining concentrations. It follows that the highly endothermic heats of solution in the solid phase determine the partition coefficient. These are related to the difference in structure of the solute elements from the Group IV semiconductors. For example, it has been shown that the heat of solution of copper in solid germanium is about 180 kJ g atom^{-1}.

Chapter 11

Physical and chemical properties of glassy and liquid silicates

The structures of the silicate minerals depend on the ratio of silica to the other metal oxides. In pure silica, the structure consists of SiO_4 tetrahedra sharing oxygen atoms or ions at each corner. The co-ordination number of silicon is therefore four, and that of oxygen two. On the addition of metal oxides, such as Na_2O or MgO, the effect, which may be described as 'bridge breaking', involves the separation of two silicon atoms joined by an oxygen ion, through the addition of another oxygen ion. The accompanying metal ion is accommodated within the structure thus,

$$Si{-}O{-}Si + MO \longrightarrow 2Si{-}O{-} + M^{2+}$$

when an alkaline earth metal oxide is added. On addition of further amounts of metal oxide, the silica structure is increasingly broken down until a sheet structure is formed with the alkali metal oxides of formula $M_2O{\cdot}2SiO_2$, corresponding to an anion of formula $Si_2O_5^{2-}$. At the composition $M_2O{\cdot}SiO_2$ or $MO{\cdot}SiO_2$, the meta-silicates, an endless series of chains are formed, in which the silicate ion may be represented as SiO_3^{2-}, and at the composition $2M_2O{\cdot}SiO_2$, or more frequently $2MO{\cdot}SiO_2$, the ortho-silicates, the structure consists of isolated SiO_4 units interspersed with metal cations in octahedral co-ordination.

The naturally occurring silicates are variable in many more ways than this. For example, the introduction of Al_2O_3 can lead to the formation of alumino-silicates in which the silica structure can include the aluminium ion providing that charge compensation is made by the addition of a balancing amount of uni- or bivalent cations. In a similar fashion phosphorus can be accommodated by the omission of a compensating amount of these cations. The structures of all of the simple and complex silicate structures can be accounted for by the use of a completely ionic model with Si^{4+}, Al^{3+} or P^{5+} ions in the main structure associated with the appropriately balancing number of cations. However, there is certainly a covalent contribution to the bonding in these structures, which at the covalent extreme would be bonded by sp^3 Si–O bonds. Bearing this in mind, the ionic model can be accepted as only a working approximation which is very useful. Apart from substituting metal cations on the silicate structure, many examples occur in which fluoride or hydroxyl ions can be substituted for oxygen ions when, again, there is the proper charge compensation by the cations.

DropBooks

The thermodynamic properties of the solid silicates show the expected entropy change of formation from the constituent oxides of nearly zero, which is typical of the reaction type

$$\text{solid} + \text{solid} \longrightarrow \text{solid}; \quad \Delta S^\circ = 0$$

The heats of formation show increasingly exothermic values as the radius of the metal ionic species increases, in a homologous series. This might be explained as reflecting the decreasing repulsive interaction between the highly charged Si^{4+} ions as the radius of the metal ion separating them in the silicate structure increases. Table 11.1 shows values of the heats of formation for a number of technically important silicates.

Table 11.1 *Standard heats of formation of some metal silicates at room temperature (from metal oxides)*

Metal ion	Composition	ΔH°_{298} (kJ mol^{-1})
Li^+	Li_2SiO_3	1648
Na^+	Na_2SiO_3	1563
	Na_4SiO_4	2101
K^+	K_2SiO_3	1590
Be^{2+}	Be_2SiO_4	2146
Mg^{2+}	$MgSiO_3$	1548
	Mg_2SiO_4	2176
Ca^{2+}	$CaSiO_3$	1628
	Ca_2SiO_4	2320
Sr^{2+}	$SrSiO_3$	1633
	Sr_2SiO_4	2303
Ba^{2+}	$BaSiO_3$	1618
	Ba_2SiO_4	2272
Alumino-silicates Mineral	Formula	ΔH°_{298} (kJ mol^{-1})
Eucryptite	$Li_2O{\cdot}Al_2O_3{\cdot}2SiO_2$	4230
β-spodumene	$Li_2O{\cdot}Al_2O_3{\cdot}4SiO_2$	6036
Leucite	$K_2O{\cdot}Al_2O_3{\cdot}4SiO_2$	6069
Cordierite	$2MgO{\cdot}2Al_2O_3{\cdot}5SiO_2$	9113
Anorthite	$CaO{\cdot}Al_2O_3{\cdot}SiO_2$	4224
Sillimanite	$Al_2O_3{\cdot}SiO_2$	2584
Talc	$3MgO{\cdot}4SiO_2{\cdot}H_2O$	5916

The structure which emerges from studies of glass is that of a metastable solid, which undergoes structural change to the equilibrium crystalline form extremely slowly. In everyday applications the properties of the glassy state can be described as those of an amorphous material, which has the properties of a a 'stiff' liquid. X-ray diffraction studies of the solid glasses show a random structure in which the basic units are the SiO_4 tetrahedra interspersed with metal cations. The oxygen ions function either as bridges between the tetrahedra with two-fold co-ordination to silicon atoms or as corners of the tetrahedra with one bond to silicon, the fraction of the latter component increasing with the metal oxide/silica ratio, as in the solid silicates. The tangled structure of a frozen glass is responsible for the stiffness in the solid state, but in the liquid state the properties such as viscosity are a marked function of the cation composition of the silicate melt, decreasing by as much as a factor of ten depending on the metal/silica ratio. As might be expected, the diffusion coefficient of silicon is very low, typically $10^{-7}\,cm^2\,s^{-1}$, while that of oxygen increases markedly with the metal/silica ratio having an average value of about $10^{-5}\,cm^2\,s^{-1}$. Metal ions, which are co-ordinated with but atomically independent of the silicate network, are quite mobile, except for those like aluminium which are part of the network and in four co-ordination with oxygen.

The viscosity of liquid silicates such as those containing barium oxide and silica show a rapid fall between pure silica and 20 mole per cent of metal oxide of nearly an order of magnitude at 2000 K, followed by a slower decrease as more metal oxide is added. The viscosity then decreases by a factor of two between 20 and 40 mole per cent. The activation energy for viscous flow decreases from 560 kJ in pure silica to $160-180\,kJ\,mol^{-1}$ as the network is broken up by metal oxide addition. The introduction of CaF_2 into a silicate melt reduces the viscosity markedly, typically by about a factor of three. There is a rapid increase in the thermal expansivity coefficient as the network is dispersed, from practically zero in solid silica to around $40\,cm^3\,mol^{-1}\,K^{-1}$ in a typical soda-lime glass.

DropBooks

The electrical conductivity also increases with increasing metal oxide content, due to the high mobility of the metal ions. For example several glass compositions have been used as solid electrolytes in galvanic cells in which other metal ions apart from the alkaline and alkaline earth ions have been incorporated. The electrochemical cell

Ag | soda glass containing Ag_2O | Ag–Au alloy

has been used to measure the acivity of silver in silver–gold alloys.

It follows that since the addition of metal oxides has such a profound effect on the properties of liquid silicates such as the viscosity, that the Reynolds number of liquid silicates in metal–silicate liquid two-phase systems will influence the boundary layer thickness to a greater extent than in the liquid metals and alloys, mainly because of the higher viscosity of the silicate.

Metal solubilities in silicate glasses

Some metals are soluble as atomic species in molten silicates, the most quantitative studies having been made with $CaO-SiO_2-Al_2O_3$(37, 26, 27 mole per cent respectively). The results at 1800 K gave solubilities of 0.055, 0.16, 0.001 and 0.101 for the pure metals Cu, Ag, Au and Pb. When these metal solubilities were compared for metal alloys which produced 1 mm Hg pressure of each of these elements at this temperature, it was found that the solubility decreases as the atomic radius increases, i.e. when the difference in vapour pressure of the pure metals is removed by alloy formation. If the solution was subjected to a temperature cycle of about 20 K around the control temperature, the copper solution precipitated copper particles which grew with time. Thus the liquid metal drops, once precipitated, remained stable thereafter.

The production of silicate glasses and glass-containing materials

Glasses and porcelains are formed from silicate minerals, largely of silica, alumina and alkali-metal oxides. For example, Soda-lime glass is about 70% silica, with 15% sodium oxide and 10% lime + magnesia, Pyrex is a borosilicate glass containing 80% silica, 10–15% boric oxide, 5–10% Na_2O, and 1–4% alumina, and Vycor is nearly pure silica containing 3–6% boric oxide.

Sheet glass has a composition close to the soda-lime glass proportions, and the material is made by melting the components in a horizontal furnace, heated by natural gas or fuel oil combustion. The liquid melt is separated into two volumes by a wall which descends to about two-thirds of the depth of the liquid. This separates the end of the furnace where the raw solid materials are introduced from the end where the liquid glass is withdrawn. It is thus possible to have two zones at different average temperatures, the end where the glass leaves the furnace being cooler than the melting zone. This produces a liquid which is more viscous than the melting zone liquid, and is therefore suitable for glass forming into sheets. In modern practice the glass sheet is floated on a pool of liquid tin before final solidification which produces a very flat glass of uniform thickness.

Glasses of this group dissolve metals under neutral atmospheres which can be made to nucleate under controlled cooling and these metal particles change the colour of the glass, Au and Cu imparting a ruby colour to the glass, and Ag a yellow colour. Glasses can also be coloured by the introduction of transition metal ions which are readily oxidized. Thus cobalt and copper divalent ions introduce a blue colour, manganese, Mn^3, a violet colour and a mixture of ferrous and ferric ions the familiar blue-green colour. These ions are all introduced into the melt as oxides, and in the case of the Ni^{2+} ion

the resultant glass is violet in glasses containing K_2O, and yellow in glasses containing Na_2O. There is thus a wide range of colours which can be used for decorative as well as physical purposes.

Pyrex glass requires a higher temperature of formation than sheet glass, around 1900 K, and is usually made in electrically heated furnaces. The production of Vycor glass requires a boro-silicate glass which undergoes phase separation in the solid state at about 900 K. When this dulpex structure is cooled, one phase contains the sodium borate, and the other is predominantly silica. The sodium phase is then dissolved in nitric acid to produce a sponge-like glass. If this material is dipped into a solution of caesium nitrate, the Cs^+ ions diffuse into the pores of the glass, and these retain their locations during subsequent fusion processes. The caesium-rich regions have a higher refractive index than the rest of the glass, and hence the surface has a higher index then the interior. Alternatively, if the boro-silicate is immersed for a longer time, so that the Cs^+ ions can diffuse throughout the glass, a second short-time immersion in water produces a material which has a lower index on the surface than in the interior.

The production of porcelains

DropBooks

These are made from such naturally occurring minerals as the feldspars, leucite, $KAl_2Si_2O_6$, and orthoclase, $KAl_2Si_3O_8$, which are low melting materials used as fluxes for the higher melting products of the decomposition of kaolinite, $Al_2(OH)_4Si_2O_5$ which is found in clay, talc, which has the formula $Mg_3(OH)_2(Si_2O_5)_2$ and natural silica (quartz or flint). A typical range of composition is 40–60% clay, 15–25% flux, and 25–30% quartz. Kaolinite has a layer structure derived from gibbsite $Al(OH)_3$ bridged by silicate sheets, and talc is derived from the $Mg(OH)_2$ layer structure joined by two layers of $Si_2O_5^{2-}$ silicate sheets by the sharing of oxygen ions (Figure 11.1).

The initial phase of porcelain formation is the release of water molecules from the kaolinite or talc particles, which creates much smaller particles than the original size distribution would show, followed by the fusion of the particles of flux at around 1300 K. Fine mullite crystals, $3Al_2O_3{\cdot}2SiO_2$, are formed from the decomposition products of the clay at around 1300–1400 K, or by interaction between the liquid flux and the clay products. The mullite crystals continue to grow by the transfer of the mullite components through a process which is probably very similar to liquid phase sintering, to produce acicular crystals. The coarser quartz then dissolves slowly in the liquid to form smaller silica particles which remain in the solidified product. This consists, then, of a glassy phase, about 50–80% by volume, with mullite crystals and fine silica particles dispersed in the solid. In modern processing where higher

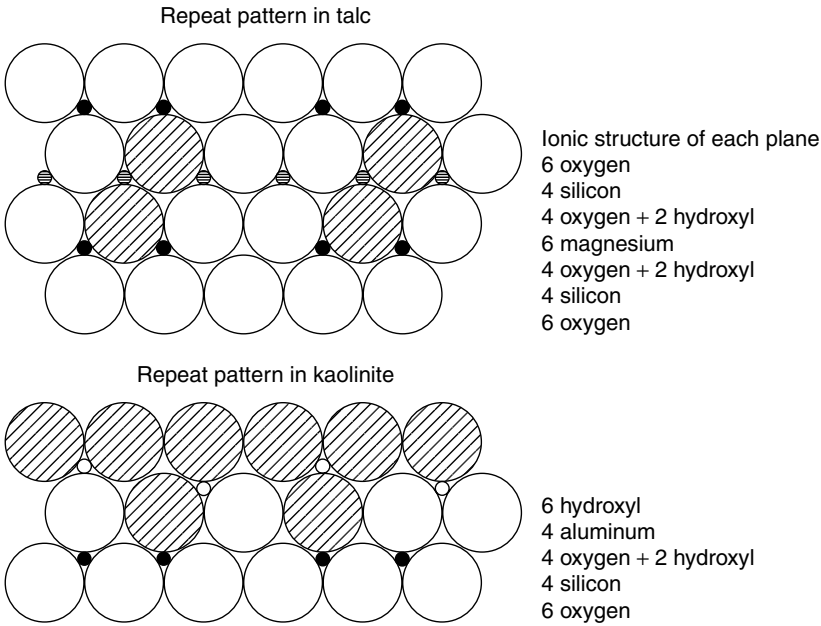


Figure 11.1 *The atomic structures of talc and kaolinite*

firing temperatures are readily available, the strength of the glass phase is improved by the addition of Al_2O_3.

A major source of weakness in porcelain objects is the presence of surface cracks or scratches. Unlike metals, ceramics and glasses cannot undergo plastic deformation, except in a few exceptions such as MgO above 1600 K. The principle mode of failure in these materials is crack propagation. The advance of a crack can be halted by the presence of small inclusions of a second phase, as in the case of cubic zirconia containing a minor amount of the tetragonal phase, when the $MgO–ZrO_2$ electrolyte is cooled rapidly. To overcome this problem, porcelain articles are usually coated with a glaze, which is a mixture of oxides applied to the surface of the porcelain object after the initial firing, as a water-based slurry. The glaze has a composition which ensures that it can be melted to cover the surface, and on cooling to be in a state of compression. This comes about because the thermal expansion coefficient of the glaze is larger than that of the underlying porcelain. The composition of the glaze used for white porcelain is very similar to that of the porcelain, but contains more flux material such as orthoclase. The main function of a glaze is to reduce the possibility of scratch or pit formation on the surface of the ceramic by contact with a harder material, which act as sources of cracks.

Ceramic electrical insulators

Materials for high voltage insulation include cordierite and steatite. The starting materials in the production of these insulators are talc and kaolinite, so the final compositions are found within the $MgO-Al_2O_3-SiO_2$ ternary phase diagram. By adjustment of the original mixture of the mineral silicates, it is possible to control the magnesia/alumina ratio and hence the final properties of the insulator. Cordierite, which has the formula $2MgO{\cdot}2Al_2O_3{\cdot}5SiO_2$ is prepared from 20% clay and the balance talc, and is typically fired to temperatures around 1600 K. Steatite is prepared in the same temperature range from a 15% clay, 85% talc mixture to which a small amount of chalk, $CaCO_3$ is added to form a flux. The final structures of these insulators contains crystals of $MgSiO_3$, enstatite and cordierite as well as a small amount of a glassy phase. The cordierite ceramics have a very low thermal expansion coefficient which makes them resistant to thermal shock.

The production of glass-ceramics

The formation of a fine dispersion of a separate phase can also have beneficial effects on the mechanical properties of ceramics. This process has been used in the stabilization of some ceramic materials from thermal shock, through the development of glass-ceramics. These materials have a fine dispersion of crystalline particles, having practically zero coefficient of expansion, in a glassy phase, and are remarkably resistant to thermal shock. The classical example is the formation of nuclei of β-eucryptite $Li_2O{\cdot}Al_2O_3{\cdot}2SiO_2$ which are transformed subsequently to β-spodumene $Li_2O{\cdot}Al_2O_3{\cdot}4SiO_2$ at 1300 K in a lithia–alumina–silica glass to form a glass-ceramic. The glass contains a small amount of TiO_2 which acts as a nucleating agent for the new phase. The initial composition is first melted and cooled to room temperature. The solid product is then heated to around 850 K to promote the nucleation of β-eucryptite, and then re-heated to allow the new phase to grow and transform to β-spodumene at 1200 K before cooling again to room temperature. The precise role of the TiO_2 nucleating agent is not clear, but the material may remain partially undissolved or be precipitated as fine particles immediately on cooling the original melt. These particles would then function as nuclei for the heterogeneous growth of the β-eucryptite. The product of this process is known familiarly as 'Pyroceram'.

A number of glass-ceramics can be made from industrial waste products, such as the Silcerams, which can be made from iron blast-furnace slag. Chromium or ferric oxides have been used as nucleating agents for the liquid slag, and on cooling, spinels of composition $MgCr_2O_4$ or magnesium-substituted $FeCr_2O_4$ separate as dispersed fine particles in a glassy mixture

DropBooks

denoted as 'pyroxene', which can be described by the general formula $Ca_{1-x}(Mg, Fe)_{1+x}(Si, Al)_2O_6$. The primary nuclei containing the magnesium spinel form at around 1625 K, and the secondary iron chromite spinel nuclei form over a wide temperature range with a maximum rate at 1200 K, and these are the major sites for nucleation of the pyroxene. The nucleation of pyroxene, which begins at around 1573 K has its maximum rate at approximately 1400 K. These glass-ceramic materials can be formed without the necessity of a complex heating cycle, as in the pyrocerams, but can be formed by direct cooling from the liquid state.

Cements

Conventional cements, such as Portland cement, comprise a mixture of silicates CS and C_3S_2 mixed with A_3S_2 and SiO_2 to form the glassy component (C = calcium, S = silica, A = alumina) with a small amount of $CaSO_4{\cdot}2H_2O$ (gypsum). The powdered material is mixed with half its weight of water, when hydrolysis of the surface of the particles slowly releases Ca^{2+} and Al^{3+} ions. These form small plate-like crystals of diameter less than 1 μm which form an interlocking network among the silicate particles.

The release of calcium is readily understood, since these ions do not play a part in the silicate network, but are isolated cations in octahedral co-ordination. The aluminium ions do form part of the network in tetrahedral co-ordination with oxygen ions, but the tetrahedron carries a negative charge due to lack of charge compensation, and hence will attract hydrogen ions from the acidic liquid phase. The strength and setting time of the cement decrease as the silica content is increased, having a maximum around 40 wt % SiO_2.

Among the many newer applications of silica-based glasses are slow release glasses including some dental cements. These applications take advantage of the ionic properties of the cations in glasses, and the applications are made possible by the diffusion rates of cations. The transport of ions is a thermally activated process in which the overall activation energy can be divided into two components. The first of these relates to the energy of separation of a cation from its immediate environment, E_s which can be approximated by the equation

$$E_s = Mz_{\text{cat}}z_{\text{an}}e^2/P(r_{\text{cat}} + r_{\text{an}})$$

where M is related to the Madelung interaction of the cation with its surroundings, z and r are the charge and radius of the cations and oxygen ions, and P is a factor related to the polarizability of the oxygen ion. The second contribution to the activation energy comes from the energy required to transport the cation through a saddle point composed of oxygen ions, which can be estimated from the bulk modulus of the glass.

An important cement which functions through the slow release of cations, is dental cement. The composition of dental cement contains a powdered glass, 15–45 μm in particle size, mixed with poly-acrylic acid. The glass is of an equimolar amount of CaF_2 and Al_2O_3 together with SiO_2 and a small amount of cryolite, Na_3AlF_6 to act as a flux. Increasing the silica content from 22 to 63 % increases the setting time from 3 to 45 minutes, and the strength of the cement increases as the setting time increases. In application, cations are slowly released from the glass to form cross-links in the organic polymer, which forms insoluble complexes.

Optical fibres

The refractive index of glass is a function of composition, and depends in large part on the polarizabilty of the octahedrally co-ordinated cations. The exchange of potassium ions for sodium ions will lead to a change in refractive index of a glass because the K^+ ion is larger than the Na^+ ion, and hence more polarizable. This property is used in the preparation of silicate optical fibres, which use internal reflection to propagate light. The sodium content near the surface of the fibre is exchanged for potassium, either by immersion in a bath of molten KNO_3 or by electrochemical exchange via an externally applied field. The former produces a typical gradient of potassium ions following the equation

$$C_K(x, t) = C_K^\circ \operatorname{erfc}(x/2(Dt)^{1/2})$$

whereas the electrochemical insertion, which produces a flatter profile, follows the equation

$$C_K(x, t) = (C_K^\circ/2) \operatorname{erfc}[(x - EM_i t)/2(Dt)^{1/2}]$$

where E is the applied electric field ($V\,cm^{-1}$), and M_i is the ionic mobility (in units of $cm^2\,V^{-1}\,s^{-1}$). Penetrations of the exchanged zone of 10 μm can readily be achieved by this means.

Chalcogenide glasses

Compounds of the elements of Group V, P, As and Sb with those of Group VI S, Se, and Te readily form amorphous solids on rapid cooling. Examples of these, As_2S_3 and As_2Se_3 are compounds in which the electronegativity difference between the elements is so small, that they may be regarded as covalent compounds. The crystal structure of the mineral, orpiment (As_2S_3) from which the structures of these compounds derive, has 12-member buckled rings

DropBooks

with alternating sulphur and arsenic atoms co-ordinated by the directed bonds of the sulphur atom. The crystalline compounds all have congruent melting points, increasing from As_2S_3(583 K) to Sb_2Se_3(863 K). These compounds in solid solutions with GeS_2 such as $As_{0.4}Te_{0.5}Ge_{0.1}S$ have interesting electron switching properties (Simmons, 1970; Ovshinsky, 1968) since they have two electronic states, one of high resistance, and the other of low resistance, and it is possible to switch from the high to the low state by applying a bias potential.

Bibliography

D.R. Uhlmann and N.J. Kriedel. *Glass: Science and Technology*, Vol. I (Glass forming systems). Academic Press (1983) TP848 G56.

L.D. Pye, W.C. La Course, H.J. Stephens. *The Physics of Non-crystalline Solid*. Taylor and Francis, London (1992).

J. Hlavac. *The Technology of Glass and Ceramics*.

M. Cable and J.M. Parker. *High Performance Glasses*. Blackie, Glasgow (1992). TP862H54.

J.G. Simmons. *Contemp. Phys.*, **11**, 21 (1970).

S.R. Ovshinsky. *Phys. Rev. Lett.* **21**, 1450 (1968).

D.W. Kingery. *J. App. Phys.*, **30**, 307 (1959).

Chapter 12

The structures and thermophysical properties of molten salts

The general trend in the melting points of the alkali and alkaline earth halides is a decrease in melting point from the fluorides to the iodides, and an entropy of fusion of the order of $6\,J\,K^{-1}$ for the fluorides, and $10–12.5\,J\,K^{-1}$, per gram-atom, for the chlorides and bromides. These entropies of fusion should be compared with typical values for the metals, $9.2\,J\,K^{-1}$. Among the oxy-salts the alkali metaborates, carbonates and sulphates have much higher melting points than the nitrates by about 550 K (Na_2CO_3, 1124 K and $NaNO_3$, 580 K).

X-ray and neutron diffraction data for the alkali metal halides indicate a significant reduction of the coordination number of the cations, from 6 to 4.5 on average, and a decrease in the cation–cation co-ordination number from 12 to about 8 for NaCl and KCl. The fusion process for these salts is accompanied by an increase in the molar volume of about 22%, which reflects the changes in structure indicated by the diffraction results. The viscosities of molten salts are determined by the fact that the anion is the larger species, except in some fluorides, and so the viscosities, which have an activation energy of about $35\,kJ\,mol^{-1}$, have typical values of one centipoise, which is comparable to that of water. The molar volumes of salt mixtures show a linear relation in the case of alkali halide mixtures, but a significant increase in mixtures of alkali halides with divalent and higher cation halides, especially in the case of caesium-containing melts, e.g. $CsCl–MgCl_2$. These observations have been taken to indicate the formation of polymeric anion structures in these solutions, and this has found support in ultra-violet absorption spectroscopic measurements, which support the existence of complex anions such as $MgCl_4^{2-}$, AlF_4^{-}, and $NiCl_4^{2-}$, and in thermodynamic measurements of the heats of formation.

The salts containing polymeric anions in the solid state melt retain the anion structure, e.g. CO_3^{2-} and NO_3^{-} on melting, while the phosphates in which the anion structure is based on the PO_4^{3-} tetrahedral ion, contain these simple units in the orthophosphates such as Na_3PO_4, but form chains with oxygen-sharing links in the phosphates with a higher P/O ratio, e.g. the metaphosphate, $NaPO_3$. It has been possible to obtain the polymeric structure of phosphate melts by chromatographic analysis of aqueous solutions of the melts (Westman and Gartaganis, 1957; Meadowcroft and Richardson, 1965). These results show that there is very little tendency to form branching chains and rings as in the silicates, but the chain lengths increase as the phosphorus/metal ratio increases.

DropBooks

The mobilities of ions in molten salts, as reflected in their electrical conductivities, are an order of magnitude larger than those in the corresponding solids. A typical value for diffusion coefficient of cations in molten salts is about $5 \times 10^{-5}\,\mathrm{cm^2\,s^{-1}}$, which is about one hundred times higher than in the solid near the melting point. The diffusion coefficients of cation and anion appear to be about the same in the alkali halides, with the cation being about 30% higher than the anion in the carbonates and nitrates.

Applying the Nernst–Einstein equation

$$\mu kT/e = D$$

to the diffusion data yields a value for the mobility of approximately $10^{-4}\,\mathrm{cm^2\,V^{-1}\,s^{-1}}$, which is to be compared with the mobilities of electron defects of about $10\text{–}100\,\mathrm{cm^2\,V^{-1}\,s^{-1}}$. It follows that a concentration of about $10^{16}\text{–}10^{17}$ of electron defects (electrons or positive holes) will lead to the same partial conductivity as that due to ionic migration.

The specific conductivities of molten salts are frequently represented, as a function of temperature by an Arrhenius equation, but it is unlikely that the unit step in diffusion has a constant magnitude, as in the corresponding solids and the results for NaCl may be expressed, within experimental error, by the alternative equations

$$\sigma = 2.20 \exp(-990/T)$$

or more accurately

$$\sigma = -2.497 + 8.043 \times 10^{-3}T - 1.42 \times 10^{-6}T^2$$

In view of Swalin's treatment of diffusion in liquid metals, the latter seems to be a better description. In binary mixtures such as NaCl–KCl the *equivalent* conductivities are a linear manner, but the $KCl\text{–}CdCl_2$ mixture shows a marked negative departure from linear behaviour, probably because of the formation of the complex ion $CdCl_3^-$.

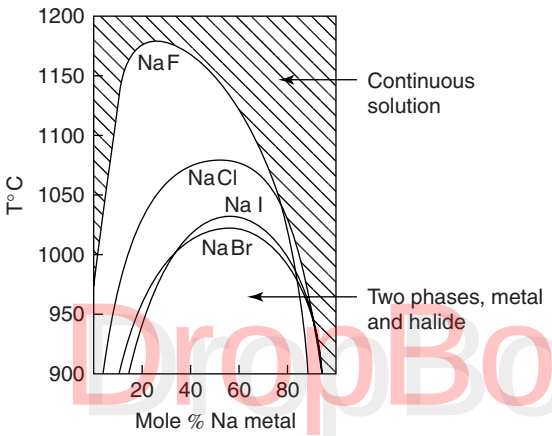
Molten sulphides are almost invariably semiconductors, and so their conductivities are typically larger than those of the average molten electrolyte. For example, the specific conductance of molten Ag_2S can be described, as a function of temperature by the equation

$$\sigma = 41.5 \exp(1280/T)$$

where the positive exponent reflects the increasing resistance to electron defect flow with increasing temperature due to the increased amplitude of vibration of the ions, probably the sulphide anions.

A significant property of the alkali metal halides is the solubility of the metals in their molten halides. Typical values of the consolute temperatures of metal–chloride melts are 1180°C in Na–NaF, 1080°C in Na–NaCl, 790°C

in K–KCl and 706°C in Rb–RbCl. In the case of the K–KCl system, the solution of 10 mole per cent in KCl increases the electrical conductivity by a factor of about twenty. As might be anticipated, the enhanced conductivity is the result of the liberation of an electron from each dissolved metal atom, so that the molten salt now takes on the electrical properties typical of a molten sulphide. The consolute temperatures of the $Ca–CaCl_2$, and the $Ba–BaCl_2$ systems are 1340°C and 1010°C. respectively, but the solution of metal in these chlorides does not increase their electrical conductivities, probably due to the formation of covalently bonded molecular species such as $Ca_2Cl_2 (Ca^0–CaCl_2)$ and similarly Ba_2Cl_2 (Figure 12.1).



DropBooks

Figure 12.1 *The solubilities of liquid sodium in the liquid sodium halides*

These facts would suggest that the electrolysis of molten alkali metal salts could lead to the introduction of mobile electrons which can diffuse rapidly through a melt, and any chemical reduction process resulting from a high chemical potential of the alkali metal could occur in the body of the melt, rather than being confined to the cathode volume. This probably explains the failure of attempts to produce the refractory elements, such as titanium, by electrolysis of a molten sodium chloride–titanium chloride melt, in which a metal 'dust' is formed in the bulk of the electrolyte.

Hot corrosion of metals by molten salts

An important industrial interest is in the corrosion of metals and ceramics by molten sodium sulphate/vanadate solutions. This is because turbines, which are usually nickel-based alloys, operating in a marine atmosphere, containing

NaCl, interact with the sulphur and vanadium oxides emitted from the combustion of technical grade hydrocarbons and the salt spray to form Na_2SO_4 and $NaVO_3$. These corrosive agents function in two modes, either the acidic mode in which for example, the sulphate has a high SO_3 thermodynamic activity, of in the basic mode when the SO_3 partial pressure is low in the combustion products. The mechanism of corrosion is similar to the hot corrosion of materials by gases with the added effects due to the penetration of the oxide coating by the molten salt.

Studies of the corrosion of nickel by molten Na_2SO_4 demonstrate the different mechanisms of these two regimes. At high pSO_3, the corrosion reaction is very similar to the effect of gaseous SO_2/O_2 mixtures in that the products are NiO and Ni_3S_2. The essential difference in the corrosive attack is that the NiO is soluble to a small extent in the molten Na_2SO_4, and so the invasion of the liquid is rapid along the grain boundaries. The result is that the corrosion is much faster than in the gaseous mixture. At low pSO_3 the thermodynamic activity of Na_2O is high and the NiO again dissolves to a small extent, but this time to form NiO^{2-} ions. The corrosive effect is again similar to that in the high pSO_3 regime, but the formation of sulphides at the oxide/metal interface is considerably reduced.

The thermodynamic data for the formation of molten Na_2SO_4 are

$$Na_2O + SO_2 + \tfrac{1}{2}O_2 = Na_2SO_4; \qquad \Delta G^\circ = -644\,500 + 339T \text{ J mol}^{-1}$$

$$Na_2O + SO_3 = Na_2SO_4; \qquad \Delta G^\circ = -533\,600 + 122T \text{ J mol}^{-1}$$

It follows from the latter equation that the equilibrium constant, which has a value of 10^{-16} at 1245 K, where

$$\log K = -\log a_{Na_2O} - \log p_{SO_3} = -16$$

indicates a minimum activity, at which the change from a high Na_2O activity (basic salt) to a high SO_3 activity (acid salt) occurs when these two activities are equal at 10^{-8}. The solubility of NiO in the melt has a minimum value at an activity of Na_2O of around -10 of about 1 ppm which is on the acidic side. The mechanism of the corrosion reaction probably depends on the reduction of the SO_3 which is released during the oxidation of the nickel, increasing the SO_2 partial pressure, which diffuses down cracks in the oxide to form a mixture of oxide and sulphide at the metal/oxide interface similar to the pure gaseous corrosion. Some of the scale can then dissolve in the salt phase to form nickelate NiO_2^- ions and to allow permeation of the oxide by the molten salt leading to a honeycomb structure in the resultant oxide.

The composition of turbine blades is a complex mixture of alloying elements in solid solution in nickel. A typical alloy would contain Al, Cr, Mo, Co or Ta in amounts up to 10 atom per cent of the particular elements which are chosen. Of these all except cobalt form substantially more stable oxides than

nickel, which react with Na_2O to form compounds, e.g. $NaCrO_2$, and $NaAlO_2$, Na_2MoO_4 and $NaTaO_3$. There are therefore a number of possible phases which could appear in the Na_2SO_4 corrosion of these commercial alloys. Vanadium can also be present in the fuel combustion products as an oxide which forms $NaVO_3$ among a number of other vanadates. All of these oxides are formed to a greater or lesser extent during the hot corrosion of the alloy, and dissolve in the molten salt phase. A potentially protective layer of Cr_2O_3 or Al_2O_3 is therefore removed from the surface of the alloy by dissolution. The presence of these oxides in solution in Na_2SO_4, especially the vanadates, lowers the melting point of Na_2SO_4 and therefore makes corrosion possible at a significantly lower temperature than in the case of pure nickel.

Molten carbonate fuel cells

Molten carbonates probably conduct electricity by the migration of oxygen ions, and thus can be used as the electrolyte in a fuel cell. The practical version of this operates with a $62\%Li_2CO_3{\cdot}38\%K_2CO_3$ mixture, at a temperature around 925 K. The electrolyte is suspended in a porous body of $LiAlO_2$, with a porous nickel anode, and a nickel oxide cathode. The practical advantage in containing the electrolyte in a porous solid, is that there will be very restricted movement in the liquid electrolyte during the inevitable thermal cycling of the power unit, and thus solution-corrosion of the container is minimized. A mixture of air and CO_2 is supplied to the cathode where the reaction

DropBooks

$$2CO_2 + O_2 + 4e^- = 2{CO_3}^{2-}$$

occurs and at the anode the reverse oxidation of hydrogen or hydrocarbon occurs according to

$$H_2 + {CO_3}^{2-} = CO_2 + H_2O + 2e^-$$

occurs. The efficiency, which is the ratio of the Gibbs energy change to the heat change of the cell reaction

$$2H_2 + O_2 = 2H_2O(g)$$

where

$$\Delta G^\circ = -494\,130 + 108T \text{ J mol}^{-1}$$

or

$$CH_4 + 3O_2 = CO_2 + 2H_2O(g)$$

$$\Delta G^\circ = -819\,110 + 239.3T \text{ J mol}^{-1}$$

and so the thermodynamic efficiency, E, for these two fuels is

$$\text{For } H_2(g) : E = \Delta G^\circ / \Delta H^\circ = 1 - T\Delta S^\circ / \Delta H^\circ = 1 - 0.20 = 80\%$$

and for $CH_4(g)$

$$= 1 - 0.27 = 73\%$$

These theoretical efficiencies are reduced in the practical situation by the three sources of energy loss, the ohmic loss I^2R in the electrolyte and the electrodes, the thermal loss of the cell to its surroundings, and the efficiency of the electrode/gas and the electrode/electrolyte reactions. These reduce the overall cell efficiency considerably so that the values for these two reactions with the liquid electrolyte might be expected to reach 60% or more when co-generation with a steam turbine is used with the exit gases from the fuel cell to augment the net power supply. Clearly, the liquid electrolyte will have a considerable advantage over the solid electrolyte cells until the conductivity of the solids can be brought close to that of the liquid, or the temperature can be substantially lower than the present operating temperatures of solid oxide fuel cells of 1000–1300 K. The latter has an advantage however when co-generation is practised because of the higher temperatures of the product gases.

Bibliography

F.D. Richardson. *Physical Chemistry of Melts in Metallurgy*, vols I & II. Academic Press, London (1974).

A.E.R. Westman and P.A. Gartaganis. *J. Amer. Chem. Soc.*, **40**, 293 (1957).

T.R. Meadowcroft and F.D. Richardson. *Trans. Far. Soc.*, **61**, 54 (1965).

Y. Waseda and J.M. Toguri *The Structure and Properties of Oxide Melts*. World Scientific, Singapore (1998) ISBN 981-02-3317-5.

Chapter 13

Extraction metallurgy

The important industry for the production of metals from naturally occurring minerals is carried out at high temperatures in *pyrometallurgical* processing, or in aqueous solutions in hydrometallurgical extraction. We are concerned only with the former in this book, and a discussion of hydrometallurgy will not be included. The pyro-processes are, however, also mainly concerned with liquids, in this case liquid metals and molten salt or silicate phases. The latter are frequently termed 'slags', since very little profitable use has been found for them, except as road fill or insulating wool.

The processes are invariably designed to obtain relatively pure liquid metals from the natural resource, sometimes in one stage, but mainly in two stages, the second of which is the *refining* stage. The movement of atoms in diffusive flow between the liquid metallic phase and the molten salt or slag, is therefore the most important rate-controlling elementary process, and the chemical reactions involved in high-temperature processing may usually be assumed to reach thermodynamic equilibrium. The diffusion coefficients in the liquid metal phase are of the order of $10^{-6}\,\mathrm{cm^2\,s^{-1}}$, but the coefficients in the molten salt and slag phases vary considerably, and are structure-sensitive, as discussed earlier.

DropBooks

As in the case of the diffusion properties, the viscous properties of the molten salts and slags, which play an important role in the movement of bulk phases, are also very structure-sensitive, and will be referred to in specific examples. For example, the viscosity of liquid silicates are in the range 1–100 poise. The viscosities of molten metals are very similar from one metal to another, but the numerical value is usually in the range 1–10 centipoise. This range should be compared with the familiar case of water at room temperature, which has a viscosity of one centipoise. An empirical relationship which has been proposed for the temperature dependence of the viscosity of liquids as an Arrhenius expression is

$$\eta = \eta_0 \exp(\Delta E/RT)$$

where the activation energy is $20–50\,\mathrm{kJ\,mol^{-1}}$ for liquid metals, and $150–300\,\mathrm{kJ\,mol^{-1}}$ for liquid slags. This expression shows that the viscosity decreases as the temperature is increased, and reflects the increasing ease with

which structural elements respond to an applied shear force with increasing temperature.

Another significant property in metal extraction is the density of the phases which are involved in the separation of metal from the slag or molten salt phases. Whereas the densities of liquid metals vary from $2.35\,\mathrm{g\,cm^{-3}}$ for aluminium, to 10.56 for liquid lead, the salt phases vary from 1.5 for boric oxide, to $3.5\,\mathrm{g\,cm^{-3}}$ for typical silicate slags. In all but a few cases, this difference in density leads to metal–slag separations which result from liquid droplets of metal descending through the liquid salt or slag phase. The velocity of descent can be calculated using Stokes' law for the terminal velocity, V_t, of a droplet falling through a viscous medium in the form

$$V_\mathrm{t} = \frac{d^2 g(\rho_\mathrm{p} - \rho)}{18\eta}$$

where d is the particle diameter, ρ and ρ_p are the densities of the slag and the particle material respectively, and η is the slag viscosity. Densities of liquid chlorides vary according to the size of the cation, from 1.4 for LiCl to 4.7 for $PbCl_2$, and so there are processes in which the metal floats on the liquid salt, as in the production of mangesium by molten chloride electrolysis.

The principles of metal extraction

Metal–slag transfer of impurities

The diffusive properties play the rate-determining role in determining the transfer of impurities from metal to slag, or salt phase, but obviously the thickness of the boundary layer is determined by the transport properties of the liquid non-metallic phase. A metal droplet will carry a boundary layer for the diffusion transport from the bulk of the metal droplet to the metal–slag interface. The flux of atoms from the metal to the slag can therefore be described in terms of the transport of atoms across two contiguous boundary layers, one in the metal and the other in the slag. In the steady state when both liquids are stationary the flux of impurity atoms out of the metal will equal the flux of atoms away from the interface and into the slag. Using the simple boundary layer approximation where

$$J = (D/\delta)(C_\mathrm{bulk} - C_\mathrm{interface})$$

and applying this to the two phases,

$$J_\mathrm{n} = J_\mathrm{s} \text{ and } \frac{D^\mathrm{M}\delta^\mathrm{S}}{D^\mathrm{S}\delta^\mathrm{M}} = \frac{(C^{\mathrm{S(I)}} - C^{\mathrm{S(B)}})}{(C^{\mathrm{M(B)}} - C^{\mathrm{M(I)}})}$$

where D and δ are the diffusion coefficient of the atoms being transferred from metal to slag, and the boundary layer thickness respectively. The concentrations, $C^{M(B)}$, $C^{S(B)}$ are in the bulk, and $C^{M(I)}$, $C^{S(I)}$, are at the metal–slag interface. Since thermodynamic equilibrium is assumed to exist at the interface, the equilibrium constant for the partition of the impurity between metal and slag K_{M-S} would be related to the interface concentrations.

$$K_{M-S} = C^{M(I)}/C^{S(I)}$$

and writing j_i for D/δ, then when $C^{S(B)} \ll C^{S(I)}$

$$j_S/j_M = K_{M-S}(C^{M(B)} - C^{M(I)})/C^{M(I)}$$

This condition applies when the equilibrium content of the slag of the impurity being transferred would be high, but the bulk of the slag is large compared to the volume of the descending metal particle. When $C^{S(B)}$ is not much less than $C^{S(I)}$

$$\begin{aligned} j_S/j_M(C^{S(I)} - C^{S(B)}) &= (C^{M(B)} - C^{M(I)}) \\ &= (j_S/j_M)((C^{M(I)}/K_{M-S}) - C^{S(B)}) \end{aligned}$$

and hence for the flux out of the metal, J_M the equation

$$J_M = j_M j_S(C^{M(B)} - C^{S(B)}K_{M-S})/K_{M-S}j_M + j_S$$

is deduced, which on re-arrangement takes the form

$$(C^{M(B)} - C^{S(B)}K_{M-S}) = J_M((1/j_M) + (K_{M-S}/j_S))$$

which is analogous to Ohm's law where $(C^{M(B)} - C^{S(B)}K^{M-S})$ is the potential drop, J_M is the current, and $(1/j_M) + (K_{M-S}/j_S)$ represents two resistances, R_M and R_S, in series.

The comparison of the magnitude of the two resistances clearly indicates whether the metal or the slag mass transfer is rate-determining. A value for the ratio of the boundary layer thicknesses can be obtained from the *Sherwood* number, which is related to the Reynolds number and the *Schmidt* number, defined by

$$N_{Sc} = \eta/\rho D$$

by the equation

$$N_{Sh} = 0.332\,N_{Re}^{1/2}N_{Sc}^{1/3}$$

DropBooks

for each of the two phases. Using the braces ( ) for the slag phase, and [ ] for the metal phase, the ratio between the Sherwood numbers of the two phases is

$$\frac{(N_{\mathrm{Sh}})}{[N_{\mathrm{Sh}}]} = \frac{k^{\mathrm{S}}D^{\mathrm{M}}}{k_{\mathrm{M}}D^{\mathrm{S}}} = \frac{(N_{\mathrm{Re}})^{1/2}(N_{\mathrm{Sc}})^{1/3}}{[N_{\mathrm{Re}}]^{1/2}[N_{\mathrm{Sc}}]^{1/3}} = \frac{(u_{\mathrm{bulk}})[\chi^{1/6}D^{1/2}]}{[u_{\mathrm{bulk}}](\chi^{1/6}D^{1/2})}$$

where χ is the kinematic viscosity, equal to η/ρ, and k is the mass transfer coefficient, and

$$k^{\mathrm{S}}/k^{\mathrm{M}} = j^{\mathrm{S}}/j^{\mathrm{M}} = D^{\mathrm{M}}\delta^{\mathrm{S}}/D^{\mathrm{S}}\delta^{\mathrm{M}}$$

it follows that

$$F(u, \chi, D) = \frac{\delta^{\mathrm{S}}}{\delta^{\mathrm{M}}} = \frac{[u_{\mathrm{bulk}}]^{1/2}(\chi^{1/6}D^{1/3})}{(u_{\mathrm{bulk}})^{1/2}[\chi^{1/6}D^{1/3}]}$$

and hence

$$R_{\mathrm{S}}/R_{\mathrm{M}} = K_{\mathrm{M-S}}F(u, \chi, D)D^{\mathrm{M}}/D^{\mathrm{S}} \approx K_{\mathrm{M-S}}(D^{\mathrm{M}}/D^{\mathrm{S}})^{2/3}$$

Usually $D^{\mathrm{S}} < D^{\mathrm{M}}$, and hence $R_{\mathrm{S}} > K_{\mathrm{M-S}}R_{\mathrm{M}}$. The transfer in the slag phase is therefore rate-determining in the transfer of a solute from the metal to the slag phase.

When the two liquid phases are in relative motion, the mass transfer coefficients in either phase must be related to the dynamical properties of the liquids. The boundary layer thicknesses are related to the Reynolds number, and the diffusive transfer to the Schmidt number. Another complication is that such a boundary cannot in many circumstances be regarded as a simple planar interface, but *eddies* of material are transported to the interface from the bulk of each liquid which change the concentration profile normal to the interface. In the simple isothermal model there is no need to take account of this fact, but in most industrial circumstances the two liquids are not in an isothermal system, but in one in which there is a temperature gradient. The simple stationary mass transfer model must therefore be replaced by an eddy mass transfer which takes account of this surface replenishment.

When only one phase is forming eddy currents, as when a gas is blown across the surface of a liquid, material is transported from the bulk of the metal phase to the interface and this may reside there for a short period of time before being submerged again in the bulk. During this *residence* time t_{r}, a quantity of matter, q_{r} will be transported across the interface according to the equation

$$q_{\mathrm{r}} = 2c_{\mathrm{bulk}}\left(\frac{D}{\pi t_r}\right)^{1/2}$$

which depends on the value of the diffusion coefficient in the liquid, D. If the container has a radius r, then the liquid is blown across the container

by a tangential stream of gas, and begins to submerge at the wall of the container. The mass transfer coefficient is given under these circumstances by an equation due to Davenport *et al.* (1967)

$$k = \left(\frac{16}{3\pi}\right)^{1/2} \left(\frac{\mu D}{r}\right)^{1/2}$$

where u is the surface velocity of the liquid. For the converse situation where an inductively heated melt is in contact with a gas, a typical value in a laboratory study involving up to about one kilogram of liquid metal, the mass transfer coefficient is approximately given by

$$k = 0.05/r^{1/2}$$

(Machlin, 1960).

When both phases are producing eddies a more complicated equation due to Mayers (1962) gives the value of the mass transfer coefficient in terms of the Reynolds and Schmidt numbers which shows that the coefficient is proportional to $D^{0.17}$.

$$k_1 = 0.0036(D_1)(\mathrm{Re}_1\mathrm{Re}_2)^{0.5} \left(\frac{\eta_1}{\eta_2}\right)^{1.9} \left(0.6 + \frac{\eta_2}{\eta_1}\right)^{-2.4} \mathrm{Sc}_1^{0.83}$$

In many studies of interphase transport, results are obtained which show a dependence on the diffusion coefficient somewhere between these two values, and therefore reflect the differing states of motion of the interface between studies.

DropBooks

The electron balance in slag–metal transfer

The transfer of an element from the metal to the slag phase is one in which the species goes from the charge-neutralized metallic phase to an essentially ionic medium in the slag. It follows that there must be some electron redistribution accompanying the transfer in order that electro-neutrality is maintained. A metallic atom which is transferred must be accompanied by an oxygen atom which will absorb the electrons released in the formation of the metal ion, thus

$$[\mathrm{Mn}] + 1/2\mathrm{O}_2 = \{\mathrm{Mn}^{2+}\} + \{\mathrm{O}^{2-}\}$$

where [Mn] indicates a manganese atom in a metallic phase and $\{\mathrm{Mn}^{2+}\}$ the ion in the slag phase. In another example electro-neutrality is maintained by the exchange of particles across the metal–slag interface

$$\{\mathrm{O}^{2-}\} + [\mathrm{S}] = \{\mathrm{S}^{2-}\} + [\mathrm{O}]$$

For any chemical species there are probably many ways in which the transfer across the metal–slag interface can be effected under the constraint of the

conservation of electric charge. Thus for the transfer of sulphur from liquid iron saturated with carbon to a silicate slag, any of the following processes would contribute

$$[S] + \{O^{2-}\} + [C] = \{S^{2-}\} + CO(g)$$

$$[S] + [Fe] = \{Fe^{2+}\} + \{S^{2-}\}$$

$$2[S] + [Si] = \{Si^{4+}\} + 2\{S^{2-}\}$$

Another result of the need to conserve electric charge in metal–slag transfer, is that elements can be transferred, initially, *up* a chemical potential gradient. Thus if a mixture of manganese metal, manganese oxide and manganese sulphide is separated from a mixture of iron, iron oxide and iron sulphide by an ionic membrane which only allows the transmission of charged species from one mixture to the other, oxygen and sulphur ions counter-diffuse across the membrane. It was found at 1500 K that oxygen transfers from iron to manganese, while sulphur transfers, atom for atom, from manganese to sulphur. Oxygen was therefore transferred from a partial pressure over the iron mixture of 9×10^{-14} atmos to the manganese mixture at a partial pressure of 9×10^{-22} atmos, forming some more manganese oxide, while sulphur was transferred from a partial pressure of 10^{-14} atmos over the manganese mixture, to the iron mixture at a pressure of 10^{-6} atmos to form more iron sulphide (Turkdogan and Grieveson, 1962).

The resolution of this apparent contradiction to the thermodynamic expectations for this transfer is that the ionic membrane will always contain a small electron/positive hole component in the otherwise predominantly ionic conductivity. Thus in an experiment of very long duration, depending on the ionic transport number of the membrane, the eventual transfer would be of both oxygen and sulphur to the manganese side of the membrane. The transfer can be shown schematically as

Mn–MnO–MnS	ionic membrane	Fe–FeO–FeS
$pO_2 = 9 \times 10^{-22}$	$\longleftarrow O^{2-}$	$pO_2 = 10^{-14}$ atmos
$pS_2 = 7 \times 10^{-14}$	$S^{2-} \longrightarrow$	$pS_2 = 10^{-6}$ atmos
$T = 1500$ K		

Bubble formation during metal extraction processes

The evolution of gases, such as in the example given above of the formation of CO(g) in the transfer of sulphur between carbon-saturated iron and a silicate slag, requires the nucleation of bubbles before the gas can be eliminated from the melt. The possibility of homogeneous nucleation seems unlikely, and the more probable source of gas bubbles would either be at the container ceramic walls, or on detached solid particles of the containing material which are

floating in the melt. This heterogeneous nucleation of the gas will take place in the spherical cap which is formed by the interplay of the surface energies of the interfaces between the container and the metal, the metal and the slag, and the container and the slag. Water models of bubbles ascending through a liquid of relatively high viscosity, such as a slag, have a near-spherical shape when the bubble diameter is less than 1 cm, and at larger sizes have the shape of a spherical cap. The velocity of ascent of spherical bubbles can be calculated by the application of Stokes' law, and the spherical-cap bubbles reach a terminal velocity of ascent of about 20–30 cm s^{-1} when their volumes approximate to that of a spherical bubble in the range of radius 1–5 cm.

In a number of refining reactions where bubbles are formed by passing an inert gas through a liquid metal, the removal of impurities from the metal is accomplished by transfer across a boundary layer in the metal to the rising gas bubbles. The mass transfer coefficient can be calculated in this case by the use of the Calderbank equation (1968)

$$N_{\mathrm{Sh}} = 1.28(N_{\mathrm{Re}}N_{\mathrm{Sc}})^{1/2}$$

where the velocity which is used in the calculation of the Reynolds' number is given by the Davies–Taylor equation

$$u = 1.02(gd/2)^{1/2} \text{ where } N_{\mathrm{Re}} = ud\rho/\eta$$

and the characteristic length is the bubble diameter, d.

The mass transfer coefficient is therefore given by

$$k = 1.08g^{1/4}d^{-1/4}D^{1/2} \quad \mathrm{cm\,s^{-1}}$$

and D is the diffusion coefficient of the element being transferred in the liquid metal. In this equation the diameter of the equivalent spherical bubble must be used for spherical-cap shaped bubbles.

The corrosion of refractories by liquid metals and slags

An important limitation on the operation of the high-temperature systems which are used in metal extraction is the chemical attack of the slags and the metals which are produced during the processing. These are of two general types. The first is the dissolution of the refractory material in the liquids, which leads to a local change in composition of the liquid phase, and hence to convection currents since there is usually a difference in density between the bulk liquid and the refractory-containing solution. The second mode of corrosion occurs at the interface between metal and slag, and at slag/gas interface. This is due to the difference in surface tension between the liquid close to the refractory wall and the rest of the interface. If the slag/gas or interfacial tensions are reduced by dissolution of material from the refractory wall,

DropBooks

there is a tendency for the dissolved material to be drawn away from the wall (Marangoni effect), leaving a corrosion notch.

The dissolution of the refractory by the first mechanism is described by an equation due to Levich (1962), where the flux, j, of the material away from the wall is calculated through the equation

$$j = -\rho_s \mathrm{d}Y_s/\mathrm{d}t = 0.65(C_0 - C_{\mathrm{bulk}})D^{3/4}\left(\frac{\Delta\rho g}{\eta}\right)^{1/4} x^{-1/4}$$

where ρ_s is the density of the solid, Y_x the thickness of the refractory wall at the time t, C_0 and C_{bulk} are the concentrations of the diffusing species at the wall and in the bulk of the corroding liquid, D is the diffusivity of the dissolving material, $\Delta\rho$ is the difference in density between the interfacial layer and the bulk, and g is the gravitational constant. The wall is of thickness Y_0 at $t = 0$ and $x = 0$. It follows that a plot of $\log(Y_0 - Y)$ against $\log x$, the corrosion depth, will have a slope of $-1/4$ when this free convection model applies. If this local equilibrium model does not fit, then there is probably a rate-determining step in the dissolution mechanism, such as the rate of transfer from the solid into the immediately neighbouring liquid (chemical control). This may be tested in the laboratory by measuring the rate of dissolution of a rotating rod of the wall material in the liquid metal or slag. If the process is chemically controlled, the rate of dissolution will be independent of the speed of rotation, but if there is diffusion control, the rate of dissolution will increase with the speed of rotation, due to a decreasing thickness of the boundary layer.

The simple model given above does not take account of the facts that industrial refractories are polycrystalline, usually non-uniform in composition, and operate in temperature gradients, both horizontal and vertical. Changes in the corrosion of multicomponent refractories will also occur when there is a change in the nature of the phase in contact with the corroding liquid for example in $CaO–MgO–Al_2O_3–Cr_2O_3$ refractories which contain several phases.

Extractive processes

The production of lead and zinc

Zinc occurs most abundantly in the mineral, Sphalerite, ZnS, which is roasted to produce the oxide before the metal production stage. The products of the roast are then reduced by carbon to yield zinc oxide and CO(g). In the older process, the Belgian *retort* process, the metal oxide and carbon are mixed together in a reactor which allows the indirect heating of the charge to produce the gaseous products followed by the condensation of zinc at a lower temperature in a zone of the reactor which is outside the heating chamber. The carbon monoxide is allowed to escape from the vessel and is immediately burnt in

air. This is clearly a batch process which uses an external heat source, and is therefore of low thermal efficiency.

An improved approach from the point of view of thermal efficiency is the *electrothermal* process in which the mixture of zinc oxide and carbon, in the form of briquettes, are heated in a vertical shaft furnace using the electrical resistance of the briquettes to allow for internal electrical heating. The zinc vapour and CO(g) which are evolved are passed through a separate condenser, the carbon monoxide being subsequently oxidized in air.

Lead: The production of lead from lead sulphide minerals, principally galena, PbS, is considerably more complicated than the production of zinc because the roasting of the sulphide to prepare the oxide for reduction produces PbO which is a relatively volatile oxide, and therefore the temperature of roasting is limited. The products of roasting also contain unoxidized galena as well as the oxide, some lead basic sulphate, and impurities such as zinc, iron, arsenic and antimony.

In the classical *Newnham hearth* process, the basic sulphate $PbSO_4 \cdot 2PbO$ reacts with lead sulphide, probably in the vapour phase, to form lead acording to the reaction

$$2PbS(g) + PbSO_4 \cdot 2PbO = 5Pb + SO_2$$

and the pressure of SO_2 reaches one atmosphere at about 1200 K.

In the blast furnace reduction slag-making materials are also added together with a small amount of iron, the function of which is to reduce any sulphide which remains, to the product of the roasting operation to produce a sinter. The sinter is then reduced with coke in a vertical shaft blast furnace in which air is blown through tuyeres at the bottom of the shaft. The temperature in the hearth where metal is produced must be controlled to avoid the vaporization of any zinc oxide in the sinter. The products of this process are normally quite complex, and can be separated into four phases. Typical compositions of these are shown in Table 13.1.

DropOfBooks

Table 13.1 *Typical compositions in wt %*

Phase	Pb	Bi	Sb	As	Fe	Ca
Metal	98.6	0.14	0.84	0.01	0.002	0.009
	Pb	S	SiO_2	FeO	CaO	
Slag	0.94	1.1	35	28.7	22.2	
	Pb	Fe	Cu	S		
Matte	10.7	44.7	12.6	23.4		
	Pb	As	Fe	Cu	S	
Speiss	4.8	19.4	55.6	4.8	11.6	

Depending on the source of the mineral, the slag phase usually contains a significant zinc oxide content, which must be subsequently removed by slag *fuming*. This is a process where powdered coal is blown through the liquid slag to reduce the ZnO to gaseous zinc.

The lead blast furnace operates at a lower temperature than the iron blast furnace, the temperature at the tuyeres being around 1600 K as opposed to 1900 K in the ironmaking furnace (see p. 333) and this produces a gas in which the incoming air is not completely reduced to CO and N_2, as much as one per cent oxygen being found in the hearth gas.

Co-production of lead and zinc in a shaft furnace

Since these metals occur together mainly as sulphides, the mineral in this process is first roasted together with lime and silica to produce a mixture of oxides in the form of a sinter, as in the lead blast furnace process. In the Imperial Smelting Process, which uses a counter-current procedure, this mixture is also reacted with coke in a shaft furnace to produce zinc vapour at the top of the shaft, and liquid lead at the bottom. The minerals also contain iron which is removed in a silicate slag as FeO at 1600 K. The need to retain iron in the slag means that the base of the furnace must be operated at a fairly high oxygen potential, when compared with the major shaft furnace operation, the ironmaking blast furnace, where all of the iron content of the input material is reduced to metal. The gas phase is produced by the oxidation of coke with air preheated to 1000 K and injected near the base of the furnace, to yield a CO/CO_2 mixture of about 1:1. Such a mixture would lead to the oxidation of the zinc vapour at the lower exit from the furnace, but this is avoided by pre-heating the coke and sinter which is loaded at the top of the furnace to 1110 K to encourage a low oxygen potential at the top of the furnace and removing the zinc vapour at this level. This vapour is trapped in falling liquid lead droplets at approximately 1200 K, and separated from the lead at a temperature between 700 and 800 K in another vessel. The activity of ferrous oxide in an $FeO-SiO_2$ mixture is approximately Raoultian, and the effect of the lime addition is to raise the activity coefficient of FeO (Figure 13.1).

This continuous process is to be compared with a batch process, such as the Belgian retort process. In this, zinc oxide, free of lead or iron is reduced with carbon to produce zinc vapour, which is condensed in the cold section of the retort. The oxygen potential in this system is very much lower than in the blast furnace, approximately at the C/CO equilibrium value. A vacuum-operated variant of this level of reduction is carried out to produce zinc vapour which is subsequently converted to zinc oxide before condensation of the metal could take place.

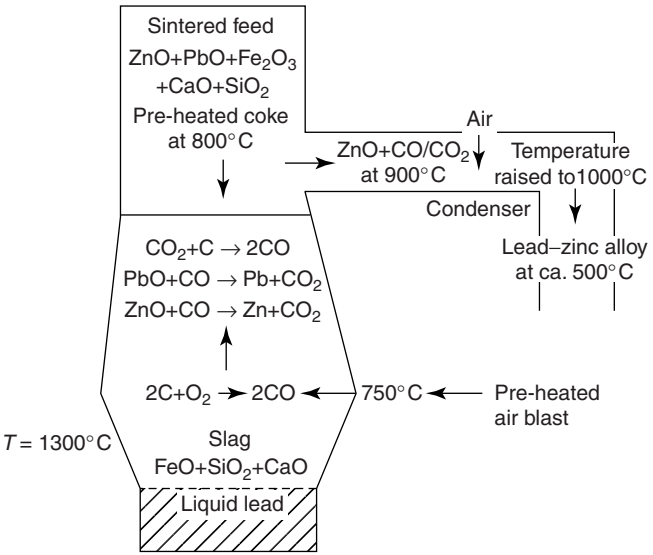


Figure 13.1 *Schematic diagram of the blast furnace for the co-production of liquid lead and zince*

The ironmaking blast furnace

DropBooks

The production of carbon-saturated iron in the blast furnace is a much larger scale of operation, both in the size of the blast furnace, and in the throughput of material which is achieved. Iron ore, in the form of haematite, is mixed with coke and slag-making materials and charged to the top of the vertical shaft furnace. Heat is generated at the bottom of the furnace by the reaction of pre-heated air, injected at high velocity through tuyeres. The carbon monoxide so produced maintains the bottom of the furnace at a sufficiently low oxygen potential to reduce any iron oxide arriving at this zone, together with some silicon from the slag-making silica and impurities such as TiO_2. The metal is saturated with carbon, and is tapped from the furnace into runners known as 'pigs', and hence the metal is known as *pig-iron*.

For the purposes of discussion, it is useful to consider the blast furnace as operating in four consecutive zones. At the fourth, bottom, zone the oxidation of coke at the tuyeres carries the temperature to levels in excess of 2100 K. The next zone, which operates in the temperature range 1600–1900 K is where the liquid metal and slag are formed. The second zone, sometimes referred to as the thermal reserve zone, is where the CO_2–C reaction to produce CO, the so-called solution reaction mainly occurs, and the reduction of iron is completed. In the first zone, at the top of the furnace, the primary reduction of

iron oxide to metallic sponge occurs, producing mainly CO_2 in the gas phase, and the decomposition of limestone to produce CaO is carried out. The liquid metal and slag arriving at the fourth zone separate according to their densities, with the metal layer on the bottom. Metal drops arriving at the supernatant slag layer from the third zone pass through the slag layer where they undergo refining reactions, such as the reduction of the sulphur content.

A heat balance for the blast furnace produced by Michard *et al.* (1967), shows that nearly 80% of the heat generated in the furnace is used to produce and melt the iron and slag. The gas which emerges from the first zone is further used to pre-heat the air injected in the tuyeres in large stoves. The process thus runs at a very high efficiency, both from the point of view of the amount of metal and slag produced and from the heat generation and utilization.

In both of these shaft furnace processes there are impurities which must be removed. The transfer of elements from the metal to the slag phase is very much dependent on the prevailing oxygen potential at the slag–metal interface. This is because elements such as sulphur or phosphorus can enter the slag phase either as elementary ions, S^{2-} or P^{3-} at low oxygen potentials, and as sulphate ($SO_4{}^{2-}$) and orthophosphate ions (PO_4^{3-}) depending on the oxygen potential. The changeover between these two alternatives occurs at about $pO_2 = 10^{-5}$ for $S_2 \rightarrow SO_4^{2-}$ and 10^{-14} atmos for $P^{3-} \rightarrow PO_4^{3-}$ in a typical $CaO–SiO_2–Al_2O_3$ slag at the metal-making temperatures given above. It is therefore clear that in the lead blast furnace these elements will be in the oxidized form in the slag, but in the ironmaking blast furnace, only phosphorus will be in the oxidized state.

The extent of transfer at any given oxygen partial pressure and temperature depends on the composition of the slag. Obviously a high CaO content with a high lime activity would encourage removal of these elements from the slag, but the upper limit on the CaO content is set by the need to have a liquid slag at the metal-making temperature. Table 13.2 shows typical data for the materials produced by weight per cent in these two blast furnace systems.

Table 13.2 *A comparison of the lead and iron blast furnaces*

The lead–zinc furnace
Metal composition Pb > 98%, Bi, Sb, As, Fe balance
Slag composition* Pb 1%, S 1%, FeO 28%, SiO_2 35%, CaO 23%
The ironmaking furnace
Metal composition Fe 95%, C 4–5%, Si 0.3%, Mn 0.2%, S 0.02%, P 0.08%.
Slag composition CaO 42%, SiO_2 35%, MgO 7–8%, Al_2O_3 10%, Fe 0.2%, S 1%

*Major constituents only.

It is the presence of a large amount of FeO in the lead–zinc furnace slag which produces a liquid at 1550 K, compared with the higher melting, virtually iron-free, slag in the other furnace.

The reduction of stable oxides in carbon arc furnaces

Stable oxides, such as those of chromium, vanadium and titanium cannot be reduced to the metal by carbon and the production of these metals, which have melting points above 2000 K, would lead to a refractory solid containing carbon. The co-reduction of the oxides with iron oxide leads to the formation of lower melting products, the ferro-alloys, and this process is successfully used in industrial production. Since these metals form such stable oxides and carbides, the process based on carbon reduction in a blast furnace would appear to be unsatisfactory, unless a product saturated with carbon is acceptable. This could not be decarburized by oxygen blowing without significant re-oxidation of the refractory metal.

The solution to this problem is the use of a carbon arc as the heat source coupled to a liquid slag as the resistance element. The choice of composition of this slag must be made to optimize the electrical resistance as well as the refining properties of the slag. The electrical coupling of the arc–slag combination can either be achieved by submerging the arc in the liquid slag, or by using a foaming slag (Ito, 1989) which forms an electrical link without bringing the carbon electrodes near the surface of the liquid alloy which is produced. Foaming slags are produced by dispersing refractory oxides, such as MgO or CaO, in a slag of a composition which produces a low surface tension. The slag is foamed by the passage of rising CO bubbles produced by reduction in the underlying metal phase. Obviously, the slag viscosity must be sufficient for the slag to form a mechanically stable bridge between the electrodes and the metal, and the composition must be chosen to produce a slag which is not too runny. An empirical equation for the effective viscosity of a slag, η_e, containing S wt % of solids dispersed in a liquid slag of viscosity, η, is

$$\eta_e = \eta(1 - 1.35S)^{5/2}$$

A compromise between these requirements for foaming slag formation, the slag composition and mechanical properties has been found with a slag containing 9 wt % MgO, 26% FeO and the residual lime/silica ratio of about 2.0. However, an equally efficient slag is formed which is less corrosive to an alumina-based refractory lining of the furnace, if 10% Al_2O_3 replaces the equivalent weight per cent of SiO_2. A comparative study of the foamability of some commonly used slags (Utigard and Zamalloa, 1993) shows that this property is increased for a given composition by temperature control, the highest workable viscosity giving the best foam formation, and for a fixed

DropBooks

viscosity, basic slags are more effective than acid slags. The overall foaming behaviour of a given slag is strongly affected by gas injection into the slag, increasing as the gas velocity increases.

Since the ferro-alloys are liquid over a wide range of composition at 1900 K, the temperature of operation of these processes is no higher than that used in electric arc steel scrap-melting furnaces, for which the technology is well established up to 100 megawatt power input.

The production of silicon by the reduction of silica with carbon in a submerged arc furnace, is complicated by the fact that pure silica has a very high viscosity at temperatures as high as 2300 K. The heat generated around the slag–electrode interface stirs the slag, and the contact of carbon at very high temperatures, probably around 4000 K, with the oxides of the slag leads to chemical reaction at the interface as well as reaction between carbon particles ejected from the surface of the electrode by evaporation and spalling. CO is generated by reactions such as

$$SiO_2 + C = SiO(g) + CO$$

$$MgO + C = Mg(g) + CO$$

and so on. Gas bubbles which are formed from the CO generated in this manner also stir the slag during evolution from the slag. Mathematical studies of the state of motion of the metal–slag system during reduction, indicate that these are the principal sources of motion in the system, and the metal phase, which should not be in contact with the electrodes, is relatively quiet.

By the correct choice of the metal oxide/carbon ratio in the ingoing burden for the furnace, the alloy which is produced can have a controlled content of carbon, which does not lead to the separation of solid carbides during the reduction reaction. The combination of the carbon electrode, the gaseous oxides and the foamed slag probably causes the formation of a plasma region between the electrode and the slag, and this is responsible for the reduction of electrical and audible noise which is found in this operation, in comparison with the arc melting of scrap iron which is extremely noisy, and which injects unwanted electrical noise into the local electrical distribution network.

A similar reduction in these sources of noise is also found in argon arc plasma furnaces, which also use carbon electrodes, but the scale of operation of carbon-arc plasma furnaces has not been developed at the present time to a power level equal to that of the conventional arc (up to 1 megawatt). One advantage which the plasma system, which functions as a high intensity radiation source, has is that the slag need not be part of the electrical conduction system, and the plasma is struck directly between carbon electrodes. This allows considerably greater scope in the choice of slag components, which can be chosen mainly for their refining properties, and not because of their electrical conductivities. A disadvantage of the plasma system, when compared

with the foaming slag–carbon electrode system, is that the latter provides a better shielding of the container walls from overheating by emitted radiation.

Steelmaking and copper production in pneumatic vessels

Steel

The production of iron relatively free of non-metal impurities was first achieved in the Bessemer furnace, in which air was blown through liquid blast furnace metal to eliminate carbon as CO(g). The bubbles of gas stir the liquid metal vigorously, thus encouraging the achievement of thermodynamic equilibrium. Using a lime–silica slag, elements such as phosphorus and manganese are removed by oxidation. This process produced liquid iron, but unfortunately introduced nitrogen, which had a deleterious effect on the physical properties of the resulting iron solid.

The replacement of air by oxygen for blast furnace metal refining in the Basic Oxygen Process (BOF), revolutionized the rate of production of iron from blast furnace metal, as well as considerably reducing the amount of physical plant which was required. The earlier refining process, the open hearth furnace was essentially a reverberatory furnace, in which carbon was eliminated as CO(g) which was nucleated on the furnace bottom. The original tests for the BOF process, in which an oxygen lance was used, were soon followed by injection of oxygen beneath the metal surface, first from the side, and eventually from the bottom of the vessel. The average rate at which refined metal can be produced in modern oxygen-injected vessels is roughly 200 tonnes in 20 minutes! Due to the severe agitation which is produced by the passage of oxygen and CO, the metal/slag system takes the form of an emulsion in which there are droplets of metal and slag as well as the gas phase. It is thought that the major refining reaction for de-carburization is between carbon dissolved in the metal droplets, and FeO dissolved in the slag. The use of pure oxygen in the basic oxygen furnace, causes severe erosion of the tuyere linings due to attack by the liquid slag containing a high FeO percentage. This has been overcome by the addition of hydrocarbon gas to the oxygen injection.

In the Bessemer furnace, silicon and manganese are removed in the first ten minutes of the blow, and after this the degree of agitation of the bath increases while the remaining carbon is removed. During the blow about 15 tonnes of oxygen are consumed to produce 200 tonnes of metal. The charge to the furnace is not only liquid blast furnace metal, but an addition of scrap metal can be made. This must be pre-heated to avoid cooling the hot metal to the solid state. The addition of lime to the reactor is usually accompanied with fluorspar, which substantially reduces the viscosity of the slag. Roughly 8% of the metal weight is added as lime, and one-tenth of this as fluorspar.

DropBooks

The mass transfer mechanism in the case of the reactive jet entering a fluid, cannot be adequately represented by the model based on a time-independent contact between the reacting species. It has been proposed that the situation in the BOF can be represented by the 'surface-renewal' model of mass transfer, in which mass transfer takes place during a limited period of time of contact, after which the two reacting phases are separated. In the case of the oxygen jet, it can be supposed that iron is oxidized at the metal/gas interface to form FeO, which, having a lower density than the metal, detaches from the interface and rises to the surface. During this ascent the oxide can react with the non-metallic elements dissolved in the metal. A model study of the removal of oxygen from liquid silver by argon produced an equation for the local mass transfer coefficient in the de-oxidation kinetics

$$k = (2DuR/\pi)^{1/2}(1/r_1)$$

where R is the radial distance from the jet axis, u is the radial velocity at the surface, D is the diffusion coefficient of oxygen in silver, and r_1 is the depth of the depression made in the liquid metal by the jet. Values of the mass transfer coefficient were found to be between 0.02 and 0.05 $\mathrm{cm\,s^{-1}}$. The diffusion coefficient of oxygen in silver is about $10^{-4}\ \mathrm{cm^2\,s^{-1}}$. The value of the product uR was estimated at $80\ \mathrm{cm^2\,s^{-1}}$. A typical value of the mass transfer coefficient in the industrial BOF process is about $0.016\ \mathrm{cm^2\,s^{-1}}$.

It should be remarked that a detailed study of the elimination of manganese and silicon from the liquid metal shows that silicon together with some of the manganese is first removed, followed by the rest of the manganese together with some of the carbon, which is finally removed together with half of the sulphur contained in the original liquid. This sequence is in accord with what would be expected from thermodynamic data for the stabilities of the oxides.

One product of the oxygen blowing of molten iron is iron 'fume', which consists of iron oxide particles, Fe_2O_3. The rate of iron fuming has been studied in the laboratory, and found to be almost equal to the free evaporation rate of liquid iron in a vacuum. The explanation of this high rate is that the boundary layer between the liquid metal and the oxygen atmosphere has a very low iron activity on the oxygen rich side, which can be obtained from the equilibrium constant for Fe_2O_3 formation from iron and oxygen at 1900 K,

$$4\mathrm{Fe} + 3\mathrm{O_2} \longrightarrow \mathrm{Fe_2O_3} : \log K_{1900} = 15.77 = -4 \log a\mathrm{Fe}$$

$$a\mathrm{Fe} = 1.14 \times 10^{-4}$$

Thus the driving force for fuming is approximately equal to that for free evaporation. Using the experimental data, and the normal expression for mass transfer across a boundary layer, it is concluded that the boundary layer thickness which would account for this rate should be about 2×10^{-4} cm (Turkdogan *et al.*, 1963).

Copper

The production of copper from sulphide minerals is accomplished with a preliminary partial roast of the sulphides before reaction with air in the liquid state, known as mattes, to form copper metal (conversion). The principal sources of copper are minerals such as chalcopyrite, $CuFeS_2$ and bornite Cu_3FeS_3, and hence the conversion process must accomplish the preferential oxidation of iron, in the form of FeO, before the copper metal appears. As mentioned before, the $FeO–SiO_2$ liquid system is practically Raoultian, and so it is relatively easy to calculate the amount of iron oxidation which can be carried out to form this liquid slag as a function of the FeO/SiO_2 ratio before copper oxidation occurs. The liquid slag has a maximum mole fraction of FeO at the matte blowing temperatures of about 0.3, at solid silica saturation.

The mineral is roasted in air as a preliminary treatment to produce a composition corresponding to the composition $Cu_2S–FeS$, and this mixture is charged to a converter, similar to the Bessemer converter, together with silica which will form the slag. The principal physical difference between the Bessemer converter and the copper converter is that whereas iron contains a substantial amount of carbon which produces heat by oxidation, copper converting is initially a process of iron and sulphur oxidation where neither element has a significant solubility in liquid copper to provide a heat source to the metal. The metal is produced *below* the molten sulphide–slag mixture, and so the converter is side-blown. Furthermore, the solubility of nitrogen in copper is very small, and nitrogen plays no part in the physical properties of the final product. As a result of this air blowing can be used, despite the fact that nitrogen in air is only a 'thermal passenger' in the process. The thermodynamic data for the liquid sulphide phase, known as a 'matte', show that the oxidation process occurs at first with the oxidation of iron and sulphur occurring in parallel. After the removal of iron, the copper sulphide is oxidized to remove the sulphur, and leave liquid copper containing oxygen, and a small amount of sulphur.

DropBooks

The thermodynamic data for $Cu_2S–FeS$ (Krivsky and Schuhmann, 1957) show that these sulphides mix to form approximately ideal ionic liquids. These are molten salts in which the heat of mixing is essentially zero, and the entropy of mixing is related to the ionic fractions of the cations and anions. In the present case the ionic fractions yield values for the activities of the two sulphides

$$a\mathrm{Cu_2S} = (n\mathrm{Cu} + /(n\mathrm{Cu^+} + n\mathrm{Fe^{2+}}))^2(n\mathrm{S^{2-}}/(n\mathrm{S^{2-}} + n\mathrm{O^{2-}}))$$

and

$$a\mathrm{FeS} = (n\mathrm{Fe^{2+}}/n\mathrm{Cu^+} + n\mathrm{Fe^{2+}})(n\mathrm{S^{2-}}/(n\mathrm{S^{2-}} + n\mathrm{O^{2-}}))$$

where the general ionic fraction is the number of cations of a given species divided by the total number of cations and similarly for the anions.

The sulphur pressure of the sulphides is a sensitive function of the metal/sulphur ratio around the stoichiometric composition, rising sharply when the sulphur content exceeds this limit. It follows from the Gibbs–Duhem equation

$$X_A d \log a_A + X_B d \log a_B = 0$$

that the copper activity in liquid Cu_2S, and the iron activity in liquid FeS drop rapidly as the composition of the sulphides exceeds the metal/sulphur ratio at the stoichiometric composition. There is a miscibility gap between the sulphides and the sulphur-containing metal phase which becomes wider as the copper/iron ratio increases. In the iron–sulphur binary system there is no miscibility gap at the temperature of copper conversion, but the liquid in contact with solid iron contains an atom fraction of sulphur of a little over 0.2.

The sulphur dissociation pressure of Fe/FeS at the matte blowing temperature of about 1573 K can be calculated from the following data

$$2Fe + S_2(g) = 2FeS; \quad \Delta G^\circ = -485\,360 + 1290T - 144.5T \log T$$

$$\log K_{1573} = 4.30 = -\log pS_2(g)\{aFe = 1\}$$

Since the Fe–S liquid system shows no miscibility gap at matte blowing temperatures, it is necessary to calculate the iron activity around the FeS composition by applying the Gibbs–Duhem equation to the data. These show that the iron activity at the *stoichiometric* composition is about 0.1, and hence the sulphur pressure is approximately 10^{-2} atmos. The sulphur pressure therefore ranges over the extreme values of 10^{-4}–10^{-2} atmos over the liquid Fe–S system. In the Cu–S system there is a substantial miscibility gap, and the sulphur pressure is about 10^{-4} atmos across this composition range. The oxygen partial pressure in equilibrium with this pressure and $pSO_2 = 0.2$, is 10^{-7} atmos. The sulphur pressure decreases with the elimination of the sulphide phase over the range 10^{-2}–10^{-7} atmos, from the Cu_2S–FeS matte to the copper phase containing 2% sulphur at the end of the blow.

The prevailing oxygen potential can be calculated during the blowing operation, assuming that the gas consists mainly of 1/5 atmosphere SO_2 with the balance as nitrogen, according to the reaction

$$2FeS + 3O_2 = 2FeO + 2SO_2(g);$$

$$\Delta G^\circ = -998\,370 + 201T$$

$$\log K_{1573} = 22.65 = \log a^2FeO\, p^2SO_2 / a^2FeS\, p^3O_2$$

At the slag–matte interface, the activity of FeO can be 0.3 as a maximum before SiO_2 saturation sets in. The activity of FeS can be assumed to vary over the activity range aFeS = 0.5–10^{-3} during the process, and so the oxygen

pressure is calculated to be in the range 10^{-8}–10^{-6} atmos. This is too low to oxidize copper, even after the sulphur content is removed, which requires an oxygen potential at this temperature of about $-125\,\text{kJ mol}^{-1}$, ($pO_2 = 8 \times 10^{-5}$). The prevailing oxygen potential during blowing makes another unwanted reaction possible, this is the oxidation of FeO to magnetite, Fe_3O_4. This is a high melting solid, and its formation can usually be avoided by the fact that the FeO is combined with silica to form the slag. The oxygen potential for magnetite formation from pure FeO corresponds to an oxygen partial pressure of about 10^{-7} atmos. However, the formation reaction

$$6FeO + O_2(g) = 2Fe_3O_4; \quad \Delta G^\circ = -624\,420 + 250.2T \quad \text{J mol}^{-1}$$

$$\Delta G^\circ_{1573} = -230\,850 \quad \text{J mol}^{-1}$$

$$\log K_{1573} = 7.67$$

shows that at 1573 K, and an oxygen partial pressure of 10^{-6} atmos, the FeO activity must be more than 0.5 in order to allow oxidation to Fe_3O_4 since

$$\Delta G^\circ = -RT \log K = 6\Delta\mu\text{FeO} + \Delta\mu O_2$$

where $\Delta\mu Fe_3O_4 = 0 (aFe_3O_4 = 1)$, and $\Delta\mu O_2 = -180\,660\,\text{J mol}^{-1}$. Hence $\Delta\mu$FeO is equal to $-8365\,\text{kJ mol}^{-1}$, and aFeO is equal to 0.53. This corresponds to a slag containing 30 wt% SiO_2 at this temperature. When the composition reaches the Cu–Cu_2S equilibrium, the oxygen potential in equilibrium with 0.2 atmos SO_2 is approximately 10^{-5} atmos, and the corresponding FeO activity in the silicate slag is 0.36 before Fe_3O_4 is formed, corresponding to a slag containing nearly the saturation content of SiO_2, 42 wt%. It is therefore preferable to remove the iron-containing slag at the end of the iron oxidation operation, so that magnetite formation does not significantly influence the process during the oxidation of Cu_2S. The product of the converter process is 'blister' copper which can be further refined in the liquid state, fire-refining, and finally by electrolytic refining with aqueous electrolytes. In the fire-refining process, the classical method of doing this was to insert a tree-trunk into the metal, a process known as 'poling', producing a copious supply of water vapour which acts to transport the impurity oxides to the surface of the liquid metal.

DropBooks

The reduction of oxides and halides by reactive metals

Magnesium

An industrial example of the reduction of stable oxides to form a metallic element as a vapour, is the Pidgeon process for the production of magnesium.

The reaction of magnesium oxide with silicon produces a very small vapour pressure of magnesium

$$2MgO + Si = 2Mg(g) + SiO_2; \quad \Delta G^\circ = 610\,860 - 285.6T \quad J\,mol^{-1}$$

and has a Gibbs energy change at 1500 K of $+182\,J\,mol^{-1}$, which corresponds to the equilibrium vapour pressure of magnesium of approximately 5×10^{-7} atmos, when silicon and silica are at unit activity. If the process is carried out using dolomite, MgO·CaO, as the source of magnesium, the activity of silica produced by this reaction is considerably reduced by formation of calcium orthosilicate, Ca_2SiO_4, and hence the vapour pressure of magnesium is considerably enhanced. In practice, ferrosilicon is used as the source of silicon, and the reaction is carried out in the solid state. The rate of the reaction is found to be directly proportional to the activity of silicon in the alloy, and this suggests that the reaction is carried forward through the distribution of the silicon potential in the briquetted mixture of reactants via the formation of SiO(g). The reaction between MgO and Si to produce SiO(g)

$$MgO + Si = Mg(g) + SiO(g); \quad \Delta G^\circ = 626\,800 - 285.6T \quad J\,mol^{-1}$$
$$\log K_{1500} = -6.9$$

produces a vapour pressure of SiO of about 3×10^{-4} atmos at 1500 K. The gas then reacts with CaO according to

$$2SiO(g) + CaO = Ca_2SiO_4; \quad \Delta G^\circ = -851\,350 + 375T \quad J\,mol^{-1}$$
$$\log K_{1500} = 10$$

It was found that the reaction rate could be significantly enhanced if a fluorspar addition is made to the briquette with the objective of producing a small amount of a liquid phase at the operating temperature. There is a eutectic in the $CaO–SiO_2–CaF_2$ system at a temperature of 1398 K. These studies show the importance of the role of a vapour species to transport chemical potentials in a solid–solid reaction, and also the desirability of introducing a small quantity of a liquid.

Chromium

The production of metals which form very stable oxides by the aluminothermic process, such as manganese, chromium and vanadium is carried out with reactants at room temperature which react to provide enough heat to raise the temperature of the products to high temperatures at which the whole system is liquid. The metal phase which is produced can therefore separate from the liquid slag which is formed. The production of chromium serves as a useful

example of this process, and the data show that for the reaction producing liquid products

$$Cr_2O_3 + 2Al = 2Cr + 3Al_2O_3;$$

$$\Delta G^\circ = -396\,300 - 2.50T \quad \text{J mol}^{-1}(2300\text{–}2800\,\text{K})$$

$$\log K_{2500} = 8.41$$

The small value of the entropy change reflects the fact that only liquids are involved in this reaction. The heat balance in carrying out this reaction may be calculted, according to Hess's law, by calculating the heat change at room temperature, and subtracting the heat required to raise the products to the final temperature. The data for this reaction are as follows:

Heat of reaction at room temperature is 541 040 J mol^{-1} Cr_2O_3. Heat required to raise the products to 2500 K is 591 080 joules. Hence there is a deficit of 50 000 joules.

The enegy deficit may be supplied by pre-heating the reactants to a temperature just below the melting point of aluminium (934 K). At 800 K, which provides a safe operating margin from the formation of liquid Al, the heat content of the reactants is 87 000 joules. This allows for heat losses through the walls of the container during the reaction as well as supplying the energy deficit. An alternative procedure is to add $Na_2Cr_2O_7$, which provides an energetically richer source of chromium, involving Cr^{6+}, the sodium oxide which remains after the reaction lowering the melting point of the slag.

DropBooks

The composition of the final slag, consisting of Al_2O_3–Cr_2O_3, may be regarded as a *Temkin* liquid in which the entropy of mixing the ions on the cation and the anion sub-lattices is ideal, and the heat of mixing is zero. The activity of the components varies in this example as the square of the mole fraction, because each mole of oxide contains two gram-ions of cation. The equilibrium constant K_{2500} which is related to the activity quotient may be approximated by the mole fraction ratio in the metal phase, and by the ionic fractions in the slag phase then becomes

$$K_{2500} = [a\text{Cr}/a\text{Al}]^2(a_{Al_2O_3}/a_{Cr_2O_3}) = [X_{Cr}/X_{Al}]^2(X_{Al_2O_3}/X_{Cr_2O_3})^2$$

Assuming that the reaction is close to completion at the final temperature, and therefore that X_{Cr} and $X_{Al_2O_3}$ are close to unity, the residual aluminum content of the metal and the amount of unreduced chromia can be obtained from the equilibrium constant

$$X_{Al}X_{Cr_2O_3} = \text{antilog} - 8.41/2 = 6.23 \times 10^{-5}$$

Manganese

The production of manganese is an example of the opposite problem, in which it is possible to produce too much heat by direct reaction of the oxide and

aluminium. Manganese may be obtained in the mineral form as pyrolusite, MnO_2, and this may be reduced to the oxides Mn_2O_3 and MnO. The heat change for the reduction of each of these oxides at 298 K is, in ascending order of metal valency, given by the reactions

$$3MnO + 2Al = 3Mn + Al_2O_3; \quad \Delta H^\circ = -519\,\text{kJ}$$

$$Mn_2O_3 + 2Al = 2Mn + Al_2O_3; \quad \Delta H^\circ = -727\,\text{kJ}$$

$$(3/2)MnO_2 + 2Al = (3/2)Mn + Al_2O_3; \quad \Delta H^\circ = -895\,\text{kJ}$$

The heat contents of the products at 2500 K are:

$$3Mn + Al_2O_3 \quad \Delta H^\circ_{2500} = 723\,780 \quad \text{joules}$$

$$2Mn + Al_2O_3 \quad = 613\,880$$

$$(3/2)Mn + Al_2O_3 \quad = 558\,920$$

It is clear that the 3+ and 4+ valencies of manganese provide oxides which can be reduced by aluminium to produce the liquid products, but further consideration of efficiency of the process from an economic point of view, must take account of the fact that the higher valencies of manganese also require more aluminium for stoichiometric reduction, since the Al/Mn ratios are 0.67 for MnO, 1.0 for Mn_2O_3, and 1.33 for MnO_2. Clearly a balance must be struck between the thermal efficiency of the higher manganese valencies against the decreasing aluminium demand of the lower valency.

Other metals having very stable oxides can be reduced by the aluminothermic reaction to produce useful ferro-alloys. Niobium oxide, NbO, can be reduced to form a ferro-alloy by the inclusion of iron in the reacting mixture as haematite or magnetite, depending on the niobium content which is required in the product.

Heat losses in crucible reactions

An upper limit of the heat losses through the reaction container wall, usually in the form of a cylindrical crucible with an increasing diameter from bottom to top, by assuming that the whole reaction mixture achieves the final reaction temperature immediately, and heat losses occur through the crucible refractory walls by conduction. The solution of Fourier's equation

$$\alpha \frac{\partial^2 T}{\partial y^2} = \frac{\partial T}{\partial t}$$

where α is the thermal diffusivity of the refractory wall material, and the y axis is along the radius of the crucible, for the boundary conditions

$T = 300\,\text{K}$ at $t = 0$

$T = 300\,\text{K}$ as $y \longrightarrow \infty$

$T = 2500\,\text{K}$ at $y = 0$

the appropriate solution for the temperature distribution is

$$T = (2500 - 300\,\text{K})\,\text{erfc}\,\frac{y}{2\sqrt{\alpha t}}$$

The total heat loss over 30 minutes, t_e, per unit area where k is the thermal conductivity of the container, is given by

$$Q = 2k.\ 2200\left(\frac{t_e}{\pi\alpha}\right)^{1/2}\text{cm}^{-2}$$

Inserting the values for a typical refractory wall,

$\alpha = 6 \times 10^{-5}\,\text{cm}^2\,\text{s}^{-1}$

$k = 5 \times 10^{-3}\,\text{J}\,\text{s}^{-1}\,\text{cm}^{-1}\,\text{K}^{-1}$

Q is then approximately equal to $136\,\text{kJ}\,\text{cm}^{-2}$.

If the crucible is assumed to be a cylinder, 1 m high by 1 m diameter, the total surface area for heat loss is $4 \times 10^4\,\text{cm}^2$, and hence the reactor loses 54 MJ during the reaction time.

Assuming that the reactor contains about 500 moles of products, which should have generated about 350 MJ, it can be seen that the upper limit of the heat loss is 15% of the heat generated by the reaction.

DropBooks

Zirconium

The Kroll process for the reduction of the halides of refractory metals by magnesium is exemplified by the reduction of zirconium tetrachloride to produce an impure metal which is subsequently refined with the van Arkel process to produce metal of nuclear reactor grade. After the chlorination of the impure oxide in the presence of carbon

$$ZrO_2 + 2Cl_2 + 2C = ZrCl_4(g) + 2CO(g)$$

the condensed chloride is heated in hydrogen to reduce the volatile $FeCl_3$ to the less volatile $FeCl_2$. Separation of sufficiently pure $ZrCl_4$ is made after this stage, and the chloride is loaded into a sealed vessel mixed with magnesium in the form of ingots or turnings. The vessel is filled with an inert gas, e.g. helium, in order to reduce the risk of oxidation of the metal product. At the reaction temperature of about 1100 K, the vapour of $ZrCl_4$ reacts with the

magnesium to form a zirconium sponge, and the magnesium chloride which is formed is molten and floats to the top of the charge.

In the production of metallic uranium the fluoride UF_4 is used for magnesium reduction since the reduction of UCl_4 does not produce sufficient heat. The chloride can be reduced with calcium, when a significantly greater amount of heat is generated to reach the desired temperature.

A useful approximation to estimate the possibility of a particular reaction which depends on internal heat generation to produce the products in the proper state for separation is to ignore the heat losses from the reactor, and assumes an average heat capacity calculated from the Neumann–Kopp law

$$C_p = 29n \quad \text{joules}$$

where n is the number of atoms in each compound. The adiabatic approximation using Hess' law, as was used above in the aluminothermic reactions, where the reaction is carried out at room temperature and the heat of the reaction is used to raise the temperature of the products to the final level.

Uranium

This approximation can be applied to the production of uranium by the reactions

$$UCl_4 + 2Mg = U + 2MgCl_2; \quad \Delta H^\circ_{298} = -230\,\text{kJ}$$

and

$$UCl_4 + 2Ca = U + 2CaCl_2; \quad \Delta H^\circ_{298} = -548\,\text{kJ}$$

in order to calculate the temperature to which the products could be raised when 7 gram-atoms per gram-atom of uranium are produced. The final temperatures are found to be 1133 K and 2699 K assuming that no latent heat must be absorbed in the products. The heats of fusion of $MgCl_2$ ($43\,\text{kJ mol}^{-1}$) and of metallic uranium ($15.5\,\text{kJ gram-atom}^{-1}$) must therefore be deducted from the heat balance if liquid products are to be formed. This requirement reduces the heat available to melt even the chloride in the magnesium reduction to below the necessary amount, whereas the calcium reduction leaves both products in the liquid form. Because of the relatively more convenient use of magnesium, the reduction of UF_4 is used. The heat change of this reaction is 330 kJ, and to compensate for insufficient heat it is necessary to pre-heat the reactants, and then the reaction may be carried out at 900–1000 K. The addition of a low-melting Mg–Pb alloy to the reaction mixture also increases the rate of reaction presumably through improving the physical contact between the reactants. The lower melting point of magnesium, 923 K, than calcium, 1115 K, is also an advantage in the reduction process.

The electrolysis of molten salts

Molten halides are liquid electrolytes in many instances, and their decomposition may be carried out in principle to produce the metal and halogen, usually in the gaseous state. The theoretical decomposition voltage, E°, is calculated from the Gibbs energy of formation through the equation

$$-\Delta G^\circ = nFE^\circ$$

where n is the valency of the cation to be reduced to metal. Since this voltage only applies to the situation where zero current is being drawn through the electrolyte, the useful applied voltage will be somewhat greater, depending on the desired rate of decomposition which is required. The desired rate of production of the metal will determine the current which must pass through the electrolyte and because of the electrical resistance of the molten salt, will add to the applied potential to supply the iR drop in the electrolyte. When there are irreversible processes, such as overvoltage at the electrodes, an additional potential will also be added.

Magnesium

The simplest industrial example of molten salt electrolysis is the production of magnesium by the electrolysis of $MgCl_2$. The electrolysis proceeds in accordance with the decomposition voltage plus an iR drop related to the conductivity of the electrolyte. The specific conductivity of molten salts is of the order of $1\,\text{ohm}^{-1}\,\text{cm}^{-1}$, corresponding to an average diffusion coefficient in the liquid state of $10^{-5}\,\text{cm}^2\,\text{s}^{-1}$. The iR drop contribution to the applied potential can therefore be estimated from these numbers for most cases. The finite resistance of the electrolyte plays a useful part in molten salt phases by supplying a heat source, i^2R, to help maintain the heating of the electrolyte, and overcome the heat losses in the reactor. Another advantage of the molten chloride route for the production of magnesium, is that the $MgCl_2$ provides both the metal and the chlorine gas which is used in the subsequent chlorination of the MgO feedstock.

DropBooks

Sodium

A complication of the extension of the electrolysis route for metal production, is that in the case of the alkali metals, there is a significant solubility of the metal which would be produced by electrolysis in the molten chloride. The dissolved metal provides very mobile electrons to the melt, thus reducing the salt resistance, and dissipating the increased current, at a given applied potential, without the production of metal. To describe this phenomenon in

another more quantitative manner, the transport number of the cations is significantly less than unity in such solutions. This fact may explain the success of the Downes' cell for the production of sodium which uses an electrolyte consisting of 40% NaCl–60% $CaCl_2$ by weight, which is molten at 873 K, the operating temperature of the cell. Since the decomposition voltages of these chlorides are very similar, 3.34 V for NaCl and 3.47 V for $CaCl_2$, it appears possible that calcium may be co-produced with sodium, but since the solubility of calcium in sodium is very limited, about 4%, the metal produced by electrolysis of the molten salt mixture can hold a very small amount of calcium at a high thermodynamic activity. The two metals can subsequently be separated on cooling of the alloy, where solid calcium separates first.

Aluminium

The most important electrochemical process for metal production is the Hall–Heroult production of aluminium which uses an electrolyte consisting of cryolite, Na_3AlF_6 together with a few weight per cent of Al_2O_3. The electrodes are made of carbon, and the products of electrolysis are aluminium metal at the cathode and a CO/CO_2 mixture at the anode, the process being carried out at about 1300 K. In a typical cell, about 4 V is required to produce the metal, and this is composed of the standard potential for the cell reaction plus the iR drop in the electrolye plus an apparent overvoltage of about 0.4 V at the anode. The practical findings are that the anode gas consists of about 20–40% CO, whereas the thermodynamic expectation would be that the gas, in equilibrium with the solid carbon anode, would be almost entirely CO at the operating temperature. The rate of anode consumption conforms to the production of CO_2 entirely at the anode and this suggests that the formation of CO occurs through an interaction between the CO_2 and the electrolyte or any dissolved metal. The decomposition potentials of aluminium and sodium were found to be very similar in this electroyte, which accounts for the damage sustained by the cathode due to sodium infiltration. The reduction of CO_2 by dissolved aluminum in the electrolyte according to

$$3CO_2 + 2\{Al\} = 3CO + \{Al_2O_3\}$$

would reduce the efficiency of metal production, and the dissolution of sodium metal in the electrolyte will introduce semiconduction in the electrolyte, which will also reduce the efficiency. Experimental studies support the empirical equation due to Pearson and Waddington,

$$\text{Current efficiency} = (1/2)(\%\ CO_2 \text{ in the anode gas}) + 50\%$$

which yields an average efficiency of 85%

Another possibility that would reduce the overall process efficiency is the kinetics of CO_2 formation at the anode. There is some evidence that the first step in the sequence

$$(1/2)O_2 + C_s \longrightarrow C - [O]$$

$$2C - [O] \longrightarrow CO_2 + C_s$$

where C_s is an active site on the carbon surface.

Refractory metals

A number of attempts to produce the refractory metals, such as titanium and zirconium, by molten chloride electrolysis have not met with success with two exceptions. The electrolysis of caesium salts such as Cs_2ZrCl_6 and $CsTaCl_6$, and of the fluorides Na_2ZrF_6 and $NaTaF_5$ have produced satisfactory products on the laboratory scale (Flengas and Pint, 1969) but other systems have produced merely metallic dusts and dendritic deposits. These observations suggest that, as in the case of metal deposition from aqueous electrolytes, e.g. Ag from $Ag(CN)_2^-$ instead of from $AgNO_3$, the formation of stable metal complexes in the liquid electrolyte is the key to success.

Thermodynamic data show that the stabilities of the caesium chloride–metal chloride complexes are greater than the corresponding sodium and potassium compounds, and the fluorides form complexes more readily than the chlorides, in the solid state. It would seem that the stabilities of these compounds would transfer into the liquid state. In fact, it has been possible to account for the heats of formation of molten salt mixtures by the assumption that molten complex salts contain complex as well as simple anions, so that the heat of formation of the liquid mixtures is the mole fraction weighted product of the pure components and the complex. For example, in the $CsCl–ZrCl_4$ system the heat of formation is given on each side of the complex compound composition, the mole fraction of the compound

$$(1/3)\Delta H^{\mathrm{m}} = X_{ZrCl_4}\Delta_f H Cs_2ZrCl_6$$

on the CsCl side of the compound composition (where $X_{ZrCl_4} = 1/3$) and

$$(2/3)\Delta H^{\mathrm{m}} = X_{CsCl}\Delta_f H Cs_2ZrCl_6$$

on the $ZrCl_4$ side of the compound composition (where $X_{CsCl} = 2/3$) where $\Delta_f H Cs_2ZrCl_6$ is the heat of formation of the compound.

Bibliography

J. Szekely and N.J. Themelis Wiley *Rate Phenomena in Process Metallurgy*. New York (1971).
R.I.L. Guthrie. *Engineering in Process Metallurgy*. Oxford University Press TA 665. G95 (1989).

DropBooks

V.G. Levich. *Physicochemical Hydrodynamics*. Englewood Cliffs, Prentice-Hall (1962).
N. Sano, W.-K. Lu, and P.V. Riboud (eds). *Advanced Physical Chemistry for Process Metallurgy*. Academic Press TN673 A325 (1997).
T. Rosenqvist. *Principles of Extractive Metallurgy*. McGraw Hill, New York TN 695 G47 (1983).
F.D. Richardson. *Physical Chemistry of Melts in Metallurgy*. Academic Press, London (1974).
W.G. Davenport, G.D.H. Wakelin and A.V. Bradshaw. *Heat and Mass Transfer in Process Metallurgy*. Inst. Min. Met. London. p. 233 (1967).
E.S. Machlin. *Trans. Met. Soc. AIME*, **218**, 314 (1960).
G.R.A. Mayers. *Chem. Eng. Sci.*, **16**, 69 (1962).
E.T. Turkdogan and P. Grieveson. *Trans. AIME*, **224**, 316 (1962).
H. Flood and J.M. Toguri. *Trans. AIME*, **227**, 525 (1963).
P.H. Calderbank. *The Chemical Engineer*, **CE220** (1968).
J. Michard, P. Dancoisne and G. Chanty. *Amer. Inst. Met Eng.*, **20**, 329 (1967).
K. Ito. *Met. Trans.*, **20B**, 515–521 (1989). Slag foaming in new iron and steelmaking processes.
E.T. Turkdogan, P. Grieveson and L.S. Darken. *J. Phys. Chem.*, **67**, 1647 (1963).
W.A. Krivsky and R. Schuhmann. *Trans. AIME*, **209**, 981 (1957).
T.A. Utigard and M. Zamalloa. *Scand. J. Metallurgy*, **22**, 83 (1993).
S.N. Flengas and P. Pint. *Can. Met. Quarterly*, **8**, 151 (1969).

Chapter 14

The refining of metals

The products which are obtained from the metal-producing processes described above are normally not sufficiently pure for modern needs. A refining stage is therefore added to the production technology to remove the unwanted elements. Depending on the metal and the particular impurity involved the process can cause the elimination of the impurity in a gaseous form, as a separate oxide phase, as an inter-metallic phase, or by electrolysis with a specifically selected electrolyte, as a deposit on an electrode. Examples of some of these will be given which will cover most of the refining steps at present in use on the large industrial scale.

The effect of slag composition on impurity transfer

DropBooks

The removal of phosphorus from steel is readily made under oxidizing conditions using a basic, or calcium oxide-rich slag. The limits of this process are set by the slag CaO/SiO_2 which is limited by the need to use a liquid slag, and hence one containing less than 40 mole per cent CaO, to achieve optimum metal–slag contact. The thermodynamic activity of lime has a maximum value around 0.01 in these slags. The removal of sulphur at this time is minimal, and, in fact, this is best carried out under reducing conditions, as in the blast furnace, where the metal is saturated with carbon.

Taking into account the need for the slag phase to be a sink for the impurities which are removed in metal-refining, it is useful to have a means of predicting, even semi-quantitatively, the effectiveness of the slag composition for the elimination of impurities. A simple model system for exchange reactions (Flood and Grjotheim, 1952) involving mixed ionic species can be obtained from a consideration of exchange reactions of halogens between gas and a molten salt containing mixed cations

$$(\mathrm{Na,\ K})\ \mathrm{Cl} + (1/2)\mathrm{Br_2(g)} \longrightarrow (\mathrm{Na,\ K})\ \mathrm{Br} + (1/2)\mathrm{Cl_2(g)}$$

ΔG (exchange) can be represented as a cycle in which the stages are:

I Separation of the cations.

$$\text{(Na, K) Cl} \longrightarrow X_{\text{NaCl}}\text{NaCl} + X_{\text{KCl}}\text{KCl}; \quad \Delta G = -\Delta G_{\text{I}}^{\text{m}} \text{ (The Gibbs energy of mixing the chlorides)}$$

II Separate exchange of the halogens

$$\text{NaCl} + (1/2)\text{Br}_2(\text{g}) \longrightarrow X_{\text{NaBr}}(\text{NaBr} + \text{Cl}_2(\text{g})); \quad X_{\text{NaBr}}\Delta G_{\text{II}}^{\circ}$$

$$\text{KCl} + (1/2)\text{Br}_2(\text{g}) \longrightarrow X_{\text{KBr}}(\text{KBr} + \text{Cl}_2(\text{g})); \quad X_{\text{KBr}}\Delta G_{\text{III}}$$

$$\text{NaBr} + \text{KBr} \longrightarrow \text{(Na, K) Br}; \quad \Delta G_{\text{IV}}^{\text{m}} \text{ (mixing of bromides)}$$

Finally the Gibbs energy for the anion exchange is given by the sum of these processes

$$\Delta G_{\text{exchange}} = \Sigma\Delta G(\text{I–IV})$$

and assuming that the mixing of the cations in stages I and IV which involved the same molar fractions of cations is ideal, the resulting equation is simply

$$\Delta G_{\text{exchange}} = X_{\text{Na}}^{+}\Delta G_{\text{II}} + X_{\text{K}}^{+}\Delta G_{\text{III}}$$

where the molar fractions X_{Na}^{+} and X_{K}^{+} are ionic fractions.

In the removal of sulphur from liquid iron the effect of slag composition can be assessed using this equation to show that the exchange equilibrium of sulphur and oxygen between iron metal and slag which occurs during desulphurization can be calculated by using data for the reactions involving only one each of the cationic species

$$[\text{O}] + \{\text{FeS}\} \longrightarrow \{\text{FeO}\} + [\text{S}]$$

$$[\text{O}] + \{\text{MnS}\} \longrightarrow \{\text{MnO}\} + [\text{S}]$$

$$[\text{O}] + \{\text{CaS}\} \longrightarrow \{\text{CaO}\} + [\text{S}]$$

$$[\text{O}] + \{\text{MgS}\} \longrightarrow \{\text{MnO}\} + [\text{S}]$$

which yields in a complex slag containing these elements

$$\Delta G^{\circ} = \Sigma_i X_i \Delta G^{\circ} \text{ (O–S exchange)}$$

Of these terms those involving iron and calcium can be compared as an example of the exchange under ironmaking conditions. Experimental values for the corresponding equilibria between gas and slag yield values of the sulphide capacities

$$C_{\text{S}} = \{\%\text{S}\}p^{1/2}\text{O}_2/p^{1/2}\text{S}_2$$

show that C_S for FeO-containing slags is somewhat higher than that of CaO-rich slags reflecting the Gibbs exchange energies

$$\mathrm{FeO} + (1/2)\mathrm{S_2(g)} = \mathrm{FeS} + (1/2)\mathrm{O_2(g)}; \quad \Delta G^\circ_{1850} = 91\,500\,\mathrm{kJ\,mol^{-1}}$$
$$\log K = -2.59$$
$$\mathrm{CaO} + (1/2)\mathrm{S_2(g)} = \mathrm{CaS} + (1/2)\mathrm{O_2(g)}; \quad \Delta G^\circ_{1850} = 81\,500\,\mathrm{kJ\,mol^{-1}}$$
$$\log K = -2.30$$

Entering into the magnitude of the sulphide capacities is the fact that the $FeO-SiO_2$ system is Raoultian, while the $CaO-SiO_2$ system shows strong negative departures from Raoult's law. Finally, the activity coefficient of sulphides in solution in slags is inversely related to the oxide activity, and hence in the equilibrium constant for the sulphide forming reaction

$$K = \frac{\gamma\mathrm{MS}\{\mathrm{MS}\}\,p\mathrm{O_2}^{1/2}}{\gamma\mathrm{MO}\{\mathrm{MO}\}\,p\mathrm{S_2}^{1/2}}$$

the activity coefficient ratio sulphide/oxide is very much higher in the case of the calcium ion than for the ferrous ion, to an extent which more than balances the equilibrium constant which appears to favour the calcium ion.

Using the method described above, the sulphide capacity of a multicomponent slag may be calculated with the exchange oxide/sulphide equilibria weighted with the metal cation fractions, thus

$$\log C_S(\mathrm{Fe^{2+}, Mn^{2+}, Ca^{2+}, Mg^{2+}})$$
$$= \Sigma X(\mathrm{Fe^{2+}, Mn^{2+}, Ca^{2+}, Mg^{2+}})$$
$$\log C_S(\mathrm{Fe^{2+}, Mn^{2+}, Ca^{2+}, Mg^{2+}})$$

Similarly the removal of phosphorus from liquid iron in a silicate slag may be represented by the equations

$$2[\mathrm{P}] + 5[\mathrm{O}] + 3\{\mathrm{O^{2-}}\} \longrightarrow 2\{\mathrm{PO_4}\}; \quad \log K = \Sigma_i x_i \log K_i$$

($i = \mathrm{Ca^{2+}}$, $\mathrm{Fe^{2+}}$ etc. which are the cationic species in the slag phase). Fellner and Krohn (1969) have shown that the removal of phosphorus from iron–calcium silicate slags is accurately described by the Flood–Grjotheim equation with

$$\log K(\mathrm{Ca^{2+}}) = 21 \text{ and } \log K(\mathrm{Fe^{2+}}) = 11$$

and concluded that the term in $x(\mathrm{Ca^{2+}}) \log K(\mathrm{Ca^{2+}})$ is the only term of importance in the dephosphorizing of iron.

DropBooks

The thermodynamics of dilute solutions

Many reactions encountered in extractive metallurgy involve dilute solutions of one or a number of impurities in the metal, and sometimes the slag phase. Dilute solutions of less than a few atomic per cent content of the impurity usually conform to Henry's law, according to which the activity coefficient of the solute can be taken as constant. However in the complex solutions which usually occur in these reactions, the interactions of the solutes with one another and with the solvent metal change the values of the solute activity coefficients. There are some approximate procedures to make the interaction coefficients in multicomponent liquids calculable using data drawn from binary data. The simplest form of this procedure is the use of the equation deduced by Darken (1950), as a solution of the ternary Gibbs–Duhem equation for a regular ternary solution, A–B–S, where A–B is the binary solvent

$$\ln \gamma_{S(A+B)} = X_A \ln \gamma_{S(A)} + X_B \ln \gamma_{S(B)} - \Delta G^{xs}_{(A+B)}/RT$$

Here, the solute S is in dilute solution, and the equation can be used across the entire composition range of the A–B binary solvent, when $X_A + X_B$ is close to one. When the concentration of the dilute solute is increased, the more concentrated solution can be calculated from Toop's equation (1965) in the form

$$\ln \gamma_{S(A+B)} = X_B/(1 - X_S) \ln \gamma_{S(B)} + X_A/(1 - X_S) \ln \gamma_{S(A)} - (1 - X_S)^2 \Delta G^{xs}_{(A+B)}/RT$$

This model is appropriate for random mixtures of elements in which the pair-wise bonding energies remain constant. In most solutions it is found that these are dependent on composition, leading to departures from regular solution behaviour, and therefore the above equations must be confined in use to solute concentrations up to about 10 mole per cent.

When there is a large difference between $\gamma_{S(A)}$ and $\gamma_{S(B)}$ in the equation above, there must be significant departures from the assumption of random mixing of the solvent atoms around the solute. In this case the quasi-chemical approach may be used as a next level of approximation. This assumes that the co-ordination shell of the solute atoms is filled following a weighting factor for each of the solute species, such that

$$n_{S-A}/n_{S-B} = X_A/X_B \exp[-(\Delta G_{exchange})/RT]$$

where n_{S-A} and n_{S-B} are the number of S–A contacts and S–B contacts respectively, and the Gibbs energy of the exchange reaction is for

$$B - S + A \longrightarrow A - S + B$$

The equation corresponding to the Darken equation quoted above is then

$$[1/\gamma_{S(A+B)}]^{1/Z} = X_A[(\gamma_{A(A+B)})/(\gamma_{S(A)})]^{1/Z} + X_B[(\gamma_{B(A+B)})/(\gamma_{S(B)})]^{1/Z}$$

In liquid metal solutions Z is normally of the order of 10, and so this equation gives values of $\gamma_{S(A+B)}$ which are close to that predicted by the random solution equation. But if it is assumed that the solute atom, for example oxygen, has a significantly lower co-ordination number of metallic atoms than is found in the bulk of the alloy, then Z in the ratio of the activity coefficients of the solutes in the quasi-chemical equation above must be correspondingly decreased to the appropriate value. For example, Jacobs and Alcock (1972) showed that much of the experimental data for oxygen solutions in binary liquid metal alloys could be accounted for by the assumption that the oxygen atom is four co-ordinated in these solutions.

The most important interactive effect in ironmaking is the raising of the activity coefficient of sulphur in iron by carbon. The result of this is that the partition of sulphur between slag and metal increases significantly as the carbon content of iron increases, thus considerably enhancing the elimination of sulphur from the metal. Other effects, such as the raising of the activity coefficient of carbon in solution in iron by silicon, due to the strong Fe–Si interaction, have less effect on the usefulness of operations at low oxygen potentials such as those at carbon-saturation in the blast furnace. The effect of one solute on the activity coefficient of another is referred to as the 'interaction coefficient', defined by

DropBooks

$$\frac{d \ln \gamma_A}{dX_B} = \varepsilon_B^A; \quad \ln \gamma_A = \ln \gamma_A^\circ + \varepsilon_B^A X_B$$

where $\gamma^\circ A$ is the activity coefficient of component A at infinite dilution in the binary M–A system, M being the solvent. The self-interaction coefficient of solute A, ε_{AA}, represents the change of the activity coefficient of solute A with increasing concentration of the solute A. In industrial practice, the logarithm to the base 10, together with the weight per cent of the components is used rather than the more formal expressions quoted above, and so the interaction coefficient, e, is given by the corresponding equation

$$\log \gamma_A = \log \gamma_A^\circ + e_B^A[\%B] \ldots \text{etc.}$$

Table 14.1 shows some experimental data for the interaction coefficients in iron as solvent.

The linear effect of the addition of the solute B only applies over a limited range of composition, probably up to 10 wt % of the solute B, because this is the limit of the composition range beyond which the solute will begin to show departures from Henry's law.

Table 14.1 *Interaction coefficients of solutes ($\times 10^2$) in liquid iron at 1850 K*

Solute A	Added element B					
	C	O	S	N	Si	Mn
C	22	−10	9	11	10	–
O	−13	−20	−9	5.5	−14	0
S	24	−18	−3	3	6.5	−2.5
Si	24	−25	5.5	9	32	0

Numbers rounded to the nearest 0.5.

The refining of lead and zinc

The metals that are produced either separately or together, as in the lead–zinc blast furnace, contain some valuable impurities. In lead, there is a significant amount of arsenic and antimony, as well as a small but economically important quantity of silver. The non-metals cause the metal to be hard, and therefore the refining stage which removes them is referred to as lead 'softening'. This is achieved by an oxidation process in which PbO is formed to absorb the oxides of arsenic and antimony, or, alternatively, these oxides are recovered in a sodium oxide/chloride slag, thus avoiding the need to oxidize lead unnecessarily. The thermodynamics of the reactions involved in either of these processes can be analysed by the use of data for the following reactions

$$(4/3)\mathrm{As} + 2\mathrm{PbO} = (2/3)\mathrm{As_2O_3} + 2\mathrm{Pb}; \quad \Delta G^\circ = 25\,580 - 82.6T\ \mathrm{J}$$

and

$$(4/3)\mathrm{Sb} + 2\mathrm{PbO} = (2/3)\mathrm{Sb_2O_3} + 2\mathrm{Pb}; \quad \Delta G^\circ = -27\,113 - 41.7T\ \mathrm{J}$$

In the case of the direct oxidation, the oxygen partial pressure must be greater than that at the Pb/PbO equilibrium, while in the process involving sodium-based salts, the oxygen pressure is less than this. The two equilibrium constants for the refining reactions

$$K_{\mathrm{As}} = a^{2/3}\{\mathrm{As_2O_3}\}/a^{4/3}[\mathrm{As}] \text{ and } K_{\mathrm{Sb}} = a^{2/3}\{\mathrm{Sb_2O_3}\}/a^{4/3}[\mathrm{Sb}]$$

(since $a_{\mathrm{Pb}} = a_{\mathrm{PbO}} = 1$) show that the relative success of these alternative processes depends on the activity coefficients of the As and Sb oxides in the slag phase. The lower these, the more non-metal is removed from the metal. There is no quantitative information at the present time, but the fact

that the sodium salts of oxy-acids are usually more stable than those of lead, would suggest that the refining is better carried out with the sodium salts than with PbO as the separate phase.

Another metal which accompanies silver in blast furnace lead is copper, which must also be removed during refining. This is accomplished by stirring elementary sulphur into the liquid, when copper is eliminated as copper sulphide(s). The mechanism of this reaction is difficult to understand on thermodynamic grounds alone, since Cu_2S and PbS have about the same stability. However, a suggestion which has been advanced, based on the fact that the addition of a small amount of silver (0.094 wt %) reduced substantially the amount of lead sulphide which was formed under a sulphur vapour-containing atmosphere, is that silver is adsorbed on the surface of lead, allowing for the preferential sulphidation of copper.

The removal of silver from lead is accomplished by the addition of zinc to the molten lead, and slowly cooling to a temperature just above the melting point of lead (600 K). A crust of zinc containing the silver can be separated from the liquid, and the zinc can be removed from this product by distillation. The residual zinc in the lead can be removed either by distillation of the zinc, or by pumping chlorine through the metal to form a zinc–lead chloride slag.

The separation of zinc and cadmium by distillation

DropBooks

An important element that must be recovered from zinc is cadmium, which is separated by distillation. The alloys of zinc with cadmium are regular solutions with a heat of mixing of $8300\, X_{Cd}X_{Zn}$ J gram-atom^{-1}, and the vapour pressures of the elements close to the boiling point of zinc (1180 K) are

$$p_{Zn} = 0.92 \text{ and } p_{Cd} = 3.90 \text{ atmos}$$

The metals can be separated by simple evaporation until the partial pressure of cadmium equals that of pure zinc, i.e.

$$p^{\circ}_{Cd}\gamma_{Cd}X_{Cd} = p^{\circ}Zn\gamma_{Zn}X_{Zn}$$

and using these data the zinc mole fraction would be 0.89 at 1180 K.

It follows that the separation of cadmium must be carried out in a distillation column, where zinc can be condensed at the lower temperature of each stage, and cadmium is preferentially evaporated. Because of the fact that cadmium–zinc alloys show a positive departure from Raoult's law, the activity coefficient of cadmium increases in dilute solution as the temperature decreases in the upper levels of the still. The separation is thus more complete as the temperature decreases.

A distillation column is composed of two types of stages. Those above the inlet of fresh material terminate in a condenser, and are called the 'rectifying'

stages. Those below the inlet terminate in a boiler and are called the 'stripping' stages. When a still is run in a steady state a material balance at one stage applies to all stages, because there is no net accumulation of material at any one stage. If the stages of the rectifying set are numbered successively from the top of the column downwards, the material balance at the nth stage is given by

$$V_{n+1} = L_n + D$$

where V_{n+1} moles of vapour approach the stage from the $(n+1)$th stage below, L_n moles of liquid reflux towards the boiler and D (distillate) moles of vapour pass to the condenser. If y_A is the fraction of the component A in an A–B vapour mixture, and x_A is the mole fraction in the co-existing liquid,

$$V_{n+1} y_{n+1}^{A} = L_n x_n^{A} + D x_D^{A}$$

where x_D^{A} is the mole fraction of component A in the product of the still, and hence

$$y_{n+1}^{A} = \frac{L_n}{L_n + D} x_n^{A} + \frac{D}{L_n + D} x_D^{A}$$

In this equation, all of the terms except y_{n+1} and x_n but including x_D^{A}, are constant. Hence the relationship between y_{n+1}^{A} and x_n^{A} is linear with a slope of $L_n/(L_n + D)$ and a line representing the relationship on a graph of y vs x must pass through $y_D = x_D$ when $x_n = x_D$, since the vapour and the liquid have the same composition in the product. This is called the rectifying operating line in a graphical representation of the distillation process.

A similar material balance for the stripping stages which are labelled 1 to $m + r$ yields

$$y_m^{A} = \frac{V_m + P}{V_m} x_{m+1}^{A} - \frac{P}{V_m} x_p^{A}$$

where V_m is the flow rate of the vapour from the mth stage and P is the flow rate of product from the bottom of the still. The graphical representation of this function is therefore a line of slope $V_m/(V_m + P)$ which passes through the point $y_p = x_p$, the stripping operating line. Any point on these lines represents a liquid which is in equilibrium with a vapour phase. The composition of the corresponding vapour phase is found by moving horizontally across the y vs x graph at the given value of x to cut the curve at the value of y which represents the corresponding equilibrium vapour composition. The composition of the feed material should ideally be made equal to that at the point of intersection of the stripping and rectifying line at which the feed material is at its boiling point. The number of stages which are required to produce a distillate of a given composition can then be calculated

by constructing intercepts in this fashion, dropping vertically at each calculated vapour composition. The slope of the rectifying stage operating line is called the 'reflux ratio', since it defines the fraction of the liquid which is returned to the stripping stage, the remainder passing on to the rectifying stage. The extent of refluxing is partly determined by the ability of the descending liquid to extract heat from the ascending vapour phase. In liquid metal systems, where the thermal conductivity is high, this extraction of heat is much more efficient than in the corresponding organic systems which are conventionally separated by distillation. The separation of metals by distillation can be expected to operate under the theoretically deduced conditions because of this (Figure 14.1).

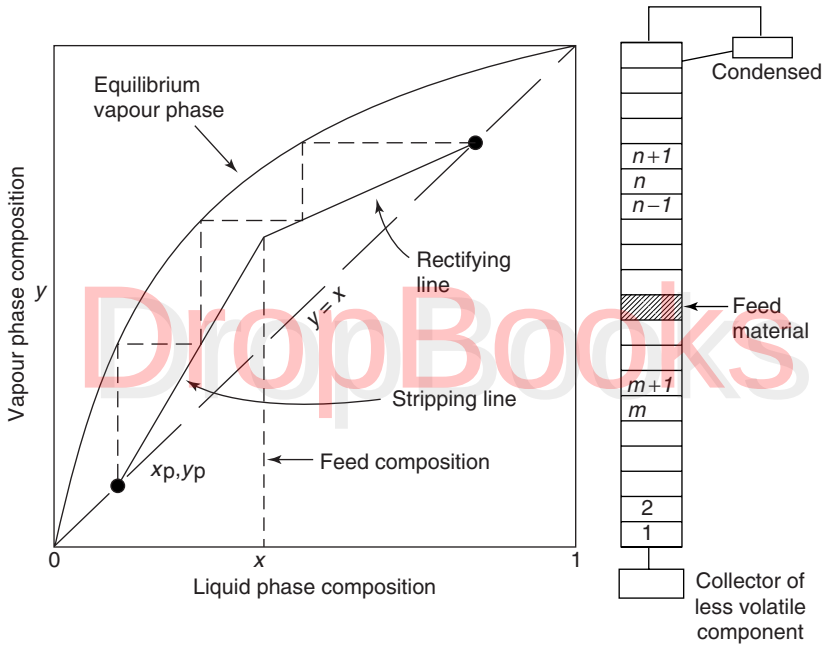


Figure 14.1 *The McCabe–Thiele diagram for the calculation of the number of theoretical stages required to separate two liquids to yield relatively pure products*

The New Jersey refining procedure for zinc refining is carried out in two stages of distillation. In the first stage, at the higher temperature, the zinc and cadmium are volatilized together, leaving a liquid phase which contains the lead impurity together with other minor impurities such as iron. In the second distillation column cadmium is removed at the top of the still and zinc is collected at the bottom at better than 99.99% purity. The activity

coefficient of cadmium in solution in zinc, which is a regular solution, depends on temperature according to

$$\log \gamma_{Cd} = 437.2\ X_{Zn}^2/T$$

the average value of the coefficient being 3.3 as $X_{Zn} \rightarrow 1$ in this temperature range, and thus it is preferable to operate the still at the lowest feasible temperature, as near to the melting point of zinc (693 K) as possible. The vapour pressures of pure cadmium and zinc can be related through the equation

$$Zn(g) + Cd(l) = Zn(l) + Cd(g)$$

$$K = p_{Cd}a_{Zn}/p_{Zn}a_{Cd} \text{ where } \Delta G^\circ = 17\,530 - 3.55\,T \quad \text{J mol}^{-1}$$

It follows that the ratio of these vapour pressures for the pure components changes from 13 at 700 K to 4.5 at 1100 K, again indicating the lowest feasible operating temperature as the preferred distillation temperature. Because the ingoing material contains cadmium at a low concentration (ca. 1 atom per cent), the relative vapour pressures will be $p_{Cd} \simeq 0.03\,p_{Zn}$.

De-oxidation of steels

The removal of carbon in the BOF process leaves the metal with an oxygen content which, if not removed, can lead to mechanical failure in the metal ingot. The removal of the unwanted oxygen can be achieved by the addition of de-oxidizing agents which are metals, such as aluminium, which have a much higher affinity for oxygen than does iron. The product of aluminium de-oxidation is the oxide Al_2O_3, which floats to the surface of the liquid steel as a finely dispersed phase, leaving a very dilute solution of the metal and a residual amount of oxygen. The equilibrium constant for the de-oxidation reaction

$$2[Al] + 3[O] = Al_2O_3$$

where [ ] represents an element in solution in liquid iron, is given by

$$K = \frac{a\mathrm{Al_2O_3}}{X_{[Al]}^2 X_{[O]}^3 \gamma_{[Al]}^2 \gamma_{[O]}^3}$$

and the final oxygen content after de-oxidation is not only determined by the stability of the oxide which is formed, but also by the mutual effects of aluminium and oxygen on their activity coefficients. Experimental data for this process at 1900 K show that the interaction coefficients of these elements

$$e_{Al}^0 = e_0^{Al} = -1300$$

hence there is a strong mutual effect. It was also found that when the aluminium content of iron is above 1 wt %, this relation no longer applies, and the de-oxidation product is hercynite, $FeO{\cdot}Al_2O_3$, and the oxygen content of the metal rises significantly above the values indicated by the iron–alumina equilibrium. There is therefore a practical limit to the extent to which iron may be de-oxidized by this method. Fine particles of alumina are found in the final solid iron product, indicating that not enough time is normally available in industrial practice to allow the alumina particles to float to the surface.

Vacuum refining of steel

An alternative, though more costly, de-oxidation procedure is the vacuum refining of liquid steel. This process takes advantage of the fact that the residual carbon content reacts with the oxygen in solution to form CO bubbles which are removed leaving no solid product in the melt. Other impurities, such as manganese, which has a higher vapour pressure than iron are also removed in this process. The removal kinetics of manganese can be calculated using the vapour pressure of the metal at steelmaking reactions in the free evaporation equation given earlier

$$m_{\mathrm{Mn}} = 44.32\gamma_{\mathrm{Mn}}X_{\mathrm{Mn}}p^{\circ}_{\mathrm{Mn}}(M_{\mathrm{Mn}}/T)^{1/2} \quad \mathrm{g\,cm^{-2}\,s^{-1}}$$

DropBooks

together with the rate of transfer of the metal, which forms a practically Raoultian solution in liquid iron, across the boundary layer

$$J = k\rho_{\mathrm{Fe}}/M_{\mathrm{Fe}}M_{\mathrm{Mn}}(X^{\mathrm{bulk}}_{\mathrm{Mn}} - X^{\mathrm{surface}}_{\mathrm{Mn}})$$

In the steady state, where these two rates are equal, the depletion of the surface, and hence the lowering of the surface concentration, and therefore the free evaporation rate of manganese below the initial value for the alloy, which is given above, is

$$(X_{\mathrm{bulk}}/X_{\mathrm{surface}}) - 1 = \frac{44.32M_{\mathrm{Fe}}}{k\rho_{\mathrm{Fe}}}\frac{\gamma_{\mathrm{Mn}}p^{\circ}_{Mn}}{(M_{\mathrm{Mn}}/T)^{1/2}}$$

For manganese which has a vapour pressure of 4.57×10^{-2} atmos at 1873 K, this depletion amounts to about one half of the bulk concentration, thus lowering the rate of manganese evaporation by half. These equations may be used to derive the condition for the preferential removal of a solute, A, from liquid iron

$$44.32p^{\circ}_{\mathrm{Fe}}(M_{\mathrm{Fe}}/T)^{1/2} \leq k(\rho_{\mathrm{Fe}}/M_{\mathrm{Fe}})M_{\mathrm{A}}(X^{\mathrm{bulk}}_{\mathrm{A}} - X^{\mathrm{surface}}_{\mathrm{A}})$$

Examples of this procedure for dilute solutions of copper, silicon and aluminium shows the widely different behaviour of these elements. The vapour pressures of the pure metals are 1.14×10^{-2}, 8.63×10^{-6} and 1.51×10^{-3} atmos at 1873 K, and the activity coefficients in solution in liquid iron are 8.0, 7×10^{-3} and 3×10^{-2} respectively. There are therefore two elements of relatively high and similar vapour pressures, Cu and Al, and two elements of approximately equal activity coefficients but widely differing vapour pressures, Si and Al. The right-hand side of the depletion equation has the values 1.89, 1.88×10^{-8}, and 1.44×10^{-3} respectively, and we may conclude that there will be depletion of copper only, with insignificant evaporation of silicon and aluminium. The data for the boundary layer were taken as $5 \times 10^{-5}\,\mathrm{cm^2\,s^{-1}}$ for the diffusion coefficient, and 10^{-3} cm for the boundary layer thickness in liquid iron.

The elimination of hydrogen and nitrogen show different kinetic behaviour during the vacuum refining of steel. Hydrogen is evolved according to the solubility and diffusion coefficient of the gas in liquid iron ($D_{\mathrm{H}} = 1.3 \times 10^{-3}\,\mathrm{cm^2\,s^{-1}}$), and has an apparent activation energy of elimination of $35\,\mathrm{kJ\,mol^{-1}}$, whereas the elimination of nitrogen showed an apparent activation energy between 100 and $250\,\mathrm{kJ\,mol^{-1}}$, increasing with increasing oxygen content of the metal. Oxygen is known to adsorb strongly on the surface of liquid iron, and it is concluded that this adsorbed layer reduces the number of surface sites at which recombination of the nitrogen atoms to form N_2 molecules can take place.

The elimination of gaseous solutes from liquid metals by the use of an inert gas purge has also been studied in two model systems. In one, the removal of oxygen from solution in liquid silver was measured, and in the other the shapes of bubbles which are formed when a gas was bubbled through water were observed. Oxygen dissolves in liquid silver to a well-defined extent, and results for the solubility having been obtained using an electrochemical cell. The experimental value deduced for the transfer of oxygen to argon which was bubbled through the liquid was $0.042\,\mathrm{cm\,s^{-1}}$. A water model study was made since water has about the same viscosity as liquid steel, and this property controls the shapes of bubbles in liquids, and it is easy to observe the effects, which are probably similar to those which take place in an opaque liquid such as steel.

The bubbles shapes in gas purging vary from small spherical bubbles, of radius less than one centimetre, to larger spherical-cap bubbles. The mass transfer coefficient to these larger bubbles may be calculated according to the equation

$$k = g^{1/4} D^{1/2} d^{-1/4}\,\mathrm{cm\,s^{-1}}$$

where d is the diameter of a spherical bubbles of equal volume. This follows from the fact that the velocity of rise through the liquid of a spherical-cap

bubble has been shown to be

$$u = 1.02(gd/2)^{1/2}$$

and this may be used, together with the diameter of the bubble, as the characteristic length, in defining the Reynolds number in the mass transfer equation

$$N_{Sh} = 1.28(N_{Re}N_{Sc})^{1/2}$$

which gives a value of the mass transfer coefficient of $4.7 \times 10^{-2}\,cm\,s^{-1}$, in good agreement with the experimental value. It should be noted that this value is also obtained from the diffusion coefficient of oxygen in silver, $5 \times 10^{-5}\,cm^2\,s^{-1}$ together with a boundary layer thickness of 10^{-3} cm.

The evolution of nitrogen from liquid steel is also dependent on the oxygen content, again because of the blocking of the surface sites which are necessary for N_2 molecule formation prior to evolution.

Refining by liquid salts and the Electroslag process

Since the alkali and alkaline metals have such a high affinity for oxygen, sulphur and selenium they are potentially useful for the removal of these non-metallic elements from liquid metals with a lower affinity for these elements. Since the handling of these Group I and II elements is hazardous on the industrial scale, their production by molten salt electrolysis during metal refining is an attractive alternative. Ward and Hoar (1961) obtained almost complete removal of sulphur, selenium and tellurium from liquid copper by the electrolysis of molten $BaCl_2$ between the metal which functioned as the cathode, and a graphite anode.

DropBooks

Another process which improves on the conditions for sulphur removal from steel is to allow the liquid metal to fall as droplets through a $CaO–CaF_2$ slag, in which the low oxygen potential of the blast furnace is reproduced, and a higher CaO activity can be achieved, as high as 0.4, at steel melting temperatures (Duckworth and Hoyle, 1969). Because of this higher CaO activity, it follows that the sulphur-holding properties of these fluoride-based molten phases will result in a much higher sulphide capacity, C_S as measured by the relation

$$C_S = (\%S)(pO_2/pS_2)^{1/2}$$

than the silicate-based slags.

The melt is heated by passing a large electrical current between two electrodes, one of which is the metal rod to be refined, and the other is the liquid metal pool standing in a water-cooled copper hearth, which collects the metal drops as they fall through the molten electrolyte. This pool therefore freezes at the bottom, forming the ingot. Under optimum circumstances the product billet takes the form of a cylindrical solid separated from the molten salt by

a thin lens of molten metal. It has been found that the temperature of the melt must not be allowed to get too high, because this leads to an ingot with unsatisfactory physical properties. To overcome this problem, Al_2O_3 is added to lower the electrical resistance. This addition is made at the cost of reducing the sulphide capacity of the melt by a factor of 10, even though the solubility of CaO in the melt is increased, but this still leaves a satisfactory,sulphur-retaining, slag.

Chapter 15

Factorial analysis of metal-producing reactions

The optimization of reactions involving a large number of variables, and in the case of metal production these might include the temperature, gas, slag and metal compositions, the state of motion of each phase, and the length of the refining period, could be analysed by the classical, so-called Newtonian method in which one variable is altered in a given series of tests while all other variables are held constant, and the results are collected in order to assess the dependence of the productivity on that variable. However, since each test would be expensive of time and labour on the industrial scale, an alternative may be adopted which reduces the number of plant trials required to separate the effects of the variables.

This practical alternative is called *factorial analysis*, and involves trials in which each variable is run at one of two values, or *levels* in the language of statistical analysis, and each trial requires the level of each variable to be set at the high or low level. For example, to test the effects of temperature, and slag–metal composition on the removal of sulphur during the refining of liquid iron containing carbon as in blast-furnace operation, there could be three variables, each at two levels, and the final content of sulphur which is produced from a given initial concentration would be measured. All other variables, such as mixing in the gas phase and stirring of the liquids and the duration of the trial, would be held constant while the chosen variables were tested. In this complex situation the factorial method reduces the number of trials which are required in comparison to the classical procedure, but the tests are truly hybrid in that some other variables would be held constant. The composition-dependent variables, such as viscosities and interfacial tension of the condensed phases are not included. Of course, the analysis could be extended to include the other independent variables, but the calculation would be lengthy, and therefore would require computer programming, which is not difficult in this context.

Labelling the variables as T, S and M, with reference symbols, a, b, c respectively in trials involving a low (l) and high (h) levels of each variable, each trial having the result x_i, the factorial procedure would produce the design code as follows:

DropBooks

Variables	Level	Symbol	Result
T, S, M	l l l l	1	x_1
	h l l l	a	x_2
	l h l l	b	x_3
	h h l l	ab	x_4
	l l h l	c	x_5
	h l h l	ac	x_6
	l h h l	bc	x_7
	h h h l	abc	x_8

The eight trials in this design have included every combination of the variables, with each variable at one of the two levels in each trial, there being four trials with each variable at one of the two levels. Needless to say, the results of the analysis will be improved if each trial is repeated (replicated) but for an initial study this is usually not necessary.

Once the results have been collected they may be analysed to show the effects of each variable separately, T, S, M, the interaction of two variables, $T–S$, $T–M$, $S–M$, and three variable interaction, $T–S–M$. These *interaction* terms measure the effect of the change in one variable on the results for the others, and $T–S–M$, the ternary interaction indicates the dependence of the results for one variable of the simultaneous change of the others.

This is a novel feature of factorial design when compared with the classical laboratory procedure which excludes indications of the interaction of the variable. The method of analysis of the data, due to Yates, which is commonly used to evaluate these effects, requires that the trials are conducted in the sequence shown above, and proceeds as follows.

The table of results is laid out in a column, and a second column is constructed in which in the first four rows the results would be added sequentially in pairs, e. g. $x_1 + x_2$, $x_3 + x_4$, $x_5 + x_6$ etc., and the lower four rows are calculated by subtracting the second value from the preceding value thus, $x_2 - x_1$, $x_4 - x_3$ etc., a third column is prepared from these results by carrying out the same sequence of operations. The process is continued until there are as many columns as the number of variables. Thus in the present three-variable, two level-study the process is repeated three times (Table 15.1), and in the general n-variable, two-level case it is repeated n times. (The general description of trials of this kind where there are n variables and two levels, is '2^n factorial trials').

Each value in the final column of the table constructed above is now divided by 4, which is the number of additions or subtractions made in each column. The results of this division show the numerical effects of each variable and the interaction between variables. The value opposite the second row shows the effect of the temperature, the third shows the effect of the slag phase composition, and, the fifth the effect of the metal composition. The interaction terms then follow the symbols of each row, the fourth showing the effect of

Table 15.1 *Schematic table of a 2^3 factorial study*

Code	Result	Column 1	Column 2	Column 3	Effect
1	x_1	$1 + a$	$1 + a + b + ab$	$1 + a + b + ab + c + ac + bc + abc$	T
a	x_2	$b + ab$	$c + ac + bc + abc$	$a - 1 + ab - b + ac - c + abc - bc$	A
b	x_3	$c + ac$	$a - 1 + ab - b$	$b + ab - 1 - a + bc + abc - c - ac$	B
ab	x_4	$bc + abc$	$ac - c + abc - bc$	$ab - b - a - 1 + abc - bc - ac + c$	AB
c	x_5	$a - 1$	$b + ab - 1 - a$	$c + ac + bc + abc - 1 - a - b - ab$	C
ac	x_6	$ab - b$	$bc + abc - c - ac$	$ac - c + abc - bc - a + 1 - ab + b$	AC
bc	x_7	$ac - c$	$ab - b - a + 1$	$bc + abc - c - ac - b - ab + 1 + a$	BC
abc	x_8	$abc - bc$	$abc - bc - ac + c$	$abc - bc - ac + c - ab + b + a - 1$	ABC

T is the total of all measurements, and so
$A = T - 2\{1 + b + c + bc\}$
$B = T - 2\{1 + a + c + ac\}$
$AB = T - 2\{a + b + bc + ac\}$
$C = T - 2\{1 + a + b + ab\}$
$AC = T - 2\{c + a + ab + bc\}$
$BC = T - 2\{b + c + ac + ab\}$
$ABC = T - 2\{1 + bc + ab + ac\}$

DropBooks

varying the temperature on the effect of the slag composition and so on. The sign of the results in the Effects column shows the way in which a variable should be altered in order to move towards the optimum. A positive sign shows that a variable must be increased in value to reach the optimum, while a negative sign indicates the opposite.

As there now exists a large body of laboratory studies on each of the variable systems, for example the effect of the lime/silica ratio in the slag on the desulphurization of liquid iron, the most appropriate phase compositions can be foreseen to some extent from these laboratory studies when attempting to optimize the complex industrial process. The factorial trials are not therefore a 'shot in the dark', but should be designed to take into account the laboratory information. Any qualitative difference between the results of a factorial trial, and the expectations predicted from physico-chemical analysis might suggest the presence of a variable which is important, but which was not included in the trials.

The effects of the individual variables can be calculated approximately if all of the interaction terms are ignored, or are subsequently shown to be negligible. The ternary interaction *ABC* is rarely of significance and can usually be ignored. In this case the trials represent four measurements of each of the variables at each of the two levels. This is equivalent to the classical laboratory procedure, and each set of four measurements at one level are *replications* of this level for this variable. When the interaction terms are found in the Yates analysis to have a value different from zero, the approximation of variable independence is called into question. The statistical *significance* of these interaction effects can be established by further tests which include, among others, an analysis of the *variance* (ANOVA), which uses the square of the standard deviations of the set of measurements to calculate the variances. The variance of the interaction data can be used together with the variance of the complete set of measurements of all effects to test the possibility that this one set of measurements does or does not belong, statistically, to the complete set.

To test the significance of the *AB* interaction a sub-set of measurements could be made in which four replications, for example, of the cells in the factorial analysis involving *A* and *B* only, *A* l, *A h*, *B* l, *B h*, would be used to give more data for this particular interaction. A simpler and more approximate method than ANOVA involves the use of the $2\sqrt{N}$ test. In this test, a comparison is made between corresponding results in the left-hand columns with the right-hand columns. This yields values of the change in going from one set to the other, and plus is assigned if the result increases from left to right, and minus in the opposite direction The difference between the (total of plus) minus (total of minus) is then compared with $2 \times \sqrt{}$ (sum of plus and minus). If the former is larger, then the interaction is significant.

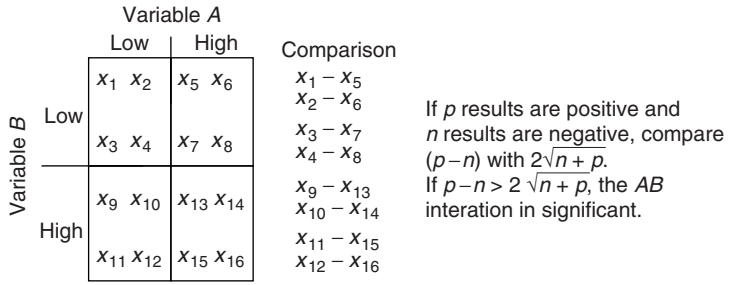


Figure 15.1 *Tableau of the experimental 2^2 analysis for the interaction between the variables A and B by the $2\sqrt{N}$ test*

Bibliography

L.S. Darken. *J. Amer. Chem. Soc.*, **72**, 2909 (1950).
F.R. de Boer, R. Boom, W.C.M. Mattens, A.R. Miedema and A.K. Niessen. *Cohesion in Metals (Transition metal alloys)*. North-Holland, Amsterdam (1988).
P. Fellner and C. Krohn. *Can. Met. Quart.*, **8**, 275 (1969).
H. Flood and K. Grjotheim. *J. Iron and Steel Inst.* **171**, 64 (1952).
L.S. Darken. *J. Amer. Chem. Soc.*, **72**, 2909 (1950).
G.W. Toop. *Trans. Met. Soc. AIME*, **233**, 850 (1965).
K.T. Jacob and C.B. Alcock. *Acta. Met.* **20**, 221 (1972).
W.E. Duckworth and G. Hoyle. *Electroslag Refining*. Chapman and Hall, London (1969).
W.E. Duckworth. *Statistical Techniques in Technological Research*. Methuen, London (1968).

BrownBooks

Index

Activation energy,
  for diffusion in metals, 172–3
  empirical estimates of, 49–50
  in gas-phase reactions, 46
  for pipe and volume diffusion, 198
Activation enthalpy, 47, 49
  for diffusion in metals, 172–4, 291
  of gas-phase transport processes, 112
Activation entropy, 47, 49
Active sites, catalytic, 120, 123
Adiabatic approximation for heat of reaction, 163–4
Adsorption,
  and bonding, 126–8
  of gases on solids, 119–24
  on nuclei, 27–8
  and surface energies of metals, 125–6
Age-hardening, 190
Air/fuel mixing in combustion systems, 58–9
Aliovalent ions, in metal oxides, 160, 228
Alloys, *see also* individual alloys
  age-hardening of, 190
  diffusion in, 177–80
  electrical conductivity of, 149, 150
  electromigration in, 153–4
  ferro-, 335–7
  formation of, from powders, 214–15
  hot corrosion of, 320–1
  in nuclear power reactors, 194–5
  Ostwald ripening of, 209
  oxidation of, 256–60
  phase transformations in, 184–95
  segregation and surface enrichment of, 126, 139–40
  solubility of, in silicate glasses, 310
  thin films of, 8–10
Alumina,
  as catalyst support, 138
  composite of, combustion synthesis of, 216–17
  electron transport in, 159
  gas–solid oxidation rate law for, 252–3
  structure of, 224
  substitution of, in nickel oxide, 228
  vaporization of, 12, 15–16
Aluminium,
  alloys, of copper, 190
  de-oxidation of steels by, 360–1
  extraction of, 348–9
  interfaces in microchips, 220
  reduction of metal oxides by, 341–4
  removal of, from steel, 362
  thermal and electrical conductivity of, 167
  vapour-phase transport of, 89–91
Aluminium arsenide–gallium arsenide alloys, 16–17
Aluminium trimethyl, 76
Aluminosilicates, 307
Aluminothermic process, 341–4
Ammonia, catalytic production of, 136–7
Andrade equations for viscosity of liquid metals, 294–5
Anharmonicity constant for vibrating molecules, 44
Antimony(III) oxide, as impurity in lead, 356–7
Antimony selenides and sulphides, 315–16

Argon arc plasma furnaces, 336–7
Aromatization, catalytic, 136
Arsenic, vaporization of, 11
Arsenic(III) oxide, as impurity in lead, 356–7
Arsenic selenides and selenides, 315–16
Arsine, photochemical dissociation of, 76
Austenite, decomposition of, 184–8

Bainite, 185, 186
Band gaps,
  in metal oxides, 158–9, 161
  in semiconductors, 155–6, 157–8
Barium oxide catalyst, 141, 142–3
Barium titanate, order–disorder transformation in, 236
Basic Oxygen Process (BOF) for steel manufacture, 337–8
Belgian retort process for zinc extraction, 330–1, 332
Beryllium–copper alloys, 257
Beryllium oxide, thermal conductivity of, 168
Bessemer furnaces, 337
Bimolecular reactions, 50, 51
Bismuth oxide, 239–42, 246–7
Blast furnace processes,
  for iron-making, 270–1, 272, 279–81, 333–5, 337–8
  for lead and zinc extraction, 331–2, 334
  for steel manufacture, 337–8
Body-centred cubic close-packed (bccp) structure, 170
Bonding, 64–7
  of adsorbed molecules, 126–8
  of gaseous heteronuclear compounds, 64, 65, 67–8, 69–70
  at ionic crystal surfaces, 232–3
  at solid catalyst surfaces, 122–4, 141
Borides, combustion synthesis of, 216–17
Borosilicate glasses, 311
Boundary layer approximation, 103–4, 105
Boundary layer diffusion at metal–slag interfaces 324–7
Boundary layer mass transfer at liquid metal–gas interface, 338
Brillouin zones, 153
Bromine, in vapour-phase transport, 91
Brownian motion, 128–9, 293–4
Bubble formation,
  in metal extraction processes, 328–9, 335–6, 337
  in water, 363–4
Burgers vector, 34

Cadmium, separation of, 357–60
Calcium,
  extraction of, 348
  reduction by, 346
Calcium chloride, electrolysis of, 348
Calcium fluoride structure, 225
Calcium oxide,
  added to ZrO_2, 228, 239
  and impurity transfer in slag, 351, 352–3
Calder Hall nuclear reactor, 294
Carbides, *see* Metal carbides
Carbon,
  alloys, of iron, 114–18
  combustion of, 273–4
  diamond, 22–3
  erosion of, 272–3
  formation of, by steam reforming, 131, 133
  graphite, 23, 274
  plasma evaporation and pyrolysis of, 23–4
Carbon arc furnace processes, 335–7
Carbon dioxide,
  erosion of carbon by, 272–3
  generation of, in Hall–Heroult process, 348–9
Carbon monoxide, adsorption of, 124–5, 127
Carbon–titanium system, 267–8
  see also Titanium carbide
Carburizing of metals, 85, 262–4, 265
Carnot engines, 60–1
Catalysis, 118–45 *passim*

DropBooks

Catalysts, 122–9
  electron supply by, 19
  industrial, 129–43 *passim*
Catalytic converters, 138–9
Cementite, 184–6, 187
Cements, silica-based, 314–15
Ceramic oxides, 234–6
  in glass-ceramics, 313–14
  hot corrosion of, by molten salts, 319–20
  as superconductors, 217, 236, 247–9
Cerium, alloy, of platinum, 139
Cerium dioxide (ceria), 239–2, 244, 246
Chain reactions,
  in CVD, 42–3, 62–3
  gas-phase combustion, 53–8
  gas-phase formation of hydrogen bromide, 52–3
Chalcogenide glasses, 315–16
Chalcopyrite, oxidation of, 275
Chemical diffusion, 177–80
Chemical potentials in two-component systems, 8–9, 94
Chemical vapour deposition (CVD),
  from a flowing gas, 106–8
  molecular dissociation and chain reactions in, 42–3, 62–3
  with solid oxide electrolytes, 242
Chemically controlled vapour-phase transport, 105
Chlorine, in vapour-phase transport, 91, 93–4
Chromium,
  alloys, of nickel, 255, 256, 258
  composite, of titanium carbide, 268
  extraction of, 342–3
  in steel, 186
Chromium(III) oxide (chromia), reduction of, 342–3
Climb, dislocation, 33, 181
Coal, combustion of, 273–4
Coalescence, of catalyst particles, 128–9
Cobalt catalyst for Fischer–Tropsch process, 135
Cobalt oxide, sulphation roasting of, 276–7
Coble equation for creep, 181
Coherency strain energy, 190, 193
Collision theory of gas-phase reactions, 45–7
Coloured glasses, 310–11
Combustion, *see also* Oxidation
  of coal, 273–4
  gas-phase, 53–9
  self-propagating, 216–19
Cooling, *see* Heat loss
Copper,
  adsorption of hydrogen sulphide by, 123
  alloys,
    of aluminium, 190
    of beryllium, 257
    catalytic activity of, 126
    of nickel, 215, 259–60
  as catalyst for water–gas shift reaction, 130
  decomposition of, 248
  diffusion in elemental semiconductors, 223
  electrical conductivity of, 150
  extraction of, 339–41
  impurity, removal of, 357, 362
  intermetallic compound, with gold, 176
  oxidation of, 253
  refinement of, 360, 363
  sintering of, 206, 207
Copper(I) oxide, formation of, 259–60
Copper sulphides, roasting of, 339–40
Cordierite ceramics, 313
Corrosion, hot,
  of metals, 283–4, 319–21
  of refractories, 329–30
Coupling reactions, of methane, 142–3
Covalent bonding, 65, 66
Creep, in metals, 180–1, 196, 208–9
Critical size, of a nucleus, 25, 27, 299
Crucibles, heat losses in, 344–5
Cryolite, electrolysis of, 348–9

De-oxidation of steels, 360–3
Debye temperature, 164–6, 167–8
Defect complexes, 229

Densification,
of combustion reaction products, 218–19
of metals, 207–9, 214–15
Density, of slags, 323–4
Dental cements, 314–15
Dephosphorization of iron and steel, 351, 353
Deposition, *see* Chemical vapour deposition (CVD); Vapour deposition
Desorption, from nuclei, 28, 119–24
Desulphurization of iron and steel, 328–9, 351, 353, 355, 363–4
factorial analysis of, 365, 368
Diamond, thin films of, 22–3
Dielectric oxides, 236–7
Diesel engines, 58, 61–2
Diffusion, 29–30
in alloys, 177–80, 257–8
coefficient, measurement of, 229–31, 242–3
control of reaction kinetics, 103–5, 251–2, 270–1
in dislocations, 197–9
in elemental semiconductors, 223–4
in gas–solid oxidation, 251–2, 255
of gases, 109, 115
in grain boundaries, 197–9, 204–7 *passim*, 219–20, 234, 251–2, 255
interdiffusion, 115, 219–21
in intermetallic compounds, 176–7
in interstitial solutions and compounds, 181–4
at metal–slag interfaces, 324–7
in metals, 170–6, 181, 199–201, 204–7, 291–4, 295
of molten salts, 318
of oxygen, 160–1, 242–3
in sintering of metal oxides, 233–4
in slags, 323
surface, 15, 199–201, 204–7 *passim*, 211–12
volume, 170–6, 181, 198–9, 204–7 *passim*, 211–12
Dilute solutions, thermodynamics of, 354–5
Dipole moments of heteronuclear gases, 65, 116
Dislocation model of grain boundaries/interfaces, 36–7, 197–9
Dislocations, 33–7, 123–4
on catalyst surfaces, 122–4
and creep in metals, 180–1
diffusion in, 197–9
in substitutional alloys, 188–9
Dispersion interaction between gas molecules, 116
Dissociation of gases, 42–3, 62–4, 72–7
Dissolution of refractories in corroding liquids, 329, 330
Distillation, to separate zinc and cadmium, 357–60
Domains, in ferroelectric oxides, 236
Downes cell, 348
Dulong and Petit's rule for heat capacity, 164

Eddy mass transfer, 326–7
Effusion, molecular, 6, 7
Einstein equation, for diffusional flux, 29–30, 31, 200
Electrical conduction mechanism in superconductors, 247–8
Electrical conductivity, 149
of alloys, 149, 150, 153
of metal oxides, 149, 160–2
of metals, 149, 150, 167, 294–5
of molten salts, 318–19
of solid solutions, 240–2
Electroceramics, 234–6
Electrolysis of molten salts, 347–9
Electrolytes, solid, 158–9, 160–3
Electromigration in alloys, 153–4
Electron bombardment, decomposition by, 72–3, 84–5
Electron diffraction techniques, 120–2
Electron switches, 316
Electronegativity, 64–5
Electrons,
effective mass of, 153, 154
transport of, 149–63
Electroslag process for desulphurization, 363–4

DropBooks

Electrothermal process for zinc extraction, 331
Energy states,
of metals, 42, 43–5, 150–3
of molecules, 43–5
Entropy, and vapour transport, 89–91
Epitaxy,
at substrate-film interfaces, 35
conditions for, 3
of GaAs-AlAs and GaAs films, 17
Equations of state for gases, 112–14
Equipartition of gases, 5
Erosion, of metals and carbon, 271–2
Ethylene, 66, 123, 127
Evaporation, *see* Vaporization
Ewald sphere, 120–1
Explosions, 55
Extraction of metals, 323–49 *passim*
Extrinsic semiconductors, 157

Face-centred cubic close-packed (fccp) structure, 170, 181–2
Factorial analysis, 365–8
Fermi surfaces and energy, 151–2
Ferrite, 184–6
Ferro-alloys, 335–7, 344
Ferroelectric oxides, 236–7
Fick's laws of diffusion,
for diffusion in alloys, 178–9
for flowing gas, 103–4, 108
for internal gas-solid reactions, 251, 257–8, 263–4
for Ostwald ripening, 209–10
for surface diffusion, 29–30, 200,?
Films, three-dimensional, 28
thin, *see* Thin films
Finite-difference technique, 80–1
Fire refining, 360
First-order reactions, 50–2
Fischer–Tropsch process, 134–6, 140, 145
Fission products, in uranium dioxide fuel rods, 249–50
Fixed bed reactors, 143–4, 145
heat transfer in, 279
for reduction of iron, 280–1
for roasting sulphides, 283
Flash photolysis, 72
Flash roasters, 283
Flowing gaseous systems, 102–8, 277–9
Fluidized bed reactors, 144–5, 282
Fluoride ion electrolytes, solid, 244
Fluorite structure, 225
Fluosolid roasters, 283
Foaming slags, 335–6, 337
Fourier equation for heat conduction, 78–81
Free electron theory of metals, 149–50
and heat capacity, 164
and structure, 170
and thermal conductivity, 167
Free radicals, *see* Radicals
Frenkel defects, 33, 226–8
Fuel cells, 244–7, 321–2
Fuels,
air/fuel mixing in combustion systems, 58–9
combustion of, *see* Combustion
nuclear fuel rods, 101–2, 249–50
Fullerenes, 23–4

Gallium arsenide,
combustion sythesis of, 218
films, 16–17, 71
surface morphology of, 124
vapour-phase transport of, 93–4
Gallium arsenide–aluminium arsenide alloys, 16–17
Gallium trimethyl, 70–1
Garnets, magnetic rare-earth, 238–9
Gas-phase reaction kinetics, 42–85
Gas–solid systems,
heat transfer in, 277–9
mass transfer in, 103–5, 338
molecular interactions in, 114–16
multicomponent, 95–9
physical properties of, 108–12
reactions of,
catalysis, 118–45
hot corrosion, 283–4
oxidation, 251–69, 283–4
vapour transport in flowing, 102–8

Gases,
bubbles of, *see* Bubble formation
equations of state for, 112–14
Gaudin–Melloy distribution, 202, 203
Gaussian distribution, 202, 211–12
Germanium,
electronic structure of, 154–6
production of, 304–5, 306
self-diffusion in, 223–4
surface morphology of, 124
Germanium dioxide (germania),
reduction of, 304
Germanium sulphide, 316
Gibbs energy of formation of metal oxides, 285–8
Gibbs–Duhem equation for ternary solutions, 354–5
Glass-ceramics, 313–14
Glasses,
chalcogenide, 315–16
metallic, 297–300
silicate, 309–11
Glazes for porcelain, 312
Gold,
as additive to nickel steam-reforming catalyst, 133
alloys, of nickel, 133, 256
apparent vapour pressure of, 103
intermetallic compound, with copper, 176
volume diffusion in, 174
Grain boundaries, 35–7
diffusion in, 197–9, 204–7 *passim*, 219–20, 234, 251–2, 255
in polycrystalline metals, 195–6, 213–14
sliding of, 181
Grain growth,
by vapour-phase transport, 100–2, 250
in polycrystalline metals, 213–14
in thin films, 30–1
Graphite, 23, 274
Greenwood equations for Ostwald ripening, 209, 210–11
Guinier–Preston zones, 190
Haber process, 137
Haematite, reduction of, 270–1, 272, 280–1
Hafnium diboride, CVD of, 106, 107
Hafnium halides, bond energies of, 68
Hall–Heroult process for aluminium production, 348
Heat capacity,
of gases at constant volume, 110
of liquid metals, 297
of reactants and products, 163–6
Heat losses,
cooling,
of austenite, 186–8
of substrate in photochemical reactions, 82
in crucible reactions, 344–5
Heat transfer, *see* Thermal transport
Heating, of substrates in photochemical reactions, 77–81
n-Heptane, oxidation of, 57
Herring 'scaling' law for sintering, 206
Hexagonal close-packed (hcp) structure, 170
Hot corrosion,
of metals, 283–4, 319–21
of refractories, 329–30
Hot pressing of metals, 207–9
Hybrid bonding, 65, 66–7
Hydrocarbons,
adsorption of, 127–8
bonding in, 66
combustion of, 273–4
ethylene, 66, 123, 127
methane, *see* Methane
oxidation of, 54–8
production of, 134–6, 142
steam reforming of, 129–31, 132–4
Hydrogen,
adsorption of, 123
oxidation of, 54
removal of, from steel, 362
thermal dissociation of, 64
Hydrogen bromide, 52–3, 73
Hydrogen chloride, 73–4

DropBooks

Hydrogen iodide,
formation and dissociation of, 45, 46–7, 49–50, 51, 73–4
heterogeneous catalytic dissociation of, 118–19
Hydrogen sulphide, adsorption of, 123
Hydroxyl groups, at catalyst metal-metal oxide interfaces, 133–4, 141, 142–3

Ideal gases, 112–14
Imperial smelting process, 332
Indium antimonide, 124
Indium–silver alloys, 258
Insulators,
ceramic oxides as, 313
electron transport in, 158–9
gas–solid oxidation rate law for, 252–3
Interaction coefficients of solutes, 354, 355
Interdiffusion,
in gases, 115
in thin films, 219–21
Interfaces, substrate-film, 35–7
Interfacial energy, 25–6, 35–7
Intermediates in gas-phase reactions, 44
Intermetallic compounds, 176–7, 220–1
Interstitial alloys, 154
Interstitial atoms, 31–2, 33
Interstitial ions, 140
Interstitial solutions and compounds, 181–4
Intrinsic semiconductors, 156
Iodine, in vapour-phase transport, 91, 92
Ion cores, diffusion of, 153–4
Ion plating, 20
Ionic solids, 232–3
Iron, *see also* Iron-making processes
alloys, of carbon, 184–8
catalyst for Fischer–Tropsch process, 135
catalyst for the Haber process, 137
ferro- to diamagnetic transformation of, 189–90
refinement of, 351, 352–3, 355
removal of, in slag, 332, 339
surface energy of liquid, 296
Iron-making processes, 272–3, 279–81, 328–9, 333–5, 337
Iron(II) oxide, 229, 237
oxidation of, 254, 340–1
Iron(III) oxide, 237, 238–9, 338
reduction of, 270–1, 279–81
Iron(II) sulphide, oxidation of, 274
Iron sulphides, roasting of, 281–3, 339–40
Irradiation, used to measure diffusion coefficents, 229–31

Jet engines, 58
Johnson–Mehl equation for *T-T-T* curves, 188

Kinetic theory of gases, 4–6, 108–12, 164, 168
Kink sites, 122, 123
Kirkendall effect, 215, 254
Knocking, in automobile engines, 57
Knudsen cells, 6–10 *passim*, 17
for deposition of alloys, 8–10
for deposition of semiconducting systems, 17, 20, 158
Kroger–Vink notation, 225
Kroll process, 345–6
Kuczynski equations for sintering, 206–7

Laminar flow, 58–9, 104–5
thermal transfer in, 277–8
Langmuir adsorption, 119–20
Laplace transform technique, 79–80
Laser techniques,
heating of substrate by, 81
nanoparticle preparation by, 23–4
thin film preparation by, 16–17, 21, 82–3
Lead,
extraction of, 331–2, 334–5
refinement of, 356–7
Lead(II) oxide, 356–7

Lead titanate, 159–60, 236
Lead zirconate, 236–7
Ledge sites, 122, 123
Lennard–Jones potential, 114–16, 199–200
Levich equation for dissolution of refractories, 330
Light,
  energy of, 77
  heating of substrates by, 77–81
  transmission, and thermal conductivity, 166–7
Line defects, *see* Dislocations
Liquid metals, 291–301
  corrosion by, 329–30
  steel, 337–8, 361–3
Liquid silicates, 309
Liquid-phase sintering, 301–4
Lithium, diffusion of, 223
Lithium oxide, 141, 142–3, 228
Lognormal distribution, 202
London theory of molecular interaction, 116

Magnéli shear plane compounds, 226
Magnesium,
  extraction of, 341–2, 347
  reduction by, 345–6
Magnesium chloride, electrolysis of molten, 347
Magnesium oxide (magnesia), 224
  catalyst, 141
  composites, combustion synthesis of, 216–17
  as crack inhibitor, 239–40
  electron transport in, 159
  reduction of, 341–2
  vaporization of, 12
Magnetic oxides, 237–9
Magnetite, 237
Magneto-hydrodynamic power conversion, 301
Magnetoplumbites, 239
Manganese,
  extraction of, 343–4
  removal of from steel, 338, 361–2
Manganese oxides,
  as catalysts, 142
  reduction of, 344
  Schottky defects in non-stoichiometric, 228
  sintering mechanism of, 233–4
Marangoni effect, 329–30
Martempering, 186
Martensite, 185–6
Mass transfer,
  across a flowing gas, 103–5
  across the metal–slag interface, 324–8, 337–8
  to bubbles in vacuum refining, 362–3
Mean free path, 5, 6, 166, 168
Mean square velocity, 5
Metal alkyls,
  bond energies of, 70
  thermal dissociation of, 68–9, 70–1
Metal carbides,
  as catalysts, 140
  combustion synthesis of, 216–17, 219
  diffusion in, 183–4, 263–4
  formation kinetics of, 263–4
  oxidation of, 266–7
  sintering of, 301
  thin films of, 85, 107
Metal carbonates, in fuel cells, 321–2
Metal carbonyls, thermal dissociation of, 71
Metal halides,
  bond energies of, 67–8
  physical properties of molten, 317, 318–19
  vapour-phase transport of, 91, 92, 93
Metal nitrides, thin films of, 84–5
Metal oxides, *see also* individual oxides
  adsorption by, 127–8
  as catalysts, 140–1
  composite, 216–17
  diffusion in, 224–9 *passim*, 229–31
  effect of, on liquid silicates, 309
  electron transport in, 158–63
  in fuel cells and membranes, 244–7
  Gibbs energy of formation of, 285–8
  magnetic, 237–9
  as metal catalyst supports, 129, 133–4

DropBooks

multilayers of, 253–4
non-stoichiometry in, 225–8
in oxygen sensors and pumps, 239–42
powders of, 234–5
reduction of, 335–7
sintering of, 233–5
structures of, 140–1, 224–9 *passim*
sulphation roasting of, 276–7
in superconductors, 217, 236, 247–9
surface properties of, 124–5, 232–3
thermal conductivity of, 167–8
Metal salts, molten, 317–19
Metal silicides, oxidation of, 266–7, 268
Metal–slag interface, 324–8, 334
Metal sulphides,
oxidation of, 274–5
roasting of, 281–3, 331, 339
as semiconductors, 318
Metallic glasses, 297–300
Metallocenes, 71
Metals, *see also* Alloys; Intermetallic compounds; Transition metals; *and under* individual metals
creep in, 180–1, 196
densification of, 207–9
diffusion in, 170–6
dissolution of, in molten halides, 318–19
electron transport in, 149–50
erosion of by oxygen, 271–2
extraction of, 323–49 *passim*
free electron theory of, 149–50
grain boundaries in, 195–6
grain growth in polycrystalline, 213–14
hot corrosion of, 283–4, 319–21
hot pressing of, 207–9
liquid, 291–301
in nuclear power reactors, 194–5
oxidation of, 252–5
powders of, 201–4, 214–15
rare earths, 7
refining of, 88, 91–3, 304–6
sintering of, 204–7
solubility of, in silicate glasses, 310, 311
Sommerfield model of, 152
sputtering of, 17–20
structure of nuclei formed from, 28
structure of, 170
surface energy of, 12–15, 125–6, 196–7
thermal conductivity of, 167–8
thin films of, 6–7, 17–21
Methane,
adsorption of, 127–8
bonding in, 66
coupling of, 142–3
oxidation of, 54–5
radical formation in reactions of, 42, 54
steam reforming of, 129–30, 131, 132–3
thermal dissociation of, 69–70
Microchip (microelectronic) structures, 219–21
Microdomains, in non-stoichiometric compounds, 229
Microwave techniques for molecular decomposition, 73
Miedema model for interaction between two metals, 176, 220–1
Misfit strain energy, 188–9
Molecular interactions, in real gases, 114–16
Molecular structure, quantum theory of, 43–5
Molten salts, 317–22
electrolysis of, 347–9, 363
in fuel cells, 321–2
hot corrosion by, 319–21
Molybdenum,
oxidation of, 266
in solid solution with uranium, 195
Molybdenum disulphide, combustion synthesis of, 216
Molybdenum oxides, 226, 250
Molybdenum–silicon system, 268
Morse equation, for the energy of diatomic molecules, 44, 292–3
Moving bed reactors, for roasting sulphides, 282, 283
Mullite, in porcelain formation, 311–12
Multicomponent gaseous systems, 95–9

n-type semiconductors, 156, 160
Nabarro–Herring volume diffusion model of creep, 181, 208
Nanoparticles, production of, 20–2, 24
Neck growth in sintering, 204–6, 303
Neumann–Kopp equation for heat capacity, 164
New Jersey refining procedure for zinc, 359–60
Newnham hearth process for lead extraction, 331
Nickel,
  added to tungsten carbide for sintering, 301
  alloys,
    of chromium, 255, 256, 258
    of copper, 259–60, 215
    of gold, 133, 256
    oxidation of, 256, 258, 259–60, 284
  as catalyst, 130, 133
  hot corrosion of, 283–4, 320–1
  oxidation of, 254–5
  refining of, 87–8
  in steel, 186, 283–4
Nickel aluminide, 216
Nickel oxide,
  as catalyst, 141
  formation of, 254–5, 258, 259–60, 284
  point defects in, 226–8
Nickel sulphide, 243–4. 284
Nickel–tungsten systems, sintering of, 301, 303–4
Niobium, 93, 266
Niobium carbide, 216
Niobium oxides, 93, 344
Nitriding of metals, 84–5, 137
Nitrogen, removal of, from steel, 362, 363
Nitrogen oxides, 50–1
Non-stoichiometry,
  and chemical potential, 8–9
  of interstitial solutions and compounds, 182
  of 123 superconductors, 248
  and oxygen potential in nuclear fuel rods, 249–50
  in semiconducting metal oxides, 143, 162, 225–8
  and thermal conductivity, 167
Nordheim's rule for conductivity of alloys, 150
Nuclear power reactors,
  fuel rods in, 101–2, 249–50
  liquid metal coolants in, 300–1
  phase transformations in metals and alloys in, 194–5
Nucleation,
  of bubbles, 328–9
  heterogeneous, 25–8, 328–9
  homogeneous, 25
  in metallic glass production, 297–9
  rate of, and phase transformations, 186, 187
  thermodynamics of, 25, 27–8, 298–9
  from the vapour phase, 24–8
Nuclei, formation of, from thin films, 28–30
Nusselt number, 278–9

Octahedral site preference energy (OSPE), 237–8
123 compounds, 247–8
Optical fibres, 315
Orbitals, electronic, 66–7
Order of chemical reactions, 50–2
Order–disorder transformations, 189–90, 236, 238
Organometallic compounds, vapour deposition from, 68–71
Orientation effect,
  for dipoles, 116
  on surfaces, 125, 126
Ostwald ripening, 128, 209–13
Otto engines, 58, 59–60, 61
Oxidation,
  of alloys, 256–60
  of carbon in ironmaking, 272–3
  gas–solid, 251–3, 260–2
  of hydrocarbons, 54–8
  of hydrogen, 54
  of metal carbides and silicides, 264–8
  of metal sulphides, 274–5, 281–3, 331

DropBooks

of metals, 253–5, 271–2, 264–6
of silicon, 255–6
of silicon carbide and nitride, 268–9
Oxygen,
blowing, in metal refining, 337–41
diffusion of, 242–3
measurement of, 231
in non-stoichiometric oxides, 161–2, 228–9
in solid electrolytes, 160–1, 245–6
effect of, in elemental semiconductors, 223–4
membranes, 247
pumps, 242, 245
removal of (de-oxidation), 360–1, 362, 363
Oxygen-deficient compounds, 140–1

p-type semiconductors, 156, 160, 161–2
Packed bed reactors, *see* Fixed bed reactors
Palladium catalysts, 129,138, 139
Parabolic rate law for oxidation, 251–2, 260–2
Partial pressure, in vapour-phase transport processes, 87–9, 94
Particle size distribution, of metal powders, 202–4
Partition functions, 48–9, 91
Pearlite, 185, 186
Pentlandite, oxidation of, 275
Perovskite structure, 224–5
Perovskites, 236
as ceramic superconductors, 236, 247–9
$La_{1-x}Sr_xMO_{3-z}$, 242, 245–7
Phase transformations in alloys, 184–95
Phonons, and thermal conductivity, 166–8
Phosphorus, iron-slag transfer of, 351, 353
Photochemical gas-phase decomposition, 72, 73–7
plasma techniques for, *see* Plasma techniques
Photolysis, by laser techniques, 82, 83
Pidgeon process for magnesium production, 341–2
Pig iron, 333
Pipe diffusion, 197–9
Plasma techniques,
argon- and carbon-arc furnaces, 336–7
for forming fullerenes, 23
for metal sputtering, 17–20
for molecular decomposition, 73, 84–5
Platinum,
adsorption by, 123
alloy, of cerium, 139
catalysts, 129, 138, 139
surface morphology of, 124
Point defects, 31–3
Kroger–Vink notation for, 225
in metal oxide catalysts, 140–1, 225–9
Pollution control, by catalytic converters, 138–9
Porcelains, 311–12
Pore size distribution, and Ostwald ripening, 212–13
Portland cement, 314
Positive holes, 140, 155–8, 161–2
Powders,
ceramic oxide, 234–5
metal, 201–4, 214–15
Prandtl number, 278
Promoters of catalysis, 141
Pyrex glass, 311
Pyrite, oxidation of, 282
Pyroceram, 313
Pyrolusite, reduction of, 344
Pyrolysis,
by laser techniques, 83
of carbon and organic molecules, 23–4
of organometallic compounds, 69
Pyroxene, 313–14
Pyrrhotite, roasting of, 282–3
PZT materials, 159–60, 236–7

Quantum efficiency, 74–5
Quantum theory of molecular structure, 43–5

Radicals,
in gas-phase reactions, 42, 54–5, 56
from pyrolysis of organometallic compounds, 68
Radioactive isotopes, used to measure diffusion coefficents, 229–31
Ranz–Marshall equation for Nusselt number, 278–9
Rare earths,
in magnetic garnets, 238–9
thin films of, 7
Reaction kinetics, theories of, 42–85
Reactors,
for catalytic processes, 143–5
nuclear power, 194–5, 300–1
Real gases, 112–16
Rectifying distillation, 357–8, 359
Reduction,
of iron ore, *see* Iron-making processes
of metal oxides, 270–1, 279–81, 304, 335–7, 341–3
of roasted galena, 331–2
of silica, 304, 336
Refining of metals, 88, 91–3, 351–64
Refractories,
combustion synthesis of, 216–17
electron transport in, 159
hot corrosion of, 329–30
liquid-phase sintering of, 301–4
metals, 7, 214, 349
Retort process, Belgian, 330–1, 332
Reynolds number, 58–9, 105, 277–8, 325, 326
Rhodium,
adsorption by, 127
catalysts, 129, 138–9
Richardson–Coulson equation for convection loss, 82
Roasting processes, 276–7, 281–3, 331
Rosin–Rammler distribution, 202, 203
Rotational energy of molecules, 43–4
Rowe–Claxton equation for heat transfer, 279
Ruddlesden–Popper compounds, 247

Sackur–Tetrode equation for entropy and partition function, 91
Schmidt number, 105, 325, 326
Schottky–Wagner sites (Schottky defects), 33, 226–8
Screen analysis of particle size distribution, 203–4
Second-order reactions, 50, 51
Sectioning technique for measuring self-diffusion coefficients, 175
Segregation ratio, for binary alloys, 126, 139–40
Selectivity of catalytic activity, 126
Self-diffusion coefficient, 170–3, 174–6, 223
Semenov equation for activation energy, 50
Semiconductors,
crystalline, 304–6
diffusion in, 223–4
electrical conductivity of, 149
electron transport in, 154–8
metal oxides, 143, 160, 162, 225–8, 236
as oxidation promoters, 143
thin films of, 16–24, 68, 69–71
Sensitizers, photochemical, 76
Shaft furnace processes, 332, 334
Shear, crystallographic, 226
Sheet glass, 311
Sherwood number, 105, 325–6
Shewmon model for chemical potential of surface atoms, 200
Shrinkage, in sintering, 207, 233–4
Silane, dissociation of, 70, 76, 84
Silica, 159, 304, 307, 336
Silicates, 309–15
Silicides,
combustion synthesis of, 216, 219
CVD of, 107
oxidation of, 8, 266–7
Silicon, 154–6
interfaces of, 220
oxidation of, 255–6
production of, 304, 336
reduction by, 341–2
removal of, from steel, 338, 362
self-diffusion in, 223–4
surface morphology of, 124

DropBooks

Silicon carbide, 10, 94, 268–9
Silicon nitride, 76–7, 269, 301
Silver,
  alloys, oxidation of, 258
  diffusion in, 198
  removal of from lead, 357
  removal of oxygen from liquid, 362
  sintering of, 206–7
  thermal and electrical conductivity of, 167
  thin films of, 6–7
Silver iodide, 243
Silver sulphide, 318
Sintering,
  by solid-state diffusion, 204–7, 233–4, 303
  by vapour-phase transport, 99–100, 204
  and densification, 207–8, 214–15
  of metal oxides, 233–5
  of metals, 204–7
  of refractory materials, 301–4
Sintering maps, 207
Skapski equation for surface energy of liquid metals, 295–6
Slags, 323–4
  in carbon arc furnace processes, 335–7
  in chromium extraction process, 343
  in copper extraction process, 339, 341
  corrosion by, 329–30
  in Electroslag process, 363–4
  and impurity transfer, 351–4
  in lead and zinc extraction, 332
  mass transfer to, 324–8
  viscosity of, 335
Sodium, extraction of, 347–8
Sodium chloride, 99–100, 347–8
Sodium sulphate, hot corrosion by, 320–1
Solid electrolytes, 158–9, 160–3
  as fuel cells and membranes, 244–7
  as oxygen sensors and pumps, 239–44
Solid solutions,
  of interstitial compounds, 182
  of metal oxides, 239–44
  of metallic alloys, 154
  of semiconductors, 158
  thermal conductivity of, 167
  uranium–molybdenum, 195
Solutes, interactions of, 354–5
Solution-diffusion, in sintering, 303
Solutions, dilute, 354–5
Sommerfield model of metals, 152
Spinel structure, 225
Spinels,
  in glass-ceramics, 313–14
  magnetic, 237–8, 239
  $NiCr_2O_4$, 256, 258
Spinodal decomposition, 190–1
Sputtering of metals, 17–20
Steam reforming of hydrocarbons, 129–31, 132–4
Steatite, 313
Steel,
  hot corrosion of, 283–4
  manufacture of,
    phase transformations during, 184–8
    in pneumatic vessels, 337–8
  refinement of, 351, 352–3, 360–3
Stefan–Boltzmann law for radiation loss, 82
Stokes–Einstein equation for diffusion of atoms in liquids, 294
Stripping distillation, 358
Strontium oxide (strontia), 246–7
Substrates,
  heating of, 77–81
  physical properties of, 83
Sulphation roasting, 276–7
Sulphides,
  oxidation of, 274–5, 281–3, 331
  roasting of, 281–3, 331, 339–41
Sulphur,
  partition of, *see* Desulphurization of iron and steel
  vaporization of, 11, 17
Sulphur dioxide, hot corrosion by, 284
Sulphur hexafluoride, 66–7
Sulphur sensors, 243
Sulphur trioxide, 119, 320
Superconductors, 217, 236, 247–9

Superexchange, in magnetic oxides, 237, 238
Supported catalysts, 128–9, 133–4, 138
Surface diffusion, 15
  in catalysts, 128
  in sintering, 204–7, 303
Surface energy,
  of alloys, 126, 139–40
  of ionic solids, 232–3
  of metals, 12–15, 125–6, 196–7, 295–6
  of nuclei, 25, 27
Surface enrichment of alloys, 126, 139–40
Surface morphology
  of catalysts, 122–5
  of metals, and temperature on, 199
  due to grain boundaries, 195–6, 197
  of nuclei, 27–8
  and surface energy, 125–6
  techniques for studying, 120–2
  and vaporization, 12–15
Swalin equation for diffusion of liquid metals, 291–4
Synthesis gas,
  production of, 134–5
  syntheses from, 142

Tantalum, 93, 349
Tantalum silicides, vaporization of, 97–9
Temperature,
  choice of for CVD, 107
  Debye, 165–6
  effect of,
    on diffusion, 30, 171–3, 174
    on gas-phase reactions, 45–6
    on gas transport properties, 112
    on nucleation of metallic glasses, 297–300
Ternary gaseous systems, 95–7, 97–9
Terrace surfaces, 122, 123–4
Thermal conductivity, 164, 166–8
  of gases, 110, 115
  of metal oxides, 167–8
  of metals, 167–8, 296–7
Thermal decomposition, to produce thin films, 106–8
Thermal deposition, *see* Chemical vapour deposition (CVD); Vapour deposition
Thermal diffusion, 102, 103
Thermal spikes, in metal sputtering, 18–19
Thermal transport,
  in condensed phases, 163–4
  in gas–solid reactions, 277–9
  in the vapour phase, 89–91, 102–3
Thin films,
  formation of, 24–37
    by gas-phase dissociation, 43
    by laser techniques, 16–17, 21, 82–3
    by metal sputtering, 17–20
    from nuclei, 28–30
    by vapour deposition, 3–16, 106–8
  interdiffusion and interaction in, 219–21
  orientation effects on, 126
  thickness of, 107–8
Third-order reactions, 50, 51
Thorium oxide (thoria), 12, 159, 239–2
Time dependence of reactions, 52–3
  T–T–N curves for nucleation of metallic glasses, 297–8, 300
  T–T–T diagrams for iron-carbon system, 187–8
Titanium, oxidation of, 254
Titanium carbide,
  composite of, with chromium, 268
  diffusion in, 183–4
  preparation of thin films of, 10, 107, 219
Titanium–carbon system, oxidation of, 267–8
Titanium diboride,
  CVD of, 106, 107
  composite of, with MgO, 216–17
Titanium halides, 68
Titanium oxides, 254, 226, 313
Titanium silicide, , 219
Titanium–silicon system, 268

DropBooks

Transition metals,
carburizing of, 262–4
as industrial catalysts, 129–143 *passim*
interstitial atoms in, 182
Transition state theory, 42, 47–9, 183
Translational energy of molecules, 43
Transport number, 160
Trimolecular reactions, 50, 51
Tungsten, 186, 266, 271–2
Tungsten carbide, sintering of, 301
Tungsten–nickel system, sintering of, 303–4
Tungsten oxides, structure of, 226
Turbulent flow, 58–9, 277–9

Unimolecular reactions, 50–2
Uranium, 194–5, 346
Uranium dioxide,
diffusion in, 228–9, 249–50
grain growth of, 101–2, 250
redistribution of fission products in, 249–50
thermal conductivity of, 167
Uranium tetrahalides, reduction of, 346

Vacant sites, 31–2, 33
energy of formation of, 173–4
in metal oxides, 225
migration of, 173–5, 176, 181, 208–9
Vacuum refining of liquid steel, 361–3
van Arkel refining of metals, 91–2
van der Waals equation for real gases, 112–14
Vanadates, hot corrosion by, 319–20, 321
Vanadium, 174, 186
Vaporization,
evaporation coefficients, 11–16
rate of, 7, 8–10
thermodynamics of, 4
Vapour deposition,
from organometallic compounds, 68–71
for thin film preparation, 3–16, 42–3, 62–3
Vapour pressure,
effect of thermal diffusion on, 103
of the elements, 4, 38–41
of two-component systems, 8
Vapour-phase transport, 86–116
grain growth by, 100–2, 250
of uranium dioxide in nuclear fuel rods, 250
Vibrational energy of molecules, 44
Viscosity,
of gases, 110, 115
of liquid metals, 294–5
of liquid silicates, 309
of molten metal halides, 317
of slags, 323–4, 335
Volume diffusion, 170–6, 181, 198–9
in Ostwald ripening, 211, 212
in oxidation, 251–2, 255
in sintering of metals, 204–7 *passim*
Vycor glass, 311

Wagner equations for growth kinetics, 211, 212
Water-cooled nuclear reactors, 194
Water-gas shift reaction, 129–30, 131–2
Work-hardening of metals, 181
Wulff's theorem, 15

Yttrium,
effect of, on nickel oxidation, 255
in ceramic superconductors 217
Yttrium iron garnet, 238–9

Zero point energy, 44
Zeroth-order reactions, 118–19
Zinc,
extraction of, 330–1, 332, 334–5
refinement and separation of, 357–60
vaporization of, 21
Zinc oxide,
fuming of, 332
nanoparticles of, 21
point defects in, 225, 226–8
Zinc sulphide, preparation of thin films of, 16
Zircalloy, 194

Zirconium,
extraction of, 345–6, 349
oxidation of, 265–6
in PZT materials, 159–60, 236
refining and purification of, 92–3
vapour-phase transport of, 87–8, 89–91
Zirconium diboride, CVD of, 107
Zirconium dioxide (zirconia),
electron transport in, 159
formation of, 265–6
in fuel cells, 244
in oxygen sensors, pumps and membranes, 239–43, 247
vacancy formation in, 228
vaporization of, 12, 16
Zirconium tetrachloride, reduction of, 345–6
Zirconium titanate, 159–60
Zone refining, 304–6

DropBooks